# Generation of sand bars under surface waves

by

Matthew James Hancock

B.Math., University of Waterloo (1998)
M.Math., University of Waterloo (1999)

Submitted to the Department of Civil and Environmental Engineering
in partial fulfillment of the requirements for the degree of

Doctor of Philosophy in Environmental Fluid Mechanics

at the

MASSACHUSETTS INSTITUTE OF TECHNOLOGY

February 2005



Author .....
Department of Civil and Environmental Engineering
November 19, 2004

Certified by .....
Chiang C. Mei
Ford Professor of Civil and Environmental Engineering
Thesis Supervisor

Accepted by .....
Andrew Whittle
Chairman, Departmental Committee on Graduate Studies

**Generation of sand bars under surface waves**

by

Matthew James Hancock

Submitted to the Department of Civil and Environmental Engineering
on November 19, 2004, in partial fulfillment of the
requirements for the degree of
Doctor of Philosophy in Environmental Fluid Mechanics

## Abstract

A quantitative theory is described for the evolution of sand bars under monochromatic surface water waves. By assuming the slopes of the waves and seabed are comparably gentle, an approximate evolution equation is found for the seabed elevation. The boundary layer structure is calculated by assuming a depth-linear or depth-independent time-invariant eddy viscosity. An empirical formula by Sleath (1978) is used to predict the bedload transport. A convective diffusion equation governs the suspended sediment transport (which includes the effects of wave-advection), and empirical formulae by Lee *et al.* (2004) and Wikramanayake & Madsen (1994) specify the time-varying concentration at the seabed. Effects of mean beach slope and narrow banded waves are also considered.

The sand bar elevation is found to evolve according to a forced-diffusion equation, where the diffusivity is the gravitational effect on bedload transport on a slope and the forcing is due to both bedload and suspended load transport mechanisms. The time scale of sand bar evolution is over four orders of magnitude longer than the wave period: days in the lab and weeks in the field. In addition to the effects of bedload considered before by Yu & Mei (2000), it is found that suspended load provides a new forcing mechanism affecting sand bar geometry when the seabed is composed of fine sediments.

When wave reflection is significant, bars and waves interact through the Bragg scattering mechanism. Under strong reflection, large regions exist where there is no change to the seabed. For weaker reflection, an inviscid return flow is present that places an additional stress on the bed. As shown by Yu & Mei (2000), any finite beach reflection is sufficient to generate and maintain sand bars.

Experiments were performed in a large wave flume to validate the theory and to study additional aspects of sand bar evolution. The wave envelope and bar profile were recorded for low and high beach reflection, monochromatic and polychromatic waves, and several sediment grain sizes. In particular, sediment sorting was demonstrated under standing waves when the seabed consisted of initially well mixed sand of two grain sizes.

Thesis Supervisor: Chiang C. Mei
Title: Ford Professor of Civil and Environmental Engineering

## Acknowledgments

I would first like to thank my advisor and mentor, Prof. Chiang Mei, for his guidance, wisdom and most of all, time. The hours we spent discussing and debating have finally produced meaningful results. I would like to thank Prof. Ole Madsen for numerous discussions regarding the theory and the experiments, and also for all his lighthearted encouragement. Thanks to Prof. Ain Sonin for being on my committee and for providing useful suggestions. Thanks to Blake Landry for the many hours we shared working on the experiments, and the wave-maker.

I thank Vladimir Barzov, supported through an MIT UROP grant, for his help with the experiments and data processing. I also thank Yile Li for his assistance during the sorting experiment, and Felice Frankel for helping to capture some high-resolution photographs of the resulting colored seabed. I am grateful to Steve Elgar, Britt Raubenheimer, Tom O'Donoghue, J. A. Battjes and R. G. Dean for providing additional field and laboratory data. I want to thank my parents for helping to proofread this thesis, despite the equations being in a "foreign language".

On a personal level, I wish to thank my parents for being there, always. I also wish to convey warm appreciation to my friends, near and far, for bringing laughter and balance to my graduate school years in Boston.

I gratefully acknowledge the funding of the present research by the Office of Naval Research (Grants N00014-89-J-3128 and N00014-04-1-0077 directed by Dr. Thomas Swean) and the US National Science Foundation (Grant CTS 0075713 directed by Dr. M. Plesniak, Dr. Roger Arndt, and Dr. John Foss).

# Contents

# List of Figures

# List of Tables

# Chapter 1

# Introduction

Sand bars and ripples are two features commonly observed on sandy beaches. Sand ripples are typically a few centimeters high and a few tens of centimeters long. Sand bars, typically numbering from a few to a few tens on a given beach, have much larger length and height and are spaced between several meters in bays to several hundred meters on a coastline (Dolan & Dean (1985) [15], Yu & Mei (2000) [70], Elgar (2003) [17] and references therein). Beaches on which sand bars appear generally have slopes less than 5%. Sand bar formation and evolution is a key component in the evolution of shoreline morphology. A better understanding of sand bar evolution may facilitate the prediction of changes to beach morphology and coastal wave climate caused by storms or the construction of nearshore structures. While it is unlikely that natural sand bars protect the shore (Yu & Mei [69]), alternative methods of beach renourishment using sand bar theory have been proposed (Boczar-Karakiewicz *et al.* (1997) [7]).

A host of sand bar generation mechanisms have been proposed, including vortex action by plunging breakers, steady currents induced by breaking waves, edge waves, harmonic decomposition of shoaling waves, the combined effect of waves and undertow, and partially-standing waves (O'Hare & Davies (1993) [52], Yu & Mei [70] and references therein). In this thesis, we focus on the generation and evolution of longshore bars outside the surf zone by non-breaking weakly nonlinear surface waves, in intermediate depths. These types of bars are generated by non-uniformities in the near-bed mass transport caused by partially-standing waves and long setup/setdown waves.

For waves propagating in shallow water, higher harmonics are produced which interact

over a larger length scale called a repetition length or recurrence length (Mei & Ünlüata [44]). The resulting non-uniformities in mass transport velocity generate sand bars whose lengths are close to the recurrence distance. This sand bar generation mechanism has been observed in the laboratory (Boczar-Karakiewicz *et al.* (1981) [6]) and in the field [3], [5], [4]. Field data suggest the spacing and crest position of these bars evolve over weeks or months. Based on the harmonic interaction mechanism, Boczar-Karakiewicz *et al.* (1987) [2] and Restrepo & Bona (1995) [53] have constructed two- and three-dimensional models, respectively, to predict the formation of sand bars in shallow water on very gently sloping beaches. Their models are generally successful at predicting bar crest locations, but not bar amplitudes or bar shapes. The models of Boczar-Karakiewicz *et al.* and of Restrepo & Bona neglect wave reflection from the shoreline and assume sediment is transported only in suspension, not via bed load. These assumptions seem to oversimplify the real situation.

Non-uniformities in the second-order current under partially-standing waves can also generate sandbars. Ocean waves incident on a shoreline, seawall, or steep slope are reflected, creating standing waves. Associated with these standing waves is a second-order mass transport current in the thin viscous boundary layer above the seabed. Theoretically, for sufficient reflection, this mass transport current reverses over a wavelength, moving sediment on the seabed toward nodes and away from antinodes of the surface wave envelope (Carter, Liu & Mei (1972) [9]). In reality, however, even when the reflection is weak, spatial variations in the mass transport velocity still exist and are sufficient to produce sand bars (O'Hare & Davies [52]).

Once bars begin to form, they can interact resonantly with the partially-standing surface waves. By placing fixed bars in a long wave flume, Heathershaw (1982) [23] has demonstrated that waves propagating over many gently sloping bars spaced at half the incident wavelength are strongly reflected via constructive interference. The linear effects of this mechanism of Bragg resonance have been studied theoretically by many authors for rigid bars (e.g. Davies (1982) [10], Mei (1985) [42], Naciri & Mei (1988) [46]). Nonlinear effects of rigid bars on waves have also been studied (Mei (1985) [42], Hara & Mei (1987) [22]). When the bars are composed of sand, the evolution of the wave-field is coupled to that of the sand bar morphology.

Several experimental studies of bar formation under standing waves have been carried out. Herbich *et al.* (1965) [24] performed experiments in a long wave flume with a seawall

inclined at different angles. Half-wavelength sand bars with ripples superposed on each were noted to form. However, a detailed account of sand bar crest locations was not given. Additional observations were made of partially-standing waves over a monolayer of sand by Carter *et al.* (1972) [9] and over a thick sandy bed by De Best, Bijker & Wichers (1971) [12], Xie (1981) [67], O'Hare & Davies (1993) [52] and Seaman & O'Donoghue (1996). De Best *et al.* (1971) [12] were the first to observe that for coarse sand (mean diameter 0.22 mm), bar crests tended to form near wave envelope nodes, while for fine sand (mean diameter 0.13 mm), crests formed near wave antinodes. Xie [67] and O'Hare & Davies [52] later repeated this finding. De Best *et al.* [12] also demonstrated sediment sorting, by generating standing waves over a seabed initially consisting of a well mixed sand of two grain sizes. The finer sand was transported toward the antinodes as suspended load, and the coarser sand toward the nodes as bed load. Furthermore, O'Hare & Davies observed that the relative position of bar crests and envelope nodes affected the degree to which wave reflection was enhanced over the bar patch. As indicated above, these authors were able to generate sand bars even when seaward reflection was weak.

Jan & Lin (1998) [28] studied the formation of sandbars and ripples under oblique standing waves in front of a seawall. Using coarse sand (mean diameter 0.27 mm), they noted that sand bar crests formed near wave nodes. A striking feature of these experiments was the drastic change in ripple geometry over a sandbar: ripple crests in sand bar troughs were perpendicular to the seawall, while ripple crests on sand bar crests were parallel to the wall. Furthermore, ripple length varied noticeably over each sand bar.

Dulou *et. al.* (2000) [16] studied sand bar formation under partially-standing waves on a gently sloping bed in a small wave tank. The distance between successive wave envelope nodes increased with depth, as did the sand bar length. In one experimental run, bars and ripples only formed over the shallower part of the bed, since the near-bed oscillation velocity in the deeper region was insufficient to create bars or ripples. In another run, an extra free harmonic present in the wave field modulated the wave envelope so that sand bars were spaced at lengths much larger than the half-wavelength of the short wave. Dulou *et. al.* also observed that ripples initially formed under wave envelope nodes, where near-bed fluid oscillations were the largest.

The coupled evolution of partially-standing surface waves and sandbars was first studied theoretically by O'Hare & Davies (1993) [52] using a numerical technique of Devillard *et.*

*al.* (1988) [13]. The wave field was computed numerically by discretizing the bed into small horizontal steps. Two types of sediment transport were considered: vortex load (for coarse grains) and suspended load (for fine grains), which account for the flux of sediment into the flow by vortex shedding off ripple crests.

Recently, Yu & Mei (2000) [70] derived a coupled set of evolution equations for the sand bar height and wave envelope, by assuming the slopes of waves and sand bars were gentle and sediment transport was dominated by bed load. Bars and waves evolve on a slow time scale (on the order of a day), and interact through the Bragg scattering mechanism described above. An important conclusion of this study is that the evolution of sand bars under partially-standing surface waves is a process of forced diffusion, in contrast to the instability mechanism involved in ripple generation. The forcing is caused by non-uniformity in the wave envelope, and hence the bottom shear stress and bedload transport. The diffusivity is due to modifications in local bed stress caused by gravitational forces on sediment grains on a sloping bed. Due to the nonlinearity of the sediment dynamics, both the mean flow (Eulerian streaming) and second time harmonic contribute to the forcing. This suggests that sand bars can be generated for any finite seaward reflection, which agrees with the experiments of O'Hare & Davies [52]. However, Yu & Mei [70] have shown that if shoreline reflection is not present, bars cannot be generated and any residual bars present initially are eventually washed out. Therefore, under the conditions of the study, finite reflection from the shore is both necessary and sufficient to generate and maintain sand bars. Yu & Mei also explained the experimental observation of O'Hare & Davies [52] that the relative position of bar crests and envelope nodes affects the wave response over the bar patch. In her thesis, Yu (1999) [68] considered the effects of narrow banded incident and reflected surface wave spectra, although she did not include the induced slowly oscillating inviscid current, which is important for low reflection. The scour in front of a seawall was also estimated and compared with the experiments of Herbich *et. al.* [24]. The model of Yu & Mei [70] is limited to two spatial dimensions (one horizontal and one vertical) and assumes a constant mean intermediate depth ($KH = O(1)$, where $K$ is the characteristic surface wavenumber and $H$ is the mean depth). Furthermore, since suspended sediment transport is neglected, the model is applicable only to seabeds composed of coarse sediment.

Prior to this study, experimental sand bar data consisted of either field data which lacked measurements of the waves that generated the bars, or laboratory data from small

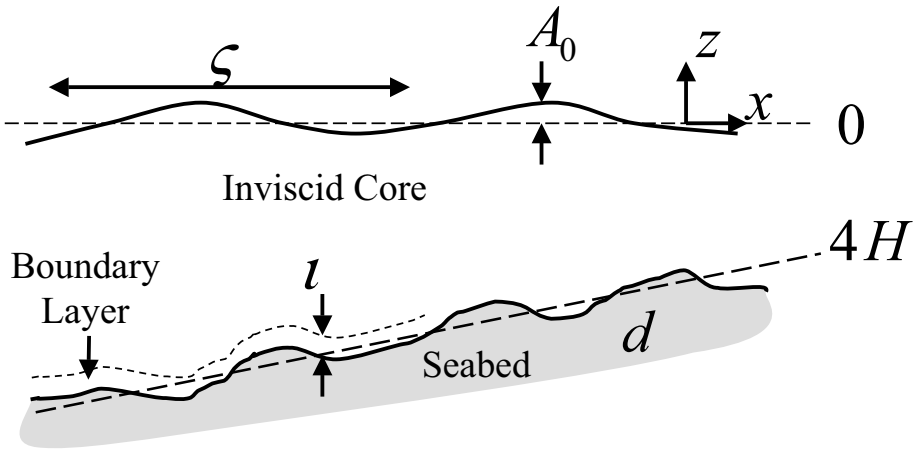


Figure 1-1: Definitional sketch of the surface ocean wave and seabed co-evolution.

flumes in which the waves were steep and the flow barely turbulent. In collaboration with B. J. Landry (2004) [33], we have performed a new set of laboratory experiments in a large wave flume and recorded complete surface wave records and bar profiles. Test conditions included low and high reflection, monochromatic and polychromatic waves, and several sediment grain sizes. In particular, an experiment was run for a seabed initially consisting of a well mixed sand of two grain sizes. Under standing waves, the finer sand was transported toward the antinodes as suspended load, and the coarser sand toward the nodes as bed load, demonstrating sediment sorting.

We proceed as follows. In the remainder of this chapter a general overview is given to the sand bar problem, including the sediment transport, boundary layer and surface wave dynamics, and scaling. In Chapter 2, we focus on monochromatic waves in water of intermediate depth over a coarse sandy bed, and analyze the wave and boundary layer dynamics and the resultant sediment transport and bar formation. Comparisons are made with past and present laboratory data, and also to field data. In Chapter 3, we consider the effects of fine sand on bar formation and further comparisons are made with laboratory data. We study bar formation under narrow banded waves in Chapter 4. In Chapter 5, we present experimental results on sand bar formation under polychromatic waves and on sediment sorting under pure standing waves.

## 1.1 General setup and assumptions

The general setup is as follows. Monochromatic progressive waves of frequency $\omega$ are incident from the sea ($x' \sim -\infty$) upon a finite patch of erodible seabed extending from $x' = 0$ to $x' = L'$ (Figure 1-1). We shall use primes to denote all physical variables. The characteristic wavelength $\lambda$ is of the order of tens to a hundred meters in water of typical depth $H_o$. The characteristic wave number and amplitude are $K = 2\pi/\lambda$ and $A_o$, respectively. In this thesis, the subscript '$o$' implies the quantity is a scale or characteristic value. The dispersion relation for the surface waves implies that $K$, $H_o$ and $\omega$ are related via

$$\omega^2 = gK \tanh KH_o. \tag{1.1}$$

In intermediate depth, $KH_o = O(1)$ and in shallow water, $KH_o \ll 1$. We assume somewhere beyond the bar patch ($x' > L'$), a boundary like a beach or seawall reflects the waves. The mechanism is immaterial; we simply need to know the reflection coefficient $R_L$ at $x' = L'$. In intermediate depth, the characteristic amplitude of the horizontal orbital velocity at the seabed is

$$A_b = \frac{A_o (1 + |R_L|)}{\sinh (KH_o)}. \tag{1.2}$$

$A_b$ and $A_o$ are of order tens of centimeters to a meter. The sediment is assumed to be cohesionless sand of uniform diameter $d$, of the order 0.1 to 1 millimeters. The slopes of the surface waves and seabed are assumed to be characterized by a small parameter $\varepsilon$:

$$\varepsilon \equiv KA_b \ll 1. \tag{1.3}$$

The free surface is assumed to be free of wind stress, so that the kinematic and stress-free conditions apply. The water column can then be divided into an inviscid core and a boundary layer of thickness $\delta$ just above the seabed. $\delta$ is typically a few centimeters. We therefore have the following separation of length scales,

$$d \ll \delta \ll (A_b,\, A_o) \ll \lambda = 2\pi/K.$$

Based on this separation of scales, we set

$$\delta K = O\left(\varepsilon^2\right), \qquad d/\delta = O\left(\varepsilon\right). \tag{1.4}$$

We assume the seabed is not sand supply-limited, i.e. profile changes are not constrained by insufficient beach sand volume.

## 1.2 Surface waves and the inviscid core

With the exception of the boundary layer above the seabed, the water column is inviscid. In this inviscid core, the flow is incompressible and irrotational and governed by (Mei 1985 [42]),

$$\phi'_{x'x'} + \phi'_{z'z'} = 0, \qquad -h' < z' < \zeta', \tag{1.5}$$

where $\phi'$ is the velocity potential, yielding the horizontal and vertical velocity components $\phi'_{x'}$, $\phi'_{z'}$, respectively. The velocity components satisfy the Euler equations,

$$\left\{\frac{\partial}{\partial t'} + \phi'_{x'}\frac{\partial}{\partial x'} + \phi'_{z'}\frac{\partial}{\partial z'}\right\}\phi'_{x'} = -\frac{1}{\rho}\frac{\partial p'}{\partial x'}, \tag{1.6}$$

$$\left\{\frac{\partial}{\partial t'} + \phi'_{x'}\frac{\partial}{\partial x'} + \phi'_{z'}\frac{\partial}{\partial z'}\right\}\phi'_{z'} = g - \frac{1}{\rho}\frac{\partial p'}{\partial z'}. \tag{1.7}$$

The seabed $z' = -h'$ is assumed impermeable, and hence

$$\phi'_{z'} = -\phi'_{x'}h'_{x'}, \qquad z' = -h'. \tag{1.8}$$

The seabed slope $\partial h'/\partial x'$ is assumed to be $O\left(\varepsilon\right)$, and hence the bottom BC (1.8) implies

$$\phi'_{z'} = O\left(\varepsilon\right), \qquad z' = -h'. \tag{1.9}$$

On the free surface $z' = \zeta'$, the kinematic and dynamic boundary conditions are, respectively,

$$\zeta'_{t'} + \phi'_{x'}\zeta'_{x'} - \phi'_{z'} = 0, \qquad z' = \zeta', \tag{1.10}$$

$$g\zeta' + \phi'_{t'} + \frac{1}{2}\left(\phi'^2_x + \phi^2_{z'}\right) = 0, \qquad z' = \zeta'. \tag{1.11}$$

Eq. (1.11) is also Bernoulli's equation on the free surface. The free surface boundary

conditions (BCs) (1.10) and (1.11) can be combined to give

$$\mathcal{L}\phi' = -\left(\phi'^2_{x'} + \phi'^2_{z'}\right)_{t'} - \frac{1}{2}\left(\phi'_{x'}\frac{\partial}{\partial x'} + \phi'_{z'}\frac{\partial}{\partial z'}\right)\left(\phi'^2_{x'} + \phi'^2_{z'}\right), \qquad z' = \zeta', \tag{1.12}$$

where

$$\mathcal{L} = \frac{\partial^2}{\partial t'^2} + g\frac{\partial}{\partial z'}.$$

Following Hara and Mei (1987), we derive a surface boundary condition in terms of $\phi'$ only. Assuming $\phi', \zeta' = O(\varepsilon)$ and expanding (1.12) and (1.11) about $z' = 0$ gives

$$\begin{aligned}\mathcal{L}\phi' &= -\left(\phi'^2_{x'} + \phi'^2_{z'}\right)_{t'} - \frac{1}{2}\left(\phi'_{x'}\frac{\partial}{\partial x'} + \phi'_{z'}\frac{\partial}{\partial z'}\right)\left(\phi'^2_{x'} + \phi'^2_{z'}\right) \\ &\quad -\zeta'\mathcal{L}_{z'}\phi' - \frac{\zeta'^2}{2}\mathcal{L}_{z'z'}\phi' - \zeta'\left(\phi'^2_{x'} + \phi'^2_{z'}\right)_{t'z'} + O\left(\varepsilon^4\right),\end{aligned} \tag{1.13}$$

$$g\zeta' + \zeta'\phi'_{t'z'} + \phi'_{t'} + \frac{1}{2}\left(\phi'^2_{x'} + \phi'^2_{z'}\right) = O\left(\varepsilon^3\right) \tag{1.14}$$

on $z' = 0$. Eq. (1.14) implies $\zeta' = -\frac{1}{g}\phi'_{t'} + O(\varepsilon)$, which can then be substituted into the higher order terms in (1.14) to give

$$\zeta' = -\frac{1}{g}\left(\phi'_{t'} - \frac{1}{g}\phi'_{t'}\phi'_{t'z'} + \frac{1}{2}\left(\phi'^2_{x'} + \phi'^2_{z'}\right)\right) + O\left(\varepsilon^3\right) \tag{1.15}$$

on $z' = 0$. Similarly, from (1.13) and (1.15), we have

$$\begin{aligned}\phi'_{t't'} &= -g\phi'_{z'} - \left(\phi'^2_{x'} + \phi'^2_{z'}\right)_{t'} - \zeta'\mathcal{L}_{z'}\phi' + O\left(\varepsilon^3\right) \\ &= -g\phi'_{z'} - \left(\phi'^2_{x'} + \phi'^2_{z'}\right)_{t'} + \frac{1}{g}\phi'_{t'}\left(\phi'_{z't't'} + g\phi'_{z'z'}\right) + O\left(\varepsilon^3\right).\end{aligned} \tag{1.16}$$

Making the replacements (1.15), (1.16) and $\phi'_{z'z'} = -\phi'_{x'x'}$ (from Laplace's equation (1.5)) in the r.h.s. of Eq. (1.13) yields, on $z' = 0$,

$$\begin{aligned}\mathcal{L}\phi' &= \left\{-\frac{1}{2}\left(\phi'^2_{x'} + \phi'^2_{z'}\right) + \frac{1}{g}\phi'_{t'}\phi'_{z't'}\right\}_{t'} - \left(\phi'_{t'}\phi'_{x'}\right)_{x'} \\ &\quad + \left\{\frac{1}{2g}\left(\phi'_{t'}\phi'^2_{x'} + \phi'_{t'}\phi'^2_{z'}\right)_{z'} - \frac{1}{g^2}\phi'_{t'}\phi'^2_{z't'} - \frac{1}{2g^2}\phi'_{z'z't'}\phi'^2_{t'}\right\}_{t'} \\ &\quad + \left\{-\frac{1}{2}\phi'_{x'}\left(\phi'^2_{x'} + \phi'^2_{z'}\right) + \frac{1}{g}\phi'_{t'}\phi'_{z't'}\phi'_{x'} + \frac{1}{2g}\phi'^2_{t'}\phi'_{x'z'}\right\}_{x'} + O\left(\varepsilon^4\right).\end{aligned} \tag{1.17}$$

### 1.2.1 Mass flux across a vertical cross-section

Following Mei (1994) [45], depth integrating Laplace's equation (1.5) for the velocity potential gives

$$\int_{-h'}^{\zeta'} \phi'_{x'x'} dz' + \phi'_{z'}\big|_{\zeta'} - \phi'_{z'}\big|_{-h'} = 0 \tag{1.18}$$

where $\phi'_{z'}\big|_{\zeta'}$ and $\phi'_{z'}\big|_{-h'}$ denote the values of $\phi'_{z'}$ on the surface $z' = \zeta'$ and on the bottom $z' = -h'$, respectively. With Leibniz's rule, Eq. (1.18) can be written as

$$\frac{\partial}{\partial x'} \int_{-h'}^{\zeta'} \phi'_{x'} dz' + \left( - \phi'_{x'}\big|_{\zeta'} \frac{\partial \zeta'}{\partial x'} + \phi'_{z'}\big|_{\zeta'} \right) - \left( \phi'_{x'}\big|_{-h'} \frac{\partial h'}{\partial x'} + \phi'_{z'}\big|_{-h'} \right) = 0. \tag{1.19}$$

The last bracketed term vanishes in view of the impermeable bottom, Eq. (1.8). Substituting the kinematic BC (1.10) into (1.19) gives (Mei 1994 [45]),

$$\frac{\partial \zeta'}{\partial t'} + \frac{\partial M'_+}{\partial x'} = 0, \qquad M'_+ = \int_{-h'}^{\zeta'} \phi'_{x'} dz'. \tag{1.20}$$

Eq. (1.20) is exact and describes the mass flux $M'_+$ across a vertical cross-section of the inviscid core.

### 1.2.2 Perturbation solutions for monochromatic waves

Following Mei (1994) [45], the velocity potential and surface elevation are expanded as

$$\phi' = \phi'_1 + \phi'_2 + \phi'_3 + \dots \tag{1.21}$$

$$\zeta' = \zeta'_1 + \zeta'_2 + \dots \tag{1.22}$$

where $\phi'_n, \zeta'_n = O(\varepsilon^n)$. On substituting into (1.5), (1.17), (1.8) and (1.15) we obtain a set of $O(\varepsilon^n)$ problems,

$$\phi'_{nx'x'} + \phi'_{nz'z'} = F'_n, \qquad -H' < z' < 0, \tag{1.23}$$

$$\mathcal{L}\phi' = G'_n, \qquad z' = 0, \tag{1.24}$$

$$\phi'_{z'} = I'_n, \qquad z' = -H', \tag{1.25}$$

$$\zeta'_n = -\frac{1}{g} \phi'_{nt'}\big|_{z'=0} + P'_n, \tag{1.26}$$

where

$$\mathcal{L} = \frac{\partial^2}{\partial t'^2} + g\frac{\partial}{\partial z'},$$

and

$$\left(F_1', G_1', I_1', P_1'\right) = 0, \tag{1.27}$$

$$F_2' = -\phi'_{1x'_1x'} - \phi'_{1x'x'_1}, \tag{1.28}$$

$$F_3' = -\left(\phi'_{1_{x'_1x'_1}} + 2\phi'_{1x'x'_2} + \phi'_{2x'x'_1} + \phi'_{2x'_1x'}\right), \tag{1.29}$$

$$G_2' = -\left(-\frac{1}{g}\phi'_{1t'}\mathcal{L}_{z'}\phi'_1 + \left(\phi'^2_{1x'} + \phi'^2_{1z'}\right)_{t'} + 2\phi'_{1t't'_1}\right), \tag{1.30}$$

$$I_2' = \left(\widetilde{h}'\phi'_{1x'}\right)_{x'} - H'_{x'_1}\phi'_{1x'}, \tag{1.31}$$

$$I_3' = -\left(\phi'_{1x'_1} + \phi'_{2x'}\right)\left(H'_{x'_1} - \widetilde{h}'_{x'}\right) - \phi'_{1x'}\left(H'_{x'_2} - \widetilde{h}'_{x'_1}\right), \tag{1.32}$$

$$+\widetilde{h}'\left(\phi'_{2x'x'} + \phi'_{1x'x'_1} + \phi'_{1x'_1x'} - \phi'_{1x'z'}\left(H'_{x'_1} - \widetilde{h}'_{x'}\right)\right) + \frac{\widetilde{h}'^2}{2}\phi'_{1x'x'z'},$$

$$P_2' = -\frac{1}{g}\left(\frac{1}{2}\left(\phi'^2_{1x'} + \phi'^2_{1z'}\right) + \phi'_{1t'_1} + \zeta'_1\phi'_{1t'z'}\right). \tag{1.33}$$

We seek a solution to the potential flow problem that is monochromatic at leading order with incident[1] and reflected components,

$$\zeta_1' = \Re\left\{\zeta_1^{[1]\prime}e^{-i\omega' t'}\right\}, \tag{1.34}$$

where

$$\zeta_1^{[1]\prime} = A'e^{iS} + B'e^{-iS}. \tag{1.35}$$

The corresponding leading order velocity potential (solution to Eqs. (1.23) – (1.26) with $n = 1$) is,

$$\phi_1' = \phi_1^{[0]\prime}\left(x_1', x_2', t_1', t_2'\right) + \frac{1}{2}\left(\phi_1^{[1]\prime}e^{-i\omega t'} + \left(\phi_1^{[1]\prime}\right)^* e^{i\omega t'}\right), \tag{1.36}$$

[1]In this thesis, the terms incident, right-going and shoreward are used interchangeably. Similarly, the terms reflected, left-going and seaward are synonymous.

where

$$\phi_1^{[1]\prime} = -\frac{ig}{\omega}\frac{\cosh k'\left(z'+H'\right)}{\cosh k'H'}\left(A'e^{iS}+B'e^{-iS}\right), \tag{1.37}$$

$$S=\int^x k'dx', \qquad \omega^2 = gk'\tanh k'H', \qquad C_g' = \frac{\omega}{2k'}\left(1+\frac{2k'H'}{\sinh 2k'H'}\right), \tag{1.38}$$

and the mean depth can vary on the long spatial scale, $H' = H'\left(x_1'\right)$.

Yu & Mei (2000) showed that the sand bars are spaced at half the incident wavelength. We derive a similar result in §2.3 for bedload dominated flows and show in §3.7 that the same holds when suspended sediment is accounted for. Therefore, the bars are $\pi$-periodic in the spatial phase $S$ and admit a spatial Fourier series of the form

$$\widetilde{h}' = \frac{1}{2}\sum_{m=1}^{\infty}\left(\widetilde{h}^{[m]\prime}e^{-2imS}+\left(\widetilde{h}^{[m]\prime}\right)^* e^{2imS}\right). \tag{1.39}$$

The first order solution (solution to Eqs. (1.23) – (1.26) with $n=2$) is

$$\zeta_2^{'} = \zeta_2^{[0]\prime}\left(x_1',x_2',t_1',t_2'\right)+\Re\left(\zeta_2^{[1]\prime}e^{-i\omega t'}+\zeta_2^{[2]\prime}e^{-2i\omega t'}\right), \tag{1.40}$$

$$\phi_2' = \phi_2^{[0]\prime}\left(x_1',x_2',t_1',t_2'\right)+\Re\left(\phi_2^{[1]\prime}e^{-i\omega t'}+\phi_2^{[2]\prime}e^{-2i\omega t'}\right), \tag{1.41}$$

where $\zeta_2^{[1]\prime}$, $\phi_2^{[1]\prime}$ are not used and hence are not listed, and

$$\zeta_2^{[2]\prime} = \frac{k'\left(1+2\cosh^2 k'H'\right)\cosh k'H'}{4\sinh^3 k'H'}\left(A'^2e^{2iS}+B'^2e^{-2iS}\right)+A^{[2]}e^{iS^{[2]}}+B^{[2]}e^{-iS^{[2]}}, \tag{1.42}$$

$$\begin{aligned}\phi_2^{[2]\prime} &= -\frac{3i\omega\cosh 2k'\left(z'+H'\right)}{8\sinh^4 k'H'}\left(A'^2e^{2iS}+B'^2e^{-2iS}\right)-\frac{i\omega A'B'\left(1-2\cosh 2k'H'\right)}{4\sinh^2 k'H'}\\ &\quad -\frac{ig}{2\omega}\frac{\cosh k^{[2]\prime}\left(z'+H'\right)}{\cosh k^{[2]\prime}H'}\left(A^{[2]\prime}e^{iS^{[2]}}+B^{[2]\prime}e^{-iS^{[2]}}\right).\end{aligned} \tag{1.43}$$

The phase of the free wave component of the second harmonic is

$$S^{[2]} = -\int^{x'} k^{[2]\prime}dx',$$

whose wavenumber $k^{[2]\prime}$ is given by

$$(2\omega)^2 = gk^{[2]\prime}\tanh k^{[2]\prime}H'. \tag{1.44}$$

In the laboratory, the free wave component of the second harmonic is a by-product of wave generation. Its amplitudes $A^{[2]\prime}$, $B^{[2]\prime}$ can be found from the wave record. We outline later how this free wave component can be canceled.

The solvability conditions for the leading order wave parameters are

$$A'_{t'_1} + C'_g A'_{x'_1} + \frac{A'}{2}\frac{\partial C'_g}{\partial x'_1} = -i\Omega'_0 \widetilde{h}^{[1]\prime} B', \tag{1.45}$$

$$B'_{t'_1} - C'_g B'_{x'_1} - \frac{B'}{2}\frac{\partial C'_g}{\partial x'_1} = -i\Omega'_0 \left(\widetilde{h}^{[1]\prime}\right)^* A', \tag{1.46}$$

where $\widetilde{h}^{[1]\prime}$ is the first (spatial) harmonic amplitude of the bar profile and

$$\Omega'_0 = \frac{\omega k'}{2\sinh 2k'H'}.$$

We now derive equations relating the energies of the incident and reflected wave trains. Adding $A'^* \times$ (1.45) and $A' \times (1.45)^*$ gives

$$\left(\left|A'\right|^2\right)_{t'_1} + \left(C'_g \left|A'\right|^2\right)_{x'_1} = 2\Omega'_0 \mathrm{Im}\left\{\widetilde{h}^{[1]\prime} A'^* B'\right\}. \tag{1.47}$$

Similarly, from (1.46) we obtain

$$\left(\left|B'\right|^2\right)_{t'_1} - \left(C'_g \left|B'\right|^2\right)_{x'_1} = -2\Omega'_0 \mathrm{Im}\left\{\widetilde{h}^{[1]\prime} A'^* B'\right\}. \tag{1.48}$$

Adding (1.47) and (1.48) gives

$$\left(\left|A'\right|^2 + \left|B'\right|^2\right)_{t'_1} + \left(C'_g\left(\left|A'\right|^2 - \left|B'\right|^2\right)\right)_{x'_1} = 0. \tag{1.49}$$

Lastly, note that due to the mean depth $H'$ varying in $x_1$, the group velocity $C'_g$ and wave number $k'$ also vary in $x_1$, hence

$$\frac{dC'_g}{dx'_1} = \frac{2\omega\left(1 - k'H'\tanh k'H'\right)}{2k'H' + \sinh 2k'H'}\frac{dH'}{dx'_1},$$

$$\frac{dk'}{dx'_1} = -\frac{2k'^2}{2k'H' + \sinh 2k'H'}\frac{dH'}{dx'_1}.$$

### 1.2.3 Mass flux

The horizontal mass flux $M'_+$ across a vertical cross-section is defined in (1.20). Substituting the perturbation expansions (1.21), (1.22) and the expressions (1.34), (1.36), (1.40), (1.41) into $M'_+$ gives

$$\begin{aligned} M'_+ &= \int_{-h'}^{\zeta'} \phi'_{x'} dz' = \int_{-H'-\widetilde{h}'}^{-H'} \phi'_{x'} dz' + \int_{-H'}^{0} \phi'_{x'} dz' + \int_{0}^{\zeta'} \phi'_{x'} dz' \\ &= -\widetilde{h}' \left.\phi'_{x'}\right|_{z'=-H'} + \int_{-H'}^{0} \phi'_{x'} dz' + \zeta' \left.\phi'_{x'}\right|_{z'=0} + O\left(\varepsilon^2\right) \\ &= -\widetilde{h}' \left.\phi'_{1x'}\right|_{z'=-H'} + \int_{-H'}^{0} \left(\phi'_{1x'} + \phi'_{2x'}\right) dz' + \zeta'_1 \left.\phi'_{1x'}\right|_{z'=0} + O\left(\varepsilon^2\right). \end{aligned} \tag{1.50}$$

We will time average $M'_+$ over the short and long times $t'$, $t'_1$. To do this, we note that the short time averages (denoted by bars) of (1.36) and (1.41) are

$$\overline{\phi'_{1x'}} = \varepsilon \phi^{[0]\prime}_{1x'_1}, \qquad \overline{\phi'_{2x'}} = \varepsilon \phi^{[0]\prime}_{2x'_1} = O\left(\varepsilon^2\right),$$

where $\phi_1^{[0]\prime} = \phi_1^{[0]\prime}(x'_1, t'_1)$ and $\phi_2^{[0]\prime} = \phi_2^{[0]\prime}(x'_1, t'_1)$ are long wave potentials. The sand bar elevation $\widetilde{h}'$ is shown later to be independent of $t'$ and $t'_1$. Thus, time averaging (1.50) over a short wave period in $t'$ gives

$$\overline{M'_+} = H' \phi^{[0]\prime}_{1x'_1} + \overline{\zeta'_1 \left.\phi'_{1x'}\right|_{z'=0}} + O\left(\varepsilon^2\right). \tag{1.51}$$

Multiplying $\zeta'_1$ and $\phi'_{1x'}$, given in (1.34), (1.35) and (1.41), (1.37) and taking the short time average yields

$$\begin{aligned} \overline{\zeta'_1 \left.\phi'_{1x'}\right|_{z'=0}} &= \frac{1}{2} \Re \left\{ \zeta_1^{[1]\prime} \left(\phi_{1x'}^{[1]\prime}\right)^* \Big|_{z'=0} \right\} \\ &= \frac{gk'}{2\omega} \left( \left|A'\right|^2 - \left|B'\right|^2 + \Re \left\{ A'^* B' e^{-2iS'} - A' B'^* e^{2iS'} \right\} \right) \\ &= \frac{gk'}{2\omega} \left( \left|A'\right|^2 - \left|B'\right|^2 \right). \end{aligned} \tag{1.52}$$

Substituting (1.52) into Eq. (1.51) for the mass flux yields

$$\overline{M'_+} = H' \phi^{[0]\prime}_{1x'_1} + \frac{gk'}{2\omega} \left( \left|A'\right|^2 - \left|B'\right|^2 \right) + O\left(\varepsilon^2\right). \tag{1.53}$$

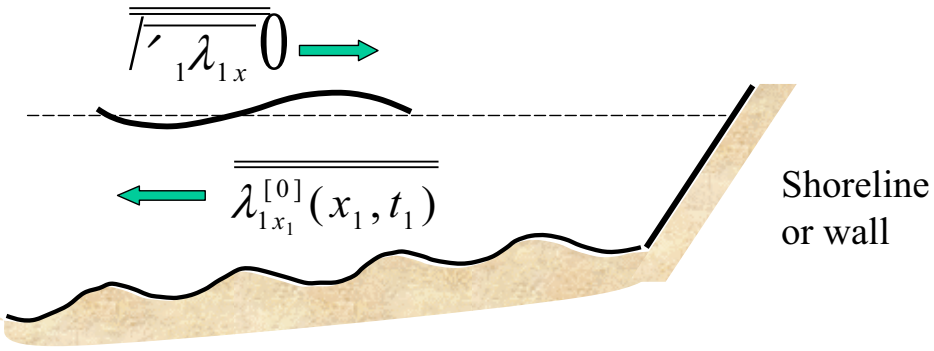


Figure 1-2: We consider the beach as a closed system bounded at one end by a shoreline or seawall.

Notice that $\overline{M'_+}$ is independent of the short spatial scale $x'$.

Substituting the perturbation expansions (1.21), (1.22), (1.34), (1.36), (1.40), (1.41) into the mass flux equation (1.20) and time averaging over the short wave period gives

$$\varepsilon \frac{\partial \zeta_2^{[0]\prime}}{\partial t'_1} + \varepsilon \frac{\partial \overline{M'_+}}{\partial x'_1} = O\left(\varepsilon^3\right). \tag{1.54}$$

Assuming the waves are periodic (or independent) of the long time scale $t_1$, we take the $t_1$-average (denoted by double bars) of Eq. (1.54) and divide by $\varepsilon$ to obtain

$$\frac{\partial}{\partial x'_1} \overline{\overline{\left(\overline{M'_+}\right)}} = -\overline{\overline{\frac{\partial \zeta_2^{[0]\prime}}{\partial t'_1}}} + O\left(\varepsilon^2\right) = O\left(\varepsilon^2\right).$$

Therefore, the mean mass flux $\overline{\overline{\left(\overline{M'_+}\right)}}$ is constant, to leading order,

$$\overline{\overline{\left(\overline{M'_+}\right)}} = c_M = \text{ constant}. \tag{1.55}$$

We consider closed systems bounded at one end by a shoreline or seawall (see Figure 1-2). At these boundaries, the mean mass flux $\overline{\overline{\left(\overline{M'_+}\right)}}$ vanishes. Thus, from (1.55), the mean mass flux must vanish everywhere,

$$\overline{\overline{\left(\overline{M'_+}\right)}} = 0 \quad \text{for all} \quad x_1. \tag{1.56}$$

This restates the well-known result (e.g. Mei [45], p. 471) that there is no net longshore

current associated with setdown waves. Taking the $t_1$-average of (1.54) and substituting (1.56) gives

$$0 = \overline{\overline{\left(\overline{M'_+}\right)}} = H' \left(\overline{\overline{\phi_1^{[0]\prime}}}\right)_{x'_1} + \frac{gk'}{2\omega}\left(\overline{\overline{|A'|^2}} - \overline{\overline{|B'|^2}}\right). \tag{1.57}$$

Hence, the mean current associated with the long waves is

$$\left(\overline{\overline{\phi_1^{[0]\prime}}}\right)_{x'_1} = -\frac{gk'}{2\omega H'}\left(\overline{\overline{|A'|^2}} - \overline{\overline{|B'|^2}}\right). \tag{1.58}$$

### 1.2.4 Long wave equation

An equation governing the evolution of the long wave potential $\phi_1^{[0]}$ is derived from the mass flux equation (1.54). Dividing (1.54) by $\varepsilon$ and substituting for $\overline{M'_+}$ from (1.53) gives

$$\frac{\partial \zeta_2^{[0]\prime}}{\partial t'_1} + \frac{\partial}{\partial x'_1}\left(H\frac{\partial \phi_1^{[0]}}{\partial x'_1}\right) + \frac{g}{2\omega^2}\frac{\partial}{\partial x'_1}\left(k'\left(\left|A'\right|^2 - \left|B'\right|^2\right)\right) = O\left(\varepsilon^2\right). \tag{1.59}$$

The mean surface elevation $\zeta_2^{[0]\prime}$ is given by time averaging (1.26) and substituting (1.33),

$$\zeta_2^{[0]\prime} = -\frac{1}{g}\overline{\frac{\partial \phi'_2}{\partial t'}} + \overline{P'_2} = -\frac{1}{g}\left(\frac{1}{2}\left(\overline{\phi'^2_{1x'}} + \overline{\phi'^2_{1z'}}\right) + \overline{\phi'_{1t'_1}} + \overline{\zeta'_1\phi'_{1t'z'}}\right). \tag{1.60}$$

Substituting $\zeta'_1$ and $\phi'_1$ given in (1.34), (1.35), (1.36), and (1.37) into Eq. (1.60), computing the time averages, and substituting the resulting expression for $\zeta_2^{[0]\prime}$ into the averaged mass flux equation (1.59) gives an equation for the long wave potential $\phi_1^{[0]\prime}$,

$$\phi^{[0]\prime}_{1t'_1t'_1} - g\left(H'\phi^{[0]\prime}_{1x'_1}\right)_{x'_1} = -\frac{gk'}{2\sinh 2k'H'}\left(\left|A'\right|^2 + \left|B'\right|^2\right)_{t'_1} + \frac{g^2}{2\omega}\left(k'\left(\left|A'\right|^2 - \left|B'\right|^2\right)\right)_{x'_1}. \tag{1.61}$$

An alternative derivation of the long wave equation (1.61) relies on the solvability of the third order mean current. We review this derivation for completeness. Taking the time average of (1.23) for $n = 3$, we have (Hara & Mei (1987) [22]),

$$\phi'_{30x'x'} + \phi'_{30z'z'} = -\phi^{[0]\prime}_{1_{x'_1x'_1}}, \qquad -H' < z' < 0, \tag{1.62}$$

$$\phi'_{30z} = \frac{1}{g}G'_{30}, \qquad z' = 0, \tag{1.63}$$

$$\phi'_{30z'} = -\left(H'_{x'_1} - \widetilde{h}'_{x'}\right)\phi^{[0]\prime}_{1x'_1}, \qquad z' = -H', \tag{1.64}$$

where $\phi'_{30}$, $G'_{30}$ are the time averages (i.e. zeroth time harmonic) of $\phi'_3$ and $G'_3$, respectively, $H' = H'(x'_1, x'_2)$ and

$$\begin{aligned} G'_{30} &= -\phi^{[0]\prime}_{1t'_1t'_1} + \left( -\left|\phi^{[1]\prime}_{1x'}\right|^2 - \left|\phi^{[1]\prime}_{1z'}\right|^2 + \frac{2\omega^2}{g}\Re\left\{\phi^{[1]\prime}_1\left(\phi^{[1]\prime}_{1z'}\right)^*\right\}\right)_{t'_1} \\ &\quad -2\omega\Re\left\{\left(i\left(\phi^{[1]\prime}_1\right)^*\phi^{[1]\prime}_{1x'}\right)_{x'_1} + \left(i\left(\phi^{[1]\prime}_1\right)^*\phi^{[1]\prime}_{1x'_1}\right)_{x'}\right\} \\ &\quad -\Re\left\{\omega i\left(\left(\phi^{[1]\prime}_1\right)^*\phi^{[1]\prime}_{2x'} + \left(\phi^{[1]\prime}_{21}\right)^*\phi^{[1]\prime}_{1x'}\right)_{x'} + \left(\left(\phi^{[1]\prime}_{1t'_1}\right)^*\phi^{[1]\prime}_{1x'}\right)_{x'}\right\}. \end{aligned} \tag{1.65}$$

Note that $G'_{30}$ is found by taking the $O\left(\varepsilon^3\right)$ terms from the time average of (1.17), and the r.h.s. of (1.64) is found by taking the $O\left(\varepsilon^3\right)$ terms from the time average of (1.32).

Taking the spatial mean of (1.62) – (1.64) across the short wavelength $2\pi/k'$ and noting that $\widetilde{h}'$ and $\phi'_1$ are $2\pi/k'$-periodic in $x'$ gives

$$\begin{aligned} \left\langle\phi'_{30z'z'}\right\rangle_{x'} &= -\phi^{[0]\prime}_{1x'_1x'_1}, \qquad -H' < z' < 0, \\ \left\langle\phi'_{30z'}\right\rangle_{x'} &= \frac{1}{g}\left\langle G'_{30}\right\rangle_{x'}, \qquad z' = 0, \\ \left\langle\phi'_{30z'}\right\rangle_{x'} &= -H'_{x'_1}\phi^{[0]\prime}_{1x'_1}, \qquad z' = -H', \end{aligned} \tag{1.66}$$

where angled brackets with subscript $x'$ denote the spatial average in $x'$ over the short wavelength $2\pi/k'$, and on $z' = 0$,

$$\begin{aligned} \left\langle G'_{30}\right\rangle_{x'} &= -\phi^{[0]\prime}_{1t'_1t'_1} - \frac{1}{4}\left\langle\left|\phi^{[1]\prime}_{1x'}\right|^2 + \left|\phi^{[1]\prime}_{1z'}\right|^2\right\rangle_{x't'_1} \\ &\quad + \frac{\omega^2}{2g}\Re\left\{\left\langle\phi^{[1]\prime}_1\left(\phi^{[1]\prime}_{1z'}\right)^*\right\rangle_{x't'_1}\right\} - \frac{\omega}{8}\Re\left\{\left(i\left\langle\left(\phi^{[1]\prime}_1\right)^*\phi^{[1]\prime}_{1x'}\right\rangle_{x'}\right)_{x'_1}\right\}. \end{aligned} \tag{1.67}$$

Substituting $\phi^{[0]\prime}_1$ from (1.37) gives

$$\left\langle G'_{30}\right\rangle_{x'} = -\phi^{[0]\prime}_{1t'_1t'_1} - \frac{gk'}{2\sinh 2k'H'}\left(\left|A'\right|^2 + \left|B'\right|^2\right)_{t'_1} + \frac{g^2}{2\omega}\left(k'\left(\left|A'\right|^2 - \left|B'\right|^2\right)\right)_{x'_1}. \tag{1.68}$$

The solvability condition for (1.66) is given by

$$-\phi^{[0]\prime}_{1x'_1x'_1}H' = \int_{-H'}^{0}\left\langle\phi'_{30z'z'}\right\rangle_{x'}dz' = \phi'_{30z'}\Big|_{-H'}^{0} = \frac{\langle G'_{30}\rangle_{x'}}{g} + H'_{x'_1}\phi^{[0]\prime}_{0x'_1}.$$

Rearranging and substituting for $\langle G'_{30} \rangle_{x'}$ from (1.68) gives the long wave equation (1.61).

### 1.2.5 Scaling

We introduce dimensionless variables

$$(x, z, h, H) = K\left(x', z', h', H'\right), \qquad x_1 = K^2 A_b x'_1, \qquad t_1 = \omega K A_b t'_1, \tag{1.69}$$

$$(A, B) = \frac{(A', B')}{A_o}, \qquad \left(\widetilde{h}, D_1\right) = \frac{\left(\widetilde{h}', \widetilde{h}^{[1]\prime}\right)}{A_b}, \qquad \left(\phi_m, \phi_m^{[n]}\right) = \frac{\left(\phi'_m, \phi_m^{[n]\prime}\right)}{A_o^m \omega K^{m-2}}, \tag{1.70}$$

$$\left(\zeta_m, \zeta_m^{[n]}\right) = \frac{\left(\zeta'_m, \zeta_m^{[n]\prime}\right)}{A_o^m K^{m-1}}, \qquad k = \frac{k'}{K}, \qquad C_g = \frac{K}{\omega} C'_g, \tag{1.71}$$

where $m = 1, 2$ and $n = 0, 1, 2, 3$. Recall that $K$, $A_o$, $\omega$ are characteristic wave parameters.

Substituting the dimensionless variables in (1.69), (1.70) into Eqs. (1.45), (1.46) and (1.49) gives

$$A_{t_1} + C_g A_{x_1} + \frac{A}{2}\frac{\partial C_g}{\partial x_1} = -i\Omega_0 D_1 B, \tag{1.72}$$

$$B_{t_1} - C_g B_{x_1} - \frac{B}{2}\frac{\partial C_g}{\partial x_1} = -i\Omega_0 D_1^* A, \tag{1.73}$$

$$\left(|A|^2 + |B|^2\right)_{t_1} + \left(C_g\left(|A|^2 - |B|^2\right)\right)_{x_1} = 0, \tag{1.74}$$

where

$$\Omega_0 = \frac{k}{2\sinh 2kH}.$$

Substituting the dimensionless variables in (1.69), (1.70) into Eqs. (1.34) – (1.38), (1.41) and (1.43) gives

$$\zeta_1 = \Re\left\{\zeta_1^{[1]} e^{-it}\right\}, \qquad \zeta_1^{[1]} = Ae^{iS} + Be^{-iS}, \tag{1.75}$$

$$\phi_1 = \phi_1^{[0]}(x_1, x_2, t_1, t_2) + \Re\left\{\phi_1^{[1]} e^{-i\omega t}\right\}, \tag{1.76}$$

$$\phi_2 = \phi_2^{[0]}(x_1, x_2, t_1, t_2) + \Re\left\{\phi_2^{[1]} e^{-i\omega t'} + \phi_2^{[2]} e^{-2i\omega t'}\right\}, \tag{1.77}$$

where

$$\phi_1^{[1]} = -\frac{igK}{\omega^2}\frac{\cosh k(z+H)}{\cosh kH}\left(Ae^{iS} + Be^{-iS}\right), \tag{1.78}$$

$$\phi_2^{[2]} = -\frac{3i\cosh 2k\,(z+H)}{8\sinh^4 kH}\left(A^2e^{2iS}+B^2e^{-2iS}\right) - \frac{iAB\,(1-2\cosh 2kH)}{4\sinh^2 kH}$$
$$-\frac{2i\cosh k^{[2]}\,(z+H)}{\sinh k^{[2]}H}\left(A^{[2]}e^{iS^{[2]}}+B^{[2]}e^{-iS^{[2]}}\right), \tag{1.79}$$

$$S=\int^x k\,(x_1)\,dx, \tag{1.80}$$

$$\frac{\omega^2}{gK}=k\,(x_1)\tanh k\,(x_1)\,H\,(x_1)\,, \qquad C_g=\frac{1}{2k}\left(1+\frac{2kH}{\sinh 2kH}\right). \tag{1.81}$$

We limit our scope to waves that are periodic in $t_1$, i.e. periodically modulated. We also drop the dependence of the variables on the long scale $x_2$, since it does not contribute to the order of accuracy retained here. Averaging (1.49) in $t_1$ gives

$$\left(C_g\left(\overline{\overline{|A|^2}}-\overline{\overline{|B|^2}}\right)\right)_{x_1}=0. \tag{1.82}$$

The complex amplitude of the first harmonic of the bottom orbital velocity is given by taking the $x$-derivative of (1.78) and setting $z=-H$,

$$U_1^{[1]} = \frac{A_o}{A_b}\,\phi_{1x}^{[1]}\Big|_{z=-H}=\frac{A_o}{A_b}\frac{1}{\sinh kH}\left(Ae^{iS}-Be^{-iS}\right)$$
$$= \frac{A_o}{A_b}\frac{|A|\,e^{i(\theta_A+\theta_R/2)}}{\sinh kH}\left(e^{i\chi}-|R|\,e^{-i\chi}\right), \tag{1.83}$$

where $\theta_R$ is the phase of the reflection coefficient $R$ (i.e. $R=|R|\,e^{i\theta_R}$) and

$$\chi=S-\theta_R/2=\int^x k\,(x_1)\,dx-\theta_R/2.$$

The complex amplitude of the zeroth and second harmonics of the (second order) bottom orbital velocity are, from (1.77), (1.79) and (1.83),

$$U_2^{[0]}=\frac{A_o}{A_b}\;\phi_{1x_1}^{[0]}\Big|_{z=-H}=\frac{A_o}{A_b}\,\phi_{1x_1}^{[0]}, \tag{1.84}$$

$$U_2^{[2]} = \frac{A_o^2}{A_b^2}\;\phi_{2x}^{[2]}\Big|_{z=-H}=\frac{3}{4}\frac{A_o^2}{A_b^2}\frac{k\,|A|^2\,e^{i(2\theta_A+\theta_R)}}{\sinh^4 kH}\left(e^{2i\chi}-|R|^2\,e^{-2i\chi}\right)$$
$$= -\frac{3i}{4\sinh^2 kH}U_1^{[1]}\frac{\partial U_1^{[1]}}{\partial x}. \tag{1.85}$$

The second equality in (1.84) follows since $\phi^{[0]}_{1x_1}$ is independent of $z$.

The dimensionless mass flux is found by substituting the dimensionless variables from (1.69) and (1.70) into Eq. (1.53) and scaling $\overline{M'_+}$ by $\varepsilon A_o \omega K^{-1}$,

$$\overline{M_+} = \frac{\overline{M'_+}}{\varepsilon A_o \omega K^{-1}} = H\phi^{[0]}_{1x_1} + \frac{A_o}{A_b}\frac{gK}{2\omega^2}k\left(|A|^2 - |B|^2\right) + O(\varepsilon). \tag{1.86}$$

The dimensionless form of the mean return flow is found by substituting the dimensionless variables from (1.69) and (1.70) into Eq. (1.58) and substituting the result into Eq. (1.84),

$$\overline{\overline{U_2^{[0]}}} = \frac{A_o}{A_b}\left(\overline{\overline{\phi_1^{[0]}}}\right)_{x_1} = -\frac{A_o^2}{2A_b^2 H \tanh kH}\left(\overline{\overline{|A|^2}} - \overline{\overline{|B|^2}}\right), \tag{1.87}$$

where double bars denote the $t_1$-average.

Substituting dimensionless variables from (1.69), (1.70) into the long wave equation (1.61) gives

$$\phi^{[0]}_{1t_1t_1} - \frac{gK}{\omega^2}\left(H\phi^{[0]}_{1x_1}\right)_{x_1} = \frac{A_o gK}{A_b\omega^2}\left(-\frac{k\left(|A|^2 + |B|^2\right)_{t_1}}{2\sinh 2kH} + \frac{gK}{2\omega^2}\left(k\left(|A|^2 - |B|^2\right)\right)_{x_1}\right). \tag{1.88}$$

## 1.3 Turbulent boundary layer

Under waves sufficiently large to produce sediment movement on the seabed, the boundary layer near the seabed is often turbulent. The turbulent intensity is quantified via the Reynolds number

$$\mathsf{R}_E = \frac{\omega A_b^2}{\nu}, \tag{1.89}$$

where $\nu$ is the kinematic viscosity of the fluid. On a smooth bed, the flow is turbulent if $\mathsf{R}_E > N \times 10^4$ where estimates of the coefficient $N$ vary from 1.26 (Jonsson 1966 [29]) to 30 (Kamphuis 1975 [31]). Huang & Mei (2003) [27] point out that most laboratory waves fall below this threshold ($A_b = 10$ cm and $\omega = \pi$ s$^{-1}$ gives $\mathsf{R}_E = 3.14 \times 10^4$). However, for a rough bed, the threshold for the transition to turbulence decreases. Based on measurements of oscillatory flow over rippled beds, Sleath (1990) [59] has given the following empirical

criterion for turbulence,

$$\left(\mathsf{R}_E \frac{\lambda_{ro}}{A_b}\left(\frac{\eta_{ro}}{\lambda_{ro}}\right)^{1.16} - 108.2\right)\left(\frac{A_b}{\lambda_{ro}}\left(\frac{\eta_{ro}}{\lambda_{ro}}\right)^{1.16} - 0.042\right) \geq 0.58, \tag{1.90}$$

where $\eta_{ro}$, $\lambda_{ro}$ are the typical ripple height (vertical distance from crest to trough) and length (distance from trough to trough or crest to crest), respectively. Furthermore, oscillatory flows over rippled beds are generally fully rough turbulent, i.e. the typical roughness[2] $k_{No}$ of the bed is considerably larger than the thickness $\nu/u_{fo}$ of the viscous sublayer, where $u_{fo}$ is the typical friction velocity. The ratio of $k_{No}$ to the viscous sublayer thickness gives a second Reynolds number,

$$\mathsf{R}_{FT} = \frac{u_f k_{No}}{\nu}. \tag{1.91}$$

Even in the small scale laboratory experiments considered in this thesis, $\mathsf{R}_{FT} > 100$, indicating the flows are fully rough turbulent.

To study the dynamics of the turbulent boundary layer, there exist many turbulence closure models, such as the eddy viscosity model, mixing length models, $k$–$\epsilon$ models, second order closure models, etc. These models combine results from theory, numerical simulation and laboratory experiments and are of varying degrees of complexity. Surveys of turbulence models for the seabed boundary layer have been given by Grant & Madsen (1986) [21] and by Sleath (1990) [59]. Of these models, the eddy viscosity model is one of the more popular and practical approaches. For example, depth-dependent eddy viscosity models have been proposed by Kajiura (1968) [30], Smith (1977) [60], Grant & Madsen (1979) [19] (see also Madsen & Salles (1998) [40] for further data comparisons and a few revisions). The effects of a time-varying eddy viscosity have been considered by Lavelle & Mofjeld (1983) [34], Trowbridge & Madsen (1984) [62], [63] and Davies (1986) [11]. The eddy viscosity $\nu_e'$ depends primarily on the orbital amplitude $A_b\omega$ and the equivalent roughness $k_{No}$. Models for eddy viscosity are generally derived for spatially uniform oscillatory flows and pure progressive waves. Under partially reflected surface waves, the local orbital amplitude $A_b\omega|U_1^{[1]}|$ and hence the turbulent intensity can vary appreciably.

The equations governing the flow in the turbulent boundary layer are the continuity and

[2]The subscript $N$ is for Nikuradse whose experiments on equivalent roughness in steady turbulent flows are well known.

Reynolds momentum equations,

$$\frac{\partial u'}{\partial x'} + \frac{\partial w'}{\partial z'} = 0, \tag{1.92}$$

$$\left\{ \frac{\partial}{\partial t'} + u' \frac{\partial}{\partial x'} + w' \frac{\partial}{\partial z'} \right\} u' = -\frac{1}{\rho} \frac{\partial p'}{\partial x'} + \frac{\partial}{\partial z'} \left( \nu_e' \frac{\partial u'}{\partial z'} \right) + \frac{\partial}{\partial x'} \left( \nu_e' \frac{\partial u'}{\partial x'} \right), \tag{1.93}$$

$$\left\{ \frac{\partial}{\partial t'} + u' \frac{\partial}{\partial x'} + w' \frac{\partial}{\partial z'} \right\} w' = -g - \frac{1}{\rho} \frac{\partial p'}{\partial z'} + \frac{\partial}{\partial z'} \left( \nu_e' \frac{\partial w'}{\partial z'} \right) + \frac{\partial}{\partial x'} \left( \nu_e' \frac{\partial w'}{\partial x'} \right). \tag{1.94}$$

The choice of eddy viscosity $\nu_e'$ depends on the particular region of the boundary layer under study. For predicting the rate of bedload transport, an accurate description of the flow is required within tens of grain diameters from the bed, where the eddy viscosity scales as the distance from the bed. For predicting the rate of suspended sediment transport, a description of the flow is required across the entire boundary layer. In this case, a depth-averaged eddy viscosity is used. In both cases, the eddy viscosity scales as $\nu_e' \sim u_{fo}\delta$, where $u_{fo}$, $\delta$ are the typical friction velocity and boundary layer thickness, respectively.

## 1.4 Boundary conforming coordinates

As in Yu [70], we introduce the boundary conforming (non-orthogonal) coordinate system $(x'', \eta')$, where

$$\eta' = z' + h'\left(x', t'\right), \qquad x'' = x', \tag{1.95}$$

and $z' = -h'$ is the seabed. The seabed elevation $h'$ has two components: a mean component $H'$ slowly varying in space and a sandbar component $\widetilde{h}'$,

$$h' = H'\left(\varepsilon x'\right) - \widetilde{h}'\left(x', t'\right). \tag{1.96}$$

The seabed slope $\partial h'/\partial x'$ is assumed to be $O\left(\varepsilon\right)$. Note that under the change of variable (1.95), we have

$$\frac{\partial f}{\partial z'} = \frac{\partial f}{\partial \eta'}, \qquad \frac{\partial f}{\partial x'} = \frac{\partial f}{\partial x''} + \frac{\partial f}{\partial \eta'} \frac{\partial h'}{\partial x'}. \tag{1.97}$$

Note that $\partial h'/\partial x' = \partial h'/\partial x''$ since $h'$ is independent of $\eta'$.

Changing variables to the boundary conforming coordinate system defined in (1.95), the continuity equation (1.92) becomes

$$\frac{\partial u'}{\partial x''} + \frac{\partial w_n'}{\partial \eta'} = 0, \tag{1.98}$$

where

$$w'_n = w' - \frac{\partial h'}{\partial x'} u' \tag{1.99}$$

is the dimensional velocity normal to the seabed.

## 1.5 Bottom shear stress and roughness

Due to bottom roughness, the flow vanishes at an elevation just above the bed, given empirically as $k'_N(x')/30$ (Grant & Madsen 1982 [20]), where $k'_N(x)$ is the local equivalent roughness that varies with the local orbital amplitude. The bottom shear stress is given by

$$\frac{\tau'}{\rho} = \nu'_e \frac{\partial u'}{\partial \eta'}\bigg|_{\eta'=k'_N(x')/30}. \tag{1.100}$$

We define the Shields parameter as

$$\Theta = \frac{\tau'}{\rho\,(s-1)\,gd}. \tag{1.101}$$

The critical Shields parameter $\Theta_{c0}$ for incipient motion of sediment on a horizontal bed is found from the modified Shields diagram. For convenience, Madsen [39] has provided the following fitting formula for $\Theta_{c0}$,

$$\Theta_{c0} = \begin{cases} 0.095 S_*^{-2/3} + 0.056\left(1 - \exp\left(-\frac{1}{20} S_*^{3/4}\right)\right), & S_* \geq 0.8, \\ 0.1 S_*^{-2/7}, & S_* < 0.8, \end{cases} \tag{1.102}$$

where $S_*$ is the fluid-sediment parameter, defined as

$$S_* = \frac{\sqrt{(s-1)\,gd^3}}{4\nu}. \tag{1.103}$$

Note that $\nu$ is the kinematic viscosity of the fluid.

The equivalent roughness $k'_N$ indicates the effect of the bedforms on the boundary layer flow. To analyze bedform geometry, Nielsen (1981) [48] defines a mobility number

$$\Psi = \Psi_o \left|U_1^{[1]}\right|^2, \qquad \Psi_o = \frac{(A_b\omega)^2}{(s-1)\,gd}. \tag{1.104}$$

Based on laboratory and field data, Nielsen found that for $\Psi < 156$, the bed is rippled;

for higher intensities, $\Psi > 156$, sheet flow conditions prevail and ripples are washed out. For moderate flow intensities $\Psi < 156$, Nielsen found the following empirical relation governing the ripple height (vertical distance from crest to trough) under regular waves in the laboratory,

$$\frac{\eta_r'}{A_b\left|U_1^{[1]}\right|} = 0.275 - 0.022\sqrt{\Psi}. \tag{1.105}$$

Grant & Madsen [20] related empirically the relative roughness $k_N'$ over a rippled bed to ripple height as

$$k_N' = 4.13\eta_r'. \tag{1.106}$$

The extension to sheet flow and a smoothed formula useful for computation are outlined in Appendix 1.9.1.

For the purpose of evaluating the criterion for turbulent flow in the laboratory, Eq. (1.90), we use Nielsen [48]'s empirical relation for the ripple steepness under regular laboratory waves,

$$\frac{\eta_{ro}}{\lambda_{ro}} = 0.182 - 0.24\,\Theta_{do}^{3/2}, \tag{1.107}$$

where $\Theta_{do}^{3/2}$ is the scale of the grain roughness Shields parameter (Eq. (1.101) with $k_N' = 2.5d$) and $(\eta_{ro}, \lambda_{ro})$ are the characteristic ripple height and length.

All of the laboratory experiments considered in this thesis have rippled beds and no sheet flow. In most cases, the ripple height is extracted from the reported seabed profiles, allowing the measured ripple height to be used directly in our theory, rather than relying on the empirical formula (1.105). For tests involving standing waves with strong reflection, large spatial variations are observed in the ripple height as it varies locally with the horizontal bottom orbital velocity $\left|U_1^{[1]}\right|$. Large sub-critical regions exist where no bedload transport occurs and ripples do not form. Based on experimental data presented later for ripples under pure standing waves, the following fitting formula well-describes the typical ripple amplitude across a bar,

$$\eta_r'(x) = \eta_{ro}\frac{\left|U_1^{[1]}\right|^2(1 - r_1\left|U_1^{[1]}\right|)}{|U_{\max}|^2(1 - r_1|U_{\max}|)}f_c, \qquad f_c = \exp\left(1 - \frac{1}{r_2}\left|U_1^{[1]}/U_{\max}\right|^{-2\,r_3}\right), \tag{1.108}$$

where $\eta_{ro}$ is the typical (or maximum) reported ripple height, $(r_1, r_2, r_3)$ are fitting con-

stants, and from Eq. (1.83),

$$|U_{\max}| = \max_x \left|U_1^{[1]}\right| = \frac{A_o A(1+|R|)}{A_b \sinh kH}. \tag{1.109}$$

The factor $f_c$ is necessary to smoothly join roughness estimates in super-critical and sub-critical regions of the bar. Over the flat sub-critical regions, the roughness scales as the grain diameter, so that Eq. (1.106) can be generalized to

$$k_N' = 4.13\eta_r'(x) + (1-f_c)d. \tag{1.110}$$

## 1.6 Bed load transport rate

The bedload transport rate on a flat bed under fluid with orbital velocity $U_0' = A_b\omega\cos\omega t'$ has been related empirically to the shear stress of the fluid on the bed by Sleath's [57] and Nielsen [50],

$$q_B' = \frac{8}{3}Q_B' \cos^4\left(\omega t' + \varpi\right) \operatorname{sgn}\left(\cos\left(\omega t' + \varpi\right)\right) \tag{1.111}$$

where $\varpi$ is the phase lead of the bedload transport relative to the fluid velocity $U_0'$ just outside the boundary layer and $Q_B'$ is the mean sediment discharge averaged over half a cycle. Madsen (1991) [37] has given a conceptual derivation of a formula for bedload sediment transport that agrees very well with Eq. (1.111). King [32] performed experiments on sloping beds and altered the formula to account for slope,

$$q_B' = \frac{8}{3}\frac{Q_B'}{1 - \frac{1}{\tan\psi_m}\frac{\partial h'}{\partial x'}\frac{\Theta}{|\Theta|}} \cos^4\left(\omega t' + \varpi\right) \operatorname{sgn}\left(\cos\left(\omega t' + \varpi\right)\right) \tag{1.112}$$

where $z' = -h'$ is the seabed and $\psi_m$ is the angle of repose of a bed whose grains are in motion.

When the bottom shear stress is in the positive $x'$ direction, the effect of the term containing $1/\tan\psi_m$ is to augment the bedload transport when the stress of the fluid on the bed is directed downslope ($\Theta > 0$ and $\partial h'/\partial x' > 0$, or $\Theta < 0$ and $\partial h'/\partial x' < 0$) and diminish it when the stress is upslope ($\Theta > 0$ and $\partial h'/\partial x' < 0$, or $\Theta < 0$ and $\partial h'/\partial x' > 0$). King (1991) found that $\psi_m = 30^o$ gave the best fit to a set of experimental data of bedload transport on sloping and flat beds, despite the considerable scatter. It will turn out that the phase difference $\varpi$ is immaterial to the mean bedload transport.

$Q'_B$ is the mean sediment discharge averaged over half a cycle given empirically by Nielsen [50] as

$$\frac{Q'_B}{\sqrt{(s-1)\,g d^3}} = 3\left(\widehat{\Theta}_d - \Theta_c\right)^{3/2} \mathrm{Hv}\left(\widehat{\Theta}_d - \Theta_c\right), \tag{1.113}$$

where $\mathrm{Hv}\,()$ is the Heaviside function and hats denote the maximum value in time of a quantity. It is important to use the grain roughness Shields parameter $\widehat{\Theta}_d$ based on the grain roughness (Eq. (1.101) with $k'_N = 2.5d$) rather than the Shields parameter based on the ripple roughness (Eq. (1.101) with $k'_N = 4\eta'_r$), since the empirical coefficient "3" in (1.113) was fit by using $\widehat{\Theta}_d$ (Nielsen [50] and Sleath [57]). Using $k'_N = 4\eta'_r$ to evaluate $\widehat{\Theta}_d$, as Yu [68] and Yu & Mei [70] have done, leads to an erroneous overestimation of the bedload transport and results in bar predictions that have several features (qualitative and quantitative) that are in stark contrast to observations. We return to this point a few times throughout the thesis.

Following Fredsøe (1974) [18], the instantaneous critical Shields parameter required for incipient motion of sediment particles on a mild slope is

$$\widetilde{\Theta}_c(t) = \Theta_{c0}\left(1 - \frac{1}{\tan\psi_s}\frac{\partial h'}{\partial x'}\frac{\Theta}{|\Theta|}\right) \tag{1.114}$$

where $\Theta_{c0}$ is the critical Shields parameter on a horizontal bed, found from the modified Shields diagram. Madsen (1991) has argued that $\tan\psi_s/\tan\psi_m \approx 2$ gives good agreement with data. Eq. (1.114) states that a smaller bed shear stress is necessary to move a particle downslope and a larger shear stress is required to move a particle upslope. Since we desire a time-independent critical Shields parameter $\Theta_c$ for use with the time-independent equation (1.113), we take $\Theta_c$ to be the minimum of $\widetilde{\Theta}_c(t)$ over a wave cycle,

$$\Theta_c = \Theta_{c0}\left(1 - \frac{1}{2\tan\psi_m}\left|\frac{\partial h'}{\partial x'}\right|\right) \tag{1.115}$$

Fredsøe used the slope modification of the critical Shields parameter $\widetilde{\Theta}_c(t)$ to modify the Shields parameter $\Theta$. However, despite $\Theta_c$ and the bedload transport rate $q'_B$ depending on slope, the Shields parameter $\Theta$ depends solely on the shear stress of the fluid on the bed. Hence, rather than modifying $\Theta$, we choose King [32]'s modification to the bedload transport rate found in Eq. (1.112).

We now convert (1.112) to an equation involving a time-varying Shields parameter $\Theta$.

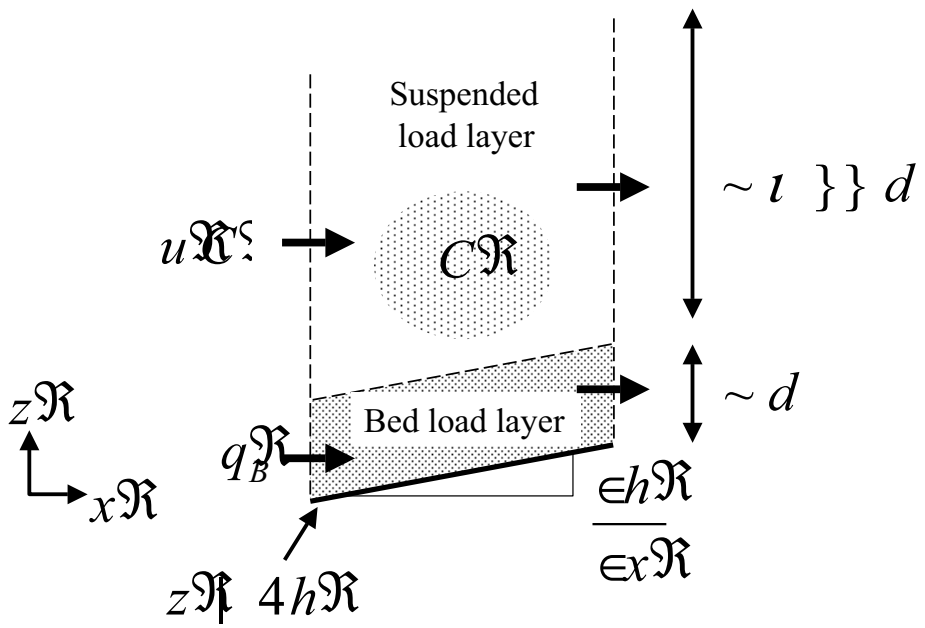


Figure 1-3: Mass budget for the sediment, both in the bed load layer near the seabed and the suspended load layer above it.

We will show that to leading order, $\Theta = \widehat{\Theta}\cos(\omega t + \varpi)$. When compared to (1.112), this motivates taking $q'_B \propto \Theta^4$,

$$q'_B = \frac{8}{3}\frac{Q'_B}{1 - \frac{1}{\tan\psi_m}\frac{\partial h'}{\partial x'}\frac{\Theta}{|\Theta|}}\left|\frac{\Theta}{\widehat{\Theta}}\right|^4 \frac{\Theta}{|\Theta|}. \tag{1.116}$$

## 1.7 Conservation of mass for sediment

We derive the conservation of mass equation for sediment transport over a seabed $z' = -h'(x', x'_1, t')$. The sediment transport is divided into two types: bed load, occurring within a few grain diameters of the bed; and suspended sediment above it (Figure 1-3). Let $q'_B$ be the volumetric bed load transport rate tangent to the bed. Let $q'_{Bx}$ be the horizontal volumetric bed load transport rate. Then

$$q'_{Bx} = q'_B \frac{1}{\sqrt{1 + \left(\frac{\partial h'}{\partial x'}\right)^2}}. \tag{1.117}$$

In two dimensions ($x'$, $z'$), conservation of mass in a thin control volume $V$ normal to the

seabed gives (Fig. 2)

$$dx'\frac{\partial}{\partial t'}\left[-\left(1-\mathcal{N}\right)h'+\int_{-h'}^{\infty}C'dz'\right] = q'_{Bx}\big|_{x'}-q'_{Bx}\big|_{x'+dx'}+\left[\int_{-h'}^{\infty}u'C'dz'\right]_{x'} - \left[\int_{-h'}^{\infty}u'C'dz'\right]_{x'+dx'}, \tag{1.118}$$

where $\mathcal{N}\approx 0.3$ is the porosity of the bed and $C'\left(x',z',t'\right)$ is the suspended sediment concentration. The left hand side of (1.118) is the time rate of change of the volume of sediment in the control volume, including the sediment in the bed and that suspended above the bed. The right hand side is the net bed load and suspended sediment flux through the control volume boundaries. We assume the suspended sediment concentration vanishes sufficiently rapidly outside the boundary layer near the seabed; hence the upper integration limits in the integrals in $z'$ are taken to be $\infty$. Therefore, (1.118) can be written as the PDE

$$\left(1-\mathcal{N}\right)\frac{\partial h'}{\partial t'}+\frac{\partial}{\partial t'}\int_{-h'}^{\infty}C'dz'=\frac{\partial}{\partial x'}\left(\frac{q'_B}{\sqrt{1+\left(\frac{\partial h'}{\partial x'}\right)^2}}+\int_{-h'}^{\infty}u'C'dz'\right). \tag{1.119}$$

Making the assumption that the seabed is gently sloping, $\partial h'/\partial x'=O\left(\varepsilon\right)$, allows (1.119) to be simplified to

$$\left(1-\mathcal{N}\right)\frac{\partial h'}{\partial t'}+\frac{\partial}{\partial t'}\int_{-h'}^{\infty}C'dz'=\frac{\partial}{\partial x'}\left(q'_B+\int_{-h'}^{\infty}u'C'dz'\right)+O(\varepsilon^2). \tag{1.120}$$

Also, with $\partial h'/\partial x'=O\left(\varepsilon\right)$, Eq. (1.117) implies that to order[3] $O\left(\varepsilon\right)$, the volumetric bed load flux is in the horizontal direction.

## 1.8 Normalization

In this section, we introduce scales and normalize the boundary layer and sediment transport quantities. First, we scale the vertical momentum equation to eliminate the pressure term in the horizontal momentum equation. To do so, we introduce the following scales in the

[3]In this thesis, the phrase "to order $O\left(\varepsilon\right)$ "means up to and including order $O\left(\varepsilon\right)$.

boundary layer,

$$x' = O\left(K^{-1}\right), \qquad t' = O\left(\omega^{-1}\right), \qquad \eta' = O\left(\delta\right), \qquad u' = O\left(A_b\omega\right), \tag{1.121}$$

$$\nu_e' = O\left(\kappa u_{fo}\delta\right) = O\left(\omega\delta^2\right), \qquad w_n' = O\left(K\delta A_b\omega\right), \qquad w' = O\left(\varepsilon A_b\omega\right). \tag{1.122}$$

Recall that $K$, $\omega$, $A_b$ are the characteristic wave number, wave angular frequency, and orbital amplitude. The scales for $w_n'$ and $w'$ were found by substituting the scales for $x$, $\eta$, $u$ into Eq. (1.98). The characteristic boundary layer thickness $\delta$ is defined by

$$\delta = \frac{2\kappa u_{fo}}{\omega}, \tag{1.123}$$

where $\kappa \approx 0.4$ is the Kármán constant. The two scalings of the eddy viscosity in Eq. (1.122) are the same in view of Eq. (1.123) for $\delta$.

From Eq. (1.97), spatial derivatives of quantities scale as

$$\frac{\partial f}{\partial z'} = \frac{\partial f}{\partial \eta'} = O\left(\frac{f}{\delta}\right), \qquad \frac{\partial f}{\partial x'} = O\left(\frac{\varepsilon f}{\delta}\right). \tag{1.124}$$

Substituting the scales in (1.121), (1.122), (1.124) into the vertical momentum equation (1.94) gives

$$1 - \frac{1}{\rho g}\frac{\partial p'}{\partial z'} = O\left(\frac{\varepsilon A_b\omega^2}{g}\right). \tag{1.125}$$

The dispersion relation (1.1) implies $\omega^2 = O\left(gK\right)$, and hence (1.125) becomes

$$1 - \frac{1}{\rho g}\frac{\partial p'}{\partial z'} = O\left(\varepsilon^2\right).$$

Thus the pressure is hydrostatic to $O\left(\varepsilon^2\right)$, implying that

$$\frac{\partial}{\partial z'}\left(-\frac{1}{\rho}\frac{\partial p'}{\partial x'}\right) = O\left(\varepsilon^2\right). \tag{1.126}$$

Thus the pressure term in the horizontal momentum equation (1.93) may be replaced by

the l.h.s. of the Euler equation (1.6) evaluated at $z' = -h'$,

$$\left\{\frac{\partial}{\partial t'} + u'\frac{\partial}{\partial x'} + w'\frac{\partial}{\partial z'}\right\}u' = \left\{\frac{\partial}{\partial t'} + U_I'\frac{\partial}{\partial x'} + W_I'\frac{\partial}{\partial z'}\right\}U_I' + \frac{\partial}{\partial z'}\left(\nu_e'\frac{\partial u'}{\partial z'}\right) + \frac{\partial}{\partial x'}\left(\nu_e'\frac{\partial u'}{\partial x'}\right), \tag{1.127}$$

where $U_I' = \phi_{x'}'\big|_{z'=-h'}$, $W_I' = \phi_{z'}'\big|_{z'=-h'}$.

Substituting the scales in (1.122) into (1.100) and (1.101) gives the scale of the Shields parameter,

$$\Theta_o = \frac{u_{fo}^2}{(s-1)\,gd}. \tag{1.128}$$

A scaling is found for the bedload transport quantities in Eqs. (1.113) and (1.116), assuming conditions exceed critical,

$$q_B', Q_B' = O\left(\sqrt{(s-1)\,gd^3}\Theta_{do}^{3/2}\right),$$

where $\Theta_{do}$ is given by (1.128), but with a friction velocity based on the grain roughness. We will write $\Theta_o$ and $\Theta_{do}$ more precisely once the characteristic friction velocity $u_{fo}$ is found via a closure relation in Chapter 2 (§2.1.3).

The scale of the relative roughness on a rippled bed follows from (1.106),

$$k_{No} = 4.13\eta_{ro}, \tag{1.129}$$

where the characteristic ripple height $\eta_{ro}$ is taken either as the maximum ripple height reported in a given experiment, or, if ripple measurements are lacking, given by replacing $\left|U_1^{[1]}\right| = 1$ and $\Psi = \Psi_0$ in (1.105),

$$\frac{\eta_{ro}}{A_b} = 0.275 - 0.022\sqrt{\Psi_o}. \tag{1.130}$$

Let all normalized variables be without primes. We introduce dimensionless variables as

$$(\eta, \eta_b) = \frac{(\eta', \eta_b')}{\delta}, \qquad (x, h, H) = K\left(x', h', H'\right), \qquad t = \omega t', \qquad \widetilde{h} = \frac{\widetilde{h}'}{A_b}, \tag{1.131}$$

$$(u, U_I) = \frac{(u', U_I')}{A_b\omega}, \qquad w_n = \frac{w_n'}{K\delta A_b\omega}, \qquad \nu_e = \frac{\nu_e'}{\kappa\, u_{fo}\delta}, \qquad u_f = \frac{u_f'}{u_{fo}}, \tag{1.132}$$

$$Q_B = \frac{Q_B'}{3\sqrt{(s-1)\, gd^3}\Theta_{do}^{3/2}}, \qquad q_B = \frac{q_B'}{8\sqrt{(s-1)\, gd^3}\Theta_{do}^{3/2}}, \qquad k_N = \frac{k_N'}{k_{No}}. \tag{1.133}$$

The numerical constants used in the normalizations of the bedload quantities $q_B'$ and $Q_B'$ are chosen to cancel those in the dimensional variables. Many of the normalizations in (1.131) – (1.133) are kept the same as those for the inviscid core, Eqs. (1.69) – (1.71), in order to facilitate the use of the bottom orbital amplitude found from the inviscid core with the boundary layer theory derived here.

We introduce the long spatial scale $x_1 = \varepsilon x$. The seabed elevation (1.96) becomes

$$h = Kh' = H(x_1) - \varepsilon\widetilde{h}(x, x_1, t). \tag{1.134}$$

Thus, as we assumed earlier, the seabed is gently sloping:

$$\frac{\partial h'}{\partial x'} = \frac{\partial h}{\partial x} = \varepsilon\left(\frac{dH}{dx_1} - \frac{\partial\widetilde{h}}{\partial x}\right). \tag{1.135}$$

Changing variables to boundary conforming coordinates via (1.95), substituting normalized variables from (1.131), (1.132), and retaining only $O(1)$ and $O(\varepsilon)$ terms, the continuity and horizontal momentum equations (1.98) and (1.127) become

$$\frac{\partial u}{\partial x} + \frac{\partial w_n}{\partial \eta} = 0, \tag{1.136}$$

$$\left\{\frac{\partial}{\partial t} + \varepsilon u\frac{\partial}{\partial x} + \varepsilon w_n\frac{\partial}{\partial \eta}\right\} u = \frac{1}{2}\frac{\partial}{\partial \eta}\left(\nu_e\frac{\partial u}{\partial \eta}\right) + \frac{\partial U_I}{\partial t} + \varepsilon U_I\frac{\partial U_I}{\partial x}. \tag{1.137}$$

The term containing $W_I'$ was dropped because it is of $O(\varepsilon^2)$ in view of Eq. (1.9). The $x'$-derivative term in the turbulent Reynolds stress was also dropped because it is of $O(\varepsilon^2)$ in view of Eqs. (1.97), (1.124).

The dimensionless bedload transport quantities are found by applying the normalization (1.133) to Eqs. (1.113) and (1.116),

$$Q_B = \frac{Q_B'}{3\sqrt{(s-1)\, gd^3}\Theta_{do}^{3/2}} = \left(\frac{\widehat{\Theta}_d - \Theta_c}{\Theta_{do}}\right)^{3/2} \mathrm{Hv}\left(\frac{\widehat{\Theta}_d - \Theta_c}{\Theta_{do}}\right),$$

$$q_B = \frac{Q_B}{\left(1 - \frac{1}{\tan\psi_m}\frac{\partial h}{\partial x}\frac{\Theta}{|\Theta|}\right)}\left|\frac{\Theta}{\widehat{\Theta}}\right|^4 \frac{\Theta}{|\Theta|}. \tag{1.138}$$

Ultimately, we desire the time averaged bedload transport $\overline{q_B}$, where bars represent the time average over a wave period.

## 1.9 Appendix

### 1.9.1 Empirical formulae for ripple geometry

In this section, a smoothed formula is found for the relative roughness $k_N$ and a factor is added to smoothly attenuate the ripples as conditions approach critical, i.e. as $\widehat{\Theta}_d \to \Theta_c$. This formula is useful for cases when the local orbital amplitude $\left|U_1^{[1]}\right|$ varies appreciably along the bed. The relative roughness for a rippled bed and for sheet flow is given by the formula of Grant & Madsen (1982) [20],

$$\frac{k_N}{A_b\left|U_1^{[1]}\right|} = 4.13\frac{\eta_r'}{A_b\left|U_1^{[1]}\right|} + 5\widehat{\Theta}_d\frac{d}{A_b\left|U_1^{[1]}\right|} \tag{1.139}$$

where $\widehat{\Theta}_d$ is amplitude of the grain roughness Shields parameter. Using the $\tanh(x)$ function, we minimize the difference between $1-\sqrt{x}$ and $\frac{1}{2} - \frac{1}{2}\tanh(a(x-b))$. A best fit analysis gives $a = 2.2$ and $b = 0.28$. We can now rewrite the formula for $k_N$:

$$\frac{k_N}{A_b\left|U_1^{[1]}\right|} = 0.57\left(1 - \tanh\left(0.014\,\Psi - 0.616\right)\right) + 5\widehat{\Theta}_d\frac{d}{A_b\left|U_1^{[1]}\right|}. \tag{1.140}$$

Lastly, we add a factor that smoothly attenuates the equivalent roughness $k_N$ near subcritical regions from the ripple roughness to the grain roughness. The particular form is not critical in view of the relatively small amount of sediment transport that occurs in these regions. We choose the factor

$$f_N = \exp\left\{-\left(3\left(\frac{\widehat{\Theta}_d - \Theta_c}{\Theta_{c0}} + \frac{1}{2}\right)\right)^{-2}\right\}\tanh\left(2\left(\frac{\widehat{\Theta}_d - \Theta_c}{\Theta_{c0}} + \frac{1}{2}\right)\right)$$

and modify (1.140) as

$$\frac{k_N}{A_b\left|U_1^{[1]}\right|}=\left\{0.57\left(1-\tanh\left(0.014\,\Psi-0.616\right)\right)+5\widehat{\Theta}_d\frac{d}{A_b\left|U_1^{[1]}\right|}\right\}f_N+\left(1-f_N\right)\frac{d}{A_b\left|U_1^{[1]}\right|}. \tag{1.141}$$

# Chapter 2

# Bars of coarse sand under monochromatic waves in intermediate depth

In this chapter, we calculate the stresses on the seabed due to surface waves that are monochromatic at leading order. We concentrate on coarse sediments, which are transported predominantly as bedload. We employ a depth-linear eddy viscosity to obtain an accurate flow description very near the seabed, where the bedload transport occurs. We derive an equation for the evolution of the sand bar elevation coupled with equations for the wave envelope.

## 2.1 Boundary layer with depth-linear eddy viscosity

Predicting bedload transport requires an accurate description of the flow within a few tens of grain diameters from the bed. In this region, the eddy viscosity scales via the "law of the wall", i.e. with distance from the seabed. In this section, we define a depth-linear model for the eddy viscosity and then use a perturbation expansion to solve the continuity and momentum equations to determine the boundary layer flow.

The depth-linear eddy viscosity is defined as

$$\nu_e' = \kappa u_f' \eta', \tag{2.1}$$

where $u'_f(x)$ is the local friction velocity. By the normalization defined in (1.132), the dimensionless eddy viscosity is

$$\nu_e = \frac{\nu'_e}{\kappa u_{fo}\delta} = u_f \eta, \tag{2.2}$$

where $u_f(x)$ is the normalized friction velocity.

We consider boundary layer flows forced by surface water waves that are monochromatic to leading order. These nearly monochromatic surface waves yield a dimensionless horizontal velocity $U_I$ at the bottom of the inviscid core ($z = -H$), just outside the boundary layer, of the form

$$U_I = \Re\left\{U_1^{[1]} e^{-it}\right\} + \varepsilon \Re\left\{U_2^{[0]} + U_2^{[1]} e^{-it} + U_2^{[2]} e^{-2it}\right\} + O\left(\varepsilon^2\right). \tag{2.3}$$

The terms $U_1^{[1]}$, $U_2^{[0]}$, $U_2^{[1]}$ and $U_2^{[2]}$ are found from potential theory governing the surface waves in the inviscid core. We expand the flow in the boundary layer in a similar manner to $U_I$,

$$u = u_1 + \varepsilon u_2 + \ldots = \Re\left\{u_1^{[1]} e^{-it}\right\} + \varepsilon \Re\left\{u_2^{[0]} + u_2^{[1]} e^{-it} + u_2^{[2]} e^{-2it}\right\} + O\left(\varepsilon^2\right), \tag{2.4}$$

$$w = w_1 + \varepsilon w_2 + \ldots = \Re\left\{w_1^{[1]} e^{-it}\right\} + O(\varepsilon). \tag{2.5}$$

The notation $f_n^{[m]}$ is used throughout the thesis to denote the time harmonic amplitude of a certain asymptotic order of a function. The subscript $n$ denotes the asymptotic order; 1 for leading order $O(1)$ and 2 for second order $O(\varepsilon)$. The superscript $m$ in square brackets denotes the time harmonic. Thus, in (2.3), $U_2^{[1]}$ is the first time harmonic of the second order ($O(\varepsilon)$) flow.

### 2.1.1 Boundary conditions on the bar surface

We derive the boundary conditions at the bottom of the boundary layer, at the bar surface. Since the bars have slope $\partial h'/\partial x' = O(\varepsilon)$ and since, as we show later, the timescale of bar evolution is $O\left(\varepsilon^{-4.5}\omega^{-1}\right)$, the normal fluid velocity at the seabed is at most $O\left(\varepsilon^{4.5}\omega A_b\right)$. Due to the depth-linear eddy viscosity and the bed roughness, the flow vanishes at an elevation just above the bed, given empirically as $k'_N(x)/30\delta$ (Grant & Madsen [20]) where $k'_N(x)$ is the local equivalent roughness (see §1.5). Recall that $k'_N$ is a function of $x$, in general, since the roughness height depends on the local orbital amplitude. Since the normal

fluid velocity at the seabed is at most $O\left(\varepsilon^{4.5}\omega A_b\right)$, to the order of accuracy retained here, we have

$$w_n = 0 \quad \text{on} \quad \eta = k'_N(x)/30\delta. \tag{2.6}$$

Yu & Mei [70] estimated that the sand grains moving as bedload within a few grain diameters of the bar surface travel with velocity $O(u'd/\delta)$. Since $d/\delta = O(\varepsilon)$, then the flow velocity at the bar surface is at most $O(\varepsilon u)$, so that

$$u = O(\varepsilon u) \quad \text{on} \quad \eta = k'_N(x)/30\delta. \tag{2.7}$$

Substituting Eqs. (2.4), (2.5) into (2.6), (2.7) and equating like powers of $\varepsilon$ gives

$$u_1^{[1]} = w_1^{[1]} = u_2^{[0]} = u_2^{[2]} = 0, \quad \text{on} \quad \eta = k'_N(x)/30\delta. \tag{2.8}$$

Outside the Stokes boundary layer, the oscillatory components of $(u, w)$ must join smoothly with those of the inviscid flow at $z = -h$,

$$u_1^{[1]} \to U_1^{[1]}, \qquad u_2^{[2]} \to U_2^{[2]}, \quad \text{as} \quad \eta \to \infty. \tag{2.9}$$

Since the bar slope is $O(\varepsilon)$, the components $U_1^{[1]}$, $U_2^{[0]}$, $U_2^{[2]}$ of the orbital velocity are the same on $z = -h$ as they are on $z = -H$; only the term $U_2^{[1]}$ will differ at these two elevations due to the effect of the $O(\varepsilon)$ bar slope. Outside the boundary layer the flow is inviscid; hence we impose a shear-free condition on the mean current $u_2^{[0]}$,

$$\nu_e \frac{\partial u_2^{[0]}}{\partial \eta} = u_f \eta \frac{\partial u_2^{[0]}}{\partial \eta} \to 0, \quad \text{as} \quad \eta \to \infty. \tag{2.10}$$

### 2.1.2 Leading order flow

Substituting the expansions for $U_I$ and $(u, w)$ from (2.3), (2.4), (2.5) into (1.137) and (1.136) yields, at leading order,

$$\frac{\partial u_1}{\partial t} = \frac{u_f(x)}{2} \frac{\partial}{\partial \eta}\left(\eta \frac{\partial u_1}{\partial \eta}\right) + \Re\left\{-iU_1^{[1]} e^{-it}\right\}, \qquad \frac{\partial w_1}{\partial \eta} = -\frac{\partial u_1}{\partial x}, \tag{2.11}$$

subject to the boundary conditions

$$u_1 = w_1 = 0 \quad \text{at } \eta = \eta_b, \qquad (u_1, w_1) \to \left( \Re \left\{ U_1^{[1]} e^{-it} \right\}, 0 \right) \quad \text{as } \eta \to \infty. \tag{2.12}$$

The solution is (Kajiura 1968 [30])

$$u_1 = \Re \left\{ u_1^{[1]} e^{-it} \right\} = \Re \left\{ U_1^{[1]} \left( 1 - \frac{\mathcal{K}_0 (Z)}{\mathcal{K}_0 (Z_b)} \right) e^{-it} \right\}, \tag{2.13}$$

where

$$Z = \frac{2\eta}{u_f (x)}, \qquad Z_b (x) = \frac{k_N' (x)}{15\delta u_f (x)}, \tag{2.14}$$

and

$$\mathcal{K}_0 (Z) = \ker 2\sqrt{Z} - i \operatorname{kei} \left( 2\sqrt{Z} \right).$$

The functions $\ker (z)$ and $\operatorname{kei} (z)$ are called Kelvin functions (see e.g. Abramowitz & Stegun [1]). Derivatives and integrals of Kelvin functions pertinent to the discussion below are discussed in Appendix 2.9.1.

The shear stress at the bed is

$$\begin{aligned} \nu_e \frac{\partial u_1^{[1]}}{\partial \eta} \bigg|_{\eta = \left( k_N'/30\delta \right)} &= u_f Z \frac{\partial u_1^{[1]}}{\partial Z} \bigg|_{Z = Z_b} \\ &= -\frac{u_f U_1^{[1]} Z_b}{\mathcal{K}_0 (Z_b)} \frac{d\mathcal{K}_0}{dZ} \bigg|_{Z = Z_b} = -\frac{1+i}{\sqrt{2}} \frac{\sqrt{Z_b} \mathcal{K}_1 (Z_b)\, u_f U_1^{[1]}}{\mathcal{K}_0 (Z_b)}, \end{aligned} \tag{2.15}$$

where $\mathcal{K}_1 (Z)$ is given in terms of Kelvin functions in (2.161) and the derivative of $\mathcal{K}_0 (Z)$ is computed in (2.162) (see Appendix 2.9.1). Also, noting that $u_1|_{\eta = \left( k_N'/30\delta \right)} = 0$, the solution for $w_1$ is

$$w_1 = -\int_{\left( k_N'/30\delta \right)}^{\eta} \frac{\partial u_1}{\partial x} d\eta = -\frac{\partial}{\partial x} \left( \int_{\left( k_N'/30\delta \right)}^{\eta} u_1 d\eta \right), \tag{2.16}$$

where Liebniz' rule was used to obtain the second equality, as well as the no-slip condition $u_1 = 0$ on $\eta = k_N'/30$. Using result (2.165) from Appendix 2.9.1, we also define

$$F_1 (Z, Z_b) = \int_{Z_b}^{Z} \left( 1 - \frac{\mathcal{K}_0 (Z')}{\mathcal{K}_0 (Z_b)} \right) dZ' = Z - Z_b + \frac{1-i}{\sqrt{2}} \frac{\sqrt{Z} \mathcal{K}_1 (Z) - \sqrt{Z_b} \mathcal{K}_1 (Z_b)}{\mathcal{K}_0 (Z_b)}. \tag{2.17}$$

Eq. (2.16) implies that $w_1 = \Re\left\{w_1^{[1]} e^{-it}\right\}$ where

$$\begin{aligned} w_1^{[1]} &= -\frac{\partial}{\partial x}\left(\frac{u_f U_1^{[1]}}{2} F_1\right) \\ &= -\frac{F_1}{2}\frac{\partial}{\partial x}\left(u_f U_1^{[1]}\right) - \frac{u_f U_1^{[1]}}{2}\frac{\partial F_1}{\partial x} \\ &= -\frac{F_1 u_f}{2}\frac{\partial U_1^{[1]}}{\partial x} - \frac{U_1^{[1]}}{2}\frac{du_f}{dx}\left(F_1 - Z\left(1 - \frac{\mathcal{K}_0(Z)}{\mathcal{K}_0(Z_b)}\right)\right) \\ &\quad -\frac{U u_f}{2}\frac{\mathcal{K}_1(Z_b)}{\sqrt{Z_b}\mathcal{K}_0(Z_b)}\left(\frac{\sqrt{Z}\mathcal{K}_1(Z)}{\mathcal{K}_0(Z_b)} - \frac{\sqrt{Z_b}\mathcal{K}_0(Z)\mathcal{K}_1(Z_b)}{\mathcal{K}_0^2(Z_b)}\right)\frac{dZ_b}{dx}. \end{aligned} \tag{2.18}$$

The term $\partial F_1/\partial x$ is computed in Appendix 2.9.1 (Eq. (2.163)) and is used to obtain (2.18).

### 2.1.3 Friction velocity and roughness

The time-independent friction velocity $u'_f(x)$ is defined in terms of the amplitude of the bottom shear stress (1.100),

$$\left(u'_f(x)\right)^2 = \frac{\widehat{\tau}}{\rho} = \kappa u'_f(x)\left|\eta' \frac{\partial u_1^{[1]\prime}}{\partial \eta'}\bigg|_{\eta'=\left(k'_N/30\right)}\right|. \tag{2.19}$$

Recall that hats denote the time amplitude of a function and parallel vertical lines indicate the modulus of a complex number and the absolute value of a real number. Inserting the scales in (1.131) – (1.133) and the shear stress in (2.15) into Eq. (2.19) gives

$$\begin{aligned} u'_f(x) &= \kappa\left|\eta' \frac{\partial u_1^{[1]\prime}}{\partial \eta'}\bigg|_{\eta'=\left(k'_N/30\right)}\right| = \kappa A_b \omega\left|\eta \frac{\partial u_1^{[1]}}{\partial \eta}\bigg|_{\eta=\left(k'_N/30\delta\right)}\right| \\ &= \kappa A_b \omega\left|U_1^{[1]}\right| \frac{\sqrt{Z_b(x)}\,|\mathcal{K}_1(Z_b(x))|}{|\mathcal{K}_0(Z_b(x))|}. \end{aligned} \tag{2.20}$$

**Scaling**

We now find scalings of the friction velocity $u'_f$ and roughness $Z_b$. Inserting the scales in (1.131) – (1.133) into Eq. (2.14) gives a scaling for $Z_b(x)$,

$$Z_b = O\left(\frac{k_{No}}{15\delta}\right), \tag{2.21}$$

where $\delta$, $k_{No}$ are the characteristic boundary layer thickness and equivalent roughness, defined in §1.5 and §1.8. Substituting (2.21) into Eq. (2.20) gives a scaling $u_{fo}$ for the eddy viscosity,

$$u_{fo} = \kappa A_b \omega \frac{\sqrt{k_{No}/15\delta}\,|\mathcal{K}_1(k_{No}/15\delta)|}{|\mathcal{K}_0(k_{No}/15\delta)|}. \tag{2.22}$$

Eliminating $u_{fo}$ from Eqs. (1.123) and (2.22) gives an equation for the boundary layer thickness $\delta$ in terms of the relative roughness $k_{No}$ and the orbital amplitude $A_b$,

$$\left(\frac{k_{No}}{15\delta}\right)^{3/2} \frac{|\mathcal{K}_1(k_{No}/15\delta)|}{|\mathcal{K}_0(k_{No}/15\delta)|} = \frac{k_{No}}{30\kappa^2 A_b}. \tag{2.23}$$

Equation (2.23) defines $k_{No}/15\delta$ implicitly as a function of the r.h.s.,

$$\frac{k_{No}}{15\delta} = f_{Zb}\left(\frac{30\kappa^2 A_b}{k_{No}}\right), \tag{2.24}$$

where, for any positive real number $r$, the function $f_{Zb}$ is defined implicitly via

$$f_{Zb}^{3/2}(r)\,\frac{|\mathcal{K}_1(f_{Zb}(r))|}{|\mathcal{K}_0(f_{Zb}(r))|} = \frac{1}{r}. \tag{2.25}$$

Figure 2-1 illustrates that $f_{Zb}(r)$ a decreasing function and hence the boundary layer thickness $\delta$ increases with increasing orbital amplitude $A_b$, and the ratio $\delta/k_{No}$ varies inversely with roughness $k_{No}$. To facilitate computation, the following explicit formula approximates $f_{Zb}(r)$,

$$f_{Zb}(r) = 10^{-0.0215(\log_{10} r)^2 - 0.6990(\log_{10} r) - 0.0509} + \epsilon, \tag{2.26}$$

with a relative error less than 1.4% and an absolute error $|\epsilon| < 0.0016$ for $1 < r < 10^4$. Once $\delta$ is found from (2.24), $u_{fo}$ is given by (1.123). Alternatively, eliminating $\delta$ from (2.24) and (1.123) gives

$$u_{fo} = \frac{\omega k_{No}}{30\kappa}\left(f_{Zb}\left(\frac{30\kappa^2 A_b}{k_{No}}\right)\right)^{-1}. \tag{2.27}$$

**Normalized friction velocity and roughness**

The normalized friction velocity is, from (1.123), (2.20), and (2.22),

$$u_f(x) = \frac{u_f'(x)}{u_{fo}} = \frac{\kappa A_b \omega}{u_{fo}}\left|U_1^{[1]}\right| \frac{\sqrt{Z_b}\,|\mathcal{K}_1(Z_b)|}{|\mathcal{K}_0(Z_b)|} = \frac{2\kappa^2 A_b}{\delta}\left|U_1^{[1]}\right| \frac{\sqrt{Z_b}\,|\mathcal{K}_1(Z_b)|}{|\mathcal{K}_0(Z_b)|}. \tag{2.28}$$

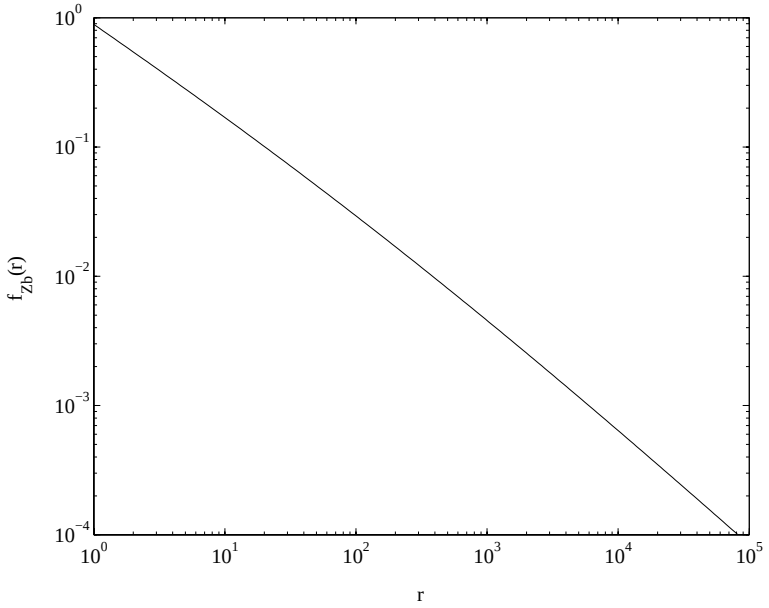


Figure 2-1: Plot of the function $f_{Zb}(r)$, defined in (2.25), used to compute the scaled roughness $Z_b$.

Eliminating $u_f(x)$ from Eqs. (2.14) and (2.28) gives

$$Z_b^{3/2}(x)\frac{|\mathcal{K}_1(Z_b(x))|}{|\mathcal{K}_0(Z_b(x))|}=\frac{k_N(x)}{\left|U_1^{[1]}(x)\right|}\frac{k_{No}}{30\kappa^2 A_b}. \tag{2.29}$$

As a check, note that in constant mean depth, when the flow velocity is maximum, i.e. $\left|U_1^{[1]}(x)\right|=1$, we have $u_f=1=k_N$ and each of (2.14) and (2.29) reduce to $Z_b=k_{No}/15\delta$. Also, comparing (2.29) with (2.23) shows that $Z_b(x)$ can be written in terms of the function $f_{Zb}(r)$ defined in (2.25),

$$Z_b=f_{Zb}\left(\frac{\left|U_1^{[1]}\right|}{k_N}\frac{30\kappa^2 A_b}{k_{No}}\right). \tag{2.30}$$

For flow over ripples, $k_N'$ can be measured directly or found from Eqs. (1.105) and (1.106) in §1.5. Substituting (1.105) and (1.106) into (2.30) gives

$$Z_b=f_{Zb}\left(\frac{1}{0.275-0.022\sqrt{\Psi_o}\left|U_1^{[1]}\right|}\frac{30\kappa^2}{4.13}\right). \tag{2.31}$$

If $\Psi_o$ is small (low or moderate flow intensity) or $\left|U_1^{[1]}\right|$ does not vary appreciably (weak reflection), then (2.31) implies $Z_b$ is approximately constant along the bed. In any case,

as the orbital amplitude $\left|U_1^{[1]}\right|$ increases, the argument of $f_{Zb}$ in Eq. (2.31) increases and, since $f_{Zb}$ is a decreasing function, $Z_b$ decreases. Once $Z_b$ is computed, $u_f$ is found from (2.14). Alternatively, substituting $Z_b$ and $\delta$ from (2.30), (1.123) into Eq. (2.14) and then substituting for $u_{fo}$ from (2.27) gives

$$u_f = k_N \frac{f_{Zb}\left(\frac{30\kappa^2 A_b}{k_{No}}\right)}{f_{Zb}\left(\frac{\left|U_1^{[1]}\right|}{k_N}\frac{30\kappa^2 A_b}{k_{No}}\right)}. \tag{2.32}$$

**Limit of small $Z_b$**

For flow motions large enough to move sediment, $Z_b$ is quite small. To see this, note that since $k_{No}$ ranges from the grain diameter to the ripple height, $A_b/k_{No}$ is large and hence (2.30) implies $Z_b(x)$ is small. At this point, most authors (e.g. Madsen 1994 [38], Mei [45]) take the limit $Z_b(x) \to 0$ and derive approximate formulae for the dependence of $u_f(x)$ on $Z_b(x)$. The reason is that, for small $Z$,

$$\mathcal{K}_0(Z) = \ker_0\left(2\sqrt{Z}\right) - i\,\mathrm{kei}_0\left(2\sqrt{Z}\right) = -\frac{1}{2}\ln(Z) - 0.5772 + \frac{i}{4} + O(Z\ln(Z)), \tag{2.33}$$

and hence

$$Z\frac{d\mathcal{K}_0}{dZ}\bigg|_{Z=0} = -\frac{1}{2}. \tag{2.34}$$

Thus, for small $Z_b$,

$$Z\frac{d\mathcal{K}_0}{dZ}\bigg|_{Z=Z_b} = -\frac{1}{2} + O(Z_b\ln(Z_b)).$$

This converges slowly; for $Z_b = 0.01$ the error can still be 10%. Furthermore, in the second order flow, some terms diverge as $Z \to 0$ so the evaluation must be made at $Z = Z_b$. We therefore do not take the limit $Z$, $Z_b \to 0$ in our theory.

### 2.1.4 Bottom shear stress

From the leading order boundary layer flow computed above, we compute the leading order terms in the bottom shear stress. The bottom shear stress is expressed in dimensionless form as a Shields parameter. From (1.100), (1.101) and (1.128), the time dependent Shields

parameter is given by

$$\frac{\Theta}{\Theta_o} = \frac{\tau'}{\rho u_{fo}^2} = \frac{1}{u_{fo}^2}\,\nu_e' \frac{\partial u'}{\partial \eta'}\bigg|_{\eta'=k_N'/30}. \tag{2.35}$$

Substituting the normalized variables from (1.131) – (1.133) gives

$$\frac{\Theta}{\Theta_o} = \frac{\kappa A_b \omega}{u_{fo}}\,\nu_e \frac{\partial u}{\partial \eta}\bigg|_{\eta=k_N'/30\delta}. \tag{2.36}$$

Substituting (2.15) into (2.36) and taking the time amplitude, denoted by hats, gives the leading order terms of the amplitude $\widehat{\Theta}$ of the Shields parameter $\Theta$,

$$\frac{\widehat{\Theta}}{\Theta_o} = \frac{\kappa A_b \omega}{u_{fo}}\left|\nu_e \frac{\partial u_1^{[1]}}{\partial \eta}\bigg|_{\eta=k_N'/30\delta}\right| + O(\varepsilon) = \frac{\kappa A_b \omega}{u_{fo}}\frac{u_f \left|U_1^{[1]}\right| \sqrt{Z_b}\,|\mathcal{K}_1(Z_b)|}{|\mathcal{K}_0(Z_b)|} + O(\varepsilon), \tag{2.37}$$

where parallel vertical lines indicate the modulus of a complex quantity and the absolute value of a real quantity. Combining (2.20) and (2.37), $\widehat{\Theta}$ is written simply as

$$\frac{\widehat{\Theta}}{\Theta_o} = u_f^2 + O(\varepsilon). \tag{2.38}$$

A simple expression is also derived for the leading order time dependent Shields parameter. To facilitate the analysis, we introduce the phase $\varpi$ which satisfies

$$e^{-i\varpi} = \frac{-|\mathcal{K}_0(Z_b)|\,\frac{d\mathcal{K}_0}{dZ}\Big|_{Z=Z_b} U_1^{[1]}}{\mathcal{K}_0(Z_b)\left|\frac{d\mathcal{K}_0}{dZ}\Big|_{Z=Z_b}\right|\left|U_1^{[1]}\right|}, \qquad e^{2i\varpi} = -i\frac{\mathcal{K}_1^*(Z_b)\,\mathcal{K}_0(Z_b)\,U_1^{[1]*}}{\mathcal{K}_1(Z_b)\,\mathcal{K}_0^*(Z_b)\,U_1^{[1]}}. \tag{2.39}$$

Substituting (2.15), (2.38), (2.39) into the shear stress (2.36) gives

$$\frac{\Theta}{\Theta_o} = u_f^2 \cos(t+\varpi) + O(\varepsilon). \tag{2.40}$$

**Grain roughness Shields parameter**

In §1.6, we outlined an empirical model for the bedload transport rate $q_B'$. The amplitude of $q_B'$ is $8Q_B'/3$, where $Q_B'$ is the mean bedload transport across a half cycle and is given empirically in Eq. (1.113) in terms of the grain roughness Shields parameter $\widehat{\Theta}_d$. The grain roughness Shields parameter $\widehat{\Theta}_d$ is defined in terms of the grain roughness, $k_N' = 2.5d$, rather than the actual bedform roughness (e.g. ripple height $\eta_r'$) on the seabed. This choice

is dictated by the empirical formula (1.113) for $Q'_B$; taking $k'_N$ other than $2.5d$ would require recomputing the empirical constants found by Nielsen [50] and Sleath [57]. For this special case, $k'_N = k_{No} = 2.5d$, Eqs. (2.27) and (2.32) become

$$u_{fo} = \frac{\omega d}{12\kappa}\left(f_{Zb}\left(\frac{12\kappa^2 A_b}{d}\right)\right)^{-1}, \qquad u_f = \frac{f_{Zb}\left(\frac{12\kappa^2 A_b}{d}\right)}{f_{Zb}\left(\left|U_1^{[1]}\right|\frac{12\kappa^2 A_b}{d}\right)}. \tag{2.41}$$

Substituting these into (1.128) and (2.38) gives

$$\Theta_{do} = \frac{1}{(s-1)\,gd}\left(\frac{\omega d}{12\kappa}\right)^2\left(f_{Zb}\left(\frac{12\kappa^2 A_b}{d}\right)\right)^{-2}, \qquad \frac{\widehat{\Theta}_d}{\Theta_{do}} = \left(\frac{f_{Zb}\left(\frac{12\kappa^2 A_b}{d}\right)}{f_{Zb}\left(\left|U_1^{[1]}\right|\frac{12\kappa^2 A_b}{d}\right)}\right)^2. \tag{2.42}$$

To avoid confusion, all instances of $Z_b$, $u_f$, and $u_{fo}$ that follow are computed with the equivalent roughness $k'_N$ given by Eq. (1.110) and based on the bedform geometry, unless otherwise noted. The only grain roughness quantities used are $\Theta_{do}$ and $\widehat{\Theta}_d$, defined in Eq. (2.42).

### 2.1.5 Second order flow : $O(\varepsilon)$ equations

The $O(\varepsilon)$ terms in the horizontal momentum equation are

$$\begin{aligned}\left\{\frac{\partial}{\partial t} - \frac{\partial}{\partial Z}\left(Z\frac{\partial}{\partial Z}\right)\right\}u_2 &= \Re\left\{\left(\frac{\partial U_1^{[1]}}{\partial t_1} + U_1^{[1]}\frac{\partial U_1^{[1]}}{\partial x} - iU_2^{[1]}\right)e^{-it} - 2iU_2^{[2]}e^{-2it}\right\} \\ &\quad - \frac{\partial u_1}{\partial t_1} - \left(u_1\frac{\partial}{\partial x} + w_1\frac{\partial}{\partial \eta}\right)u_1.\end{aligned} \tag{2.43}$$

Substituting (2.3), (2.13), (2.16) and (2.18), the r.h.s. of (2.43) can be written as

$$rhs = \Re\left\{-iU_2^{[1]}e^{-it} - 2iU_2^{[2]}e^{-2it}\right\} + rhs^{[0]} + \Re\left\{rhs^{[1]}e^{-it} + rhs^{[2]}e^{-2it}\right\},$$

where

$$\begin{aligned}rhs^{[0]} &= \frac{1}{2}\Re\left\{U_1^{[1]*}\frac{\partial U_1^{[1]}}{\partial x} - u_1^{[1]*}\frac{\partial u_1^{[1]}}{\partial x} - w_1^{[1]}\frac{\partial u_1^{[1]*}}{\partial \eta}\right\} \\ &= \frac{1}{2}\Re\left\{U_1^{[1]*}\frac{\partial U_1^{[1]}}{\partial x}\frac{\partial c_{01}}{\partial Z} + \frac{\left|U_1^{[1]}\right|^2}{Z_b}\frac{dZ_b}{dx}\frac{\partial c_{02}}{\partial Z} + \frac{\left|U_1^{[1]}\right|^2}{u_f}\frac{du_f}{dx}\frac{\partial c_{03}}{\partial Z}\right\},\end{aligned} \tag{2.44}$$

$$
\begin{aligned}
rhs^{[2]} &= \frac{1}{2}U_1^{[1]}\frac{\partial U_1^{[1]}}{\partial x} - \frac{1}{2}\left(u_1^{[1]}\frac{\partial u_1^{[1]}}{\partial x} + w_1^{[1]}\frac{\partial u_1^{[1]}}{\partial \eta}\right) \\
&= \frac{U_1^{[1]}}{2}\frac{\partial U_1^{[1]}}{\partial x}c_{04}\left(Z,Z_b\right) + \frac{U_1^{[1]2}}{2Z_b}\frac{dZ_b}{dx}c_{05}\left(Z,Z_b\right) + \frac{U_1^{[1]2}}{2u_f}\frac{du_f}{dx}c_{06}\left(Z,Z_b\right), \qquad (2.45)
\end{aligned}
$$

and the functions $c_{0n}\left(Z,Z_b\right)$ are given by

$$
\begin{aligned}
c_{01}\left(Z,Z_b\right) &= \int_Z^\infty \left(1 - \left|1 - \frac{\mathcal{K}_0\left(Z\right)}{\mathcal{K}_0\left(Z_b\right)}\right|^2 - \frac{F_1\left(Z,Z_b\right)}{\mathcal{K}_0^*\left(Z_b\right)}\frac{d\mathcal{K}_0^*}{dZ}\right)dZ, \\
c_{02}\left(Z,Z_b\right) &= \left(Z - Z_b + \frac{iZ_b}{\mathcal{K}_0^*\left(Z_b\right)}\left.\frac{d\mathcal{K}_0}{dZ}\right|_{Z_b}\right)\frac{\mathcal{K}_0^*\left(Z\right)}{\mathcal{K}_0^*\left(Z_b\right)} \qquad (2.46) \\
&\quad + \left(1 + \frac{Z_b}{\mathcal{K}_0\left(Z_b\right)}\left.\frac{d\mathcal{K}_0}{dZ}\right|_{Z_b}\right)\int_Z^\infty \frac{F_1}{\mathcal{K}_0^*\left(Z_b\right)}\frac{d\mathcal{K}_0^*}{dZ}dZ + \int_Z^\infty \frac{\mathcal{K}_0^*\left(Z\right)}{\mathcal{K}_0^*\left(Z_b\right)}dZ \\
&\quad - \frac{Z_b}{\mathcal{K}_0\left(Z_b\right)}\left.\frac{d\mathcal{K}_0}{dZ}\right|_{Z_b}\int_Z^\infty \left(\frac{\left(Z - Z_b\right)}{\mathcal{K}_0^*\left(Z_b\right)}\frac{d\mathcal{K}_0^*}{dZ} + \left(1 - \frac{\mathcal{K}_0^*\left(Z\right)}{\mathcal{K}_0^*\left(Z_b\right)}\right)\frac{\mathcal{K}_0\left(Z\right)}{\mathcal{K}_0\left(Z_b\right)}\right)dZ, \\
c_{03}\left(Z,Z_b\right) &= \left(Z - Z_b + \frac{iZ_b}{\mathcal{K}_0\left(Z_b\right)}\left.\frac{d\mathcal{K}_0}{dZ}\right|_{Z_b}\right)\frac{\mathcal{K}_0^*\left(Z\right)}{\mathcal{K}_0^*\left(Z_b\right)},
\end{aligned}
$$

$$
\begin{aligned}
c_{04}\left(Z,Z_b\right) &= 1 - \left(1 - \frac{\mathcal{K}_0\left(Z\right)}{\mathcal{K}_0\left(Z_b\right)}\right)^2 - \frac{F_1\left(Z,Z_b\right)}{\mathcal{K}_0\left(Z_b\right)}\frac{d\mathcal{K}_0}{dZ}, \\
c_{05}\left(Z,Z_b\right) &= \frac{Z_b}{\mathcal{K}_0\left(Z_b\right)}\left.\frac{d\mathcal{K}_0}{dZ}\right|_{Z_b}\left(\frac{1}{\mathcal{K}_0\left(Z_b\right)}\frac{d\mathcal{K}_0}{dZ}\left(F_1\left(Z,Z_b\right) - \left(Z - Z_b\right)\right)\right. \qquad (2.47) \\
&\quad \left. - \frac{\mathcal{K}_0\left(Z\right)}{\mathcal{K}_0\left(Z_b\right)} + \left(\frac{\mathcal{K}_0\left(Z\right)}{\mathcal{K}_0\left(Z_b\right)}\right)^2\right), \\
c_{06}\left(Z,Z_b\right) &= -\frac{F_1\left(Z,Z_b\right)}{\mathcal{K}_0\left(Z_b\right)}\frac{d\mathcal{K}_0}{dZ}.
\end{aligned}
$$

The derivatives of functions $c_{01}$, $c_{02}$, $c_{03}$ are written in (2.44) to facilitate later notation. The integrals in (2.46) are computed in Appendix 2.9.2. The term $rhs^{[1]}$ is not used here and hence is not listed.

Based on the form of the rhs of (2.43), we write the solution $u_2$ as

$$
u_2 = \frac{1}{2}\left(u_2^{[0]} + u_2^{[1]}e^{-it} + u_2^{[2]}e^{-2it} + *\right), \qquad (2.48)
$$

where $u_2^{[n]}$ depends on $x$, $y$, $x_1$, $y_1$, $t_1$, $\bar{t}$. It turns out later that only $u_2^{[0]}$ and $u_2^{[2]}$ are needed. The equations for $u_2^{[n]}$ are, from (2.43),

$$\frac{\partial}{\partial Z}\left(Z\frac{\partial u_2^{[n]}}{\partial Z}\right) + ni\left(u_2^{[n]} - U_2^{[n]}\right) = -rhs^{[n]}, \qquad n = 0, 2. \tag{2.49}$$

### 2.1.6 Eulerian current $u_2^{[0]}$

To include the effect of the inviscid current $U_2^{[0]}$, defined in (1.84) and (1.87), on the bed shear stress, we split the mean flow $u_2^{[0]}$ into two pieces,

$$u_2^{[0]} = u_{2W}^{[0]} + u_{2C}^{[0]} \tag{2.50}$$

where $u_{2W}^{[0]}$ is the Eulerian current in the boundary layer induced by the oscillatory components $u_1^{[1]}$ and $U_1^{[1]}$, and the component $u_{2C}^{[0]}$ is the current induced by the inviscid Eulerian current $U_2^{[0]}$. The current $u_{2W}^{[0]}$ satisfies (2.49) with $n = 0$,

$$\frac{\partial}{\partial Z}\left(Z\frac{\partial u_{2W}^{[0]}}{\partial Z}\right) = -rhs^{[0]}. \tag{2.51}$$

Integrating (2.51) once yields

$$Z\frac{\partial u_{2W}^{[0]}}{\partial Z} = \int_Z^\infty rhs^{[0]} dZ' + c_1. \tag{2.52}$$

Imposing the shear-free condition (2.10) gives $c_1 = 0$.

For the flow $u_{2C}^{[2]}$ induced by the inviscid current $U_2^{[0]}$, the transition from an inviscid current to a turbulent current is complicated. For the purpose of computing the bedload transport rate, our interest lies only in the bed shear stress, given in Eq. (2.58). We therefore make an order of magnitude estimate of the bed shear stress induced by $U_2^{[0]}$,

$$Z\frac{\partial u_{2C}^{[0]}}{\partial Z}\bigg|_{Z=Z_b} = \Lambda_2^{[0]} U_2^{[0]}, \tag{2.53}$$

where $\Lambda_2^{[0]}$ has order unity and acts as a fitting parameter in our theory. Thus, from (2.52)

and (2.53), the mean bed stress due to the Eulerian current $u_2^{[0]}$ is

$$\nu_e \frac{\partial u_2^{[0]}}{\partial \eta}\bigg|_{\eta=k_N'/30\delta} = u_f \, Z \frac{\partial u_2^{[0]}}{\partial Z}\bigg|_{Z=Z_b} = u_f \int_{Z_b}^{\infty} rhs^{[0]} dZ + u_f \Lambda_2^{[0]} U_2^{[0]}. \tag{2.54}$$

The last term is the effect of the inviscid mean flow $U_2^{[0]}$ on the bed shear stress. It is also important to note that since $rhs^{[0]}$ is divergent as $Z \to 0$, the shear stress must be evaluated at $Z = Z_b$ and not at $Z = 0$ (unlike boundary layer theories employing depth-independent eddy viscosities).

To compute the integral in the r.h.s. of (2.54), we integrate (2.44) to obtain

$$\begin{aligned} \int_{Z_b}^{\infty} rhs^{[0]}(Z,x)\, dZ &= \frac{1}{2}\Re\left\{ U_1^{[1]*} \frac{\partial U_1^{[1]}}{\partial x} c_{01}(Z_b, Z_b) \right. \\ &\left. + \frac{\left|U_1^{[1]}\right|^2}{Z_b}\frac{dZ_b}{dx} c_{02}(Z_b, Z_b) + \frac{\left|U_1^{[1]}\right|^2}{u_f}\frac{du_f}{dx} c_{03}(Z_b, Z_b) \right\}. \end{aligned} \tag{2.55}$$

From Eqs. (2.175) and (2.176) in Appendix 2.9.2, we have

$$c_{01}(Z_b, Z_b) = \frac{1+i}{\sqrt{2}}\sqrt{Z_b}\frac{\mathcal{K}_1^*(Z_b)}{\mathcal{K}_0^*(Z_b)} \tag{2.56}$$

$$\Re\{c_{02}(Z_b, Z_b)\} = 0 = \Re\{c_{03}(Z_b, Z_b)\}. \tag{2.57}$$

Substituting (2.56) and (2.57) into (2.55) and (2.54) gives the mean bed stress

$$\nu_e \frac{\partial u_2^{[0]}}{\partial \eta}\bigg|_{\eta=k_N'/30\delta} = \frac{u_f}{2}\Re\left\{ \frac{1+i}{\sqrt{2}}\sqrt{Z_b}\frac{\mathcal{K}_1^*(Z_b)}{\mathcal{K}_0^*(Z_b)} U_1^{[1]*}\frac{\partial U_1^{[1]}}{\partial x} \right\} + u_f \Lambda_2^{[0]} U_2^{[0]}, \tag{2.58}$$

where $\Lambda_2^{[0]}$ is a fitting parameter of order unity and $U_2^{[0]}$ is the inviscid current defined in (1.84) and (1.87).

### 2.1.7 Oscillatory flow component $u_2^{[2]}$

The second harmonic of the second order flow $u_2^{[2]}$ is found from (2.49),

$$\left\{ \frac{\partial^2}{\partial Z^2} + \frac{1}{Z}\frac{\partial}{\partial Z} + \frac{2i}{Z} \right\}\left( U_2^{[2]} - u_2^{[2]} \right) = \frac{rhs^{[2]}(x,Z)}{Z}. \tag{2.59}$$

From (2.8) and (2.9), the boundary conditions are

$$u_2^{[2]} = 0 \quad \text{on} \quad Z = Z_b, \tag{2.60}$$

$$u_2^{[2]} \to U_2^{[2]} \quad \text{as} \quad Z \to \infty. \tag{2.61}$$

The homogeneous solutions of (2.59) are $\mathcal{K}_0(2Z)$ and $\mathcal{I}_0(2Z)$. Thus (e.g. §1.9 of Hildebrand [25]),

$$\begin{aligned} U_2^{[2]} - u_2^{[2]} &= -\mathcal{K}_0(2Z) \int^Z \frac{rhs^{[2]}(x, Z')\, \mathcal{I}_0(2Z')}{ZW\left[\mathcal{K}_0(2Z), \mathcal{I}_0(2Z)\right]} dZ' \\ &\quad + \mathcal{I}_0(2Z) \int^Z \frac{rhs^{[2]}(x, Z')\, \mathcal{K}_0(2Z')}{ZW\left[\mathcal{K}_0(2Z), \mathcal{I}_0(2Z)\right]} dZ' \\ &\quad + c_1 \mathcal{K}_0(2Z) + c_2 \mathcal{I}_0(2Z), \end{aligned} \tag{2.62}$$

where the Wronskian is given by Hildebrand ([25], §1.10, Eq. (65)) by noting the coefficient $Z^{-1}$ of $\partial/\partial Z$ in (2.59),

$$W\left[\mathcal{K}_0(2Z), \mathcal{I}_0(2Z)\right] = 2\left(\mathcal{K}_0(2Z)\,\mathcal{I}_0'(2Z) - \mathcal{K}_0'(2Z)\,\mathcal{I}_0(2Z)\right) = \frac{1}{2} e^{-\int^Z Z^{-1} dZ} = \frac{1}{2Z}. \tag{2.63}$$

Substituting (2.63) into (2.62) gives

$$\begin{aligned} U_2^{[2]} - u_2^{[2]} &= -2\mathcal{K}_0(2Z) \int_{Z_b}^Z rhs^{[2]}\left(x, Z'\right) \mathcal{I}_0\left(2Z'\right) dZ' \\ &\quad + 2\mathcal{I}_0(2Z) \int_{Z_b}^Z rhs^{[2]}\left(x, Z'\right) \mathcal{K}_0\left(2Z'\right) dZ' \\ &\quad + c_1 \mathcal{K}_0(2Z) + c_2 \mathcal{I}_0(2Z). \end{aligned} \tag{2.64}$$

The integration constants $c_1$ and $c_2$ are found by imposing $u_2^{[2]} = 0$ at $Z = Z_b$ (the no-slip condition (2.60)) and $u_2^{[2]} \to U_2^{[2]}$ as $Z \to \infty$ (the matching condition (2.61)). As $Z \to \infty$, $\mathcal{K}_0(2Z) \to 0$ and $|\mathcal{I}_0(2Z)| \to \infty$ so that the matching condition (2.61) implies

$$c_2 = -2 \int_{Z_b}^\infty rhs^{[2]}\left(x, Z'\right) \mathcal{K}_0\left(2Z'\right) dZ'. \tag{2.65}$$

As $Z \to Z_b$, the integrals vanish, so that the no-slip condition (2.60) implies

$$c_1 = \frac{U_2^{[2]} - c_2 \mathcal{I}_0 (2Z_b)}{\mathcal{K}_0 (2Z_b)}. \tag{2.66}$$

Substituting $c_1$ and $c_2$ from (2.65), (2.66) into (2.64) gives

$$\begin{aligned} u_2^{[2]} &= \left(1 - \frac{\mathcal{K}_0 (2Z)}{\mathcal{K}_0 (2Z_b)}\right) U_2^{[2]} + 2\mathcal{K}_0 (2Z) \int_{Z_b}^{Z} rhs^{[2]} \left(x, Z'\right) \mathcal{I}_0 \left(2Z'\right) dZ' \\ &\quad + 2\mathcal{I}_0 (2Z) \int_{Z}^{\infty} rhs^{[2]} \left(x, Z'\right) \mathcal{K}_0 \left(2Z'\right) dZ' \\ &\quad - \frac{2\mathcal{K}_0 (2Z) \mathcal{I}_0 (2Z_b)}{\mathcal{K}_0 (2Z_b)} \int_{Z_b}^{\infty} rhs^{[2]} \left(x, Z'\right) \mathcal{K}_0 \left(2Z'\right) dZ'. \end{aligned} \tag{2.67}$$

It is easy to show that each term converges as $Z \to \infty$, since $rhs^{[2]}$ contains $\mathcal{K}_m (2Z)$ and not $\mathcal{I}_m (2Z)$.

To find the bottom shear stress, we differentiate (2.67) in $Z$, set $Z = Z_b$ and multiply by $Z_b$,

$$\begin{aligned} Z_b \left.\frac{\partial u_2^{[2]}}{\partial Z}\right|_{Z=Z_b} &= -\frac{1+i}{\sqrt{2}} \frac{U_2^{[2]} \sqrt{Z_b 2} \mathcal{K}_1 (2Z_b)}{\mathcal{K}_0 (2Z_b)} \\ &\quad + 2Z_b \left( \left.\frac{d\mathcal{I}_0 (2Z)}{dZ}\right|_{Z=Z_b} - \left.\frac{d\mathcal{K}_0 (2Z)}{dZ}\right|_{Z=Z_b} \frac{\mathcal{I}_0 (2Z_b)}{\mathcal{K}_0 (2Z_b)} \right) \\ &\quad \times \int_{Z_b}^{\infty} rhs^{[2]} \left(x, Z'\right) \mathcal{K}_0 \left(2Z'\right) dZ'. \end{aligned} \tag{2.68}$$

Eq. (2.68) can be simplified by using the Wronskian $W \left[\mathcal{K}_0 (2Z), \mathcal{I}_0 (2Z)\right]$ given in (2.63). Note that

$$\begin{aligned} Z_b \left( \left.\frac{d\mathcal{I}_0 (2Z)}{dZ}\right|_{Z=Z_b} - \left.\frac{d\mathcal{K}_0 (2Z)}{dZ}\right|_{Z=Z_b} \frac{\mathcal{I}_0 (2Z_b)}{\mathcal{K}_0 (2Z_b)} \right) &= Z_b \frac{W \left[\mathcal{K}_0 (2Z), \mathcal{I}_0 (2Z)\right]_{Z=Z_b}}{\mathcal{K}_0 (2Z_b)} \\ &= \frac{1}{2\mathcal{K}_0 (2Z_b)}. \end{aligned} \tag{2.69}$$

Substituting (2.69) into (2.68) gives

$$\begin{aligned}\nu_e \frac{\partial u_2^{[2]}}{\partial \eta}\bigg|_{\eta=\eta_0} &= u_f\, Z \frac{\partial u_2^{[2]}}{\partial Z}\bigg|_{Z=Z_b} \\ &= -\frac{1+i}{\sqrt{2}} \frac{u_f U_2^{[2]} \sqrt{Z_b} 2 \mathcal{K}_1(2Z_b)}{\mathcal{K}_0(2Z_b)} + \frac{u_f}{\mathcal{K}_0(2Z_b)} \int_{Z_b}^{\infty} rhs^{[2]}(x, Z')\, \mathcal{K}_0(2Z')\, dZ'.\end{aligned} \tag{2.70}$$

Substituting $rhs^{[2]}(x, Z)$ from (2.45) gives

$$\begin{aligned}\nu_e \frac{\partial u_2^{[2]}}{\partial \eta}\bigg|_{\eta=\eta_0} &= -\frac{(1+i)\, u_f U_2^{[2]} \sqrt{Z_b} \mathcal{K}_1(2Z_b)}{\mathcal{K}_0(2Z_b)} \\ &+ \frac{u_f}{2} U_1^{[1]} \frac{\partial U_1^{[1]}}{\partial x} \int_{Z_b}^{\infty} c_{04}(Z, Z_b) \frac{\mathcal{K}_0(2Z)}{\mathcal{K}_0(2Z_b)} dZ \\ &+ \frac{1}{2} \left(U_1^{[1]}\right)^2 \frac{u_f}{Z_b} \frac{dZ_b}{dx} \int_{Z_b}^{\infty} c_{05}(Z, Z_b) \frac{\mathcal{K}_0(2Z)}{\mathcal{K}_0(2Z_b)} dZ \\ &+ \frac{1}{2} \left(U_1^{[1]}\right)^2 \frac{du_f}{dx} \int_{Z_b}^{\infty} c_{06}(Z, Z_b) \frac{\mathcal{K}_0(2Z)}{\mathcal{K}_0(2Z_b)} dZ,\end{aligned} \tag{2.71}$$

where the $c_{0n}(Z, Z_b)$ are listed above in Eq. (2.46). The integrals in (2.71) are expanded and given in terms of three simpler integrals that must be computed numerically, in Eqs. (2.177) – (2.179) in Appendix 2.9.2.

### 2.1.8 Bottom shear stress

From the flow components computed above, we compute the bottom shear stress of the flow on the seabed, expressed in dimensionless form as a Shields parameter. From (2.36), the time dependent Shields parameter is given by

$$\begin{aligned}\frac{\Theta}{\Theta_o} &= \frac{\kappa A_b \omega}{u_{fo}}\, \nu_e \frac{\partial u}{\partial \eta}\bigg|_{\eta=\left(k_N'/30\delta\right)} \\ &= \frac{\kappa A_b \omega}{u_{fo}}\, \Re\left\{ \nu_e \frac{\partial u_1^{[1]}}{\partial \eta}\bigg|_{\eta=\left(k_N'/30\delta\right)} e^{-it} + \varepsilon\, \nu_e \frac{\partial u_2^{[0]}}{\partial \eta}\bigg|_{\eta=\left(k_N'/30\delta\right)} \right. \\ &\qquad \left. + \varepsilon\, \nu_e \frac{\partial u_2^{[1]}}{\partial \eta}\bigg|_{\eta=\left(k_N'/30\delta\right)} e^{-it} + \varepsilon\, \nu_e \frac{\partial u_2^{[2]}}{\partial \eta}\bigg|_{\eta=\left(k_N'/30\delta\right)} e^{-2it} \right\}.\end{aligned} \tag{2.72}$$

The individual components of stress are given in (2.15), (2.54) and (2.71).

## 2.2 Mean bedload transport rate

Using the shear stress components computed in the previous section, we find the corresponding mean bedload transport rate. Taking the time average, denoted by bars, of (1.138) over a wave cycle and expanding in powers of $\varepsilon$ (recall $\partial h'/\partial x' = O(\varepsilon)$) gives

$$\overline{q_B} = \frac{Q_B}{\widehat{\Theta}^4}\overline{|\Theta|^3\,\Theta} + \frac{\varepsilon Q_B}{\tan\psi_m}\left(\frac{\partial H}{\partial x_1} - \frac{\partial h}{\partial x}\right)\frac{\overline{|\Theta|^4}}{\widehat{\Theta}^4} + O\left(\varepsilon^2\right). \tag{2.73}$$

From (2.40), $\Theta$ is simple harmonic to leading order,

$$\frac{\Theta}{\Theta_o} = u_f^2\cos\left(t+\varpi\right) + O\left(\varepsilon\right). \tag{2.74}$$

The time averages in Eq. (2.73) involve integrals of powers of $|\cos t|$. We now review the pertinent integral relations. Since $\cos t$ and $\sin t$ are $2\pi$-periodic, then for any continuous function $f$ and any real numbers $a$ and $b$,

$$\begin{aligned}
\overline{f\left(\cos n\left(t+a\right),\sin m\left(t+a\right)\right)} &= \frac{1}{2\pi}\int_0^{2\pi} f\left(\cos n\left(t+a\right),\sin m\left(t+a\right)\right)dt \qquad (2.75)\\
&= \frac{1}{2\pi}\int_{-a}^{2\pi-a} f\left(\cos s,\sin s\right)ds, \qquad s = t+a,\\
&= \frac{1}{2\pi}\int_{b}^{2\pi+b} f\left(\cos s,\sin s\right)ds,\\
&= \overline{f\left(\cos nt,\sin mt\right)}.
\end{aligned}$$

Thus, any time interval of length $2\pi$ can be used to compute the time average. Also, for any positive integers $n$, $m$, since $|\cos t|$ is an even function of $t$ and since $\sin mt$ is odd,

$$\overline{|\cos t|^n\sin mt} = \int_{-\pi}^{\pi}|\cos t|^n\sin mt\,dt = 0. \tag{2.76}$$

Next, for any $n > 0$,

$$\overline{|\cos t|^n\cos t} = \int_{-\pi/2}^{3\pi/2}|\cos t|^n\cos t\,dt = \int_{-\pi/2}^{\pi/2}|\cos t|^n\cos t\,dt + \int_{\pi/2}^{3\pi/2}|\cos t|^n\cos t\,dt.$$

Making the change of variable $s = t - \pi$ in the second integral gives

$$\overline{|\cos t|^n \cos t} = \int_{-\pi/2}^{\pi/2} |\cos t|^n \cos t \, dt - \int_{-\pi/2}^{\pi/2} |\cos s|^n \cos s \, ds = 0. \tag{2.77}$$

Combining (2.76) with $m = 1$ and (2.77) gives

$$\overline{|\cos t|^n e^{-it}} = \overline{|\cos t|^n \cos t} - i\overline{|\cos t|^n \sin t} = 0. \tag{2.78}$$

Lastly, it is easy to show that

$$\overline{|\cos t|^3} = \frac{4}{3\pi}, \qquad \overline{|\cos t|^3 \cos 2t} = \frac{4}{5\pi}, \qquad \overline{|\cos t|^4} = \frac{3}{8}. \tag{2.79}$$

For $m = 2$ and $n = 3$, combining (2.76) and the second equality in (2.79) gives

$$\overline{|\cos t|^3 e^{-2it}} = \overline{|\cos t|^3 \cos 2t} - i\overline{|\cos t|^3 \sin 2t} = \frac{4}{5\pi}. \tag{2.80}$$

Note that from (2.74) and results (2.75) and (2.77),

$$\overline{|\Theta|^3 \Theta} = u_f^8 \overline{|\cos(t+\varpi)|^3 \cos(t+\varpi)} + O(\varepsilon) = 0 + O(\varepsilon). \tag{2.81}$$

Substituting (2.81) into (2.73) gives $\overline{q_B} = O(\varepsilon)$, i.e. the bedload transport $q_B$ averages to zero at leading order. This is a consequence of the flow being monochromatic. To compute the $O(\varepsilon)$ terms in $\overline{|\Theta|^3 \Theta}$, Eq. (2.72) is used,

$$\begin{aligned} \frac{\overline{|\Theta|^3 \Theta}}{\Theta_o^4} &= \varepsilon \frac{4\kappa A_b \omega \, u_f^6}{u_{fo}} \Re \left\{ \nu_e \frac{\partial u_2^{[0]}}{\partial \eta}\bigg|_{\eta=\left(k_N'/30\delta\right)} \overline{|\cos(t+\varpi)|^3} \right. \\ &\quad + \nu_e \frac{\partial u_2^{[1]}}{\partial \eta}\bigg|_{\eta=\left(k_N'/30\delta\right)} \overline{|\cos(t+\varpi)|^3 e^{-it}} \\ &\quad \left. + \nu_e \frac{\partial u_2^{[2]}}{\partial \eta}\bigg|_{\eta=\left(k_N'/30\delta\right)} \overline{|\cos(t+\varpi)|^3 e^{-2it}} \right\} + O\left(\varepsilon^2\right). \end{aligned} \tag{2.82}$$

Computing the time averages on the first, second and third lines of (2.82) from Eqs. (2.79),

(2.78) and (2.80), respectively, gives

$$\frac{\overline{|\Theta|^3\,\Theta}}{\Theta_o^4} = \varepsilon\,\frac{16\kappa A_b\omega u_f^6}{\pi u_{fo}}\,\Re\left\{\frac{1}{3}\,\nu_e\frac{\partial u_2^{[0]}}{\partial\eta}\bigg|_{\eta=\left(k_N'/30\delta\right)} + \frac{e^{2i\varpi}}{5}\,\nu_e\frac{\partial u_2^{[2]}}{\partial\eta}\bigg|_{\eta=\left(k_N'/30\delta\right)}\right\} + O\left(\varepsilon^2\right). \tag{2.83}$$

Lastly, from (2.74) and the last equality of (2.79),

$$\frac{\overline{|\Theta|^4}}{\widehat{\Theta}^4} = \overline{|\cos\left(t+\varpi\right)|^4} + O\left(\varepsilon\right) = \frac{3}{8} + O\left(\varepsilon\right). \tag{2.84}$$

The mean bedload transport $\overline{q_B}$ is found by substituting (2.38), (2.83) and (2.84) into (2.73),

$$\frac{\overline{q_B}}{(1-\mathcal{N})} = \varepsilon q_\tau + \varepsilon D_\nu\left(\frac{\partial H}{\partial x_1} - \frac{\partial\widetilde{h}}{\partial x}\right) + O\left(\varepsilon^2\right), \tag{2.85}$$

where

$$D_\nu = \frac{3Q_B}{8\left(1-\mathcal{N}\right)\tan\psi_m}, \tag{2.86}$$

$$q_\tau = \frac{16\kappa A_b\omega}{5\pi(1-\mathcal{N})u_{fo}}\frac{Q_B}{u_f^2}\,\Re\left\{\frac{5}{3}\,\nu_e\frac{\partial u_2^{[0]}}{\partial\eta}\bigg|_{\eta=\left(k_N'/30\delta\right)} + e^{2i\varpi}\,\nu_e\frac{\partial u_2^{[2]}}{\partial\eta}\bigg|_{\eta=\left(k_N'/30\delta\right)}\right\}, \tag{2.87}$$

$$Q_B = \left(\frac{\widehat{\Theta}_d-\Theta_c}{\Theta_{do}}\right)^{3/2}\mathrm{Hv}\left(\frac{\widehat{\Theta}_d-\Theta_c}{\Theta_{do}}\right), \tag{2.88}$$

where $\widehat{\Theta}_d$ is given in (2.42) and $\Theta_c$ in (1.115). Note that we do not need the first time harmonic of $u_2$ to compute $\overline{q_B}$. Furthermore, since $\overline{q_B} = O\left(\varepsilon\right)$, only the leading order terms in $Q_B$ (and hence $\widehat{\Theta}_d$) are required, to the order of accuracy retained.

Substituting (2.28), (2.54), (2.71), and (2.38) into (2.87) gives

$$\begin{aligned} q_\tau \;=\; & \frac{16\kappa A_b\omega}{5\pi(1-\mathcal{N})u_{fo}}\frac{Q_B}{u_f}\left(\Re\left\{M_1\left(Z_b\right)U_1^{[1]*}\frac{\partial U_1^{[1]}}{\partial x} + M_2\left(Z_b\right)\frac{U_1^{[1]*}U_2^{[2]}}{U_1^{[1]}}\right\}\right. \\ & \left. + \frac{5}{3}\Lambda_2^{[0]}U_2^{[0]} + M_3\left(Z_b\right)\frac{\left|U_1^{[1]}\right|^2}{Z_b}\frac{dZ_b}{dx} + M_4\left(Z_b\right)\frac{\left|U_1^{[1]}\right|^2}{u_f}\frac{du_f}{dx}\right), \end{aligned} \tag{2.89}$$

where

$$M_1\left(Z_b\right) = \frac{5\left(1+i\right)\sqrt{2Z_b}\mathcal{K}_1^*\left(Z_b\right)}{12\mathcal{K}_0^*\left(Z_b\right)} - \frac{i}{2}\frac{\mathcal{K}_1^*\left(Z_b\right)\mathcal{K}_0\left(Z_b\right)}{\mathcal{K}_1\left(Z_b\right)\mathcal{K}_0^*\left(Z_b\right)}\int_{Z_b}^{\infty} c_{04}\left(Z,Z_b\right)\frac{\mathcal{K}_0\left(2Z\right)}{\mathcal{K}_0\left(2Z_b\right)}dZ, \tag{2.90}$$

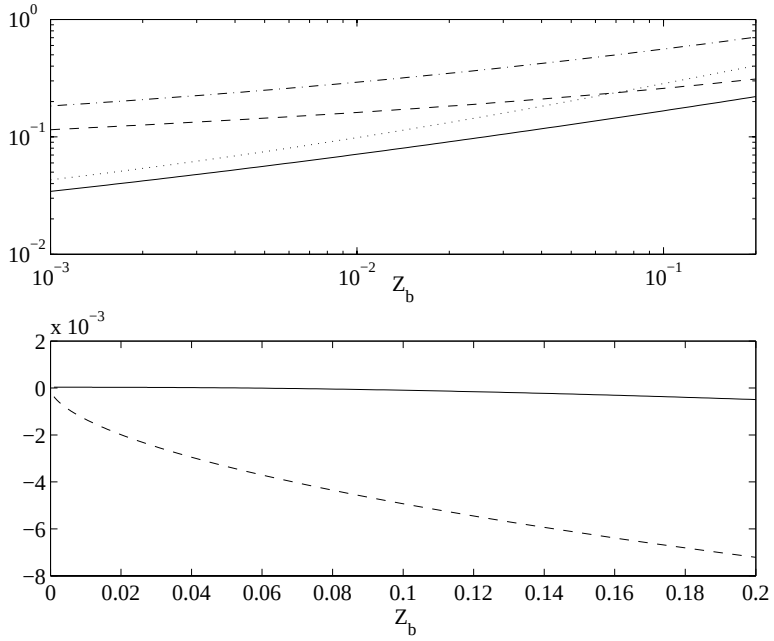


Figure 2-2: The functions $M_n(Z_b)$ in the bedload forcing $q_\tau$. In the top plot, $\Re(M_1)$ (solid), $-\Im(M_1)$ (dash), $\Re(M_2)$ (dash-dot), $\Im(M_2)$ (dot). In the bottom plot, $M_3$ (solid) and $M_4$ (dash).

$$M_2\left(Z_b\right) = -\frac{\left(1-i\right)\sqrt{Z_b}\mathcal{K}_1\left(2Z_b\right)\mathcal{K}_1^*\left(Z_b\right)\mathcal{K}_0\left(Z_b\right)}{\mathcal{K}_0\left(2Z_b\right)\mathcal{K}_1\left(Z_b\right)\mathcal{K}_0^*\left(Z_b\right)}, \tag{2.91}$$

$$M_3\left(Z_b\right) = \Re\left\{-\frac{i}{2}\frac{\mathcal{K}_1^*\left(Z_b\right)\mathcal{K}_0\left(Z_b\right)}{\mathcal{K}_1\left(Z_b\right)\mathcal{K}_0^*\left(Z_b\right)}\int_{Z_b}^{\infty} c_{05}\left(Z, Z_b\right)\frac{\mathcal{K}_0\left(2Z\right)}{\mathcal{K}_0\left(2Z_b\right)}dZ\right\}, \tag{2.92}$$

$$M_4\left(Z_b\right) = \Re\left\{-\frac{i}{2}\frac{\mathcal{K}_1^*\left(Z_b\right)\mathcal{K}_0\left(Z_b\right)}{\mathcal{K}_1\left(Z_b\right)\mathcal{K}_0^*\left(Z_b\right)}\int_{Z_b}^{\infty} c_{06}\left(Z, Z_b\right)\frac{\mathcal{K}_0\left(2Z\right)}{\mathcal{K}_0\left(2Z_b\right)}dZ\right\}. \tag{2.93}$$

From (2.14), the derivative of $Z_b$ can be written in terms of the derivatives of the friction velocity $u_f$ and the equivalent roughness $k_N$,

$$\frac{dZ_b}{dx} = \frac{d}{dx}\left(\frac{Z_{bo}k_N}{u_f}\right) = Z_b\left(\frac{1}{k_N}\frac{dk_N}{dx} - \frac{1}{u_f}\frac{du_f}{dx}\right). \tag{2.94}$$

The functions $M_n\left(Z_b\right)$ are given in terms of three simpler integrals in Eqs. (2.177) – (2.179) in Appendix 2.9.2, and are plotted in Figure 2-2. It is apparent that $M_1$, $M_2$ are significantly larger than the coefficients $M_3$, $M_4$ of the terms with $dZ_b/dx$ and $du_f/dx$ in the bedload forcing $q_\tau$.

## 2.3 Sand bar equation

Using the formula for mean bedload transport derived in the previous section, we derive an equation for the evolution of sand bars of coarse grains. Substituting the scales in (1.133) into the equation for conservation of sediment mass (1.120) and ignoring suspended sediment terms gives

$$\frac{\partial h}{\partial t} = \frac{1}{\alpha_1 \varepsilon} \frac{\partial q_B}{\partial x}, \tag{2.95}$$

where

$$\alpha_1 = \frac{A_b \omega}{8 \varepsilon \Theta_{do}^{3/2} K \sqrt{(s-1)\, g d^3}}. \tag{2.96}$$

In the parameter regime of interest, the characteristic grain roughness Shields parameter $\Theta_{do} \precsim O(1)$ and hence $\alpha_1 = O\left(\varepsilon^{-4.5}\right)$ and $\partial h/\partial t = O\left(\varepsilon^{3.5}\right)$. Thus $h$ is independent of the short wave time $t$ and varies over a much longer timescale $\bar{t}$ such that $\bar{t}/t \precsim O\left(\varepsilon^{3.5}\right)$. Recall that we split the depth $h$ into its mean $H(x_1)$ and sand bar component $\widetilde{h}$ via Eq. (1.134). Time averaging Eq. (2.95) over a wave period and substituting $h$ from (1.134) and the mean bedload transport rate $q_B$ from (2.85) gives

$$\frac{\partial \widetilde{h}}{\partial \bar{t}} - \frac{\partial}{\partial x}\left(D_\nu \frac{\partial \widetilde{h}}{\partial x}\right) = -\frac{\partial}{\partial x}\left(q_\tau + D_\nu \frac{dH}{dx_1}\right). \tag{2.97}$$

Eq. (2.97) governs the evolution of the sand bar elevation $\widetilde{h}$ over the long time $\bar{t} = t/\alpha_1$. The gravity driven diffusivity $D_\nu$ is given in Eq. (2.86). The forcing $-\partial q_\tau/\partial x$ is due to bedload transport, where $q_\tau$ is given in Eq. (2.89).

Yu & Mei [70] derived an equation similar in form to (2.97), but used the Shields parameter $\widehat{\Theta}$ based on the bedform roughness to compute $Q_B$. As noted in §1.6, the grain roughness Shields parameter $\widehat{\Theta}_d$ is the proper Shields parameter with which to compute $Q_B$, the scaled mean bedload transport over a half period. Since $Q_B$ multiplies both the diffusivity and bedload forcing in the sand bar equation (2.97), many of our conclusions differ from those of Yu & Mei.

It is important to note that the bedload forcing $-\partial q_\tau/\partial x$ (see Eqs. (2.87) and (2.89)) is proportional not only to the 3/2 power of the leading order stresses via $\widehat{\Theta}_d$ in $Q_B$, but also to the *second order* stresses. In other words, when the leading order flow is monochromatic, any second order effect in the flow field will have a leading order effect on $q_\tau$ and, via Eq.

(2.97), the sand bar evolution. In the laboratory, this means that the weak return flow and any wave-maker induced free harmonics can have a significant effect on bar formation.

The mean seabed slope $dH/dx_1$ adds a downslope forcing term to the sand bar equation (2.97). This effect is derived from the downslope gravitational pull on sediment particles on a slope, included in the bedload transport formula (1.112).

### 2.3.1 Review of constant parameters

In this section we outline the calculation of the constant parameters. The parameters that must be specified are the wave period $T$ (or the angular frequency $\omega = 2\pi/T$), the incident wave amplitude $A_o$, the reflection coefficient at the shoreline or seawall $R_L$, the sediment grain diameter $d$, the length of the bar patch $L'$ and the typical water depth $H_o$. Auxiliary constants are the porosity $\mathcal{N} = 0.3$, the gravitational acceleration $g = 9.81$ m/s$^2$, the Kármán constant $\kappa = 0.41$, the angle of repose $\psi_m = 30^o$ and the properties of fresh water: at $20^o$ C, density $\rho = 1.00$ g/cm$^3$, kinematic viscosity $\nu = 0.0101$ cm$^2$/s and sediment specific gravity $s = 2.65$. For seawater, the salinity alters slightly the water density, viscosity and sediment specific gravity: at $15^o$C, $\rho = 1.03$ g/cm$^3$, $\nu = 0.0115$ cm/sec$^2$, $s = 2.57$.

With $\omega = 2\pi/T$, we compute the typical wavenumber $K$ from the dispersion relation (1.1),

$$\omega^2 = gK \tanh KH_o.$$

From $A_o$, $R_L$, $K$ we compute $A_b$ from (1.2),

$$A_b = \frac{A_o\left(1 + |R_L|\right)}{\sinh\left(KH_o\right)}.$$

The wave slope is $\varepsilon = KA_b$. From (2.42), the characteristic grain roughness Shields parameter is

$$\Theta_{do} = \frac{1}{(s-1)\,gd}\left(\frac{\omega d}{12\kappa}\right)^2\left(f_{Zb}\left(\frac{12\kappa^2 A_b}{d}\right)\right)^{-2},$$

where the function $f_{Z_b}$ is defined in (2.25) and a fitting formula is given in (2.26),

$$f_{Zb}\left(r\right) = 10^{-0.0215(\log_{10} r)^2 - 0.6990(\log_{10} r) - 0.0509} + \epsilon,$$

with a relative error less than 1.4% and an absolute error $|\epsilon| < 0.0016$ for $1 < r < 10^4$. The critical Shields parameter $\Theta_{C0}$ for incipient motion on a flat bed is found from the modified

Shields diagram, or, equivalently, Madsen [39]'s formula (1.102). From Eq. (2.96),

$$\alpha_1 = \frac{A_b \omega}{8\varepsilon \Theta_{do}^{3/2} K \sqrt{(s-1)\, g d^3}}.$$

The ripple height $\eta_r'$ and relative roughness $k_N'$ and their characteristic values $\eta_{ro}$ and $k_{No}$ are either measured directly from experiments or predicted from empirical formulae (see §2.1.3 and Appendix 1.9.1). From $k_{No}$ and $A_b$, we compute $\delta$ from (2.24),

$$\delta = \frac{k_{No}}{15} \left( f_{Zb} \left( \frac{30\kappa^2 A_b}{k_{No}} \right) \right)^{-1},$$

and $u_{fo} = \delta\omega/(2\kappa)$ from (1.123). The characteristic value of the Shields parameter is then given by (1.128),

$$\Theta_o = \frac{u_{fo}^2}{(s-1)\, g d}.$$

We can now compute all the parameters given $T$, $A_o$, $R_L$, $d$ and $H_o$. Three sample calculations are presented in Table 2.1. For the parameters used, the left hand side of Sleath's criterion for turbulence, Eq. (1.90), is between 405 and 3651, and the values of $\mathsf{R}_{FT}$ are all significantly greater than 100, indicating the corresponding boundary layers are all fully rough turbulent.

Recall that in §1.6 we argued that the grain roughness Shields parameter $\widehat{\Theta}_d$, with typical value $\Theta_{do}$, must be used to estimate the mean bedload transport $Q_B'$ over a half cycle, rather than the Shields parameter $\widehat{\Theta}$, with scale $\Theta_o$, based on the bedform roughness. Note that in Table 2.1, $\Theta_o$ is roughly ten times larger than $\Theta_{do}$. Thus, using $\widehat{\Theta}$ instead of $\widehat{\Theta}_d$ to compute $Q_B'$ would lead to a large overestimation of the bedload transport.

In Figures 2-3 and 2-4, the sand bar time scale $\alpha_1/\omega$ is plotted for various parameter values, for both laboratory and field conditions. Figure 2-3 illustrates that in the lab, sand bars form over a day or so; in the field, they form over tens of days. All else being equal, bars form more quickly under larger waves (precisely, larger $A_b$) and form more slowly for finer sediment. Figure 2-4 elucidates the dependence of $\alpha_1/\omega$ on the wave slope $\varepsilon = KA_b$ and on the dispersion parameter $KH$. Bars under steeper waves or in shallower water grow more quickly. Note that the curves in 2-3 and 2-4 do not depend on the ripple geometry, since only the grain roughness $2.5d$ is required to compute $\alpha_1$.

We should point out that the slope of the lines in the log-log plot in Figure 2-4($i$)

| Test | $T$ [s] | $H_o$ [cm] | $A_o$ [cm] | $R_L$ | $d$ [mm] | $\eta_{ro}$ [cm] | $\eta_{ro}/\lambda_{ro}$ |
|---|---|---|---|---|---|---|---|
| 1 | 2.5 | 60 | 6.36 | 0.1 | 0.20 | 2.00 | 0.20 |
| 2 | 8.0 | 600 | 40 | 0.25 | 0.50 | 9.81 | 0.16 |
| 3 | 8.0 | 600 | 40 | 0.25 | 0.20 | 4.20 | 0.11 |

| Test | $\lambda$ [m] | $\delta$ [cm] | $\alpha_1/\omega$ [days] | $A_b\omega$ [cm/s] | $u_f$ [cm/s] | $w_S$ [cm/s] | $\eta_{ro}(N)$ [cm] |
|---|---|---|---|---|---|---|---|
| 1 | 5.67 | 2.12 | 1.74 | 24.6 | 6.67 | 2.02 | 1.73 |
| 2 | 57.5 | 13.9 | 25.4 | 55.8 | 13.6 | 6.42 | 9.81 |
| 3 | 57.5 | 11.2 | 37.6 | 55.8 | 11.0 | 2.02 | 4.20 |

| Test | $\varepsilon$ | $KH_o$ | $\Theta_{c0}$ | $\Theta_{do}$ | $\Theta_o$ | $Z_b$ | $\mathsf{R}_E$ | $\mathsf{R}_{FT}$ | Eq. (1.90) |
|---|---|---|---|---|---|---|---|---|---|
| 1 | 0.11 | 0.66 | 0.053 | 0.153 | 1.38 | 0.25 | 24121 | 5512 | 405 |
| 2 | 0.08 | 0.66 | 0.034 | 0.224 | 2.29 | 0.19 | 396604 | 55236 | 3651 |
| 3 | 0.08 | 0.66 | 0.053 | 0.431 | 3.72 | 0.10 | 396604 | 19021 | 1865 |

Table 2.1: Sample calculations for constant parameters. The values of $\mathsf{R}_E$, $\mathsf{R}_{FT}$ and the l.h.s. of Eq. (1.90) indicate the boundary layers in all tests are fully rough turbulent.

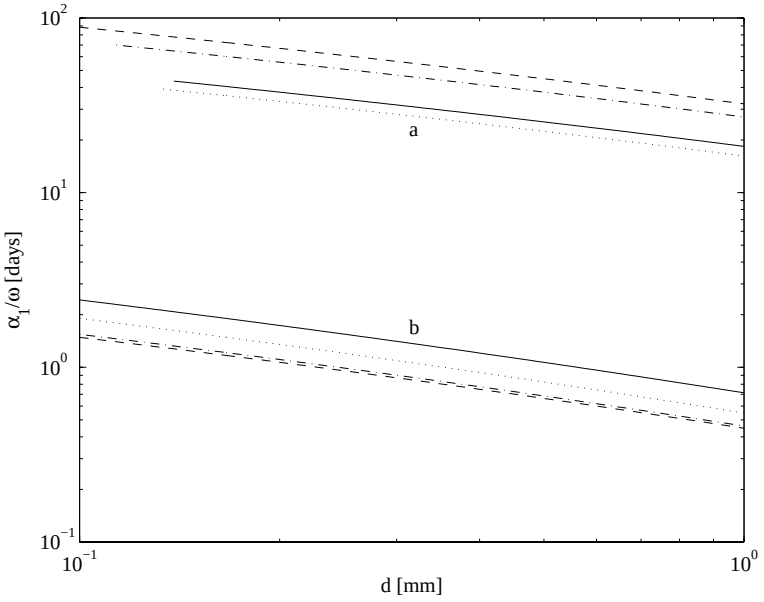


Figure 2-3: Dependence of the time scale for sand bar evolution $\alpha_1/\omega$ on the grain diameter $d$, for various parameter sets. Field conditions are plotted in group (a), with $T = 8$ s, $H_o = 6$ m, $A_o(1+|R_L|) = 50$ cm (solid); the other curves have these values except $A_o(1+|R_L|) = 50$ cm (dash), $H_o = 7$ m (dash-dot), $T = 7.5$ s (dot). Lab conditions are plotted in group (b), with $T = 2.5$ s, $H_o = 60$ cm, $A_o(1 + |R_L|) = 7$ cm (solid); the other curves have these values, except $A_o(1 + |R_L|) = 8.5$ cm (dash), $H_0 = 50$ cm (dash-dot), $T = 2.2$ s (dot).

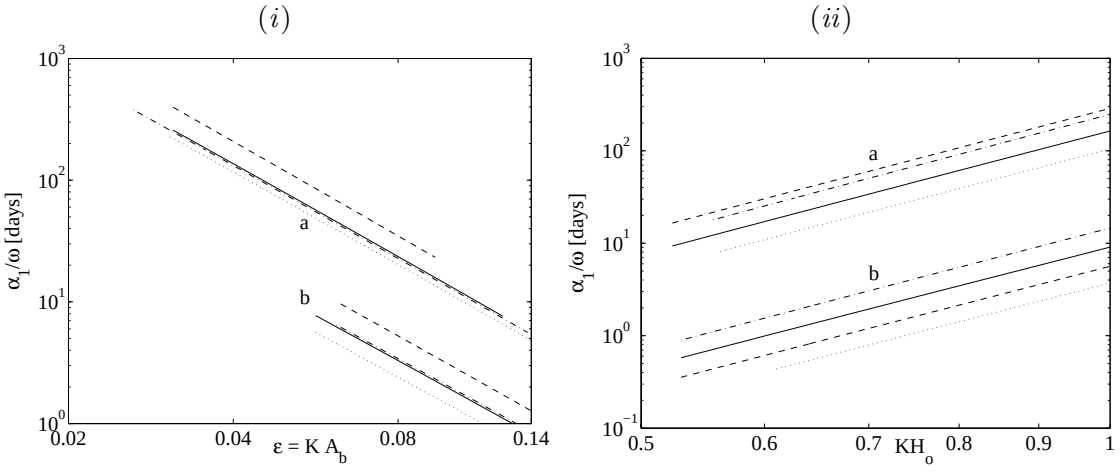


Figure 2-4: $(i)$ Dependence of the time scale for sand bar evolution $\alpha_1/\omega$ on the wave slope $\varepsilon$, for various parameter sets. Field conditions are plotted in group (a), with $T = 8$ s, $H_o = 6$ m, $d = 0.5$ mm (solid); the other curves have these values, except $d = 0.2$ mm (dash), $H_o = 7$ m (dash-dot), $T = 7.5$ s (dot). Lab conditions are plotted in group (b), with $T = 2.5$ s, $H_0 = 60$ cm, $d = 0.25$ mm (solid); the other curves have these values, except $d = 0.10$ mm (dash), $H_o = 50$ cm (dash-dot), $T = 2.2$ s (dot).

$(ii)$ Dependence of the time scale for sand bar evolution $\alpha_1/\omega$ on the dispersion parameter $KH_o$, for various parameter sets. Field conditions are plotted in group (a), with $T = 8$ s, $A_o(1 + |R_L|) = 50$ m, $d = 0.5$ mm (solid); the other curves have these values, except $A_o(1 + |R_L|) = 40$ cm (dash), $d = 0.2$ mm (dash-dot), $T = 7.5$ s (dot). Lab conditions are plotted in group (b), with $T = 2.5$ s, $A_o(1 + |R_L|) = 50$ cm, $d = 0.25$ mm (solid); the other curves have these values, except $A_o(1 + |R_L|) = 8.5$ cm (dash), $d = 0.10$ mm (dash-dot), $T = 2.2$ s (dot).

are approximately $-2.5$, in other words, the curves suggest $\alpha_1 = O(\varepsilon^{-2.5})$, which seems to contradict our scaling argument that $\alpha_1 = O(\varepsilon^{-4.5})$. The apparent discrepancy arises because the empirical formula (1.105) for the ripple height $\eta_r/A_b$ approaches a small, but constant value 0.275 for small wave intensity (i.e. small $\Psi$), rather than decreasing with wave slope via $\eta_r/A_b = O(\varepsilon)$ as our scaling assumption assumes. Thus, there is really no discrepancy; it is just that the empirical formula is written in terms of constants, rather than the wave slope. In the parameter regime of interest, $\eta_r/A_b$ and $\varepsilon$ are similar in numerical value.

Lastly, note that no sediment motion occurs below the critical Shields parameter $\Theta_c$ and our theory is invalid in shallow water; hence $A_b$, $K$ and $\varepsilon = KA_b$ cannot be taken arbitrarily small. This is the reason some of the curves in Figures 2-4$(i)$, $(ii)$ do not extend across the entire domain of $\varepsilon$ or $KH$. Similarly, we have limited our scope to rippled flow, and hence we halt the computation if the wave intensity (or mobility number $\Psi$) becomes

too large for ripples to be maintained (for a discussion, see §1.5).

## 2.4 Bars of coarse sand under perfectly tuned monochromatic waves

This section contains a detailed discussion of bedload dominated sand bar evolution under perfectly tuned ($t_1$-independent) surface waves that are monochromatic at leading order. Equations governing the wave envelope and bedload forcing are reviewed and the various coefficients in the sand bar equation are analyzed. Steady state sand bar profiles are calculated and give insight into the effect of the wave and sediment parameters on sand bar shape. Simulations of a single sand bar in an infinite bar patch under constant waves provide further information such as the bar growth rate.

We consider a coarse sand patch from $0 < x_1 < \varepsilon L$, and assume that outside this region either the bed is non-erodible or the water is sufficiently deep that the bed shear stress is too weak to cause erosion. Since the sand is coarse, bedload dominates the sediment transport. We assume the waves are perfectly tuned, so that $A$ and $B$ are independent of $t_1$. Note that $A$ and $B$ do depend on the bar evolution time $\bar{t}$. However, since $\bar{t} = O(\varepsilon^{4.5}t)$, i.e. the time scale of bar evolution is many orders of magnitude longer than the wave period, the dependence of $A$ and $B$ on $\bar{t}$ is parametric. We introduce the (complex) reflection coefficient $R = B/A$ and find equations for $A$, $R$ from (1.72) and (1.73),

$$\frac{\partial A}{\partial x_1} = -\frac{A}{C_g}\left(\frac{1}{2}\frac{\partial C_g}{\partial x_1} + i\Omega_0 D_1 R\right), \qquad \frac{\partial R}{\partial x_1} = \frac{i\Omega_0}{C_g}\left(D_1^* + D_1 R^2\right), \tag{2.98}$$

where

$$\Omega_0 = \frac{k}{2\sinh 2kH}, \qquad \tilde{h} = \Re\left\{\sum_{m=1}^{\infty} D_m e^{2miS}\right\}, \qquad C_g = \frac{1}{2k}\left(1 + \frac{2kH}{\sinh 2kH}\right).$$

The form of the Bragg scattering equations in (2.98) is more numerically convenient than those presented by Yu & Mei (2000). In one of their equations, $R$ appeared in the denominator and made numerical schemes difficult when $R$ was small. From (1.35), the wave envelope is given by

$$\zeta_{env} = \left|\zeta_1^{[1]}\right| = |A|\sqrt{1 + |R|^2 + 2|R|\cos(2\chi)}$$

where

$$\chi = S - \theta_R/2 = \int^x k\,(x_1)\,dx - \theta_R/2,$$

and $\theta_R$ is the phase of the complex reflection coefficient $R$. Terms needed in the sand bar equation involving the leading order bottom horizontal orbital velocity are, from (1.83),

$$\left|U_1^{[1]}\right| = \frac{A_o}{A_b}\frac{|A|}{\sinh kH}\sqrt{1+|R|^2-2\,|R|\cos 2\chi}, \tag{2.99}$$

$$U_1^{[1]*}\frac{\partial U_1^{[1]}}{\partial x} = k\left(\frac{A_o}{A_b}\frac{|A|}{\sinh kH}\right)^2\left(i\left(1-|R|^2\right)+2\,|R|\sin 2\chi\right). \tag{2.100}$$

The complex amplitude of the zeroth harmonic of the bottom orbital velocity is, from (1.84) and (1.87),

$$U_2^{[0]} = -\frac{A_o}{2A_b}\frac{|A|^2\left(1-|R|^2\right)}{H\tanh kH} = -\frac{A_o}{2A_b}\frac{|A\,(0)|^2\left(1-|R\,(0)|^2\right)}{H\tanh kH}\frac{C_g\,(0)}{C_g}. \tag{2.101}$$

The second equality in (2.101) follows from (1.49), which reduces to

$$C_g\left(|A|^2-|B|^2\right) = C_g\,|A|^2\left(1-|R|^2\right) = const$$

since $A$, $B$, $R$ are independent of $t_1$. Lastly, recall from Eq. (1.85) that the second harmonic of the bottom orbital velocity satisfies

$$U_2^{[2]} = -\frac{3i}{4\sinh^2 kH}U_1^{[1]}\frac{\partial U_1^{[1]}}{\partial x}. \tag{2.102}$$

For a flat mean seabed ($dH/dx_1 = 0$), Eqs. (1.72) and (1.73) reduce to

$$C_g\frac{\partial A}{\partial x_1} = -i\Omega_0 B, \qquad -C_g\frac{\partial B}{\partial x_1} = -i\Omega_0^* A, \tag{2.103}$$

since $A$, $B$ are independent of $t_1$. Multiplying the first equation by $A^*$ and the second by $B^*$, we obtain

$$C_g\frac{\partial\,|A|^2}{\partial x_1} = \Im\left\{\widehat{\Omega}_0\right\}|A|\,|B|\,, \qquad -C_g\frac{\partial\,|B|^2}{\partial x_1} = -\Im\left\{\widehat{\Omega}_0\right\}|A|\,|B|\,, \tag{2.104}$$

where $\widehat{\Omega}_0 = \Omega_0 e^{i\theta_R}$ and $\theta_R$ is the phase of the reflection coefficient $R$. These equations were

obtained by Yu & Mei [70] and show that if $\Im\left\{\widehat{\Omega}_0\right\} > 0$, $|A|$ and $|B|$ increase shoreward as energy is transferred from the reflected wave to the incident wave, i.e. from $B$ to $A$. Conversely, if $\Im\left\{\widehat{\Omega}_0\right\} < 0$, $|A|$ and $|B|$ decrease shoreward as energy is transferred from $A$ to $B$. Note that the energy $\frac{1}{2}|B|^2$ in the reflected wave propagates seaward. Furthermore, Yu & Mei [70] showed that the relative position of the bar crest and the wave node determines the sign of $\Im\left\{\widehat{\Omega}_0\right\}$. In particular, if the bar crest is shoreward of the antinode and seaward of the node, $\Im\left\{\widehat{\Omega}_0\right\} > 0$, and vice versa. This is a key mechanism for sand bar and surface wave evolution under weak reflection.

For perfectly tuned surface waves, inserting (1.83), (2.99), (2.102) into the bedload transport formula (2.89) yields

$$\begin{aligned} q_\tau &= \frac{16\kappa A_b \omega}{5\pi(1-\mathcal{N})u_{fo}}\frac{Q_B}{u_f}\left(\Re\left\{\left(M_1 - \frac{3iM_2}{4\sinh^2 kH}\right)U_1^{[1]*}\frac{\partial U_1^{[1]}}{\partial x}\right\}\right. \\ &\qquad \left. + \frac{5}{3}\Lambda_2^{[0]}U_2^{[0]} + M_3\frac{\left|U_1^{[1]}\right|^2}{Z_b}\frac{dZ_b}{dx} + M_4\frac{\left|U_1^{[1]}\right|^2}{u_f}\frac{du_f}{dx}\right), \end{aligned} \tag{2.105}$$

where $\left|U_1^{[1]}\right|$, $U_1^{[1]*}U_{1x}^{[1]}$ and $U_2^{[0]}$ are found from (2.99), (2.100) and (2.101), respectively, $Z_b$, $u_f$ are found from (2.30) and (2.14), and the $M_n$ are given in (2.90) – (2.93).

The sand bar evolution is governed by Eq. (2.97),

$$\frac{\partial \widetilde{h}}{\partial \bar{t}} - \frac{\partial}{\partial x}\left(D_\nu \frac{\partial \widetilde{h}}{\partial x}\right) = -\frac{\partial}{\partial x}\left(q_\tau + D_\nu \frac{dH}{dx_1}\right), \tag{2.106}$$

where $q_\tau$ is given in (2.105) and $D_\nu$ in (2.86).

The fact that $\left|U_1^{[1]}\right|$ is $\pi$-periodic over the short scale $x$ leads to special properties of the sand bars. The $\pi$-periodicity of $\left|U_1^{[1]}\right|$ implies the same for $D_\nu$ and $q_\tau$. Hence, if the initial bar profile $\widetilde{h}(x,0)$ is $\pi$-periodic, then the sand bar profile $\widetilde{h}(x,\bar{t})$ is $\pi$-periodic for all time. Integrating (2.97) in $x$ across a bar wavelength $\pi$ gives

$$\frac{\partial}{\partial \bar{t}}\int_0^\pi \widetilde{h}(x,\bar{t})\,dx = \int_0^\pi \frac{\partial}{\partial x}\left(D_\nu\left(\frac{\partial \widetilde{h}}{\partial x} - \frac{\partial H}{\partial x_1}\right) - q_\tau\right)dx = 0, \tag{2.107}$$

since $D_\nu$, $q_\tau$ and $\widetilde{h}$ are $\pi$-periodic. We assume that the initial bar profile $\widetilde{h}(x,0)$ satisfies

$\int_0^\pi \widetilde{h}\,(x,0)\,dx = 0$ and hence (2.107) implies

$$\int_0^\pi \widetilde{h}\,(x,\bar{t})\,dx = 0. \tag{2.108}$$

When the mean depth $H$ is constant, Eq. (2.97) is similar in form to that derived by Yu & Mei [70]. A detailed comparison between Yu & Mei's theory and our theory is presented in §2.8. Some general qualitative features are common to both theories. Yu & Mei [70] noted that the slope modification to bedload transport leads to a diffusion term $D_\nu$ and a forcing term $q_\tau$. For zero reflection, these terms are constants, and hence bars cannot form. However, for any nonzero reflection, $D_\nu$ and $q_\tau$ are not constant (provided, of course, that conditions are supercritical $\widehat{\Theta}_d > \Theta_c$) and bars form. This implies that bars can form even if circulation cells do not form in the Eulerian mean flow $u_2^{[0]}$, as noted experimentally by O'Hare & Davies [52]. This is due in part to the bedload transport depending on both the Eulerian mean flow $u_2^{[0]}$ and also the second harmonic $u_2^{[2]}$. Carter, Liu & Mei [9] expected that the mean flow $u_2^{[0]}$ was solely responsible for bar formation.

### 2.4.1 Diffusivity and forcing

Given the wave envelope parameters $A$, $R$ and the mean depth $H$, we present in this section a step-by-step procedure to find the diffusivity and forcing functions in the sand bar equation. For single bar simulations or to plot functions like forcing or diffusivity over a single bar, we take constant values for the wave parameters: $H = KH_o$, $C_g = C_{g0}$, $A = 1$, $R = R_L$. For multi-bar simulations, $H$ is specified and the wave number $k$ is found from (1.81),

$$\frac{\omega^2}{gK} = k \tanh kH.$$

The discretization and solution of the wave envelope ODEs (2.98) is deferred until §2.4.4 on the evolution of an entire bar patch. We simply assume here that $A$, $R$, $k$, $H$ are given. From these, we find $\left|U_1^{[1]}\right|$ and $U_1^{[1]}U_{1x}^{[1]*}$ from (2.99) and (2.100), respectively. Then, the amplitude of the grain roughness Shields parameter is found from (2.42),

$$\frac{\widehat{\Theta}_d}{\Theta_{do}} = \left( \frac{f_{Zb}\left(\frac{12\kappa^2 A_b}{d}\right)}{f_{Zb}\left(\left|U_1^{[1]}\right| \frac{12\kappa^2 A_b}{d}\right)} \right)^2,$$

where the function $f_{Z_b}$ is defined in (2.25) and a fitting formula is given in (2.26). The local critical Shields parameter is given by (1.115),

$$\Theta_c = \Theta_{c0}\left(1 - \frac{\varepsilon}{2\tan\psi_m}\left|\frac{\partial\widetilde{h}}{\partial x}\right|\right).$$

The bedload transport rate over a half cycle is given by (2.88),

$$Q_{B0} = \left(\frac{\widehat{\Theta}_d - \Theta_c}{\Theta_{do}}\right)^{3/2} \mathrm{Hv}\left(\frac{\widehat{\Theta}_d - \Theta_c}{\Theta_{do}}\right).$$

The diffusivity is given in (2.86),

$$D_\nu = \frac{3Q_{B0}}{8\,(1-\mathcal{N})\tan\psi_m}.$$

From $\left|U_1^{[1]}\right|$, we find the local ripple height $\eta_r = \eta_r'/\eta_{ro}$ and the relative roughness $k_N = k_N'/k_{No}$ either from measurements or from empirical formulae (1.105) and (1.106) in §1.5. From these, Eq. (2.30) gives

$$Z_b = f_{Zb}\left(\frac{\left|U_1^{[1]}\right|}{k_N}\frac{30\kappa^2 A_b}{k_{No}}\right), \tag{2.109}$$

and the functions $M_n$ are then found from (2.90) – (2.93). The bedload transport term $q_\tau$ then follows from (2.105).

The wave envelope $\zeta_{env}$, diffusivity $D_\nu$ and bedload forcing $-\partial q_\tau/\partial x$ are plotted across a single bar in Figure 2-5 for various reflection coefficients $R_L$. When plotting these we take $\Theta_c = \Theta_{c0}$, as only minor differences exist near slopes and sub-critical regions. The orbital amplitude $A_b = A_o(1+|R_L|)/\sinh KH_o$ is kept the same as $R_L$ varies; thus higher reflection coefficients correspond to lower incident amplitudes $A_o$.

Figure 2-5 illustrates that the diffusivity $D_\nu$ is non-negative and symmetric with respect to the wave node for all $|R|$, and takes a maximum under the wave node and a minimum under the wave antinode, along with the bed shear stress and the bedload transport rate. The gravity-driven diffusivity $D_\nu$ limits the bar growth. In principle, an equilibrium can be reached between the gravity-driven diffusivity and the shear-driven bedload forcing, so that the bedload transport rate is uniform across a bar.

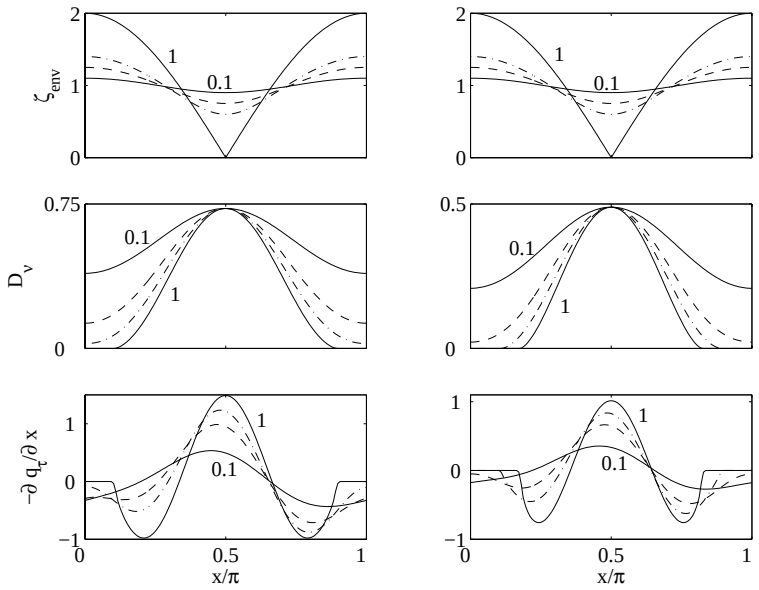


Figure 2-5: Wave envelope $\zeta_{env}$, diffusivity $D_\nu$ and forcing $-\partial q_\tau/\partial x$ across one bar length for various reflection coefficients, $|R_L| = 0.1$ (solid), $|R_L| = 0.25$ (dash), $|R_L| = 0.4$ (dash-dot), $|R_L| = 1.0$ (solid). Numbers adjacent to curves indicate the value of the reflection coefficient. Field conditions are plotted in the left column, $T = 8$ s, $H_o = 6$ m, $A_o(1 + |R_L|) = 50$ cm, $d = 0.5$ mm and $\eta_r'$ is found empirically using Nielsen's formula (1.105) (see §1.5). Lab conditions are plotted in the right column, $T = 2.5$ s, $H_o = 60$ cm, $A_o(1 + |R_L|) = 7$ cm, $d = 0.2$ mm and $\eta_r' = 1$ cm. In all cases, $\Lambda_2^{[0]} = 1.5$.

The bedload forcing $-\partial q_\tau/\partial x$, plotted in Figure 2-5, is asymmetric except for $R = 1$, takes its maximum near the node (under the node for $R = 1$) and takes its minimum between the node and the antinode. Under a wave node, the bedload forcing is positive, so that deposition occurs and bar crests form. Near or under the antinode, the bedload forcing becomes negative, so that scouring occurs and bar troughs form.

For sufficiently high reflection, sub-critical regions exist where $\widehat{\Theta}_d < \Theta_c$ and both $D_\nu$ and $q_\tau$ vanish, leaving the bed unchanged. On a flat bed (no bars), the half width $X_c$ of the sub-critical region between two bar troughs is predicted from the wave and sediment characteristics by solving $\widehat{\Theta}_d(X_c) = \Theta_{c0}$, where $\widehat{\Theta}_d$ is the local grain roughness Shields parameter defined in (2.42) and $\Theta_{c0}$ is the flat bed critical Shields parameter found from the Shields diagram (more precisely, Eq. (1.102)). As time evolves, scouring near the sub-critical regions increases the local bar slope and decreases the local value of the slope-dependent critical Shields parameter $\Theta_c$, defined in (1.115). The local diffusivity $D_\nu$ and bedload forcing then become nonzero and the size of the sub-critical region is reduced. Through

this mechanism, the trough slopes neighboring sub-critical regions are generally kept small. If scouring occurs too fast and large slopes form before the gravity-driven diffusion can reduce them, our model fails since it was derived assuming mild slopes, $\partial h'/\partial x' = O(\varepsilon)$. In reality, large slopes may also be smoothed by local avalanches. A better model would include these and other finite slope effects.

We should point out that the width $X_c$ of the sub-critical region is mainly dependent on the prediction of $\Theta_{c0}$ from the modified Shields diagram. Despite the inherent variability in the Shields diagram, $X_c$ seems to be well-predicted in most of the experimental comparisons made in this thesis. However, in cases where discrepancies exist, the width $X_c$ of the sub-critical region is measured directly from the experiments and the corresponding value of $\Theta_{c0}$ is inferred via $\Theta_{c0} = \widehat{\Theta}_d(X_c)$.

The dependence of the diffusivity $D_\nu$ and bedload forcing $-\partial q_\tau/\partial x$ on the sediment diameter is illustrated in the left column of Figure 2-6. Two grain sizes, $d = 0.2$ and $0.5$ mm, are considered for field conditions under two reflection coefficients, $R_L = 0.25$ and 1. No appreciable difference is observed between the diffusivity or forcing for the two grain sizes, for both reflection coefficients, despite the values of the roughness $Z_b$ more than doubling when going from $d = 0.2$ mm to $d = 0.5$ mm. In Chapter 3, a new forcing term due to suspended sediment is considered which alters the bar geometry for fine sediments.

The dependence of the wave envelope $\zeta_{env}$, diffusivity $D_\nu$ and bedload forcing $-\partial q_\tau/\partial x$ on the wave amplitude $A_o$ is shown in the right column of Figure 2-6, for lab conditions and weak reflection $R_L = 0.25$. Four amplitudes, expressed in dimensionless form as wave slopes, are considered. For sufficiently small wave amplitude, sub-critical regions appear where the diffusivity and forcing vanish. As the amplitude increases, the sub-critical regions disappear. Also, as the wave amplitude (and hence, wave slope) increase, so do the diffusivity and bedload forcing magnitude. However, as shown, the diffusivity can grow faster than the magnitude of bedload forcing.

The bedload forcing $q_\tau$, given in (2.105), has a term containing $\sinh kH$ in the denominator, derived from the second harmonic $U_2^{[2]}$ of the bottom orbital velocity. Thus, in shallow water where $kH$ approaches zero, $q_\tau$ will increase exponentially in $kH$ and our sand bar model becomes invalid.

The dependence of the forcing, diffusivity and resultant sand bar form on the return flow stress coefficient $\Lambda_2^{[0]}$ is illustrated in the next section when we consider the steady state

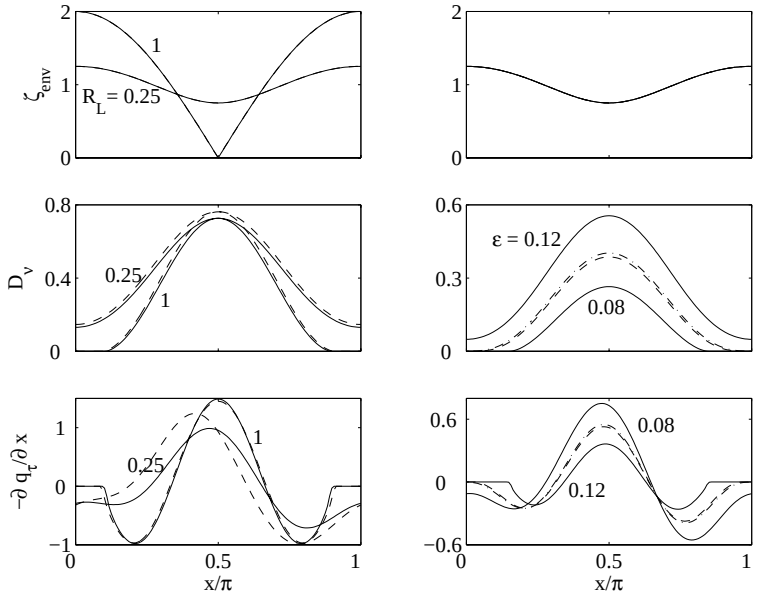


Figure 2-6: Dependence of the wave envelope $\zeta_{env}$, diffusivity $D_\nu$, and bedload forcing $-\partial q_\tau/\partial x$ on the sediment diameter (left column) and on wave amplitude (right column). In the left column, field conditions ($T = 8$ s, $H_o = 6$ m, $A_o = 50$ cm) are plotted with $d = 0.05$ cm (solid), $d = 0.02$ cm (dash, dash-dot) and numbers adjacent to curves indicate the value of the reflection coefficient. In the right column, lab conditions ($T = 2.5$ s, $H_o = 60$ cm, $R_L = 0.25$, $d = 0.25$ mm) are plotted with $\varepsilon = 0.08$ ($A_o = 4.13$ cm, solid); $\varepsilon = 0.093$ ($A_o = 4.80$ cm, dash); $\varepsilon = 0.095$ ($A_o = 4.90$ cm, dash-dot), $\varepsilon = 0.12$ ($A_o = 6.19$ cm, solid), and numbers adjacent to curves indicate the value of $\varepsilon$. The ripple height $\eta_{ro}$ is taken as 2 cm for lab conditions and found from Eq. (1.105) for field conditions. In all cases, $\Lambda_2^{[0]} = 1.5$.

of the sand bar evolution.

### 2.4.2 Steady state bars

Though in a field setting, the wave parameters usually change after a few hours, it is natural at least in an academic sense to consider the steady state bar profiles. These lend insight to the dependence of bar shape on the wave and sediment characteristics. In the following we take the mean depth and the wave parameters $A$, $R$ to be constant, real and positive. Thus $H = KH_o$, $dH/dx_1 = 0$, $k = 1$ and $\chi = x$. Following Yu & Mei [70], the steady state bar profiles are given by setting $\partial\widetilde{h}/\partial\bar{t} = 0$ and $\widetilde{h}\,(x,\bar{t}) = \widetilde{h}_S\,(x)$ in the sand bar equation (2.97) and integrating, to obtain

$$D_\nu \frac{d\widetilde{h}_S}{dx} = q_\tau - q_e, \tag{2.110}$$

where $q_e$ is a constant of integration and represents the equilibrium net bedload transport across a bar. Integrating gives

$$\widetilde{h}_S = \widetilde{h}_0 + \int_{x_0}^{x} D_\nu^{-1} \left(q_\tau - q_e\right) dx \tag{2.111}$$

where $x = x_0$ is an arbitrary point on the bar and $\widetilde{h}_0 = \widetilde{h}_S \left(x_0\right)$. The ratio of the bed load forcing to diffusivity is given by (2.86) and (2.105),

$$\begin{aligned} \frac{q_\tau}{D_\nu} \;=\; & \frac{128 \tan\left(\psi_m\right) \kappa A_b \omega}{15\pi u_{fo}\, u_f} \left( \Re\left\{ \left( M_1 - \frac{3iM_2}{4\sinh^2 kH} \right) U_1^{[1]*} \frac{\partial U_1^{[1]}}{\partial x} \right\} \right. \\ & \left. + \frac{5}{3} \Lambda_2^{[0]} U_2^{[0]} + M_3 \frac{\left|U_1^{[1]}\right|^2}{Z_b} \frac{dZ_b}{dx} + M_4 \frac{\left|U_1^{[1]}\right|^2}{u_f} \frac{du_f}{dx} \right), \end{aligned} \tag{2.112}$$

Note that $128 \tan\left(\psi_m\right) / 15\pi = 1.6$.

In regions where $\hat{\Theta}_d < \Theta_c$, effectively no bedload transport takes place and the flow is called sub-critical; where $\hat{\Theta}_d > \Theta_c$, the flow is called supercritical. For the purpose of finding the steady state, we take $\Theta_c = \Theta_{c0}$ and neglect the mild slope effect on the critical Shields parameter. From (2.99), the minimum and maximum of $\left|U_1^{[1]}\right|$ occur at $x = 0$ and $\pi/2$, respectively, since $R$ is taken real. From Eq. (2.42), $\widehat{\Theta}_d$ increases with $\left|U_1^{[1]}\right|$, since $f_{Zb}$ defined in (2.25) is a decreasing function. Hence the minimum and maximum of $\hat{\Theta}_d$ coincide with those of $\left|U_1^{[1]}\right|$, namely, at $x = 0$ and $\pi/2$, respectively. Therefore, if $\widehat{\Theta}_d \left(0\right) > \Theta_{c0}$ the reflection is sufficiently weak so that no sub-critical region exists, and if $\widehat{\Theta}_d \left(0\right) \leq \Theta_{c0}$ the reflection is sufficiently high (or the orbital amplitude $A_b$ sufficiently small) that a sub-critical region exists.

**Weak reflection**

When the bottom shear stress exceeds the critical shear stress for sediment motion across a bar, i.e. $\hat{\Theta}_d > \Theta_{c0}$ for all $x$, we take $x_0 = 0$. The constants $q_e$ and $\widetilde{h}_0$ are determined by imposing the condition (2.108) and $\pi$–periodicity plus continuity at $x = 0$ and $\pi$,

$$h_S \left(0\right) = h_S \left(\pi\right). \tag{2.113}$$

Imposing (2.113) on (2.111) gives

$$\widetilde{h}_0 = \widetilde{h}_S(0) = \widetilde{h}_S(\pi) = \widetilde{h}_0 + \int_0^\pi D_\nu^{-1}(q_\tau - q_e)\,dx$$

Rearranging gives

$$q_e = \frac{\int_0^\pi q_\tau D_\nu^{-1} dx'}{\int_0^\pi D_\nu^{-1} dx'} = \frac{3}{8(1-\mathcal{N})\tan\psi_m}\frac{\int_0^\pi q_\tau D_\nu^{-1} dx'}{\int_0^\pi Q_{B0}^{-1} dx'}. \tag{2.114}$$

Substituting (2.114) into (2.111) with $x_0 = 0$ yields

$$\widetilde{h}_S = \widetilde{h}_0 + \left\{\int_0^x dx' - \Gamma(x)\int_0^\pi dx'\right\}\frac{q_\tau}{D_\nu}, \tag{2.115}$$

where

$$\mathcal{G}(x) = \frac{\int_0^x D_v^{-1} dx'}{\int_0^\pi D_v^{-1} dx'} = \frac{\int_0^x Q_{B0}^{-1} dx'}{\int_0^\pi Q_{B0}^{-1} dx'}. \tag{2.116}$$

Substituting (2.115) into (2.108) yields

$$\widetilde{h}_0 = -\frac{1}{\pi}\left\{\int_0^\pi\int_0^x dx' - \int_0^\pi \Gamma(x')\,dx'\int_0^\pi dx'\right\}\frac{q_\tau}{D_\nu}. \tag{2.117}$$

Since $D_\nu$ only depends on $x$ via the function of $\cos 2x$, result (2.181) from Appendix 2.9.4 implies

$$\int_0^\pi \mathcal{G}(x')\,dx' = \frac{\int_0^\pi\int_0^{x'} D_v^{-1} dx'' dx'}{\int_0^\pi D_v^{-1} dx'} = \frac{\pi}{2}. \tag{2.118}$$

Substituting (2.117) and (2.118) into (2.115) gives

$$\widetilde{h}_S(x) = \left\{\int_0^x dx' - \frac{1}{\pi}\int_0^\pi\int_0^x dx' dx + \left(\frac{1}{2} - \mathcal{G}(x)\right)\int_0^\pi dx\right\}\frac{q_\tau}{D_\nu}. \tag{2.119}$$

The form of Eq. (2.119) is similar to that given in Yu & Mei [70], although the integrals cannot be calculated analytically due to our form of $q_\tau/D_\nu$.

The total height of the steady state bar profile is given by

$$\max\{h_S\} - \min\{h_S\} = \max\{f(x)\} - \min\{f(x)\}, \tag{2.120}$$

where

$$f(x) = \int_0^x \frac{q_\tau}{D_\nu} dx' - \mathcal{G}(x)\int_0^\pi \frac{q_\tau}{D_\nu} dx.$$

Note that $f(0) = 0 = f(\pi)$. Let $x_{\min}$ and $x_{\max}$ be the extrema of $f(x)$. These extrema satisfy $df/dx = 0$ or,

$$\frac{q_\tau}{D_\nu} Q_{B0} = \frac{\int_0^\pi \frac{q_\tau}{D_\nu} dx}{\int_0^\pi Q_{B0}^{-1} dx}.$$

Based on the plots of $h_S$ and $q_\tau/D_\nu$ below, $x_{\min} < x_{\max}$ for small Eulerian current $U_2^{[0]}$ and the reverse holds when $U_2^{[0]}$ is significant. Eq. (2.120) becomes

$$\begin{aligned} \max\{h_S\} - \min\{h_S\} &= \int_{x_{\min}}^{x_{\max}} \frac{q_\tau}{D_\nu} dx' - (\mathcal{G}(x_{\max}) - \mathcal{G}(x_{\min})) \int_0^\pi \frac{q_\tau}{D_\nu} dx \\ &= \int_{x_{\min}}^{x_{\max}} \frac{q_\tau}{D_\nu} dx' - \frac{\int_{x_{\min}}^{x_{\max}} Q_{B0}^{-1} dx}{\int_0^\pi Q_{B0}^{-1} dx} \int_0^\pi \frac{q_\tau}{D_\nu} dx. \end{aligned} \tag{2.121}$$

**Strong reflection**

When $\hat{\Theta}_d(0) < \Theta_c$, there exists a region of the bed where the wave-intensity is below the threshold necessary for sediment transport, i.e. $Q_{B0} = D_\nu = q_\tau = 0$. Hence (2.110) implies the net sediment transport across a bar is zero, $q_e = 0$. Assuming the flow intensity is above critical over part of the bed, i.e. that $\hat{\Theta}_d(\pi/2) > \Theta_{c0}$, the flow is sub-critical in the interval $-X_c \le x \le X_c$, where $X_c$ satisfies

$$\hat{\Theta}_d(X_c) = \Theta_{c0}, \qquad 0 < X_c < \pi/2. \tag{2.122}$$

Eq. (2.122) can be solved numerically for $X_c$. For the purpose of finding a steady state, we assume the bed is flat in the sub-critical regions, $\widetilde{h}_S(x) = 0$ for $-X_c \le x \le X_c$. Under this assumption and that of $\pi$-periodicity plus continuity at $x = \pi$, we have $\widetilde{h}_S(0) = \widetilde{h}_S(\pi) = 0$. Eq. (2.111) becomes, with $x_0 = X_c$,

$$\begin{aligned} \widetilde{h}_S(x) &= 0, && 0 \le x \le X_c, \\ \widetilde{h}_S(x) &= \widetilde{h}_0 + \int_{X_c}^x \frac{q_\tau}{D_v} dx', && X_c \le x \le \pi - X_c, \\ \widetilde{h}_S(x) &= 0, && \pi - X_c \le x \le \pi. \end{aligned} \tag{2.123}$$

Again, the form of Eq. (2.123) is similar to that given in Yu & Mei [70], although the integral cannot be calculated analytically due to the form of $q_\tau/D_\nu$. The profile may be

discontinuous at $x = X_c$ and $\pi - X_c$. Substituting (2.123) into (2.108) gives

$$\widetilde{h}_0 = -\frac{1}{\pi - 2X_c} \int_{X_c}^{\pi - X_c} \int_{X_c}^{x} \frac{q_\tau}{D_v} dx' dx.$$

Substituting this back into (2.123) gives

$$\widetilde{h}_S(x) = \left\{ \int_{X_c}^{x} dx' - \frac{1}{\pi - 2X_c} \int_{X_c}^{\pi - X_c} \int_{X_c}^{x} dx' dx \right\} \frac{q_\tau}{D_v} \tag{2.124}$$

for $X_c \leq x \leq \pi - X_c$.

The total height of the steady state bar profile is given by

$$\max\left\{\widetilde{h}_S(x)\right\} - \min\left\{\widetilde{h}_S(x)\right\} = \max\{f(x)\} - \min\{f(x)\}, \tag{2.125}$$

where

$$f(x) = \int_{X_c}^{x} \frac{q_\tau}{D_v} dx'.$$

By finding the extrema of $f(x)$, either at $X_c$, $\pi - X_c$, or solutions of $q_\tau(x) = 0$, the steady state bar height can be computed.

**Steady state bar profiles and bar height**

Steady state bar profiles $\widetilde{h}_S(x)$ are plotted in Figure 2-7 along with the wave envelope $\zeta_{env}$ and the bedload forcing to diffusivity ratio $q_\tau / D_\nu$, for lab and field conditions and various reflection coefficients. Notice that for weak reflection, the flow is super-critical across the entire bar, $\widehat{\Theta}_d > \Theta_c$ everywhere, while for strong reflection, sub-critical regions exist where $\widehat{\Theta}_d < \Theta_c$. Also, for weak reflection, the bar height increases with increasing reflection, while for strong reflection, the bar height can actually decrease with increasing reflection, since the sub-critical regions are also increasing in size, leaving less sand available for bar growth. This effect is also observed later in Figure 2-11, where bar height is plotted vs. the reflection coefficient.

The steady state bar profiles for lab and field conditions are qualitatively similar. The only noticeable difference is that for strong reflection, the lab profiles have larger sub-critical regions. For low reflection, the position of the bar crest relative to the wave node is affected by the return flow stress coefficient $\Lambda_2^{[0]}$. The values of $\Lambda_2^{[0]}$ suitable for the

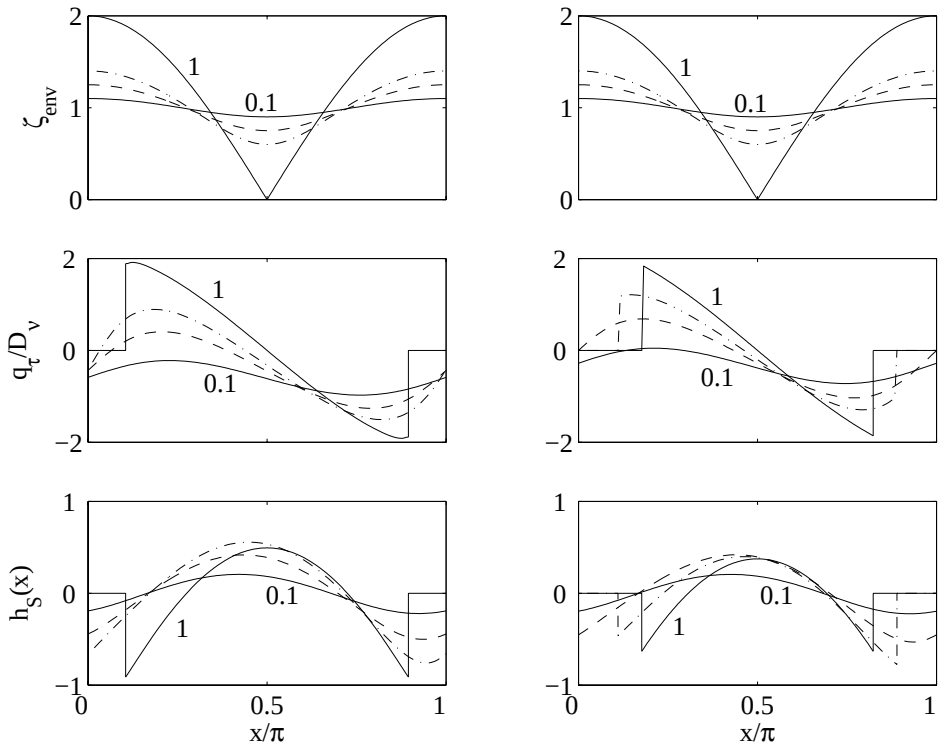


Figure 2-7: Wave envelope $\zeta_{env}$, bedload forcing to diffusivity ratio $q_\tau/D_\nu$, and the resultant steady state bar profile $\widetilde{h}_S(x)$ for various reflection coefficients, $|R_L| = 0.1$ (solid), $|R_L| = 0.25$ (dash), $|R_L| = 0.4$ (dash-dot), $|R_L| = 1.0$ (solid) for the field (left column) and lab (right column) conditions listed in Figure 2-5. Numbers adjacent to curves indicate the value of the reflection coefficient.

laboratory have been verified experimentally; those for the field have not, since we have no field measurements relating the relative positions of bar crests and wave nodes.

The grain diameter $d$ dependence of the wave envelope $\zeta_{env}$, bedload forcing to diffusivity ratio $q_\tau/D_\nu$, and the resultant steady state bar profiles $\widetilde{h}_S(x)$ is illustrated in the left column of Figure 2-8. Two grain sizes, $d = 0.2$ and 0.5 mm, are considered for field conditions. As was the case for the diffusivity and bedload forcing plotted separately in Figure 2-6, no appreciable difference is observed for either low reflection $R_L = 0.25$ or high reflection $R_L = 1$. In Chapter 3, a new forcing term due to suspended sediment is considered which alters the bar geometry for fine sediments.

The wave amplitude $A_o$ dependence of the wave envelope $\zeta_{env}$, bedload forcing to diffusivity ratio $q_\tau/D_\nu$, and the resultant steady state bar profiles $\widetilde{h}_S(x)$ is shown in the right column of Figure 2-8, for lab conditions and weak reflection $R_L = 0.25$. Four wave amplitudes are considered, expressed in dimensionless form by wave slopes. For sufficiently

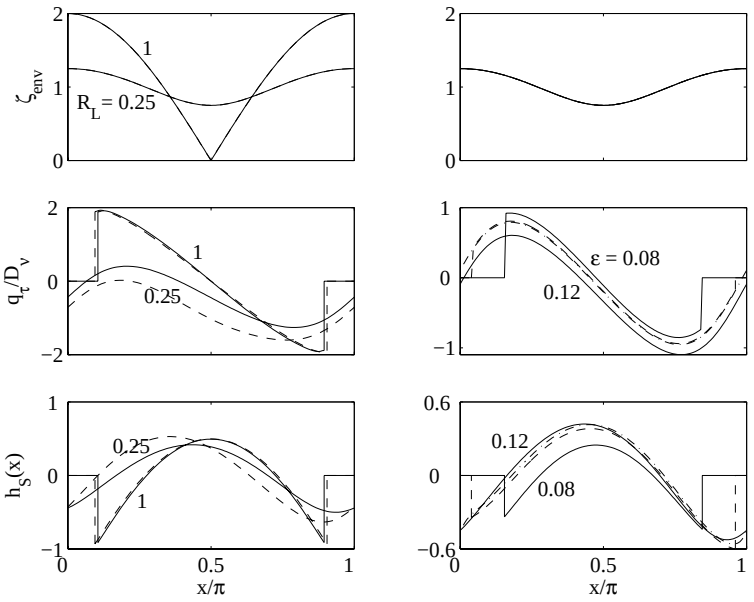


Figure 2-8: Dependence of the wave envelope $\zeta_{env}$, bedload forcing to diffusivity ratio $q_\tau/D_\nu$, and the resultant steady state bar profile $\widetilde{h}_S(x)$ on grain size (left column, $d = 0.05$ cm (solid), $d = 0.02$ cm (dash, dash-dot)) and on wave amplitude (right column, $\varepsilon = 0.08, 0.093, 0.095, 0.12$ (solid, dash, dash-dot, solid)). The parameters for each curve are the same as those in Figure 2-6. Numbers adjacent to curves indicate the reflection coefficient in the left column, and the wave slope $\varepsilon$ in the right column.

small amplitude, sub-critical regions appear where the diffusivity and forcing vanish. As the wave amplitude increases, the sub-critical regions disappear. As we show below in plots of the steady state bar height, as the sub-critical regions decrease in length, more sand is available for transport and the bar height increases. Once the sub-critical regions disappear, increasing the wave amplitude (and hence, wave slope) further leads to a decrease in the steady bar height. As discussed in the previous section, this is caused by the diffusivity growing faster than the forcing, leading to a decrease in $q_\tau/D_\nu$ and thus in the steady state bar height.

The effect of the return flow bed stress coefficient $\Lambda_2^{[0]}$ on the bedload forcing $q_\tau$ and resultant steady state bar profiles $h_S(x)$ is illustrated in Figure 2-9. Increasing $\Lambda_2^{[0]}$ increases the bed shear stress due to the return flow, moving the peak of the forcing seaward (negative $x$-direction). Since the diffusivity is independent of the return flow, the predicted bar crests also shift seaward as $\Lambda_2^{[0]}$ increases. Recall that $\Lambda_2^{[0]}$ has no effect on bar formation for high reflection since the return flow is small, $U_2^{[0]} \propto (1 - |R_L|^2)$.

The effect of the ripple height $\eta_r'$ on the bedload forcing $-\partial q_\tau/\partial x$ and resultant steady

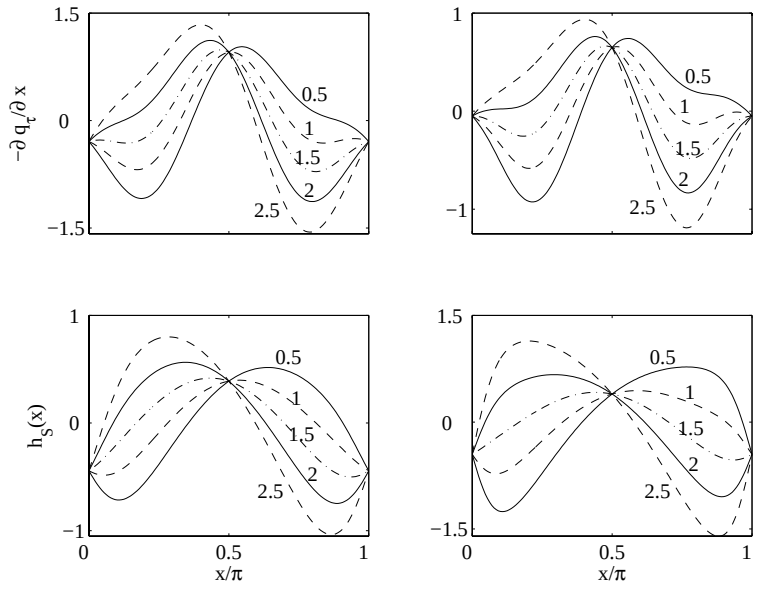


Figure 2-9: Dependence of the bedload forcing and the steady state bar profiles on the return flow bed stress coefficient $\Lambda_2^{[0]}$ for field (left column) and lab (right column) conditions. Numbers adjacent to curves indicate the value of $\Lambda_2^{[0]}$. The reflection coefficient is $R_L = 0.25$. All other parameters are the same as those in Figure 2-5.

state bar profiles $h_S(x)$ is illustrated in Figure 2-10. For both lab and field conditions, doubling the ripple height has a negligible effect for high reflection $R_L = 1$. For low reflection, doubling the ripple height while keeping $\Lambda_2^{[0]}$ fixed moves the crests shoreward and closer to the wave nodes. The reason is that, while $\Lambda_2^{[0]}$ is assumed to be independent of the ripple height (for simplicity), other terms in the bedload forcing $q_\tau$ increase with ripple height (see Eq. (2.105)). Thus, increasing the ripple height counters the effect of the return flow. Lastly, if the local ripple height $\eta_r'(x)$ is prescribed by Eq. (1.108) with $(r_1, r_2, r_3) = (0.68, 3, 2)$ and $\eta_{ro} = 2$ cm, the resulting forcing and steady state bar profiles are indistinguishable (to the resolution plotted) from the solid lines in Figure 2-10 corresponding to a constant ripple height $\eta_r' = \eta_{ro} = 2$ cm. The reason is that the ripple height $\eta_r'(x)$ in Eq. (1.108) is approximately constant over most of the bar, and only diminishes rapidly near the sub-critical regions where the bedload transport rate is low.

The dependence of the steady state bar height on the reflection coefficient is plotted in Figure 2-11 for lab and field conditions. Starting from weak reflection, the bar height increases until a cusp is reached, and then may slowly decrease or increase. The value of the reflection coefficient at the cusp is the critical value below which the entire bar is

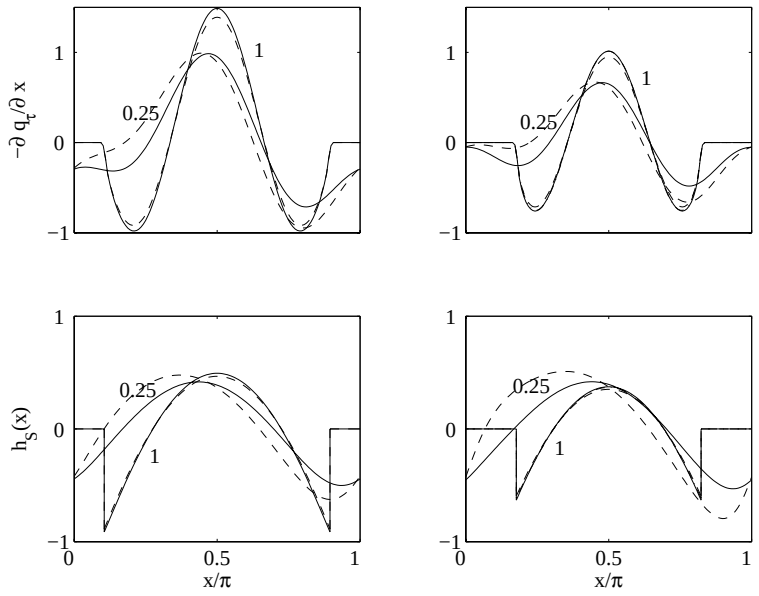


Figure 2-10: Dependence of the bedload forcing and the steady state bar profiles on the ripple height $\eta_{ro}$ for $R_L = 0.25$, 1. Field conditions are plotted in the left column, $H_o = 6$ m, $T = 8$ s, $A_o(1 + |R_L|) = 50$ cm, $d = 0.5$ mm. The ripple height $\eta_{ro}$ for the solid lines is found from Eq. (1.105); the dashed lines have half the ripple height of the corresponding solid line (of the same $R_L$). Lab conditions are plotted in the right column, $H_o = 60$ cm, $T = 2.5$ s, $A_o(1 + |R_L|) = 7$ cm, $d = 0.2$ mm, with $\eta_r' = \eta_{ro} = 2$ cm (solid), $\eta_r' = \eta_{ro} = 1$ cm (dash), and $\eta_r'$ found from Eq. (1.108) with $(r_1, r_2, r_3) = (0.68, 3, 2)$ and $\eta_{ro} = 2$ cm (dash-dot). The dash-dot line is so close to the solid line it is not visible. Numbers adjacent to curves indicate the value of $R_L$. In all cases, $\Lambda_2^{[0]} = 1.5$.

super-critical, i.e. $\widehat{\Theta}_d > \Theta_c$ everywhere, and above which there exists a sub-critical region where the bedload transport vanishes $\widehat{\Theta}_d < \Theta_c$. In Figure 2-11(top), the near-bed orbital amplitude $A_b = A_o(1 + |R_L|)/\sinh KH_o$ is held fixed as $|R_L|$ is varied. For reflection sufficiently strong to create sub-critical regions, the bar heights decrease with increasing reflection since the sub-critical regions are increasing in width, leaving less sand available for bar growth. In Figure 2-11(bottom), the incident amplitude $A_o$ is held fixed and thus increasing $R_L$ also increases the orbital amplitude $A_b$. In particular, the increase in orbital amplitude can offset the increase in the width of the sub-critical regions, allowing the bar heights to increase with $R_L$ even for strong reflection. Also, for the same $R_L$, the near-bed orbital amplitude in the bottom plot is $1 + |R_L|$ times greater than that in the top plot. Thus, the cusps occur at different critical reflection coefficients in the top and bottom plots.

Another interesting feature illustrated in Figure 2-11 is that for a given set of parameters, increasing the wave amplitude can lead to a decrease in bar height for weak reflection, and

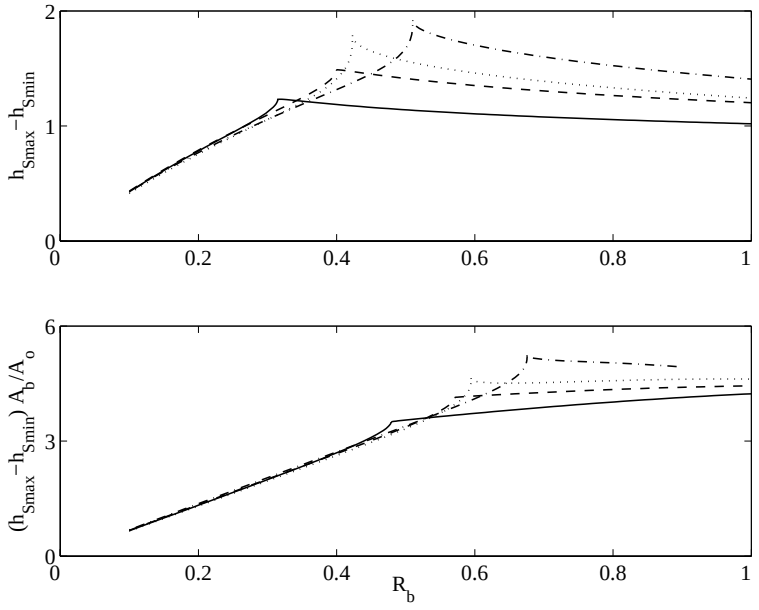


Figure 2-11: Dependence of the steady state bar height on the reflection coefficient. The lab conditions are $T = 2.5$ s, $H_o = 60$ cm, $d = 0.25$ mm, $\eta_r' = \eta_{ro} = 2$ cm and $A_o(1 + |R_L|) = 7$ cm (top, solid), $A_o(1 + |R_L|) = 8.5$ cm (top, dash), $A_o = 7$ cm (bottom, solid), $A_o = 8.5$ cm (bottom, dash). The field conditions are $T = 8$ s, $H_o = 6$ m, $d = 0.5$ mm, $\eta_r'$ found from Eq. (1.105), and $A_o(1 + |R_L|) = 50$ cm (top, dash-dot), $A_o(1 + |R_L|) = 40$ cm (top, dot), $A_o = 50$ cm (bottom, dash-dot), $A_o = 40$ cm (bottom, dot). In all cases, $\Lambda_2^{[0]} = 1.5$. The dash-dot line (bottom plot) ends prematurely at $R_L = 0.9$ as the rippled bed approaches sheet flow conditions ($\Phi_0 \sim 140$).

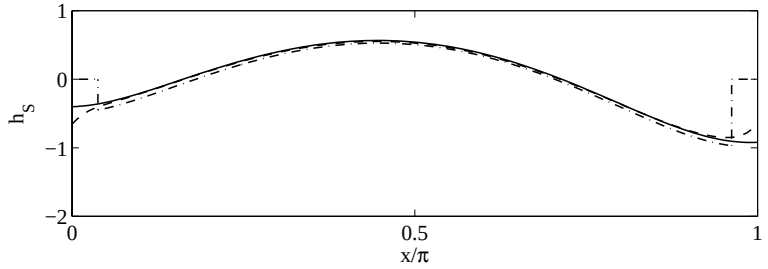


Figure 2-12: Steady state bar profiles near the critical value of the reflection coefficient where sub-critical regions appear. The parameters are the same as the dashed line in Figure 2-11(top), with $R_L = R_{\text{crit}} = 0.3994$ (solid), $R_L = R_{\text{crit}} - 0.01$ (dash), $R_L = R_{\text{crit}} + 0.02$ (dash-dot).

an increase in bar height for strong reflection (compare solid to dashed lines, and dash-dot to dotted lines). The former is reasonable since, from Eq. (2.121), the steady state bar height depends on the ratio of the bedload forcing to the diffusivity, and in this case as the wave amplitude increases, the diffusivity increases faster than the bedload forcing, leading to smaller bars. For strong reflection, increasing the wave amplitude decreases the size of the sub-critical region, allowing more sand to be available for bar growth.

To understand the source of the cusp in the steady state bar heights in Figure 2-11, steady state bar profiles are plotted in Figure 2-12 for three reflection coefficients close to the critical value. Changes in the reflection coefficient of 0.01 or 0.02 result in significant changes in the bar shape and height. In nature, these sudden changes could be smoothed somewhat by local avalanches.

The dependence of the steady state bar height on the wave slope

$$\varepsilon = KA_b = \frac{KA_o(1+|R_L|)}{\sinh KH_o}$$

is illustrated in Figure 2-13(top), for weak and strong reflection and for lab and field conditions. For each curve, the wave amplitude $A_o$ is varied while the other parameters are held fixed. For all but the solid curve, the bar height increases with increasing wave amplitude. More variations occur for lab conditions than for field conditions. In particular, for field conditions under weak reflection $R_L = 0.25$ (dash-dot), almost no variation in the steady state bar height is observed for the range of wave amplitudes plotted. The exception is the solid line, which contains a cusp at the critical wave slope below which a sub-critical region exists. As the wave amplitude (and slope) increase, the sub-critical region diminishes in length and the bar height increases. As the wave amplitude increases beyond the critical point, the sub-critical region vanishes and the steady state bar height decreases. As we said earlier, this striking feature occurs because, in this case, the diffusivity is increasing faster than the bedload forcing, leading to smaller steady state bars. To illustrate this point further, we plotted the diffusivity, bedload forcing and steady state bar height corresponding to four points on this solid curve ($\varepsilon = 0.08, 0.093, 0.095, 0.12$) in the right columns of Figures 2-6 and 2-8.

Figure 2-13(bottom) illustrates the dependence of the steady state bar height on the dispersion parameter $KH_o$. For each curve, the mean depth $H_o$ is varied as the other

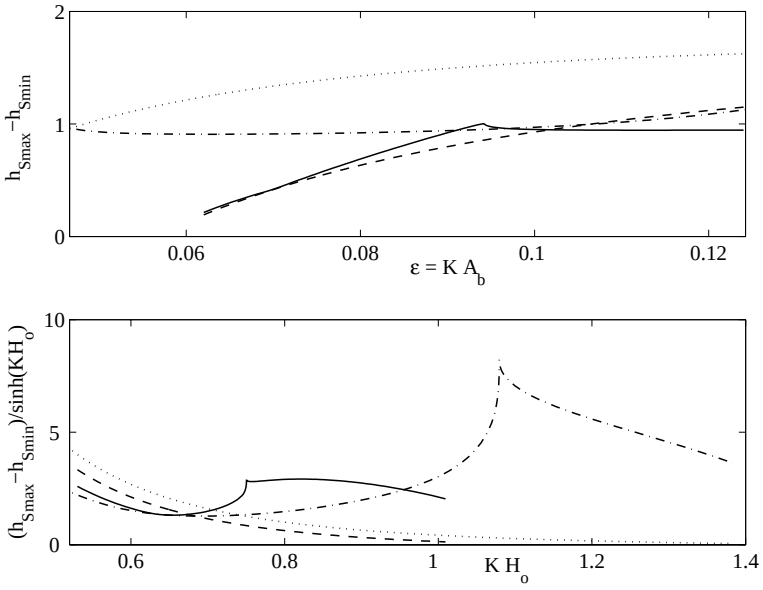


Figure 2-13: Dependence of the steady state bar height on the wave slope $\varepsilon = KA_b$ (top) and on the dispersion parameter $KH_o$ (bottom). In the top plot, the lab conditions are $T = 2.5$ s, $H_o = 60$ cm, $d = 0.25$ mm and $R_L = 0.25$ (solid), $R_L = 1$ (dash) and the field conditions are $T = 8$ s, $H_o = 6$ m, $d = 0.5$ mm and $R_L = 0.25$ (dash-dot), $R_L = 1$ (dot). In the bottom plot, the lab conditions are $T = 2.5$ s, $A_o(1 + |R_L|) = 7$ cm, $d = 0.25$ mm and $R_L = 0.25$ (solid), $R_L = 1$ (dash) and the field conditions are $T = 8$ s, $A_o(1 + |R_L|) = 50$ cm, $d = 0.5$ mm and $R_L = 0.25$ (dash-dot) and $R_L = 1$ (dot). In all cases, $\Lambda_2^{[0]} = 1.5$. The ripple height $\eta_r'$ is 2 cm for lab conditions and is found from Eq. (1.105) for field conditions.

parameters, in particular the wavenumber $K$, are held fixed. In general, as the mean depth increases, the bar height decreases. The exception is that for weak reflection, the diffusivity may decrease faster than the return flow component of the bedload forcing, over a certain depth range. This, however, partially depends on the return flow bed stress coefficient $\Lambda_2^{[0]}$, whose depth dependence has not been verified experimentally. Thus a definitive statement of the depth-dependence of bar heights under weak reflection must be deferred until further experimental comparisons can be made.

Figure 2-14 illustrates the dependence of the steady state bar height on the grain diameter. For weak reflection in the lab (solid line), as the grain diameter increases, the steady state bar height initially decreases and then increases to a cusp where a sub-critical region appears ($X_c > 0$). Further increases in grain diameter cause the sub-critical region to increase in length, leaving less sand available for transport and smaller steady state bar heights. For weak reflection in the field (dash-dot), as the grain diameter increases, the bar height initially decreases and then levels off, without sub-critical regions appearing (for

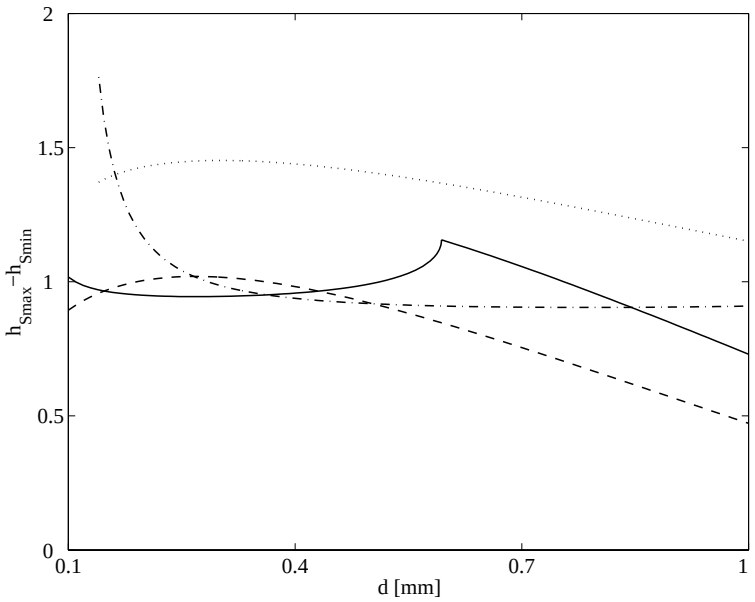


Figure 2-14: Dependence of the steady state bar height on the grain diameter $d$. The lab conditions are $T = 2.5$ s, $H_o = 60$ cm, $A_o(1 + |R_L|) = 7$ cm, $\eta_r' = 2$ cm, and $R_L = 0.25$ (solid), $R_L = 1$ (dash). The field conditions are $T = 8$ s, $H_o = 6$ m, $A_o(1 + |R_L|) = 50$ cm, $\eta_r'$ found from Eq. (1.105), and $R_L = 0.25$ (dash-dot), $R_L = 1$ (dot). In all cases, $\Lambda_2^{[0]} = 1.5$.

this range of $d$). For strong reflection in the lab and field (dashed and dotted lines, respectively), the bar height and length of the associated sub-critical regions initially increase and then decrease as the grain diameter increases. The lower grain-diameter cutoffs for the field conditions correspond to the transition from a rippled bed to sheet flow, which is not considered here.

### 2.4.3 Single bar simulations

In this section we focus on the evolution of a single bar in an infinite bar patch. Periodic boundary conditions are imposed at the bar ends. The Bragg Scattering effect of bars on waves is neglected for the moment, and the wave amplitude $A$ and reflection coefficient $R$ are held fixed. Despite the oversimplified setting, much insight is gained into the dependence of bar shape and growth rate on the wave and sediment characteristics.

Bar profile snapshots are plotted at different times and compared to the corresponding steady state profiles in Figure 2-15. Since the time interval between the solid profiles is the same, $\Delta\bar{t} = 0.2$, the relative distance between solid curves indicates the bar growth rate. Initially, the growth rate is high; at later times, the growth rate diminishes as the

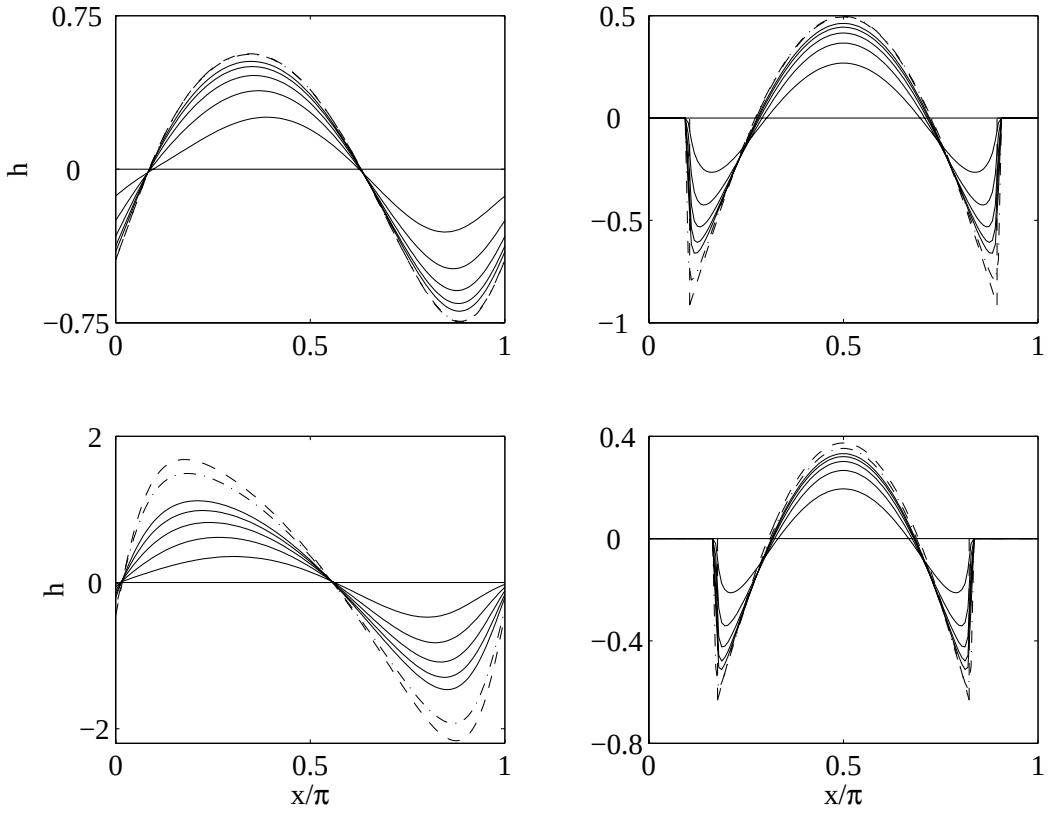


Figure 2-15: Bar profile snapshots at different times for $R_L = 0.25$ (left column) and $R_L = 1$ (right column). The time between each solid line profile is $\Delta\bar{t} = 0.2$. The dash-dot profile is at $\bar{t} = 4$. Steady state profiles are plotted as dashed lines for comparison. Field parameters are used in the top row, $T = 8$ s, $H_o = 6$ m, $A_o(1 + |R_L|) = 50$ cm, $d = 0.5$ mm, $\eta_r'$ found from Eq. (1.105). Lab conditions are used in the bottom row, $T = 2.5$ s, $H_o = 60$ cm, $A_o(1 + |R_L|) = 7$ cm, $d = 0.2$ mm, $\eta_r' = 2$ cm. In all cases, $\Lambda_2^{[0]} = 1.5$.

bars approach their steady state. Notice that for strong reflection ($R_L = 1$), the broad crests approach a steady state faster than the narrow scour regions. Thus, the maximum bar elevation achieves a steady state faster than the depth of scour.

Time evolutions of the bar crest elevation, $\max_x(\widetilde{h}(x,\bar{t}))$, scaled by the steady state crest elevation $\max_x(\widetilde{h}_S(x))$ are plotted in Figure 2-16 for field (left) and lab (right) conditions. The growth rate is large initially and then diminishes as the bars approach their steady state. The evolutions are plotted vs. the sand bar time $\bar{t} = t/\alpha_1$, so that large variations due to $\alpha_1$ are removed. Only minor differences are noticeable as the parameters vary. Increases in the wave amplitude (compare solid to dotted lines) and in the reflection coefficient (solid and dashed lines) and decreases in the mean water depth (solid and dash-dot lines) lead to larger bar growth rates initially and hence faster convergence to the steady state. The

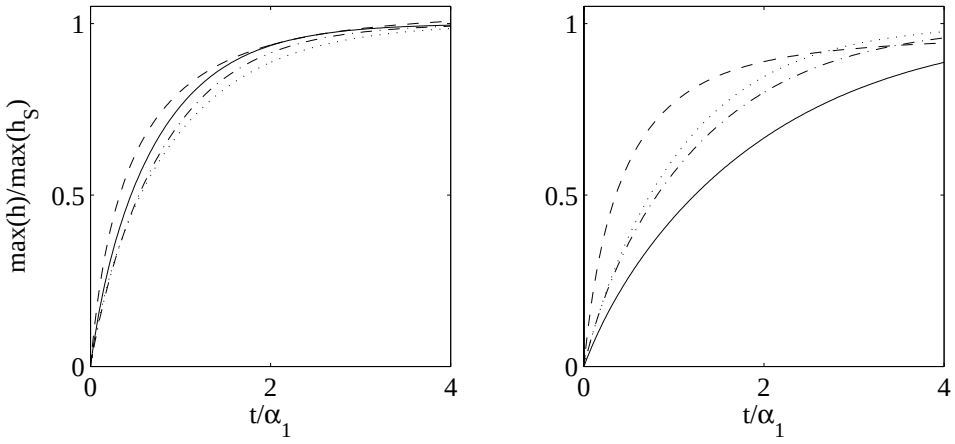


Figure 2-16: Evolution of the maximum bar elevation $\max_x \widetilde{h}(x,\bar{t})$, scaled by the corresponding steady state bar elevation $\max_x \widetilde{h}_S(x)$, in terms of the sand bar time $\bar{t} = t/\alpha_1$. Field conditions are plotted at left, with $T = 8$ s, $A_o(1 + |R_L|) = 50$ cm, $d = 0.5$ mm, $H_o = 6$ m, $\eta_r'$ found from Eq. (1.105), $R_L = 0.25$ (solid); the other curves have these parameters, except $R_L = 1$ (dash), $H_o = 7$ m (dash-dot), $A_o(1 + |R_L|) = 40$ cm (dot). Lab conditions are plotted at right, with $T = 2.5$ s, $A_o(1 + |R_L|) = 7$ cm, $d = 0.2$ mm, $\eta_r' = 2$ cm, $R_L = 0.25$ (solid); the other curves have these values, except $R_L = 1$ (dash), $H_o = 50$ cm (dash-dot) and $A_o(1 + |R_L|) = 8.5$ cm (dot). In all cases, $\Lambda_2^{[0]} = 1.5$.

variations for field conditions are not as significant as those for lab conditions, for similar changes in the parameters.

### 2.4.4 Waves and bars over a sandy region (multi-bar simulations)

Consider a bar patch $0 < x < L$. Seaward of the bar patch ($x < 0$), we assume that the water depth is too deep for bar formation or that the seabed is non-erodible. On the shoreward side of the patch, we assume that either a wall exists at $x = L$ or a beach exists at some $x > L$. The dimensionless incident amplitude $A(0)$ is specified at the seaward end of the bar patch and the reflection coefficient $R_L$ is specified at $x = L$ ($x_1 = \varepsilon L$).

The sand bar elevation is assumed to vanish, $\widetilde{h} = 0$, at the ends $x = 0, L$ of the bar patch. For strong reflection, the ends are chosen to coincide with sub-critical regions, where the forcing is zero and thus $\widetilde{h} = 0$ in any case. For weak reflection, these boundary conditions crudely simulate a non-erodible region. In addition, for weak reflection, the forcing is damped within a quarter bar length of $x = 0, L$ to maintain smoothness. An alternative would be to set the bedload transport rate to zero (Yu (1999)); however, this neglects sediment transported from the erodible region to the non-erodible region. We

admit that conditions near the shoreline of a real beach are very complicated with sediment transported to and from the surf zone. Thus, the nearshore condition for weak reflection is oversimplified and our predictions near this region are tentative.

The solution method is now outlined. Initially the bed is flat, $\widetilde{h}\,(x, \bar{t} = 0) = 0 = D_1$. The incident wave amplitude $A$ and reflection coefficient $R$ are solved from the Bragg Scattering equations (2.98) subject to the boundary conditions $A = A(0)$ at $x_1 = 0$ and $R = R_L$ at $x_1 = \varepsilon L$. A fixed step 4'th order Runge-Kutta scheme performs the spatial integration in $x_1$. We first integrate from $x_1 = \varepsilon L$ to 0 to find $R$ and then integrate from $x_1 = 0$ to $\varepsilon L$ to find $A$. If the mean depth varies, $H = H(x_1)$, then the local wavenumber $k(x_1)$ and group velocity $C_g(x_1)$ are found from (1.81) and the phase $S(x)$ is found from Eq. (1.80) by numerically integrating $k(x_1) = k(\varepsilon x)$ in $x$ from 0 to $x$. The wave parameters $A$, $R$ are then interpolated over the short scale $x$ and used to compute the forcing $q_\tau$ and diffusivity $D_\nu$ in the sand bar equation (2.105). We discretize the spatial derivatives in the sand bar equation (2.105) using finite differences. The sand bar elevation $\widetilde{h}$ is then updated in time using adaptive step 4th-5th order Runge-Kutta scheme (more precisely, the ode45 routine in Matlab), subject to the boundary conditions $\widetilde{h} = 0$ at $x_1 = 0,\ \varepsilon L$. The bar amplitude $D_1$ is then calculated from the updated sand bar elevation $\widetilde{h}$ using the Fast Fourier Transform (fft in Matlab). The wave parameters $A$, $R$ are then updated from the Bragg Scattering equations, followed by the bar elevation $\widetilde{h}$. The process repeats in this manner until the bar evolution is found for the desired time interval $\left[0, \bar{t}_f\right]$.

A second method, employed by Yu (1999) and Yu & Mei (2000), involves evolving a single bar at each grid point of $x_1$. Periodic boundary conditions are applied at the ends of each single bar. The values of the wave amplitude $A$, reflection coefficient $R$, mean depth $H$ and wavenumber $k$ are constant across each bar, but vary from bar to bar. The periodicity assumption is not valid at the ends of the bar patch if the seabed is non-erodible outside the bar patch. Furthermore, due to Bragg scattering, the boundary conditions on $A$ and $R$ will not be constant in time if bars exist outside the bar patch. Thus, like the theory presented in this thesis, the boundary conditions imposed by Yu & Mei render bar predictions at the ends of the bar patch tentative, at least for weak reflection.

For the constant depth comparisons with the MIT experimental data presented in §2.6 below, the difference between the two solution methods presented above is negligible everywhere except for the first and last half bars in each bar patch under weak reflection, where

predictions are tentative in any case.

## 2.5 Comparison to small scale laboratory experiments

Prior to our experiments, other researchers have investigated sand bar evolution in the laboratory. The experiments are generally performed in small tanks, where the water depth is generally less than 30 cm. In order to keep the boundary layer turbulent, the surface waves are often steep and higher harmonics in the flow may grow due to nonlinearity. We have assumed in this thesis that the waves are weakly nonlinear (small slope) and, in this chapter, monochromatic at leading order. Another common feature of small scale laboratory data is that the ripple heights are of the same order as the bar height. This is problematic in two ways. First, the acoustic sounding records of bars on real beaches made by Dolan & Dean (1985) [15] do not show the prevalence of ripples. This does not imply there are no ripples, but that the ripple heights are negligible compared to the bar heights. Second, our theory assumes that the ripple heights are an order of magnitude smaller than the bar heights. Despite these drawbacks, we offer comparisons of our theory with these small scale laboratory experiments for completeness.

Yu (1999) [68] argued that small scale laboratory experiments could not mimic real bars on beaches. The argument presented here follows hers, although some of our conclusions differ due to our use of the grain roughness Shields parameter $\widehat{\Theta}_d$, rather than the full Shields parameter $\widehat{\Theta}$, to properly calculate the mean bedload transport $Q_B$ over a half cycle. Guided by past theories, Yu [68] has shown that ripples in the laboratory and in nature are dynamically similar if $(A_b\omega)_{\text{lab}} = (A_b\omega)_{\text{field}}$. This scaling, readily achieved in the laboratory, is consistent with the empirical formulae of Nielsen [48] and Grant & Madsen [20], including Nielsen's Eq. (1.105) for ripple height.

For laboratory generated sand bars to be dynamically similar to those in nature, the situation is more complicated. Based on the current scaling, the sand bar evolution equation (2.106) and the supporting Eqs. (2.86), (2.105) for the diffusivity and bedload forcing depend on three main parameters: the wave slope $\varepsilon = KA_b$, the sand bar time coefficient $\alpha_1$, and the grain roughness Shields parameter $\widehat{\Theta}_{do}$. To simulate bars on a beach in the

laboratory, it is necessary that

$$\frac{(\alpha_1)_m}{(\alpha_1)_p} = \frac{(\varepsilon)_m}{(\varepsilon)_p} = \frac{\left(\widehat{\Theta}_{do}\right)_m}{\left(\widehat{\Theta}_{do}\right)_p} = 1, \tag{2.126}$$

where the subscripts $m$ and $p$ denote model and prototype, respectively. The similarity of the wave slope $\varepsilon$ gives

$$\frac{(A_b)_m}{(A_b)_p} = \frac{(K)_p}{(K)_m}. \tag{2.127}$$

From Eqs. (2.96), (1.128) and (1.38), it follows that

$$\frac{(\alpha_1)_m}{(\alpha_1)_p} = \left(\frac{(K)_p}{(K)_m}\right)^{3/2} \left(\frac{\left((s-1)\,gd^3\right)_p}{\left((s-1)\,gd^3\right)_m} \frac{(\tanh KH_o)_m}{(\tanh KH_o)_p}\right)^{1/2}, \tag{2.128}$$

$$\frac{\left(\widehat{\Theta}_{do}\right)_m}{\left(\widehat{\Theta}_{do}\right)_p} = \frac{\left(u_{fo}^2\right)_m}{\left(u_{fo}^2\right)_p} \left(\frac{\left((s-1)\,gd^3\right)_p}{\left((s-1)\,gd^3\right)_m}\right)^{1/2}, \tag{2.129}$$

where the friction velocities are based on the grain roughness $2.5d$. For water of intermediate depth, $KH_o = O\,(1)$ and thus $\tanh KH_o$ is approximately the same for model and prototype. Assuming natural sand and water are used in the laboratory, $s$ is the same for both model and prototype. Thus to have the same $\alpha_1$, Eq. (2.128) implies

$$(Kd)_p \simeq (Kd)_m\,. \tag{2.130}$$

The same result was obtained by Yu (1999) [68] using $\widehat{\Theta}_o$ instead of $\widehat{\Theta}_{do}$. In small scale experiments, a typical ratio of wavelengths is $(K)_m\,/\,(K)_p \sim 50$, so that $(d)_m\,/\,(d)_p \sim 1/50$. Thus, if field scale sand bars of very coarse sand, e.g. $(d)_p = 1$ mm, are simulated using a large laboratory wave flume, so that, say $(K)_m\,/\,(K)_p \sim 10$, the laboratory sand would have to have $(d)_m = 0.1$ mm. However, the laboratory experiments of De Best *et al.* (1971), Xie (1981), Dulou (2000), as well as our own experiments, indicate that sand of diameter $(d)_m = 0.1$ mm acts like a very fine sand in a laboratory setting. In Chapter 3, we show that sand bars of fine grains have different shapes than those of coarse grains, and are described by additional dimensionless parameters. Therefore, even though $\alpha_1$ and $\varepsilon$ are matched, these other parameters would not match and the bar shapes would differ significantly. Furthermore, the mean grain sizes in the field sand bar observations of Dolan

(1983) and Elgar *et al.* (2003) are approximately 0.25 mm and 0.3 mm, respectively. Thus, it seems virtually impossible to simulate bars in the lab whose evolution and geometry are dynamically similar to those in the field.

However, in sections 2.4.1, 2.4.2 and 2.4.3, we showed that the diffusivity and forcing terms in the sand bar equation and the resulting bar predictions look qualitatively similar for lab and field conditions. The parameter $\alpha_1$ only affects the growth rate and not the sand bar shape. Note also that it is the sand bar shape (i.e. spatial dependence) that determines variation of the envelope of the surface waves. If only $\widehat{\Theta}_{do}$ and $\varepsilon$ are made dynamically similar, Eq. (2.129) implies

$$\frac{(u_{fo})_m}{(u_{fo})_p} = \left(\frac{(d)_m}{(d)_p}\right)^{3/4}, \tag{2.131}$$

where the friction velocities are based on the grain roughness $2.5d$. Since the friction velocities are proportional to $A_b\omega$ and depend only weakly on the grain roughness via $Z_b$, and since the grain diameter $d$ in the lab and field are similar, Eq. (2.131) reduces to the condition

$$(A_b\omega)_m = (A_b\omega)_p\,. \tag{2.132}$$

We commented above that (2.132) is readily achieved in the laboratory. Therefore, it should not be surprising that the sand bar shapes and the sand bar interaction with waves found in the laboratory can mimic those found in nature.

Based on our theory, the larger ratio of ripple to bar height in the laboratory would only significantly affect the scale of the surface roughness, and not the bar shape. The reason is that the magnitude of the bedload transport depends mainly on the grain roughness Shields parameter $\widehat{\Theta}_{do}$, which depends only on the grain diameter $d$ and not on the ripple geometry. We should point out that a detailed analysis of the boundary layer flow around ripples may lead to further effects not included here.

We now consider four sets of experiments on laboratory generated sand bars.

### 2.5.1 Experiments of Herbich *et al.* (1965)

Herbich, Murphy & Van Weele (1965) [24] performed experiments in a wave tank 20.6 m long, 61 cm wide and deep. A flap-type wavemaker was positioned at one end and a seawall at the other. The inclination of the seawall was set at 15°, 30°, 45°, 67.5° and 90° with

respect to the horizontal bottom. A layer of sand, 12.7 cm thick, was placed at the bottom for a distance of 12.28 m in front of the seawall. Before each test the sand bed was leveled. A false bottom was mounted in front of the wavemaker to the edge of the sand bed so that the entire bed was flat initially. The sand was well washed before the test to eliminate fine particles. The mean grain diameter of the sand bed was $d = 0.48$ mm.

We consider only the experiments with the three steep seawalls (45°, 67.5° and 90°) for which the beach reflection was essentially perfect, i.e. $|R_L| \simeq 1.0$. The wall inclination only affects the phase of the reflection coefficient. Half-wavelength sand bars with ripples superposed on each were noted to form. However, a detailed account of sand bar crest locations was not given. All that was reported was the relative depth of scour corresponding to $\min_x(h(x,\bar{t}))$ over the time duration $t'_f$ of each test. Also, no detailed account of the ripple height was given, except that the maximum ripple height was approximately $\eta_{ro} = 2.54$ cm (1 inch). We showed in Figure 2-10 that for high reflection, the bar profiles are insensitive to the precise ripple height. Therefore, we simply use a constant ripple height for our predictions, $\eta'_r = \eta_{ro}$. The experimental parameters are listed in Table 2.2. For comparison, the ripple height predicted by Nielsen's formula (1.105) is listed in Table 2.2 as $\eta_{ro}(N)$. $\eta_{ro}(N)$ under-predicts $\eta_{ro}$ by about 50% for tests 1 and 2 and by about 25% for test 3. The ripple steepness $\eta_{ro}/\lambda_{ro}$, not reported by Herbich, is computed from Nielsen's formula (1.107). Lastly, the left hand side of Sleath's criterion for turbulence, Eq. (1.90), is between 57 and 225, and the values of $\mathsf{R}_{FT}$ are all significantly greater than 100, indicating the corresponding boundary layers are all fully rough turbulent.

Using the parameters listed in Table 2.2 and setting $R_L = 1$, predictions of both the depth of scour $\min_x \widetilde{h}(x,\bar{t})$ and the maximum bar elevation $\max_x \widetilde{h}(x,\bar{t})$ are made with the single bar simulations described in §2.4.3. In Figure 2-17, we have compared our predictions of the scour depth $\min_x \tilde{h}'/(4A_o)$ (dash) and the maximum bar elevation $\max_x \tilde{h}'/(4A_o)$ (solid) to Herbich's measurements. The shapes of the scour curves mimic very well the corresponding measured curves. In particular, the rate of approach to the steady state is very similar. The actual depth of scour is not as well predicted; the best prediction is made for the second case, Figure 2-17(middle). Note that in all cases, the total wave height $4A_o$ is approximately half the mean water depth $H_o$, which violates our assumption that $A_o/H_o = O(\varepsilon) \ll 1$. As a snapshot of the waves in Herbich's Figure 15 illustrates, the nonlinearity in the waves is significant and cannot be neglected. Yu & Mei [70] achieved

| Test | $T$ [s] | $H_o$ [cm] | $A_o$ [cm] | $R_L$ | $d$ [mm] | $\eta_{ro}$ [cm] | $\eta_{ro}/\lambda_{ro}$ | $t_f'$ [hr] |
|---|---|---|---|---|---|---|---|---|
| 1 | 1.5 | 12.7 | 1.56 | 1 | 0.48 | 2.54 | 0.17 | 21.30 |
| 2 | 1.5 | 17.4 | 2.05 | 1 | 0.48 | 2.54 | 0.17 | 23.80 |
| 3 | 2.0 | 21.29 | 2.36 | 1 | 0.48 | 2.54 | 0.17 | 27.00 |

| Test | $\lambda$ [m] | $\delta$ [cm] | $\alpha_1/\omega$ [hr] | $A_b\omega$ [cm/s] | $u_f$ [cm/s] | $w_S$ [cm/s] | $\eta_{ro}(N)$ [cm] |
|---|---|---|---|---|---|---|---|
| 1 | 1.61 | 1.60 | 1.47 | 25.3 | 8.38 | 6.20 | 1.26 |
| 2 | 1.86 | 1.70 | 1.60 | 27.6 | 8.90 | 6.20 | 1.34 |
| 3 | 2.79 | 2.21 | 3.51 | 29.7 | 8.68 | 6.20 | 1.88 |

| Test | $\varepsilon$ | $KH_o$ | $\Theta_{c0}$ | $\Theta_{do}$ | $\Theta_o$ | $Z_b$ | $\mathsf{R}_E$ | $\mathsf{R}_{FT}$ | Eq. (1.90) |
|---|---|---|---|---|---|---|---|---|---|
| 1 | 0.24 | 0.50 | 0.034 | 0.110 | 0.90 | 0.42 | 15318 | 8788 | 57 |
| 2 | 0.22 | 0.59 | 0.034 | 0.126 | 1.01 | 0.39 | 18138 | 9338 | 79 |
| 3 | 0.21 | 0.48 | 0.034 | 0.128 | 0.96 | 0.30 | 28149 | 9108 | 225 |

Table 2.2: Parameters for the experiments of Herbich *et al.* [24]. $\eta_{ro}(N)$ is the ripple height predicted by the empirical formula (1.105). The values of $\mathsf{R}_E$, $\mathsf{R}_{FT}$ and the l.h.s. of Eq. (1.90) indicate the boundary layers in all tests were fully rough turbulent.

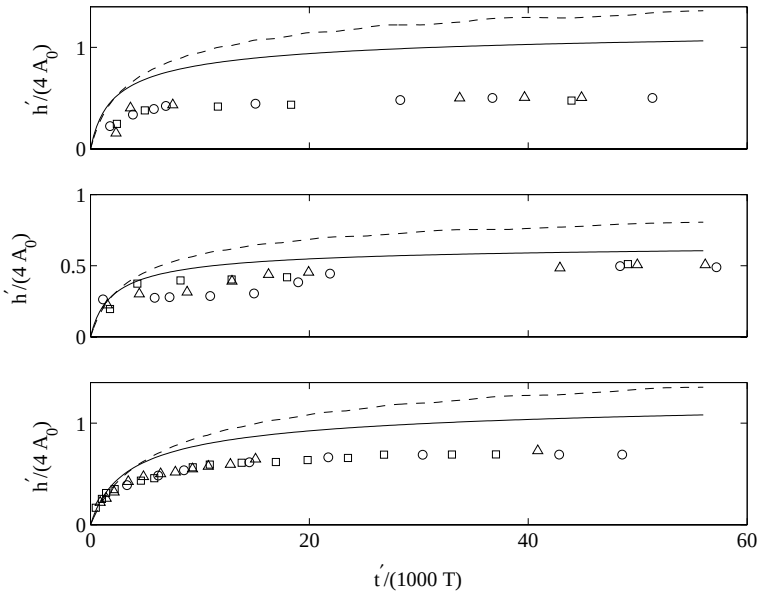


Figure 2-17: Predicted relative depth of scour $\min_x \tilde{h}'/(4A_o)$ (dash) and maximum bar elevation $\max_x \tilde{h}'/(4A_o)$ (solid) for the experiments of Herbich *et al.* [24]. The predictions are made from single bar simulations, described in §2.4.3, based on $R_L = 1$ and the parameters in Table 2.2, for Tests 1 (top), 2 (middle), and 3 (bottom). The data of Herbich *et al.* [24] is plotted for seawalls inclined at 45° (△), 67.5° (□) and 90° (○).

better agreement with Herbich's data since they employed a fitting parameter adjusted to match the predicted and measured steady state bar heights. The theory presented here (with $R_L = 1$) uses no fitting parameters; all empirical parameters are found in the general literature.

### 2.5.2 Experiments of de Best *et al.* (1971)

De Best, Bijker & Wichers (1971) [12] performed experiments in a wave tank 10 m long and 50 cm wide. A wavemaker was positioned at one end and a vertical seawall at the other. A layer of sand roughly 10 cm thick was placed at the bottom for a distance of at least one half wavelength in front of the seawall. Before each test the sand bed was leveled. Coarse and fine grained sands were used, as well as various wave periods. In one experiment, coarse and fine sand was mixed; the sand was sorted under the wave action. We consider our own sediment sorting experiments in Chapter 5.

The parameters for three of De Best *et al.*'s tests are listed in Table 2.3. In this section, we consider only test SA III with the coarse sand; the tests with finer grains are presented in Chapter 3. De Best *et al.* reported photographs of characteristic bed profiles for each of these three tests. The raw profiles were digitized from the reported profile photographs. A clock positioned in each photograph gives the time duration $t'_f$ of the test. The left hand side of Sleath's criterion for turbulence, Eq. (1.90), is between 233 and 537, and the values of $\mathsf{R}_{FT}$ are all significantly greater than 100, indicating the corresponding boundary layers are all fully rough turbulent.

Figure 2-18(top) shows that our steady state prediction and single bar simulations after 4.5 and 9 hours compare favorably with the measured bed profiles. The steady state profile overestimates the scour in the troughs, since the flat-bed critical Shields parameter $\Theta_{C0}$ is used for steady state predictions. The single bar simulations employed the slope-dependent critical Shields parameter $\Theta_C$ of Fredsøe, Eq. (1.115), which decreases with increasing bed slope. The single bar simulations thus more accurately predict the size of the sub-critical region and also the depth of scour in the trough.

The ripple heights were obtained by averaging the measured bed profiles across a ripple length and subtracting the average from the measured profile. The ripple elevations are plotted in Figure 2-18(middle) along with the fitting formula Eq. (1.108) with $(r_1, r_2, r_3) = (0.71, 3, 2)$ and $\eta_{ro}$ listed in Table 2.3. For comparison, the characteristic ripple height

| Test | $T$ [s] | $H_o$ [cm] | $A_o$ [cm] | $R_L$ | $d$ [mm] | $\eta_{ro}$ [cm] | $\eta_{ro}/\lambda_{ro}$ | $t'_f$ [hr] |
|---|---|---|---|---|---|---|---|---|
| SA III | 2.0 | 31 | 3.00 | 1 | 0.22 | 1.84 | 0.16 | 9.00 |
| SE III | 2.0 | 31 | 3.00 | 1 | 0.16 | 1.56 | 0.16 | 7.00 |
| SB III | 2.0 | 31 | 3.00 | 1 | 0.13 | 1.42 | 0.20 | 5.00 |

| Test | $\lambda$ [m] | $\delta$ [cm] | $\alpha_1/\omega$ [hr] | $A_b\omega$ [cm/s] | $u_f$ [cm/s] | $w_S$ [cm/s] | $\eta_{ro}(N)$ [cm] |
|---|---|---|---|---|---|---|---|
| SA III | 3.31 | 2.05 | 7.22 | 30.2 | 8.05 | 2.33 | 1.56 |
| SE III | 3.31 | 1.96 | 8.48 | 30.2 | 7.70 | 1.42 | 1.38 |
| SB III | 3.31 | 1.91 | 9.38 | 30.2 | 7.51 | 1.01 | 1.24 |

| Test | $\varepsilon$ | $KH_o$ | $\Theta_{c0}$ | $\Theta_{do}$ | $\Theta_o$ | $Z_b$ | $\mathsf{R}_E$ | $\mathsf{R}_{FT}$ | Eq. (1.90) |
|---|---|---|---|---|---|---|---|---|---|
| SA III | 0.18 | 0.59 | 0.049 | 0.217 | 1.82 | 0.24 | 29055 | 6114 | 233 |
| SE III | 0.18 | 0.59 | 0.064 | 0.269 | 2.29 | 0.21 | 29055 | 4960 | 258 |
| SB III | 0.18 | 0.59 | 0.076 | 0.309 | 2.68 | 0.19 | 29055 | 4403 | 537 |

Table 2.3: Parameters for the experiments of De Best *et al.* (1971) [12]. $\eta_{ro}(N)$ is the ripple height predicted by the empirical formula Eq. (1.105). The values of $\mathsf{R}_E$, $\mathsf{R}_{FT}$ and the l.h.s. of Eq. (1.90) indicate the boundary layers in all tests were fully rough turbulent.

predicted by Nielsen's formula (1.105) is listed in Table 2.3 as $\eta_{ro}(N)$ and gives reasonable estimates of the measured ripple heights.

The predicted evolution of the maximum bar elevation scaled by the steady state bar height, $\max_x \widetilde{h} \,/\, \max_x \widetilde{h}_S$, is plotted in Figure 2-18(bottom) and shows that the predicted bar crest height at 9 hours is close to its (predicted) steady state value.

### 2.5.3 Experiments of Xie (1981)

Xie (1981) [67] performed experiments in two tanks: a small tank 38 m long, 0.8 m wide and 0.6 m deep; and a large tank 46 m long, 0.8 m wide and 1.0 m deep. Wavemakers were installed at one end of each tank and vertical seawalls at the opposing ends. For the small flume, the distance between the wave paddle and the wall was 32.9 m. A 6 m long, 15 cm thick horizontal sand bed was placed in front of the wall. A 1:30 slope linked the sand bed to the flume bottom. The water depth in the flume is 0.45 m; that over the sand bed was $H_o = 30$ cm. The larger flume had 36.2 m between the wave board and the opposing vertical wall. The length of the horizontal sand bed in front of the wall was 11 m. The water depths used in the flume were 0.45, 0.55 and 0.65 m; the water depths over the sand bed were 0.3, 0.4 and 0.5 m respectively.

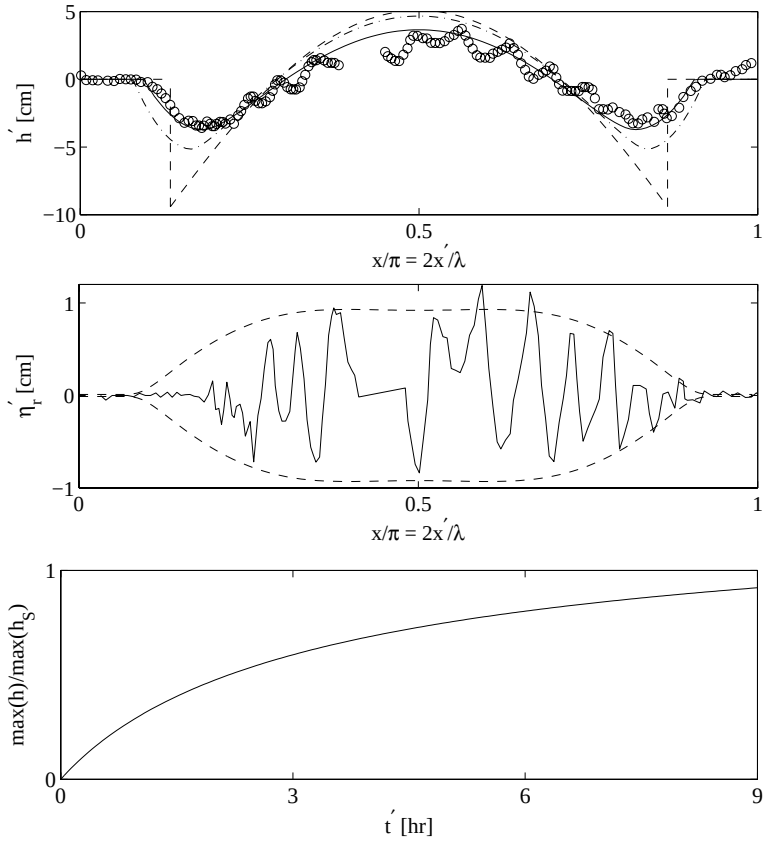


Figure 2-18: Comparison of predictions with the experimental bar profiles of De Best *et al.* (1971) [12]. Top: the measured ($\circ$) bar profile after 9 hours for test SA III of De Best *et al.*, with our single bar prediction $\widetilde{h}'$ after 4.5 (solid) and 9 (dash-dot) hours, and our steady state profile (dash). The test parameters are listed in Table 2.3. Middle: dashed lines $\pm\eta_r'/2$ are compared to the measured ripple elevation, where $\eta_r'$ is the fitted ripple height from Eq. (1.108) with $(r_1, r_2, r_3) = (0.71, 3, 2)$ and $\eta_{ro}$ listed in Table 2.3. Bottom: the predicted evolution of the maximum bar height scaled by steady state value, $\max_x \tilde{h}/\max_x \tilde{h}_S$. Gaps in the data are due to a vertical tank support blocking the view.

Both fine and coarse sands were used in the tests. For each test presented here, the sand bed was initially level. Wave records were taken by wave height meters placed at the antinodes. In some tests, the orbital velocities of the standing waves at the nodes and halfway between the nodes and the antinodes were measured by a current flow meter. The seabed profiles were measured by an electric profile indicator developed at Delft Hydraulics Laboratory. The bar profiles were averaged spatially to remove the ripples; ripple height and steepness measurements compared favorably with Nielsen (1979)'s empirical formulae, Eqs. (1.105) and (1.107), presented in §1.5. Xie reports equilibrium bar profiles and the time evolution of the depth of scour. The equilibrium bar profiles are presented in a scaled

| Test | $T$ [s] | $H_o$ [cm] | $A_o$ [cm] | $R_L$ | $d$ [mm] | $\eta_{ro}$ [cm] | $\eta_{ro}/\lambda_{ro}$ | $t'_f$ [hr] |
|---|---|---|---|---|---|---|---|---|
| 23a | 1.5 | 30 | 3.25 | 1 | 0.78 | 1.58 | 0.17 | 3.00 |
| 13a | 1.5 | 30 | 3.25 | 1 | 0.15 | 1.02 | 0.14 | N/A |
| 8b | 2.0 | 50 | 3.75 | 1 | 0.20 | 1.45 | 0.16 | N/A |

| Test | $\lambda$ [m] | $\delta$ [cm] | $\alpha_1/\omega$ [hr] | $A_b\omega$ [cm/s] | $u_f$ [cm/s] | $w_S$ [cm/s] | $\eta_{ro}(N)$ [cm] |
|---|---|---|---|---|---|---|---|
| 23a | 2.40 | 1.64 | 1.56 | 30.70 | 8.40 | 9.63 | 1.58 |
| 13a | 2.40 | 1.46 | 3.87 | 30.70 | 7.48 | 1.28 | 1.02 |
| 8b | 4.01 | 1.78 | 14.1 | 27.47 | 7.05 | 2.02 | 1.45 |

| Test | $\varepsilon$ | $KH_o$ | $\Theta_{c0}$ | $\Theta_{do}$ | $\Theta_o$ | $Z_b$ | $\mathsf{R}_E$ | $\mathsf{R}_{FT}$ | Eq. (1.90) |
|---|---|---|---|---|---|---|---|---|---|
| 23a | 0.20 | 0.79 | 0.034 | 0.111 | 0.56 | 0.25 | 22950 | 5493 | 231 |
| 13a | 0.20 | 0.79 | 0.067 | 0.315 | 2.31 | 0.18 | 22950 | 3166 | 135 |
| 8b | 0.14 | 0.78 | 0.053 | 0.198 | 1.54 | 0.21 | 23774 | 4211 | 210 |

Table 2.4: Parameters for the experiments of Xie (1981) [67]. The ripple height $\eta_{ro}(N)$ and steepness $\eta_{ro}/\lambda_{ro}(N)$ are estimated empirically from Eqs. (1.105) and (1.107). The values of $\mathsf{R}_E$, $\mathsf{R}_{FT}$ and the l.h.s. of Eq. (1.90) indicate the boundary layers in all tests were fully rough turbulent. Lastly, the values listed for the critical Shields parameter $\Theta_{c0}$ are found from Eq. (1.102).

manner: the elevations are scaled by the incident wave height $2A_o$ and the horizontal spatial coordinate is translated relative to the measured length $X_c$ of the equilibrium sub-critical region and scaled by the wavelength $\lambda$. In our plots below, we have unraveled these transformations and plotted the bar elevations vs. $x$. Lastly, Xie reports the time durations $t'_f$ required to reach equilibrium for some tests, but not all.

We focus on the tests with relatively coarse grains for which bar profiles are reported. The relevant parameters are listed in Table 2.4. For the tests listed, the left hand side of Sleath's criterion for turbulence, Eq. (1.90), evaluates to between 135 and 231, and the values of $\mathsf{R}_{FT}$ are significantly greater than 100, indicating the corresponding boundary layers are fully rough turbulent.

Figure 2-19 shows that our steady state prediction and single bar simulations compare favorably with the measured bed profiles. The steady state profile overestimates the scour in the troughs, since the flat-bed critical Shields parameter was used for steady state predictions. Figure 2-20 shows good agreement between measurements and our prediction of the time evolution of the depth of scour. Motivated by the reported agreement between Xie's

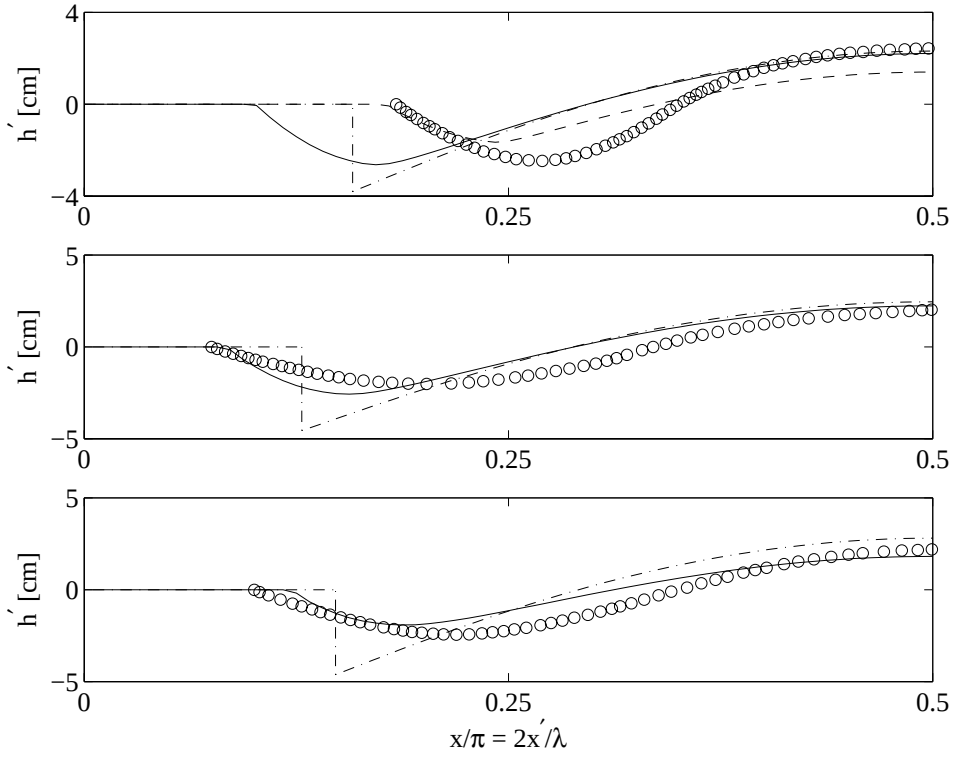


Figure 2-19: Comparison of predictions with the experimental bar profiles of Xie (1981) [67] for test 23a (top), 13a (middle) and 8b (bottom). Each plot has measured elevations (∘), and our single bar prediction $\widetilde{h}'$ (solid) and steady state profile $\widetilde{h}_S(x)$ (dash-dot) based on test parameters in Table 2.4. The top plot also has a single bar prediction with $\Theta_{c0} = 0.065$ (dash). The single bar predictions are plotted at the reported time of $t'_f = 3$ hours in the top plot, and 12000 wave periods for the middle and bottom plots. Ripple predictions are found from Eqs. (1.105) and (1.110).

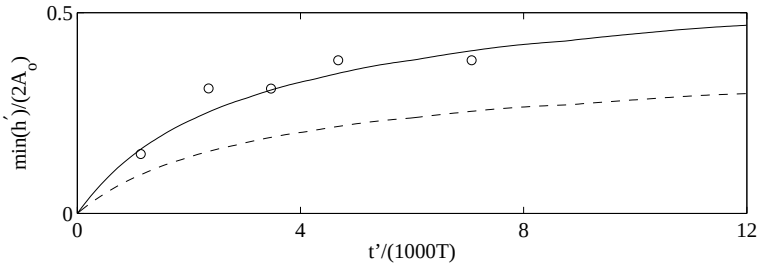


Figure 2-20: Comparison of predictions with the measured depth of scour (∘) for test 23a of Xie (1981) [67]. The predictions (solid, dash) correspond to the profiles (solid, dash) in Figure 2-19(top).

data and Nielsen's formulae for ripple geometry, the ripple height and equivalent roughness are found from Nielsen's Eq. (1.105) and Eq. (1.110).

In §2.4.1, we discussed the relation between the width $X_c$ of the sub-critical region under the wave antinode and the critical Shields parameter $\Theta_{c0}$. In tests 13a and 8b, $X_c$ is well-predicted by choosing $\Theta_{c0}$ from the Shields diagram, i.e. Eq. (1.102). However, perhaps owing to the relatively large grain diameter (for a laboratory setting) used in test 23a, the Shields diagram estimate of $\Theta_{c0} = 0.034$ is apparently too small since the predicted profile (solid line, Figure 2-19(top)) has a narrower sub-critical region than the measured profile. Figure 2-19(bottom) shows that the evolution of the bar height is well predicted, however. If $\Theta_{c0}$ is instead set to 0.065 (dashed line, Figure 2-19(top)), the width of the flat region is better predicted, but the overall bar height is not as well predicted.

### 2.5.4 Experiments of Seaman & O'Donoghue (1996)

Seaman & O'Donoghue (1996) [56] performed experiments in a wave tank 20 m long and 45 cm wide. A paddle-type wavemaker was positioned at one end and a vertical seawall at the other. The mean water depth in front of the wavemaker was 70 cm. A 1/20 slope perspex panel beach extended from the wavemaker all the way to the surface of a sand bed mounted on supports. The mean water depth over the sand bed was 15 cm. The sand bed was 20 cm deep with a mean diameter of $d = 0.32$ mm and extended for a distance of 3 m in front of the seawall. The sand bed was leveled before each test. The relevant parameters are listed in Table 2.5. The time duration $t'_f$ of each test was not reported, although the tests were run until the bars reached an apparent equilibrium. The left hand side of Sleath's criterion for turbulence, Eq. (1.90), is 67 and 80 for tests 3a and b, and the values of $\mathsf{R}_{FT}$ are significantly greater than 100, indicating the corresponding boundary layers are fully rough turbulent.

Seaman & O'Donoghue reported the equilibrium bar profiles for two tests. In Figure 2-21, the equilibrium profiles are compared with our steady state predictions and with single bar simulations at $\bar{t} = 8$, corresponding to $t' = 12.7$ hours for test 3a and 4.42 hours for test 3b. The agreement between the measured and predicted bar amplitudes is good; however, there appears to be a discrepancy between the predicted and measured bar length. Due to the other favorable theory/lab data comparisons, it is surprising that the measured bar length is not closer to half the surface wavelength.

| Test | $T$ [s] | $H_o$ [cm] | $A_o$ [cm] | $R_L$ | $d$ [mm] | $\eta_{ro}$ [cm] | $\eta_{ro}/\lambda_{ro}$ | $t'_f$ |
|---|---|---|---|---|---|---|---|---|
| 3a | 1.1 | 15 | 1.50 | 1 | 0.32 | 0.70 | 0.17 | N/A |
| 3b | 0.9 | 15 | 2.00 | 1 | 0.32 | 0.70 | 0.17 | N/A |

| Test | $\lambda$ [m] | $\delta$ [cm] | $\alpha_1/\omega$ [days] | $A_b\omega$ [cm/s] | $u_f$ [cm/s] | $w_S$ [cm/s] | $\eta_{ro}(N)$ [cm] |
|---|---|---|---|---|---|---|---|
| 3a | 1.24 | 0.77 | 0.066 | 20.3 | 5.43 | 3.87 | 0.75 |
| 3b | 0.97 | 0.76 | 0.023 | 24.4 | 6.55 | 3.87 | 0.70 |

| Test | $\varepsilon$ | $KH_o$ | $\Theta_{c0}$ | $\Theta_{do}$ | $\Theta_o$ | $Z_b$ | $\mathsf{R}_E$ | $\mathsf{R}_{FT}$ | Eq. (1.90) |
|---|---|---|---|---|---|---|---|---|---|
| 3a | 0.18 | 0.76 | 0.039 | 0.111 | 0.57 | 0.24 | 7258 | 1569 | 67 |
| 3b | 0.23 | 0.97 | 0.039 | 0.161 | 0.83 | 0.24 | 8587 | 1895 | 80 |

Table 2.5: Parameters for the experiments of Seaman & O'Donoghue (1996) [56]. $\eta_{ro}(N)$ is the ripple height predicted by the empirical formula Eq. (1.105). The values of $\mathsf{R}_E$, $\mathsf{R}_{FT}$ and the l.h.s. of Eq. (1.90) indicate the boundary layers in all tests were fully rough turbulent.

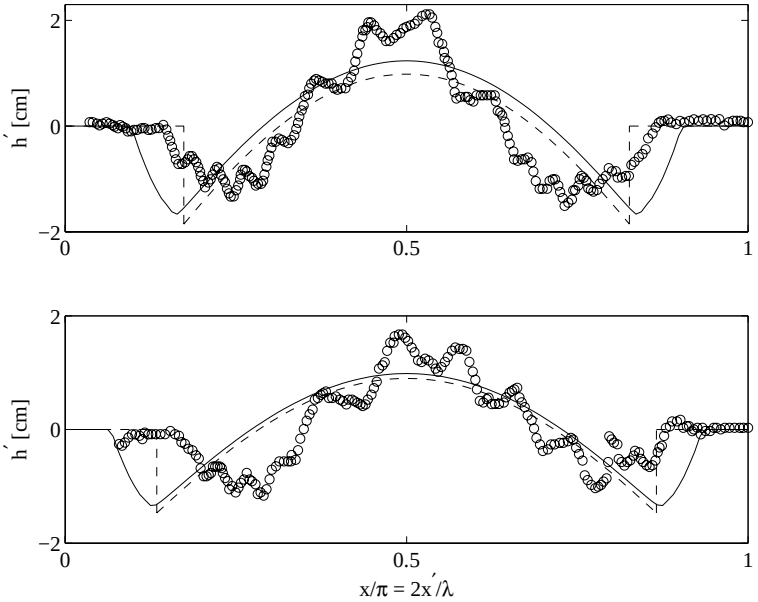


Figure 2-21: Predicted and measured bar profiles $\widetilde{h}$ for the experiments of Seaman & O'Donoghue (1996) [56]. The solid profile $\widetilde{h}\prime$ is the result of a single bar simulation, described in §2.4.3, after $\bar{t} = 8$. The dashed line is our steady state profile. The test parameters are listed in Table 2.5 for the top (test 3a) and bottom (test 3b) plots.

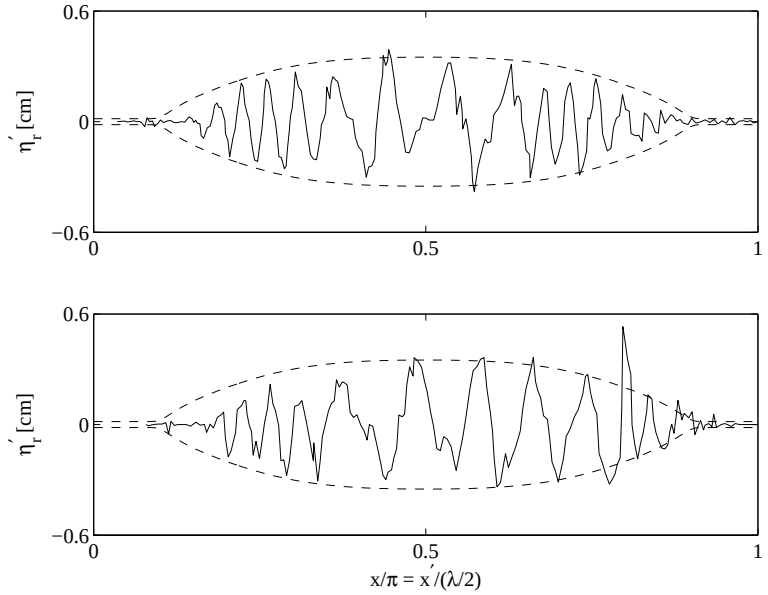


Figure 2-22: Measured ripple elevations (solid line) for the experiments of Seaman & O'Donoghue (1996) [56] for test 3a (top) and test 3b (bottom). The dashed lines indicate $\pm\eta_r'/2$, where $\eta_r'$ is the fitted ripple height from (1.108) with $(r_1, r_2, r_3) = (0.62, 3, 4)$ and $\eta_{ro}$ listed in Table 2.5.

The ripple heights were obtained by averaging the measured bed profiles across a ripple length and subtracting the average from the measured profile. The ripple elevations are plotted in Figure 2-22 along with the fitting formula Eq. (1.108) with $(r_1, r_2, r_3) = (0.62, 3, 4)$ and $\eta_{ro}$ listed in Table 2.5. Seaman & O'Donoghue reported that the characteristics of the ripples remained largely unchanged throughout the experiments as the underlying bars developed. This validates our use of the ripple height in Eq. (1.108) throughout our simulation. Recall that in our single bar simulations, the wave parameters are held fixed in time, and thus, the ripple height is also fixed. Also, for comparison, the ripple height predicted by Nielsen's formula (1.105) is listed in Table 2.5 as $\eta_{ro}(N)$ and again gives reasonable estimates of the measured ripple height.

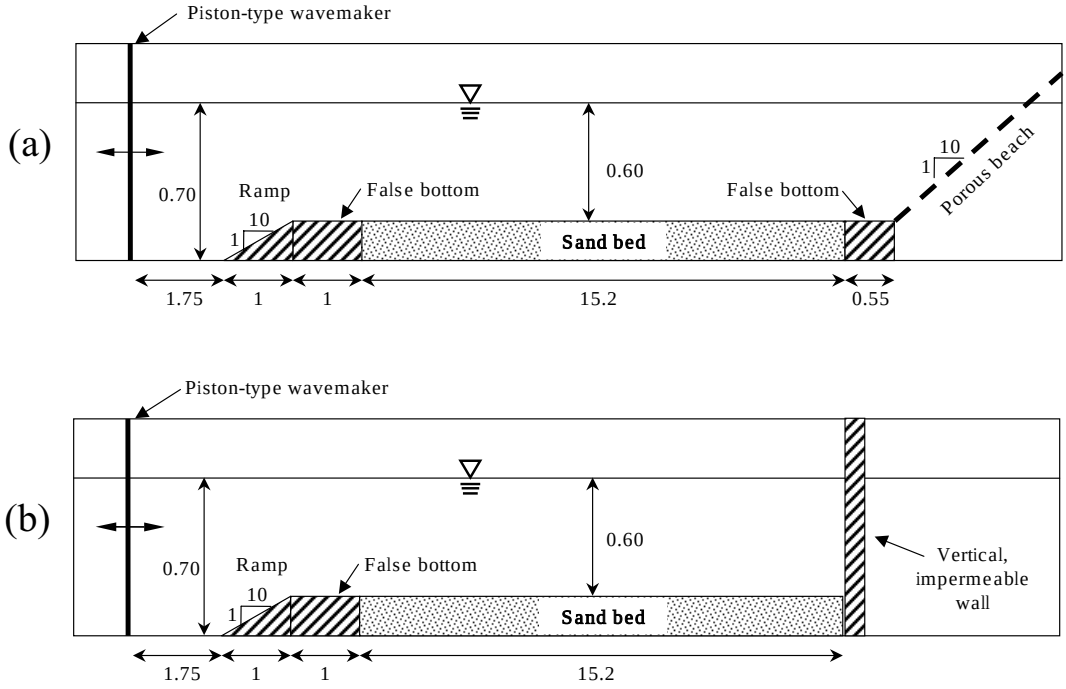


Figure 2-23: Schematic of the experimental setup for the MIT experiments. Two configurations of the wave flume were used: (a) a porous beach and (b) a wall. All lengths are in meters.

## 2.6 Comparison to MIT laboratory experiments

Due to the drawbacks of the available small scale laboratory data, we performed a new set of larger scale laboratory experiments to properly validate our theory. In collaboration with Blake Landry [33], experiments were run during the spring of 2003 in a large wave flume 25 m long, 70 cm wide and 80 cm deep. A piston-type wavemaker was positioned at one end and either an artificial beach or vertical seawall at the other. A layer of sand, 10 cm thick, was placed at the bottom for a distance of 15.2 m in front of the beach or seawall. Before each test, the sand bed was leveled. Tests were run for various grain sizes and wave conditions. More precise information regarding the experimental facilities can be found in Carter (2002) [8], Mathisen (1993) [41] and Rosengaus (1987) [55].

The precise initial bathymetry is illustrated in Figure 2-23. We denote by $X'$ the distance from the mean wavemaker position. The mean water depth in front of the wavemaker was 70 cm from $X' = 0$ to $X' = 1.75$ m. A false-bottom ramp and platform were installed to meet the edge of the sand bed. The 1:10 sloping ramp started at $X' = 1.75$ m and ended

at $X' = 2.75$ m, where the water depth was 60 cm. A horizontal platform extended from $X' = 2.75$ m to $X' = 3.75$ m, and the sand bed test section extended from $X' = 3.75$ m to $X' = 18.95$ m, for a total length $L' = 15.2$ m. For experiments with the wall, the side of the wall facing the wavemaker was positioned at $X' = 18.95$ m. For experiments with the artificial beach, a horizontal false bottom extended from the edge of the sand bed at $X' = 18.95$ m to the toe of the beach at $X' = 19.5$ m. The artificial beach was made porous by drilling 3" holes in the beach over approximately half the water depth. The beach was covered with 2" horsehair mesh to further reduce the beach reflection.

The wave fields for each test were chosen to maximize sediment movement on the bed while keeping the wave slope as mild as possible. Monochromatic wavemaker piston displacements generate a spurious free wave component to the second harmonic. Since this free second harmonic wave component would not be present for simple harmonic waves naturally generated (e.g. by the wind) and propagating in a semi-infinite expanse of water toward a beach or seawall, the free second harmonic is canceled, as described below, by adding a second harmonic component to the wavemaker piston displacement.

For each test run, wave records and bar profiles were measured at periodic time intervals. Three probes mounted on a movable cart measured the wave elevation. By positioning the cart at successive points along the tank, time records of the surface elevation, each 1024 s in duration, were taken at 25 cm intervals across the sand bed section. One set of wave measurements required 49 minutes to complete. A digital camera was mounted on a side arm of the same cart and positioned at the level of the initial surface of the sand bed. Images of successive portions of the seabed were taken and later stitched to obtain the profile of the entire sand bed. Each set of seabed images required 10 minutes to shoot. Lastly, CCD cameras recorded ripple and initial bar evolution.

Four sand bar tests, labeled as[1] 324, 430, 508 and 519 were then run as described above and progressed as follows. Initially the sand bed was smooth and horizontal. Roughly ten to twenty minutes after the wavemaker started, ripples forming on the seabed reached a quasi-steady state. Over several hours, sand bars began to form. Tests 324 and 508 used the artificial beach configuration of the wave flume (see Figure 2-23(a)), and had weak beach reflection $|R_L| \simeq 0.24$. Tests 430 and 519 used the seawall configuration of the wave flume (see Figure 2-23(b)) and had pure standing waves, $R_L = 1$. Tests 324, 430 and 508 had

[1]These tests are labeled according to the starting date, e.g. 324 means March 24, 2003, etc.

relatively coarse sand, $d = 0.2$ mm, while test 519 had relatively fine sand, $d = 0.125$ mm.

Over the next few sections, the wave generation and parametrization procedure is described and then the measurements from each bar test are compared with our predictions.

### 2.6.1 Wave generation and parameterization

Given the wavemaker piston displacement

$$\xi'(t) = \xi_1' \cos \omega t' + \xi_2' \sin\left(2\omega t' + \psi_2\right), \tag{2.133}$$

Madsen (1971) [36] derived a theory to predict resultant surface waves under zero beach reflection. In general, if the wavemaker piston motion is monochromatic ($\xi_2' = 0$), free and forced second harmonics appear in the resultant surface waves. Since the free second harmonic has wave number $k^{[2]} \neq 2k$, we show experimentally in Chapter 5 that the waves and bars are not spatially periodic. Furthermore, the amplitude of the second harmonic is significantly modulated across the tank, leading to varying bar shapes across the tank. As noted above, since this free second harmonic wave component is an artifact of the wavemaker and would not be present for simple harmonic waves naturally generated (e.g. by the wind) and propagating in a semi-infinite expanse of water toward a beach or seawall, the free second harmonic is canceled, as described below, by adding a second harmonic component to the wavemaker piston displacement.

We focus on the laboratory case where the mean water depth is constant. By keeping the second harmonic piston amplitude $\xi_2'$ small, the resultant surface waves have a first harmonic amplitude of

$$\left|\zeta^{[1]\prime}\right| = \left|A'\right| \sqrt{1 + |R|^2 + 2\,|R| \cos\left(2k'x' - \theta_R\right)}. \tag{2.134}$$

Initially, the bed is flat (no bars) so that $A'$ and $R'$ are constants. By adjusting the time coordinate $t'$, we may assume that $A' = |A'| > 0$. The complex amplitude of the weak second harmonic is given by Eq. (1.42). Along the sand bed, the mean water depth is

constant, and hence (1.42) becomes

$$\begin{aligned}\zeta_2^{[2]\prime} &= \frac{k'\left(1+2\cosh^2 k'H'\right)\cosh k'H'}{4\sinh^3 k'H'}A'^2\left(e^{2ik'x'}+R^2e^{-2ik'x'}\right)\\ &\quad + A^{[2]\prime}\left(e^{ik^{[2]\prime}x'}+R^{[2]}e^{-ik^{[2]\prime}x'}\right),\end{aligned} \tag{2.135}$$

where $A'$ ($=|A'|$) and $R$ were previously found. The parameters of the free wave component, $A^{[2]\prime}$ and $R^{[2]}$, are both complex, in general, since the phase of the second harmonic amplitude will differ from that of the first harmonic. Also, $A^{[2]\prime}$, $R^{[2]}$ are constant because the mean depth is constant.

Unfortunately, the steep ramp in front of our wavemaker leading to the sand bed rendered Madsen [36]'s theory, derived for a flat bottom, inapplicable. Thus, the details of the transformation from the wavemaker piston position to the resultant surface waves in the tank are complicated and are not considered.

Instead of predicting the waves, measurements of the surface elevation are made directly at regular intervals along the tank and allow the parameters of the first and second harmonics, $|A'|$, $R$ and $A^{[2]\prime}$, $R^{[2]}$, respectively, to be found. Technically, only three measurements of the first harmonic and four of the second harmonic are needed to compute the phases and magnitudes of these wave parameters. However, to overcome experimental variation, measurements are taken every 25 cm along the tank and $|A'|$, $R$, $A^{[2]\prime}$, $R^{[2]}$ are found by a least squares minimization of the error between the theoretical profiles (2.134), (2.135) and the measured first and second harmonic amplitudes along the tank. Note that the phase of the reflection coefficient governs the position of the wave nodes and antinodes, so the values are readily found by aligning the positions of the theoretical nodes to the measured nodes.

Typical observed wave spectra at fixed locations along the tank are shown in Figure 2-24. Near antinodes, the first harmonic dominates; near nodes, the second harmonic can be comparable to the first. Also, the thin spiked spectra indicate the waves are perfectly tuned ($t_1$-independent).

The first and second harmonic wave amplitudes across the tank are plotted at various times in Figure 2-25 for tests 324, 508 and 430. The corresponding fitted parameters of the initial wave profiles (before the bars formed $\widetilde{h} \approx 0$) are given in Table 2.6. The variations in the waves after that time are due to the Bragg Scattering effect of the bars on the waves, and also possibly the wavemaker (for test 508). In test 324 and 508, the beach reflection

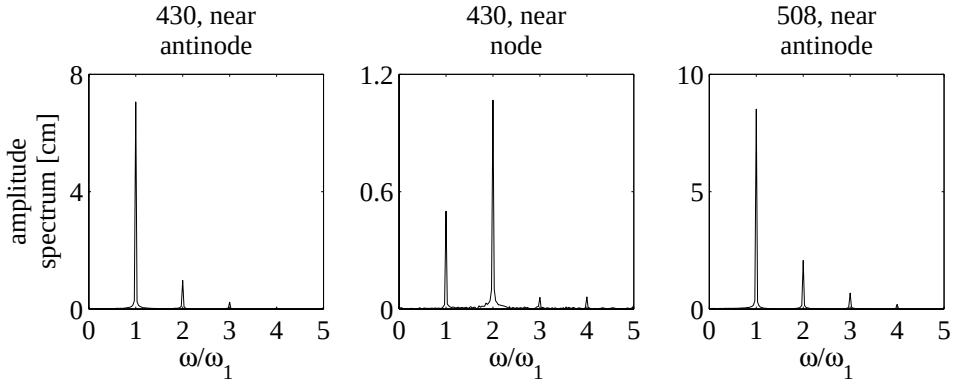


Figure 2-24: Sample wave amplitude spectra near an antinode ($X' = 9$ m) and near a node ($X' = 7.75$) for test 430, and near an antinode ($X' = 6.25$) for test 508.

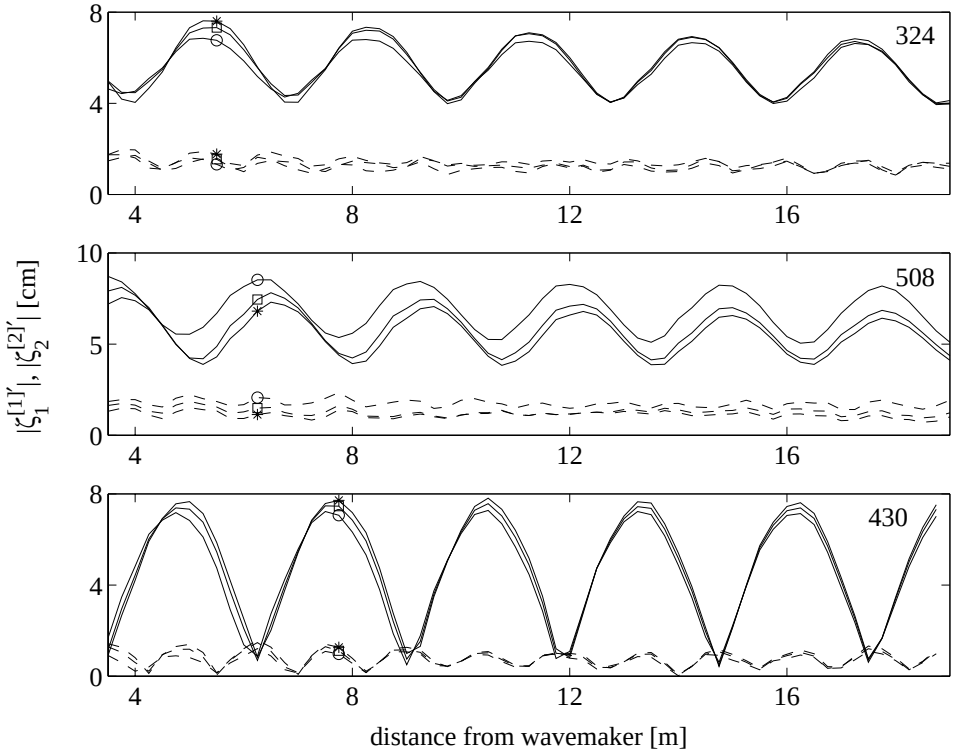


Figure 2-25: Amplitudes of first (solid) and second (dash) wave harmonics across the tank for tests 324 (top), 508 (middle) and 430 (bottom) after the following times, in days, 0 ($\circ$), 1.5 ($\square$), 3.0 ($*$) for test 324 and 0 ($\circ$), 2.0 ($\square$), 4.0 ($*$) for tests 508 and 430.

| Test | $A_1^{[1]}$ [cm] | $R_1^{[1]}$ | $A_2^{[2]}$ [cm] | $R_2^{[2]}$ |
|---|---|---|---|---|
| 324 | 5.46 | $0.24e^{5.22i}$ | $0.17e^{-0.21i}$ | $e^{4.53i}$ |
| 508 | 7.01 | 0.23 | $0.12e^{4.36i}$ | $e^{3.90i}$ |
| 430 | 3.68 | 1.0 | $\approx 0$ | |

Table 2.6: Fitted parameters for the initial wave profiles in tests 324, 508 and 430 of the MIT experiments. The phases are with respect to $x = 0$ which corresponds to distances of 2.8 m, 3.5 m, and 4.78 m from the wavemaker for tests 324, 508 and 430, respectively. The mild wave attenuation in the initial profiles of tests 324 and 508, due to viscous dissipation, is neglected; the incident amplitude is taken with respect to $x = 0$.

$|R_L| \simeq 0.24$ was weak; test 430 had pure standing waves, $R_L = 1$. The nodes (locations of minimum surface displacement) and antinodes (location of maximum surface displacement) are quite visible in all cases. The wave period for test 324 is $T = 2.63$ s, while that for tests 508 and 430 is $T = 2.5$ s. Therefore, the wavelength in test 324 is somewhat longer than those in tests 508 and 430. Mild wave attenuation due to viscous dissipation is visible in the initial profiles of tests 324 and 508. This feature is neglected in our predictions.

The desired surface waves are those with small wave slope $k'A'$ that produce sufficient sand motion on the bed. For the purpose of finding the appropriate wavemaker settings, the piston displacement was initially taken as monochromatic ($\xi_2' = 0 = \psi_2$). Measurements of the resultant surface waves for different values of $\xi_1'$ yielded an empirical relation between the piston amplitude $\xi_1'$ and the wave amplitude $A'$. Observations were made of the amount of sediment movement on the bed, and a value $\xi_1' = \xi_{1D}'$ was chosen for the first harmonic piston amplitude. As noted above, this monochromatic wavemaker displacement generates an unwanted free second harmonic wave component. We now discuss how the wavemaker piston displacement was adjusted to cancel this spurious free wave component.

### 2.6.2 Obtaining a wave field without the free second harmonic

In this section, we outline a three-step procedure to adjust the wavemaker piston displacement and cancel the free wave component of the second harmonic generated by the wavemaker piston motion.

1. First, the surface waves resulting from the monochromatic wavemaker piston displacement $\xi(t) = \xi_{1D}' \cos \omega t'$ are measured across the tank and the parameters $|A'|$, $R'$, $A^{[2]}$, $R^{[2]}$ are fitted to these data (both magnitude and phase are fitted for those that are

complex). The free wave component of the second harmonic is denoted as

$$\zeta_{F1}^{[2]\prime} = A_{F1}^{[2]\prime}\left(e^{ik^{[2]\prime}x'} + R_{F1}^{[2]}e^{-ik^{[2]\prime}x'}\right). \tag{2.136}$$

The subscript 'F1' on $\zeta_{F1}^{[2]\prime}$, $A_{F1}^{[2]\prime}$, $R_{F1}^{[2]}$ denotes the free wave component of step 1.

2. We now add a second harmonic to the wave piston displacement,

$$\xi\left(t\right) = \xi_{1D}'\cos\omega t' + \xi_2'\sin 2\omega t', \tag{2.137}$$

for $\xi_2 > 0$ but $\psi_2 = 0$. There is nothing special about the use of cos and sin in (2.137); it is merely that this was the form of the input in the wavemaker control program. The resultant waves are measured, yielding a new set of fitted wave parameters. The corresponding free second harmonic is

$$\zeta_{F2}^{[2]\prime} = A_{F2}^{[2]\prime}\left(e^{ik^{[2]\prime}x'} + R_{F2}^{[2]}e^{-ik^{[2]\prime}x'}\right). \tag{2.138}$$

The subscript 'F2' on $\zeta_{F2}^{[2]\prime}$, $A_{F2}^{[2]\prime}$, $R_{F2}^{[2]}$ denotes the free wave component of step 2. We write $\zeta_{F2}^{[2]\prime}$ as the sum of the free second harmonic $\zeta_{F1}^{[2]\prime}$ from step 1 plus the additional piece $\zeta_{FWM}^{[2]\prime}$, added in step 2, due to the second harmonic of the wavemaker displacement,

$$\begin{aligned}
\zeta_{F2}^{[2]\prime} &= \zeta_{FWM}^{[2]\prime} + \zeta_{F1}^{[2]\prime}, \\
&= A_{WM}^{[2]\prime}\left(e^{ik^{[2]\prime}x'} + R_{WM}^{[2]}e^{-ik^{[2]\prime}x'}\right) + A_{F1}^{[2]\prime}\left(e^{ik^{[2]\prime}x'} + R_{F1}^{[2]}e^{-ik^{[2]\prime}x'}\right), \\
&= \left(A_{WM}^{[2]\prime} + A_{F1}^{[2]\prime}\right)\left(e^{ik^{[2]\prime}x'} + \frac{A_{WM}^{[2]}R_{WM}^{[2]} + A_{F1}^{[2]\prime}R_{F1}^{[2]}}{A_{WM}^{[2]\prime} + A_{F1}^{[2]\prime}}e^{-ik^{[2]\prime}x'}\right).
\end{aligned} \tag{2.139}$$

From Eqs. (2.138) and (2.139), the unknown parameters $A_{WM}^{[2]\prime}$, $R_{WM}^{[2]}$ are found in terms of the other measured parameters as

$$A_{WM}^{[2]\prime} = A_{F2}^{[2]\prime} - A_{F1}^{[2]\prime}, \qquad R_{WM}^{[2]} = \frac{A_{F2}^{[2]\prime}R_{F2}^{[2]} - A_{F1}^{[2]\prime}R_{F1}^{[2]}}{A_{F2}^{[2]\prime} - A_{F1}^{[2]\prime}}. \tag{2.140}$$

Thus, adding a second harmonic $\xi_2'\sin 2\omega t'$ to the piston displacement has resulted in an additional free second harmonic component of amplitude

$$A_{WM}^{[2]\prime} = A_{F2}^{[2]\prime} - A_{F1}^{[2]\prime}.$$

In order to cancel the original free second harmonic of step 1, $\zeta_{F1}^{[2]\prime}$, the additional second harmonic $\zeta_{FWM}^{[2]\prime}$ must be equal in magnitude and opposite in phase to $\zeta_{F1}^{[2]\prime}$. It follows that we desire

$$\left|A_{WM}^{[2]\prime}\right| = \left|A_{F1}^{[2]\prime}\right|.$$

By varying $\xi_2'$, measuring the resultant waves, and computing $\left|A_{WM}^{[2]\prime}\right|$ from (2.140), we construct an empirical curve of $\left|A_{WM}^{[2]\prime}\right| - \left|A_{F1}^{[2]\prime}\right|$ vs. $\xi_2'$. We choose the value $\xi_2' = \xi_{2D}'$ that makes $\left|A_{WM}^{[2]\prime}\right| - \left|A_{F1}^{[2]\prime}\right| = 0$.

3. The third and final step to canceling the free second harmonic wave component involves adjusting the phase of the second harmonic piston displacement $\psi_2$,

$$\xi(t) = \xi_{1D}' \cos\omega t' + \xi_{2D}' \sin\left(2\omega t' + \psi_2\right).$$

By varying $\psi_2$ between 0 and $2\pi$, measuring the resultant waves, and fitting the wave parameters, an empirical relation is found between the amplitude of the incident free second harmonic, $\left|A^{[2]}\right|$, and the second harmonic piston displacement phase $\psi_2$. We choose the value $\psi_2 = \psi_{2D}$ that minimizes $\left|A^{[2]}\right|$.

Following the preceding three step process yields a wavemaker piston displacement

$$\xi(t) = \xi_{1D}' \cos\omega t' + \xi_{2D}' \sin\left(2\omega t' + \psi_{2D}\right)$$

whose resultant surface waves do not have a significant free second harmonic.

The free second harmonic cancellation method was used several times to obtain wave fields for use in our sand bar experiments. To demonstrate the method, experimental wave profiles are shown in Figure 2-26 after steps 1 (top), 2 (middle), and 3 (bottom) corresponding to the wavemaker piston displacements

$$\text{After Step 1:} \quad \xi(t) = \xi_{1D}' \cos\omega t', \tag{2.141}$$

$$\text{After Step 2:} \quad \xi(t) = \xi_{1D}' \cos\omega t' + \xi_{2D}' \sin\left(2\omega t'\right), \tag{2.142}$$

$$\text{After Step 3:} \quad \xi(t) = \xi_{1D}' \cos\omega t' + \xi_{2D}' \sin\left(2\omega t' + \psi_{2D}\right), \tag{2.143}$$

where $\xi_{1D} = 10.0$ cm, $\xi_{2D} = 0.60$ cm, $\psi_{2D} = -0.50$. A closeup of the second harmonic amplitudes after each step is shown in Figure 2-27. In particular, the modulation in the second

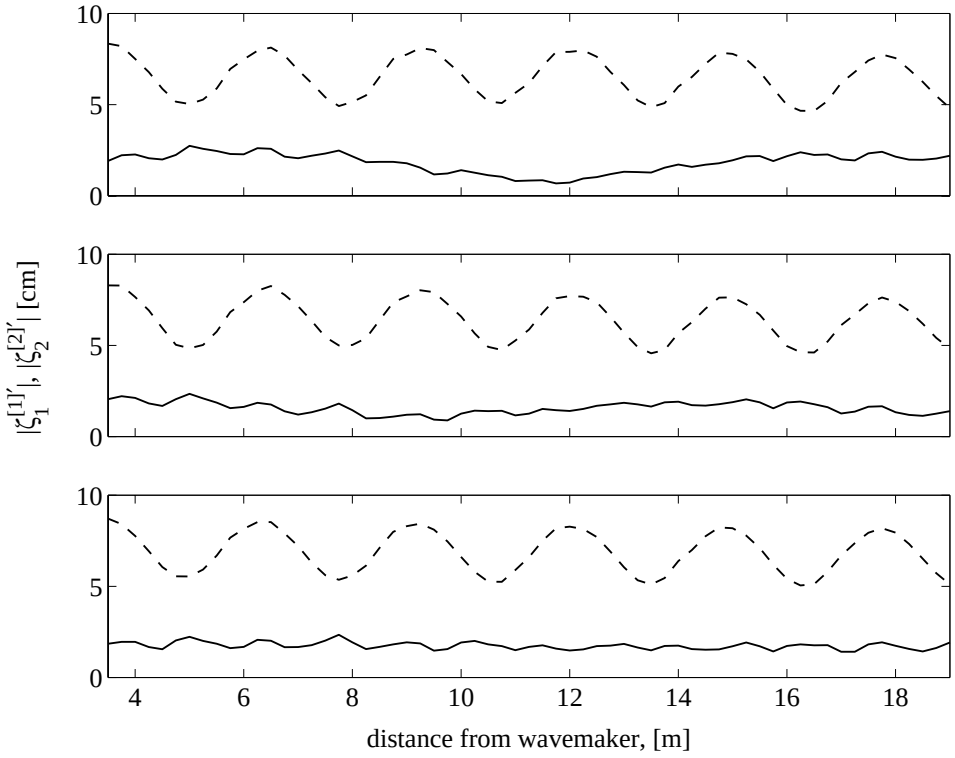


Figure 2-26: Experimental first and second wave harmonic amplitudes $|\zeta_1^{[1]\prime}|$ (dash) and $|\zeta_2^{[2]\prime}|$ (solid), respectively, after step 1 (top), 2 (middle) and 3 (bottom) of the free second harmonic cancellation procedure. The piston displacements that produced these wave profiles on the MIT test bed (Figure 2-23(top)) are given in Eqs. (2.141) – (2.143). The wave profile after step 3 (bottom) is that used for the sand bar test 508.

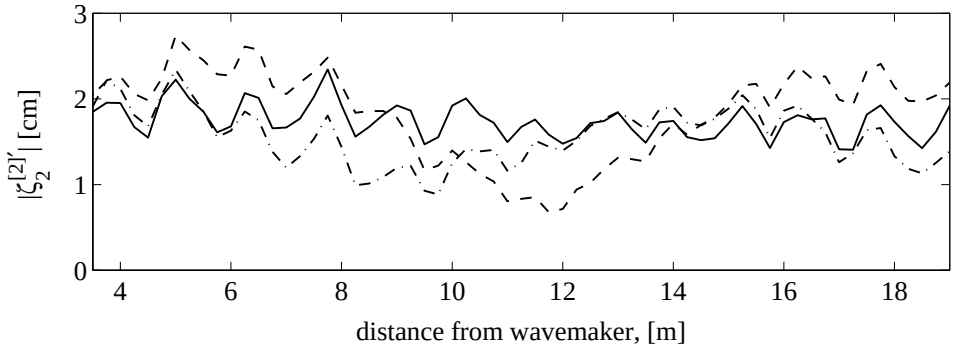


Figure 2-27: Closeup of the second harmonic amplitudes after step 1 (dash), 2 (dash-dot) and 3 (solid) of the free second harmonic cancellation procedure.

harmonic amplitude is significantly reduced after step 3. This indicates the amplitude of the free second harmonic is significantly reduced, leaving only the bound second harmonic.

The reason this three step process works is that the surface waves and piston displacements are weakly nonlinear and monochromatic to leading order. Thus, the leading order monochromatic piston displacement generates a second order, second harmonic free wave. A second order, second time harmonic correction is applied to the wavemaker piston displacement to cancel this second harmonic free wave. The adjustment can be done in two steps, amplitude first and phase second, since any nonlinear coupling between the phase and amplitude is of third order.

The waves in Figure 2-26(bottom) are those used in Test 508. The corresponding fitted parameters are listed in Table 2.6. Admittedly, the free second harmonic, though weak, is still present in the wave field. Time constraints did not allow us to perform more wave tests and better estimate the second harmonic wavemaker piston parameters $\xi_{2D}$ and $\psi_{2D}$ needed to cancel the free second harmonic.

Lastly, we comment on the spatial resolution required for the wave measurements. A coarser spatial resolution takes much less time to obtain; a fine spatial resolution facilitates determining the wave parameters, especially the phase of the complex amplitude of the free second harmonic, required in step 2. The typical wavelength in experiments was 6 m. For steps 1 and 3, taking wave measurements every 50 cm gave sufficient resolution to determine $A^{[1]}$, $R^{[1]}$ and $|A^{[2]}|$. In step 2, where it is necessary to determine the phase of $|A^{[2]}|$, the wave measurements were taken every 25 cm.

### 2.6.3 Experimental parameters

Following the procedure outlined in the previous section, piston inputs were found that generated waves with insignificant free second harmonic components. The four tests 324, 430, 508 and 519 were then run as described above. The recorded waves and resultant bar profiles are presented below, along with our predictions. The relevant parameters are listed in Table 2.7. The reflection was weak in tests 324 and 508, and strong in tests 430 and 519. Tests 324, 430 and 508 had relatively coarse sand, $d = 0.2$ mm, while test 519 had relatively fine sand, $d = 0.125$ mm.

From the parameters in Table 2.7, the constants in our model are calculated as described in §2.3.1 and the terms in the sand bar equation are computed as in §2.4.1. The correspond-

| Test | $T$ [s] | $H_o$ [cm] | $A_o$ [cm] | $R_L$ | $d$ [mm] | $\eta_{ro}$ [cm] | $\eta_{ro}/\lambda_{ro}$ | $t'_f$ [days] |
|---|---|---|---|---|---|---|---|---|
| 324 | 2.6 | 60 | 5.46 | $0.24e^{-1.06i}$ | 0.20 | 2.00 | 0.20 | 3.04 |
| 430 | 2.5 | 60 | 3.68 | 1 | 0.20 | 2.24 | 0.20 | 4.04 |
| 508 | 2.5 | 60 | 7.00 | $0.25e^{0.04i}$ | 0.20 | 2.00 | 0.20 | 3.98 |
| 519 | 2.5 | 60 | 3.44 | 1 | 0.12 | 2.00 | 0.20 | 4.10 |

| Test | $\lambda$ [m] | $\delta$ [cm] | $\alpha_1/\omega$ [days] | $A_b\omega$ [cm/s] | $u_f$ [cm/s] | $w_S$ [cm/s] | $\eta_{ro}(N)$ [cm] |
|---|---|---|---|---|---|---|---|
| 324 | 6.01 | 2.18 | 2.09 | 24.2 | 6.50 | 2.02 | 1.80 |
| 430 | 5.67 | 2.27 | 1.53 | 25.9 | 7.14 | 2.02 | 1.77 |
| 508 | 5.67 | 2.65 | 1.00 | 30.7 | 8.32 | 2.02 | 1.89 |
| 519 | 5.67 | 2.10 | 2.33 | 24.2 | 6.59 | 0.88 | 1.45 |

| Test | $\varepsilon$ | $KH_o$ | $\Theta_{c0}$ | $\Theta_{do}$ | $\Theta_o$ | $Z_b$ | $\mathsf{R}_E$ | $\mathsf{R}_{FT}$ | Eq. (1.90) |
|---|---|---|---|---|---|---|---|---|---|
| 324 | 0.11 | 0.63 | 0.053 | 0.15 | 1.30 | 0.24 | 24470 | 5365 | 415 |
| 430 | 0.11 | 0.66 | 0.053 | 0.17 | 1.57 | 0.26 | 26666 | 6602 | 438 |
| 508 | 0.14 | 0.66 | 0.053 | 0.22 | 2.14 | 0.25 | 37449 | 6873 | 680 |
| 519 | 0.11 | 0.66 | 0.082 | 0.21 | 2.24 | 0.25 | 23301 | 5443 | 388 |

Table 2.7: Parameters for the MIT sand bar experiments. $\eta_{ro}(N)$ is the ripple height predicted by the empirical formula Eq. (1.105). The values of $\mathsf{R}_E$, $\mathsf{R}_{FT}$ and the l.h.s. of Eq. (1.90) indicate the boundary layers in all tests were fully rough turbulent.

ing sand bar predictions are found by running our model on a bar patch $0 < x < L$ and imposing the boundary conditions $A(0) = 1$ and $R(L) = R_L$ on the waves, where $L = KL'$ is the scaled length of the tank and $K$ is the wave number. For tests 430 and 519, the origin of the normalized $x$-axis used in our theory corresponds to $X' = 4.78$ m, which is five bar lengths ($5\lambda/2$) from the vertical seawall. The origin of the $x$-axis corresponds to $X' = 2.80$ m for test 324, and to $X' = 3.5$ m for test 508. This choice makes $x = 0$ an antinode for 430 and 519, and places $x = 0$ close to where the measured bar elevation is zero for tests 324 and 508, thereby improving the validity of our boundary condition that $\widetilde{h} = 0$ at $x = 0$. Further computational details are outlined above in §2.4.4.

The physical (dimensional) forms of the predicted wave amplitudes and bar elevation are compared with measurements. Recall from our normalizations (1.71) and (1.131) that the normalized and physical wave amplitude and bar elevation are related via

$$\zeta_1^{[1]\prime} = A_o\zeta_1^{[1]}, \qquad \zeta_2^{[2]\prime} = A_o^2 K\zeta_2^{[2]}, \qquad \widetilde{h}' = A_b\widetilde{h}. \tag{2.144}$$

Lastly, recall that obtaining complete wave and bar records along the tank required 49 and 10 minutes, respectively. The time used to compare predictions to measurements is taken as the halfway point of the bar measurements. Since the waves evolved slowly over several days (see Figure 2-24) and the bars over several hours, their change over the duration of each measurement was negligible.

### 2.6.4 Test 430

The evolution of sand bars in front of a wall, i.e. under pure standing waves, is studied in test 430. Our model predictions based on the parameters listed in Table 2.7 are compared to the measured sand bar profiles for test 430 in Figures 2-28 to 2-31. Note that for $R_L = 1$ our model contains no fitting parameters, since the return flow $U_2^{[0]}$ vanishes and our model does not depend on $\Lambda_2^{[0]}$. The agreement between the predicted and measured bar crest amplitude and position is very satisfactory. The predicted and observed bar crests occur directly under the wave node, making the coupling coefficient $\Im\left(D_1 e^{i\theta_R}\right)$ less than 0.015 over the entire duration of the simulation and experiment. This renders the Bragg scattering effect negligible in both the predictions and the experiments. Lastly, sub-critical (flat) regions occur where the intensity of the flow is sub-critical, i.e. $\Theta_d < \Theta_c$. The agreement between the predicted and measured sub-critical region length and position is also very satisfactory.

Predicted and measured time histories of bar heights are shown in Figure 2-32. Agreement is, again, very satisfactory. The bar growth rate is large initially, but diminishes as the bars approach their steady state. Lastly, ripple profiles are plotted in Figure 2-33 along with the fitted ripple height $\eta_r'(x)$ from Eq. (1.108) with $(r_1, r_2, r_3) = (0.68, 3, 2)$ and $\eta_{ro} = 2.24$ cm. Note that the sub-critical regions are also visible in the ripple profiles.

Landry (2004) [33] has reported the ripple progression for several tests, including 430. Initially, the entire bed is flat (without ripples). Once the wavemaker is started, ripples begin to form under the wave nodes and the rippled region grows toward the antinodes. After approximately 30 to 60 minutes of wave action, the rippled region has filled the entire super-critical region and ceases growing in length. Beyond that point in time, scouring slowly decreases the length of the sub-critical region until the bar profiles reach equilibrium. This latter process is evident in the measured bar profiles in Figures 2-29 – 2-31. Our predictions mimic this behavior as the predicted sub-critical regions also decrease in length

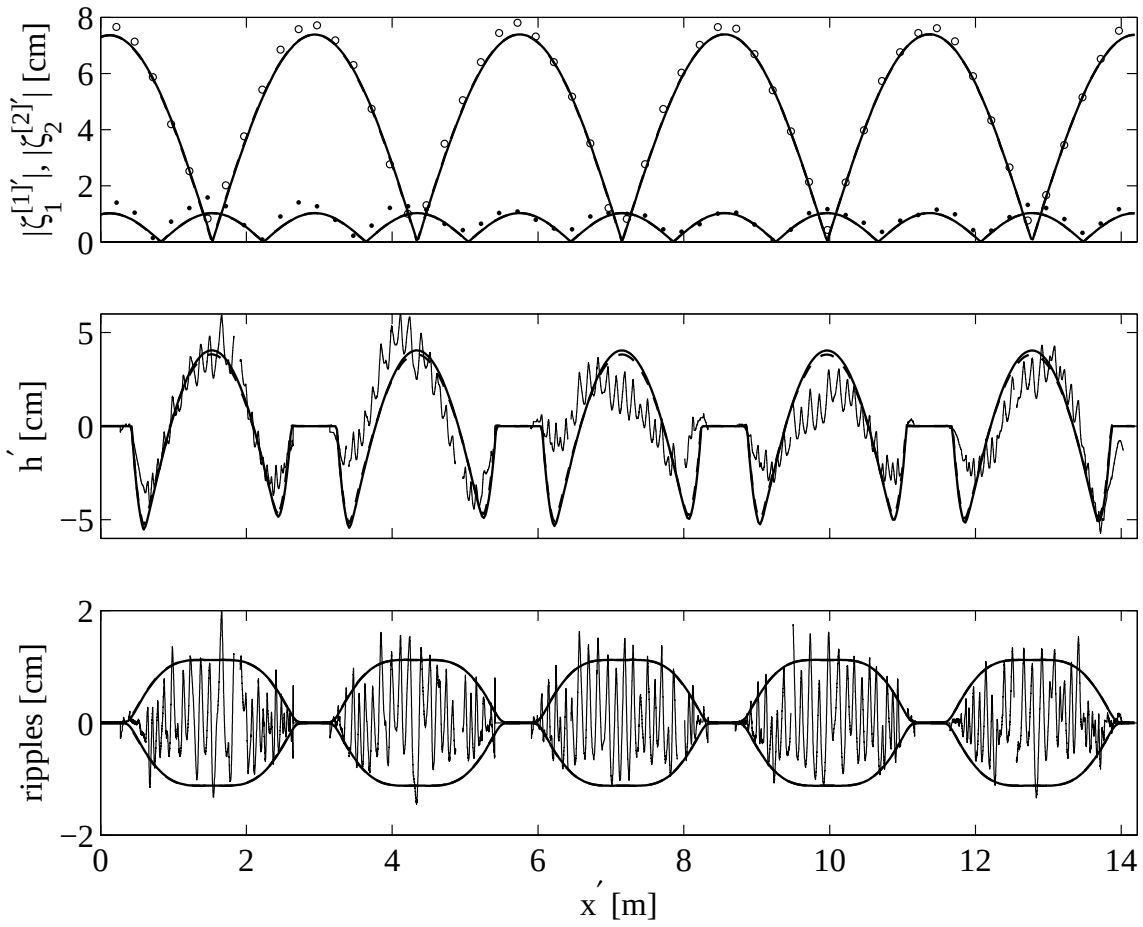


Figure 2-28: Comparison of measured and predicted wave amplitudes (top) and bar elevations (middle) along the tank for test 430 at $t' = 4.02$ days (waves) and $t' = 4.04$ days (bars). The measured first and second harmonic wave amplitudes $\zeta'_{env} = |\zeta_1^{[1]\prime}|$ ($\circ$) and $|\zeta_2^{[2]\prime}|$ ($\bullet$) are plotted above the bar elevation $\widetilde{h}'$ (jagged line). Corresponding predictions are made by neglecting (smooth solid line) and including (smooth dash line) suspended sediments. In the bottom plot, measured ripple elevations (jagged line) are compared to the ripple envelope (smooth line) formed by $\pm\eta'_r/2$, where the ripple height $\eta'_r$ is found from Eq. (1.108) with $(r_1, r_2, r_3) = (0.68, 3, 2)$ and $\eta_{ro} = 2.24$ cm. $x' = 0$ is 4.78 m from the mean wavemaker position. Gaps in the bar and ripple data are due to vertical tank supports blocking the view.

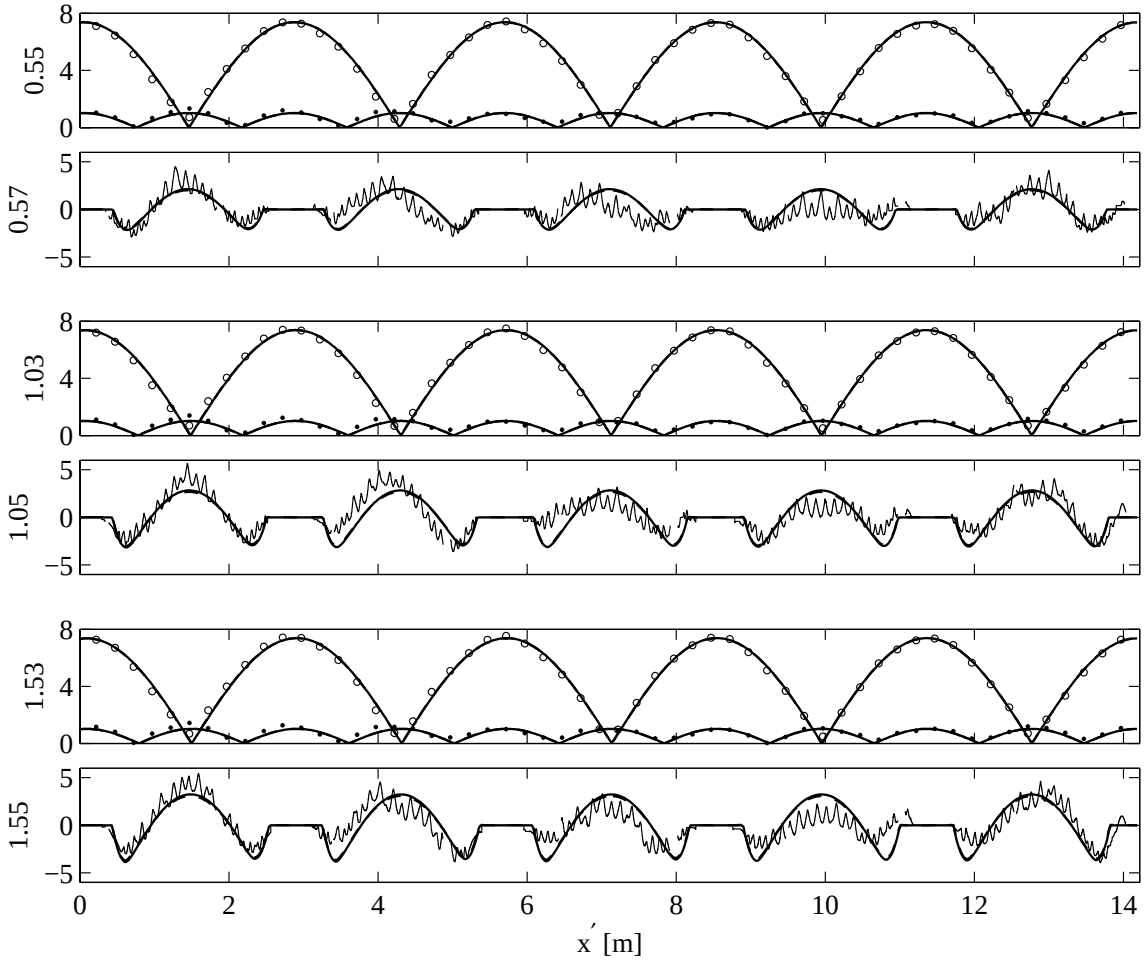


Figure 2-29: Pairs of wave and bar comparisons along the tank for test 430 at various times. For each plot pair, the measured first and second harmonic wave amplitudes $\zeta'_{env} = |\zeta_1^{[1]\prime}|$ ($\circ$) and $|\zeta_2^{[2]\prime}|$ ($\bullet$) are plotted above bar elevations $\widetilde{h}'$ (jagged lines). Corresponding predictions are made by neglecting (smooth solid line) and including (smooth dash line) suspended sediments. All vertical scales are in [cm]. $x' = 0$ is 4.78 m from the mean wavemaker position. Numbers left of the wave and seabed elevation plots indicate the corresponding elapsed time in days. Gaps in the bar data are due to vertical tank supports blocking the view.

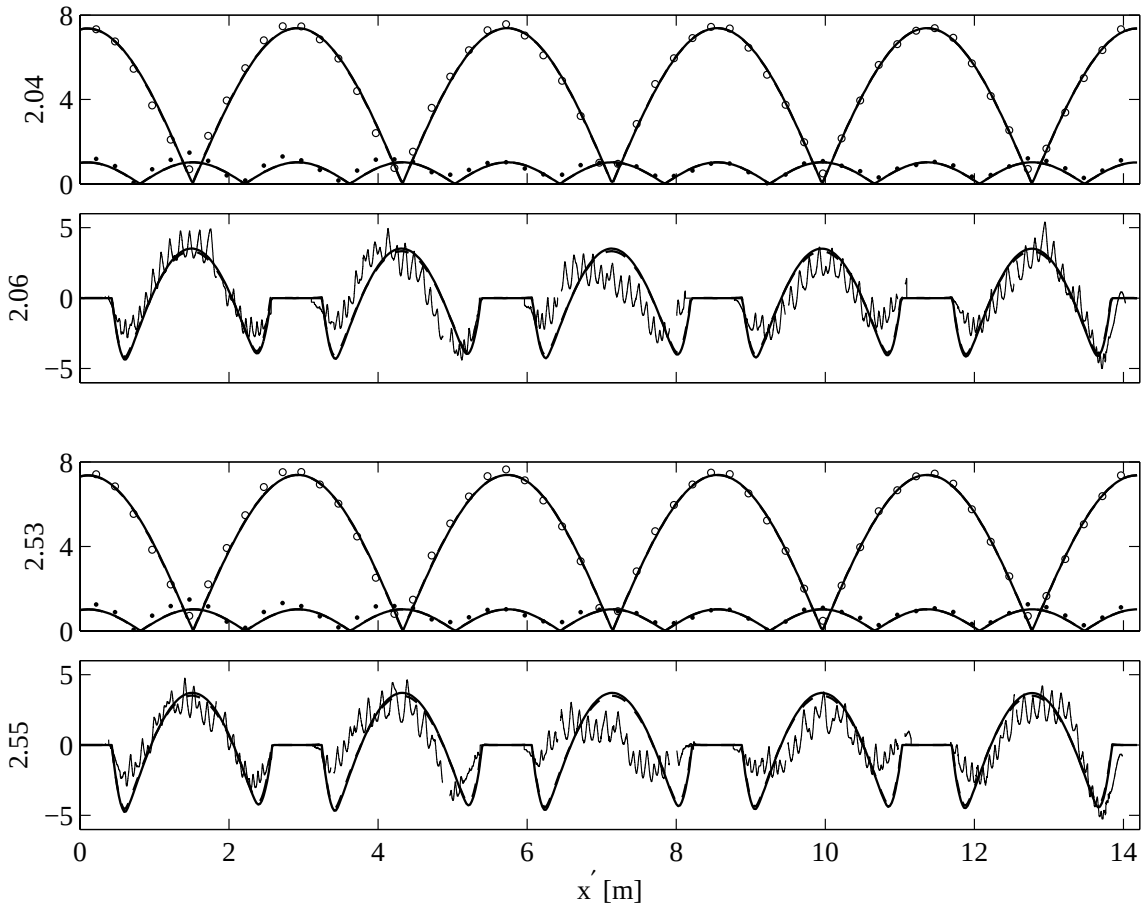


Figure 2-30: See caption of Figure 2-29.

and agree well with the measurements. In our model, which assumes a fully rippled supercritical region, scouring increases the bar slope adjacent to the sub-critical regions, thereby decreasing the local value of the slope-dependent critical Shields parameter $\Theta_C$ (see Eq. (1.115)). This decrease in $\Theta_C$ effectively shortens the sub-critical region, i.e. the region where $\widehat{\Theta}_d < \Theta_C$, allowing further scouring to occur. The process repeats until the bars reach equilibrium.

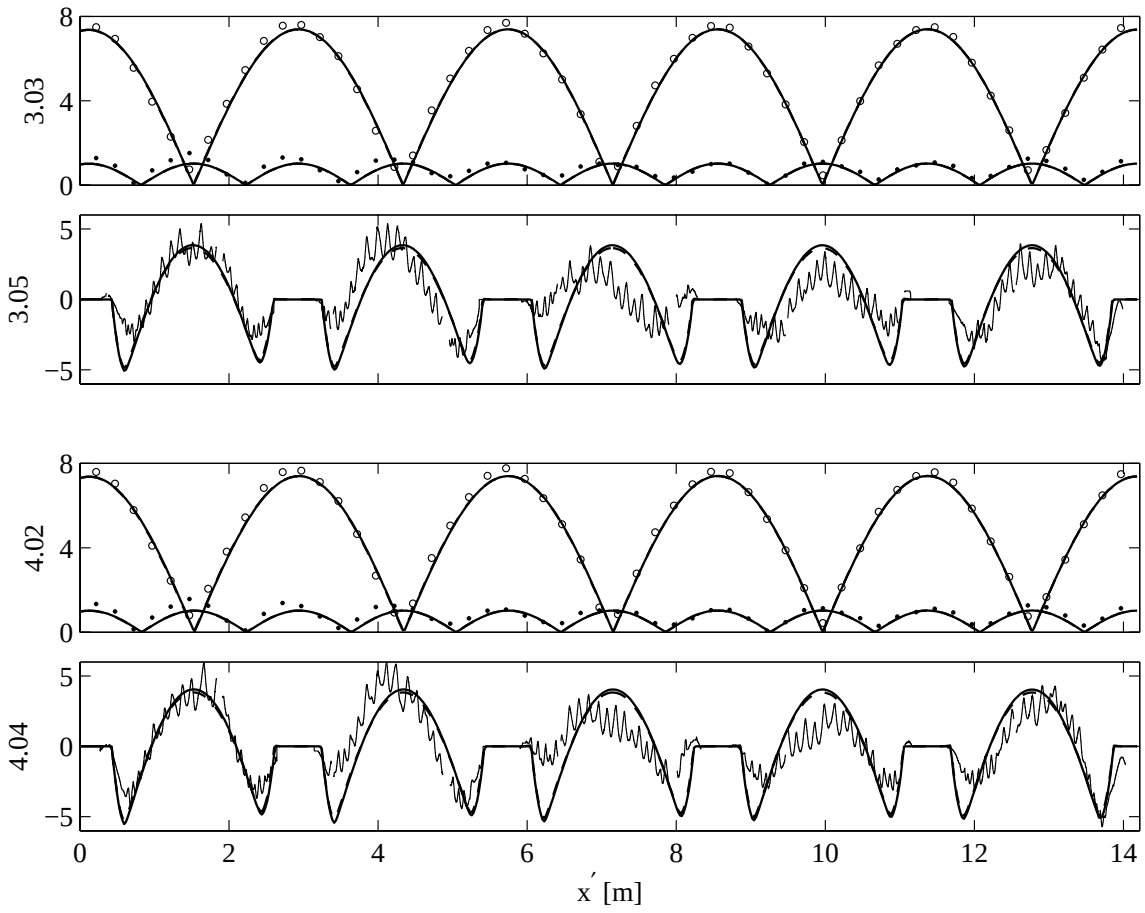


Figure 2-31: See caption of Figure 2-29.

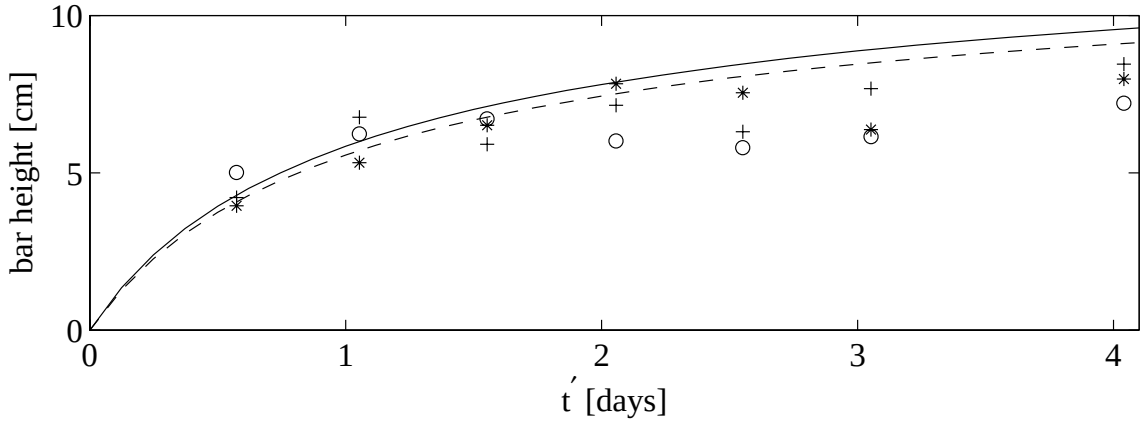


Figure 2-32: Measured and predicted bar height evolution in time, for test 430. The measured bar heights correspond to the first ($\circ$), second ($+$) and fifth ($*$) bars, counted from the left in Figures 2-28 to 2-31. Predictions of bar height $\max(\widetilde{h}') - \min(\widetilde{h}')$ are made by neglecting (solid line) and including (dashed line) suspended sediments.

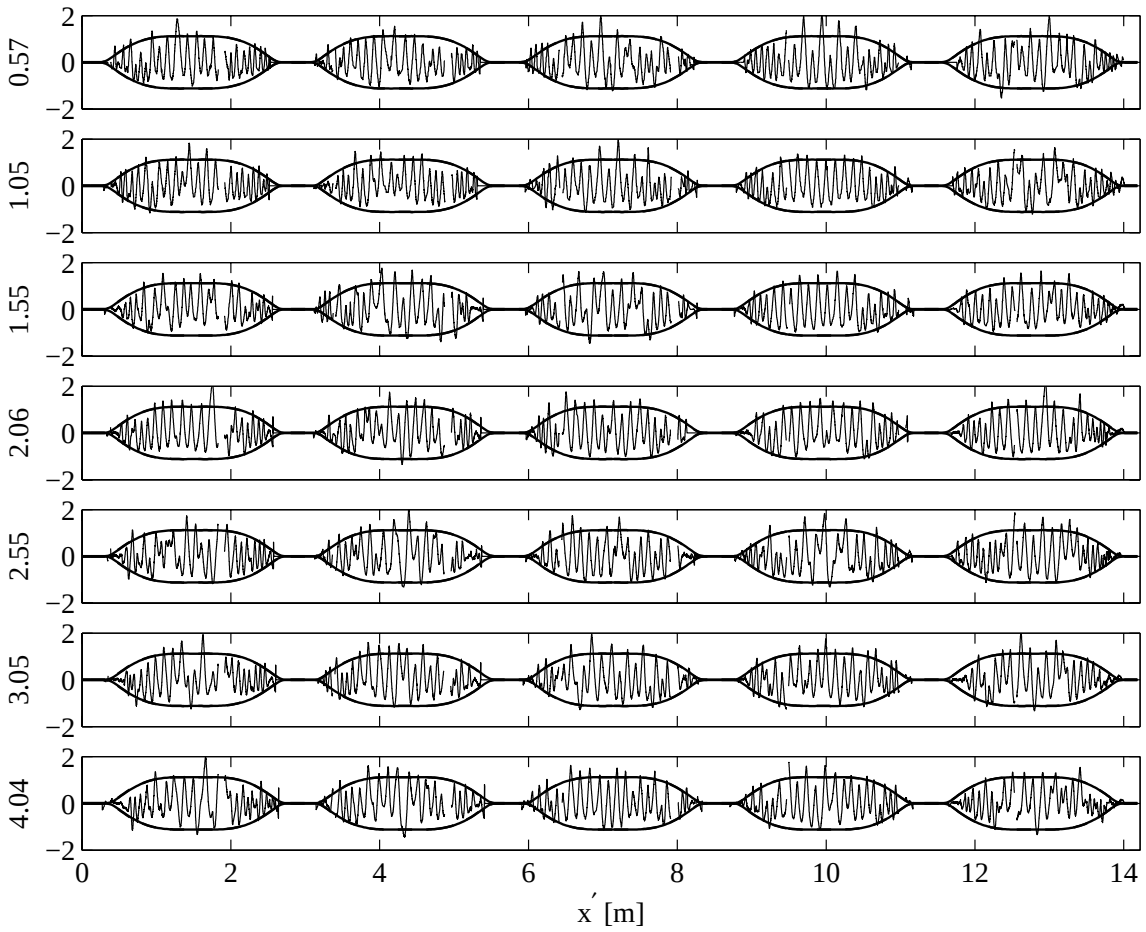


Figure 2-33: Comparison of measured ripple elevations (jagged lines) to the fitted ripple envelope formed by $\pm\eta_r'/2$ at various times in test 430. The ripple height $\eta_r'$ is found from Eq. (1.108) with $(r_1, r_2, r_3) = (0.68, 3, 2)$ and $\eta_{ro} = 2.24$ cm. Numbers left of the ripple elevation plots indicate the corresponding elapsed time in days. Gaps in the ripple data are due to vertical tank supports blocking the view.

### 2.6.5 Tests 324 and 508

Bar evolution in front of a beach, i.e. under weak reflection, is studied in tests 324 and 508. Tests 324 and 508 differ in wave period and amplitude. In test 508, the incident wave amplitude at $x = 0$ decreased with time (see Figure 2-25) according to

$$A(0, \bar{t}) = 0.0091\,\bar{t}^2 - 0.0795\,\bar{t} + 0.9929. \tag{2.145}$$

This decrease was likely due to the effect of the large wave loading on the wavemaker. As the bars grew, reflection was enhanced over the bar patch and hence the wave height near the wavemaker increased. The increased loading on the wavemaker piston led to a minor reduction in piston displacement amplitude. The phase of the shoreline reflection coefficient $R_L$ also changed with time, probably owing to the change in incident wave amplitude,

$$\theta_R(L, \bar{t}) = -0.0250\,\bar{t}^2 + 0.2051\,\bar{t} + 0.0722. \tag{2.146}$$

The magnitude of $R_L$ was constant in time. Note that for all other tests, the incident wave amplitude $A(0, \bar{t})$ and shoreline reflection coefficient $R_L$ were constant and the corresponding wave heights were generally at least 10% smaller. To allow for the decrease in $A(0, \bar{t})$ in our model, the Bragg Scattering equations (2.98) are solved as before, but are now subject to the boundary condition (2.145).

The return flow stress coefficient $\Lambda_2^{[0]}$ is taken as 1.8 for test 324 and 1.4 for test 508. To illustrate more clearly the effect of $\Lambda_2^{[0]}$, bar profiles for various values of $\Lambda_2^{[0]}$ are plotted in Figures 2-34 and 2-35 for tests 324 and 508, respectively. As $\Lambda_2^{[0]}$ increases, the predicted bar crests move seaward, from in front of the wave node for $\Lambda_2^{[0]} = 0, 1$ to behind the node for larger values. Note that when the bar crests are in front of the wave node, the coupling coefficient $\Im\left\{D_1 e^{i\theta_R}\right\} > 0$, meaning that energy is transferred from the reflected wave to the incident wave, so that the reflection coefficient and the wave and bar amplitudes increase in the shoreward direction. In contrast, when the bar crests are behind the wave node, the coupling coefficient $\Im\left\{D_1 e^{i\theta_R}\right\} < 0$, meaning that energy is transfered from the incident wave to the reflected wave, so that the reflection coefficient and wave and bar amplitudes decrease in the shoreward direction. In the laboratory, the bar crests appear behind the node and the bar amplitudes decrease shoreward. Thus, the value of $\Lambda_2^{[0]}$ must be taken

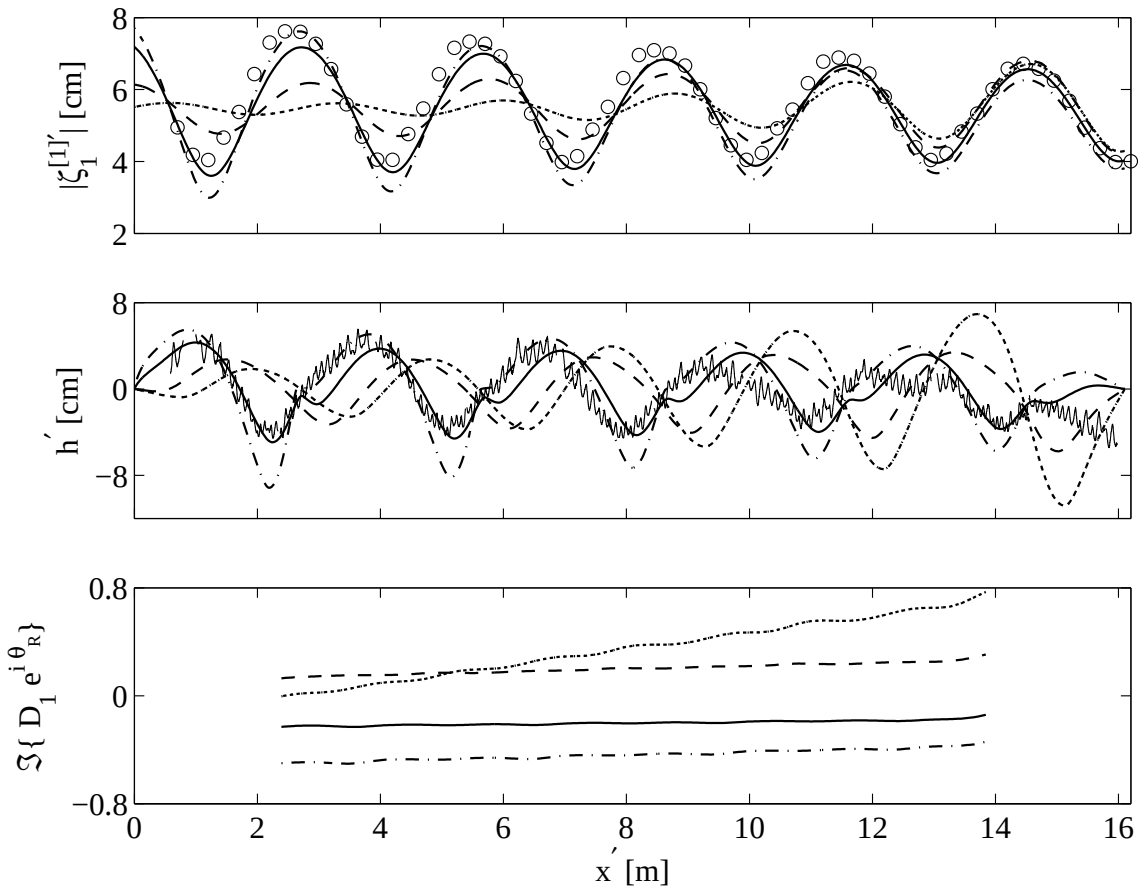


Figure 2-34: The effect of the return flow stress coefficient $\Lambda_2^{[0]}$ on wave (top) and bar (middle) predictions corresponding to test 324: $\Lambda_2^{[0]} = 0$ (solid-dot), 1 (dash), 1.8 (solid), 2.2 (dash-dot). Comparison is made to the measured first harmonic wave amplitude $\zeta'_{env} = |\zeta_1^{[1]'}|$ ($\circ$, top) and bar elevations $\widetilde{h}'$ (jagged line, middle) along the tank for test 324 at $t' = 3.02$ days (waves) and $t' = 3.04$ days (bars). The bar/wave coupling coefficient $\Im\left\{D_1 e^{i\theta_R}\right\}$ is plotted (bottom) along the tank. $x' = 0$ is 2.80 m from the mean wavemaker position. Gaps in the bar data are due to vertical tank supports blocking the view.

sufficiently large to move the predicted bar crests behind the node. However, choosing $\Lambda_2^{[0]}$ sufficiently large to make the predicted and measured bar crests coincide leads to an overestimation of the predicted bar amplitudes. Thus, a trade-off exists when choosing a value for $\Lambda_2^{[0]}$.

The predicted and measured sand bar profiles for tests 324 and 508 are shown in Figures 2-36 to 2-39 and 2-42 to 2-45, respectively. The agreement for both tests 324 and 508 are encouraging, considering the level of variability associated with the empirical constants used in our model and the return flow stress coefficient $\Lambda_2^{[0]}$. The predictions of the location of the crest and the sand bar amplitude agree favorably with the data. The shoreward decrease in

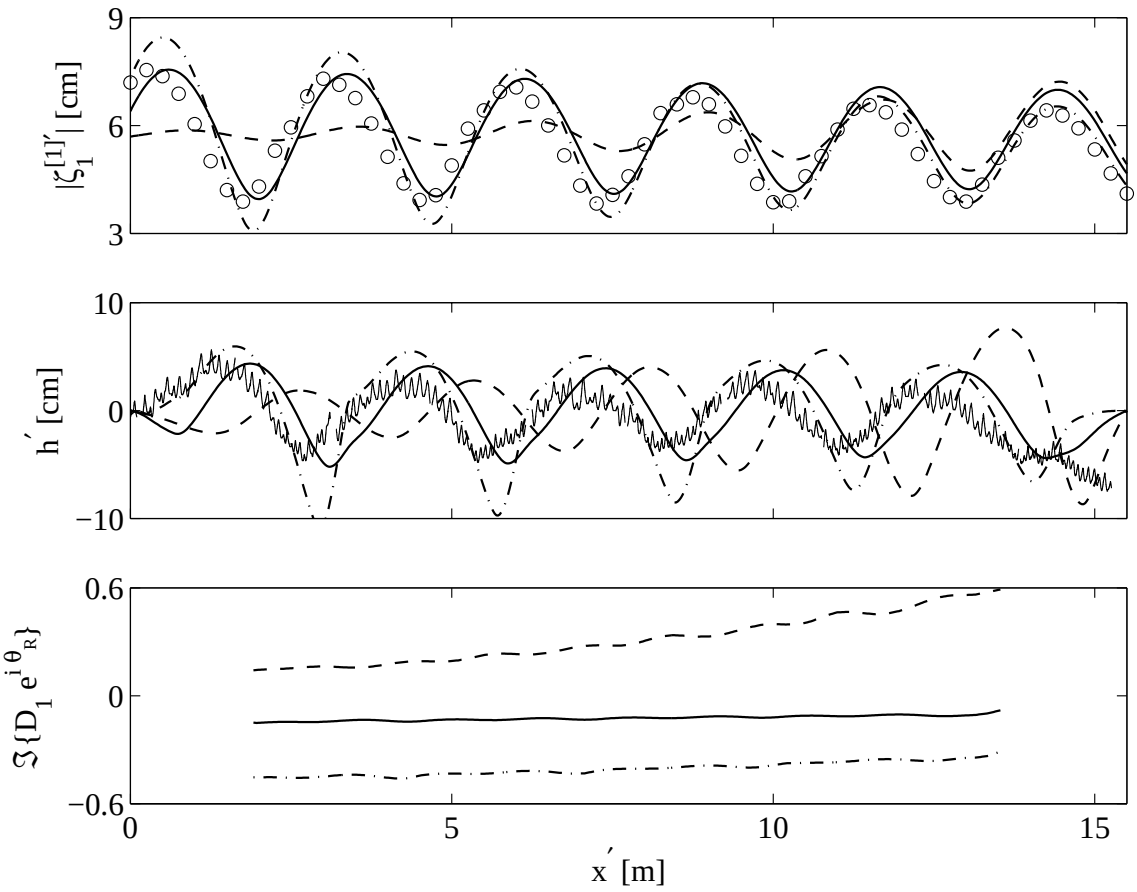


Figure 2-35: The effect of the return flow stress coefficient $\Lambda_2^{[0]}$ on wave (top) and bar (middle) predictions corresponding to test 508: $\Lambda_2^{[0]} = 0$ (dot), 1 (dash), 1.4 (solid), 1.8 (dash-dot). Comparison is made to the measured first harmonic wave amplitude $\zeta'_{env} = |\zeta_1^{[1]'}|$ ($\circ$, top) and bar elevations $\widetilde{h}'$ (jagged line, middle) along the tank for test 508 at $t' = 3.96$ days (waves) and $t' = 3.98$ days (bars). The bar/wave coupling coefficient $\Im\left\{D_1 e^{i\theta_R}\right\}$ is also plotted (bottom) along the tank. $x' = 0$ is 3.5 m from the mean wavemaker position. Gaps in the bar data are due to vertical tank supports blocking the view.

total wave and bar height is also predicted well, demonstrating the effect of Bragg scattering on the coupled bar/wave evolution.

Predicted and measured time histories of bar heights are shown in Figures 2-40 and 2-46. Predictions are given for the heights of the first and last bar. The bar growth is large initially, but diminishes quickly as the bars approach a steady state.

Lastly, ripple profiles are plotted in Figures 2-41 and 2-47 along with the fitted ripple

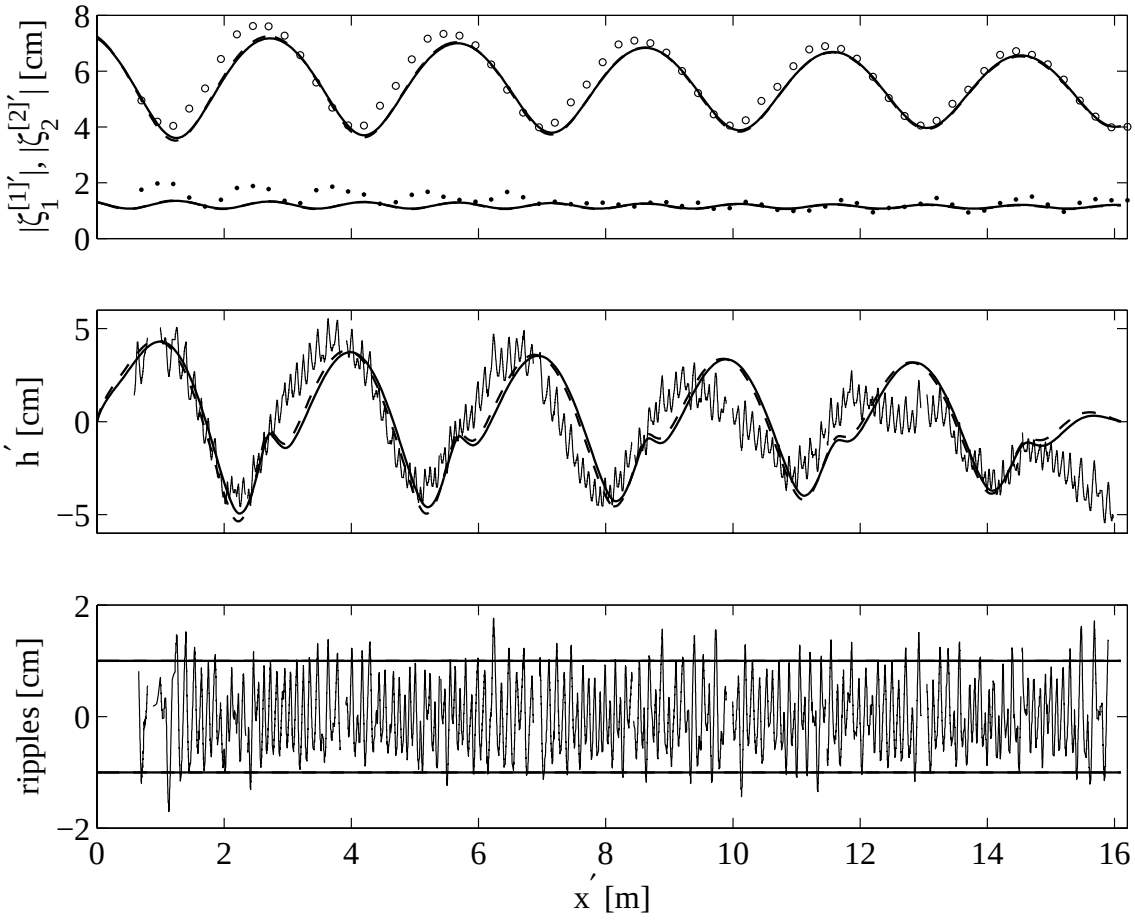


Figure 2-36: Comparison of measured and predicted wave amplitudes (top) and bar elevations (middle) along the tank for test 324 at $t' = 3.02$ days (waves) and $t' = 3.04$ days (bars). The measured first and second harmonic wave amplitudes $\zeta'_{env} = |\zeta_1^{[1]\prime}|$ ($\circ$) and $|\zeta_2^{[2]\prime}|$ ($\bullet$) are plotted above the bar elevation $\widetilde{h}'$ (jagged line). Corresponding predictions are made by neglecting (smooth solid line) and including (smooth dash line) suspended sediments. In the bottom plot, measured ripple elevations (jagged line) are compared to the fitted ripple envelope (smooth line) $\pm\eta'_r = \pm 1$ cm. $x' = 0$ is 2.80 m from the mean wavemaker position. Gaps in the bar and ripple data are due to vertical tank supports blocking the view.

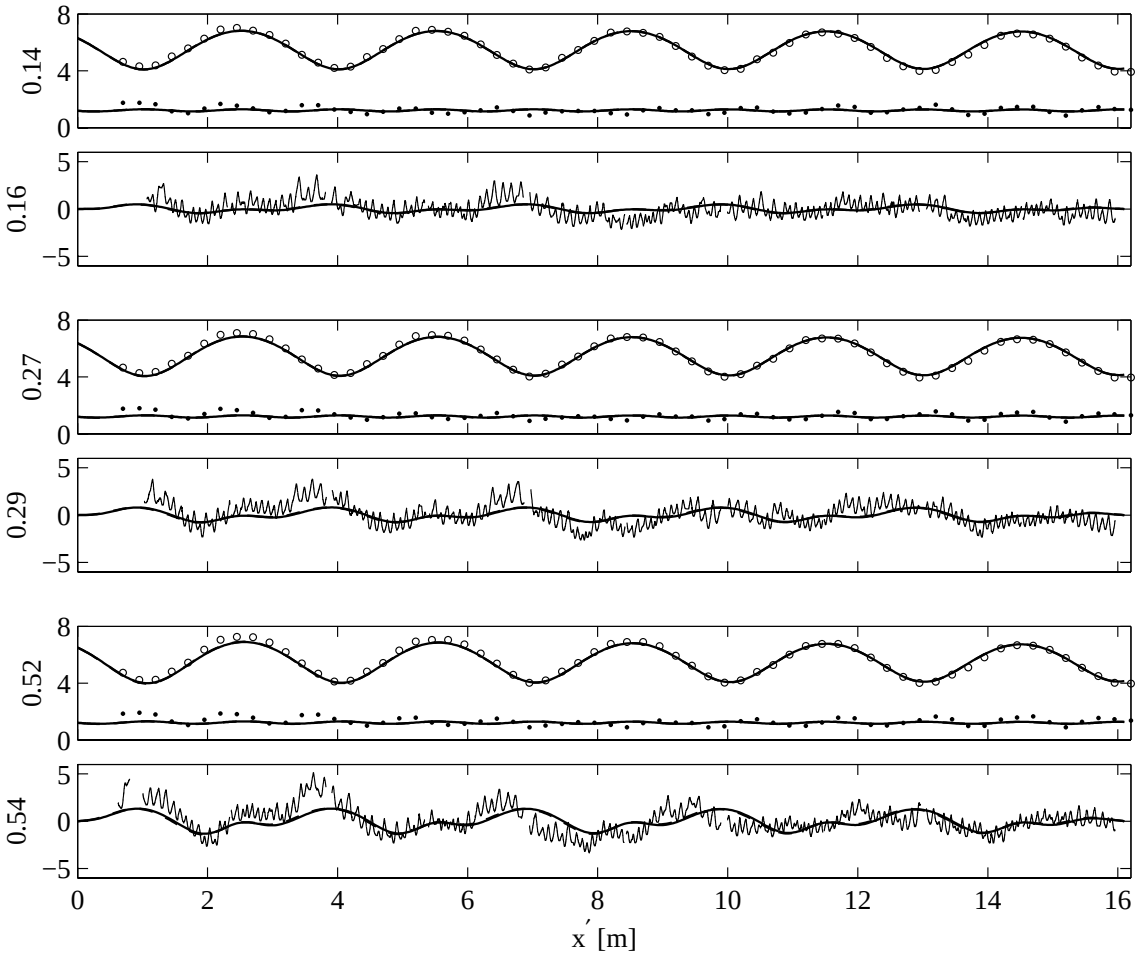


Figure 2-37: Pairs of wave and bar comparisons along the tank for test 324 at various times. For each plot pair, the measured first and second harmonic wave amplitudes $\zeta'_{env} = |\zeta_1^{[1]\prime}|$ ($\circ$) and $|\zeta_2^{[2]\prime}|$ ($\bullet$) are plotted above bar elevations $\widetilde{h}'$ (jagged lines). Corresponding predictions are made by neglecting (smooth solid line) and including (smooth dash line) suspended sediments. All vertical scales are in [cm]. $x' = 0$ is 2.80 m from the mean wavemaker position. Numbers left of the wave and seabed elevation plots indicate the corresponding elapsed time in days. Gaps in the bar data are due to vertical tank supports blocking the view.

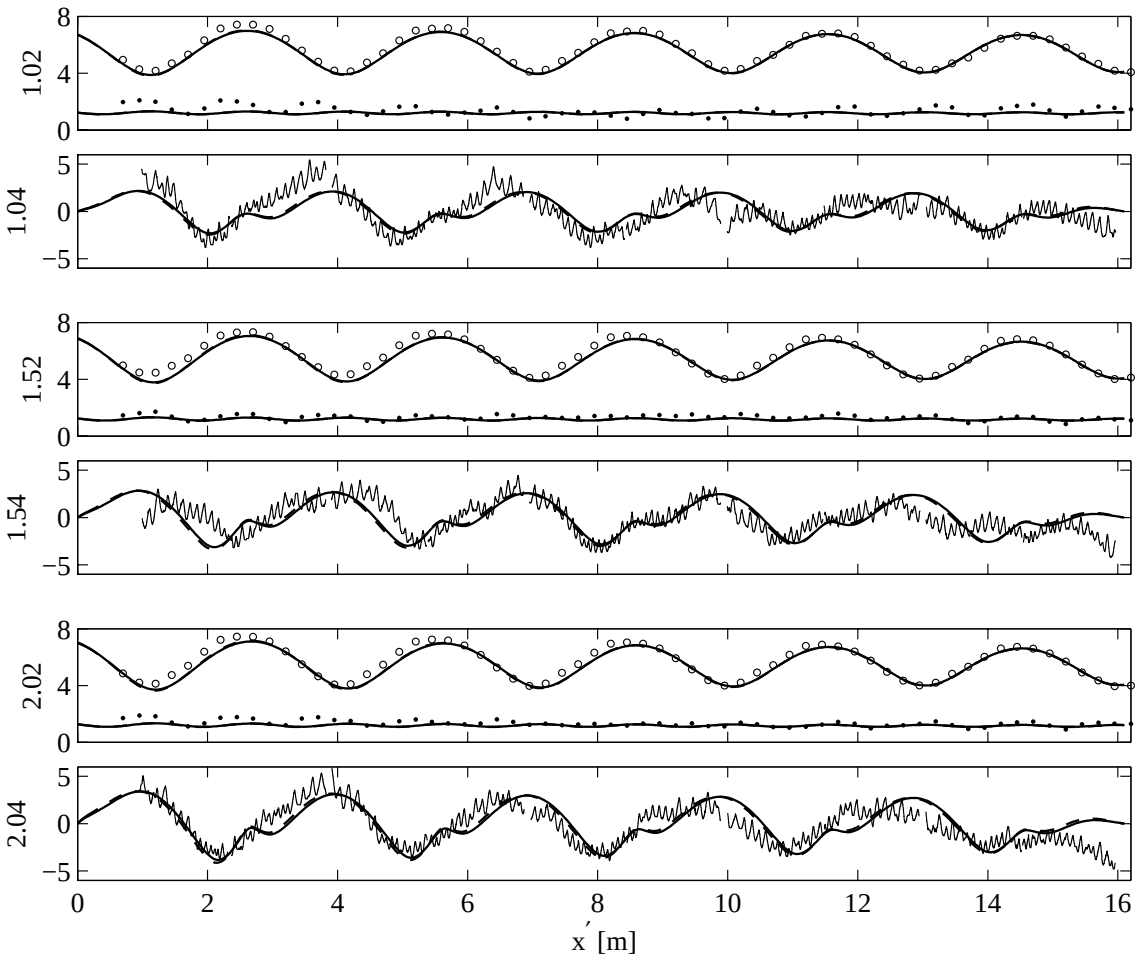


Figure 2-38: See caption of Figure 2-37.

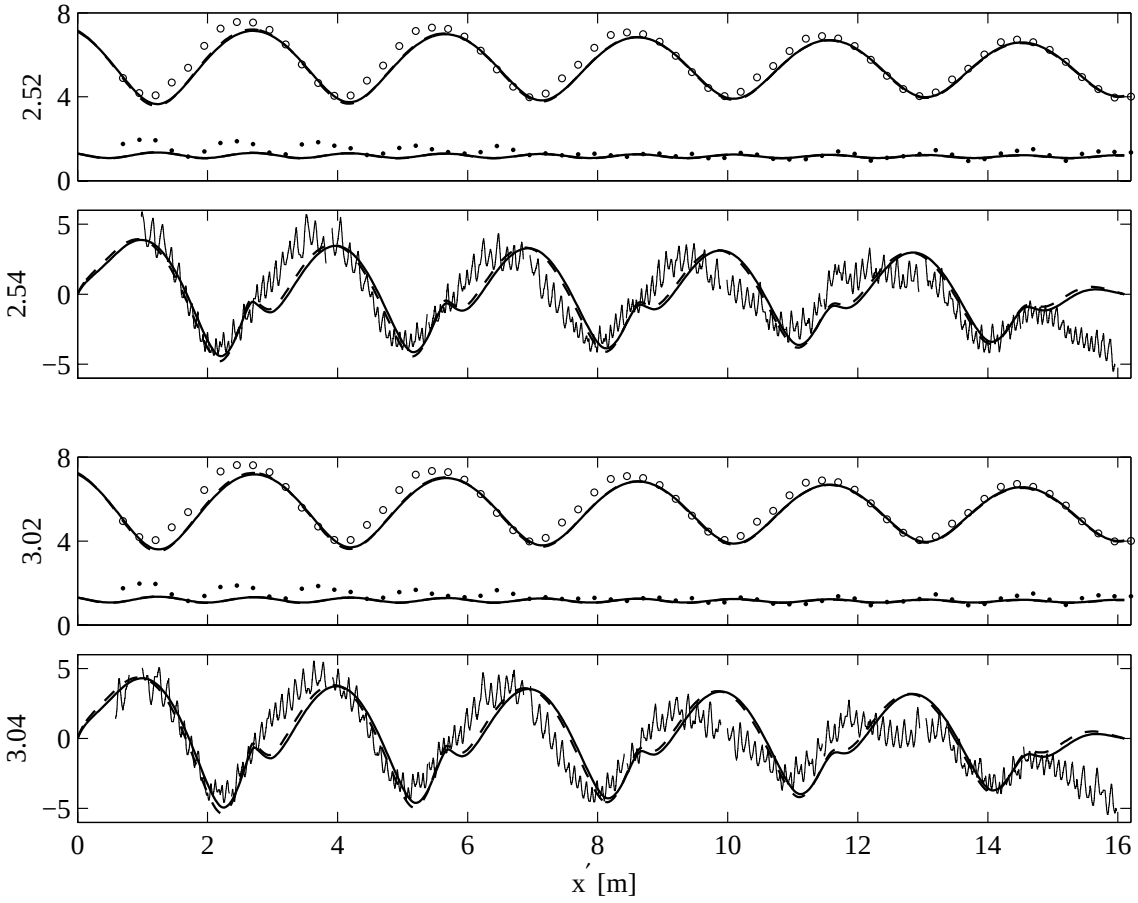


Figure 2-39: See caption of Figure 2-37.

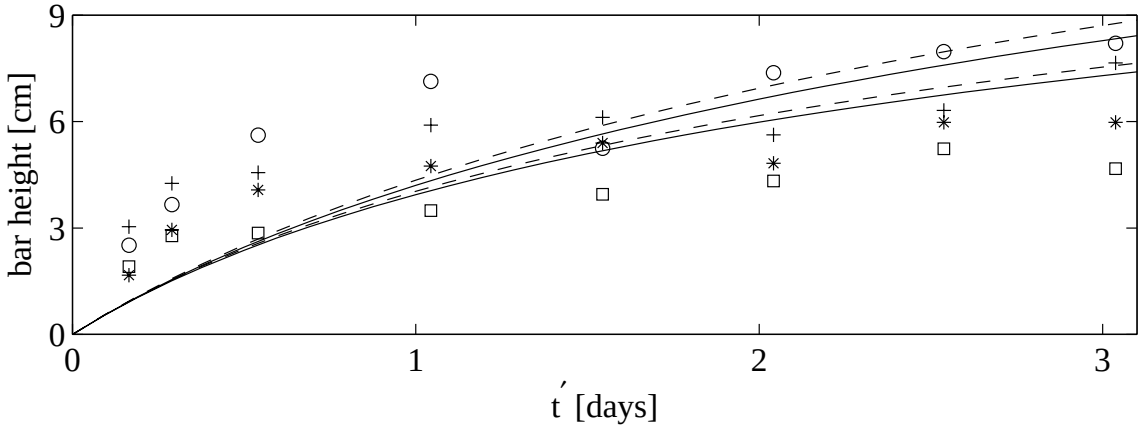


Figure 2-40: Measured and predicted bar height evolution in time, for test 324. The measured bar heights correspond to the first (∘), second (+) and fifth (△) bars, counted from the left in Figures 2-36 to 2-39. Predictions of the heights $\max(\widetilde{h}') - \min(\widetilde{h}')$ of the first and last bars are made by neglecting (solid lines) and including (dashed lines) suspended sediments.

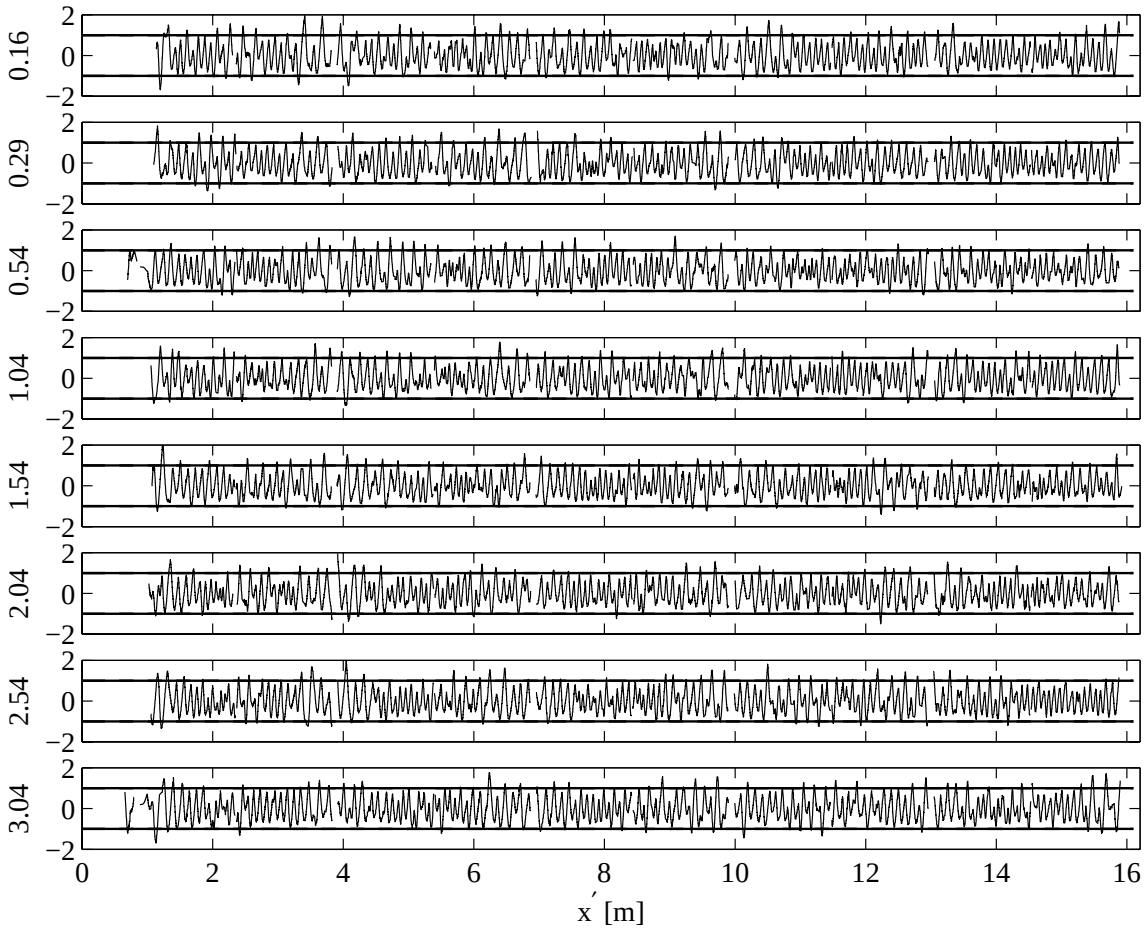


Figure 2-41: Comparison of measured ripple elevations (jagged lines) to the fitted ripple envelope formed by $\pm\eta_r' = \pm 1$ cm. All vertical scales are in [cm]. Numbers left of the ripple elevation plots indicate the corresponding elapsed time in days. Gaps in the ripple data are due to vertical tank supports blocking the view.

height $\eta_r' = \eta_{ro} = 2$ cm for test 324 and, for test 508,

$$\eta_r' = 2\frac{\left(0.85 + 0.4\left|U_2^{[1]}\right|\right)}{0.85 + 0.4\left|U_{max}\right|^2}, \tag{2.147}$$

where $U_{\max}$ was defined in Eq. (1.109),

$$|U_{\max}| = \max_x \left|U_1^{[1]}\right| = \frac{A_o A(1+|R|)}{A_b \sinh kH}.$$

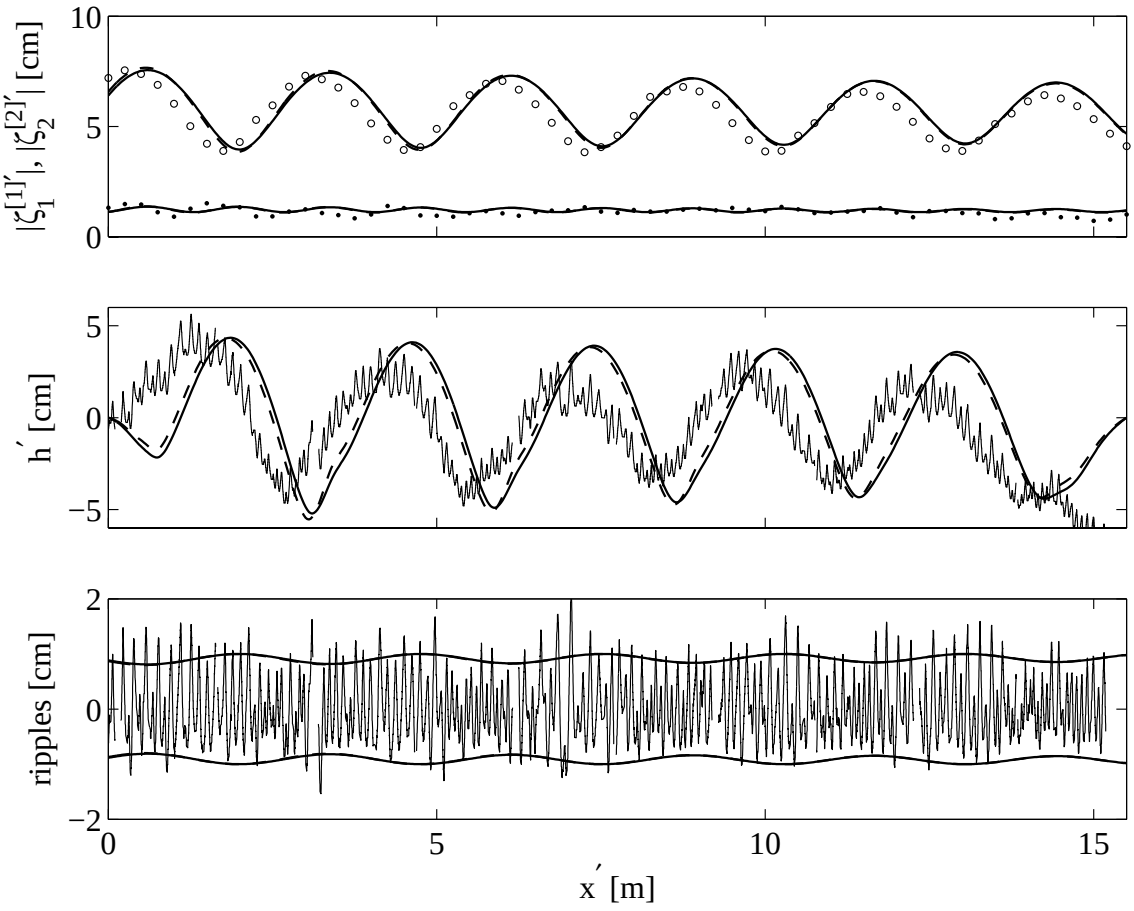


Figure 2-42: Comparison of measured and predicted wave amplitudes (top) and bar elevations (middle) along the tank for test 508 at $t' = 3.96$ days (waves) and at $t' = 3.98$ days (bars). The measured first and second harmonic wave amplitudes $\zeta'_{env} = |\zeta_1^{[1]\prime}|$ ($\circ$) and $|\zeta_2^{[2]\prime}|$ ($\bullet$) are plotted above the bar elevation $\widetilde{h}'$ (jagged line). Corresponding predictions are made by neglecting (smooth solid line) and including (smooth dash line) suspended sediments. In the bottom plot, measured ripple elevations (jagged line) are compared to the ripple envelope (smooth line) formed by $\pm\eta'_r/2$, where the ripple height $\eta'_r$ is found from Eq. (2.147). $x' = 0$ is 3.5 m from the mean wavemaker position. Gaps in the bar and ripple data are due to vertical tank supports blocking the view.

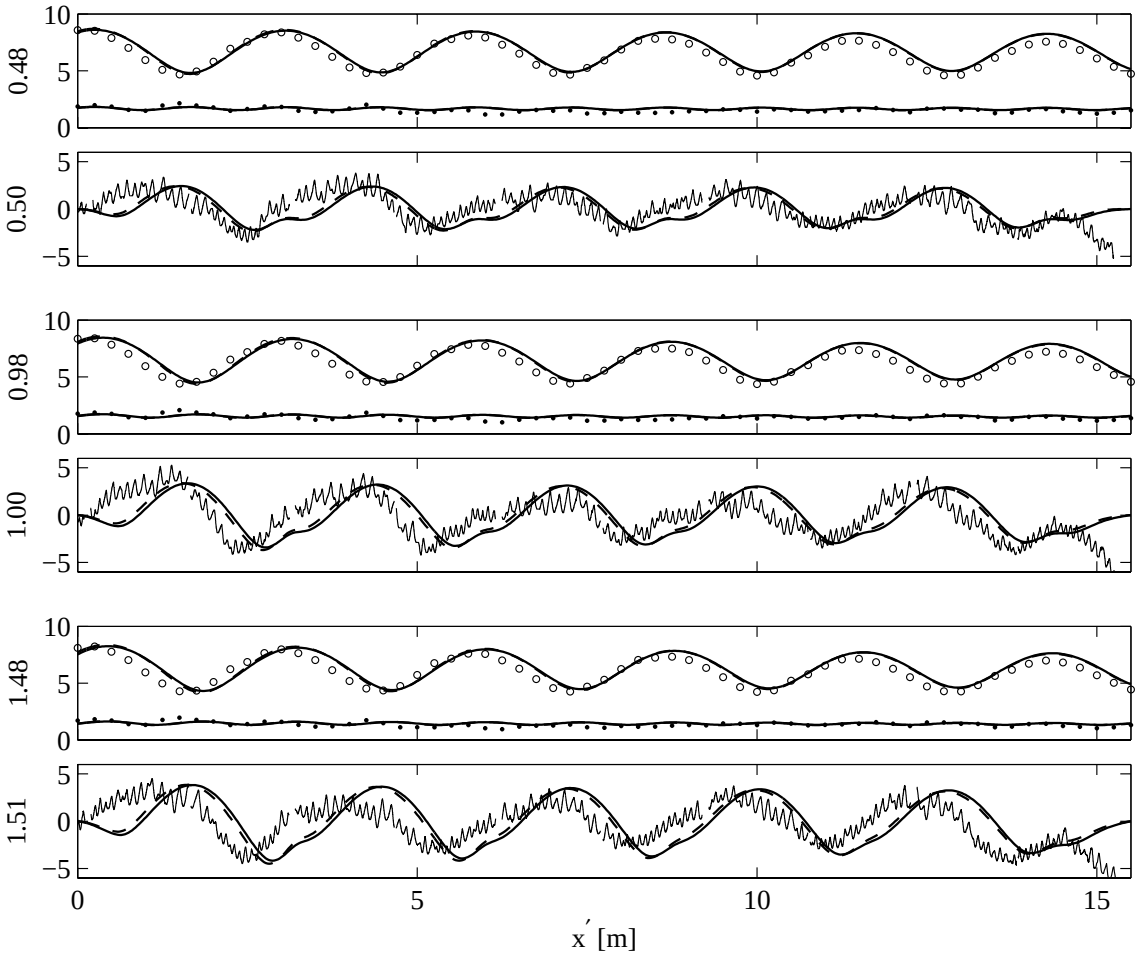


Figure 2-43: Pairs of wave and bar comparisons along the tank for test 508 at various times. For each plot pair, the measured first and second harmonic wave amplitudes $\zeta'_{env} = |\zeta_1^{[1]\prime}|$ ($\circ$) and $|\zeta_2^{[2]\prime}|$ ($\bullet$) are plotted above bar elevations $\widetilde{h}'$ (jagged lines). Corresponding predictions are made by neglecting (smooth solid line) and including (smooth dash line) suspended sediments. All vertical scales are in [cm]. $x' = 0$ is 3.5 m from the mean wavemaker position. Numbers left of the wave and seabed elevation plots indicate the corresponding elapsed time in days. Gaps in the bar data are due to vertical tank supports blocking the view.

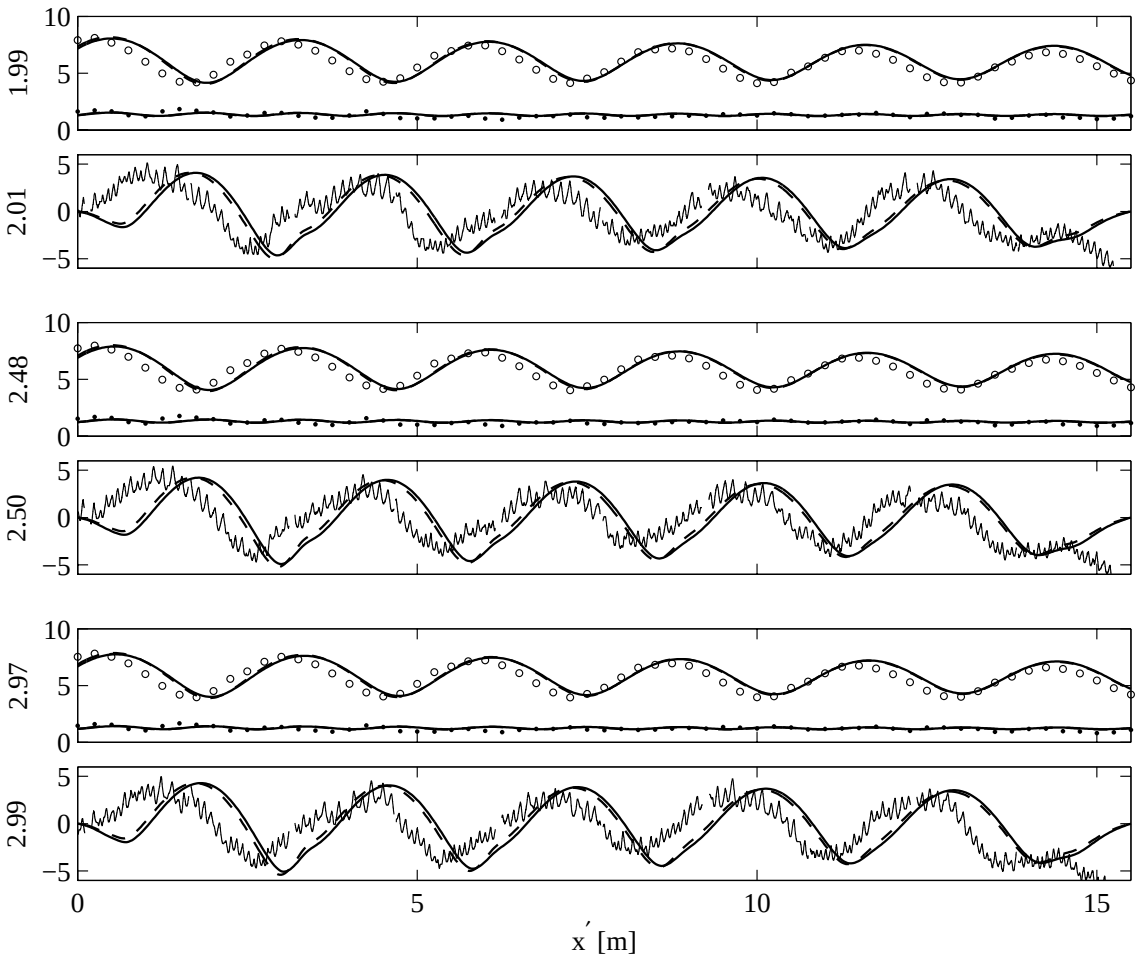


Figure 2-44: See caption of Figure 2-43.

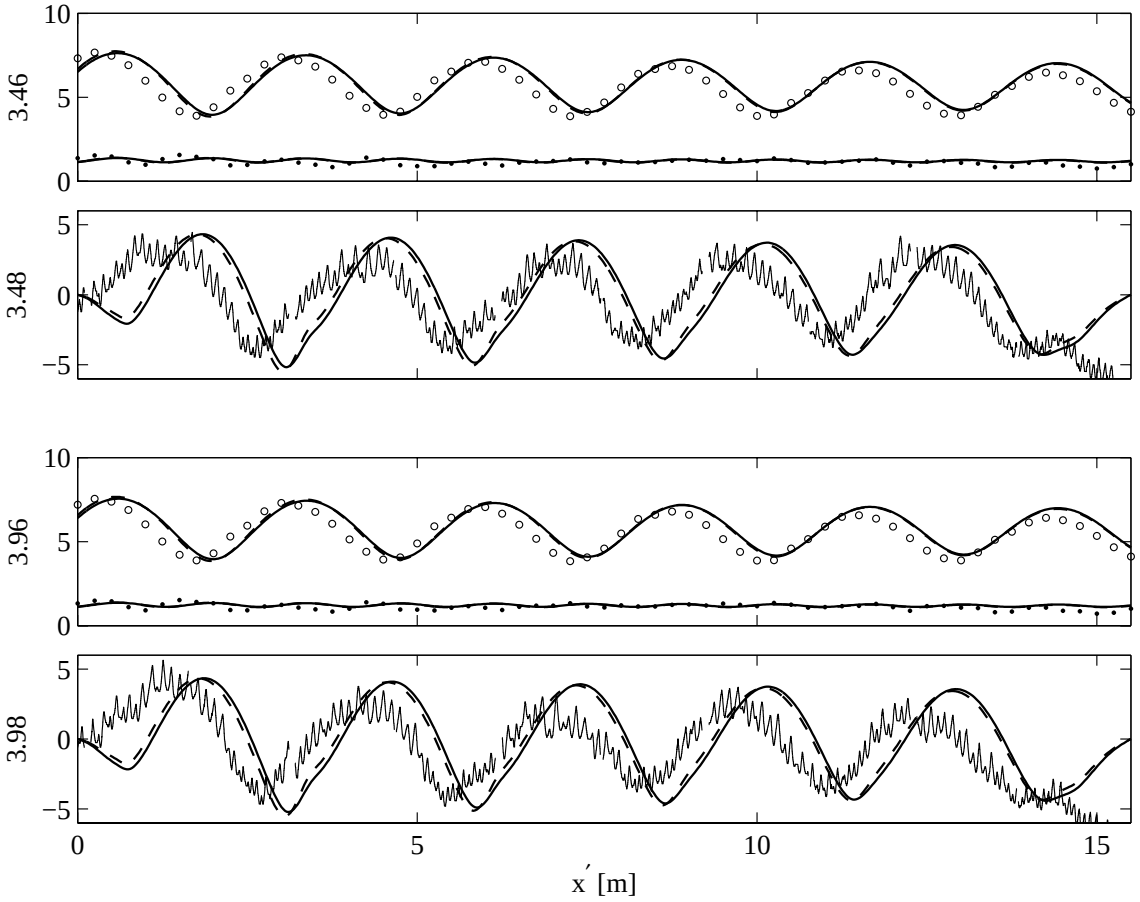


Figure 2-45: See caption of Figure 2-43.

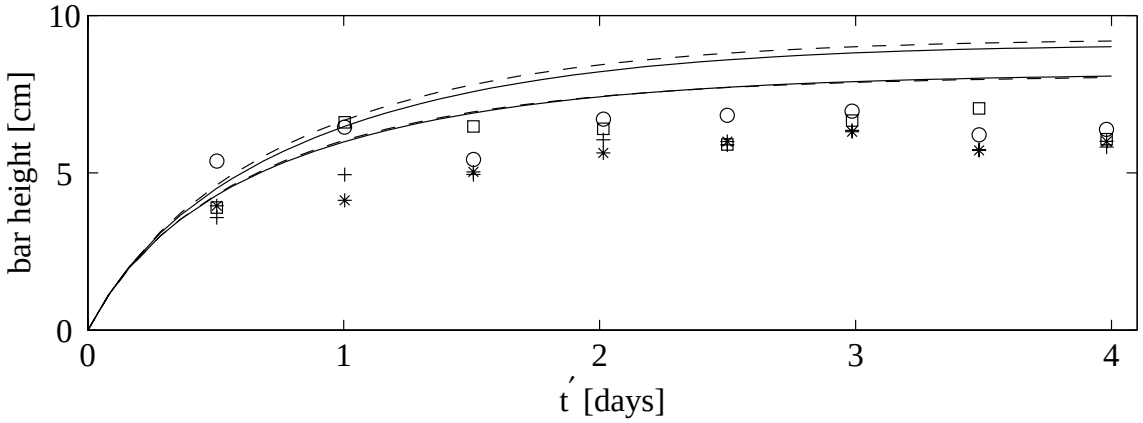


Figure 2-46: Measured and predicted bar height evolution in time, for test 508. The measured bar heights correspond to the first (∘), second (+) and fifth (△) bars, counted from the left in Figures 2-42 to 2-45. Predictions of the heights $\max(\widetilde{h}') - \min(\widetilde{h}')$ of the first and last bars are made by neglecting (solid lines) and including (dashed lines) suspended sediments.

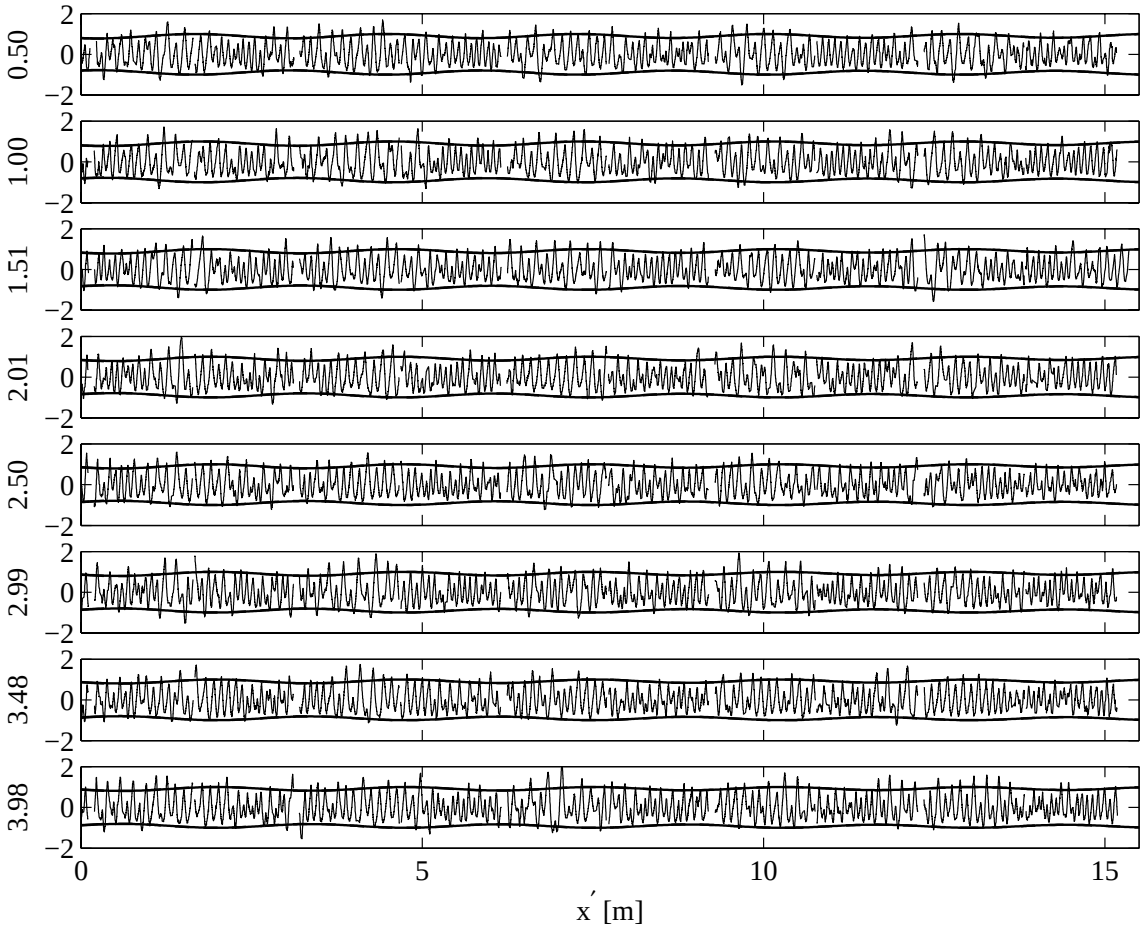


Figure 2-47: Comparison of measured ripple elevations (jagged lines) to the fitted ripple envelope formed by $\pm\eta_r'/2$ at various times in test 508. The ripple height $\eta_r'$ is found from Eq. (2.147). All vertical scales are in [cm]. Numbers left of the ripple elevation plots indicate the corresponding elapsed time in days. Gaps in the ripple data are due to vertical tank supports blocking the view.

## 2.7 Bars in the field

With our sand bar model validated against laboratory data, we now turn to the real goal: the prediction of sand bars in nature. Unfortunately, no records exist of simultaneous wave and sand bar evolution in the field. The field observations considered here are the acoustic soundings of Dolan & Dean (1985) [15] of bars in Chesapeake Bay and, more recently, the observations of Elgar *et al.* (2003) [17] of bars in Cape Cod Bay. Tentative predictions are made by using measured wave parameters over existing bars (in the case of Elgar *et al.*) or by estimating the wave period from local bar lengths and water depth (for the observations of Dolan & Dean), and by adjusting the phase of the reflection coefficient so that the predicted and measured bar crests coincide. In both cases, the wave estimates involve small values of the dispersion parameter $KH_o$ (0.1 to 0.3), indicating that a shallow water theory is more suited to making predictions of these observations. We also make theoretical predictions of bar formation in more intermediate depths on a prototypical sloping beach. Lastly, for completeness, we use parameters associated with seawater in all the predictions in this section, i.e sediment specific gravity $s = 2.57$, fluid viscosity $\nu = 0.0115$ cm$^2$/s and water density $\rho = 1.03$ g/cm$^3$. The effect of using these parameters instead of those for fresh water is admittedly insignificant.

We consider two empirical formulae to help estimate the ripple roughness under irregular waves in the field. Despite considerable scatter, Nielsen [48] proposed the following formula for the ripple height,

$$\frac{\eta_{ro}}{A_{b\,\mathrm{rms}}} = 21\Psi_{\mathrm{rms}}^{-1.85}, \quad \text{for} \quad \Psi_{\mathrm{rms}} > 10, \tag{2.148}$$

where $A_{b\,\mathrm{rms}}$ and $\Psi_{\mathrm{rms}}$ are the orbital amplitude and mobility number (defined in (1.104)) based on the significant wave height. Wikramanayke & Madsen (1990) [65] have also given a formula for ripple height in the field,

$$\frac{\eta_{ro}}{A_{b\,\mathrm{rms}}} = 7.0 \times 10^{-4} Z^{-1.23}, \qquad 0.012 < Z < 0.18, \tag{2.149}$$

where $Z = \Theta_{do\mathrm{rms}}/S_*$, the ratio of the grain roughness Shields parameter $\Theta_{do\mathrm{rms}}$ (based on the significant wave height) and the fluid sediment parameter $S_*$ defined in (1.103).

All prototypical simulations with strong shoreline reflection $|R_L| = 1$ are run using the first method outlined in §2.4.4, in which the sand bar patch is evolved as a single unit and

zero boundary conditions are imposed at the patch ends. When the shoreline reflection is $|R_L| = 1$, the bar patch ends are set to correspond to sub-critical regions, where the bar elevation is zero at all times. All prototypical simulations for weak shoreline reflection $|R_L| < 0.5$ are run using the second numerical solution method discussed in §2.4.4, namely, evolving a single sand bar at each $x_1$ gridpoint and applying periodic boundary conditions at the ends of each bar.

### 2.7.1 Observations of Dolan & Dean (1985)

Dolan & Dean (1985) [15] made acoustic soundings of sand bars at eighteen sites in upper Chesapeake Bay (Maryland, USA) during July 1982. The sites exhibited between 5 and 17 bars spaced between 12 and 70 m in water depths of 0.5 to 2 m. Bar heights ranged from 0.03 to 0.67 m. Based on 16 years of aerial photography, little change was observed in the number or shape of the bars at the 18 sites. Multiple bars were also observed throughout the year and thus are not a seasonal phenomenon.

For most sites, Dolan & Dean report the mean grain diameter at up to four cross-shore locations. For our predictions, we take $d$ as the average of the grain diameters reported at the three most offshore locations. For those sites without a reported mean grain diameter, $d$ is estimated from that of neighboring sites.

Since no wave data was recorded, we must make tentative estimates of the wave parameters. The wave length is estimated as twice the local bar length, and the wave period is then found from the dispersion relation using the local water depth. The phase of the reflection coefficient is adjusted to make the predicted and observed bar crests coincide as closely as possible. The magnitude of shoreline reflection $|R_L|$ is deemed to be relatively low since no sub-critical regions are evident in the observations. In the absence of wave data, we set the total wave amplitude at the shallowest bar as 25 cm and the magnitude of shoreline reflection as $|R_L| = 0.25$. The characteristic depth $H_o$ is chosen as the mean of the depth $H$ over $0 < x_1 < \varepsilon L$. Under the assumption of non-breaking waves, the offshore wave amplitude (in depth $H'(0)$) and the characteristic wave amplitude (in depth $H_o$) are found using conservation of wave energy flux,

$$A'(0) = \sqrt{\frac{C_{gi}}{C_{gs}}} 25 \text{ cm}, \qquad A_o = \sqrt{\frac{C_{gi}}{C_{go}}} 25 \text{ cm},$$

| Site | $d$ [mm] | $S_*$ | $T$ [s] | $H_o$ [m] | $A_o$ [cm] | $A'(0)$ [cm] | $R_L$ | $\varepsilon$ | $KH_o$ | $\Psi_{\text{rms}}$ | $\widehat{\Theta}_{do}$ | $\eta_{ro}$ [cm] |
|---|---|---|---|---|---|---|---|---|---|---|---|---|
| 1 | 0.19* | 2.20 | 12 | 1.76 | 22.1 | 16.0 | $\frac{e^{-0.94i}}{4}$ | 0.16 | 0.22 | 143 | 0.55 | 1.0 |
| 5 | 0.19 | 2.20 | 13 | 1.25 | 20.9 | 18.2 | $\frac{e^{0.63i}}{4}$ | 0.21 | 0.17 | 181 | 0.66 | 1.0 |
| 6 | 0.22 | 2.85 | 17 | 1.57 | 21.1 | 17.3 | $\frac{e^{0.31i}}{4}$ | 0.17 | 0.15 | 124 | 0.45 | 1.2 |

Table 2.8: Parameters used for predictions of the observations of Dolan & Dean (1985) [15] and Dolan (1983) [14]. The grain diameter $d$ is found from Dolan's measurements. Asterisks on the grain diameter $d$ indicate the value was found from neighboring sites. All other parameters are tentative estimates based on the local bar length, water depth, and bar crest positions.

where $C_{gi}$, $C_{go}$, and $C_{gs}$ are the group velocities in the offshore depth $H'(0)$, the characteristic depth $H_o$, and the shallowest depth $H'(\varepsilon L')$, respectively. The scaled offshore amplitude $A'(0)/A_o$ and the shoreline reflection $R_L$ are the boundary values of the wave amplitude $A$ and reflection coefficient $R$ used in our sand bar simulation. The parameters are summarized in Table 2.8.

Although Dolan & Dean measured bars at 18 sites, many of the bars were in very shallow water (small $KH_o$). The mean depth $H$ is found by fitting a smooth profile to the observed beach topography. We limit our comparisons to the sites with the largest water depths, and make predictions of the bars in the deeper portions of those sites. The parameters used for predictions are summarized in Table 2.8. Despite choosing only the sites with the largest water depths, the water is still relatively shallow. Hence the term proportional to $1/\sinh^2 kH$ dominates the bedload forcing. In particular, the return flow term is dominated by the $1/\sinh^2 kH$ term, and hence the precise value taken for $\Lambda_2^{[0]}$ is immaterial (we chose $\Lambda_2^{[0]} = 1.5$).

Dolan & Dean noted multiple wave breaking events over the bars at various sites. As the bars grow, the water depth over the bar crests diminishes, causing waves to break. In shallow water, waves break when the ratio of wave height to water depth exceeds a critical value generally between 0.7 and 1.2 (Mei [45] and references therein). The range of $\gamma$ is due to the considerable scatter in the field measurements.

Since our model can only predict bar formation under non-breaking waves, we can only make sand bar predictions outside the surf zone. Our predictions indicate that under non-breaking waves, bar height should increase as the mean water depth decreases. For each of the three sites considered, the first 3-5 bars increase in height and the next 2-3 bars decrease

in height, as the water depth decreases in the shoreward direction. We estimate that the surf zone begins where bar height begins to decrease with decreasing water depth in the shoreward direction. Near those locations, our predicted wave heights are between 0.4 to 0.6 times the water depth over the bar crests, near the critical range for breaking.

Under non-breaking waves, the timescale of bar evolution is $\alpha_1/\omega$. For Sites 1, 5 and 6, $\alpha_1/\omega$ is between 14 and 41 days. However, wave breaking reduces the local wave height and tempers bar growth. A steady state could possibly be reached on a much shorter timescale than $\alpha_1/\omega$ between the bars and breaking waves. It is thus more likely that the phenomenon limiting bar growth in the field is wave breaking rather than gravity dominated diffusion.

The presence or absence of ripples was not reported by Dolan & Dean. The reported bar profiles seem to be smooth, but this is probably due to the relatively low horizontal resolution in the reported profiles (50 m of beach corresponds to 1-3 cm on the printed page). Given the sediment and wave parameters, ripple estimates are made using formulae (2.148) and (2.149). For our predictions, we take the ripple height $\eta_r' = \eta_{ro}$ to be the greater of these two estimates and 1 cm.

Sand bar predictions based on the parameters listed in Table 2.8 and corresponding to the bars in the deeper portions of Sites 1, 5 and 6 are shown in Figures (2-48) and (2-49). The mean depth is added to the predicted bar elevation and their sum is plotted against the measured seabed profiles. The data is taken from Dolan & Dean (1985) [15] and Dolan (1983) [14]. In all cases, the agreement is satisfactory given the tentative estimates made for the wave parameters, shoreline reflection and the duration of the wave action.

### 2.7.2 Observations of Elgar *et al.* (2003)

Between August and October of 2001, Elgar *et al.* (2003) [17] made repeated surveys of sand bars, wave spectra, and currents in Cape Cod Bay near Truro, MA, USA. The bars did not evolve significantly during the observation period, and hence it is not known what sea spectrum generated the bars. However, the Elgar *et al.* did report the amount of reflection from the shoreline as a function of wave frequency, which gives an estimate of $|R_L|$. The mean grain diameter along the transect was approximately $d = 0.33$ mm (S. Elgar and B. Raubenheimer, personal communication, 2004).

The mean depth $H$ is found by fitting a smooth profile to the observed beach topography. In water deeper than 3.2 m, where there seemed to be no bars, we use the reported depth

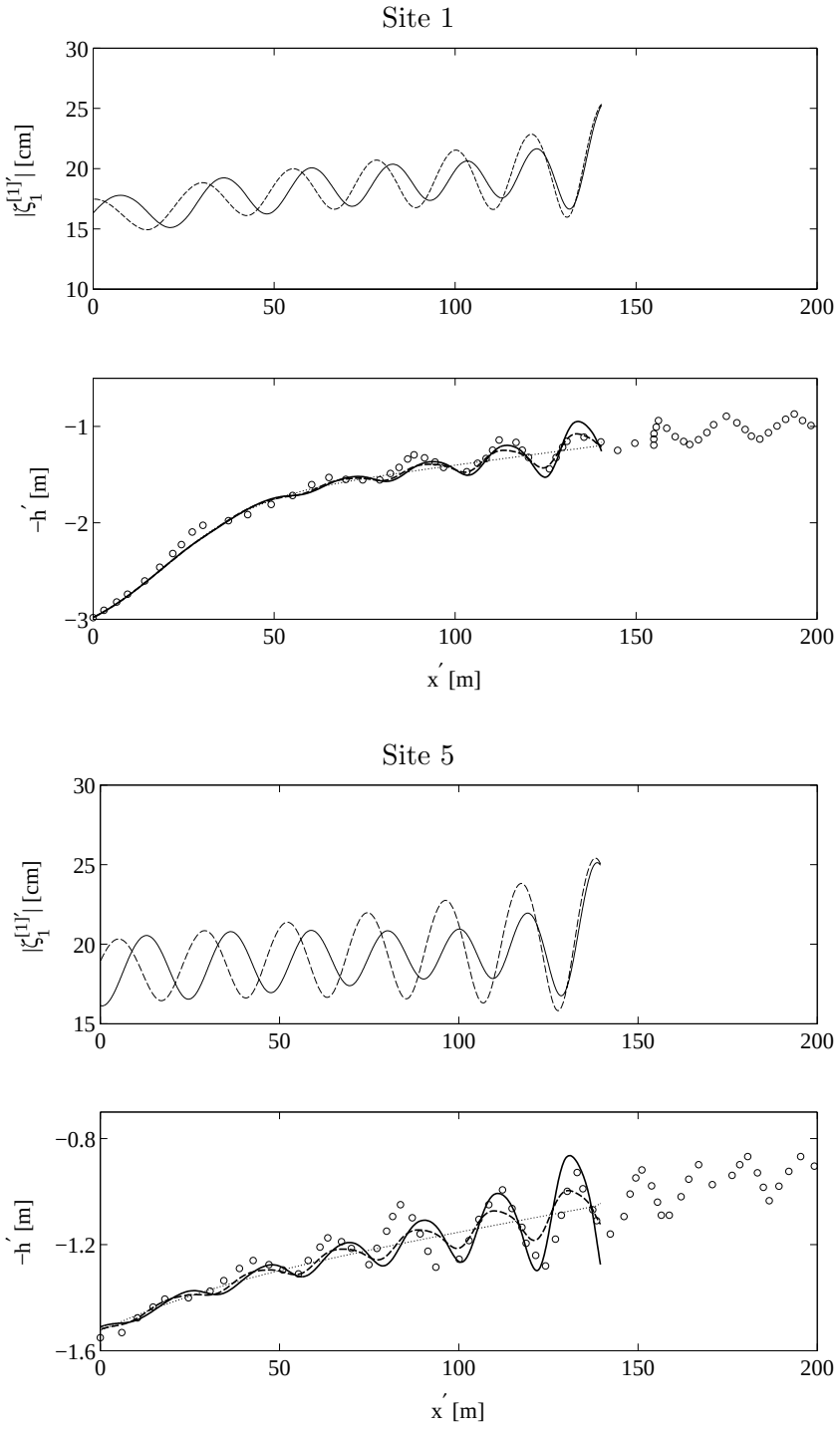


Figure 2-48: Comparison of our predictions with Dolan & Dean (1985) [15]'s observations of bars at Sites 1 and 5 in Chesapeake Bay (data (∘) from Dolan (1983) [14]). Predictions based on the parameters listed in Table 2.8 of wave amplitudes $|\zeta_1^{[1]\prime}|$ and bar profiles $\widetilde{h}'$ are given after 4 (dash) and 8 (solid) hours of wave action. Bar elevations $\widetilde{h}'$ are superposed on the mean beach profile $z' = -H'$ (also the initial condition), indicated by dotted lines.

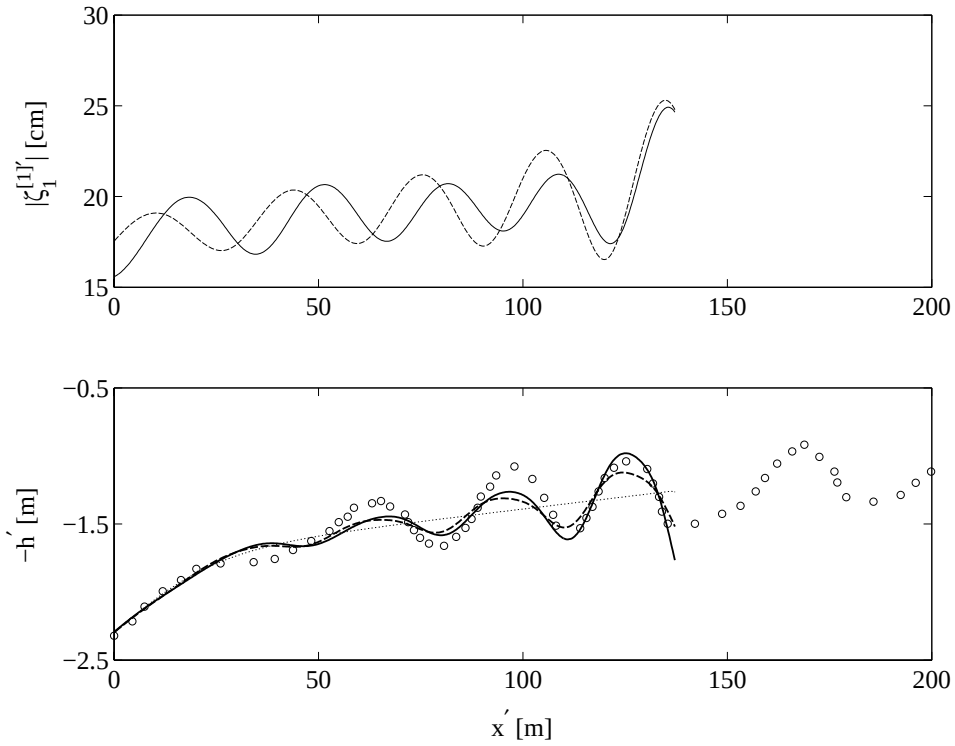


Figure 2-49: Same as caption for Figure 2-48 but for Site 6. Predictions are after 1 (dash) and 3 (solid) hours of wave action.

profile directly.

To obtain wave records, Elgar *et al.* deployed collocated bottom-mounted pressure gages and acoustic Doppler current meters at 5 cross-shore locations. Various types of waves were recorded, including low energy Atlantic swell (typical frequency $f \approx 0.07$ Hz) and infra-gravity waves ($f \approx 0.01$ Hz) and higher energy local wind waves ($f \approx 0.25$ Hz). Resonant frequencies are in the range $f \approx 0.037 - 0.044$ Hz and correspond to surface wavelengths equal to twice the typical bar length in the given water depth. Also, large reflection coefficients were observed for low-energy waves and low-frequency waves and the reflection coefficients decreased as the wave frequency and energy increased. Since strong shoreline reflection leads to prominent sub-critical regions on the bed, which were not observed, the bars were most likely generated by high energy waves with frequencies in the resonant range $f \approx 0.037 - 0.044$ Hz.

During a storm, Elgar *et al.* recorded a 1 hour interval consisting of very large waves of frequency $f = 0.042$ Hz that broke over the first bar and proceeded unbroken until the shoreline, where 80% of the energy was dissipated ($|R_L|^2 = 0.2$). Since these storm waves

| $d$ [mm] | $S_*$ | $T$ [s] | $H_o$ [m] | $A_o$ [cm] | $A'(0)$ [cm] | $R_L$ | $\varepsilon$ | $KH_o$ | $\Psi_{\text{rms}}$ | $\widehat{\Theta}_{do}$ | $\eta_{ro}$ [cm] |
|---|---|---|---|---|---|---|---|---|---|---|---|
| 0.33 | 5.11 | 23.8 | 2.80 | 23.1 | 21.2 | $\frac{9e^{-2.51i}}{20}$ | 0.12 | 0.14 | 76.2 | 0.28 | 5.8 |

Table 2.9: Parameters used for predictions of Elgar *et al.* (2003) [17]'s observations.

satisfy our criteria for resonant frequency and low reflection, we choose the corresponding parameters to make our predictions: $f = 0.042$ Hz ($T = 23.8$ s) and $|R_L|^2 = 0.2$. For this wave event, the significant wave height, defined as four times the standard deviation of the surface fluctuations, was 0.8 m at the seaward sensor in 2.8 m water depth. After breaking over the first bar, the wave energy decreased by 30%, reducing the wave height by a factor of $\sqrt{0.7}$. Since our model is only valid for non-breaking waves and since the observed waves of reduced height propagated unbroken until the shoreline, we choose the characteristic wave height as the reduced wave height $2A_o(1 + |R_L|) = 80\sqrt{0.7}$ cm in a characteristic water depth of $H_o = 2.8$ m, for our predictions. Neglecting the wave breaking event over the first bar, we set the offshore wave amplitude to be that of the "reduced" wave and use conservation of wave energy flux to obtain

$$A'(0) = A_o\sqrt{\frac{C_{gi}}{C_{go}}}$$

where $C_{gi}$ and $C_{go}$ are the group velocities in the offshore depth $H'(0) = 4.02$ m and the characteristic depth $H_o = 2.8$ m, respectively. For the parameters listed, $\sqrt{C_{gi}/C_{go}} = 0.868$ and $A'(0) = 21.2$ cm. The scaled offshore amplitude $A'(0)/A_o$ and the shoreline reflection $R_L$ are the boundary values of the wave amplitude $A$ and reflection coefficient $R$ used in our sand bar simulation.

Elgar *et al.* reported that wave-orbital ripples were observed on the bar crests by SCUBA divers and when the bar crests were exposed during the spring low tide. A photograph of ripples found on a bar crest (Figure 1(c) in Elgar *et al.*), suggests that the typical ripple height was approximately 4-6 cm and length 10-20 cm. Of course, the geometry of the bedforms that existed (if at all) when the bars were formed is not known. Given the sediment and wave parameters, the greater of the ripple estimates (2.148) and (2.149) is 5.8 cm. Thus, for our predictions, we use the ripple height $\eta'_r = \eta_{ro} = 5.8$ cm.

The parameters used for predictions are summarized in Table 2.9. Note that the water is

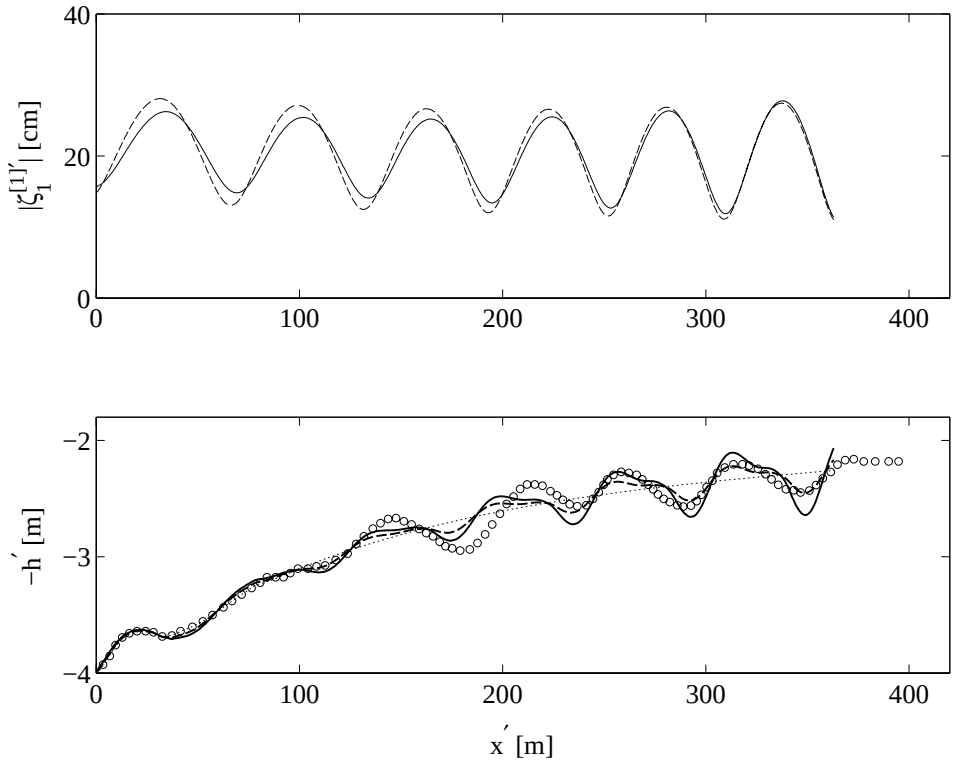


Figure 2-50: Comparison of our predictions with Elgar *et al.* [17]'s observations (∘) of bars in Cape Cod Bay. The predictions are based on the parameters listed in Table 2.9. The amplitude of the first wave harmonic $|\zeta_1^{[1]\prime}|$ (top) and seabed profiles $z' = -h' = -H' + \widetilde{h}'$ (bottom) are given after 8 hours (dash) and 16 hours (solid) of wave action. The mean beach profile $z' = -H'$ (the initial condition) is indicated by the dotted line.

relatively shallow ($KH_o = 0.14$), and hence the term proportional to $1/\sinh^2 kH$ dominates the bedload forcing. Thus, despite taking $\Lambda_2^{[0]} = 1.5$, the precise value is immaterial since the return flow term is dominated by the $1/\sinh^2 kH$ term. A sand bar theory for shallow water would be better suited to making predictions.

Sand bar predictions based on the parameters listed in Table 2.9 are shown in Figure 2-50. The sum of the mean depth and the predicted bar elevation is plotted against the measured seabed profiles after 8 (dash) and 16 (solid) hours of wave action. The agreement is encouraging given the tentative estimates of the wave parameters, the phase of the shoreline reflection, and the duration of wave action. We should point out that the first crest at $x' = 5$ m is not a predicted bar, but a feature of the mean topography $H'$. Also, our prediction of the first (most offshore) sand bar is poor because we have neglected the wave-breaking that occurred over that bar.

The timescale of bar evolution $\alpha_1/\omega$ corresponding to the bar predictions in Figure 2-50

and the parameters in Table 2.9 is very large, 159 days. Thus, as we hypothesized in the previous section, the phenomena that limit bar growth in the field are (a) a change in the incident waves and (b) wave breaking, neither of which is included in our model. We have therefore only made predictions for the first 16 hours of bar formation.

### 2.7.3 Bars on a beach in water of intermediate depth

To make predictions better suited to our model, namely those in water of intermediate depth, we consider a beach that mimics the shapes of those in Dolan [14] and Elgar *et al.* [17]'s observations, but that is set in deeper water (minimum depth $H_o = 4$ m),

$$H'(x') = \frac{H_o}{4}\left(7 - \tanh\left(\frac{x'}{12.5H_o} - \frac{1}{2}\right)\right) - \frac{x'}{200}. \tag{2.150}$$

As $x'$ increases from 0 at the offshore boundary to $L' = 400$ m at the shoreward boundary, the depth $H'$ decreases from 7.46 to 4 m. The slope is steep (1/50) on the seaward side and mildly sloping (1/200) closer to the shore. The nearshore slope is consistent with the observations of Dolan [14] and Elgar *et al.*, who reported beach slopes between 0.0012 and 0.0052. Introducing dimensionless variables from Eq. (1.69), the normalized mean depth is given by

$$H(x_1) = \frac{KH_o}{4}\left(7 - \tanh\left(\frac{x_1}{12.5\varepsilon KH_o} - \frac{1}{2}\right)\right) - \frac{x_1}{200\varepsilon}. \tag{2.151}$$

If a beach ends at a seawall or steep shoreline, the shoreline reflection $R_L$ can be very strong. Elgar *et al.* [17] have given evidence of strong shoreline reflection due to a steep shore. If the shore has a mild slope, the waves are more likely to break and the shoreline reflection can be weak. Predictions are made of sand bars on the prototypical beach (2.151) for both weak ($|R_L| = 0.25$) and strong ($|R_L| = 1$) shoreline reflection.

The waves are chosen to have period $T = 10$ s and characteristic total amplitude $A_o(1 + |R_L|) = 50$ cm. Under the assumption of non-breaking waves, the offshore wave amplitude (in depth $H'(0)$) is found using conservation of wave energy flux,

$$A'(0) = A_o\sqrt{\frac{C_{gi}}{C_{go}}}$$

where $C_{gi}$ and $C_{go}$ are the group velocities in the offshore depth $H'(0)$ and the characteristic depth $H_o$, respectively. The scaled offshore amplitude $A'(0)/A_o$ and the shoreline reflection

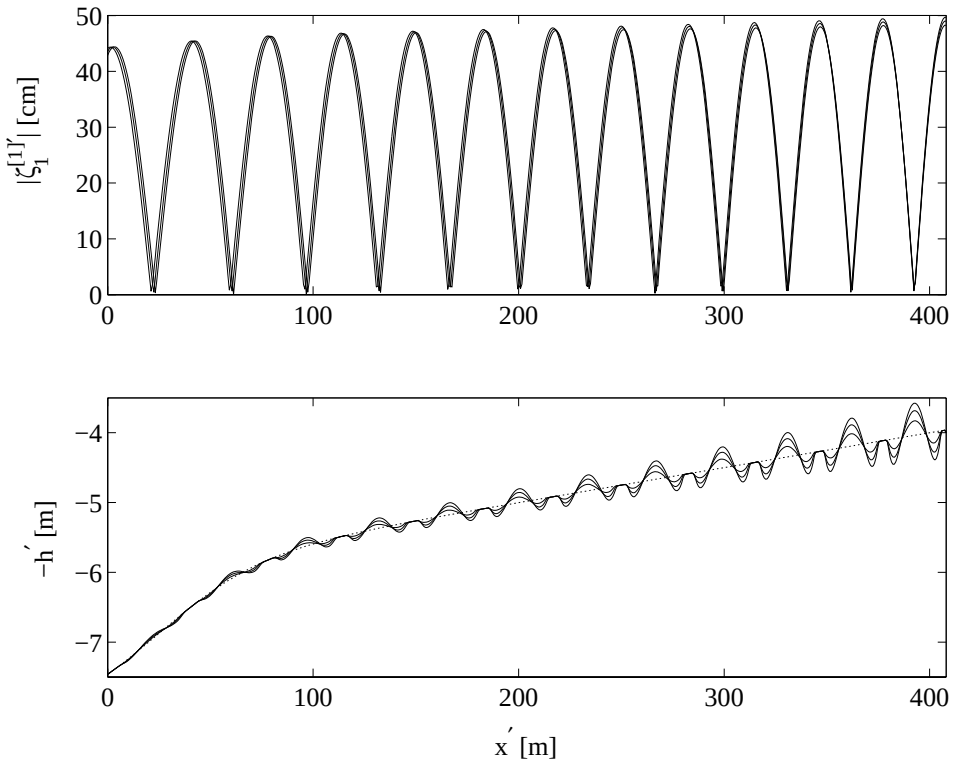


Figure 2-51: Snapshots of wave amplitude $|\zeta_1^{[1]\prime}|$ (top) and seabed profiles $z' = -H' + \widetilde{h}'$ (bottom) for the prototypical sloping beach (2.151) with strong shoreline reflection $R_L = 1$, after 1, 2, and 3 days of wave action (solid curves). The mean beach profile $z' = -H'$ (the initial condition) is indicated by the dotted line. The other parameters are $T = 10$ s, $A'(0) = 22.2$ cm, $A_o(1 + |R_L|) = 50$ cm, $H_o = 4$ m, $d = 0.5$ mm, $\eta_r' = 5.5$ cm.

$R_L$ are the boundary values of the wave amplitude $A$ and reflection coefficient $R$ used in our sand bar simulation. Changing the phase of $R_L$ merely shifts the bar crests and wave nodes seaward or shoreward; the relative position of the bar crests and the wave nodes remains unchanged. We therefore assume that $R_L = |R_L| > 0$.

We consider a seabed composed of uniform coarse grains of diameter $d = 0.5$ mm. Given the sediment and wave parameters, across the mildly sloping section of the beach (2.151), the greater of the ripple estimates (2.148) and (2.149) ranges from 5 to 6 cm. For our predictions, we take the ripple height $\eta_r' = \eta_{ro} = 5.5$ cm.

Sand bar predictions under strong reflection $R_L = 1$ are shown in Figure 2-51. The mean depth $H$ has been added to the predicted bar elevations $\widetilde{h}$ and the evolving seabed $h$ is plotted after 1, 2, and 3 days of wave action. The flat sub-critical regions on the seabed, under the wave antinodes, are indicative of strong reflection. As depth increases, the bar heights diminish and the bar lengths increase.

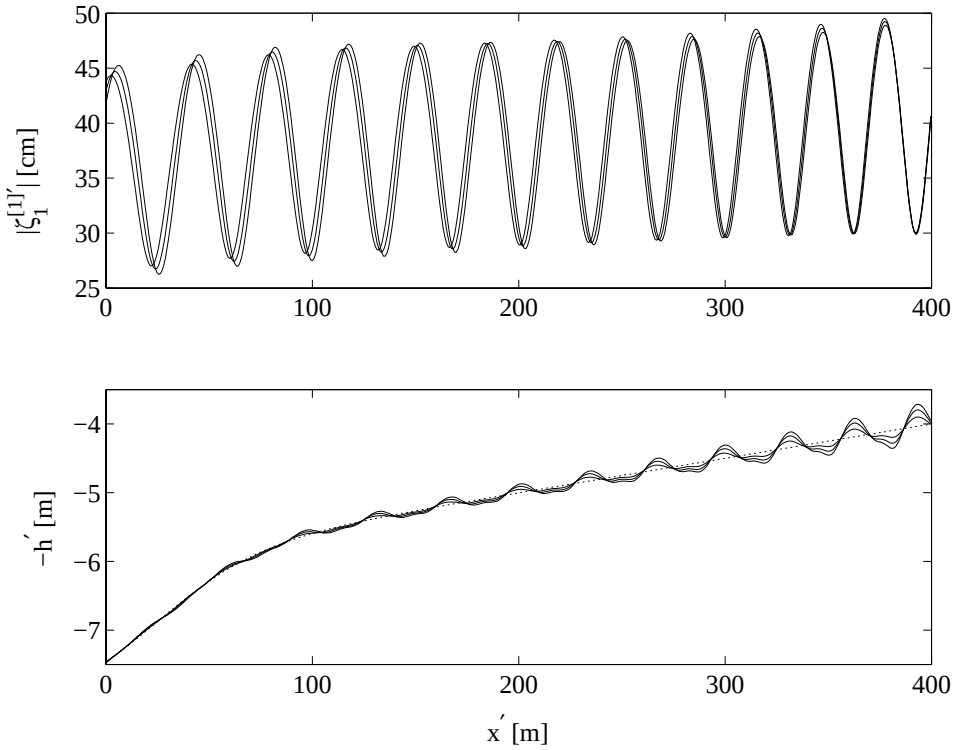


Figure 2-52: Snapshots of wave amplitude $|\zeta_1^{[1]\prime}|$ (top) and seabed profiles $z' = -H' + \widetilde{h}'$ (bottom) for the prototypical sloping beach (2.151) with weak shoreline reflection $R_L = 0.25$, after 1, 2, and 3 days of wave action (solid curves). The mean beach profile $z' = -H'$ (the initial condition) is indicated by the dotted line. The other parameters are $T = 10$ s, $A'(0) = 35.5$ cm, $A_o(1 + |R_L|) = 50$ cm, $H_o = 4$ m, $d = 0.5$ mm, $\eta_r' = 5.5$ cm, $\Lambda_2^{[0]} = 2$.

Sand bar predictions under weak reflection $R_L = 0.25$ are shown in Figures 2-52 and 2-53. In Figure 2-52, the seabed profile $h$ is plotted after 1, 2, and 3 days of wave action. No sub-critical regions appear and as depth increases, the bar heights diminish and the bar lengths increase. The effect of the return flow bed stress coefficient $\Lambda_2^{[0]}$ on predicted bar heights is illustrated in Figure 2-53. The mechanism was described in §2.6.5. For small values of $\Lambda_2^{[0]}$, bar crests are positioned in front of the wave nodes, causing energy to be transferred from the reflected wave to the incident wave. For larger values of $\Lambda_2^{[0]}$, the bar crests are positioned behind the wave node and the energy transfer is reversed. Since the mean depth decreases in the shoreward direction, the waves also shoal. Therefore, for large values of $\Lambda_2^{[0]}$ (see long dash line in Figure 2-53), the total wave height can initially decrease and then increase. In any case, larger values of $\Lambda_2^{[0]}$ are associated with larger bar heights in deeper water.

For both strong and weak reflection, bars are predicted along the entire mildly sloping

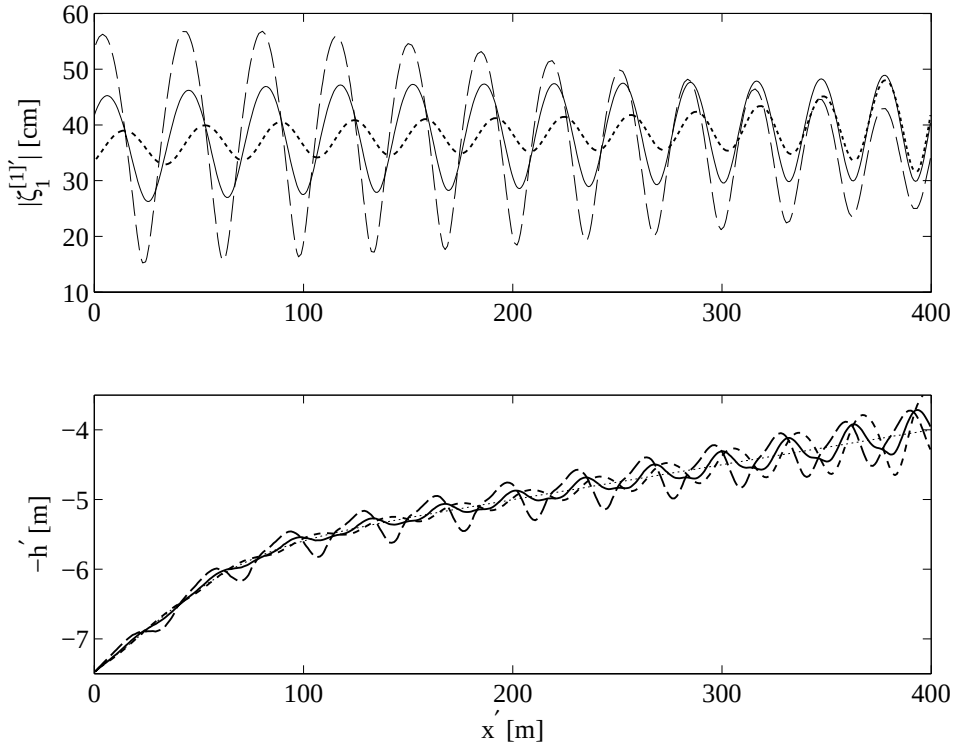


Figure 2-53: The effect of return flow on wave amplitude $|\zeta_1^{[1]\prime}|$ (top) and seabed profiles $z' = -H' + \widetilde{h}'$ (bottom) for the prototypical sloping beach (2.151) with weak shoreline reflection $R_L = 0.25$, after 3 days of wave action. The value of the return flow bed stress coefficient for each curve is $\Lambda_2^{[0]} = 0$ (short dash), $\Lambda_2^{[0]} = 2$ (solid), $\Lambda_2^{[0]} = 4$ (long dash). The other parameters are the same as those in Figure 2-52. The mean beach profile $z' = -H'$ (the initial condition) is indicated by the dotted line.

section of the prototypical beach. On the steep section of the beach, however, the bar heights diminish rapidly as the water depth increases. We conclude that the number of bars on a beach is determined by the underlying beach shape: beaches with longer mildly sloping sections in relatively shallow water will have more bars. This conclusion is supported by the observations of Dolan [14], where the bars were only observed to exist along mildly sloping sections of the beach.

## 2.8 Comparison to the theory of Yu & Mei (2000)

The sand bar/surface wave interaction model derived in this thesis is based in part on the work of Yu (1999) [68] and Yu & Mei (2000) [70]. It is therefore important to compare the two theories directly. Yu & Mei's model is outlined in the introduction and is referred to throughout the thesis. Their sand bar equation has the same form as ours, Eq. (2.106), for

a horizontal mean seabed ($dH/dx_1 = 0$),

$$\frac{\partial \widetilde{h}}{\partial \bar{t}_{\mathrm{YM}}} - \frac{\partial}{\partial x}\left(D_{\mathrm{YM}} \frac{\partial \widetilde{h}}{\partial x}\right) = \frac{\partial q_{\mathrm{YM}}}{\partial x}, \tag{2.152}$$

where the diffusivity and bedload forcing are given by

$$D_{\mathrm{YM}} = \frac{2\sqrt{2}\beta}{\pi\left(1-\mathcal{N}\right)} \frac{Q_{\mathrm{YM}}}{|A|\left(1+|R|^2-2\,|R|\cos 2\chi\right)}, \tag{2.153}$$

$$q_{\mathrm{YM}} = \frac{\Theta_{\mathrm{YM}}}{\pi\left(1-\mathcal{N}\right)}\left(\frac{2+\sqrt{2}}{3} + \frac{1}{\sin^2\left(KH_o\right)}\right) Q_{\mathrm{YM}}\ |A|\ \frac{1-|R|^2+2\,|R|\sin 2\chi}{1+|R|^2-2\,|R|\cos 2\chi}, \tag{2.154}$$

and $\chi = x - \theta_R/2$. We have rewritten the equations of Yu & Mei [70] using our variables. In particular, Yu & Mei used the time dependence $e^{it}$ rather than $e^{-it}$ and also wrote $\zeta_1 = \Re\left\{\left(Ae^{-ix} - Be^{ix}\right)e^{it}\right\}$. Thus, we have made the transformations $A \to A^*$, $\theta_R \to \theta_R + \pi$ in their equations. Yu & Mei used Bragg scattering equations, mathematically equivalent to the equations in 2.98, to solve for the magnitudes and phases of $A$ and $R$ across the bar patch. The form of our Bragg scattering equations is more suitable for numerical solution, since it is equally stable for high and low reflection. One of Yu & Mei's equations involved the term $|R|^{-1}$ which is large for small reflection.

Yu & Mei's sand bar formation time variable is

$$\bar{t}_{\mathrm{YM}} = \frac{\varepsilon \Theta_{\mathrm{YM}}^{1/2}}{\alpha_{\mathrm{YM}}} t,$$

where

$$\alpha_{\mathrm{YM}} = \frac{A_{\mathrm{YM}}\,\omega}{8K\sqrt{(s-1)\,gd^3}},$$

and $\Theta_{\mathrm{YM}}$ is the characteristic Shields parameter based on the full roughness,

$$\Theta_{\mathrm{YM}} = \frac{A_{\mathrm{YM}}\,\omega\,\nu_{e\mathrm{YM}}}{(s-1)\,gd\delta_{\mathrm{YM}}}. \tag{2.155}$$

In the above, $A_{\mathrm{YM}}$ is orbital amplitude based on the the incident wave amplitude $A_o$, i.e. $A_{\mathrm{YM}} = A_o/\sinh KH_o$ and $\delta_{\mathrm{YM}}$ is the boundary layer thickness defined as $\delta_{\mathrm{YM}} = \sqrt{2\nu_{e\mathrm{YM}}/\omega}$.

Yu & Mei employed a constant eddy viscosity $\nu_{e\mathrm{YM}}$ defined in terms of a friction factor,

$$\nu_{e\mathrm{YM}} = \frac{f_w}{4\omega}\left(\kappa\, A_{\mathrm{YM}}\,\omega\right)^2,$$

where $f_w$ is the wave friction factor (Madsen 1994 [38])

$$\begin{aligned} f_w &= \exp\left\{7.02\left(\frac{A_{\mathrm{YM}}}{k_{No}}\right)^{-0.078} - 8.82\right\}, \qquad 0.2 < \frac{A_{\mathrm{YM}}}{k_{No}} < 10^2, \\ f_w &= \exp\left\{5.61\left(\frac{A_{\mathrm{YM}}}{k_{No}}\right)^{-0.109} - 7.30\right\}, \qquad 10^2 < \frac{A_{\mathrm{YM}}}{k_{No}} < 10^4, \end{aligned}$$

and $k_{No}$ is the equivalent roughness defined in §1.5.

The diffusivity $D_{\mathrm{YM}}$ in Yu & Mei's sand bar equation (2.152) is derived from the slope-effect on the critical Shields parameter (due to Fredsøe [18]). In contrast, our diffusivity $D_\nu$ is based on the slope effect on the bedload transport, found empirically by King [32]. The two resulting diffusivities $D_{\mathrm{YM}}$ and $D_\nu$ have the same form, although Yu & Mei's diffusivity involves a fitting parameter $\beta = O\left(\Theta_c\right)$ to adjust the bar height. When comparing with laboratory experiments, the parameter $\beta$ is chosen by first comparing the steady state bar height to the experimentally measured equilibrium bar height, and then finding the time varying bar profiles by numerically solving the sand bar equation (2.152).

The most important difference between our theory and that of Yu & Mei concerns the estimate of the mean bedload transport over half a wave period, $Q_{\mathrm{YM}}$ (Yu & Mei) and our $Q_B$. Yu & Mei's $Q_{\mathrm{YM}}$ is defined as

$$\begin{aligned} Q_{\mathrm{YM}} &= \left(\sqrt{2}\,|A|\left(1 + |R|^2 - 2\,|R|\cos 2\chi\right) - \frac{\Theta_{c0}}{\Theta_{\mathrm{YM}}}\right)^{3/2} \\ &\qquad \times \mathrm{Hv}\left(\sqrt{2}\,|A|\left(1 + |R|^2 - 2\,|R|\cos 2\chi\right) - \frac{\Theta_{c0}}{\Theta_{\mathrm{YM}}}\right), \end{aligned} \tag{2.156}$$

where $\Theta_{c0}$ is the flat-bed critical Shields parameter, defined in (1.102), and $\mathrm{Hv}(\bullet)$ is the Heaviside function. For comparison, our $Q_B$ is defined as (see Eq. (2.88))

$$Q_B = \left(\frac{\widehat{\Theta}_d - \Theta_c}{\Theta_{do}}\right)^{3/2} \mathrm{Hv}\left(\frac{\widehat{\Theta}_d - \Theta_c}{\Theta_{do}}\right).$$

The main difference between Yu & Mei's $Q_{\mathrm{YM}}$ and our $Q_B$ concerns the type of Shields

parameter used. Yu & Mei have used the Shields parameter $\Theta_{\text{YM}}$ based on the full roughness to compute their $Q_{\text{YM}}$, while we use the grain roughness Shields parameter $\widehat{\Theta}_d$ to compute $Q_B$. We have argued before that the empirical formula developed by Sleath [57] and Nielsen [50] for the mean bedload transport over half a wave period was developed using a Shields parameter based on the grain roughness. Yu & Mei's use of $\Theta_{\text{YM}}$, approximately 10 times larger than $\widehat{\Theta}_d$, leads to a large overestimation of the bedload transport. The overestimation was not evident because the fitting parameter $\beta$ could be adjusted to match predicted and measured bar heights. We will see that, despite the adjustment of $\beta$, qualitative differences due to the choice of $\Theta_{\text{YM}}$ remain between Yu & Mei's predictions and our experimental data.

Lastly, the effect of the return flow $U_2^{[0]}$ on boundary layer was not included in Yu & Mei's sand bar model. We will see this leads to poor predictions of laboratory generated sand bars under weak wave reflection.

The derivation of our steady state sand bar solution followed that of Yu & Mei. The steady state solution of Yu & Mei's sand bar equation (2.152) is

$$\begin{aligned} \widetilde{h}_S &= \frac{\sqrt{2}\Theta_{\text{YM}}}{4\beta}\left(\frac{2+\sqrt{2}}{3}+\frac{1}{\sinh^2 KH_o}\right) \\ &\quad \times |A|^2\left(\left(1-|R|^2\right)\left(\chi-\pi\mathcal{G}_{\text{YM}}\left(\chi\right)\right)-|R|\cos 2\chi-\frac{|R|\sin 2\chi_c}{\pi-2\chi_c}\right) \end{aligned} \tag{2.157}$$

for $\chi_c \le \chi \le \pi-\chi_c$, where $\chi = x-\theta_R/2$, $\chi_c$ is the half-width of the sub-critical region, and

$$\begin{aligned} \mathcal{G}_{\text{YM}}\left(x\right) &= \frac{\int_0^\chi D_{\text{YM}}^{-1}d\chi'}{\int_0^\pi D_{\text{YM}}^{-1}d\chi'} = \frac{\int_0^\chi \left|U_1^{[1]}\right| Q_{\text{YM}}^{-1}d\chi'}{\int_0^\pi \left|U_1^{[1]}\right| Q_{\text{YM}}^{-1}d\chi'}, \qquad \chi_c = 0, \\ \mathcal{G}_{\text{YM}}\left(x\right) &= \frac{1}{2}, \qquad \chi_c > 0. \end{aligned} \tag{2.158}$$

We have shifted Yu & Mei's solution by $\Delta x = \pi/2$ so that the wave node appears at $\chi = \pi/2$. Recall that we also made the transformation $\theta_R \to \theta_R + \pi$. Eq. (2.157) is analogous to our Eq. (2.119) for weak reflection and to (2.124) for strong reflection.

The regions of weak reflection have no sub-critical regions, i.e. $\chi_c = 0$. The regime of

strong reflection is characterized by sub-critical regions ($\chi_c > 0$) where

$$|R| > 1 - \frac{\Theta_{c0}}{\Theta_{\rm YM}\sqrt{2}\,|A|}.$$

Over one bar length $0 \le \chi \le \pi$, the sub-critical regions are the intervals $[0, \chi_c]$ and $[\pi - \chi_c, \pi]$, where $\chi_c$ is the position where the Shields parameter takes the critical value,

$$\sqrt{1 + |R|^2 - 2\,|R| \cos 2\chi_c} \;=\; \frac{\Theta_{c0}}{\sqrt{2}\,|A|\,\Theta_{\rm YM}}. \tag{2.159}$$

Solving (2.159) for $\chi_c$ gives Yu & Mei's estimate of the half-width of the sub-critical region. We will see that this estimate severely under-predicts the width of the measured sub-critical regions, due to their choice of $\Theta_{\rm YM}$ rather than $\widehat{\Theta}_d$ (approximately 10 times smaller) to compute $Q_{\rm YM}$.

Yu & Mei's predictions corresponding to test 430 are plotted in Figure 2-54. The fitting parameter $\beta$ is set to 0.46 to match the predicted and measured bar heights. Since Yu & Mei's model only allows the characteristic ripple height to be specified, we set the ripple height at $\eta_{ro} = 2$ cm (characteristic for test 430) and take $k_{No} = 4.13\eta_{ro}$. The other parameters used are those listed for test 430 in Table 2.7, namely, $T = 2.5$ s, $H_o = 60$ cm, $A_o = 3.68$, $R_L = 1$, and $d = 0.20$ mm. Based on Eq. (2.152), a single bar is evolved for 4 days and is plotted with the steady state bar profile (2.157). To evolve a single bar in time, the wave amplitudes are held fixed and periodic boundary conditions are imposed at the bar ends. Yu & Mei's model severely under-predicts the size of the sub-critical region. Also, their predicted growth rate is too large initially, and their model reaches a steady state too quickly. Our predictions, based on the parameters listed in Table 2.7, are plotted for comparison and seem to agree better with the measured bar growth rate and measured bar profiles near the sub-critical region.

Yu & Mei's predictions corresponding to test 324 are plotted in Figure 2-55 for a single bar and in Figure 2-56 for the entire bar patch. The fitting parameter $\beta$ is set to 0.45 to match the predicted and measured bar heights. The other parameters used are those listed for test 324 in Table 2.7, namely, $T = 2.63$ s, $H_o = 60$ cm, $A_o = 5.46$, $R_L = 0.24e^{-1.06i}$, $d = 0.20$ mm, and $\eta_{ro} = 2$ cm. Based on Eq. (2.152), a single bar is evolved for 3 days and is plotted with the steady state bar profile (2.157). To evolve a single bar in time, the wave amplitudes are held fixed and periodic boundary conditions are imposed at the bar ends.

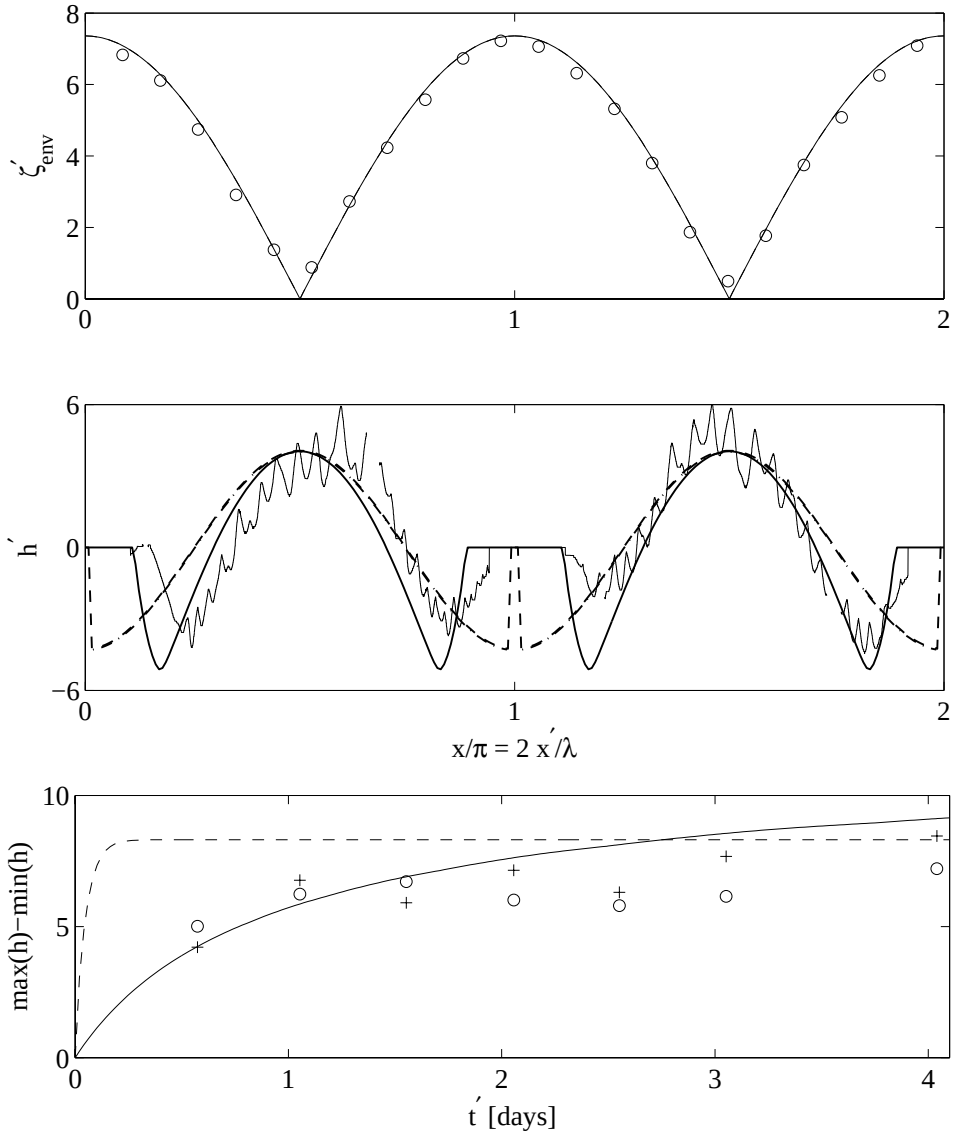


Figure 2-54: Comparison of our predictions (solid) with those of Yu & Mei (2000) (dash, dash-dot) for test 430. The measured first harmonic wave amplitude $\zeta'_{env} = |\zeta_1^{[1]\prime}|$ (top, $\circ$) at $t' = 0$ is plotted above the bar elevation $\widetilde{h}'$ (middle, jagged line) after $t' = 4$ days of wave action. In the middle plot, Yu & Mei's steady state bar profile Eq. (2.157) (dash-dot) and their time evolved bar profile (dash), as well as our time evolved bar profile (solid) are shown after $t' = 4$ days of wave action. To obtain the time evolved predictions, the waves are held fixed and periodic boundary conditions are applied at the bar ends. The predicted time history of bar height $\max(\widetilde{h}') - \min(\widetilde{h}')$ is plotted at bottom, for our theory (solid) and that of Yu & Mei (2000) (dash). The measured bar heights are also plotted for the first ($\circ$) and second ($+$) bars.

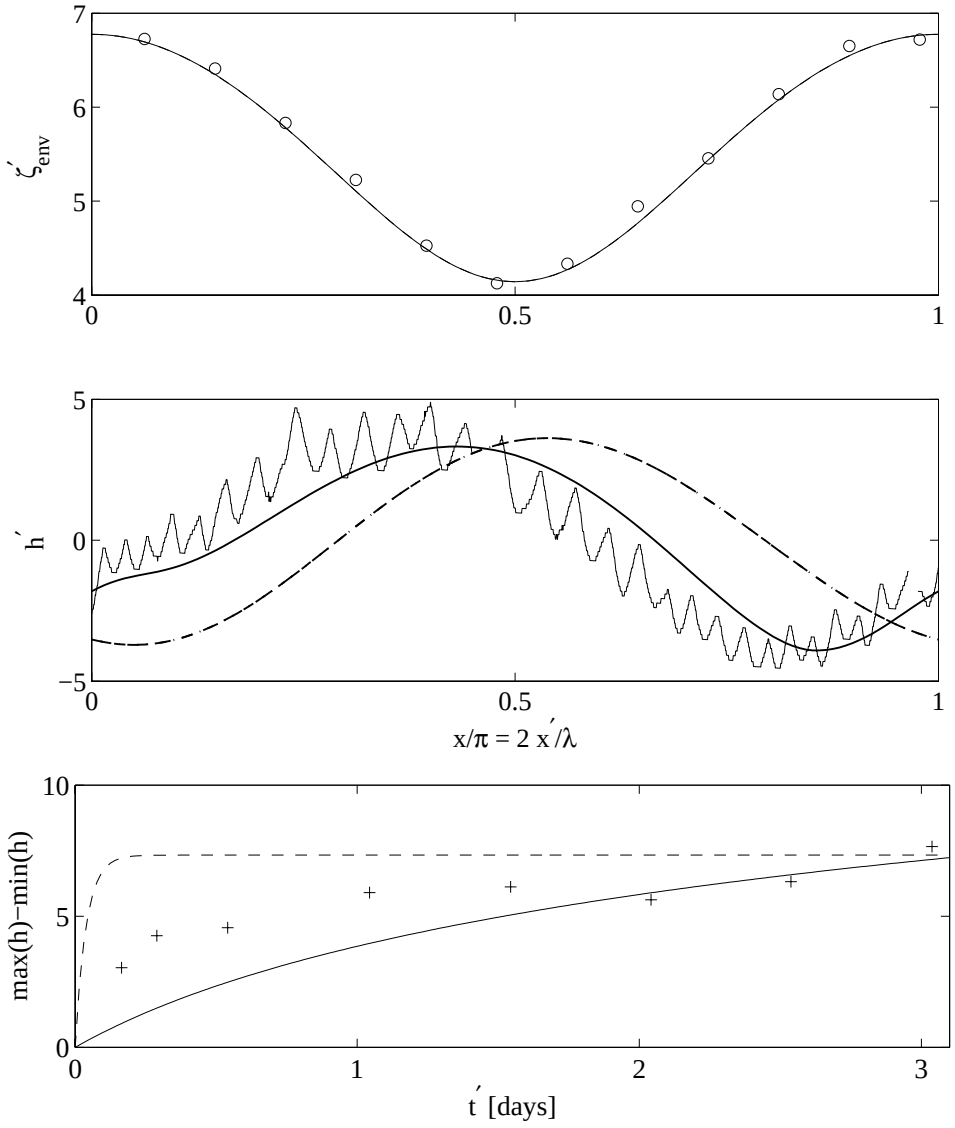


Figure 2-55: Comparison of our predictions (solid) with those of Yu & Mei (2000) (dash, dash-dot) for test 324. The measured first harmonic wave amplitude $\zeta'_{env} = |\zeta_1^{[1]\prime}|$ (top, $\circ$) at $t = 0$ is plotted above the bar elevation $\widetilde{h}'$ (middle, jagged line) after $t' = 3$ days of wave action. In the middle plot, Yu & Mei's steady state bar profile Eq. (2.157) (dash-dot) and their time evolved bar profile (dash), as well as our time evolved bar profile (solid) are shown after $t' = 3$ days of wave action. To obtain the time evolved predictions, the waves are held fixed and periodic boundary conditions are applied at the bar ends. The predicted time history of bar height $\max(\widetilde{h}') - \min(\widetilde{h}')$ is plotted at bottom, for our theory (solid) and that of Yu & Mei (2000) (dash). The measured bar height (+) is also plotted.

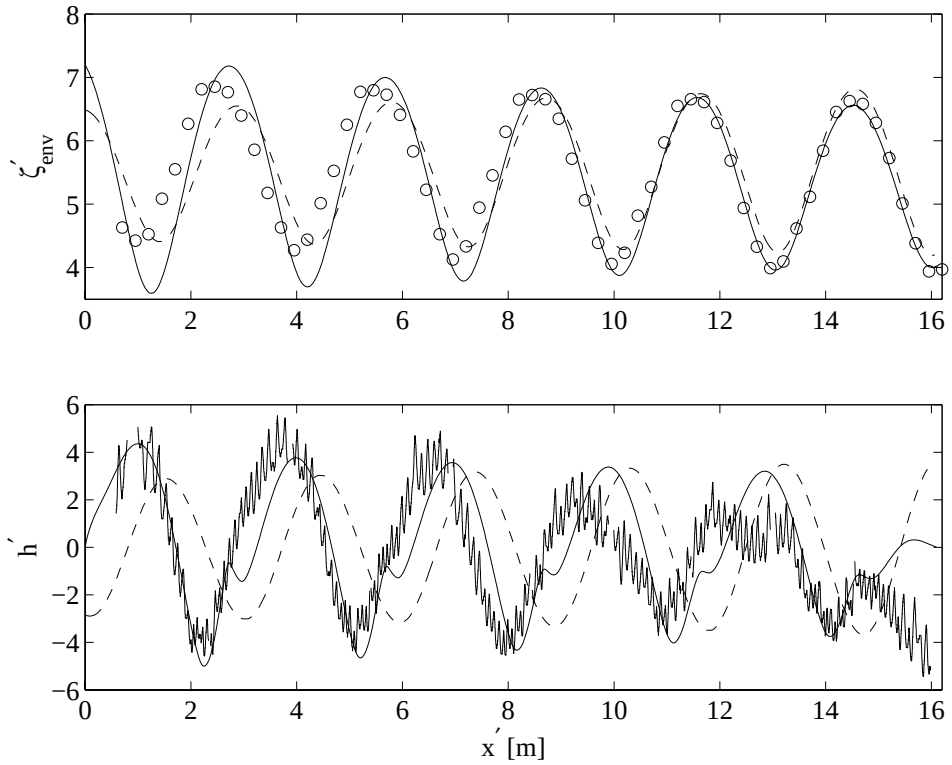


Figure 2-56: Comparison of our predictions (solid) with those of Yu & Mei (2000) (dash) for test 324. The measured first harmonic wave amplitude $\zeta'_{env} = |\zeta_1^{[1]\prime}|$ (top, $\circ$) is plotted above the bar elevation $\widetilde{h}'$ (bottom, jagged line), both after $t' = 3$ days of wave action.

Again, Yu & Mei over-predict the bar growth rate initially and their model reaches a steady state too quickly. Furthermore, due to the absence of return flow effects in their model, Yu & Mei predict the bar crests appear shoreward of the wave nodes, which is the opposite of what was observed. Since our theory includes the effect of return flow, our predicted bar crests are seaward of the wave node, by choice of our fitting parameter $\Lambda_2^{[0]} = 1.8$.

To obtain Yu & Mei's prediction of the evolution of the entire bar patch corresponding to test 324, Yu (1999)'s solution method is employed; namely, evolving single bars at each $x_1$ grid point and applying periodic boundary conditions at the bar endpoints (see §2.4.4). The results are shown in Figure 2-56. Again, the absence of the return flow effect in their model predictions causes the bar crests to appear shoreward of the wave nodes, causing energy to be transferred from the incident to reflected waves and the total wave and bar height to increase shoreward. Based on the bar and wave measurements for test 324, the opposite is observed to happen. Since our theory includes the effect of return flow, our predicted bar crests are seaward of the wave nodes and our predicted wave and bar heights

decrease shoreward.

In Chapter 5 of her thesis, Yu [68] attempted to study the effects of a locally varying eddy viscosity $\nu_{e\mathrm{YM}}(x)$. When computing the first order flow, Yu made a change of variable

$$y = \frac{\eta}{\sqrt{\nu_{e\mathrm{YM}}(x)}}$$

However, when computing $x$-derivatives, the $\partial y/\partial x$ was neglected (see Yu [68]'s equations 5.2.13 to 5.2.26). Consequently, the coefficient of $\partial\nu_{e\mathrm{YM}}/\partial x$ in Yu's second order flow is incorrect, and thus the dependence of the sand bar formation on $\nu_{e\mathrm{YM}}$ is also incorrect. Furthermore, Yu [68] noted that the local variation of the eddy viscosity enhanced the forcing and led to larger bar heights. However, a large portion of the enhanced forcing is due to Yu's use of a characteristic orbital amplitude $A_{\mathrm{YM}}$ based on the incident wave amplitude $A_o$ and not the total wave amplitude $A_o(1+|R_L|)$. The additional factor $(1+|R_L|)$ is present in the local orbital amplitude, but not the characteristic amplitude $A_{\mathrm{YM}}$. Therefore, the constant eddy viscosity $\nu_{e\mathrm{YM}}$ based on the characteristic orbital amplitude is a factor $(1+|R_L|)^2$ less than the locally varying eddy viscosity $\nu_{e\mathrm{YM}}(x)$ based on the local orbital amplitude. The enhanced local eddy viscosity will of course lead to enhanced forcing, due mainly to the additional factor $(1+|R_L|)^2$ rather than the spatial variation.

## 2.9 Appendix

### 2.9.1 Useful facts about Kelvin functions

In this section we list some useful results for the functions $\mathcal{K}_m(nZ)$. The function $\mathcal{K}_0(Z)$ satisfies the ODE

$$\frac{d}{dZ}\left(Z\frac{d\mathcal{K}_0}{dZ}\right) + i\mathcal{K}_0 = 0; \qquad \lim_{Z\to\infty}\mathcal{K}_0(Z) = 0. \tag{2.160}$$

We define Kelvin functions of order $m$ ($m$ an integer) depending on $nZ$ ($n$ an integer) as

$$\mathcal{K}_m(nZ) = \mathrm{ker}_m\left(2\sqrt{nZ}\right) - i\mathrm{kei}_m\left(2\sqrt{nZ}\right), \quad \mathcal{I}_m(nZ) = \mathrm{ber}_m\left(2\sqrt{nZ}\right) - i\mathrm{bei}_m\left(2\sqrt{nZ}\right). \tag{2.161}$$

Note that from Eq. (9.9.2) in Abramowitz & Stegun [1],

$$\mathcal{K}_m(nZ) = e^{im\pi/2}K_m\left(2\sqrt{nZ}e^{-i\pi/4}\right) = i^m K_m\left(2\sqrt{nZ}e^{-i\pi/4}\right)$$

where $K_m$ is the modified Bessel function of order $m$.

We compute $d\mathcal{K}_0/dZ$ in terms of other Kelvin functions (Abramowitz & Stegun [1], Eq. (9.6.27)),

$$\frac{d\mathcal{K}_0}{dZ} = \frac{K_0'\left(2\sqrt{Z}e^{-i\pi/4}\right)}{\sqrt{Z}} = -e^{-i\pi/4}\frac{K_1\left(2\sqrt{Z}e^{-i\pi/4}\right)}{\sqrt{Z}} = (1+i)\,\frac{\mathcal{K}_1(Z)}{\sqrt{2Z}}. \tag{2.162}$$

Next, we compute some derivatives used in our theory. From (2.17), we have

$$\frac{\partial F_1(Z,Z_b)}{\partial Z} = 1 - \frac{\mathcal{K}_0(Z)}{\mathcal{K}_0(Z_b)}, \qquad \frac{\partial F_1(Z,Z_b)}{\partial Z_b} = -\frac{1}{\mathcal{K}_0(Z_b)}\left.\frac{d\mathcal{K}_0}{dZ}\right|_{Z_b}(F_1 - (Z - Z_b)).$$

Thus, using the chain rule, we have

$$\begin{aligned}
\frac{\partial F_1}{\partial x} &= \frac{\partial F_1(Z,Z_b)}{\partial Z}\frac{\partial Z(\eta,x)}{\partial x} + \frac{\partial F_1(Z,Z_b)}{\partial Z_b}\frac{dZ_b}{dx} \\
&= -Z\left(1 - \frac{\mathcal{K}_0(Z)}{\mathcal{K}_0(Z_b)}\right)\frac{1}{u_f}\frac{du_f}{dx} - \frac{1}{\mathcal{K}_0(Z_b)}\left.\frac{d\mathcal{K}_0}{dZ}\right|_{Z_b}(F_1 - (Z - Z_b))\frac{dZ_b}{dx} \\
&= -Z\left(1 - \frac{\mathcal{K}_0(Z)}{\mathcal{K}_0(Z_b)}\right)\frac{1}{u_f}\frac{du_f}{dx} \\
&\quad -\frac{\mathcal{K}_1(Z_b)}{\sqrt{Z_b}\mathcal{K}_0(Z_b)}\left(\frac{\sqrt{Z}\mathcal{K}_1(Z)}{\mathcal{K}_0(Z_b)} - \frac{\sqrt{Z_b}\mathcal{K}_0(Z)\mathcal{K}_1(Z_b)}{(\mathcal{K}_0(Z_b))^2}\right)\frac{dZ_b}{dx},
\end{aligned} \tag{2.163}$$

$$\frac{\partial}{\partial x}\left(\frac{\mathcal{K}_0(Z)}{\mathcal{K}_0(Z_b(x))}\right) = -\frac{1}{u_f}\frac{du_f}{dx}\frac{Z}{\mathcal{K}_0(Z_b)}\frac{d\mathcal{K}_0}{dZ} - \frac{\mathcal{K}_0(Z)}{(\mathcal{K}_0(Z_b))^2}\left.\frac{d\mathcal{K}_0}{dZ}\right|_{Z_b}\frac{dZ_b}{dx}. \tag{2.164}$$

In (2.163) and (2.164), we used the fact that

$$\begin{aligned}
\mathcal{K}(Z_b,Z_b) &= 1, \\
\frac{\partial Z(\eta,x)}{\partial x} &= -\frac{2\eta}{u_f^2}\frac{\partial u_f}{\partial x} = -\frac{Z}{u_f}\frac{\partial u_f}{\partial x}, \\
\frac{\partial \mathcal{K}_0(Z)}{\partial x} &= \frac{d\mathcal{K}_0}{dZ}\frac{\partial Z}{\partial x} = -\frac{d\mathcal{K}_0}{dZ}\frac{Z}{u_f}\frac{\partial u_f}{\partial x}.
\end{aligned}$$

Some integrals we encounter in this thesis are

$$\int_Z^\infty \mathcal{K}_0(Z')\,dZ = \frac{1-i}{\sqrt{2}}\sqrt{Z}\mathcal{K}_1(Z), \tag{2.165}$$

$$\int_{Z_b}^{\infty}\left(\frac{\mathcal{K}_0(Z)}{\mathcal{K}_0(Z_b)}\right)^2 dZ = -Z_b\left(1+\frac{\mathcal{K}_1^2(Z_b)}{\mathcal{K}_0^2(Z_b)}\right), \tag{2.166}$$

$$\int_{Z_b}^{\infty}\left|\frac{\mathcal{K}_0(Z)}{\mathcal{K}_0(Z_b)}\right|^2 dZ = -\sqrt{Z_b}\Re\left(e^{-i\pi/4}\frac{\mathcal{K}_1(Z_b)}{\mathcal{K}_0(Z_b)}\right). \tag{2.167}$$

For $nZ \geq 16$ ($n \geq 1$), the function $\mathcal{K}_0(nZ)$ is approximated by (Abramowitz & Stegun [1], Eqs. (9.11.9) and (9.11.11))

$$\mathcal{K}_0(nZ) = \sqrt{\frac{\pi}{4\sqrt{nZ}}}\exp\left[-(1+i)\sqrt{2nZ}+\theta\left(-2\sqrt{nZ}\right)\right](1+\epsilon_1), \tag{2.168}$$

where $|\epsilon_1| < 10^{-7}$ and $|\Re\{\theta(x)\}| < 0.01$ for $|x| \geq 10$. Therefore, for $nZ > 25$,

$$|\Re\{\mathcal{K}_0(nZ)\}|, \quad |\Im\{\mathcal{K}_0(nZ)\}| \leq |\mathcal{K}_0(nZ)| \leq \frac{\exp\left(-\sqrt{2nZ}\right)}{(nZ)^{1/4}}. \tag{2.169}$$

We define the integral limit truncation error as

$$er(n,m,a) = \left|\int_a^{\infty} Z^{p_1} f_n^{p_2}(Z)\, g_m^{p_3}(Z)\, dZ\right|, \tag{2.170}$$

where $n, m$ are non-negative integers, $p_n$ are non-negative real numbers, and the functions $f_n(Z)$, $g_n(Z)$ are any of

$$\{\Re\{\mathcal{K}_0(nZ)\}, \Im\{\mathcal{K}_0(nZ)\}, \mathcal{K}_0(nZ)\}. \tag{2.171}$$

Using the square of Eq. (2.169), for any $a \geq 10$, $n, m \geq 1$, $0 \leq p_1 \leq 1$, $p_2, p_3 \geq 1$, Eq. (2.170) yields

$$\begin{aligned} er(n,m,a) &\leq \int_a^{\infty} |\mathcal{K}_0(nZ)|\,|\mathcal{K}_0(mZ)|\, Z dZ \\ &\leq (nm)^{-1/4}\int_a^{\infty} Z^{1/2} e^{-\left(\sqrt{n}+\sqrt{m}\right)\sqrt{2Z}} dZ \\ &= (nm)^{-1/4}\frac{\left(\sqrt{2}+2\sqrt{a}\left(\sqrt{n}+\sqrt{m}\right)+\sqrt{2}a\left(\sqrt{n}+\sqrt{m}\right)^2\right)}{\left(\sqrt{n}+\sqrt{m}\right)^3} e^{-\left(\sqrt{n}+\sqrt{m}\right)\sqrt{2a}}. \end{aligned} \tag{2.172}$$

For $a \geq 100$,

$$er\,(n,m,a) \leq er\,(1,1,a) < 10^{-10}, \tag{2.173}$$

for $n, m \geq 1$, and hence the integrals only need to be computed to an upper limit of 100.

We now estimate the decay of $d\mathcal{K}_1/dZ$. For $Z > 25$, we have (Abramowitz & Stegun [1], Eqs. (9.11.12) and (9.11.13)),

$$\begin{aligned}
\frac{d\mathcal{K}_1}{dZ} &= \frac{1}{\sqrt{Z}}\frac{d}{dZ}\left(\ker Z + i\mathrm{kei}Z\right) \\
&= -\frac{1}{\sqrt{Z}}\sqrt{\frac{\pi}{4\sqrt{Z}}}\exp\left[-\left(1+i\right)\sqrt{2Z} + \theta\left(-2\sqrt{Z}\right)\right]\gamma\left(-2\sqrt{Z}\right)\left(1+\epsilon_3\right)
\end{aligned}$$

where $|\epsilon_3| < 3 \times 10^{-7}$ and $|\gamma\,(x)| < 1.1$ for $|x| > 8$. Thus for $Z \geq 25$,

$$\left|\frac{d\mathcal{K}_1}{dZ}\right| < \frac{\exp\left(-\sqrt{2Z}\right)}{Z^{1/4}} \tag{2.174}$$

and hence $d\mathcal{K}_1/dZ$ may be included in the list of functions in (2.171) for which result (2.172) holds.

### 2.9.2 Second order flow terms

Integrals in and involving the functions $c_{0n}\,(Z,x)$ $(n = 1,2,..,6)$ defined in §2.1.5 in Eqs. (2.46) and (2.47) are computed here. Integrating by parts, using (2.165) – (2.167), and noting that $F\,(Z_b, Z_b) = 0$ yields

$$\int_{Z_b}^{\infty}\frac{(Z-Z_b)}{\mathcal{K}_0^*\,(Z_b)}\frac{d\mathcal{K}_0^*}{dZ}dZ = (Z-Z_b)\,\frac{\mathcal{K}_0^*\,(Z)}{\mathcal{K}_0^*\,(Z_b)}\Big|_{Z=Z_b}^{\infty} - \int_{Z_b}^{\infty}\frac{\mathcal{K}_0^*\,(Z)}{\mathcal{K}_0^*\,(Z_b)}dZ = -\int_{Z_b}^{\infty}\frac{\mathcal{K}_0^*\,(Z)}{\mathcal{K}_0^*\,(Z_b)}dZ,$$

$$\begin{aligned}
\int_{Z_b}^{\infty}\frac{F_1\,(Z,Z_b)}{\mathcal{K}_0^*\,(Z_b)}\frac{d\mathcal{K}_0^*}{dZ}dZ &= F_1\frac{\mathcal{K}_0^*\,(Z)}{\mathcal{K}_0^*\,(Z_b)}\Big|_{Z_b}^{\infty} - \int_{Z}^{\infty}\left(\frac{\mathcal{K}_0^*\,(Z)}{\mathcal{K}_0^*\,(Z_b)} - \left|\frac{\mathcal{K}_0\,(Z)}{\mathcal{K}_0\,(Z_b)}\right|^2\right)dZ \\
&= -\int_{Z_b}^{\infty}\left(\frac{\mathcal{K}_0^*\,(Z)}{\mathcal{K}_0^*\,(Z_b)} - \left|\frac{\mathcal{K}_0\,(Z)}{\mathcal{K}_0\,(Z_b)}\right|^2\right)dZ.
\end{aligned}$$

Substituting these into Eq. (2.46) gives

$$c_{01}\left(Z_b,Z_b\right)=\int_{Z_b}^{\infty}\left(\frac{\mathcal{K}_0\left(Z\right)}{\mathcal{K}_0\left(Z_b\right)}+2\frac{\mathcal{K}_0^*\left(Z\right)}{\mathcal{K}_0^*\left(Z_b\right)}-2\left|\frac{\mathcal{K}_0\left(Z\right)}{\mathcal{K}_0\left(Z_b\right)}\right|^2\right)dZ=\frac{1+i}{\sqrt{2}}\sqrt{Z_b}\frac{\mathcal{K}_1^*\left(Z_b\right)}{\mathcal{K}_0^*\left(Z_b\right)},\tag{2.175}$$

$$\begin{aligned}c_{02}\left(Z_b,Z_b\right) &= \frac{iZ_b}{\mathcal{K}_0\left(Z_b\right)}\left.\frac{d\mathcal{K}_0}{dZ}\right|_{Z_b}-\frac{Z_b}{\mathcal{K}_0\left(Z_b\right)}\left.\frac{d\mathcal{K}_0}{dZ}\right|_{Z_b}\int_{Z_b}^{\infty}\frac{\mathcal{K}_0\left(Z\right)}{\mathcal{K}_0\left(Z_b\right)}dZ\\ &\quad+\left(1+\frac{2Z_b}{\mathcal{K}_0\left(Z_b\right)}\left.\frac{d\mathcal{K}_0}{dZ}\right|_{Z_b}\right)\int_{Z_b}^{\infty}\left|\frac{\mathcal{K}_0\left(Z\right)}{\mathcal{K}_0\left(Z_b\right)}\right|^2dZ\\ &= \frac{1+i}{2\sqrt{2}}\sqrt{Z_b}\frac{\mathcal{K}_1^*\left(Z_b\right)}{\mathcal{K}_0^*\left(Z_b\right)}-\frac{1-i}{2\sqrt{2}}\sqrt{Z_b}\frac{\mathcal{K}_1\left(Z_b\right)}{\mathcal{K}_0\left(Z_b\right)}+iZ_b\left|\frac{\mathcal{K}_1\left(Z_b\right)}{\mathcal{K}_0\left(Z_b\right)}\right|^2,\end{aligned}$$

$$c_{03}\left(Z_b,Z_b\right)=\frac{iZ_b}{\mathcal{K}_0\left(Z_b\right)}\left.\frac{d\mathcal{K}_0}{dZ}\right|_{Z_b}+\int_{Z_b}^{\infty}\frac{\mathcal{K}_0^*\left(Z\right)}{\mathcal{K}_0^*\left(Z_b\right)}dZ=-\frac{1-i}{\sqrt{2}}\sqrt{Z_b}\frac{\mathcal{K}_1\left(Z_b\right)}{\mathcal{K}_0\left(Z_b\right)}+\frac{1+i}{\sqrt{2}}\sqrt{Z_b}\frac{\mathcal{K}_1^*\left(Z_b\right)}{\mathcal{K}_0^*\left(Z_b\right)}.$$

Notice that

$$\Re\left\{c_{02}\left(Z_b,Z_b\right)\right\}=0=\Re\left\{c_{03}\left(Z_b,Z_b\right)\right\}.\tag{2.176}$$

The integrals of $c_{0n}\left(Z_b\right)$ for $n=4,5,6$ are given below in terms of three integrals $\mathcal{A}_m\left(Z_b\right)$:

$$\begin{aligned}&\int_{Z_b}^{\infty}c_{04}\left(Z,Z_b\right)\frac{\mathcal{K}_0\left(2Z\right)}{\mathcal{K}_0\left(2Z_b\right)}dZ\\ =\;&\int_{Z_b}^{\infty}\left(2\frac{\mathcal{K}_0\left(Z\right)}{\mathcal{K}_0\left(Z_b\right)}-\left(\frac{\mathcal{K}_0\left(Z\right)}{\mathcal{K}_0\left(Z_b\right)}\right)^2-\frac{F_1\left(Z,Z_b\right)}{\mathcal{K}_0\left(Z_b\right)}\frac{d\mathcal{K}_0}{dZ}\right)\frac{\mathcal{K}_0\left(2Z\right)}{\mathcal{K}_0\left(2Z_b\right)}dZ\\ =\;&2\left(1-i\right)\sqrt{Z_b}\left(\frac{\mathcal{K}_1\left(2Z_b\right)}{\mathcal{K}_0\left(2Z_b\right)}-\frac{1}{\sqrt{2}}\frac{\mathcal{K}_1\left(Z_b\right)}{\mathcal{K}_0\left(Z_b\right)}\right)-\mathcal{A}_1\left(Z_b\right)-\mathcal{A}_2\left(Z_b\right),\end{aligned}\tag{2.177}$$

$$
\begin{aligned}
&\int_{Z_b}^{\infty} c_{05}\left(Z, Z_b\right) \frac{\mathcal{K}_0\left(2Z\right)}{\mathcal{K}_0\left(2Z_b\right)} dZ \\
= \quad & \frac{Z_b}{\mathcal{K}_0\left(Z_b\right)} \left.\frac{d\mathcal{K}_0}{dZ}\right|_{Z_b} \\
& \times \int_{Z_b}^{\infty} \left( \frac{d\mathcal{K}_0}{dZ} \frac{F_1\left(Z, Z_b\right) - \left(Z - Z_b\right)}{\mathcal{K}_0\left(Z_b\right)} - \frac{\mathcal{K}_0\left(Z\right)}{\mathcal{K}_0\left(Z_b\right)} + \left( \frac{\mathcal{K}_0\left(Z\right)}{\mathcal{K}_0\left(Z_b\right)} \right)^2 \right) \frac{\mathcal{K}_0\left(2Z\right)}{\mathcal{K}_0\left(2Z_b\right)} dZ \\
= \quad & -\frac{\sqrt{2} Z_b \mathcal{K}_1\left(Z_b\right)}{\mathcal{K}_0\left(Z_b\right)} \left( \frac{\mathcal{K}_1\left(2Z_b\right)}{\mathcal{K}_0\left(2Z_b\right)} - \frac{1}{\sqrt{2}} \frac{\mathcal{K}_1\left(Z_b\right)}{\mathcal{K}_0\left(Z_b\right)} \right) \\
& \quad + \frac{Z_b}{\mathcal{K}_0\left(Z_b\right)} \left.\frac{d\mathcal{K}_0}{dZ}\right|_{Z_b} \left( \mathcal{A}_1\left(Z_b\right) + \mathcal{A}_2\left(Z_b\right) - \mathcal{A}_3\left(Z_b\right) \right), \qquad (2.178)
\end{aligned}
$$

$$
\int_{Z_b}^{\infty} c_{06}\left(Z, Z_b\right) \frac{\mathcal{K}_0\left(2Z\right)}{\mathcal{K}_0\left(2Z_b\right)} dZ = -\int_{Z_b}^{\infty} F_1\left(Z, Z_b\right) \frac{\mathcal{K}_0\left(2Z\right)}{\mathcal{K}_0\left(Z_b\right) \mathcal{K}_0\left(2Z_b\right)} \frac{d\mathcal{K}_0}{dZ} dZ = -\mathcal{A}_2\left(Z_b\right), \qquad (2.179)
$$

where

$$
\begin{aligned}
\mathcal{A}_1\left(Z_b\right) &= \int_{Z_b}^{\infty} \frac{\mathcal{K}_0^2\left(Z\right) \mathcal{K}_0\left(2Z\right)}{\mathcal{K}_0^2\left(Z_b\right) \mathcal{K}_0\left(2Z_b\right)} dZ, \\
\mathcal{A}_2\left(Z_b\right) &= \int_{Z_b}^{\infty} F_1\left(Z, Z_b\right) \frac{\mathcal{K}_0\left(2Z\right)}{\mathcal{K}_0\left(Z_b\right) \mathcal{K}_0\left(2Z_b\right)} \frac{d\mathcal{K}_0}{dZ} dZ, \\
\mathcal{A}_3\left(Z_b\right) &= \int_{Z_b}^{\infty} \left(Z - Z_b\right) \frac{\mathcal{K}_0\left(2Z\right)}{\mathcal{K}_0\left(Z_b\right) \mathcal{K}_0\left(2Z_b\right)} \frac{d\mathcal{K}_0}{dZ} dZ.
\end{aligned}
$$

The functions $\mathcal{A}_n\left(Z_b\right)$ must be computed numerically. From (2.172) and (2.173), these integrals need only be computed to an upper limit of 100 to obtain errors less than $10^{-10}$. To derive Eqs. (2.177)–(2.179), we used the fact that

$$
\int_{Z_b}^{\infty} \frac{\mathcal{K}_0\left(Z\right) \mathcal{K}_0\left(2Z\right)}{\mathcal{K}_0\left(Z_b\right) \mathcal{K}_0\left(2Z_b\right)} dZ = \left(1 - i\right) \sqrt{Z_b} \left( \frac{\mathcal{K}_1\left(2Z_b\right)}{\mathcal{K}_0\left(2Z_b\right)} - \frac{1}{\sqrt{2}} \frac{\mathcal{K}_1\left(Z_b\right)}{\mathcal{K}_0\left(Z_b\right)} \right).
$$

### 2.9.3 Perturbation of the absolute value of a sinusoid

In our theory, we use the perturbation theory approximation to the average $\overline{\left|\cos t + a \cos 2t\right|}^t$ for $a \ll 1$. Here we compare this approximation against the numerically computed average

for small $a$. Note that

$$\begin{aligned} |\cos t + a\cos 2t| &= |\cos t| \left|1 + a\frac{\cos 2t}{\cos t}\right| \\ &= |\cos t| \left(1 + a\frac{\cos 2t}{\cos t}\right) + O\left(a^2\right) \\ &= |\cos t| + a\frac{|\cos t|}{\cos t}\cos 2t + O\left(a^2\right) \end{aligned}$$

The time average of the perturbation approximation is

$$\overline{|\cos t + a\cos 2t|}^t = \frac{2}{\pi} + O\left(a^2\right)$$

Comparing the exact average (computed numerically) to the perturbation average truncated at $O\left(a^2\right)$ yields an error bound of $0.6a^2$.

### 2.9.4 Integral simplification used in steady state

Consider a single variable continuous function $f$ and the integral

$$I_f \equiv \int_0^\pi \left(\int_0^x f\left(\cos 2x'\right) dx'\right) dx. \tag{2.180}$$

The double integral can be simplified by using the transformations $x'' = \pi - x'$, $Y = \pi - x$,

$$\begin{aligned} I_f &= \int_0^\pi \left(-\int_\pi^{\pi-x} f\left(\cos 2x''\right) dx''\right) dx = -\int_\pi^0 \left(-\int_\pi^Y f\left(\cos 2x''\right) dx''\right) dY \\ &= \int_0^\pi \left(\int_x^\pi f\left(\cos 2x'\right) dx'\right) dx. \end{aligned}$$

Thus,

$$\begin{aligned} I_f &= \frac{I_f}{2} + \frac{I_f}{2} = \frac{1}{2}\int_0^\pi \left(\int_0^x f\left(\cos 2x'\right) dx'\right) dx + \frac{1}{2}\int_0^\pi \left(\int_x^\pi f\left(\cos 2x'\right) dx'\right) dx, \\ &= \frac{1}{2}\int_0^\pi \left(\int_0^\pi f\left(\cos 2x'\right) dx'\right) dx = \frac{\pi}{2}\int_0^\pi f\left(\cos 2x\right) dx. \end{aligned} \tag{2.181}$$

The double integral $I_f$ defined in (2.180) has been rewritten as a single integral.

# Chapter 3

# Bars on a bed of fine sand

In this chapter, we study the effects of fine sediments on sand bar formation under monochromatic waves in intermediate depth. We consider the mass conservation equation for suspended sediments and, coupled with the flow, compute the flux of suspended sediment and a new forcing term in the sand bar equation. Since fine grains are present across the boundary layer, an accurate description of the flow is also required across the boundary layer. Thus, a depth-averaged model for the eddy viscosity is employed with the continuity and horizontal momentum equations (1.136), (1.137) to predict the boundary layer flow.

The concentration $C'(x', z', t')$ of a dilute cloud of suspended sediment obeys the conservation equation

$$\frac{\partial C'}{\partial t'} + \frac{\partial}{\partial x'}\left(u'C'\right) + \frac{\partial}{\partial z'}\left[\left(-w_S + w'\right)C'\right] = \frac{\partial}{\partial x'}\left(D'_h \frac{\partial C'}{\partial x'}\right) + \frac{\partial}{\partial z'}\left(D'_v \frac{\partial C'}{\partial z'}\right), \qquad (3.1)$$

where ($u'$,$w'$) are the horizontal and vertical components of fluid velocity, respectively, $-w_S$ is the fall velocity of suspended particles, $(D'_h, D'_v)$ are the horizontal and vertical eddy mass diffusivities, and $d$ is the sediment grain diameter. Equation (3.1) is a good approximation when $C'$ is sufficiently small that the presence of suspended sediment does not significantly alter the fluid flow. A sediment grain is considered fine if its fall velocity $w_S$ is smaller than the friction velocity $u'_f$, since in this case the turbulent eddies are more likely to keep the grain in suspension. Thus, fine grains will closely follow the flow, implying that the mass diffusivities scale as the eddy viscosity, $\nu_{eo}$. For the situations we are modeling, we expect the concentration to be significant only in the boundary layer near the seabed. Hence we

impose the upper BC

$$C' \to 0, \qquad z' + h' \gg \delta. \tag{3.2}$$

## 3.1 Bottom BC : reference concentration

For a wide range of field conditions, Lee, Dade, Friedrichs & Vincent (2004) [35] developed an empirical formula for the mean reference concentration at 1 cm above the bed,

$$\overline{C\,(1\text{ cm}, x, t)} = \frac{2.58\text{ g/l}}{\rho_S}\left(\frac{\widehat{\Theta}_d^{3/2}}{w_S\sqrt{(s-1)gd}}\right)^{1.45}, \tag{3.3}$$

where $\widehat{\Theta}_d$ is the grain roughness Shields parameter defined in (2.42). The 95% confidence interval for the coefficient 2.58 is approximately $\pm 45\%$ and that for the exponent 1.45 is $\pm 3\%$. To find the fitting coefficients in Eq. (3.3), Lee *et al.* [35] used a regression method to fit Rouse-type profiles $(z/z_0)^{-P}$ to measured mean suspended sediment concentration profiles $\overline{C\,(z, x, t)}$.

The Rouse-type suspended sediment concentration profile is derived by assuming a mass diffusivity that is depth-linear. We show below that these profiles do not decay fast enough away from the bed to be used with our theory, and so we employ a depth-averaged mass diffusivity. One could argue that the fitted formula (3.3) for $\overline{C\,(1\text{ cm}, x, t)}$ would change if exponential profiles $e^{-Pz}$, derived using a depth-independent eddy viscosity, were used instead to fit the data. However, the scatter in the data makes this difference less important. The functional form of (3.3) is desirable because, unlike other formulae, it does not vanish at a finite Shields parameter and it includes the fall velocity $w_S$, which is small for fine sediments. Nielsen [49] provides a fitting formula for the reference concentration based on exponential profiles and presents experimental evidence that suspension exists even below the threshold $\Theta < \Theta_c$. However, his formula depends only on $\widehat{\Theta}_d$ and not on the fall velocity $w_S$.

We show below that the mean concentration is given by $\overline{C'\,(z, x, t)} = \widehat{C}' e^{-Pz/\delta}$ where $\widehat{C}'$ is the mean reference concentration at $\eta' = 0$. Since (3.3) gives the mean concentration at $z = 1$ cm, the reference concentration $\widehat{C}'$ at $z' = 0$ is given by

$$\widehat{C}' = \frac{0.00258}{s}\left(\frac{\widehat{\Theta}_d}{\Theta_{do}}\right)^{2.175} e^{P(1\text{ cm})/\delta}\left(\frac{\Theta_{do}^{3/2}}{w_S\sqrt{(s-1)gd}}\right)^{1.45}, \tag{3.4}$$

where $s$ is the specific gravity of the sediment in water and $\Theta_{do}$ is the characteristic grain roughness Shields parameter defined in (1.128) with $k_{No} = 2.5d$. We choose the scale of the reference concentration to be

$$C_o = \frac{0.00258\, e^{P(1\text{ cm})/\delta}}{s} \left( \frac{\Theta_{do}^{3/2}}{w_S \sqrt{(s-1)gd}} \right)^{1.45}, \tag{3.5}$$

The neglect of time varying components in the reference concentration assumes that the variation from the mean is not important. However, research on the transient entrainment and suspension from rippled and flat beds has shown that the concentration near the bed is highly time dependent and varies as much as 100% from the mean (Homma *et al.* 1965 [26], Nakato *et al.* 1977 [47], Sleath 1982 [58] and more recently by Staub *et al.* 1996 [61] and Ribberink & Al-Salem 1994 [54]). Wikramanayake & Madsen (1994) [66], therefore, proposed a time varying reference concentration which is proportional to the excess bed shear stress, $C'(0,t') \propto (\Theta - \Theta_c)\,\mathrm{Hv}(\Theta - \Theta_c)$, where $\mathrm{Hv}(\bullet)$ is the Heaviside function. Agreement with the data of Vincent & Green (1990) [64], where $d = 0.018$ and 0.023 cm, is acceptable, although there is considerable scatter. Due to the scatter and for simplicity, we merely write

$$C'\big|_{z'=0} = \widehat{C}' \left|\tau'_{b0}\right| \left( \overline{\left|\tau'_{b0}\right|} \right)^{-1}, \tag{3.6}$$

where horizontal bars denote the time average over the wave period $[0, 2\pi]$, $\tau'_{b0}$ is the leading order bottom shear stress and $\widehat{C}'$ is the mean reference concentration given in (3.4). We further assume that the phase shift between $\tau'_{b0}$ and the horizontal velocity outside the boundary layer is that computed from our boundary layer analysis. No additional phase shift is introduced.

A key assumption made in this section is that the suspended sediment concentration near the bed is determined solely from the bed shear stress. Therefore, if the bed shear stress at a particular location remains the same, the suspended sediment concentration will also remain the same, regardless of the amount of sediment being moved to and from this location. The reason is that the bed is assumed to be composed of uniform sand grains and the sand is not supply-limited, so even if scouring or deposition occurs at a particular location, the concentration of the sand grains on the surface of the bed remains constant. The suspension reacts quickly to any change in the local turbulence: when turbulent intensity decreases, grains fall to the bed; when turbulent intensity increases, so too does the bed shear stress and

more grains are brought into suspension. The picture would change somewhat if multiple sediment sizes were present in the bed, in which case the near-bed concentration would also be a function of the grain size fraction at each point along the bed. The picture would also change if only a limited amount of sand were present on the bed or suspended in the water column (see e.g. Mei & Chian [43]). In this limited sand supply scenario, the near-bed concentration also depends on the amount of sand on the seabed available for transport.

## 3.2 Scaling

In addition to the normalized variables in (1.131), we introduce the normalized concentrations and mass diffusivities

$$\left(C, \widehat{C}\right) = \frac{\left(C', \widehat{C}'\right)}{C_o}, \qquad (D_h, D_v) = \frac{(D'_h, D'_v)}{\nu_{eo}}. \tag{3.7}$$

In terms of the boundary conforming coordinate defined in (1.95) and the normalized variables defined in (1.131) and (3.7), Eq. (3.1) becomes an equation for the normalized suspended sediment concentration $C(x, t, \eta)$,

$$\begin{aligned} & \frac{\partial C}{\partial t} - \frac{\partial}{\partial \eta}\left(\frac{D_v}{2}\frac{\partial C}{\partial \eta}\right) - \frac{P}{2}\frac{\partial C}{\partial \eta} \\ = \; & -\varepsilon \frac{\partial}{\partial x}(uC) - \varepsilon \frac{\partial}{\partial \eta}(w_n C) + \frac{\varepsilon^2 D_h}{2}\left(-\frac{\partial H}{\partial x_1} + \frac{\partial \widetilde{h}}{\partial x}\right)^2 \frac{\partial^2 C}{\partial \eta^2} \qquad (3.8) \\ = \; & -\varepsilon u \frac{\partial C}{\partial x} - \varepsilon w_n \frac{\partial C}{\partial \eta} + \frac{\varepsilon^2 D_h}{2}\left(-\frac{\partial H}{\partial x_1} + \frac{\partial \widetilde{h}}{\partial x}\right)^2 \frac{\partial^2 C}{\partial \eta^2}, \qquad (3.9) \end{aligned}$$

where $P = 2w_S/\delta\omega$ is the Peclet number. The outer boundary condition (3.2) becomes

$$C \to 0, \qquad \eta \to \infty. \tag{3.10}$$

From (3.4), (3.5) and (3.7), the scaled mean reference concentration $\widehat{C}$ is given by

$$\widehat{C} = \frac{\widehat{C}'}{C_o} = \left(\frac{\widehat{\Theta}_d}{\Theta_{do}}\right)^{2.175}, \tag{3.11}$$

where $\widehat{\Theta}_d$ is the maximum (over a wave cycle) grain roughness Shields parameter defined

in (2.42). Note that $\widehat{C}(x,t_1,\bar{t})$ varies spatially with the grain roughness Shields parameter $\widehat{\Theta}_d(x,t_1,\bar{t})$, and both depend on the long times $t_1,\ \bar{t}$. From Eqs. (1.101), (2.40), (3.6) and (3.7), the bottom boundary condition for $C$ on $\eta=0$ becomes

$$C\left(x,t,0\right)=\widehat{C}\frac{\left|\tau_{b0}'/\left(\left(s-1\right)gd\right)\right|}{\left(\overline{\left|\tau_{b0}'/\left(\left(s-1\right)gd\right)\right|}\right)}=\widehat{C}\frac{\left|\Theta_0\right|}{\left(\overline{\left|\Theta_0\right|}\right)}=\widehat{C}\frac{\left|\cos\left(t+\varpi\right)\right|}{\left(\overline{\left|\cos\left(t+\varpi\right)\right|}\right)}=\frac{\pi}{2}\widehat{C}\left|\cos\left(t+\varpi\right)\right|, \tag{3.12}$$

where $\widehat{C}$ is given in (3.11) and $\varpi$ in (2.39). This boundary condition can be written as a Fourier series

$$C\left(x,t,0\right)=\widehat{C}(x,t_1,\bar{t})+\sum_{n=1}^{\infty}\frac{1}{2}\left(\widehat{C^{[2n]}}(x,t_1,\bar{t})\,e^{-2int}+*\right), \tag{3.13}$$

where, for $n=1,2,3\ldots$,

$$\widehat{C^{[2n]}}=\pi\widehat{C}\overline{\left|\cos\left(t+\varpi\right)\right|e^{2int}}=\pi\widehat{C}e^{-2in\varpi}\overline{\left|\cos t\right|e^{2int}}=\frac{2\widehat{C}\left(-1\right)^{n-1}e^{-2in\varpi}}{\left(2n\right)^2-1}. \tag{3.14}$$

## 3.3 Mass diffusivity

In this section, we discuss the choice of mass diffusivity $D_v$, by linearizing and time averaging Eq. (3.8) over a wave period,

$$-\frac{\partial}{\partial\eta}\left(\frac{D_v}{2}\frac{\partial\overline{C}}{\partial\eta}\right)-\frac{P}{2}\frac{\partial\overline{C}}{\partial\eta}=0. \tag{3.15}$$

We have implicitly assumed $D_v$ is time independent. If we employ a depth-linear mass diffusivity $D_v=\alpha\eta$, then (3.15) becomes

$$-\frac{\partial}{\partial\eta}\left(\frac{\alpha\eta}{2}\frac{\partial\overline{C}}{\partial\eta}\right)-\frac{P}{2}\frac{\partial\overline{C}}{\partial\eta}=0. \tag{3.16}$$

Integrating in $\eta$ and imposing the outer BC (3.10) gives

$$\overline{C}=c_{zc}\left(\frac{\eta_c}{\eta}\right)^{-P/\alpha},$$

where $c_{zc}$ is the mean concentration at some near-bed reference level $\eta_c$. For fine sediments, the turbulent intensity $\alpha=O\left(u_f\right)$ will be larger than the sediment's fall velocity, so that $P/\alpha<1$. Therefore, the predicted net mean sediment in a vertical column of water,

$\int_{\eta_c}^{\infty} \overline{C}' dz$, is unbounded. The problem occurs since the linearly varying mass diffusivity over-predicts the turbulent correlation $\overline{\widetilde{w}\widetilde{C}}^{\tilde{t}}$ for $\eta' > \delta$, i.e. away from the bed, where $\widetilde{C}$ and $\widetilde{w}$ are the turbulent variations in the concentration and vertical velocity over the turbulent timescale $\tilde{t}$. The depth-linear eddy viscosity proved useful for bedload transport, where only near-bed accuracy was needed. In this case, however, we need accuracy across the boundary layer. The sediment mass diffusivity would need to be damped away from the bed, long before the free surface is reached. The flow could still be calculated using a depth-linear eddy viscosity. However, for simplicity, we employ depth-independent mass diffusivities $D'_v$ and $D'_h$ and eddy viscosity $\bar{\nu}_e$, and assume these are equal,

$$D_v = D_h = \bar{\nu}_e. \tag{3.17}$$

The choice of $\bar{\nu}_e$ and the resulting flow are considered next.

## 3.4 Boundary layer with depth-independent eddy viscosity

The scales and normalized variables introduced in §1.4 are used to analyze the flow in the boundary layer due to a depth-independent eddy viscosity $\bar{\nu}_e$ (time and $z$-independent). The dimensionless continuity and horizontal momentum equations are (1.136) and (1.137) with $\nu_e = \bar{\nu}_e$. The boundary conditions are those derived in §2.1: no-slip at the seabed (2.8) and continuous approach of the oscillatory harmonics to the inviscid core flow (2.9). The solution method is similar to that in §2.1.

### 3.4.1 Leading order flow

Expanding the orbital velocities as

$$U_I = \Re\left\{U_1^{[1]} e^{-it}\right\} + \varepsilon \Re\left\{U_2^{[0]} + U_2^{[1]} e^{-it} + U_2^{[2]} e^{-2it}\right\} + O\left(\varepsilon^2\right), \tag{3.18}$$

$$u = u_1 + \varepsilon u_2 + \cdots, \qquad w_n = w_1 + \varepsilon w_2 + \cdots, \tag{3.19}$$

and substituting into (1.137) and (1.136) yields, at leading order,

$$\frac{\partial u_1}{\partial t} = \frac{\bar{\nu}_e}{2} \frac{\partial^2 u_1}{\partial \eta^2} + \Re\left\{-i U_1^{[1]} e^{-it}\right\}, \qquad \frac{\partial w_1}{\partial z} = -\frac{\partial u_1}{\partial x}, \tag{3.20}$$

subject to the boundary conditions

$$u_1 = w_1 = 0, \qquad \text{at } \eta = 0; \qquad (u_1, w_1) \to \left( \Re \left\{ U_1^{[1]} e^{-it} \right\}, 0 \right), \qquad \text{as } \eta \to \infty. \tag{3.21}$$

The solution is

$$u_1 = \Re \left\{ U_1^{[1]} F' \left( \frac{\eta}{\sqrt{\bar{\nu}_e}} \right) e^{-it} \right\}, \qquad w_1 = -\Re \left\{ \frac{\partial}{\partial x} \left( U_1^{[1]} \sqrt{\bar{\nu}_e} F \right) e^{-it} \right\}, \tag{3.22}$$

where

$$F(s) = s - \frac{1+i}{2} \left( 1 - e^{-(1-i)s} \right).$$

Notice that the solution involves exponentials and not logarithms, as was the case for a depth-linear eddy viscosity. Hence we can take the bottom at $\eta = 0$. The shear stress on the bed is

$$\bar{\nu}_e \frac{\partial u_1^{[1]}}{\partial \eta} \bigg|_{\eta=0} = \sqrt{\bar{\nu}_e} (1-i) U_1^{[1]}. \tag{3.23}$$

### 3.4.2 Eddy viscosity

The depth-independent eddy viscosity is found by averaging the depth-linear eddy viscosity across the boundary layer from $\eta' = 0$ to $\eta' = \delta$,

$$\bar{\nu}'_e = \frac{1}{\delta} \int_0^\delta \kappa u'_f \eta' d\eta' = \frac{u'_f \delta}{2}, \tag{3.24}$$

where $u'_f$ is given in (2.28) and its computation was discussed in the previous chapters. Thus, we are using some of the results for the depth-linear eddy viscosity to help predict $\bar{\nu}'_e$. However, away from the bed ($\eta' > \delta$), $\bar{\nu}'_e$ will not grow arbitrarily large with $\eta'$, as does the depth-linear eddy viscosity. Since the scale of the eddy viscosity was kept as $\nu_{eo} = \kappa u_{fo} \delta$, the dimensionless depth-independent eddy viscosity is

$$\bar{\nu}_e = \frac{\bar{\nu}'_e}{\nu_{eo}} = \frac{u_f}{2}, \tag{3.25}$$

where the normalized friction velocity $u_f$ is given in Eq. (2.32).

### 3.4.3 Second order flow : $O(\varepsilon)$ equations

The $O(\varepsilon)$ equations are found by substituting the expansions (3.18) and (3.19) into (1.137) and (1.136) and collecting $O(\varepsilon)$ terms,

$$\left\{\frac{\partial}{\partial t}-\frac{\bar{\nu}_e}{2}\frac{\partial^2}{\partial\eta^2}\right\}u_2=-\frac{\partial u_1}{\partial t_1}+\frac{\partial U_{I1}}{\partial t_1}+\frac{\partial U_{I2}}{\partial t}+U_{I1}\frac{\partial U_{I1}}{\partial x}-\left(u_2\frac{\partial}{\partial x}+w_2\frac{\partial}{\partial\eta}\right)u_2. \tag{3.26}$$

Substituting (2.3), (3.22), the r.h.s. of (3.26) can be written as

$$rhs=rhs^{[0]}+\Re\left\{rhs^{[1]}e^{-it}+rhs^{[2]}e^{-2it}\right\}, \tag{3.27}$$

where

$$rhs^{[0]} = \Re\left\{\frac{1+\bar{\nu}_e\left(FF^*_{\eta\eta}-|F_\eta|^2\right)}{2}U_1^{[1]*}\frac{\partial U_1^{[1]}}{\partial x}+\frac{FF^*_{\eta\eta}}{4}\left|U_1^{[1]}\right|^2\frac{\partial\nu_e}{\partial x}\right\}, \tag{3.28}$$

$$rhs^{[2]} = -2iU_2^{[2]}+\frac{1+\bar{\nu}_e\left(FF_{\eta\eta}-F_\eta^2\right)}{2}U_1^{[1]}\frac{\partial U_1^{[1]}}{\partial x}+\frac{FF_{\eta\eta}}{4}U_1^{[1]2}\frac{\partial\nu_e}{\partial x}. \tag{3.29}$$

We do not use $rhs_1^{[1]}$, and hence omit writing it. We write $u_2$ as

$$u_2(\eta,x,x_1,t,t_1,\bar{t}) = u_2^{[0]}(\eta,x,x_1,t_1,\bar{t})+\Re\left\{u_2^{[1]}(\eta,x,x_1,t_1,\bar{t})\,e^{-it}+u_2^{[2]}(\eta,x,x_1,t_1,\bar{t})\,e^{-2it}\right\}. \tag{3.30}$$

Substituting (3.30) into the l.h.s. of (3.26) and using (3.27) – (3.29) gives

$$-niu_2^{[n]}-\frac{\bar{\nu}_e}{2}\frac{\partial^2u_2^{[n]}}{\partial\eta^2}=rhs^{[n]},\qquad n=0,1,2. \tag{3.31}$$

The boundary conditions are, from (2.8) and (2.9),

$$u_2^{[0],[2]}=0,\qquad \text{on } \eta=0, \tag{3.32}$$

$$\lim_{\eta\to\infty}u_2^{[2]}=U_2^{[2]}. \tag{3.33}$$

As in §2.1.6, the inviscid return current $U_2^{[0]}$ adds an additional shear stress $u_f\Lambda_2^{[0]}U_2^{[0]}$

(see Eq. 2.58) to the mean current in the boundary layer,

$$\bar{\nu}_e \frac{\partial u_2^{[0]}}{\partial \eta} = \bar{\nu}_e \frac{\partial u_{2W}^{[0]}}{\partial \eta} + u_f \Lambda_2^{[0]} U_2^{[0]}, \tag{3.34}$$

where $u_{2W}^{[0]}$ is the component of the current due to the first order oscillatory terms and satisfies Eq. (3.31) with $n = 0$,

$$\frac{\bar{\nu}_e}{2} \frac{\partial^2 u_{2W}^{[0]}}{\partial \eta^2} = -rhs^{[0]}. \tag{3.35}$$

Since the oscillatory components that generate $u_{2W}^{[0]}$ are shear free outside the boundary layer, we assume that $u_{2W}^{[0]}$ is also shear free as $\eta \to \infty$,

$$\lim_{\eta \to \infty} \frac{\partial u_{2W}^{[0]}}{\partial \eta} = 0. \tag{3.36}$$

Integrating (3.35) and applying the BC (3.36) gives

$$\bar{\nu}_e \frac{\partial u_{2W}^{[0]}}{\partial \eta} = 2 \int_\eta^\infty rhs^{[0]} d\eta. \tag{3.37}$$

Substituting the shear stress due to $u_{2W}^{[0]}$, Eq. (3.37), into the shear stress due to the total mean current, Eq. (3.34), integrating, and imposing the no-slip condition (3.32) gives

$$u_2^{[0]} = \Re \left\{ F_1 \left( \frac{\eta}{\sqrt{\bar{\nu}_e}} \right) U_1^{[1]*} \frac{\partial U_1^{[1]}}{\partial x} - F_2 \left( \frac{\eta}{\sqrt{\bar{\nu}_e}} \right) \frac{\left| U_1^{[1]} \right|^2}{2\bar{\nu}_e} \frac{\partial \bar{\nu}_e}{\partial x} \right\} + 2\,\eta \Lambda_2^{[0]} U_2^{[0]}, \tag{3.38}$$

where

$$F_1(s) = \frac{1+3i}{2} e^{-(1+i)s} - \frac{i}{2} e^{-(1-i)s} + \frac{1-i}{4} e^{-2s} - \frac{s}{2}(1-i)\, e^{-(1+i)s} - \frac{3}{4}(1+i), \tag{3.39}$$

$$F_2(s) = \frac{i}{4} e^{-2s} - \frac{1}{2} e^{-(1+i)s} (1 + 2i - (1-i)\, s) + \frac{2+3i}{4}. \tag{3.40}$$

Integrating (3.31) for $n = 2$ and applying the BCs (3.32), (3.33) yields

$$u_2^{[2]} = U_2^{[2]} \left( 1 - e^{-(1-i)\sqrt{2/\bar{\nu}_e}\eta} \right) + F_3 \left( \eta/\sqrt{\bar{\nu}_e} \right) U_1^{[1]} \frac{\partial U_1^{[1]}}{\partial x} + F_4 \left( \eta/\sqrt{\bar{\nu}_e} \right) \frac{U_1^{[1]2}}{\bar{\nu}_e} \frac{\partial \bar{\nu}_e}{\partial x}, \tag{3.41}$$

where

$$F_3(s) = \frac{s}{2}(1+i)\,e^{-(1-i)s} - \frac{i}{2}e^{-(1-i)s} + \frac{i}{2}e^{-(1-i)\sqrt{2}s}, \tag{3.42}$$

$$F_4(s) = \frac{1}{4}e^{-(1-i)s}\left((1+i)\,s - 3i\right) - \frac{i}{8}e^{-2(1-i)s} + \frac{7i}{8}e^{-(1-i)\sqrt{2}s}. \tag{3.43}$$

Special cases of these boundary layer flow equations were given by Mei [45] and by Yu [68].

## 3.5 Suspended sediment concentration

In this section, we use the boundary layer flow just derived to calculate the suspended sediment concentration. Recall that the flow was expanded as

$$u = u_1 + \varepsilon u_2 + O\left(\varepsilon^2\right), \qquad w_n = w_1 + \varepsilon w_2 + O\left(\varepsilon^2\right).$$

Similarly, we expand the suspended sediment concentration as

$$C(x,t,t_1,z) = C_1(x,t,t_1,z) + \varepsilon C_2(x,t,t_1,z) + O\left(\varepsilon^2\right). \tag{3.44}$$

Substituting these expansions and Eq. (3.17) into Eq. (3.9) and collecting leading order terms gives

$$\frac{\partial C_1}{\partial t} - \frac{\bar{\nu}_e}{2}\frac{\partial^2 C_1}{\partial \eta^2} - \frac{P}{2}\frac{\partial C_1}{\partial \eta} = 0. \tag{3.45}$$

The boundary conditions are

$$C_1 \to 0, \qquad \eta \to \infty, \tag{3.46}$$

$$C_1(x,t,0) = \widehat{C}(x,t_1,\bar{t}) + \sum_{n=1}^{\infty}\frac{1}{2}\left(\widehat{C^{[2n]}}(x,t_1,\bar{t})\,e^{-2int} + *\right), \tag{3.47}$$

where $\widehat{C}$, $\widehat{C^{[2n]}}$ are given in (3.11) and (3.14). The solution to (3.45) – (3.47) is

$$C_1 = \widehat{C}(x,t_1,\bar{t})\exp\left(-\frac{P\eta}{\bar{\nu}_e}\right) + \sum_{n=1}^{\infty}\frac{1}{2}\left(\widehat{C^{[2n]}}(x,t_1,\bar{t})\exp\left(-\frac{P\beta_{2n}\eta}{\bar{\nu}_e}\right)e^{-2int} + *\right) \tag{3.48}$$

where

$$\beta_n = \frac{1}{2} + \frac{1}{2}\sqrt{1 - \frac{8in\bar{\nu}_e}{P^2}}.$$

The second order terms in (3.9) yield

$$\frac{\partial C_2}{\partial t} - \frac{\bar{\nu}_e}{2}\frac{\partial^2 C_2}{\partial \eta^2} - \frac{P}{2}\frac{\partial C_2}{\partial \eta} = -u_1\frac{\partial C_1}{\partial x} - w_1\frac{\partial C_1}{\partial \eta} - \frac{\partial C_1}{\partial t_1}, \tag{3.49}$$

subject to the boundary conditions

$$C_2 \to 0, \qquad \eta \to \infty, \tag{3.50}$$

$$C_2\,(x,t,0) = 0. \tag{3.51}$$

We expand $C_2$ in time-harmonics as

$$C_2 = \frac{1}{2}\left(C_2^{[0]} + C_2^{[1]}e^{-it} + C_2^{[2]}e^{-2it}\cdots\right) + *. \tag{3.52}$$

In §3.7, we show that $C_2^{[1]}$ is the only component of $C_2$ that is used in our theory. Substituting (3.52) and the flow equations (3.22) into (3.49) and isolating the first time harmonic gives an equation for $C_2^{[1]}$,

$$\left\{i + \frac{P}{2}\frac{\partial}{\partial \eta} + \frac{\bar{\nu}_e}{2}\frac{\partial^2}{\partial \eta^2}\right\} C_2^{[1]} = u_1^{[1]}\frac{\partial C_1^{[0]}}{\partial x} + \frac{u_1^{[1]*}}{2}\frac{\partial C_1^{[2]}}{\partial x} + w_1^{[1]}\frac{\partial C_1^{[0]}}{\partial \eta} + \frac{w_1^{[1]*}}{2}\frac{\partial C_1^{[2]}}{\partial \eta}. \tag{3.53}$$

From (3.50) and (3.51), we have

$$C_2^{[1]}\Big|_{\eta\to\infty} = 0, \qquad C_2^{[1]}\Big|_{\eta=0} = 0. \tag{3.54}$$

The expression for $C_2^{[1]}$ is lengthy and is listed as Eq. (3.75) in Appendix 3.14.1.

The equation for the second order correction $C_2^{[0]}$ to the mean concentration is found by taking the time average (in $t$) of Eq. (3.49),

$$\left\{\frac{P}{2}\frac{\partial}{\partial \eta} + \frac{\bar{\nu}_e}{2}\frac{\partial^2}{\partial \eta^2}\right\} C_2^{[0]} = \frac{\partial C_1^{[0]}}{\partial t_1}$$

Assuming that the waves are either perfectly tuned (independent of $t_1$) or periodic in $t_1$, the corresponding flow and sediment transport quantities are also independent of $t_1$ or periodic

in $t_1$, respectively, and averaging over the long time $t_1$ gives

$$\left\{ \frac{P}{2}\frac{\partial}{\partial \eta} + \frac{\bar{\nu}_e}{2}\frac{\partial^2}{\partial \eta^2} \right\} \overline{\overline{C_2^{[0]}}} = 0$$

where double bars denote the average with respect to $t_1$. Imposing the BCs (3.50) and (3.51) gives the solution

$$\overline{\overline{C_2^{[0]}}}\,(\eta) = 0. \tag{3.55}$$

For perfectly tuned waves (independent of $t_1$), result (3.55) implies that

$$\overline{C(x,t,0)} = \overline{C_1(x,t,0)} + \varepsilon \overline{C_2(x,t,0)} + O(\varepsilon^2) = \widehat{C}(x,\bar{t}) + O(\varepsilon^2). \tag{3.56}$$

Thus, to $O(\varepsilon^2)$, the mean concentration at the bottom $\eta = 0$ is just $\widehat{C}$. Similarly, for waves that are also periodic in $t_1$, result (3.55) implies that

$$\overline{\overline{\left(\overline{C(x,t,0)}\right)}} = \overline{\overline{\widehat{C}(x,t_1,\bar{t})}} + O(\varepsilon^2). \tag{3.57}$$

Lastly, the scaled mean concentration at the bed, $\widehat{C}$, is plotted in Figure 3-1 for field conditions under weak and strong reflection. The magnitude of $\widehat{C}$ follows that of the shear stress: the maximum concentration occurs under the node, while the minimum occurs near the antinodes. We will soon show that under strong reflection, suspended sediment is transported from the nodes to the antinodes. This process of scouring fine sand from under the node and depositing it under the antinode does not alter the bed concentration $\widehat{C}$, which is purely a function of the shear stress, since the same amount of sand is always available for transport at the surface of the seabed.

## 3.6 Conservation of sediment mass

Substituting the dimensionless variables in Eqs. (1.133), (3.7) into the equation for the conservation of sediment mass, Eq. (1.120), gives

$$\frac{\partial \widetilde{h}}{\partial t} = -\frac{1}{\alpha_1 \varepsilon}\frac{\partial}{\partial x}\left(q_B + \alpha_2 \langle uC \rangle\right) + \frac{\alpha_2}{\alpha_1 \varepsilon^2}\frac{\partial}{\partial t}\langle C \rangle\,, \tag{3.58}$$

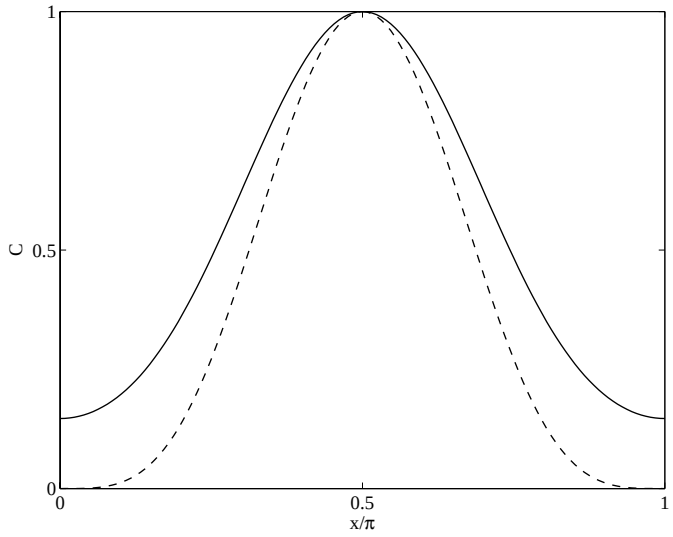


Figure 3-1: Near bed mean suspended sediment concentration $\widehat{C}$ across a bar length for field conditions, under weak (solid, $R_L = 0.25$) and strong (dashed, $R_L = 1$) reflection. The field conditions are $T = 8$ s, $H_o = 6$ m, $A_o(1 + |R_L|) = 60$ cm, $d = 0.2$ mm, and $\eta_r'$ found from Eq. (1.105). Wave antinodes occur at $x = 0, \pi$ and a wave node at $x = \pi/2$.

where $\langle \bullet \rangle$ denotes depth integration,

$$\langle uC \rangle = \int_0^\infty uC d\eta,$$

and

$$\alpha_1 = \frac{A_b \omega}{8\varepsilon \Theta_{do}^{3/2} K \sqrt{(s-1)\, g d^3}}, \qquad \alpha_2 = \frac{\varepsilon \alpha_1 K \delta C_o}{1 - \mathcal{N}}. \tag{3.59}$$

In the parameter regime of interest, $\Theta_o \precsim O(1)$ and hence $\alpha_1 = O\left(\varepsilon^{-4.5}\right)$ and $\alpha_2 \precsim O(1)$. Thus (3.58) implies $\partial h/\partial t = O\left(\varepsilon^{2.5}\right)$, so that once again $h$ is independent of the fast time $t$ and varies over a much longer timescale, assumed *a priori* to be $\bar{t} = t/\alpha_1$.

From (3.22) and (3.48), the leading order horizontal velocity $u_1$ contains only the first time harmonic and the harmonics in $C_1$ are all even. Thus, the wave period time average of the product $u_1 C_1$ is zero, i.e. $\overline{u_1 C_1} = 0$, and the mean suspended sediment transport $\overline{\langle uC \rangle}$ is $O(\varepsilon)$,

$$\overline{\langle uC \rangle} = \varepsilon \left( \overline{\langle u_2 C_1 \rangle} + \overline{\langle u_1 C_2 \rangle} \right). \tag{3.60}$$

For the remainder of this chapter, we assume the waves are perfectly tuned (independent of $t_1$) and only depend on the short time $t$ and the sand bar time $\bar{t}$. Thus, from the solution for $C$ (Eqs. (3.48) and (3.75)), $C$ also only depends on $t$ and $\bar{t}$, so that the time average of

the last term in (3.58) becomes

$$\frac{\alpha_2}{\alpha_1\varepsilon^2}\overline{\frac{\partial}{\partial t}\langle C\rangle} = \frac{\alpha_2}{\varepsilon^2}\overline{\frac{\partial}{\partial \widetilde{t}}\langle C\rangle}. \tag{3.61}$$

Since the time averages of the other terms in (3.58) have order $O\left(\alpha_1^{-1}\right) = O\left(\varepsilon^{-4.5}\right)$, the time average in (3.61) is of higher order and negligible.

The depth-independent eddy viscosity is used to predict the suspended sediment, because it is better suited to be used across the entire boundary layer than the depth-linear model. However, the depth-linear eddy viscosity is a far better model very close to the bed where the bedload transport occurs. Hence we treat the bedload forcing and suspended sediment transport as separate entities, and use the eddy viscosity model best suited for each region where the particular type of sediment transport occurs. Thus, the bedload formula Eq. (2.105) derived from the depth-linear eddy viscosity model is used to predict $q_\tau$.

Time averaging (3.58) over a wave period, substituting (2.85), (3.60), (3.61), and retaining leading order terms gives

$$\frac{\partial \widetilde{h}}{\partial \widetilde{t}} - \frac{\partial}{\partial x}\left(D_\nu \frac{\partial \widetilde{h}}{\partial x}\right) = -\frac{\partial}{\partial x}\left(q_\tau + D_\nu \frac{\partial H}{\partial x_1} + \alpha_2 \overline{q_S}\right), \tag{3.62}$$

where $D_\nu$ and $q_\tau$ are given in (2.86) and (2.105), respectively, and the scaled mean suspended sediment flux is given by

$$\overline{q_S} = \overline{\langle u_2 C_1\rangle} + \overline{\langle u_1 C_2\rangle}. \tag{3.63}$$

Comparing the sand bar equation (3.62) with that for bedload dominated flows, Eq. (2.106), illustrates that the effect of fine grains is to add an additional forcing term $\alpha_2\overline{q_S}$. The diffusivity $D_\nu$ is purely due to the gravitational effect on the bedload transport rate.

The magnitude of the suspended sediment forcing depends on the coefficient $\alpha_2$ and, as will be shown in the next section, on the Peclet number $P = 2w_S/(\delta\omega)$. The dependence of $\alpha_2$ and $P$ on the grain diameter $d$, wave slope $\varepsilon = KA_b$, and dispersion parameter $KH_o$ is illustrated in Figures 3-2 to 3-4, respectively, for field and lab conditions. Figure 3-2 shows that $\alpha_2$ increases and $P$ decreases with decreasing grain diameter $d$, and all else being equal, $\alpha_2$ increases and $P$ decreases with decreasing depth $H_o$ and increasing wave amplitude $A_o$ and period $T$. Figure 3-3 shows that $\alpha_2$ increases and $P$ decreases with

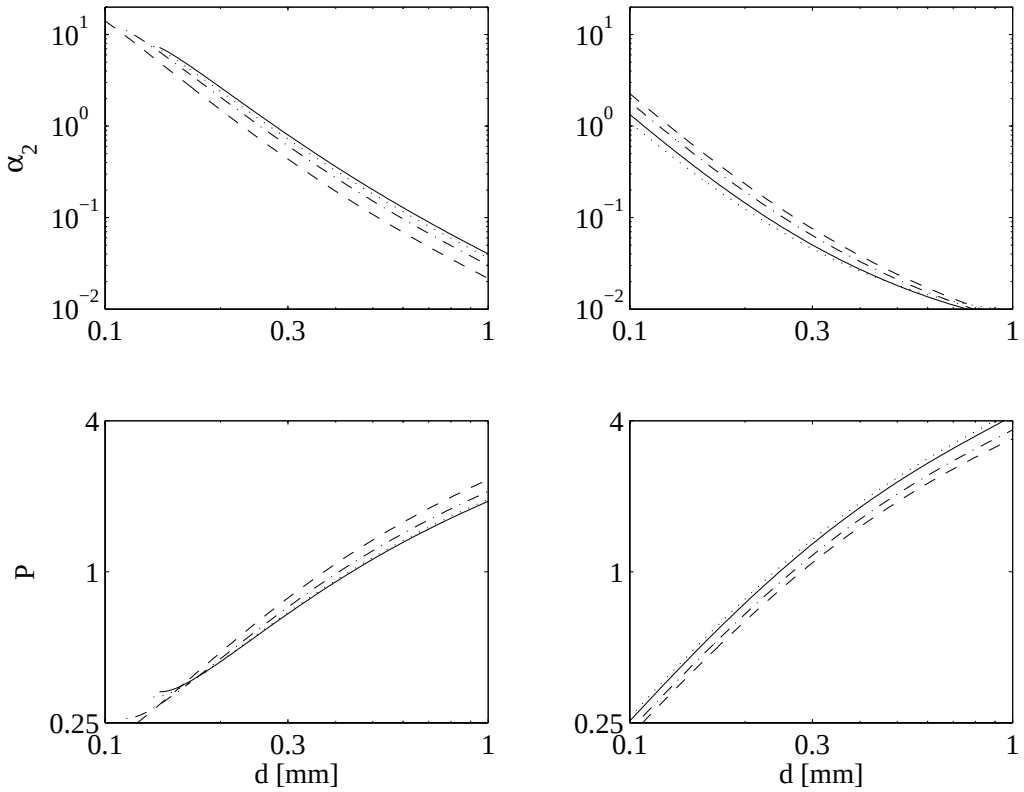


Figure 3-2: Dependence of the suspended sediment forcing coefficient $\alpha_2$ and the Peclet number $P = 2w_S/(\delta\omega)$ on the grain diameter $d$. Field scales are plotted in the left column, $T = 8$ s, $H_o = 6$ m, $\eta_r'$ found from Eq. (1.105), $A_o(1 + |R_L|) = 50$ cm (solid); the others curves have these values, except $A_o(1+|R_L|) = 40$ cm (dash), $H_o = 7$ m (dash-dot), $T = 7.5$ s (dot). Lab scales are plotted in the right column, $T = 2.5$ s, $H_0 = 60$ cm, $\eta_r' = 1$ cm, $A_o(1 + |R_L|) = 7$ cm (solid); the other curves have these values, except $A_o(1 + |R_L|) = 8.5$ cm (dash), $H_0 = 50$ cm (dash-dot), $T = 2.2$ s (dot).

increasing wave slope $\varepsilon$. Lastly, Figure 3-4 shows that $\alpha_2$ increases and $P$ decreases with decreasing dispersion parameter $KH_o$, i.e. decreasing depth $H_o$ and increasing wavelength $\lambda = 2\pi/K$. Note that in Figure 3-3, the apparent increase in $\alpha_2$ from $H_o = 6$ m (solid line) to $H_o = 7$ m (dash-dot line) is merely an artifact of $\alpha_2$ being plotted vs. $\varepsilon$, which also depends on the depth. For the same value of $\varepsilon$, the $H_o = 6$ m curve is associated with a lower orbital amplitude $A_b$, and hence a lower $\alpha_2$, than the $H_o = 7$ m curve.

## 3.7 Suspended sediment flux

In this section we compute the suspended sediment flux $\overline{qs}$. From Eqs. (3.22) and (3.30) in §3.4.1, the leading order flow has the form $u_1 = \Re\left\{u_1^{[1]}e^{-it}\right\}$ and the $O(\varepsilon)$ flow has the

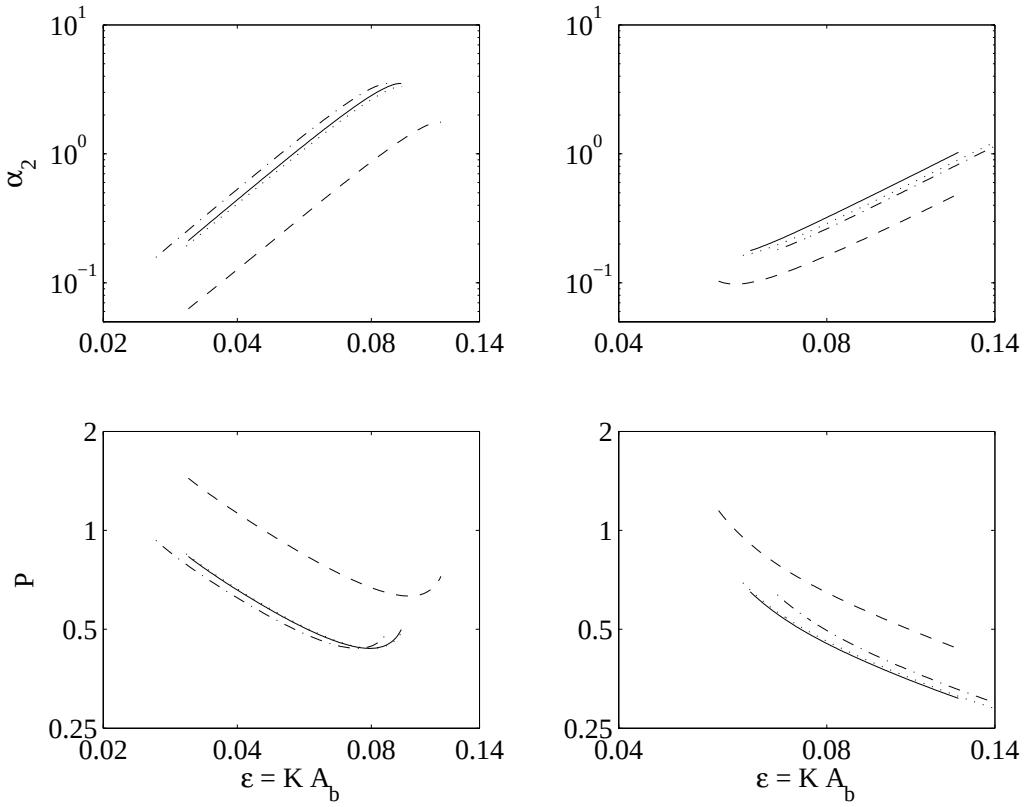


Figure 3-3: Dependence of the suspended sediment forcing coefficient $\alpha_2$ and the Peclet number $P = 2w_S/(\delta\omega)$ on the wave slope $\varepsilon = KA_b$. Field scales are plotted in the left column, $T = 8$ s, $H_o = 6$ m, $\eta_r'$ found from Eq. (1.105), $d = 0.2$ mm (solid); the other curves have these values, except $d = 0.3$ mm (dash), $H_o = 7$ m (dash-dot), $T = 7.5$ s (dot). Lab scales are plotted in the right column, $T = 2.5$ s, $H_o = 60$ cm, $\eta_r' = 1$ cm, $d = 0.12$ mm (solid); the other curves have these values, except $d = 0.15$ mm (dash), $H_o = 50$ cm (dash-dot), $T = 2.2$ s (dot).

form

$$u_2 = u_2^{[0]} + \Re\left\{u_2^{[1]}e^{-it} + u_2^{[2]}e^{-it}\right\}. \tag{3.64}$$

Substituting these and also $C_1$, $C_2$ from (3.48), (3.52) into the suspended sediment flux (3.63) gives

$$\overline{q_S} = \left\langle u_2^{[0]}C_1^{[0]}\right\rangle + \frac{1}{2}\Re\left(\left\langle u_1^{[1]*}C_2^{[1]}\right\rangle + \left\langle u_2^{[2]}C_1^{[2]*}\right\rangle\right). \tag{3.65}$$

This shows that the mean suspended sediment flux depends on coupling between the mean and time varying components of the flow and of the suspended sediment concentration. In the literature (e.g. Boczar-Karakiewicz *et al.* [2], O'Hare & Davies [52], Restrepo & Bona [53]), only the correlation $\left\langle u_2^{[0]}C_1^{[0]}\right\rangle$ between the Eulerian flux and the mean concentration are treated. We first list formulae for each correlation and also $\overline{q_S}$, and then plot the various

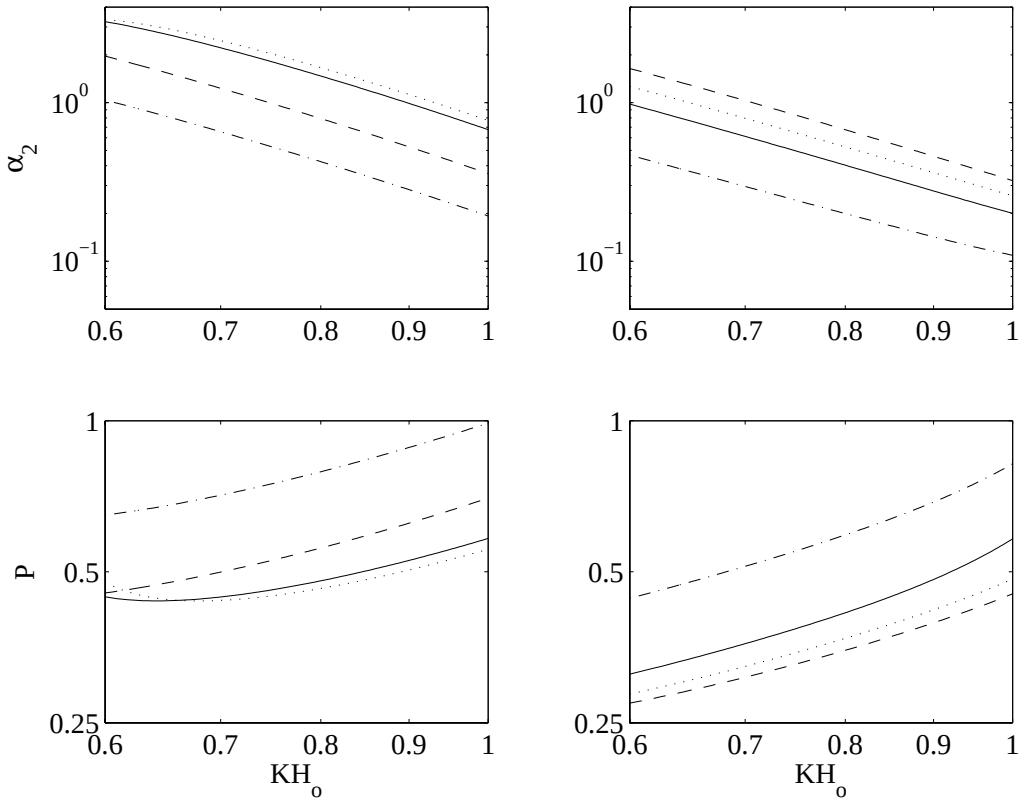


Figure 3-4: Dependence of the suspended sediment forcing coefficient $\alpha_2$ and the Peclet number $P = 2w_S/(\delta\omega)$ on the dispersion parameter $KH_o$. Field scales are plotted in the left column, $T = 8$ s, $A_o(1 + |R_L|) = 50$ m, $\eta_r'$ found from Eq. (1.105), $d = 0.2$ mm (solid); the other curves have these values, except $A_o(1 + |R_L|) = 40$ m (dash), $d = 0.3$ mm (dash-dot), $T = 7.5$ s (dot). Lab scales are plotted in the right column, $T = 2.5$ s, $A_o(1 + |R_L|) = 7$ cm, $\eta_r' = 1$ cm, $d = 0.12$ mm (solid); the other curves have these values, except $A_o(1 + |R_L|) = 8.5$ cm (dash), $d = 0.15$ mm (dash-dot), $T = 2.2$ s (dot).

correlations to show that $\left\langle u_1^{[1]*} C_2^{[1]} \right\rangle$ can be as large as $\left\langle u_2^{[0]} C_1^{[0]} \right\rangle$. In other words, it cannot be neglected.

The correlations in Eq. (3.65) are found by forming the various products of the boundary layer components $u_1^{[1]}$, $u_2^{[0]}$, $u_2^{[2]}$ from (3.22), (3.38), (3.41) and the concentrations $C_1$, $C_2$ from (3.48) and (3.75) and depth-integrating to obtain

$$\left\langle u_2^{[0]} C_1^{[0]} \right\rangle = \widehat{C}\sqrt{\bar{\nu}_e} \left( \Re\left\{ F_{00}\left(\frac{P}{\sqrt{\bar{\nu}_e}}\right) U_1^{[1]*} \frac{\partial U_1^{[1]}}{\partial x} \right\} + F_{01}\left(\frac{P}{\sqrt{\bar{\nu}_e}}\right) \frac{\left|U_1^{[1]}\right|^2}{\bar{\nu}_e} \frac{\partial \bar{\nu}_e}{\partial x} \right) + \frac{2\widehat{C}\Lambda_2^{[0]} U_2^{[0]} \bar{\nu}_e^2}{P^2}, \tag{3.66}$$

$$\left\langle u_1^{[1]*} C_2^{[1]} \right\rangle = \sqrt{\bar{\nu}_e} U_1^{[1]*} \left( F_{11} U_1^{[1]} \frac{\partial \widehat{C}}{\partial x} + F_{12} U_1^{[1]*} \frac{\partial \widehat{C^{[2]}}}{\partial x} + \left( F_{13} \widehat{C} + F_{14} \widehat{C^{[2]}} \right) \frac{\partial U_1^{[1]*}}{\partial x} \right.$$
$$\left. + \left( F_{15} U_1^{[1]} \widehat{C} + F_{16} U_1^{[1]*} \widehat{C^{[2]}} \right) \frac{1}{\bar{\nu}_e} \frac{\partial \bar{\nu}_e}{\partial x} \right), \tag{3.67}$$

$$\left\langle u_2^{[2]*} C_1^{[2]} \right\rangle = \sqrt{\bar{\nu}_e} \widehat{C^{[2]}} \left( F_{20} \left( \frac{P\beta_2}{\sqrt{\bar{\nu}_e}} \right) U_1^{[1]*} \frac{\partial U_1^{[1]*}}{\partial x} + F_{21} \left( \frac{P\beta_2}{\sqrt{\bar{\nu}_e}} \right) U_1^{[2]*} \right. \tag{3.68}$$
$$\left. + F_{22} \left( \frac{P\beta_2}{\sqrt{\bar{\nu}_e}} \right) \frac{U_1^{[1]*2}}{\bar{\nu}_e} \frac{\partial \bar{\nu}_e}{\partial x} \right),$$

where the functions $F_{mn}$ are listed in Eqs. (3.79) – (3.84) in Appendix 3.14.2. Substituting (1.85), (2.39), (3.14) into Eqs. (3.66) – (3.68) and (3.65) yields

$$\frac{\overline{q_S}}{\widehat{C}\sqrt{\bar{\nu}_e}} = \Re \left\{ \left( E_1 + \frac{E_2}{\sinh^2 kH} \right) U_1^{[1]*} \frac{\partial U_1^{[1]}}{\partial x} \right\} + E_3 \frac{\left| U_1^{[1]} \right|^2}{\widehat{C}} \frac{\partial \widehat{C_0}}{\partial x} + E_4 \frac{\left| U_1^{[1]} \right|^2}{\bar{\nu}_e} \frac{\partial \bar{\nu}_e}{\partial x}$$
$$+ \frac{2\Lambda_2^{[0]} U_2^{[0]} \bar{\nu}_e^{3/2}}{P^2} + \left| U_1^{[1]} \right|^2 E_5 \frac{dZ_b}{dx}, \tag{3.69}$$

where the functions $E_n(P/\sqrt{\bar{\nu}_e}, Z_b)$ are listed in Eqs. (3.88) – (3.92) in Appendix 3.14.2. The coefficients are plotted in Figure 3-5, illustrating that $E_1$ is the dominant coefficient, $E_4$ is somewhat important, and $E_2$, $E_3$, $E_5$ are numerically insignificant. Also, $E_1$, $E_3$ and $E_4$ do not vary significantly with $Z_b$, while the numerically insignificant coefficients $E_2$ and $E_5$ do vary appreciably with $Z_b$. We should point out that the term with $\partial \widehat{C}/\partial x$ acts like a diffusion term in the sand bar equation. However, since $E_3$ is numerically insignificant, this source of diffusion is negligible.

We now briefly review the computational steps needed in addition to those in §2.3.1 and §2.4. First, all the parameters listed in §2.3.1 are computed. Using these, we then compute the Peclet number $P = 2w_S/(\delta\omega)$, the reference concentration $C_o$ from (3.5), and then $\alpha_2$ from (3.59). The procedure outlined in §2.4 is then followed to compute the wave envelope $\zeta_{env}$, the grain roughness Shields parameter $\widehat{\Theta}_d$, the diffusivity $D_\nu$ and the bedload forcing $q_\tau$. Using $\widehat{\Theta}_d$, the local reference concentration $\widehat{C_0}$ is found from Eq. (3.11). From Eq. (2.32) for $u_f$, the depth-averaged eddy viscosity $\bar{\nu}_e$ is calculated from (3.25). Using $P$, $\bar{\nu}_e$ and $Z_b$, the coefficients $E_m(P/\bar{\nu}_e, Z_b)$ are found from Eqs. (3.88) – (3.92) in Appendix

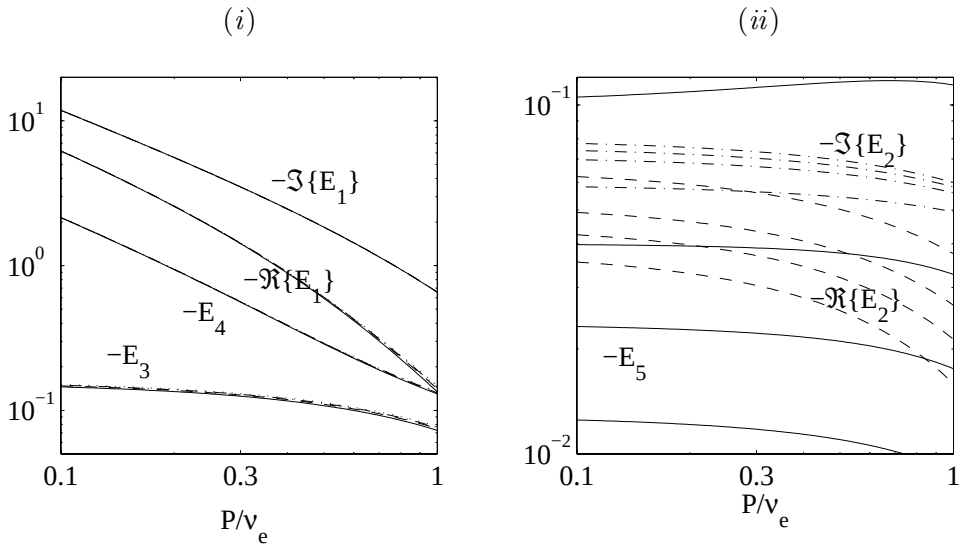


Figure 3-5: The coefficients $E_m(P/\bar{\nu}_e, Z_b)$ in the suspended load forcing $\overline{q_S}$, plotted vs. $P/\bar{\nu}_e$ for various $Z_b$. In plot $(i)$, $E_1$, $E_3$ and $E_4$ are plotted for $Z_b = 0.01$ (solid), 0.05 (dash), 0.1 (dash-dot) and 0.2 (dot). In plot $(ii)$, $\Re\{E_2\}$ (dash), $\Im\{E_2\}$ (dash-dot), $E_5$ (solid) are plotted for the same values of $Z_b$. For $\Re\{E_2\}$ and $E_5$, the value of $Z_b$ increases from top to bottom; for $\Im\{E_2\}$, the value of $Z_b$ decreases from top to bottom.

3.14.2. The flow/concentration correlations are then found from Eqs. (3.66) – (3.68) and the suspended sediment forcing from Eq. (3.69).

Three of the correlations in the suspended sediment forcing, $-\partial\left(\Re\langle u_1^{[1]*}C_2^{[1]}\rangle\right)/\partial x$, $-\partial\left(\langle u_2^{[0]}C_1^{[0]}\rangle\right)/\partial x$ and $-\partial\left(\Re\langle u_2^{[2]*}C_1^{[2]}\rangle\right)/\partial x$ are plotted in Figure 3-6 for laboratory and field conditions. Note that in some cases, the correlation $-\partial\left(\Re\langle u_1^{[1]*}C_2^{[1]}\rangle\right)/\partial x$ dominates, while in others, all three correlations are important. To reiterate the point made above, the correlation of the mean flow and mean concentration used by most authors, $\left\langle u_2^{[0]*}C_1^{[0]}\right\rangle$, is not the only significant correlation in any of the cases plotted!

We commented above that there is considerable experimental evidence that a suspension can exist even if the Shields parameter is less than the critical value given by the Shields diagram. The empirical formula (3.11) for the reference concentration $\widehat{C}$ is based on a large data set, for super-critical and sub-critical flows, and does not vanish at a finite value of the Shields parameter $\Theta_d$. Therefore, for the case of high reflection, the suspended sediment forcing can be nonzero even though the bedload forcing and diffusivity vanish. This is illustrated in the right column of Figure 3-6, where dotted lines mark the edges of the sub-critical regions near the antinodes.

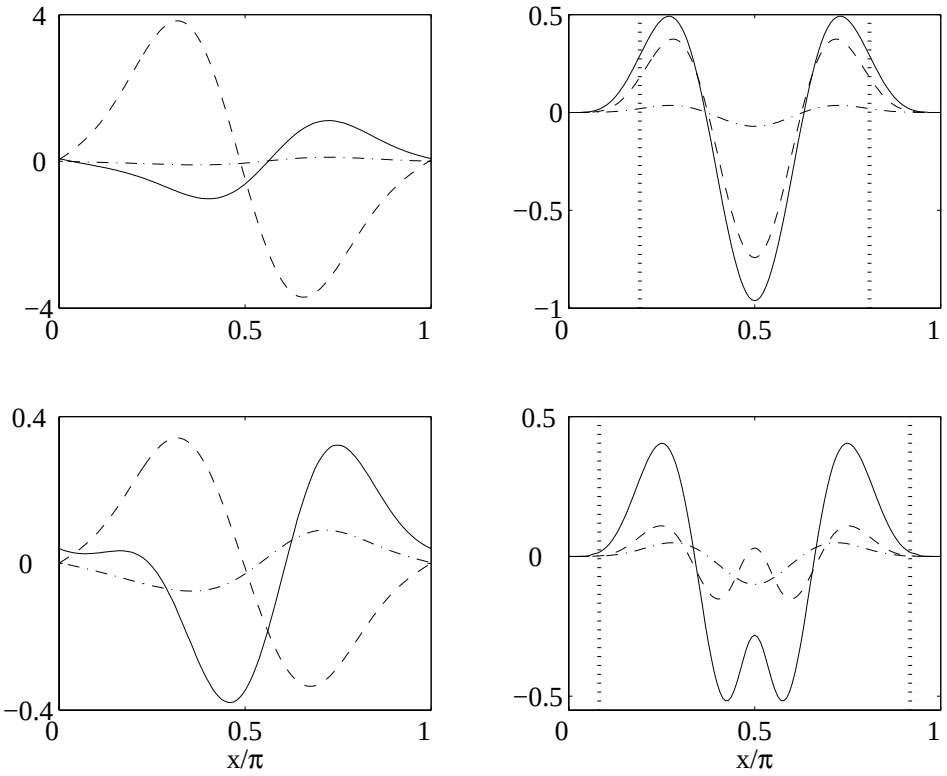


Figure 3-6: Flow/concentration correlations in the suspended sediment forcing, $-\partial\left(\Re\langle u_1^{[1]*}C_2^{[1]}\rangle\right)/\partial x$ (solid), $-\partial\left(\langle u_2^{[0]}C_1^{[0]}\rangle\right)/\partial x$ (dash), $-\partial\left(\Re\langle u_2^{[2]*}C_1^{[2]}\rangle\right)/\partial x$ (dash-dot). In the top row, lab conditions are plotted with $T = 2.5$ s, $H_o = 60$ cm, $A_o(1 + |R_L|) = 7$ cm, $d = 0.11$ mm, $\eta_r' = 1$ cm, and $R_L = 0.25$ (left), $R_L = 1$ (right). In the bottom row, field conditions are plotted with $T = 8$ s, $H_o = 6$ m, $A_o(1 + |R_L|) = 60$ cm, $\eta_r'$ found from Eq. (1.105), and $d = 0.4$ mm, $R_L = 0.25$ (left) and $d = 0.2$ mm, $R_L = 1$ (right). Dotted lines in the right column indicate edge of the the sub-critical regions near the antinodes.

Finally, for small Peclet number $P \ll 1$, Eq. (3.69) becomes

$$\overline{q_S} = \frac{2\widehat{C}\Lambda_2^{[0]}U_2^{[0]}\bar{\nu}_e^2}{P^2} - \frac{\widehat{C}\bar{\nu}_e}{4P}\left(\Re\left\{(3+5i)U_1^{[1]*}\frac{\partial U_1^{[1]}}{\partial x}\right\} + \frac{\left|U_1^{[1]*}\right|^2}{\bar{\nu}_e}\frac{\partial\bar{\nu}_e}{\partial x}\right) + O(P^0). \qquad (3.70)$$

Thus, the magnitude of the suspended sediment forcing $-\alpha_2\partial\overline{q_S}/\partial x$ increases as $\alpha_2$ increases and as $P$ decreases. From the plots of $\alpha_2$ and $P$ in Figures 3-2, 3-3, 3-4, the magnitude of the suspended sediment forcing increases as the grain diameter $d$ and dispersion parameter $KH_o$ decrease and as the wave slope $\varepsilon$ increases. Also, the contribution due to the return flow induced stress is proportional to $P^{-2}$, and hence dominates the suspended sediment forcing for fine grains (small $P$).

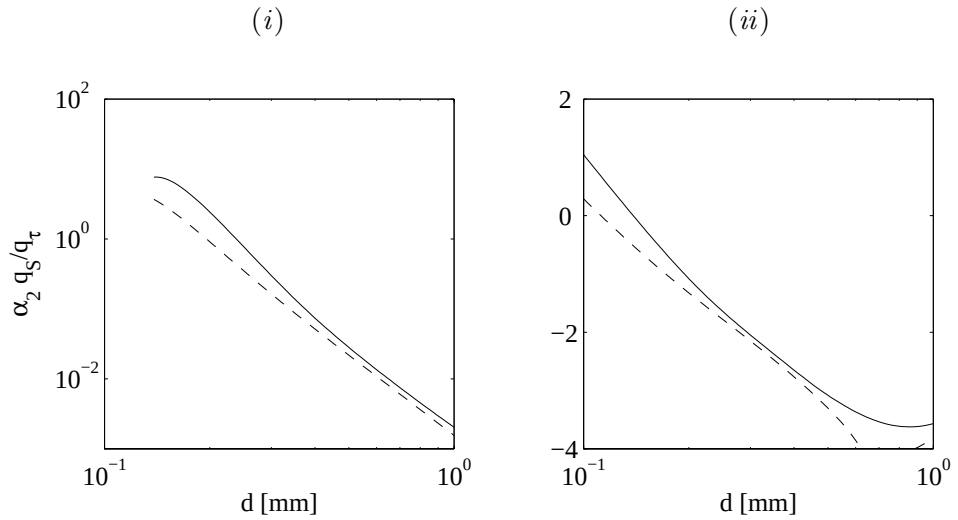


Figure 3-7: Dependence of the ratio of the maximum suspended sediment forcing to maximum bedload forcing across a bar length, $(\max - \min)\left(\alpha_2 \overline{q_S}\right) / (\max - \min) q_\tau$ on grain diameter $d$, for $(i)$ field conditions ($T = 8$ s, $H_o = 6$ m, $A_o(1 + |R_L|) = 50$ cm) and $(ii)$ lab conditions ($T = 2.5$ s, $H_o = 60$ cm, $A_o(1 + |R_L|) = 7$ cm). The reflection coefficient and return-flow matching elevation are $R = 0.25$ (solid) and $R = 1$ (dash). In all cases, ripple amplitudes $\eta_r'$ are found from Eq. (1.105) and $\Lambda_2^{[0]} = 1.5$.

## 3.8 Sand bar forcing

The effect of fine grains on the sand bar forcing is illustrated by considering the ratio of the suspended sediment and bedload forcing and by comparing these two forcing mechanisms for various grain diameters, reflection coefficients, and lab and field conditions.

The ratio of the maximum suspended sediment forcing to the maximum bedload forcing across a bar length, $(\max - \min)_x \left(\alpha_2 \overline{q_S}\right) / (\max - \min)_x q_\tau$, is plotted against various parameters in Figures 3-7 to 3-9. Figure 3-7 shows that this ratio increases exponentially as the grain size $d$ decreases. In other words, the magnitude of the suspended sediment forcing is sensitive to the grain diameter for fine sediments. Figure 3-8 shows that the suspended sediment becomes important at high wave intensities in the field, and at high and low wave intensities in the lab. Figure 3-9 illustrates that suspended sediments become important in shallow water in the field, and in shallow and deeper water in the lab.

Next, the bedload and suspended load contributions to forcing are plotted across a bar for various sediment diameters for field and lab conditions in Figures 3-10 and 3-11, respectively. The qualitative picture in both regimes is the same: as the grain diameter decreases, the variation in bedload forcing is limited, if not negligible, while the suspended

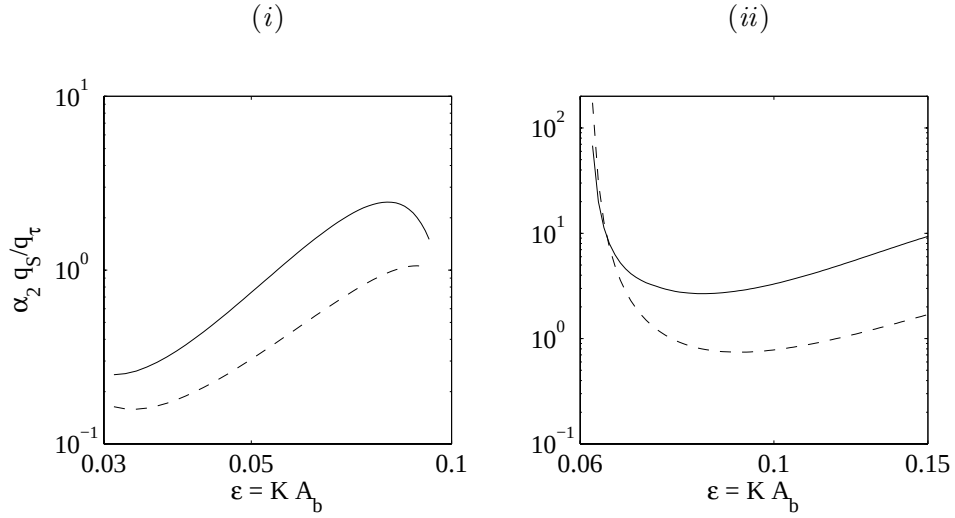


Figure 3-8: Dependence of the ratio of the maximum suspended sediment forcing to maximum bedload forcing across a bar length, $(\max - \min)_x \left(\alpha_2 \overline{q_S}\right) / (\max - \min)_x q_\tau$ , on wave slope $\varepsilon = KA_b$ for $(i)$ field conditions ($T = 8$ s, $H_o = 6$ m, $d = 0.2$ mm) and $(ii)$ lab conditions ($T = 2.5$ s, $H_o = 60$ cm, $d = 0.115$ mm). The reflection coefficients are $R = 0.25$ (solid) and $R = 1$ (dash). For a given wave slope $\varepsilon$, the total wave height $A_o(1 + |R_L|)$ is kept the same for each value of $R_L$ plotted. In all cases, ripple amplitudes $\eta_r'$ are found from Eq. (1.105) and $\Lambda_2^{[0]} = 1.5$.

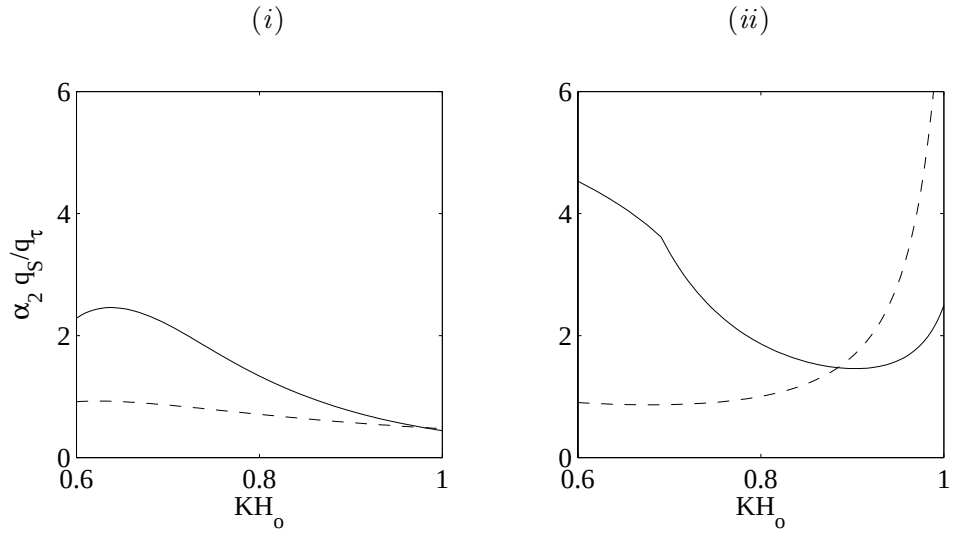


Figure 3-9: Dependence of the ratio of the maximum suspended sediment forcing to maximum bedload forcing across a bar length, $(\max - \min)_x \left(\alpha_2 \overline{q_S}\right) / (\max - \min)_x q_\tau$ , on the dispersion parameter $KH_o$ for $(i)$ field conditions ($T = 8$ s, $d = 0.2$ mm, $A_o(1 + |R_L|) = 50$ cm) and $(ii)$ lab conditions ($T = 2.5$ s, $d = 0.115$ mm, $A_o(1 + |R_L|) = 7$ cm). The reflection coefficients are $R = 0.25$ (solid) and $R = 1$ (dash). In all cases, ripple amplitudes $\eta_r'$ are found from Eq. (1.105) and $\Lambda_2^{[0]} = 1.5$.

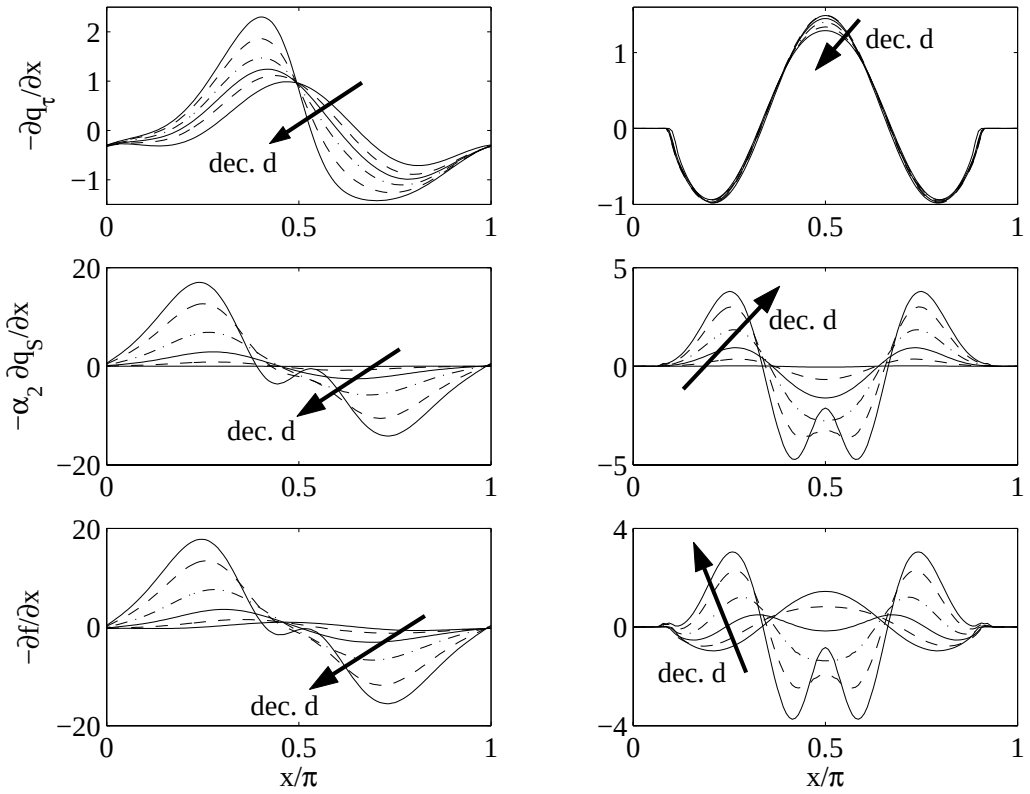


Figure 3-10: The dependence of the bedload forcing $-\partial q_\tau/\partial x$ and the suspended load forcing $-\alpha_2 \partial \overline{q_S}/\partial x$ on the grain diameter $d$ for field conditions, $T = 8$ s, $H_o = 6$ m, $A_o(1+|R_L|) = 50$ cm, $\Lambda_2^{[0]} = 1.5$ and $\eta_r'$ found empirically using Nielsen's formula (1.105). Arrows indicate the direction of decreasing grain diameter, $d = 0.5,\ 0.25,\ 0.2,\ 0.17,\ 0.15,\ 0.14$ mm (solid, dash, solid, dash-dot, dash, solid). The reflection coefficient is $R_L = 0.25$ (left) and 1 (right).

sediment forcing becomes dominant. As the grain size diminishes, crests shift seaward for low reflection, and, for high reflection, troughs form under the wave node and crests form near the sub-critical regions.

The effect of the return flow bed stress coefficient $\Lambda_2^{[0]}$ on the bedload forcing $-\partial q_\tau/\partial x$ and the suspended load forcing $-\alpha_2 \partial \overline{q_S}/\partial x$ is illustrated in Figure 3-12. For both lab and field scales, increasing $\Lambda_2^{[0]}$ increases the shear stress in the boundary layer due to the return flow and shifts the peak of the bedload forcing seaward (negative $x$-direction). Increasing $\Lambda_2^{[0]}$ dramatically increases the magnitude of the suspended sediment forcing, despite making very little change to its peak position, which is always well behind the wave node. Thus, increasing $\Lambda_2^{[0]}$ increases the magnitude of the combined forcing and shifts its peak seaward of the wave node.

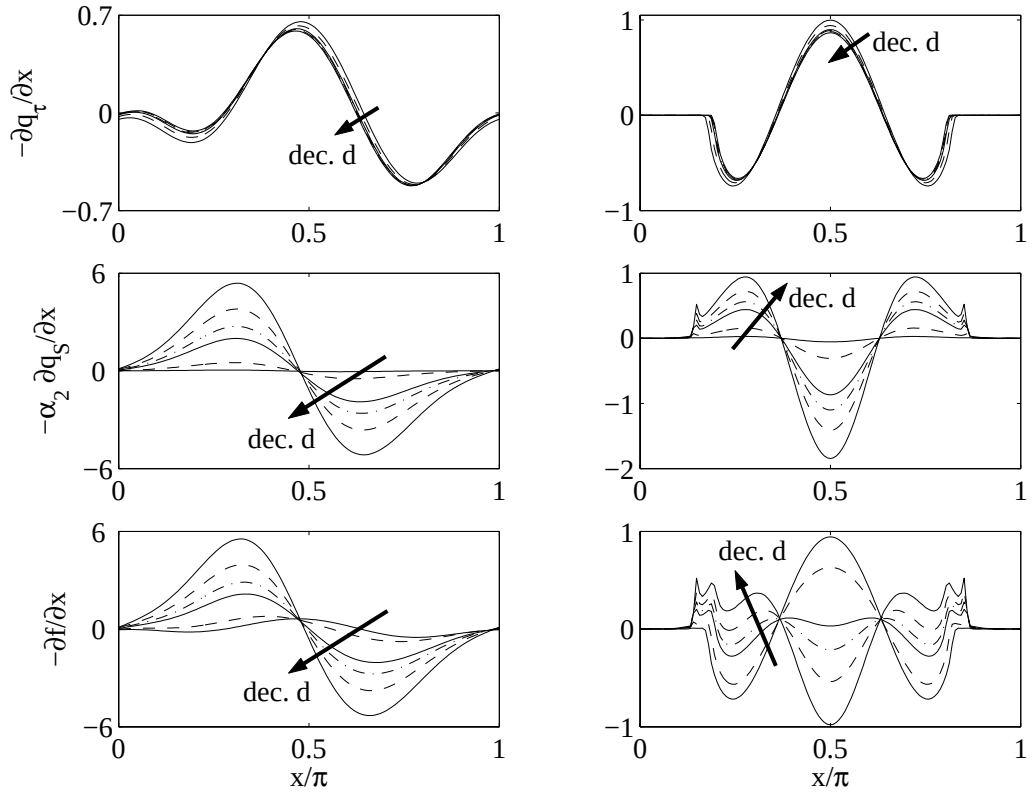


Figure 3-11: The dependence of the bedload forcing $-\partial q_\tau/\partial x$ and the suspended load forcing $-\alpha_2 \partial \overline{qs}/\partial x$ on the grain diameter $d$ for lab conditions, $T = 2.5$ s, $H_o = 60$ cm, $A_o(1 + |R_L|) = 7$ cm, $\Lambda_2^{[0]} = 1.5$ and $\eta_r'$ found empirically using Nielsen's formula (1.105). Arrows indicate the direction of decreasing grain diameter, $d = 0.02, 0.014, 0.0115, 0.011, 0.0105, 0.01$ (solid, dash, solid, dash-dot, dash, solid). The reflection coefficient is $R_L = 0.25$ (left) and 1 (right).

The effect of ripple height on the bedload and suspended load forcing is shown in Figure 3-13 for fine grains. Doubling the ripple height has little effect on the bedload and suspended load forcing for high reflection ($R_L = 1$), consistent with the result for coarse grains in Chapter 2. For weak reflection, doubling the ripple height shifts the peak of the bedload forcing shoreward, but shifts the peak of the suspended load seaward. Since the suspended sediment forcing dominates the bedload forcing for fine grains, the crest of the overall forcing is shifted seaward. Also, for the grain diameters used in Figure 3-13, doubling the ripple height increases the magnitude of the suspended sediment forcing by approximately 50% and the overall forcing by 25%. Thus, the ripple height has a significant impact on the sand bar forcing for fine grains.

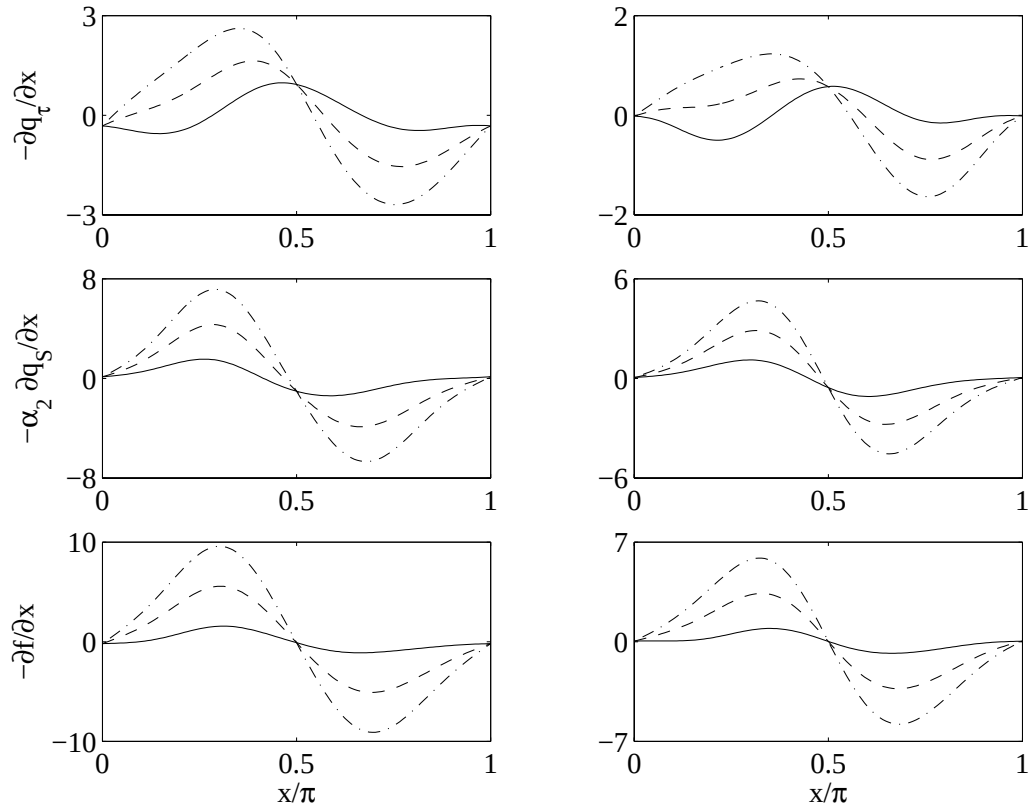


Figure 3-12: The dependence of the bedload forcing $-\partial q_\tau/\partial x$ and the suspended load forcing $-\alpha_2 \partial \overline{qs}/\partial x$ on the return flow bed stress coefficient, $\Lambda_2^{[0]} = 1$ (solid), 2 (dash) and 3 (dash-dot), for field (left column) and lab (right column) conditions. The reflection coefficient is $R_L = 0.25$. All other parameters are the same as those in Figures 3-10 and 3-11 for field and lab conditions, respectively.

## 3.9 Steady state

The sand bar equation (3.62) does not admit a steady state solution for strong reflection, since sub-critical regions ($\widehat{\Theta}_d < \Theta_c$) exist under the wave antinode where the diffusivity $D_\nu$ vanishes, but the suspended sediment forcing $-\alpha_2 \, \partial \overline{qs}/\partial x$ does not. Unlike the diffusivity and bedload forcing, the suspended sediment flux $\overline{qs}$ does not vanish at a finite value of the Shields parameter. For fine grains, this amounts to continual deposition in a narrow region overlapping the sub-critical regions. In reality, local avalanches will limit the growth of the narrow crests near the sub-critical regions. Since avalanche and steep-slope effects are not included in our model, the steady state can only be predicted when the diffusivity $D_\nu$ is nonzero everywhere across the bar, i.e. for weak reflection.

Note that bar predictions under strong reflection can still be made, but will only be valid

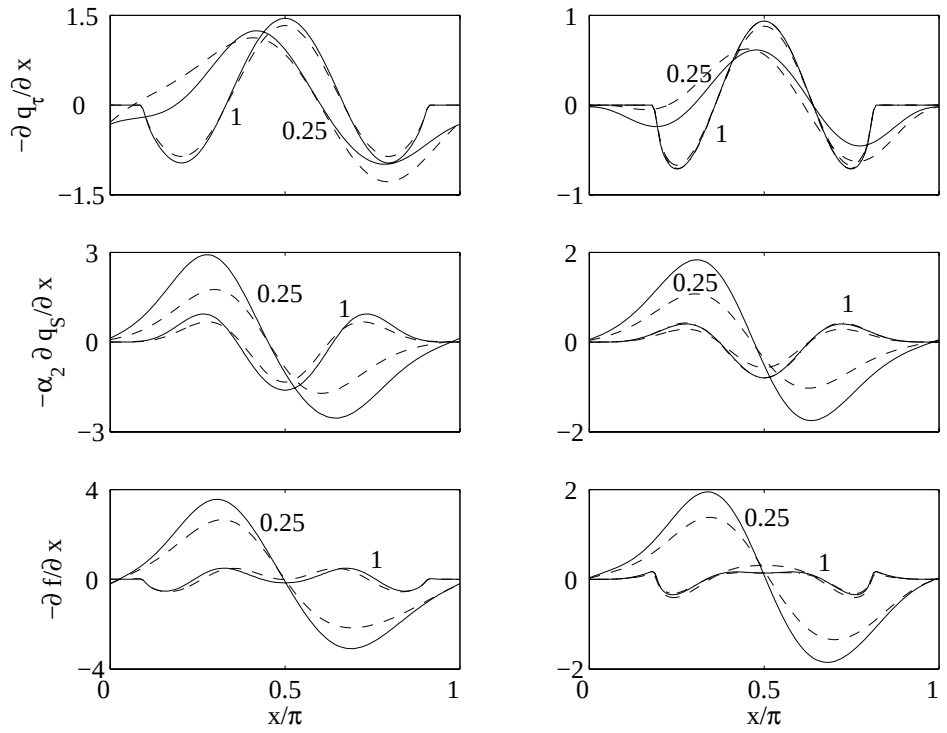


Figure 3-13: Dependence of the bedload forcing $-\partial q_\tau/\partial x$ and the suspended load forcing $-\alpha_2 \partial \overline{q_S}/\partial x$ on the ripple height $\eta_r'$ for $R_L = 0.25, 1$. Field conditions are plotted in the left column, $H_o = 6$ m, $T = 8$ s, $A_o(1 + |R_L|) = 50$ cm, $d = 0.2$ mm, and ripple height $\eta_r' = \eta_{ro}$ (solid) and $\eta_r' = \eta_{ro}/2$ (dash), where $\eta_{ro}$ is found from Eq. (1.105). Lab conditions are plotted in the right column, $H_o = 60$ cm, $T = 2.5$ s, $A_o(1 + |R_L|) = 7$ cm, $d = 0.12$ mm, with $\eta_r' = 2$ cm (solid), $\eta_r' = 1$ cm (dash), and $\eta_r'$ found from Eq. (1.108) with $(r_1, r_2, r_3) = (0.68, 3, 2)$ and $\eta_{ro} = 2$ cm (dash-dot). The dash-dot line is so close to the solid line it is not visible. Numbers adjacent to curves indicate the value of $R_L$. In all cases, $\Lambda_2^{[0]} = 1.5$.

as long as the predicted bar slopes are small. In practice, this is not a serious limitation, since the bar growth is very weak near the sub-critical regions.

If the reflection is weak, the derivation of the steady state bar profile is identical to that in §2.4.2 with the bedload forcing $q_\tau$ replaced by the total forcing $q_\tau + \alpha_2 \overline{q_S}$. Under this replacement, the steady state bar profiles for fine grains are given by Eq. (2.119),

$$\widetilde{h}_S(x) = \left\{ \int_0^x dx' - \frac{1}{\pi} \int_0^\pi \int_0^x dx' dx + \left( \frac{1}{2} - \mathcal{G}(x) \right) \int_0^\pi dx \right\} \frac{q_\tau + \alpha_2 \overline{q_S}}{D_\nu}, \tag{3.71}$$

where $\mathcal{G}(x)$ is still the ratio of integrals of $D_\nu^{-1}$ given in Eq. (2.116).

The effects of fine grains on the steady state bar height are illustrated in Figures 3-14 through 3-16. Figure 3-14 shows that for fine grains, the steady state bar height increases

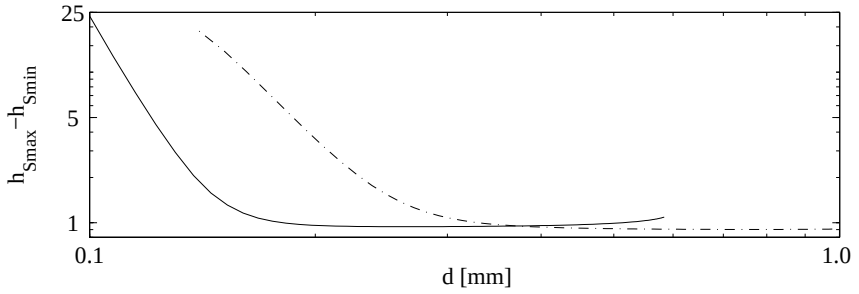


Figure 3-14: The effects of fine grains on the steady state bar height for field (dash-dot) and lab (solid) conditions. The lab conditions are $T = 2.5$ s, $H_o = 60$ cm, $A_o(1 + |R_L|) = 7$ cm, $\eta_r' = 2$ cm. The field conditions are $T = 8$ s, $H_o = 6$ m, $A_o(1 + |R_L|) = 50$ cm, and $\eta_r'$ is found from Eq. (1.105). In all cases, $\Lambda_2^{[0]} = 1.5$. The right limit of the solid line corresponds to the critical reflection coefficient above which a sub-critical region exists.

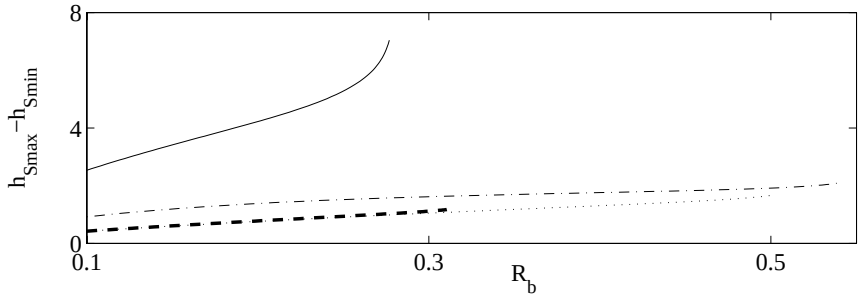


Figure 3-15: Dependence of the steady state bar height on the reflection coefficient, for fine and coarse grains. The lab conditions are $T = 2.5$ s, $H_o = 60$ cm, $A_o(1 + |R_L|) = 7$ cm, $\eta_r' = 2$ cm, and $d = 0.12$ mm (solid) and $d = 0.25$ mm (dash). The field conditions are $T = 8$ s, $H_o = 6$ m, $A_o(1 + |R_L|) = 50$ cm, $\eta_r'$ found from Eq. (1.105), and $d = 0.25$ mm (dash-dot) and $d = 0.5$ mm (dot). In all cases, $\Lambda_2^{[0]} = 1.5$. The right limit of each curve corresponds to the the critical reflection coefficient above which a sub-critical region exists, and the steady state (with suspended sediment) does not exist.

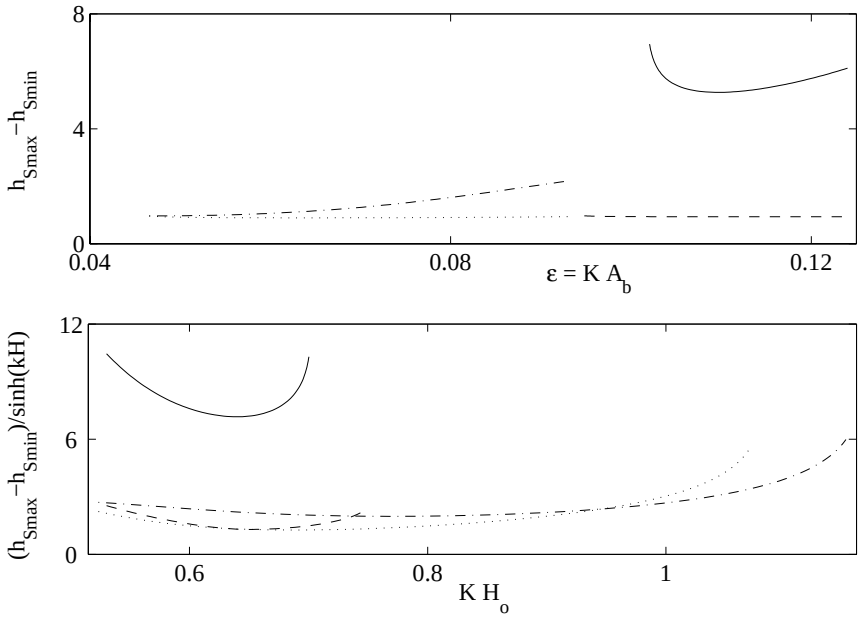


Figure 3-16: Dependence of the steady state bar height on the wave slope $\varepsilon = KA_b$ (top) and on the dispersion parameter $KH_o$ (bottom). The reflection coefficient is $R_L = 0.25$ for all curves. In the top plot, the lab conditions are $T = 2.5$ s, $H_o = 60$ cm, and $d = 0.12$ mm (solid) and $d = 0.25$ mm (dash). The field conditions are $T = 8$ s, $H_o = 6$ m, and $d = 0.25$ mm (dash-dot) and $d = 0.5$ mm (dot). In the bottom plot, the lab conditions are $T = 2.5$ s, $A_o(1 + |R_L|) = 7$ cm, and $d = 0.12$ mm (solid) and $d = 0.25$ mm (dash). The field conditions are $T = 8$ s, $A_o(1 + |R_L|) = 50$ cm, and $d = 0.25$ mm (dash-dot) and $d = 0.5$ mm (dot). In all cases, $\Lambda_2^{[0]} = 1.5$. The ripple height $\eta_r'$ is 2 cm for lab conditions and is found from Eq. (1.105) for field conditions.

dramatically as a power-law of the grain diameter, both in the lab and in the field.

The dependence of the steady state bar height on the reflection coefficient is plotted in Figure 3-15 for lab and field conditions. The total wave height $A_o\,(1 + |R_L|)$ is held constant while the reflection $R_L$ is varied. As for coarse grains, the bar heights increase with the amount of reflection. However, the bar height in the lab is greater and increases faster for fine grains than for coarse grains (compare solid to dashed lines). For field conditions, the rate of increase is similar, but the bar heights for fine grains are still larger (compare dash-dot to dotted lines). The reflection coefficients are kept below the threshold where sub-critical regions exist and a steady state does not.

The dependence of the steady state bar height on the wave slope $\varepsilon = KA_b$ is illustrated in Figure 3-16(top), for fine and coarse grains. The scaled bar heights for coarse grains (dash-dot, dotted lines) in the lab and the field are relatively independent of the wave slope, indicating that the physical bar elevation $\widetilde{h}' = A_b\widetilde{h}$ varies linearly with wave amplitude. For

fine grains (solid, dashed lines), however, the steady state bar height increases with wave slope for field scales and decreases and then increases for laboratory scales. Also, the bar heights associated with fine grains are larger than those for coarse grains, as illustrated in Figure 3-14.

Figure 3-16(bottom) illustrates the dependence of the steady state bar height on the dispersion parameter $KH_o$. For each curve, the mean depth $H_o$ is varied as the other parameters, in particular the wavenumber $K$, are held fixed. In general, as the mean depth increases, the bar heights decrease and then increase. For field conditions, the bar heights for coarse grains can actually become greater than those for fine grains as depth increases.

## 3.10 Single bar simulations

We now investigate the effects of fine grains on overall bar shape and growth rate. As for coarse grains in Chapter 2, we consider a single bar in a patch of infinitely many bars, apply periodic boundary conditions at the bar ends, and fix the wave parameters ($A$, $R$).

Bar profile snapshots are plotted at different times in Figure 3-17 for weak ($R_L = 0.25$) and strong ($R_L = 1$) reflection. Since the time interval between the solid profiles is the same, $\Delta\bar{t} = 0.2$ for $R_L = 0.25$ (left column) and $\Delta\bar{t} = 0.1$ for $R_L = 1$ (right column), the relative distance between solid curves indicates the bar growth rate. Initially, the growth rate is high; at later times, the growth rate diminishes. In the case of weak reflection, the bars approach their steady state, indicated by a dashed line in the figure. For strong reflection, crests grow near the sub-critical regions under the antinodes as scouring occurs under the wave node. Notice that even though the bar growth rate diminishes with time, the crests near the antinodes continue to grow, as indicated by the dash-dot bar profile at $\bar{t} = 4$. The growth rate of the crests seems to be larger than that of the scour under the node, since the scour region is broad and the crests are narrow. In reality, local avalanching would erode these crests and spread sediment further into the sub-critical region. Since our theory is only valid for mild slopes, the simulation is halted when the crests near the antinodes become steep.

Under weak reflection, time evolutions of the bar crest elevation, $\max_x(\widetilde{h}(x,\bar{t}))$, scaled by the steady state crest elevation $\max_x(\widetilde{h}_S(x))$ are plotted in Figure 3-18 for field (left) and lab (right) conditions. The growth rate is large initially and then diminishes as the bars

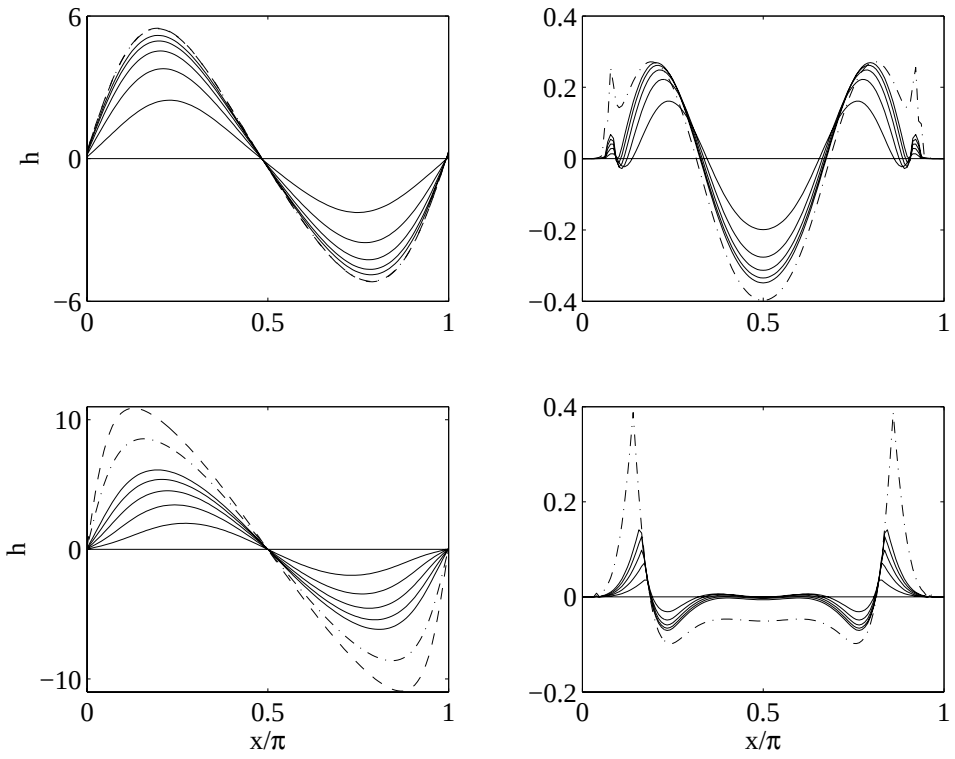


Figure 3-17: Bar profile snapshots at different times for $R_L = 0.25$ (left column) and $R_L = 1$ (right column). The time between each solid line profile is $\Delta\bar{t} = 0.2$ in the left column and $\Delta\bar{t} = 0.1$ in the right column. The dash-dot profile is at $\bar{t} = 4$. For comparison, steady state profiles are plotted in the left column as dashed lines. Field parameters are used in the top row, $T = 8$ s, $H_o = 6$ m, $A_o(1+|R_L|) = 50$ cm, $d = 0.16$ mm and $\eta_r'$ found from Eq. (1.105). Lab scales are used in the bottom row, $T = 2.5$ s, $H_o = 60$ cm, $A_o(1 + |R_L|) = 7$ cm, $d = 0.115$ mm, $\eta_r' = 2$ cm. In all cases, $\Lambda_2^{[0]} = 1.5$.

approach their steady state. The evolutions are plotted vs. the sand bar time $\bar{t} = t/\alpha_1$, so that large variations due to $\alpha_1$ are removed. Only minor differences, analogous to those for coarse grains, are noticeable as the parameters vary.

Snapshots at $\bar{t} = 4$ of bar profiles for various grain diameters are plotted in Figure 3-19. Under strong reflection, the dependence of bar shape on sediment diameter is striking. As the grain diameter decreases from coarse to fine, the crest under the wave node becomes a trough, and the troughs neighboring the sub-critical regions become crests. In Figure 3-20, the corresponding evolutions of the bar elevation under the wave node are plotted vs. the sand bar time $\bar{t} = t/\alpha_1$, so that large variations due to $\alpha_1$ are removed. Under weak reflection, decreases in the grain diameter mainly lead to larger bar heights and bar crests that are further behind the wave node. The corresponding evolutions of the bar crest

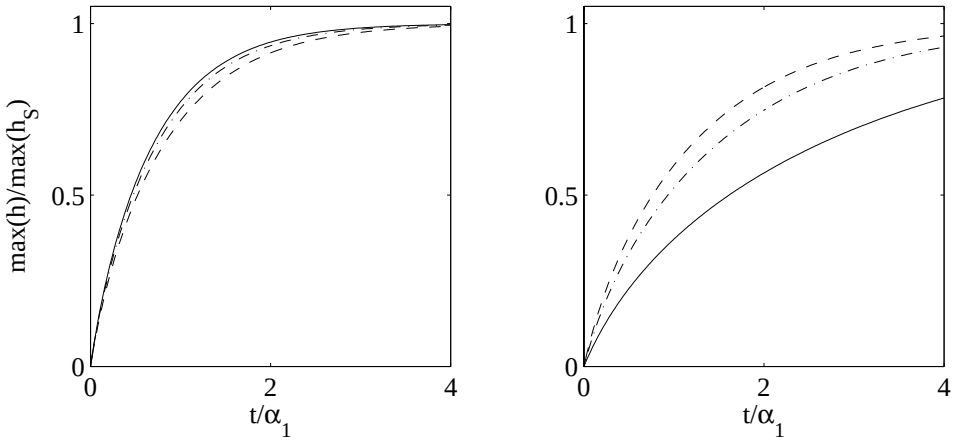


Figure 3-18: Evolution of the maximum bar elevation $\max_x \widetilde{h}(x,\bar{t})$, scaled by the corresponding steady state bar elevation $\max_x \widetilde{h}_S(x)$, in terms of the sand bar time $\bar{t} = t/\alpha_1$, for weak reflection $R_L = 0.25$. Field conditions are plotted at left, with $T = 8$ s, $H_o = 6$ m, $A_o(1+|R_L|) = 50$ cm, $\eta_r'$ found from Eq. (1.105) and $d = 0.16$ mm (solid); the other curves have these parameters, except $d = 0.20$ mm, $H_o = 7$ m (dash-dot) and $d = 0.20$ mm, $A_o(1+|R_L|) = 40$ cm (dash). Lab conditions are plotted at right, with $T = 2.5$ s, $A_o(1+|R_L|) = 7$ cm, $\eta_r' = 2$ cm, $d = 0.2$ mm (solid); the other curves have these values, except $H_o = 50$ cm (dash-dot) and $A_o(1+|R_L|) = 8.5$ cm (dash). In all cases, $\Lambda_2^{[0]} = 1.5$.

elevations are shown in Figure 3-21. For field scales (left), crest heights evolve in a similar fashion, for all grain diameters, on the scaled time $\bar{t} = t/\alpha_1$. For lab conditions, bar crests of fine grains approach their steady state more slowly in the scaled time $\bar{t}$ than those of coarse grains. Recall that longer bar formation timescales $\alpha_1/\omega$ (see Chapter 2) are associated with fine grains.

## 3.11 Comparison to past small scale laboratory experiments

Analogous to §2.5 for coarse grains, we compare our theory to three sets of small scale laboratory experiments concerning sand bars composed of fine grains. Both De Best *et al.* (1971) [12] and Xie (1981) [67], whose setup and coarse grained data were reviewed in §2.5, also performed tests with fine sand. Recently, Dulou, Belzons & Rey (2000) [16] performed fine-grained sand bar experiments on a mean slope.

### 3.11.1 Fine-grained experiments of De Best *et al.* (1971)

The experiments of De Best *et al.* (1971) [12] were introduced in §2.5.2, and our bar predictions were compared to the tests with coarse grains. De Best *et al.* (1971) performed

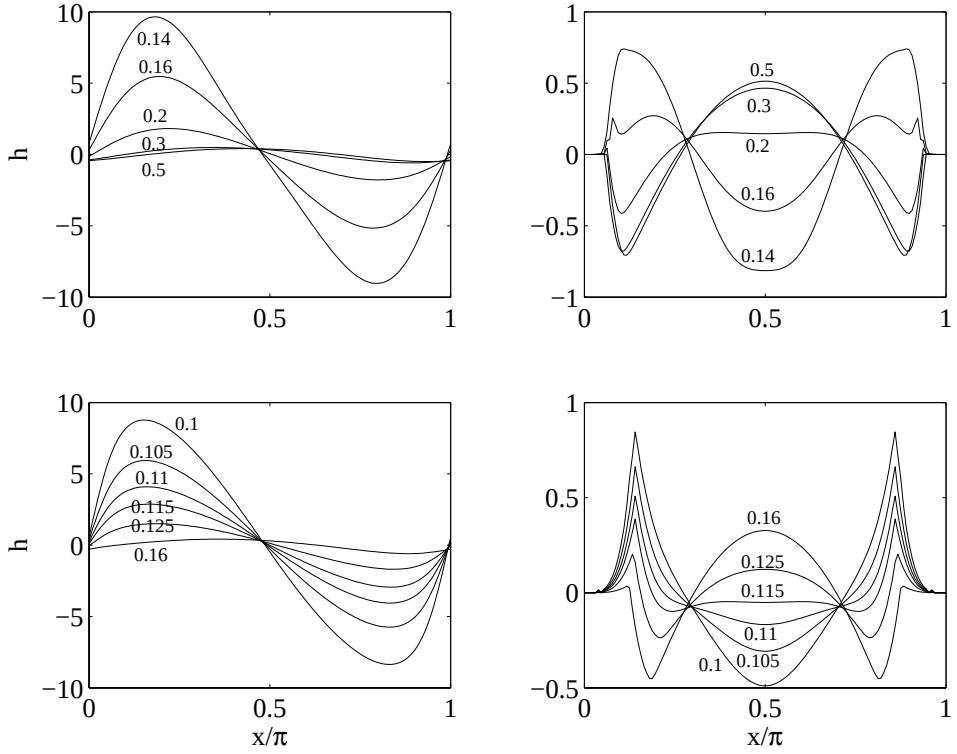


Figure 3-19: The dependence of bar profiles $\widetilde{h}$ at $\bar{t} = 4$ on the grain diameter $d$, for field (top row) and laboratory (bottom row) conditions, for weak ($R_L = 0.25$, left column) and strong ($R_L = 1$, right column) reflection. Numbers adjacent to curves indicate the grain diameter $d$ in mm. The field conditions are $T = 8$ s, $H_o = 6$ m, $A_o(1 + |R_L|) = 50$ cm, $\eta_r'$ found from Eq. (1.105). The lab conditions are $T = 2.5$ s, $A_o(1 + |R_L|) = 7$ cm, $\eta_r' = 2$ cm. In all cases, $\Lambda_2^{[0]} = 1.5$.

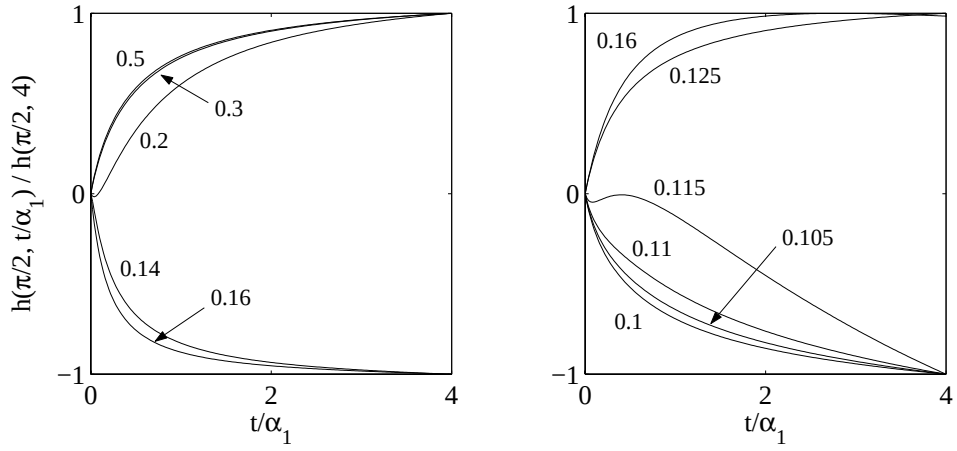


Figure 3-20: The time evolution of the bar elevation under the wave node for various grain sizes and strong reflection $R_L = 1$ in the field (left) and the lab (right). The bar elevations are scaled by their value at $\bar{t} = 4$, $\widetilde{h}(\pi/2, 4)$. Numbers adjacent to curves indicate the grain diameter $d$ in mm. The corresponding field and lab conditions are listed in Figure 3-19.

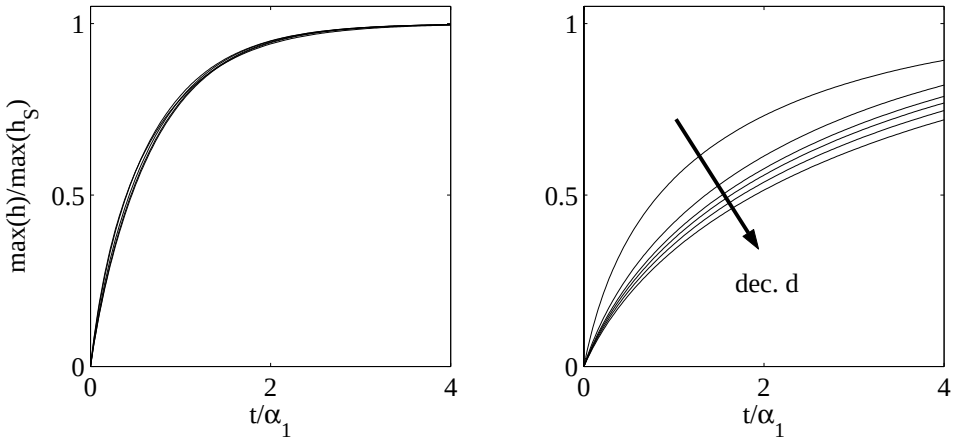


Figure 3-21: The time evolution of the bar crest elevation $\max_x \widetilde{h}$ for various grain sizes under weak reflection $R_L = 0.25$ in the field (left) and the lab (right). The bar crest elevations are scaled by the steady state bar crest elevation $\max_x \widetilde{h}_S(x)$. For field conditions (left), the curves virtually coincide; for lab conditions (right), the arrow indicates the direction of decreasing grain diameter $d$. The corresponding field and lab conditions, including the grain diameters $d$, are listed in Figure 3-19.

tests with coarse (SA III), intermediate (SE III) and fine (SB III) grains. The relevant parameters are listed in Table 2.3 in §2.5.2 and in Table 3.1 here. In §2.5.2, we verified the flows are all fully rough turbulent.

Since the suspended sediment forcing is quite sensitive to the grain diameter and increases rapidly as the grain diameter decreases, we have, in some cases, made predictions using smaller grain diameters than the experimental value. These extra predictions are listed with the label (sim) in Table 3.1, and correspond to larger $\alpha_2$ and smaller $P$ than for the actual grain size used in the particular experiment.

Our single bar simulations are compared with De Best *et al.*'s tests SA III, SE III and SB III in Figure 3-22. Figure 3-22(top) shows our predictions for test SA III after 9 hours with (solid) and without (dash) suspended sediment forcing. The lines are virtually indistinguishable, indicating the sand grains are coarse, i.e. the effects of fine grains are negligible. Figure 3-22(middle) shows our predictions for test SE III after 7 hours for $d = 0.16$ mm (solid) and $d = 0.12$ mm (dash). Note that $d = 0.16$ mm is the experimental mean grain diameter for test SE III. However, for this value, our theory over-predicts the crest height and the trough depth. Taking $d$ 25% smaller in our simulation, $d = 0.12$ mm, gives excellent agreement with the experimental profile. Figure 3-22(bottom) shows our predictions for test SB III after 5 hours for $d = 0.13$ mm (solid), $d = 0.11$ mm (dash) and

| Test | $d$ [mm] | $\alpha_2$ | $P$ | $w_S/u_f$ | $C_o$ |
|---|---|---|---|---|---|
| SA III | 0.22 | 0.17 | 0.69 | 0.29 | 0.00019 |
| SE III | 0.16 | 0.43 | 0.44 | 0.19 | 0.00044 |
| SE III (sim) | 0.12 | 1.13 | 0.27 | 0.11 | 0.00100 |
| SB III | 0.13 | 0.84 | 0.32 | 0.13 | 0.00078 |
| SB III (sim) | 0.11 | 1.51 | 0.24 | 0.10 | 0.00132 |
| SB III (sim) | 0.10 | 2.13 | 0.20 | 0.09 | 0.00178 |

Table 3.1: Parameters relevant to the suspended sediment forcing for the experiments of De Best *et al.* (1971) [12]. The label (sim) indicates that the set of parameters is used for predictions and corresponds to a finer grain diameter than that used in the given experimental test.

$d = 0.1$ mm (dash-dot). Note that $d = 0.13$ mm is the experimental mean grain diameter for test SB III. However, for this value, our theory predicts a crest under the node and no crests near the antinode. Taking $d$ 25% smaller in our simulation, $d = 0.1$ mm, yields a prediction with a trough under the node and crests near the antinodes. The crest height is within a factor of 2 of the measured height, but the predicted position is further from the antinode than the observed crest. For comparison, the prediction for $d = 0.1$ mm is also given, illustrating the sensitivity of the predictions to the precise value of the grain diameter.

The degree to which the bars have reached a steady state is indicated by the evolution of the bar crest elevation $\widetilde{h}(\pi/2, \bar{t})$ in Figure 3-23. For all simulations, the change in the bar crests is small by the end of the test.

The ripple heights were obtained by averaging the measured bed profiles across a ripple length and subtracting the average from the measured profile. The ripple elevations are plotted in Figure 3-24 for each test along with the fitting formula Eq. (1.108) with $\eta_{ro}$ given in Table 2.3 in §2.5.2 and $(r_1, r_2, r_3) = (0.71, 3, 2)$ for test SA III, $(r_1, r_2, r_3) = (0.77, 3, 2)$ for test SE III, $(r_1, r_2, r_3) = (0.79, 3, 0.5)$ for test SB III. For comparison, the characteristic ripple height predicted by Nielsen's formula (1.105) is listed in Table as $\eta_{ro}(N)$ and gives reasonable estimates of the measured ripple heights.

### 3.11.2 Fine-grained experiments of Xie (1981)

The experiments of Xie (1981) [67] were introduced in §2.5.3, and bar predictions were given for the tests with coarse grains. Here we present predictions for the tests with fine

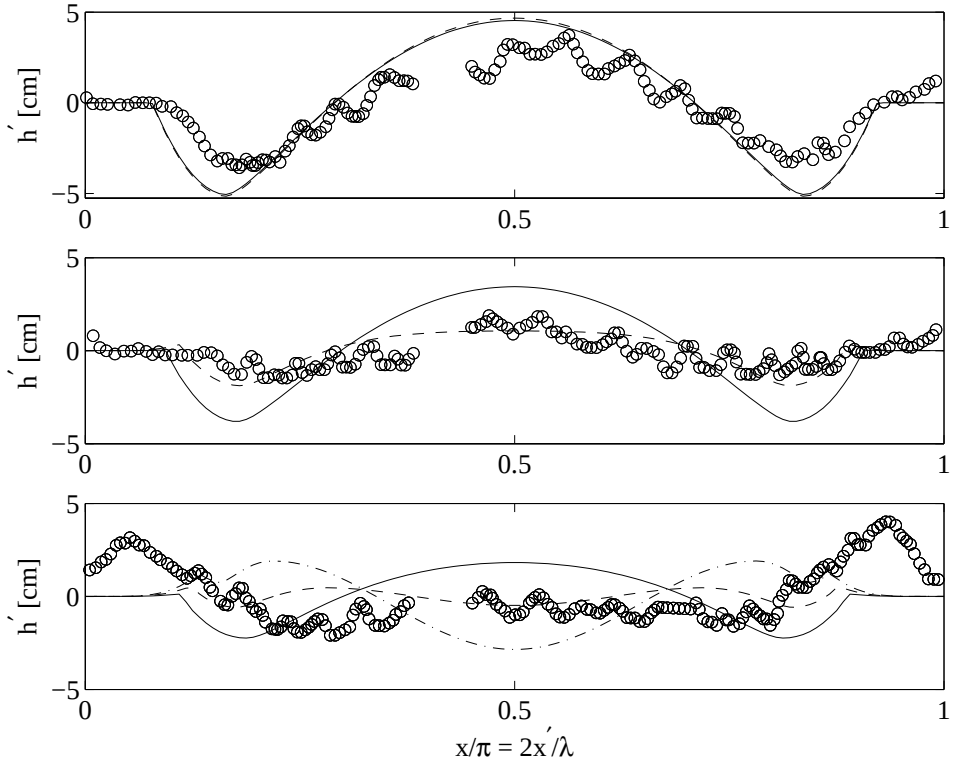


Figure 3-22: Comparison of predicted bar profiles $\widetilde{h}'$ with the experiments of De Best *et al.* (1971) [12] demonstrating the effect of fine grains. The measured bar profiles are denoted by ($\circ$). Predictions are made with our single bar simulation. Top: predicted bar profile after 9 hours for test SA III, with (solid) and without (dash, $\alpha_2 = 0$) the suspended sediment forcing. Middle: predicted bar profile after 7 hours for test SE III, for $d = 0.16$ mm (solid) and $d = 0.12$ mm (dash). Bottom: predicted bar profile after 5 hours for test SB III, for $d = 0.13$ mm (solid), $d = 0.11$ mm (dash) and $d = 0.10$ mm (dash-dot). Gaps in the data are due to a vertical tank support blocking the view.

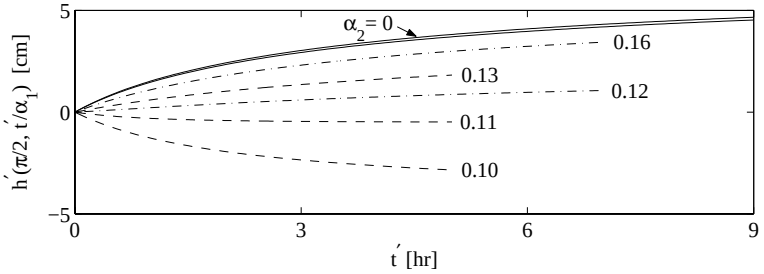


Figure 3-23: Predicted evolution of bar crest elevation $\widetilde{h}'(\pi/2, \bar{t})$ corresponding to the experiments De Best *et al.* (1971) [12]: test SA III (solid), SB III (dash) and SE III (dash-dot). Numbers adjacent to curves indicate the grain diameter $d$ used for the simulation. The solids lines correspond to $d = 0.22$ mm with and without ($\alpha_2 = 0$) the suspended sediment forcing.

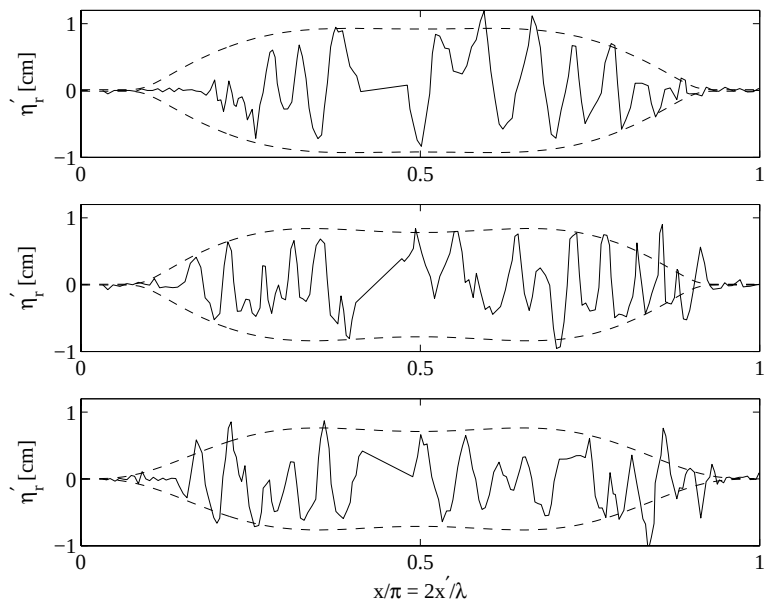


Figure 3-24: Comparison of ripple height fit with measured ripple elevations (jagged lines) for the experiments of De Best *et al.* (1971) [12]. The dashed lines are $\pm\eta_r'/2$, where $\eta_r'$ is the fitted ripple height from Eq. (1.108) with $\eta_{ro}$ given in Table 2.3 in §2.5.2 and $(r_1, r_2, r_3) = (0.71, 3, 2)$ (test SA III), $(r_1, r_2, r_3) = (0.77, 3, 2)$ (test SE III), $(r_1, r_2, r_3) = (0.79, 3, 0.5)$ (test SB III). Gaps in the data are due to a vertical tank support blocking the view.

grains. Xie performed approximately 40 tests, mostly for fine grained sands. We compare our theoretical predictions to the tests whose conditions were significantly above critical, $\Theta_{do} > 4\Theta_{C0}$, which is the regime of interest for coastal erosion.

The relevant parameters are listed in Table 2.4. For the tests listed, the left hand side of Sleath's criterion for turbulence, Eq. (1.90), is 88 or greater, and the values of $\mathsf{R}_{FT}$ are significantly greater than 100, indicating the corresponding boundary layers are fully rough turbulent.

Xie reported the grain size distribution (Figure 5 in Xie [67]) for the various sands used in the test bed. Since the suspended sediment forcing is quite sensitive to the grain diameter and increases rapidly as the grain diameter decreases, we have, in some cases, run simulations with $d_{25}$, the grain diameter for which 25% of the mass of a sediment sample is finer, for the particular sand bed. Also, the ripple heights $\eta_{ro}$ for tests 2a and 6a were found from Xie's Figure 25, using the corresponding the values of $\Psi_0$ and $d$. For the other tests, Nielsen's formula (1.105) gave accurate predictions of $\eta_{ro}$.

Our single bar simulations are compared with the experimental bar profiles of Xie's tests 6a, 2a and 16b in Figure 3-25. For each test, our predictions correctly predict a trough under

| Test | $T$ [s] | $H_o$ [cm] | $A_o$ [cm] | $R_L$ | $d$ [mm] | $\eta_{ro}$ [cm] | $\eta_{ro}/\lambda_{ro}$ | $t'_f$ [hr] |
|---|---|---|---|---|---|---|---|---|
| 2a | 1.3 | 30 | 3.75 | 1 | 0.106 | 0.97 | 0.20 | 3.98 |
| 2a ($d_{25}$) | 1.3 | 30 | 3.75 | 1 | 0.083 | 0.97 | 0.20 | 3.98 |
| 6a | 1.9 | 30 | 4.50 | 1 | 0.106 | 0.94 | 0.20 | 3.47 |
| 16b | 1.7 | 50 | 4.25 | 1 | 0.106 | 0.94 | 0.13 | 4.99 |
| 16b ($d_{25}$) | 1.7 | 50 | 4.25 | 1 | 0.083 | 0.79 | 0.12 | 4.99 |
| 18b | 2.4 | 50 | 5.00 | 1 | 0.106 | 1.00 | 0.09 | 6.98 |

| Test | $\lambda$ [m] | $\delta$ [cm] | $\alpha_1/\omega$ [hr] | $A_b\omega$ [cm/s] | $u_f$ [cm/s] | $w_S$ [cm/s] | $\eta_{ro}(N)$ [cm] |
|---|---|---|---|---|---|---|---|
| 2a | 2.00 | 1.35 | 2.516 | 32.84 | 8.05 | 0.71 | 0.69 |
| 2a ($d_{25}$) | 2.00 | 1.35 | 2.835 | 32.84 | 8.05 | 0.62 | 0.53 |
| 6a | 3.00 | 2.21 | 2.935 | 45.42 | 9.31 | 0.71 | 0.45 |
| 16b | 3.33 | 1.47 | 10.941 | 28.79 | 6.79 | 0.71 | 0.94 |
| 16b ($d_{25}$) | 3.33 | 1.40 | 12.305 | 28.79 | 6.48 | 0.62 | 0.79 |
| 18b | 5.00 | 2.42 | 13.396 | 39.09 | 7.93 | 0.71 | 1.00 |

| Test | $\varepsilon$ | $KH_o$ | $\Theta_{c0}$ | $\Theta_{do}$ | $\Theta_o$ | $Z_b$ | $\mathsf{R}_E$ | $\mathsf{R}_{FT}$ | Eq. (1.90) |
|---|---|---|---|---|---|---|---|---|---|
| 2a | 0.22 | 0.94 | 0.092 | 0.467 | 3.78 | 0.19 | 22663 | 3211 | 419 |
| 2a ($d_{25}$) | 0.22 | 0.94 | 0.108 | 0.552 | 4.83 | 0.19 | 22663 | 3211 | 419 |
| 6a | 0.28 | 0.63 | 0.092 | 0.724 | 5.05 | 0.11 | 61074 | 3620 | 1278 |
| 16b | 0.15 | 0.94 | 0.092 | 0.345 | 2.69 | 0.17 | 22427 | 2638 | 120 |
| 16b ($d_{25}$) | 0.15 | 0.94 | 0.108 | 0.408 | 3.13 | 0.15 | 22427 | 2104 | 88 |
| 18b | 0.19 | 0.63 | 0.092 | 0.520 | 3.66 | 0.11 | 58358 | 3282 | 114 |

| Test | $d$ [mm] | $\alpha_2$ | $P$ | $w_S/u_f$ | $C_o$ |
|---|---|---|---|---|---|
| 2a | 0.106 | 1.66 | 0.21 | 0.09 | 0.00278 |
| 2a ($d_{25}$) | 0.083 | 2.70 | 0.18 | 0.08 | 0.00403 |
| 6a | 0.106 | 4.68 | 0.18 | 0.08 | 0.00674 |
| 16b | 0.106 | 1.30 | 0.25 | 0.10 | 0.00146 |
| 16b ($d_{25}$) | 0.083 | 2.05 | 0.23 | 0.10 | 0.00214 |
| 18b | 0.106 | 3.56 | 0.21 | 0.09 | 0.00329 |
| 8b | 0.200 | 0.17 | 0.68 | 0.29 | 0.000187 |
| 13a | 0.150 | 0.47 | 0.41 | 0.17 | 0.000725 |
| 23a | 0.780 | 0.01 | 2.73 | 1.15 | $5.0 \times 10^{-5}$ |

Table 3.2: Parameters for the fine-grained experiments of Xie (1981) [67]. The ripple height $\eta_{ro}(N)$ and steepness $\eta_{ro}/\lambda_{ro}(N)$ are estimated empirically from Eqs. (1.105) and (1.107). The ripple heights $\eta_{ro}$ for tests 2a and 6a are estimated directly from Xie [67]'s Figure 25. For all other tests, $\eta_{ro} = \eta_{ro}(N)$. The values listed for the critical Shields parameter $\Theta_{c0}$ are found from Eq. (1.102). The values of $\mathsf{R}_E$, $\mathsf{R}_{FT}$ and the l.h.s. of Eq. (1.90) indicate the boundary layers in all tests were fully rough turbulent. The label ($d_{25}$) denotes parameters based on the grain diameter that is coarser than 25% of the sediment by mass, for the particular test bed.

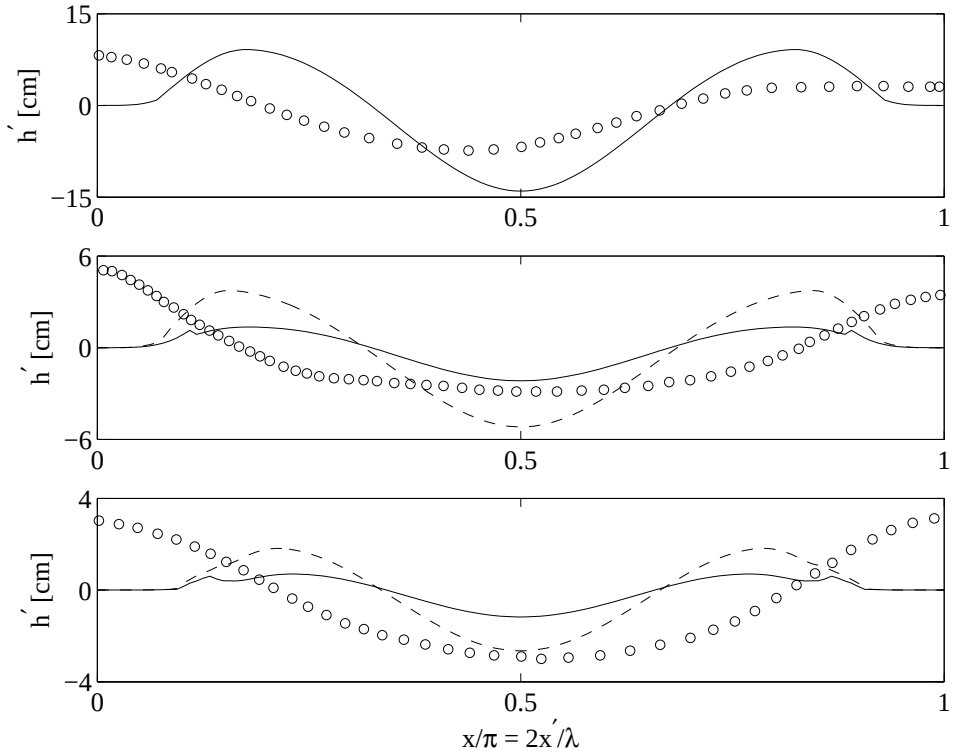


Figure 3-25: Comparison of predictions $\widetilde{h}'$ with the fine-grained experimental bar profiles ($\circ$) of Xie (1981) [67] for test 6a (top), 2a (middle) and 16b (bottom). Our single bar predictions are plotted for grain diameter $d = d_{50} = 0.106$ mm (solid) and $d = d_{25} = 0.083$ mm (dash). The other parameters corresponding to each test are listed in Table 3.2.

the wave node and crests near the antinode. The trough depth and crest heights have the correct order of magnitude, although may over- or under-estimate the measured quantities. The measured crest position is very near the antinode, while our predicted crest positions are further away. Simulations using $d_{25}$ yield better predictions for tests 2a and 16b, a consequence of the large variability associated with fined-grained experiments. Figure 3-26 shows good agreement between measurements and our predictions of the time evolution of the depth of scour $\min_x \widetilde{h}'$ for tests 2a, 16b, and 18b, and moderate agreement for test 6a. We should point out that the wave slope in test 6a was large, $\varepsilon = 0.28$, and our over-prediction is reminiscent of our comparison with Herbich's data in §2.5.1.

### 3.11.3 Fine-grained experiments of Dulou *et al.* (2000)

Dulou, Belzons & Rey (2000) [16] performed laboratory sand bar experiments on a sloping seabed of fine grains in a glass-walled tank 4.7 m long and 0.38 m wide with a maximum

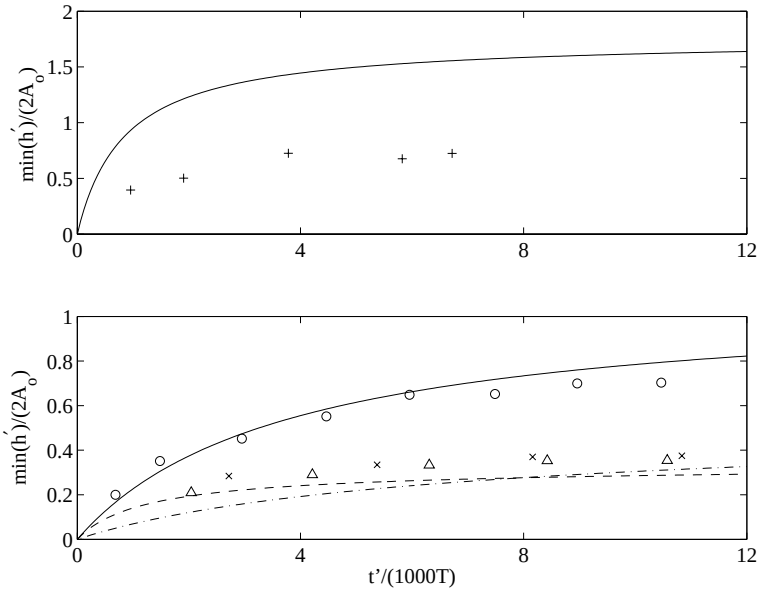


Figure 3-26: Comparison of predictions with the measured depth of scour $\min_x \widetilde{h}'$ on a bed of fine grains by Xie (1981) [67], for test 6a (top, +), 2a (×), 16b (△), 18b (○). The predictions are plotted for test 6a (top, solid), 2a (dash), 16b ($d_{25}$) (dash-dot), 18b (bottom, solid).

water depth of 15 cm. A paddle-type wavemaker was installed at one end of the tank and an artificial beach was placed shoreward of the sand bed at the other end. The slope of the artificial beach could be varied to adjust the amount of reflection. A layer of artificial cohesionless sand (glass spheres of specific gravity $s = 2.7$, mean diameter $d = 0.080$ mm) was placed in a region extending from 1.2 m downstream of the wavemaker to 0.26 m upstream of the toe of the beach slope. A false bottom 0.26 m long was mounted between the end of the sand bed and the artificial beach. For each test, the initial sand bed was a sloping plane of typical length 2 m extending from a water depth of 8 cm to 4 cm.

Wave records and bed profiles were measured by ultrasonic probes mounted on a cart, which was moved along the tank by a stepping motor. Dulou *et al.* recorded the surface displacement and bed profile minutes after the wavemaker started, when only ripples were present on the bed, and also at later times when bars had formed.

We focus on the three tests whose wave fields did not possess significant free second harmonic components. The data corresponding to these tests is reported in Figures 3, 6 and 9 of Dulou *et al.* (2000). The relevant parameters are listed in Table 3.3; the primary difference is the amount of shoreline reflection. Also, for the tests listed, the left hand side of Sleath's criterion for turbulence, Eq. (1.90), evaluates to between 8 and 30 and the values

| Test | $T$ [s] | $H_o$ [cm] | $A_o$ [cm] | $R_L$ | $d$ [mm] | $\eta_{ro}$ [cm] | $\eta_{ro}/\lambda_{ro}$ | $t'_f$ [hr] |
|---|---|---|---|---|---|---|---|---|
| 3 | 0.7 | 4 | 0.84 | 0.31 | 0.080 | 0.28 | 0.20 | 20.0 |
| 6 | 0.7 | 4 | 0.77 | 0.42 | 0.080 | 0.24 | 0.20 | 3.33 |
| 9 | 0.7 | 4 | 0.63 | 0.16 | 0.080 | 0.24 | 0.20 | 33.3 |

| Test | $\lambda$ [m] | $\delta$ [cm] | $\alpha_1/\omega$ [hr] | $A_b\omega$ [cm/s] | $u_f$ [cm/s] | $w_S$ [cm/s] | $\eta_{ro}(N)$ [cm] |
|---|---|---|---|---|---|---|---|
| 3 | 0.39 | 0.34 | 0.54 | 15.2 | 3.95 | 0.59 | 0.27 |
| 6 | 0.39 | 0.32 | 0.56 | 15.0 | 3.75 | 0.59 | 0.27 |
| 9 | 0.39 | 0.24 | 1.47 | 10.1 | 2.81 | 0.59 | 0.08 |

| Test | $\varepsilon$ | $KH_o$ | $\Theta_{c0}$ | $\Theta_{do}$ | $\Theta_o$ | $Z_b$ | $\mathsf{R}_E$ | $\mathsf{R}_{FT}$ | Eq. (1.90) |
|---|---|---|---|---|---|---|---|---|---|
| 3 | 0.26 | 0.64 | 0.109 | 0.194 | 1.17 | 0.22 | 2458 | 457 | 30 |
| 6 | 0.26 | 0.64 | 0.109 | 0.190 | 1.06 | 0.20 | 2395 | 372 | 28 |
| 9 | 0.17 | 0.64 | 0.109 | 0.100 | 0.59 | 0.26 | 1084 | 278 | 8 |

| Test | $d$ [mm] | $\alpha_2$ | $P$ | $w_S/u_f$ | $\overline{C_0}$ |
|---|---|---|---|---|---|
| 3 | 0.080 | 0.41 | 0.36 | 0.15 | 0.00106 |
| 6 | 0.080 | 0.42 | 0.38 | 0.16 | 0.00112 |
| 9 | 0.080 | 0.33 | 0.50 | 0.21 | 0.000673 |

Table 3.3: Parameters for the fine-grained experiments of Dulou *et al.* (2000) [16]. The test numbers correspond to the figure number in [16]. The ripple height $\eta_{ro}(N)$ and steepness $\eta_{ro}/\lambda_{ro}(N)$ are estimated empirically from Eqs. (1.105) and (1.107). The values listed for the critical Shields parameter $\Theta_{c0}$ are found from Eq. (1.102). The values of $\mathsf{R}_{FT}$ and the l.h.s. of Eq. (1.90), based on a measured ripple slope of 0.2, indicate the boundary layers in all tests were fully rough turbulent.

of $\mathsf{R}_{FT}$ are greater than 100, indicating the corresponding boundary layers are fully rough turbulent.

Our predictions corresponding to Dulou *et al.*'s tests 3, 6 and 9 are shown in Figures 3-27, 3-28 and 3-29, respectively. All predictions are made on a slope fitted to the initial sloping seabed. The ripple height $\eta'_r$ used in our predictions is found from the measured ripple elevations. Averaging the measured bed profiles across a ripple length and subtracting this average from the measured profile yields the ripple elevation across the bed. The following formula, based on the shoreline reflection coefficient $R_L$, gives a reasonable fit to the measured ripple elevation in tests 3, 6 and 9,

$$\eta'_r = \eta_{ro}\, F_{rip}\, \frac{\sqrt{1+|R_L|^2-2|R_L|\cos\left(2S-\theta_R(L)\right)}}{1+|R_L|} \tag{3.72}$$

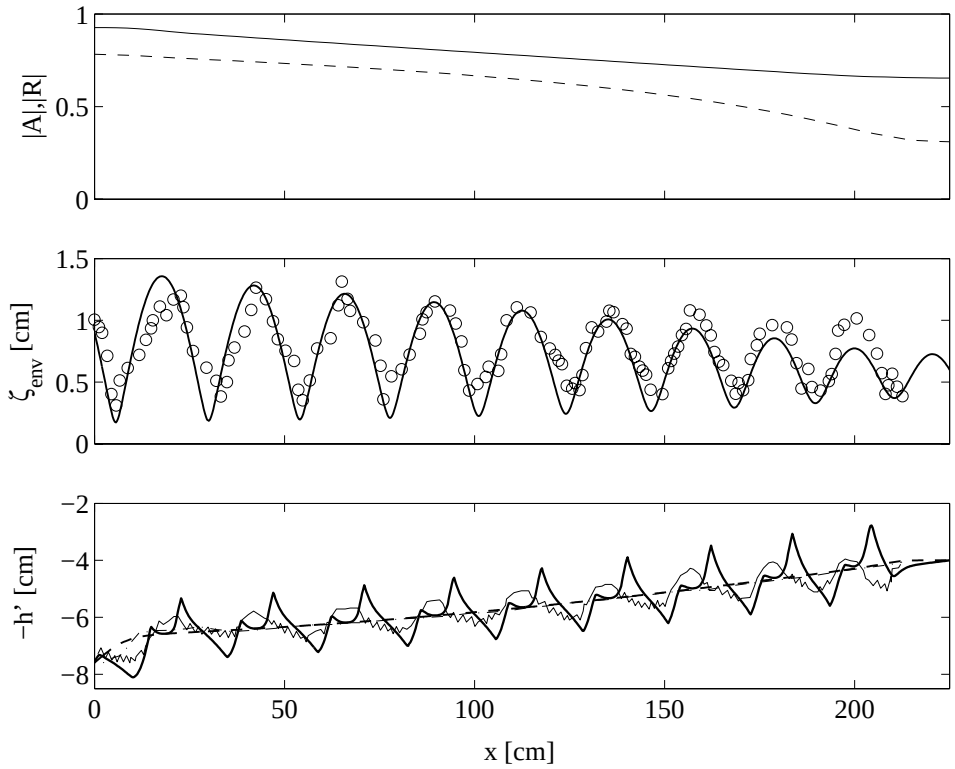


Figure 3-27: Comparison of predictions with test 3 of the fine-grained sand bar experiments of Dulou *et al.* (2000) [16], after $t'_f = 7.2 \times 10^4$s = 20 hrs of wave action. Top: Predicted incident amplitude $|A|$ (solid) and reflection coefficient $R$ (dash). Middle: Predicted (solid) and measured ($\circ$) amplitude of the first harmonic $|\zeta_1^{[1]\prime}|$. Bottom: Predicted seabed elevation $-h' = -H' + \widetilde{h}'$ (thick solid), measured seabed elevation (jagged solid), experimental initial seabed (dash-dot), mean seabed used in simulation $-H'$ (dash). Parameters: $T = 1/1.5$ s, $A_r = 0.8$ cm, $R_L = 0.31e^{-0.3\pi i}$, $\Lambda_2^{[0]} = 1.4$. The ripple height $\eta'_r$ used in the predictions is found from Eq. (3.72) with $F_{rip} = 1$.

where $S = \int_0^x k(\varepsilon x)dx$ is the phase, the fitted values of $\eta_{ro}$ are listed in Table 3.3, and $F_{rip} = 1$ for tests 3 and 6. For test 9, ripples do not appear on the deeper portion of the bed and the factor $F_{rip}$ is needed to reduce the ripple height smoothly to zero in this region,

$$F_{rip} = \exp\left(\frac{1}{10^8\left(\max_{x_1}|U_{\max}|^2 - 0.55\right)^8} - \frac{1}{10^8\left(|U_{\max}|^2 - 0.55\right)^8}\right), \tag{3.73}$$

where $|U_{\max}|$ is given by Eq. (1.109),

$$|U_{\max}| = \max_x \left|U_1^{[1]}\right| = \frac{A_o A(1+|R|)}{A_b \sinh kH}. \tag{3.74}$$

Over the region where $\eta'_r = 0$, the roughness $k'_N$ is set to the grain diameter $d$.

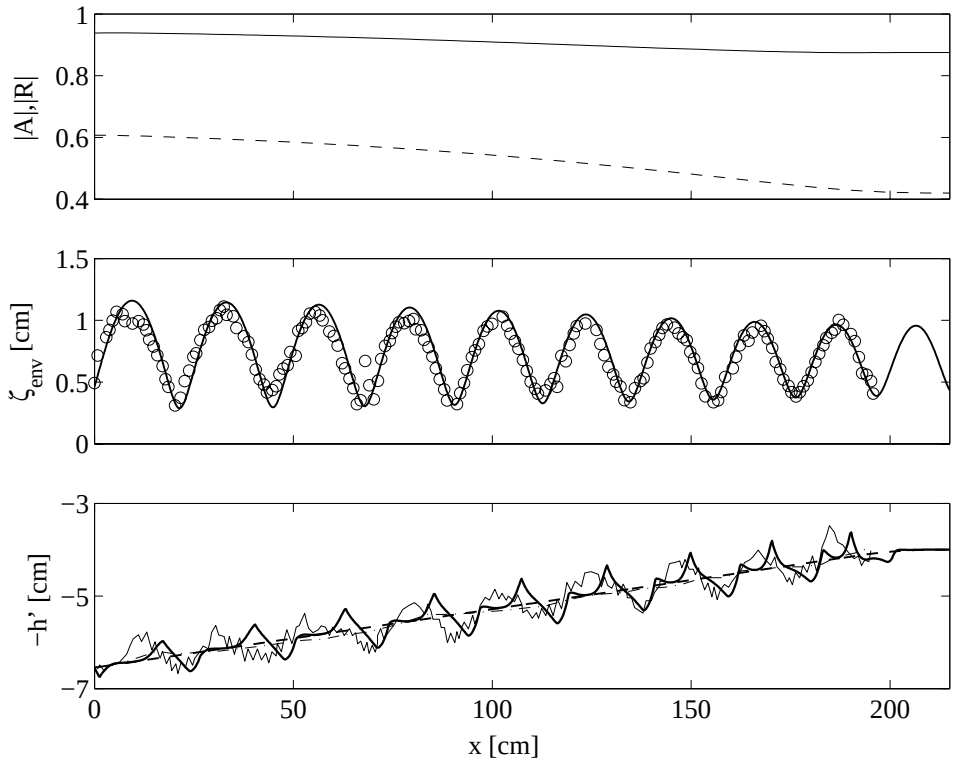


Figure 3-28: Comparison of predictions with test 6 of the fine-grained sand bar experiments Dulou *et al.* (2000) [16], after $t'_f = 1.2 \times 10^4$s $= 3.33$ hrs of wave action. Top: Predicted incident amplitude $|A|$ (solid) and reflection coefficient $R$ (dash). Middle: Predicted (solid) and measured ($\circ$) amplitude of the first harmonic $|\zeta_1^{[1]\prime}|$. Bottom: Predicted seabed elevation $-h' = -H' + \widetilde{h}'$ (thick solid), measured seabed elevation (jagged solid), experimental initial seabed (dash-dot), mean seabed used in simulation $-H'$ (dash). Parameters: $T = 1/1.5$ s, $A_r = 0.73$ cm, $R_L = 0.42e^{0.9\pi i}$, $\Lambda_2^{[0]} = 1.2$. The ripple height $\eta'_r$ used in the predictions is found from Eq. (3.72) with $F_{rip} = 1$.

The computational steps are the same as those for coarse grains outlined in §2.4.4. The only difference is the presence of the new forcing term $-\alpha_2 \partial \overline{q_S}/\partial x$ in the sand bar equation (3.62). Zero boundary conditions are imposed on $\widetilde{h}$ at the ends of the bar patch and the forcing is damped near the ends of the bar patch.

Figures 3-27, 3-28 and 3-29 show that our predictions compare favorably with the measured bed profiles. In particular, the effect of suspended sediments in our model leads to accurate bar height predictions. The predicted and measured bar crests appear close to the antinodes, where the flow is weak. Notice that virtually no ripples appear on the measured bar crests, indicating the shear stress on the bed in those regions is sub-critical. In these sub-critical regions, the bedload transport vanishes, leaving only suspended sediment trans-

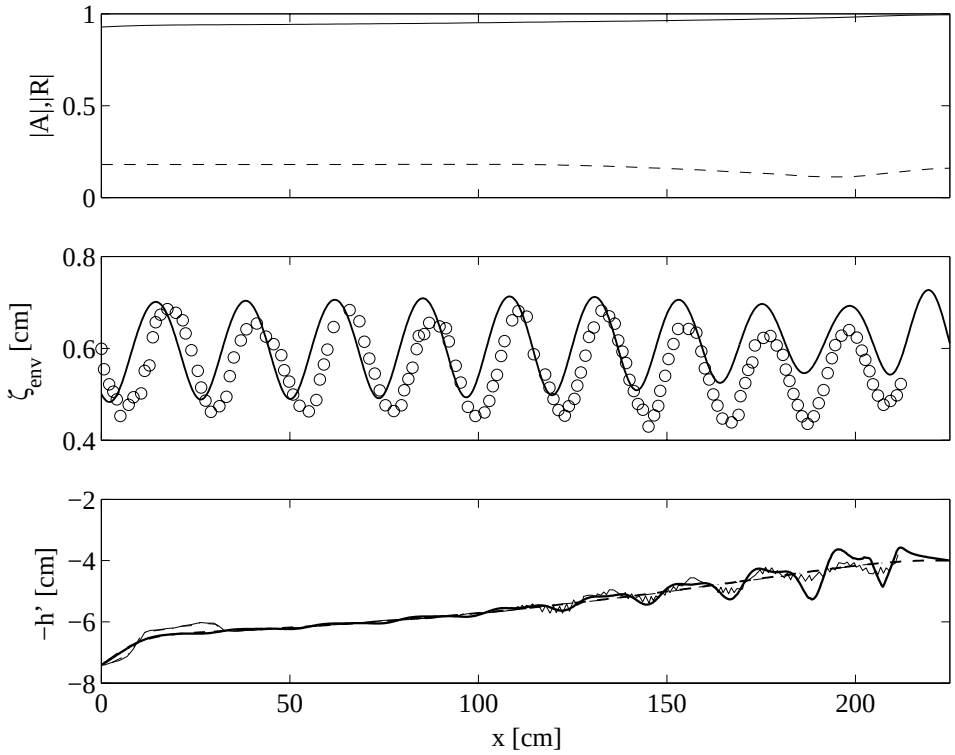


Figure 3-29: Comparison of predictions with test 9 of the fine-grained sand bar experiments Dulou *et al.* (2000) [16], after $t'_f = 1.2 \times 10^5$s = 33.3 hrs of wave action. Top: Predicted incident amplitude $|A|$ (solid) and reflection coefficient $R$ (dash). Middle: Predicted (solid) and measured ($\circ$) amplitude of the first harmonic $|\zeta_1^{[1]\prime}|$. Bottom: Predicted seabed elevation $-h' = -H' + \widetilde{h}'$ (thick solid), measured seabed elevation (jagged solid), experimental initial seabed (dash-dot), mean seabed used in simulation $-H'$ (dash). Parameters: $T = 1/1.5$ s, $A_r = 0.6$ cm, $R_L = 0.16e^{-\pi i/4}$, $\Lambda_2^{[0]} = 0.75$. The ripple height $\eta'_r$ used in the predictions is found from Eq. (3.72) with $F_{rip}$ given in (3.73).

port and local avalanching to control the bar shape. The bedload forcing $-\partial q_\tau/\partial x$ and diffusivity $D_\nu$ in our model also vanish under the antinodes and hence near the bar crests. Furthermore, since avalanching is not included in our model, our predictions contain sharp bar crests, unlike the rounded crests in the observations. Lastly, to gage the importance of suspended sediment in our model, predictions neglecting suspended load transport ($\alpha_2 = 0$) are made in Figure 3-30. These predictions are in very poor agreement with the observations: when suspended sediments are neglected, no bars are predicted on the deeper portion of the slope, bar crests are predicted where troughs are observed, and vice versa. Thus, the addition of suspended sediment transport to our sand bar model leads to significantly better predictions of sand bars on beds of fine grains.

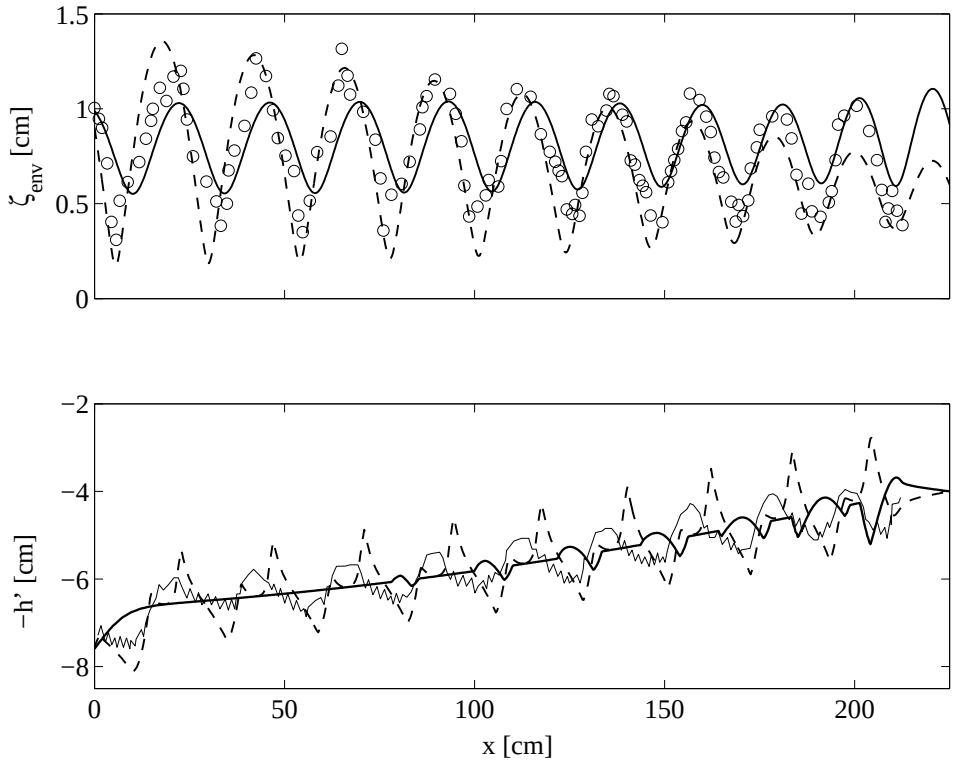


Figure 3-30: Comparison of predictions including and excluding the effects of suspended sediment, for test 3 of the fine-grained sand bar experiments Dulou *et al.* (2000) [16], after $t'_f = 7.2 \times 10^4$s = 20 hrs of wave action. Top: Predicted (solid, dash) and measured ($\circ$) amplitude of the first harmonic $|\zeta_1^{[1]\prime}|$. Bottom: Predicted seabed elevation $-h' = -H' + \widetilde{h}'$ including (dash) and excluding ($\alpha_2 = 0$, thick solid) the effects of suspended sediment, measured seabed elevation (jagged solid). Parameters: $T = 1/1.5$ s, $A_r = 0.8$ cm, $R_L = 0.31e^{-0.3\pi i}$, $\Lambda_2^{[0]} = 1.4$. The ripple height $\eta'_r$ used in the predictions is found from Eq. (3.72) with $F_{rip} = 1$.

| Test | $d$ [mm] | $\alpha_2$ | $P$ | $w_S/u_f$ | $C_o$ |
|---|---|---|---|---|---|
| 324 | 0.200 | 0.14 | 0.74 | 0.31 | $9.17 \times 10^{-5}$ |
| 430 | 0.200 | 0.17 | 0.67 | 0.28 | 0.000117 |
| 508 | 0.200 | 0.25 | 0.61 | 0.26 | 0.000206 |
| 519 | 0.120 | 0.73 | 0.32 | 0.13 | 0.000387 |
| 519 (sim) | 0.110 | 0.99 | 0.27 | 0.11 | 0.000505 |

Table 3.4: Parameters relevant to the suspended sediment forcing for the MIT experiments. The label (sim) indicates a set of parameters used for predictions and associated with a finer grain diameter than that used in the given experimental test.

## 3.12 Comparison with MIT laboratory experiments

The effect of fine grains on bar formation was also investigated in the MIT experiments. Several tests were run with a test bed of fine grains of diameter $d = 0.125$ mm. A test was also run with a mixture of fine and coarse grains (see Chapter 5). In this section, we focus on the tests with beds of uniform sand under nearly monochromatic wave fields that have negligible free second harmonic components. The tests include 324, 430, 508, and 519. The overall setup of the MIT experiments was described in §2.6.

The parameters relevant to diffusion and bedload forcing are listed in Table 2.7 in §2.6 and those relevant to the suspended sediment forcing are listed in Table 3.4. Based on the grain diameters used in the experiments, the ratio of sediment fall velocity to the friction velocity $w_S/u_f < 1/3$ in all cases, indicating that the turbulent eddies in the boundary layer can maintain the sediment in suspension. However, the values of $\alpha_2$ for the tests with the coarse grains of diameter $d = 0.2$ mm are less than $1/4$, suggesting that suspended sediments play a limited role in tests 324, 430 and 508. Predictions based on the parameters for tests 324, 430 and 508 that included effects of suspended sediment were run and plotted as dashed lines in the experimental comparisons in §2.6 of Chapter 2, Figures 2-28 to 2-32 for test 430, Figures 2-36 to 2-40 for test 324, and Figures 2-42 to 2-46 for test 508. In these figures, the predictions with (dashed lines) and without (solid lines) suspended sediment forcing differ very little, consistent with the small values of $\alpha_2$.

The evolution of bars of fine grains of mean diameter $d = 0.120$ mm under pure standing waves ($R_L = 1$) is studied in test 519. The wave parameters are nearly the same as those for Test 430; the main difference is the finer grain diameter. Unfortunately, there was insufficient fine sand available to completely build up the sand bed to a uniform 10 cm

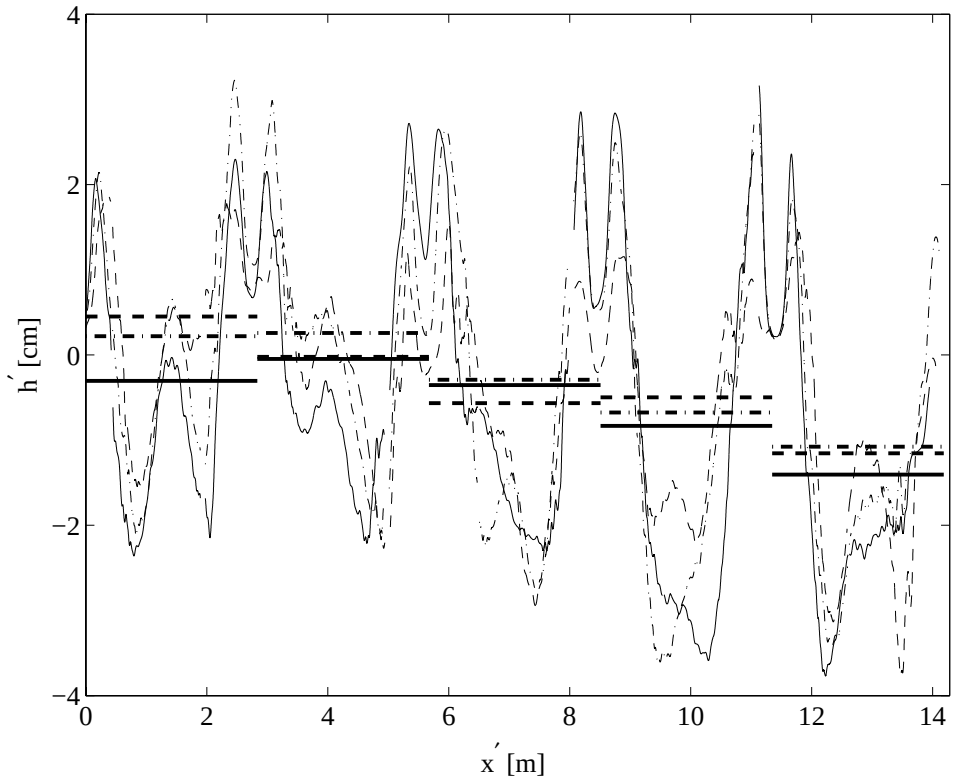


Figure 3-31: Seabed profiles and mean seabed elevation (straight horizontal lines) for test 519 after 0.5 (dash), 2.0 (dash-dot), and 4.1 (solid) days of wave action. $x' = 0$ is 4.78 m from the mean wavemaker position. Gaps in the seabed data are due to vertical tank supports blocking the view.

thickness. Therefore, the sand bed thickness over the last two bars was smaller than that of the first three bars. Also, though the wall at the end of the tank perfectly reflected the waves, it did not completely stop the flow. Seepage occurred under the wall which transported fine grains from the last bar. Due to the laboratory closure for construction, this test could not be repeated. Three seabed profiles after 0.5, 2, and 4 days are shown in Figure 3-31 along with the mean seabed height along each bar. The mean seabed height is 1 to 1.5 cm lower over the last two bars than over the first three. The variation in mean seabed height over the duration of the experiment is within the measurement error and sand bar variability, which we show in Chapter 5 to be approximately 1 cm. Due to the decrease in mean seabed elevation over the last two bars, these are omitted in the comparisons and interpretations that follow.

The wave amplitudes and seabed profiles for test 519 after 4.1 days of wave action are shown in Figure 3-32. The effect of fine grains on sand bar formation is illustrated

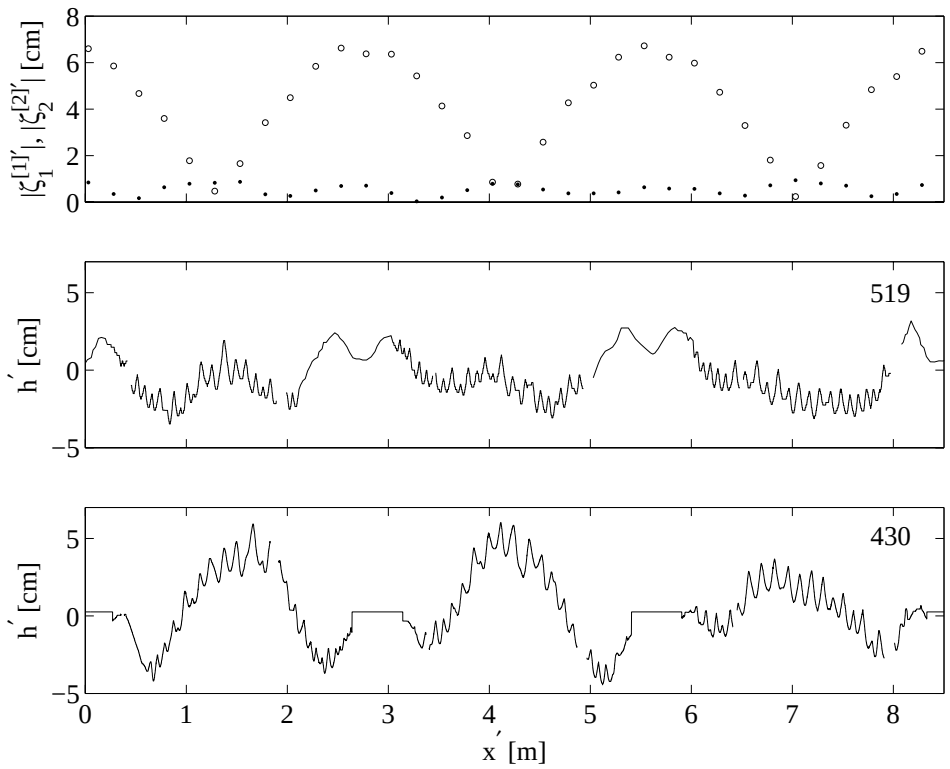


Figure 3-32: Final wave amplitudes and seabed profile (the first three bar lengths) for test 519 after 4.1 days of wave action. Top: first and second harmonic wave amplitudes $\zeta'_{env} = |\zeta_1^{[1]\prime}|$ (○) and $|\zeta_2^{[2]\prime}|$ (●). Middle: seabed profile (ripples and bars). Bottom: for comparison, seabed profile for test 430 after 4.0 days. $x' = 0$ is 4.78 m from the mean wavemaker position. Gaps in the seabed data are due to vertical tank supports blocking the view.

by comparing the final seabed with that of test 430, which had nearly the same wave amplitude and had the same reflection coefficient and mean water depth. For fine grains, the seabed elevation is significantly reduced under the wave node and small narrow crests form adjacent to the sub-critical regions under the wave antinodes, confirming the transport of fine sediments from the wave node toward the wave antinodes. The experiments exhibit considerable variability. The first sand bar has a small sunken crest under the wave node, while the third bar has a trough.

Our predictions are compared to the first three bars in test 519 in Figure 3-33 after 4.1 days of wave action. A time history of the measured and predicted wave amplitudes and bar elevations is shown in Figure 3-34. The agreement is expectedly far less satisfactory than for coarse grains, due to the sensitive dependence of the suspended sediment forcing on the grain diameter. For this experiment, 25% of the mass of each sample of sediment is

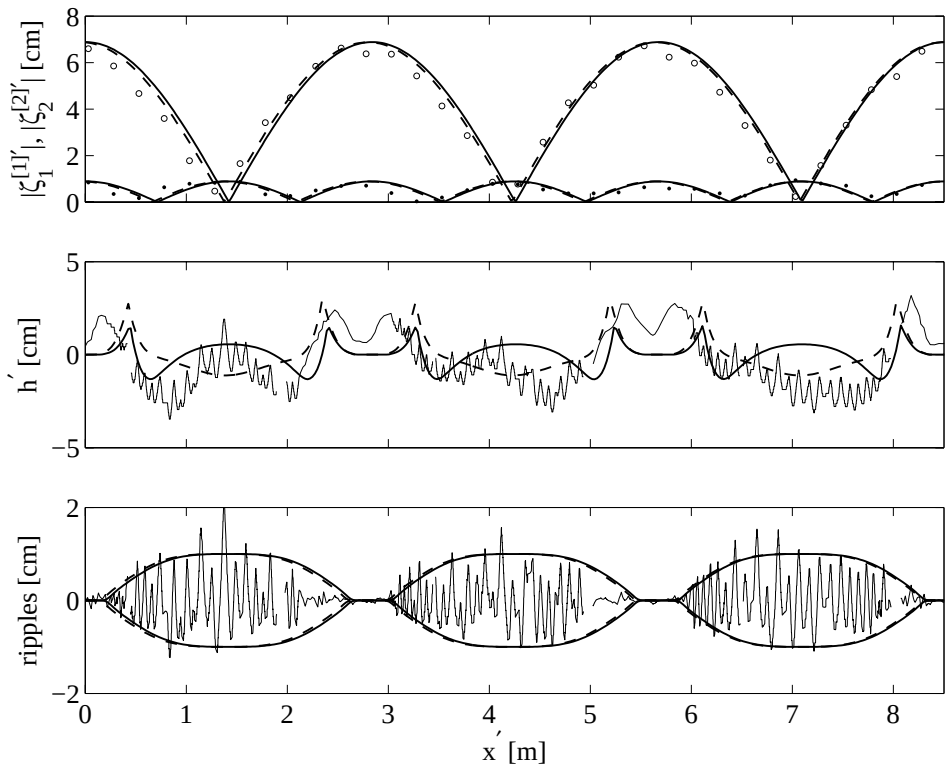


Figure 3-33: Comparison of measured and predicted wave amplitudes (top) and bar elevations (middle) for the first three bars along the tank for test 519 at $t' = 4.06$ days (waves) and $t' = 4.1$ days (bars). The measured first and second harmonic wave amplitudes $\zeta'_{env} = |\zeta_1^{[1]\prime}|$ ($\circ$) and $|\zeta_2^{[2]\prime}|$ ($\bullet$) are plotted above the bar elevation $\widetilde{h}'$ (jagged line). Corresponding predictions are made with $d = 0.120$ mm (smooth solid line) and $d = 0.110$ mm (dashed line). In the bottom plot, measured ripple elevations (jagged line) are compared to the ripple envelope (smooth line) formed by $\pm\eta'_r/2$, where the ripple height $\eta'_r$ is found from Eq. (1.108) with $(r_1, r_2, r_3) = (0.65, 4, 3)$ and $\eta_{ro} = 2.0$ cm. $x' = 0$ is 4.78 m from the mean wavemaker position. Gaps in the bar and ripple data are due to vertical tank supports blocking the view.

finer than $d_{25} = 0.094$ mm. We have made predictions using both the mean grain diameter $d = 0.120$ mm (smooth solid lines in the Figures) and a slightly finer diameter $d = 0.110$ mm (dashed line in the Figures), which is between the mean grain diameter and $d_{25}$. This small difference in grain diameter corresponds to a significant change in the predicted bar shape: bars with $d = 0.120$ mm have small crests under the wave node while those for $d = 0.110$ mm have troughs under the node. The large sensitivity in our theoretical predictions, though unfortunate, is consistent with the variability in the experimental seabed profiles. Despite the sensitivity to grain size, the predictions for both grain sizes have small crests near the wave antinodes, in qualitative agreement with the experiments.

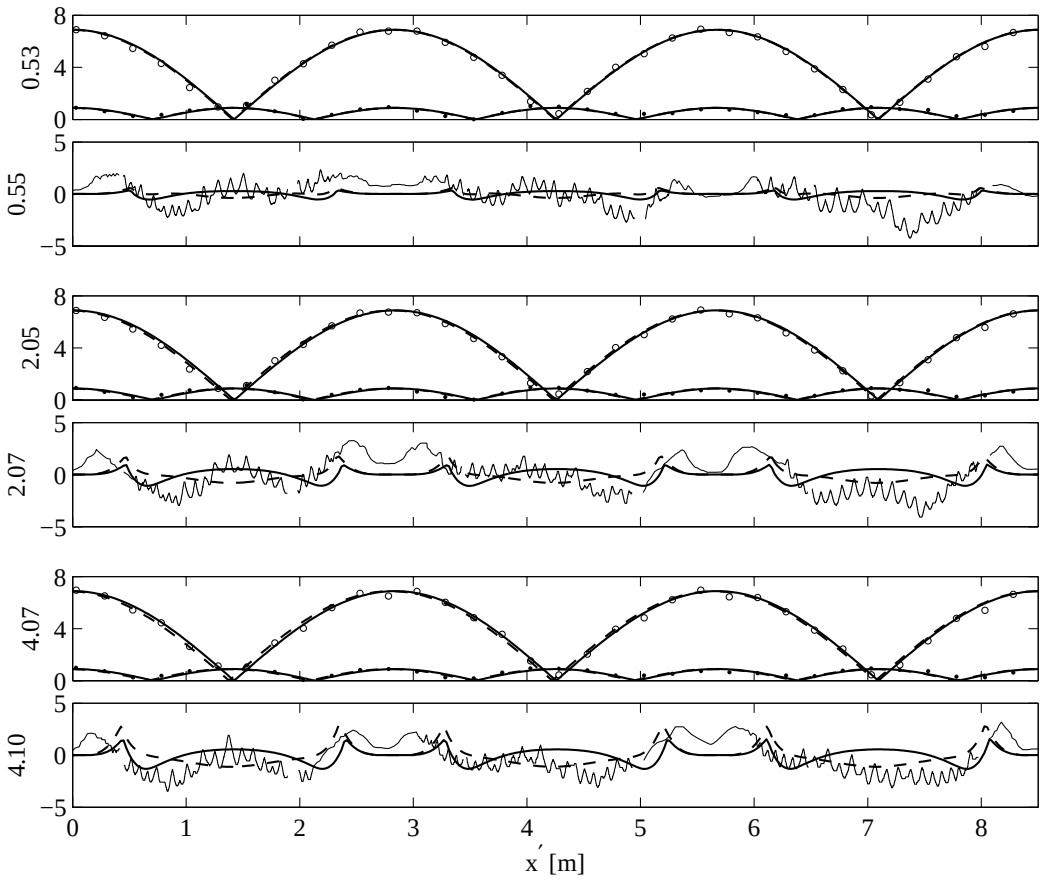


Figure 3-34: Pairs of wave and bar comparisons along the tank for test 519 at various times. For each plot pair, the measured first and second harmonic wave amplitudes $\zeta'_{env} = |\zeta_1^{[1]\prime}|$ ($\circ$) and $|\zeta_2^{[2]\prime}|$ ($\bullet$) are plotted above bar elevations $\widetilde{h}'$ (jagged lines). Corresponding predictions are made with $d = 0.120$ mm (smooth solid line) and $d = 0.110$ mm (dashed line). All vertical scales are in [cm]. $x' = 0$ is 4.78 m from the mean wavemaker position. Numbers left of the wave and seabed elevation plots indicate the corresponding elapsed time in days. Gaps in the bar data are due to vertical tank supports blocking the view.

Lastly, ripple profiles are plotted in Figure 3-33 along with the fitted ripple height $\eta'_r(x)$ from Eq. (1.108) with $(r_1, r_2, r_3) = (0.65, 4, 3)$ and $\eta_{ro} = 2.0$ cm.

| Test | $d$ [mm] | $\alpha_2$ | $P$ | $w_S/u_f$ | $C_o$ |
|---|---|---|---|---|---|
| Dolan 1 | 0.188 | 8.32 | 0.43 | 0.12 | 0.00251 |
| Dolan 5 | 0.188 | 10.18 | 0.42 | 0.15 | 0.00292 |
| Dolan 6 | 0.223 | 5.14 | 0.60 | 0.20 | 0.00102 |
| Elgar | 0.330 | 2.84 | 0.76 | 0.26 | 0.00033 |
| Sim | 0.200 | 6.46 | 0.45 | 0.19 | 0.00253 |
| Sim | 0.500 | 0.52 | 1.02 | 0.43 | 0.00020 |

Table 3.5: Parameters relevant to fine grains for bar predictions corresponding to the observations of Dolan [14] (sites 1, 5, 6) and of Elgar *et al.* [17], and for predictions on the prototypical beach (2.151), denoted by Sim.

## 3.13 The effect of fine grains on bars in the field

The effect of fine grains on bars in the field is investigated by including the suspended sediment forcing in bar predictions corresponding to the field observations considered in §2.7. Predictions are also made of the formation of bars of fine grains on the prototypical beach (2.151).

Parameters relevant to fine grains are listed in Table 3.5 for the observations of Dolan & Dean (1985) [15] (sites 1, 5, 6) and of Elgar *et al.* [17]. Note that $\alpha_2 > 1$ and $P < 1$ in all cases, suggesting that the effect of fine grains is important. However, recall from Tables 2.8 and 2.9 that the dispersion parameters $KH_o$ associated with these observations are quite small, and the term $1/\sinh^2 KH_o$ dominates the bedload transport. Thus, in our bar predictions, the inclusion of the suspended sediment forcing has a negligible effect for the observations of Elgar, and only a mild effect for the observations of Dolan & Dean. Figure 3-35 illustrates the effect of fine grains on bar predictions corresponding to Dolan & Dean [15]'s site 5. Predictions are made with (solid) and without (dash) the suspended sediment forcing. The amplitude of the rightmost bar is increased somewhat with the inclusion of suspended sediment forcing. This increase alters the local reflection coefficient, which in turn affects the waves seaward of that point.

Next, predictions analogous to those in §2.7.3 are made for bars of fine sand on the prototypical beach (2.151). The parameters are the same as those used in §2.7.3, except that small grain diameters are considered. In particular, the time scale of sand bar formation $\alpha_1/\omega$ is between 25 and 40 days. In the field, the properties of the incident waves are only steady for half a day, at most. Thus, we limit the duration of our predictions to 3 days,

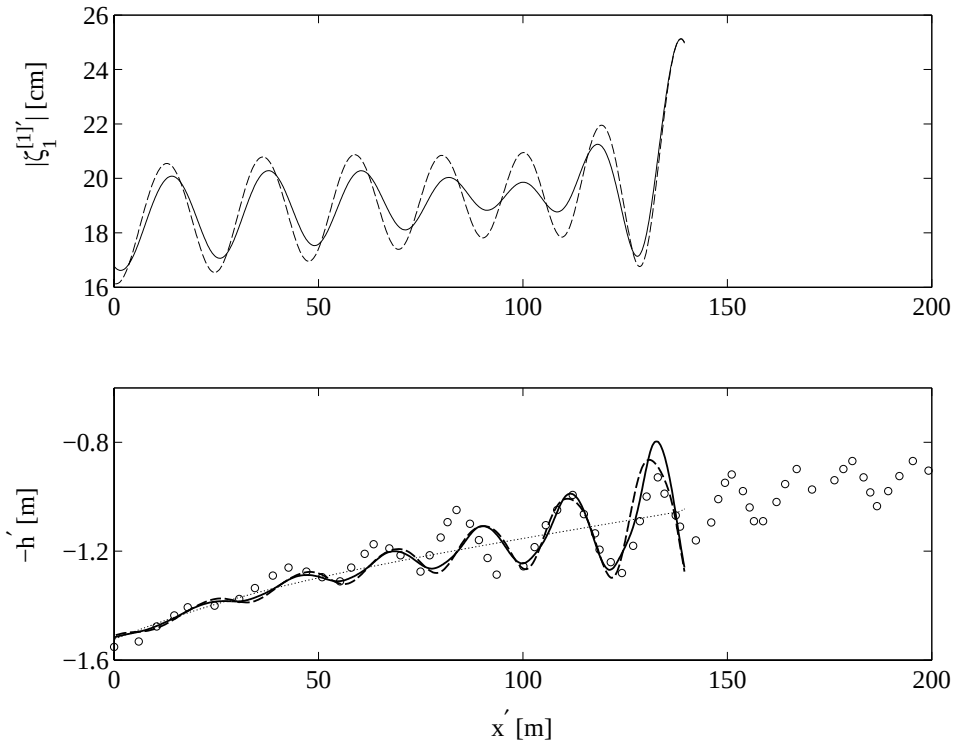


Figure 3-35: The effects of fine grains on our predictions corresponding to Dolan & Dean (1985) [15]'s observations of bars at Site 5 in Chesapeake Bay (data (∘) from Dolan (1983) [14]). The predictions are based on the parameters listed for Site 5 in Tables 2.8 and 3.5. The amplitude of the first wave harmonic $|\zeta_1^{[1]\prime}|$ (top) and seabed profiles $z' = -h' = -H' + \widetilde{h}'$ (bottom) are given after 8 hours of wave action for predictions with (solid) and without ($\alpha_2 = 0$, dash) the suspended sediment forcing. The mean beach profile $z' = -H'$ (the initial condition) is indicated by the dotted line.

which corresponds to the early stage of bar formation. Parameters relevant to suspended sediment are listed in Table 3.5.

Figure 3-36 illustrates that under strong shoreline reflection $R_L = 1$ (waves in front of a seawall or steep shore), bars of fine grains (solid line) have the characteristic troughs under the wave nodes and crests near the sub-critical regions, while those of coarse grains (dashed line) have crests under the wave nodes and troughs neighboring the sub-critical regions. The bar heights associated with coarse grains are larger than those for fine grains.

Under weak shoreline reflection $R_L = 0.25$, the difference between bars of fine and coarse sand relies on the particular value of the return flow stress parameter $\Lambda_2^{[0]}$. Figure 3-37($i$) shows a striking difference between bars of coarse and fine sand for $\Lambda_2^{[0]} = 2$. Crests of the fine-grained bars appear behind the wave nodes and the corresponding wave height decreases shoreward. Crests of the coarse-grained bars appear directly under or just ahead

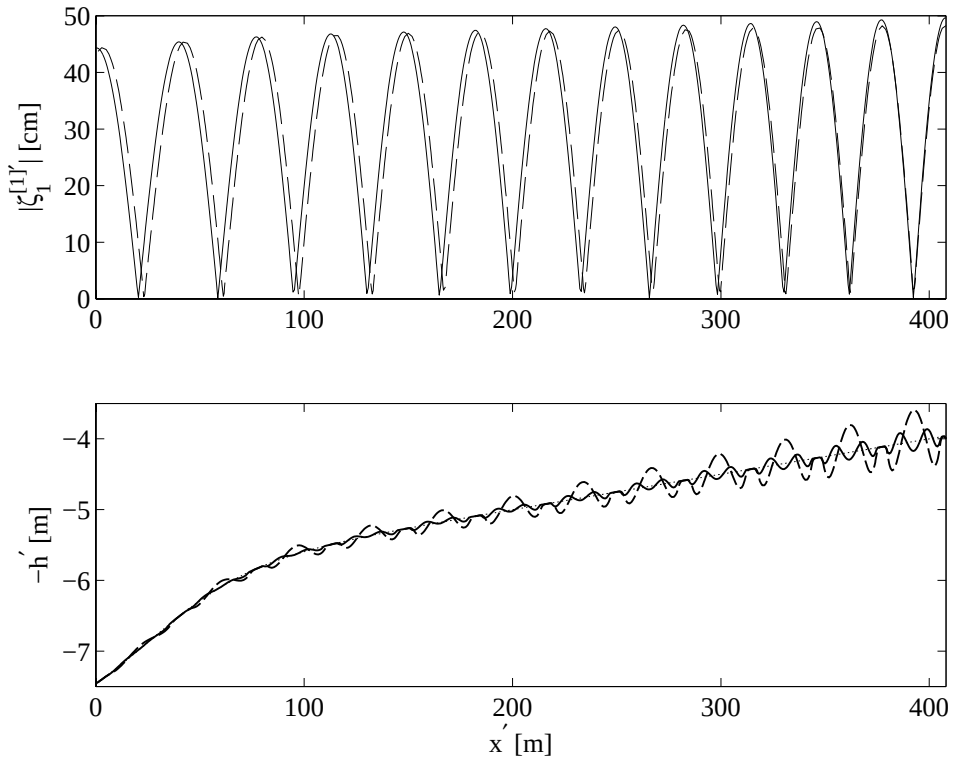


Figure 3-36: Wave amplitude $|\zeta_1^{[1]\prime}|$ (top) and bar profiles $\widetilde{h}$ (bottom) on the prototypical beach $H'$ (2.151) with strong shoreline reflection $R_L = 1$, after 3 days of wave action for bars of fine (solid) and coarse (dash) grains. The other parameters are $T = 10$ s, $A'(0) = 22.2$ cm, $A_o(1 + |R_L|) = 50$ cm, $H_o = 4$ m, and $d = 0.2$ mm, $\eta_r' = 1$ cm (solid) and $d = 0.5$ mm, $\eta_r' = 5.5$ cm (dash). The mean beach profile $z = -H'$ (the initial condition) is indicated by the dotted line.

of the wave node, and the corresponding wave height increases shoreward. The heights of the fine-grained bars are larger than those of the coarse-grained bars along the deeper section of the beach. The situation is different for smaller values of $\Lambda_2^{[0]}$. Figure 3-37($ii$) shows that for $\Lambda_2^{[0]} = 1$, the fine-grained bar crests appear in front of the wave node, as do those for coarse grains. The bar and wave heights associated with both fine and coarse grains are very similar. The wave amplitude and seabed profiles for different return flow bed stress coefficients $\Lambda_2^{[0]}$ are plotted together in Figure 3-38. The conclusion is that the effect of the return flow is important and demands further experimental study.

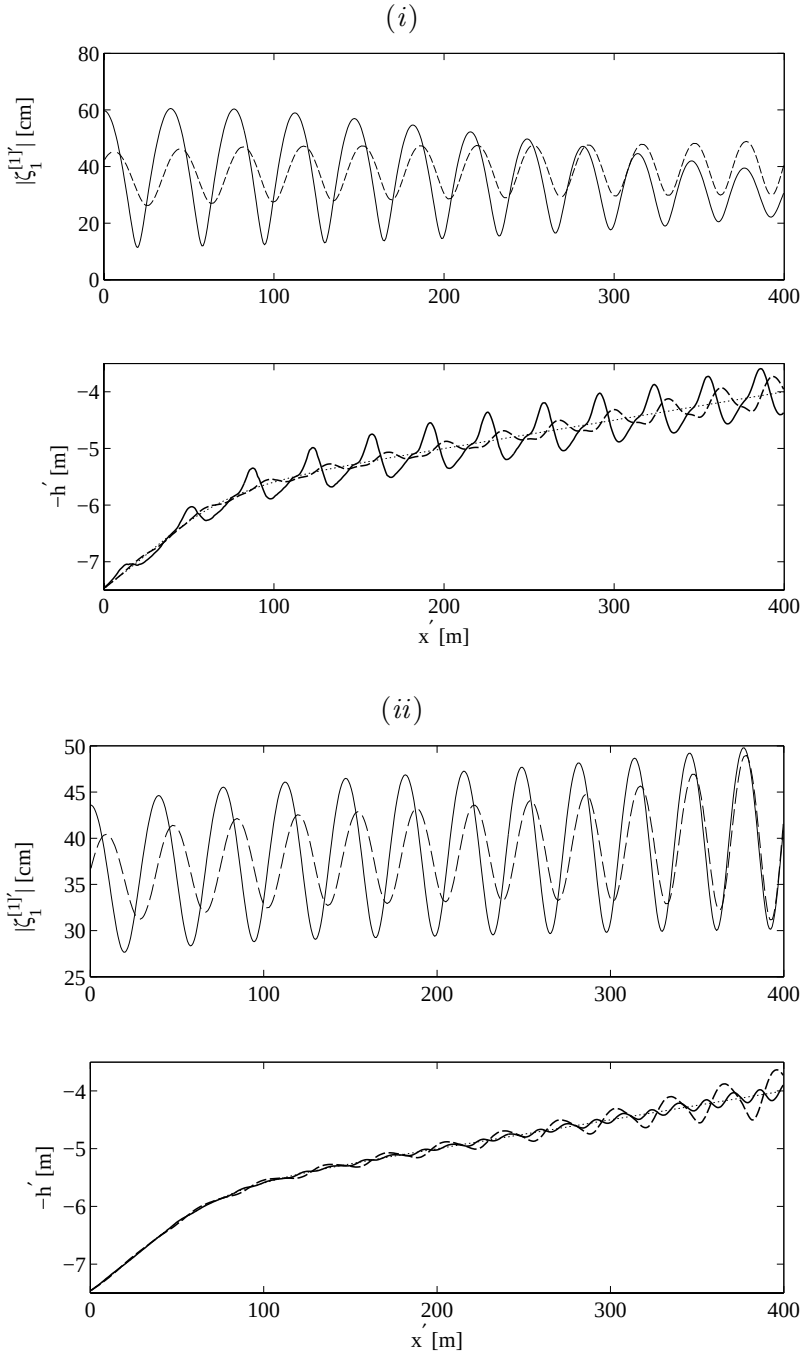


Figure 3-37: Wave amplitude $|\zeta_1^{[1]\prime}|$ and bar profiles $\widetilde{h}'$ on the prototypical beach (2.151) with weak shoreline reflection $R_L = 0.25$, after 3 days of wave action. Predictions for fine grains ($d = 0.2$ mm, $\eta_r' = 1$ cm, solid lines) and coarse grains ($d = 0.5$ mm, $\eta_r' = 5.5$ cm, dashed lines) are shown. The return flow stress coefficient is $(i)$ $\Lambda_2^{[0]} = 2$ and $(ii)$ $\Lambda_2^{[0]} = 1$. The other parameters are $T = 10$ s, $A'(0) = 35.5$ cm, $A_o(1 + |R_L|) = 50$ cm, and $H_o = 4$ m. Bar elevations $\widetilde{h}'$ are superposed on the mean beach profile $z = -H'$ (also the initial condition), indicated by the dotted line.

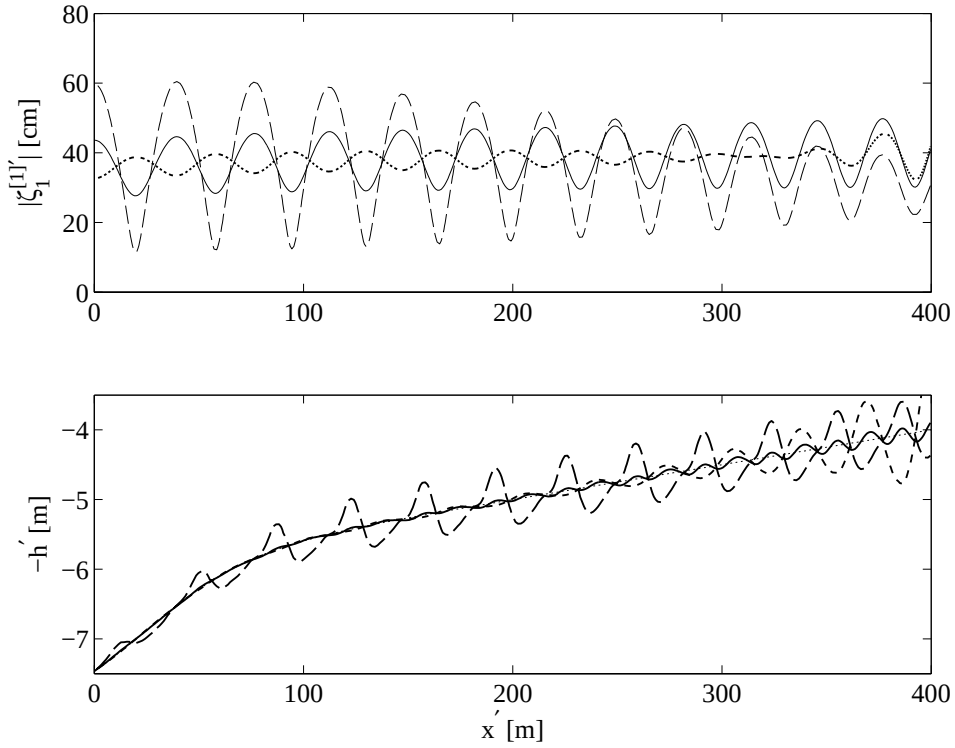


Figure 3-38: The effect of return flow on predictions of bars of fine grains ($d = 0.2$ mm) on the prototypical beach (2.151) with weak shoreline reflection $R_L = 0.25$. The wave amplitude $|\zeta_1^{[1]\prime}|$ (top) and bar profiles $\widetilde{h}'$ (bottom) are plotted after 3 days of wave action. The value of the return flow bed stress coefficient for each curve is $\Lambda_2^{[0]} = 0$ (short dash), $\Lambda_2^{[0]} = 2$ (solid), $\Lambda_2^{[0]} = 4$ (long dash). The other parameters are $T = 10$ s, $A'(0) = 35.5$ cm, $A_o(1 + |R_L|) = 50$ cm, $H_o = 4$ m, and $\eta_r' = 1$ cm. Bar elevations $\widetilde{h}'$ are superposed on the mean beach profile $z = -H'$ (also the initial condition), indicated by the dotted line.

## 3.14 Appendix

### 3.14.1 First order concentration

The solution to (3.53) and (3.54) is

$$\begin{aligned} C_2^{[1]} \;=\; & -e^{-\widetilde{P}\widetilde{\eta}}\left(A_1 i + \left(\frac{\widetilde{P}}{2} + i\widetilde{\eta}\right)(A_2 + A_5)\right) \\ & -\frac{e^{-\Gamma_4\widetilde{\eta}}}{\widetilde{P}}\left((1+i)\left(A_1 + \frac{\widetilde{\eta}}{2}A_5\right) + \frac{i}{\widetilde{P}}\left(\frac{\widetilde{P}}{2} + 1 - i\right)A_5\right) \\ & +\frac{e^{-\widetilde{P}\beta_2\widetilde{\eta}}}{\Gamma_1}\left(A_3 + \left(\widetilde{\eta} + \frac{\Gamma_2}{\Gamma_1}\right)\left\{A_4 + A_6\left(1 + \frac{4i}{\widetilde{P}\beta_2\Gamma_2}\right)\right\}\right) \\ & -\frac{e^{-\Gamma_5\widetilde{\eta}}}{\Gamma_3}\left(A_3 + A_6\left(\frac{1}{2} + \frac{4i}{\widetilde{P}\beta_2\Gamma_2}\right)\left(\frac{\Gamma_2 + 2(1+i)}{\Gamma_3} + \widetilde{\eta}\right)\right) + A_7 e^{-\widetilde{P}\beta_1\widetilde{\eta}}, \end{aligned} \tag{3.75}$$

where $\widetilde{\eta} = \eta/\sqrt{\nu_e}$, $\widetilde{P} = P/\sqrt{\nu_e}$ and

$$\Gamma_1 = \frac{P^2\beta_2}{\nu_e}(\beta_2 - 1) + 2i, \qquad \Gamma_2 = \frac{P}{\sqrt{\nu_e}}(2\beta_2 - 1), \qquad \Gamma_3 = \Gamma_1 + (1+i)\Gamma_2 + 2i,$$

$$\Gamma_4 = \frac{P}{\sqrt{\nu_e}} + 1 - i, \qquad \Gamma_5 = \frac{P\beta_2}{\sqrt{\nu_e}} + 1 + i$$

$$\begin{aligned}
A_1 &= U_1^{[1]}\frac{\partial \widehat{C}}{\partial x} - \frac{1+i}{4}(2A_2 + A_5), \qquad A_2 = \frac{P}{\sqrt{\nu_e}}\widehat{C}\frac{\partial U_1^{[1]}}{\partial x}, \\
A_3 &= U_1^{[1]*}\frac{\partial \widehat{C^{[2]}}}{\partial x} - \frac{1-i}{4}(2A_4 + A_6), \qquad A_4 = \frac{P\beta_2}{\sqrt{\nu_e}}\widehat{C^{[2]}}\,\frac{\partial U_1^{[1]*}}{\partial x}, \qquad (3.76) \\
A_5 &= P\widehat{C}\frac{U_1^{[1]}}{\nu_e^{3/2}}\frac{\partial \nu_e}{\partial x}, \qquad A_6 = P\beta_2\widehat{C^{[2]}}\frac{U_1^{[1]*}}{\nu_e^{3/2}}\frac{\partial \nu_e}{\partial x},
\end{aligned}$$

$$\begin{aligned}
A_7 &= \frac{i\Gamma_4\sqrt{\nu_e}}{P}A_1 + \frac{P}{2\sqrt{\nu_e}}A_2 + \left(\frac{1}{\Gamma_3} - \frac{1}{\Gamma_1}\right)A_3 - \frac{\Gamma_2}{\Gamma_1^2}\left(A_4 + \frac{A_6}{2}\right) \qquad (3.77) \\
&+ \left(\frac{P}{2\sqrt{\nu_e}} + \frac{i\nu_e}{P^2}\left(\frac{P}{2\sqrt{\nu_e}} + 1 - i\right)\right)A_5 \\
&+ \left(\frac{1}{2} + \frac{4i\sqrt{\nu_e}}{P\beta_2\Gamma_2}\right)\left(\frac{\Gamma_2 + 2(1+i)}{\Gamma_3^2} - \frac{\Gamma_2}{\Gamma_1^2}\right)A_6.
\end{aligned}$$

### 3.14.2 Suspended sediment flux

Defining

$$\begin{aligned}
I_1(q) &\equiv \frac{1}{q} - \frac{1}{1+i+q}, \\
I_2(q) &\equiv \frac{1}{q^2} - \frac{1}{(1+i+q)^2},
\end{aligned}$$

we readily compute

$$\begin{aligned}\frac{\left\langle u_1^{[1]*}C_2^{[1]}\right\rangle}{\sqrt{\nu_e}U_1^{[1]*}} &= -\left(A_1 i+\frac{\widetilde{P}}{2}\left(A_2+A_5\right)\right)I_1\left(\widetilde{P}\right)-i\left(A_2+A_5\right)I_2\left(\widetilde{P}\right)\\ &+\frac{A_3 I_1\left(\widetilde{P}\beta_2\right)}{\Gamma_1}+A_7 I_1\left(\widetilde{P}\beta_1\right)-\frac{1+i}{2\widetilde{P}}A_5 I_2\left(\Gamma_4\right)-\frac{A_3 I_1\left(\Gamma_5\right)}{\Gamma_3} \qquad (3.78)\\ &-\frac{1}{\widetilde{P}}\left(\left(1+i\right)A_1+\frac{i}{\widetilde{P}}\left(\frac{\widetilde{P}}{2}+1-i\right)A_5\right)I_1\left(\Gamma_4\right)\\ &+\frac{1}{\Gamma_1}\left(I_2\left(\widetilde{P}\beta_2\right)+\frac{\Gamma_2}{\Gamma_1}I_1\left(\widetilde{P}\beta_2\right)\right)\left(A_4+A_6\left(1+\frac{4i}{\widetilde{P}\beta_2\Gamma_2}\right)\right)\\ &-\frac{A_6}{\Gamma_3}\left(\frac{1}{2}+\frac{4i}{\widetilde{P}\beta_2\Gamma_2}\right)\left(\frac{\Gamma_2+2\left(1+i\right)}{\Gamma_3}I_1\left(\Gamma_5\right)+I_2\left(\Gamma_5\right)\right).\end{aligned}$$

where $\widetilde{P}=P/\sqrt{\bar{\nu}_e}$. Rearranging gives Eq. (3.67),

$$\begin{aligned}\left\langle u_1^{[1]*}C_2^{[1]}\right\rangle &= \sqrt{\bar{\nu}_e}U_1^{[1]*}\left(F_{11}U_1^{[1]}\frac{\partial\widehat{C}}{\partial x}+F_{12}U_1^{[1]*}\frac{\partial\widehat{C^{[2]}}}{\partial x}+F_{13}\widehat{C}\frac{\partial U_1^{[1]}}{\partial x}\right.\\ &\left.+F_{14}\widehat{C^{[2]}}\frac{\partial U_1^{[1]*}}{\partial x}+\left(F_{15}U_1^{[1]}\widehat{C}+F_{16}U_1^{[1]*}\widehat{C^{[2]}}\right)\frac{1}{\bar{\nu}_e}\frac{\partial\bar{\nu}_e}{\partial x}\right),\end{aligned}$$

where

$$F_{11} = \frac{\left(2-6i\right)\left(1+\widetilde{P}\right)+\left(1-i\right)\widetilde{P}^2}{\widetilde{P}\left(2+\widetilde{P}\right)\left(\widetilde{P}^2+2\widetilde{P}+2\right)}+\frac{i}{\widetilde{P}}\Gamma_4 I_1\left(\widetilde{P}\beta_1\right), \qquad (3.79)$$

$$F_{12} = \frac{I_1\left(\widetilde{P}\beta_2\right)}{\Gamma_1}-\frac{I_1\left(\Gamma_5\right)}{\Gamma_3}+\left(\frac{1}{\Gamma_3}-\frac{1}{\Gamma_1}\right)I_1\left(\widetilde{P}\beta_1\right), \qquad (3.80)$$

$$F_{13}=-\frac{1+i}{2}-\frac{i}{\widetilde{P}}-\frac{i}{2+\widetilde{P}}+\frac{1-i}{\Gamma_4^{*2}}+\frac{4i-\left(1-3i\right)\widetilde{P}}{\widetilde{P}^2+2\widetilde{P}+2}+\frac{\widetilde{P}^2+\left(1-i\right)\widetilde{P}-2i}{2}I_1\left(\widetilde{P}\beta_1\right), \qquad (3.81)$$

$$\frac{F_{14}}{\widetilde{P}\beta_2}=\frac{1}{\Gamma_1}\left(\frac{1-i}{2}-\frac{\Gamma_2}{\Gamma_1}\right)\left(I_1\left(\widetilde{P}\beta_1\right)-I_1\left(\widetilde{P}\beta_2\right)\right)+\frac{I_2\left(\widetilde{P}\beta_2\right)}{\Gamma_1}+\frac{1-i}{2\Gamma_3}\left(I_1\left(\Gamma_5\right)-I_1\left(\widetilde{P}\beta_1\right)\right), \qquad (3.82)$$

$$
\begin{aligned}
F_{15} &= -\frac{1-i+2\widetilde{P}}{4}\widetilde{P}I_1\left(\widetilde{P}\right)-\frac{1+i}{\widetilde{P}}I_1\left(\Gamma_4\right)-i\widetilde{P}I_2\left(\widetilde{P}\right)-\frac{(1+i)\,I_2\left(\Gamma_4\right)}{2} \\
&\quad +\frac{(1-i)\,\widetilde{P}^3-i\widetilde{P}^2+4}{2\,(1-i)\,\widetilde{P}}I_1\left(\widetilde{P}\beta_1\right),
\end{aligned}
\tag{3.83}
$$

$$
\begin{aligned}
\frac{F_{16}}{\widetilde{P}\beta_2} &= \left(\frac{1-i}{4}\Gamma_1-\Gamma_2-\frac{4i}{\widetilde{P}\beta_2}\right)\frac{I_1\left(\widetilde{P}\beta_1\right)-I_1\left(\widetilde{P}\beta_2\right)}{\Gamma_1^2} \\
&\quad +\left(1+i+\frac{\Gamma_2}{2}-\frac{1-i}{4}\Gamma_3+\frac{4}{\widetilde{P}\beta_2}\left(i-\frac{2\,(1-i)}{\Gamma_2}\right)\right)\frac{I_1\left(\widetilde{P}\beta_1\right)-I_1\left(\Gamma_5\right)}{\Gamma_3^2} \\
&\quad +\frac{I_2\left(\widetilde{P}\beta_2\right)}{\Gamma_1}-\frac{I_2\left(\Gamma_5\right)}{2\Gamma_3}+\frac{4i}{\widetilde{P}\beta_2\Gamma_2}\left(\frac{I_2\left(\widetilde{P}\beta_2\right)}{\Gamma_1}-\frac{I_2\left(\Gamma_5\right)}{\Gamma_3}\right).
\end{aligned}
\tag{3.84}
$$

Note also that

$$
\begin{aligned}
F_{00}\left(q\right) &= \frac{1}{2q\,(2+q)}\left(1-i-\frac{4}{q^2+2q+2}-\frac{2i\,(q+2+2i)}{(q+1+i)^2}\right), \\
F_{01}\left(q\right) &= -\frac{1}{q\left(q^2+2q+2\right)^2}, \\
F_{20}\left(q\right) &= \frac{q\left(1-1/\sqrt{2}\right)(1-i)+1}{\left(q+\sqrt{2}\,(1+i)\right)(q+1+i)^2}, \\
F_{21}\left(q\right) &= \frac{1}{q}-\frac{1}{q+\sqrt{2}\,(1+i)}, \\
F_{22}\left(q\right) &= i\frac{2\,(1+i)+3q}{4\,(q+1+i)^2}+\frac{i}{8\,(q+2+2i)}-\frac{7i}{8\left(q+\sqrt{2}\,(1+i)\right)}.
\end{aligned}
\tag{3.85}
$$

We now specialize the above results to monochromatic (partially) standing waves in intermediate depth. From Eqs. (3.14) and (2.39),

$$
\widehat{C^{[2]}}\left(x\right)=\frac{2}{3}\widehat{C}e^{-2i\varpi}=\frac{2i}{3}\widehat{C}\frac{\mathcal{K}_1\left(Z_b\right)\mathcal{K}_0^*\left(Z_b\right)U_1^{[1]}}{\mathcal{K}_1^*\left(Z_b\right)\mathcal{K}_0\left(Z_b\right)U_1^{[1]*}}.
\tag{3.86}
$$

Differentiating (3.86) gives

$$\frac{\partial\widehat{C^{[2]}}}{\partial x} = \frac{2i}{3U_1^{[1]*}}\frac{\mathcal{K}_1(Z_b)\mathcal{K}_0^*(Z_b)}{\mathcal{K}_1^*(Z_b)\mathcal{K}_0(Z_b)}\left(U_1^{[1]}\frac{\partial\widehat{C}}{\partial x}+\widehat{C}\left(\frac{U_1^{[1]*}}{U_1^{[1]*}}\frac{\partial U_1^{[1]}}{\partial x}-\frac{U_1^{[1]}}{U_1^{[1]*}}\frac{\partial U_1^{[1]*}}{\partial x}\right)\right) + \frac{2iU_1^{[1]}}{3U_1^{[1]*}}\widehat{C_0}(x)\frac{d}{dx}\left(\frac{\mathcal{K}_1(Z_b)\mathcal{K}_0^*(Z_b)}{\mathcal{K}_1^*(Z_b)\mathcal{K}_0(Z_b)}\right). \tag{3.87}$$

Substituting (1.85), (3.86), (3.87) into Eqs. (3.66) – (3.68) and (3.65) yields Eq. (3.69),

$$\frac{\overline{qs}}{\widehat{C}\sqrt{\bar{\nu}_e}} = \left(E_1+\frac{E_2}{\sinh^2 kH}\right)U_1^{[1]*}\frac{\partial U_1^{[1]}}{\partial x}+E_3\frac{\left|U_1^{[1]}\right|^2}{\widehat{C}}\frac{\partial\widehat{C_0}}{\partial x}+E_4\frac{\left|U_1^{[1]}\right|^2}{\bar{\nu}_e}\frac{\partial\bar{\nu}_e}{\partial x} + \frac{2U_2^{[0]}\bar{\nu}_e^{3/2}}{Z_1u_fP^2}+\left|U_1^{[1]}\right|^2E_5\frac{dZ_b}{dx},$$

where

$$E_1 = F_{00}\left(\frac{P}{\sqrt{\bar{\nu}_e}}\right)+\frac{2i}{3}\Re\left\{F_{12}e^{i\varpi_E}\right\}+\frac{1}{2}F_{13}-\frac{i}{3}e^{-i\theta_E}\left(F_{14}^*+F_{20}^*\left(\frac{P\beta_2^*}{\sqrt{\bar{\nu}_e}}\right)\right), \tag{3.88}$$

$$E_2 = -\frac{1}{4}e^{-i\theta_E}F_{21}^*\left(\frac{P\beta_2^*}{\sqrt{\bar{\nu}_e}}\right), \tag{3.89}$$

$$E_3 = \Re\left\{\frac{1}{2}F_{11}+\frac{i}{3}e^{i\theta_E}F_{12}\right\}, \tag{3.90}$$

$$E_4 = \Re\left\{F_{01}\left(\frac{P}{\sqrt{\bar{\nu}_e}}\right)+\frac{1}{2}F_{15}+\frac{i}{3}e^{i\theta_E}\left(F_{16}+F_{22}\left(\frac{P\beta_2}{\sqrt{\bar{\nu}_e}}\right)\right)\right\}, \tag{3.91}$$

$$E_5 = \frac{\sqrt{2}}{3\sqrt{Z_b}}\Re\left\{\frac{F_{12}}{\mathcal{K}_1^{*2}(Z_b)\mathcal{K}_0^2(Z_b)}\right\}\mathrm{Im}\left\{(1+i)\left(\mathcal{K}_1^2(Z_b)+\mathcal{K}_0^2(Z_b)\right)\mathcal{K}_1^*(Z_b)\mathcal{K}_0^*(Z_b)\right\}, \tag{3.92}$$

$$e^{i\theta_E} = \frac{\mathcal{K}_1(Z_b)\mathcal{K}_0^*(Z_b)}{\mathcal{K}_1^*(Z_b)\mathcal{K}_0(Z_b)}.$$

### 3.14.3 Net mean suspended sediment flux

In this section we discuss an alternative bottom boundary condition for the suspended sediment concentration: the mean net flux. We first derive an equation for the mean net flux and then relate it to the reference concentration. Substituting (3.44) into (3.8),

averaging over the short wave period, and integrating in $\eta$ across the boundary layer gives

$$\begin{aligned}\left\{\frac{P}{2}C_3^{[0]}+\frac{\nu_e}{2}\frac{\partial C_3^{[0]}}{\partial\eta}\right\}_{\eta=0} &= -\frac{\partial\left\langle C_1^{[0]}\right\rangle}{\partial t_2}-\frac{\partial}{\partial x}\left(\left\langle\overline{u_1C_2}\right\rangle+\left\langle\overline{u_2C_1}\right\rangle\right)-\left\{w_1C_2+w_2C_1\right\}_{\eta=0}^{\infty}\\ &\quad -\frac{D_h}{2}\left(-\frac{\partial H}{\partial x_1}+\frac{\partial\widetilde{h}}{\partial x}\right)^2\frac{\partial\overline{C}}{\partial\eta}\Big|_{\eta=0}\\ &= -\frac{\partial\widehat{C}}{\partial t_2}\frac{\bar{\nu}_e}{P}-\frac{\partial\overline{q_S}}{\partial x}+\frac{PD_h}{2\bar{\nu}_e}\left(-\frac{\partial H}{\partial x_1}+\frac{\partial\widetilde{h}}{\partial x}\right)^2\widehat{C}, \qquad (3.93)\end{aligned}$$

where $t_2=\varepsilon^2t$ and we used (2.6) and (3.48) for $w_1$ and $C_1$, respectively. Notice that the net mean flux of sediment from the seabed into suspension is, from (3.48) and (3.55),

$$\varepsilon^2\overline{F_{net}}=-\overline{\left\{\frac{P}{2}C+\frac{\nu_e}{2}\frac{\partial C}{\partial\eta}\right\}_{\eta=0}}=-\varepsilon^2\left\{\frac{P}{2}C_3^{[0]}+\frac{\nu_e}{2}\frac{\partial C_3^{[0]}}{\partial\eta}\right\}_{\eta=0}.$$

Therefore, substituting (3.48) into (3.93) gives the net mean flux

$$\overline{F_{net}}=-\frac{\partial\widehat{C}}{\partial t_2}-\frac{P}{\nu_e}\frac{\partial\overline{q_S}}{\partial x}+\frac{P^2D_h}{2\nu_e^2}\left(-\frac{\partial H}{\partial x_1}+\frac{\partial\widetilde{h}}{\partial x}\right)^2\widehat{C}. \qquad (3.94)$$

For a flat bed ($\partial H/\partial x_1=0$, $\widetilde{h}=0$), Mei and Chian (1994) defined the net mean flux $\overline{F_{net}}$ empirically to *deduce* the mean suspended sediment concentration $\widehat{C}$. Here, instead, we specified $\widehat{C}$ via the empirical relation (3.11) in terms of the Shields parameter $\widehat{\Theta}_d$. Since $\widehat{\Theta}_d$ depends only on the wave amplitude, which evolves on the sand bar time scale $\bar{t}=\varepsilon^{4.5}t$, then $\partial\widehat{C}/\partial t_2=O\left(\varepsilon^{2.5}\right)$. Hence, we can deduce the net flux of sediment from the seabed into suspension from (3.94),

$$\overline{F_{net}}=-\frac{P}{\nu_e}\frac{\partial\overline{q_S}}{\partial x}+\frac{P^2D_h}{2\nu_e^2}\left(-\frac{\partial H}{\partial x_1}+\frac{\partial\widetilde{h}}{\partial x}\right)^2\widehat{C}. \qquad (3.95)$$

# Chapter 4

# Narrow banded waves over a bar patch

Waves in nature have frequencies spread over a finite spectrum. To gain insight into the effects of such waves on bar formation, we consider a simple model of narrow banded waves. Specifically, the incident waves consist of two frequencies: $\omega(1 \pm \varepsilon\Omega)$. The dimensionless bandwidth is $\Omega = O(1)$. In dimensionless form, the leading order surface elevation is the sum of waves of these two frequencies,

$$\begin{aligned}\zeta_1 &= \Re\left\{\left(\widehat{A}_- e^{iS} + \widehat{B}_- e^{-iS}\right) e^{-i(1+\varepsilon\Omega)t}\right\} \\ &\quad + \Re\left\{\left(\widehat{A}_+ e^{iS} + \widehat{B}_+ e^{-iS}\right) e^{-i(1-\varepsilon\Omega)t}\right\} \\ &= \Re\left\{\left(A(x_1,t_1)e^{iS} + B(x_1,t_1)e^{-iS}\right) e^{-it}\right\} \qquad (4.1)\end{aligned}$$

where

$$A(x_1,t_1) = \widehat{A}_- e^{-i\Omega t_1} + \widehat{A}_+ e^{i\Omega t_1}, \qquad B(x_1,t_1) = \widehat{B}_- e^{-i\Omega t_1} + \widehat{B}_+ e^{i\Omega t_1} \qquad (4.2)$$

The subscripts $+$, $-$ stand for upper and lower sideband.

## 4.1 Sand bar equation

The discussion and results derived in Chapter 1 and in sections §2.1–2.4 and §3.1–3.6 (up to and including Eq. (3.60)) of Chapters 2 and 3 are valid for any incident and reflected wave amplitudes $A(x_1,t_1)$, $B(x_1,t_1)$. In particular, sand bars of coarse grains under the

narrow banded waves (4.1) with $A(x_1,t_1)$, $B(x_1,t_1)$ given in (4.2) evolve according to the sand bar equation (2.97). The diffusivity $D_\nu$ and forcing $-\partial q_\tau/\partial x$, given in (2.86) and (2.105), respectively, now depend on $t_1$. Since the time scale of sand bar evolution $\bar{t}=t/\alpha_1$ is longer than $t_1$ by a factor $\varepsilon/\alpha_1=O\left(\varepsilon^{-3.5}\right)$, the $t_1$-scale fluctuations only affect the sand bar elevation $\widetilde{h}$ at order $O(\varepsilon^{3.5})$. Therefore, to leading order, the evolution of the sand bar elevation $\widetilde{h}$ is simply the average of Eq. (2.97) with respect to $t_1$,

$$\frac{\partial\widetilde{h}}{\partial\bar{t}}-\frac{\partial}{\partial x}\left(\overline{\overline{D_\nu}}\frac{\partial\widetilde{h}}{\partial x}\right)=-\frac{\partial}{\partial x}\left(\overline{\overline{q_\tau}}+\overline{\overline{D_\nu}}\frac{dH}{dx_1}\right), \tag{4.3}$$

where double bars denote the average with respect to $t_1$. Due to the nonlinearity of the sediment transport formulae, the diffusivity $D_\nu$, forcing $-\partial q_\tau/\partial x$ and sand bar elevation $\widetilde{h}$ depend nonlinearly on the amplitudes and phases of the two wave components in (4.1).

Including the effects of fine grains requires an extra step in the derivation. Recall that, in Chapter 3, we derived the dimensionless equation for conservation of sediment mass, Eq. (3.58), which allowed for the variation of $A$, $B$ with $t_1$,

$$\alpha_1\frac{\partial\widetilde{h}}{\partial t}=-\frac{1}{\varepsilon}\frac{\partial}{\partial x}\left(q_B+\alpha_2\left\langle uC\right\rangle\right)+\frac{\alpha_2}{\varepsilon^2}\frac{\partial}{\partial t}\left\langle C\right\rangle. \tag{4.4}$$

Time averaging (4.4) over the short-wave period (i.e. in $t$) and substituting (2.85), (3.60) and $\bar{t}=t/\alpha_1$ gives

$$\frac{\partial\widetilde{h}}{\partial\bar{t}}-\frac{\partial}{\partial x}\left(D_\nu\frac{\partial\widetilde{h}}{\partial x}\right)=-\frac{\partial}{\partial x}\left(q_\tau+D_\nu\frac{\partial H}{\partial x_1}+\alpha_2\overline{q_S}\right)+\frac{\alpha_2}{\varepsilon^2}\overline{\frac{\partial}{\partial t}\left\langle C\right\rangle}+O\left(\varepsilon\right). \tag{4.5}$$

In Chapter 3, we then focused on perfectly tuned waves (independent of $t_1$), in which case the term involving $\overline{\partial\left\langle C\right\rangle/\partial t}$ is negligible. However, for narrow banded waves, the depth-integrated mean concentration $\left\langle\overline{C}\right\rangle$ depends on the long scale $t_1$, so that

$$\frac{\alpha_2}{\alpha_1\varepsilon^2}\overline{\frac{\partial}{\partial t}\left\langle C\right\rangle}=\frac{\alpha_2}{\varepsilon}\frac{\partial}{\partial t_1}\left\langle\overline{C}\right\rangle. \tag{4.6}$$

Substituting (4.6) into (4.5) gives

$$\frac{\partial\widetilde{h}}{\partial\bar{t}}-\frac{\partial}{\partial x}\left(D_\nu\frac{\partial\widetilde{h}}{\partial x}\right)=-\frac{\partial}{\partial x}\left(q_\tau+D_\nu\frac{\partial H}{\partial x_1}+\alpha_2\overline{q_S}\right)+\frac{\alpha_2}{\varepsilon}\frac{\partial}{\partial t_1}\overline{\left\langle C\right\rangle}+O\left(\varepsilon\right). \tag{4.7}$$

Even with the last term, $\partial\widetilde{h}/\partial t_1 = \varepsilon^{3.5}\partial\widetilde{h}/\partial\bar{t} \precsim O\left(\varepsilon^{3.5}\alpha_2\varepsilon^{-1}\right) = O\left(\varepsilon^{2.5}\right)$. Thus, the $t_1$-scale fluctuations only affect the sand bar elevation $\widetilde{h}$ at order $O(\varepsilon^{2.5})$. Therefore, to leading order, the evolution of the sand bar elevation $\widetilde{h}$ is simply the average of Eq. (4.7) with respect to $t_1$ (denoted by double bars)

$$\frac{\partial\widetilde{h}}{\partial\bar{t}} - \frac{\partial}{\partial x}\left(\overline{\overline{D_\nu}}\frac{\partial\widetilde{h}}{\partial x}\right) = -\frac{\partial}{\partial x}\left(\overline{\overline{q_\tau}} + \overline{\overline{D_\nu}}\frac{dH}{dx_1} + \alpha_2\overline{\overline{(q_S)}}\right) + \frac{\alpha_2}{\varepsilon}\overline{\overline{\frac{\partial}{\partial t_1}\overline{\langle C\rangle}}} + O\left(\varepsilon\right). \tag{4.8}$$

Since the narrow banded waves are periodic in the long scale $t_1$ (with scaled period $2\pi/\Omega$), so too are the corresponding flows and sediment transport. Thus,

$$\overline{\overline{\frac{\partial}{\partial t_1}\overline{\langle C\rangle}}} = \frac{\alpha_1}{\varepsilon}\frac{\partial}{\partial\bar{t}}\overline{\overline{\left(\overline{\langle C\rangle}\right)}} = O\left(\varepsilon^{3.5}\right)$$

Hence, once again, this term is negligible and (4.8) becomes, retaining leading order terms,

$$\frac{\partial\widetilde{h}}{\partial\bar{t}} - \frac{\partial}{\partial x}\left(\overline{\overline{D_\nu}}\frac{\partial\widetilde{h}}{\partial x}\right) = -\frac{\partial}{\partial x}\left(\overline{\overline{q_\tau}} + \overline{\overline{D_\nu}}\frac{dH}{dx_1} + \alpha_2\overline{\overline{(q_S)}}\right). \tag{4.9}$$

The mean suspended sediment flux $\overline{q_S}$ is given in Eq. (3.65) in terms of correlations between harmonics in the flow and suspended sediment concentration,

$$\overline{q_S} = \left\langle u_2^{[0]}C_1^{[0]}\right\rangle + \frac{1}{2}\Re\left(\left\langle u_1^{[1]*}C_2^{[1]}\right\rangle + \left\langle u_2^{[2]}C_1^{[2]*}\right\rangle\right). \tag{4.10}$$

Equations for the flow components $u_1^{[1]}$, $u_2^{[0]}$, $u_2^{[2]}$ and concentration components $C_1^{[0]}$, $C_1^{[2]}$, $C_2^{[1]}$ were derived in Chapters 2 and 3, and are valid when the wave amplitudes $A$, $B$ depend on $t_1$. Furthermore, the formulae for $\left\langle u_2^{[0]}C_1^{[0]}\right\rangle$, $\left\langle u_1^{[1]*}C_2^{[1]}\right\rangle$, $\left\langle u_2^{[2]}C_1^{[2]*}\right\rangle$ and $\overline{q_S}$ derived in §3.7 are also valid when the wave amplitudes $A$, $B$ depend on $t_1$. Hence, $\overline{q_S}$ is given by Eq. (3.69),

$$\begin{aligned}\frac{\overline{q_S}}{\widehat{C}\sqrt{\bar{\nu}_e}} &= \Re\left\{\left(E_1 + \frac{E_2}{\sinh^2 kH}\right)U_1^{[1]*}\frac{\partial U_1^{[1]}}{\partial x}\right\} + E_3\frac{\left|U_1^{[1]}\right|^2}{\widehat{C}}\frac{\partial\widehat{C_0}}{\partial x} + E_4\frac{\left|U_1^{[1]}\right|^2}{\bar{\nu}_e}\frac{\partial\bar{\nu}_e}{\partial x} \\ &\quad + \frac{2\Lambda_2^{[0]}U_2^{[0]}\bar{\nu}_e^{3/2}}{P^2} + \left|U_1^{[1]}\right|^2 E_5\frac{dZ_b}{dx}.\end{aligned} \tag{4.11}$$

The dependence on $t_1$ is implicit via the orbital amplitude $U_1^{[1]}$, reference concentration $\widehat{C}$, eddy viscosity $\bar{\nu}_e$, etc. Due to the nonlinear dependence of $\overline{q_S}$ on the orbital amplitude $U_1^{[1]}$,

the $t_1$-average of $\overline{q_S}$, i.e. $\overline{\overline{(\overline{q_S})}}$, is nonzero.

Once equations for the incident and reflected wave amplitudes, $A$ and $B$, and the return flow $U_2^{[0]}$ are found, the diffusivity and forcing terms in the sand bar equation can be calculated and sand bar predictions can be made. For narrow banded waves, the detuning modulates the amplitudes $A$ and $B$ in space. Also, the return flow $U_2^{[0]}$ has two parts, a mean part found in Chapter 1 by specifying zero net mass flux and an oscillatory part found from the long wave equation. The effects of these new features of the flow on bar formation are subsequently considered.

## 4.2 Short wave envelope equations and boundary conditions

Substituting the narrow banded wave amplitudes (4.2) into the Bragg Scattering equations (1.72), (1.73) and separating the harmonics $e^{\pm i\Omega t_1}$ gives evolution equations for each harmonic amplitude,

$$C_g\widehat{\mathcal{A}}_{\pm x_1} + \left(\frac{1}{2}\frac{\partial C_g}{\partial x_1} \pm i\Omega\right)\widehat{\mathcal{A}}_{\pm} = -i\Omega_0 D_1\widehat{\mathcal{B}}_{\pm}, \tag{4.12}$$

$$C_g\widehat{\mathcal{B}}_{\pm x_1} + \left(\frac{1}{2}\frac{\partial C_g}{\partial x_1} \mp i\Omega\right)\widehat{\mathcal{B}}_{\pm} = i\Omega_0 D_1^*\widehat{\mathcal{A}}_{\pm}. \tag{4.13}$$

Recall that $D_1$ is the dimensionless spatial amplitude of the first harmonic of the sand bars ($D_1 = \widetilde{h}_1^{[1]\prime}/A_b$). Substituting $\widehat{\mathcal{B}}_{\pm} = R_{\pm}\widehat{\mathcal{A}}_{\pm}$ into (4.13) and then substituting for $\widehat{\mathcal{A}}_{\pm x_1}$ using (4.12) gives

$$\frac{\partial R_{\pm}}{\partial x_1} = \frac{i\Omega_0}{C_g}\left(D_1^* + D_1R_{\pm}^2\right) \pm 2i\frac{\Omega}{C_g}R_{\pm}. \tag{4.14}$$

The terms $R_{\pm}$ act like reflection coefficients, but since there are two harmonics and not one, $R_{\pm}$ can be greater than 1 in magnitude. Using $R_{\pm}$ expedites the solution of $\widehat{\mathcal{A}}_{\pm}$ and $\widehat{\mathcal{B}}_{\pm}$, since Eq. (4.14) is decoupled from $\widehat{\mathcal{A}}_{\pm}$ and $\widehat{\mathcal{B}}_{\pm}$.

We consider a bar patch $0 < x_1 < \varepsilon L$. The boundary condition at the incident end of the bar patch is

$$\left(\widehat{\mathcal{A}}_+,\, \widehat{\mathcal{A}}_-\right) = \text{given}, \qquad \text{at} \quad x_1 = 0. \tag{4.15}$$

For simplicity in this study, we assume the phases are zero, so that

$$\left(\widehat{\mathcal{A}}_+,\, \widehat{\mathcal{A}}_-\right) = \left|\widehat{\mathcal{A}}_0\right|, \qquad \text{at} \quad x_1 = 0. \tag{4.16}$$

Because the frequencies are so close, the magnitude of shoreline reflection is approximately the same for both waves, although the phase of the reflected waves could be different at $x_1 = \varepsilon L$, depending on the location and length of the bar patch. Thus, at the shoreward end of the bar patch, the boundary condition is

$$\left(\left|\frac{\widehat{\mathcal{B}}_+}{\widehat{\mathcal{A}}_+}\right|, \left|\frac{\widehat{\mathcal{B}}_-}{\widehat{\mathcal{A}}_-}\right|\right) = (|R_+|\,, |R_-|) = |R_L|\,, \qquad (\theta_{R+}, \theta_{R-}) = \text{ given}, \qquad \text{at} \quad x_1 = \varepsilon L. \tag{4.17}$$

As Mei (1994) [45] and Hara & Mei (1987) [22] showed, the amount of detuning governs the behavior of the wave envelope and long waves. The dimensional detuning ratio is defined as

$$\frac{\Omega'}{\Omega'_0} = \frac{\Omega}{\Omega_0\,|D_1|}$$

where $|D_1|$ is the amplitude of the first spatial Fourier mode of the bar elevation $\widetilde{h}$. There are four cases for the detuning frequency $\Omega' = \omega\Omega$ relative to the cutoff frequency $\Omega'_0 = \omega\Omega_0 D_1$: perfect tuning ($\Omega' = 0$), below cutoff ($0 < \Omega'/\Omega'_0 < 1$), at cutoff $\Omega' = \Omega'_0$ and above cutoff $\Omega' > \Omega'_0$. As waves approach from deeper water, where there are no bars, the detuning $\Omega'$ will be above the cutoff $\Omega'_0 = 0$. As the depth decreases and the bars become large, the detuning $\Omega'$ may go below the cutoff.

Equations relating the wave and bar amplitudes are found by adding $\widehat{\mathcal{A}}^*_\pm \times$ ( Eq. (4.12) ) to $\widehat{\mathcal{A}}_\pm \times$ ( conjugate of Eq. (4.12) ),

$$\left(C_g \left|\widehat{\mathcal{A}}_\pm\right|^2\right)_{x_1} = 2\Omega_0 \mathrm{Im}\left\{D_1 \widehat{\mathcal{A}}^*_\pm \widehat{\mathcal{B}}_\pm\right\}. \tag{4.18}$$

Similarly, adding $\widehat{\mathcal{B}}^*_\pm \times$ Eq. (4.13) to $\widehat{\mathcal{B}}_\pm \times$ ( conjugate of (4.13) ) gives

$$\left(C_g \left|\widehat{\mathcal{B}}_\pm\right|^2\right)_{x_1} = 2\Omega_0 \mathrm{Im}\left\{D_1 \widehat{\mathcal{A}}^*_\pm \widehat{\mathcal{B}}_\pm\right\}. \tag{4.19}$$

Thus, as for (perfectly tuned) monochromatic waves, Bragg scattering by bars transfers energy between the incident and reflected waves, but only within the same wave component (i.e. either + or -). The amount and direction of energy transfer depends on the complex bar amplitude $D_1$, which in turn depends nonlinearly on the shear stresses due to both wave components. Subtracting (4.18) and (4.19) yields an energy flux equation for each

wave component,

$$\left(C_g\left(\left|\widehat{\mathcal{A}}_{\pm}\right|^2-\left|\widehat{\mathcal{B}}_{\pm}\right|^2\right)\right)_{x_1}=0. \tag{4.20}$$

Thus, the energy flux for each wave component (+/-) is constant across the bar patch.

The total surface wave envelope oscillates in $t_1$ and is given by

$$\begin{aligned}\zeta_{env}^2 &= \left|Ae^{iS}+Be^{-iS}\right|^2\\ &= |A|^2+|B|^2+2\Re\left\{AB^*e^{2iS}\right\}\\ &= \zeta_{env+}^2+\zeta_{env-}^2+2\Re\left\{\left(\widehat{\mathcal{A}}_-e^{iS}+\widehat{\mathcal{B}}_-e^{-iS}\right)\left(\widehat{\mathcal{A}}_+^*e^{-iS}+\widehat{\mathcal{B}}_+^*e^{iS}\right)e^{-2i\Omega t_1}\right\}\end{aligned}$$

where

$$\zeta_{env\pm}=\sqrt{\left|\widehat{\mathcal{A}}_{\pm}\right|^2+\left|\widehat{\mathcal{B}}_{\pm}\right|^2+2\Re\left\{\widehat{\mathcal{A}}_{\pm}\widehat{\mathcal{B}}_{\pm}^*e^{2iS}\right\}}$$

Thus the square of the total surface envelope is the sum of the squares of the stationary envelopes of each wave component (+/-) plus a term that oscillates with $t_1$. As the total surface wave envelope oscillates in $t_1$, its maximum and minimum are, respectively,

$$\zeta_{\max}^2 = \zeta_{env+}^2+\zeta_{env-}^2+\left|\left(\widehat{\mathcal{A}}_-e^{iS}+\widehat{\mathcal{B}}_-e^{-iS}\right)\left(\widehat{\mathcal{A}}_+^*e^{-iS}+\widehat{\mathcal{B}}_+^*e^{iS}\right)\right|, \tag{4.21}$$

$$\zeta_{\min}^2 = \zeta_{env+}^2+\zeta_{env-}^2-\left|\left(\widehat{\mathcal{A}}_-e^{iS}+\widehat{\mathcal{B}}_-e^{-iS}\right)\left(\widehat{\mathcal{A}}_+^*e^{-iS}+\widehat{\mathcal{B}}_+^*e^{iS}\right)\right|. \tag{4.22}$$

Lastly, the $t_1$-rms wave envelope is

$$\zeta_{rms}=\sqrt{\overline{\overline{\zeta_{env}^2}}}=\sqrt{\zeta_{env+}^2+\zeta_{env-}^2}. \tag{4.23}$$

## 4.3 Long wave equation and return flow

The long wave component $\phi_1^{[0]}(x_1,t_1)$ of the flow is governed by Eq. (1.88),

$$\phi_{1t_1t_1}^{[0]}-\frac{gK}{\omega^2}\left(H\phi_{1x_1}^{[0]}\right)_{x_1}=\frac{A_ogK}{A_b\omega^2}\left(-\frac{k\left(|A|^2+|B|^2\right)_{t_1}}{2\sinh 2kH}+\frac{gK}{2\omega^2}\left(k\left(|A|^2-|B|^2\right)\right)_{x_1}\right). \tag{4.24}$$

The incident and reflected wave amplitudes $A$, $B$ each contain two wave components, defined in (4.2), with amplitudes $\widehat{\mathcal{A}}_{\pm}$, $\widehat{\mathcal{B}}_{\pm}$ found from Eqs. (4.12) and (4.13). The long waves

generate a return flow

$$U_2^{[0]} = \frac{A_b}{A_o}\phi_{1x_1}^{[0]} \tag{4.25}$$

that appears in the bedload and suspended load forcing terms. For narrow banded waves, $\phi_1^{[0]}$ and $U_2^{[0]}$ have mean and oscillatory components in the long time $t_1$, which will add new effects to the bedload and suspended load forcing.

Eq. (4.24) for the long wave potential $\phi_1^{[0]}(x_1, t_1)$ involves the terms $\left(|A|^2 + |B|^2\right)_{t_1}$ and $\left(k\left(|A|^2 + |B|^2\right)\right)_{x_1}$. We now write these in terms of $\widehat{\mathcal{A}}_\pm$, $\widehat{\mathcal{B}}_\pm$, using the energy flux equation (1.74),

$$\left(C_g\left(|A|^2 - |B|^2\right)\right)_{x_1} = -\left(|A|^2 + |B|^2\right)_{t_1}. \tag{4.26}$$

From (4.2), we have

$$|A|^2 = \left|\widehat{\mathcal{A}}_+\right|^2 + \left|\widehat{\mathcal{A}}_-\right|^2 + 2\Re\left\{\widehat{\mathcal{A}}_+^*\widehat{\mathcal{A}}_- e^{-2i\Omega t_1}\right\}, \tag{4.27}$$

$$|B|^2 = \left|\widehat{\mathcal{B}}_+\right|^2 + \left|\widehat{\mathcal{B}}_-\right|^2 + 2\Re\left\{\widehat{\mathcal{B}}_+^*\widehat{\mathcal{B}}_- e^{-2i\Omega t_1}\right\}. \tag{4.28}$$

Adding (4.27) and (4.28) gives

$$|A|^2 + |B|^2 = \left|\widehat{\mathcal{A}}_+\right|^2 + \left|\widehat{\mathcal{A}}_-\right|^2 + \left|\widehat{\mathcal{B}}_+\right|^2 + \left|\widehat{\mathcal{B}}_-\right|^2 + 2\Re\left\{\left(\widehat{\mathcal{A}}_+^*\widehat{\mathcal{A}}_- + \widehat{\mathcal{B}}_+^*\widehat{\mathcal{B}}_-\right)e^{-2i\Omega t_1}\right\}. \tag{4.29}$$

Differentiating (4.29) in the long time $t_1$ and substituting into (4.26) gives

$$\left(C_g\left(|A|^2 - |B|^2\right)\right)_{x_1} = -\left(|A|^2 + |B|^2\right)_{t_1} = -4\Omega\Im\left\{\left(\widehat{\mathcal{A}}_+^*\widehat{\mathcal{A}}_- + \widehat{\mathcal{B}}_+^*\widehat{\mathcal{B}}_-\right)e^{-2i\Omega t_1}\right\}. \tag{4.30}$$

To find an expression for $\left(k\left(|A|^2 - |B|^2\right)\right)_{x_1}$, we note that

$$\begin{aligned}\left(k\left(|A|^2 - |B|^2\right)\right)_{x_1} &= k\left(|A|^2 - |B|^2\right)_{x_1} + \left(|A|^2 - |B|^2\right)k_{x_1} \\ &= \frac{k}{C_g}\left(C_g\left(|A|^2 - |B|^2\right)\right)_{x_1} + \left(|A|^2 - |B|^2\right)C_g\left(\frac{k}{C_g}\right)_{x_1}.\end{aligned} \tag{4.31}$$

Substituting (4.30) gives

$$\left(k\left(|A|^2 - |B|^2\right)\right)_{x_1} = -\frac{4\Omega k}{C_g}\Im\left\{\left(\widehat{\mathcal{A}}_+^*\widehat{\mathcal{A}}_- + \widehat{\mathcal{B}}_+^*\widehat{\mathcal{B}}_-\right)e^{-2i\Omega t_1}\right\} + \left(|A|^2 - |B|^2\right)C_g\left(\frac{k}{C_g}\right)_{x_1}. \tag{4.32}$$

To find an expression for $|A|^2 - |B|^2$, we subtract (4.27) and (4.28),

$$|A|^2 - |B|^2 = \left|\widehat{\mathcal{A}}_+\right|^2 - \left|\widehat{\mathcal{B}}_+\right|^2 + \left|\widehat{\mathcal{A}}_-\right|^2 - \left|\widehat{\mathcal{B}}_-\right|^2 + 2\Re\left\{\left(\widehat{\mathcal{A}}_+^*\widehat{\mathcal{A}}_- - \widehat{\mathcal{B}}_+^*\widehat{\mathcal{B}}_-\right)e^{-2i\Omega t_1}\right\}. \quad (4.33)$$

Integrating (4.20) in $x_1$ and applying the BCs at $x_1 = 0$ gives

$$\left|\widehat{\mathcal{A}}_\pm\right|^2 - \left|\widehat{\mathcal{B}}_\pm\right|^2 = \frac{C_{g0}}{C_g}\left(\left|\widehat{\mathcal{A}}_0\right|^2 - \left|\widehat{\mathcal{B}}_\pm(0)\right|^2\right) \quad (4.34)$$

where $\widehat{\mathcal{B}}_\pm(0)$ is the value of $\widehat{\mathcal{B}}_\pm$ at $x_1 = 0$ and is found after solving for $\widehat{\mathcal{B}}_\pm$. Substituting (4.34) into (4.33) gives

$$|A|^2 - |B|^2 = \left(2\left|\widehat{\mathcal{A}}_0\right|^2 - \left|\widehat{\mathcal{B}}_+(0)\right|^2 - \left|\widehat{\mathcal{B}}_-(0)\right|^2\right)\frac{C_{g0}}{C_g} + 2\,\Re\left\{\left(\widehat{\mathcal{A}}_+^*\widehat{\mathcal{A}}_- - \widehat{\mathcal{B}}_+^*\widehat{\mathcal{B}}_-\right)e^{-2i\Omega t_1}\right\}. \quad (4.35)$$

Finally, substituting (4.30), (4.31) and (4.33) into the long wave equation (4.24) gives

$$\begin{aligned}
&\phi^{[0]}_{1t_1t_1} - \frac{gK}{\omega^2}\left(H\phi^{[0]}_{1x_1}\right)_{x_1} = \\
&\quad - \frac{A_o}{A_b}\frac{2gKk\Omega}{\omega^2}\left(\frac{1}{\sinh 2kH} + \frac{gK}{\omega^2 C_g}\right)\Im\left\{\left(\widehat{\mathcal{A}}_+^*\widehat{\mathcal{A}}_- + \widehat{\mathcal{B}}_+^*\widehat{\mathcal{B}}_-\right)e^{-2i\Omega t_1}\right\} \\
&\quad + \frac{A_o}{A_b}\left(\frac{gK}{\omega^2}\right)^2\left(\frac{k}{C_g}\right)_{x_1} C_g\,\Re\left\{\left(\widehat{\mathcal{A}}_+^*\widehat{\mathcal{A}}_- - \widehat{\mathcal{B}}_+^*\widehat{\mathcal{B}}_-\right)e^{-2i\Omega t_1}\right\} \\
&\quad + \frac{A_o}{2A_b}\left(\frac{gK}{\omega^2}\right)^2\left(\frac{k}{C_g}\right)_{x_1}\left(2\left|\widehat{\mathcal{A}}_0\right|^2 - \left|\widehat{\mathcal{B}}_+(0)\right|^2 - \left|\widehat{\mathcal{B}}_-(0)\right|^2\right)C_{g0}.
\end{aligned} \quad (4.36)$$

The forcing terms on the r.h.s. of Eq. (4.36) are either constant in the long time $t_1$ or oscillate with frequency $2\Omega$. This motivates splitting the long wave potential into its mean and oscillatory components,

$$\phi_1^{[0]} = \overline{\overline{\phi_1^{[0]}}} + \Re\left\{\widetilde{\phi_1^{[0]}}e^{-2i\Omega t_1}\right\}. \quad (4.37)$$

The corresponding return flow $U_2^{[0]}$, given in (4.25), is also split into its mean and oscillatory components,

$$U_2^{[0]} = \overline{\overline{U_2^{[0]}}} + \Re\left\{\widetilde{U_2^{[0]}}e^{-2i\Omega t_1}\right\}, \qquad \overline{\overline{U_2^{[0]}}} = \frac{A_o}{A_b}\frac{\partial\overline{\overline{\phi_1^{[0]}}}}{\partial x_1}, \qquad \widetilde{U_2^{[0]}} = \frac{A_o}{A_b}\frac{\partial\widetilde{\phi_1^{[0]}}}{\partial x_1}. \quad (4.38)$$

The mean return flow $\overline{\overline{U_2^{[0]}}}$ was found in §1.2.3 to cancel the mean forward flux $\overline{\overline{(\zeta_1\phi_{1x})}}$ in the inviscid core. The $t_1$-average of Eq. (4.36) merely gives back the equation for $\overline{\overline{U_2^{[0]}}}$. To see this, we substitute (4.37) into (4.36) and isolate the mean components to obtain

$$\frac{\partial}{\partial x_1}\left(H\frac{\partial}{\partial x_1}\overline{\overline{\phi_1^{[0]}}}\right) = -\frac{A_o}{A_b}\frac{gKC_{g0}}{2\omega^2}\left(2\left|\widehat{\mathcal{A}}_0\right|^2 - \left|\widehat{\mathcal{B}}_+(0)\right|^2 - \left|\widehat{\mathcal{B}}_-(0)\right|^2\right)\left(\frac{k}{C_g}\right)_{x_1}. \tag{4.39}$$

Upon integrating in $x_1$ and imposing zero mean mass flux gives Eq. (1.87) for the mean return flow $\overline{\overline{U_2^{[0]}}}$, in view of (4.35),

$$\overline{\overline{U_2^{[0]}}} = \frac{A_o}{A_b}\frac{\partial}{\partial x_1}\left(\overline{\overline{\phi_1^{[0]}}}\right) = -\frac{A_o^2 gKC_{g0}}{2A_b^2\omega^2}\left(2\left|\widehat{\mathcal{A}}_0\right|^2 - \left|\widehat{\mathcal{B}}_+(0)\right|^2 - \left|\widehat{\mathcal{B}}_-(0)\right|^2\right)\frac{k(x_1)}{H(x_1)C_g(x_1)}. \tag{4.40}$$

The oscillatory component $\widetilde{U_2^{[0]}}$ of the return flow is a new component due to the narrow banded waves, and modifies the effects of the return flow on the bedload and suspended load transport. To find $\widetilde{U_2^{[0]}}$, we must first solve for the oscillatory long wave potential $\widetilde{\phi_1^{[0]}}$. Subtracting (4.39) from (4.36) gives an equation for $\widetilde{\phi_1^{[0]}}$,

$$\begin{aligned}\frac{\partial}{\partial x_1}\left(H\frac{\partial}{\partial x_1}\widetilde{\phi_1^{[0]}}\right) + \frac{4\Omega^2\omega^2}{gK}\widetilde{\phi_1^{[0]}} &= -2ik\Omega\frac{A_o}{A_b}\left(\frac{1}{\sinh 2kH} + \frac{gK}{\omega^2 C_g}\right)\left(\widehat{\mathcal{A}}_+^*\widehat{\mathcal{A}}_- + \widehat{\mathcal{B}}_+^*\widehat{\mathcal{B}}_-\right)\\ &\quad - \frac{A_o}{A_b}\frac{gK}{\omega^2}\left(\frac{k}{C_g}\right)_{x_1} C_g\left(\widehat{\mathcal{A}}_+^*\widehat{\mathcal{A}}_- - \widehat{\mathcal{B}}_+^*\widehat{\mathcal{B}}_-\right).\end{aligned} \tag{4.41}$$

Once the envelopes for the incident and reflected short waves ($\widehat{\mathcal{A}}_\pm$, $\widehat{\mathcal{B}}_\pm$) are found from Eqs. (4.12) and (4.13), the oscillatory long wave potential is found from Eq. (4.41) subject to boundary conditions specified at $x_1 = 0$ and $x_1 = \varepsilon L$.

### 4.3.1 Boundary conditions for the oscillatory long wave potential

Boundary conditions for the oscillatory long wave potential $\widetilde{\phi_1^{[0]}}$ are specified at $x_1 = 0,\ \varepsilon L$. We assume a shoreline or seawall exists at the shoreward end of the bar patch ($x_1 = \varepsilon L$). Thus, at $x_1 = \varepsilon L$, the mass flux, expressed in dimensionless form in Eq. (1.86), must vanish,

$$\overline{M_+} = H\frac{\partial\phi_1^{[0]}}{\partial x_1} + \frac{A_o}{A_b}\frac{gK}{2\omega^2}k\left(|A|^2 - |B|^2\right) = 0, \qquad x_1 = \varepsilon L. \tag{4.42}$$

Note that the $t_1$-averaged mass flux $\overline{\overline{(\overline{M_+})}}$ vanishes everywhere (Eq. (1.56)), but the $t$-averaged mass flux $\overline{M_+}$ is only required to vanish at the shore or wall. Substituting (4.37)

into (4.42) and isolating the oscillatory component gives

$$H\Re\left\{\frac{\partial}{\partial x_1}\widetilde{\phi_1^{[0]}}e^{-2i\Omega t_1}\right\}+\frac{A_o}{A_b}\frac{gK}{2\omega^2}k\left(|A|^2-|B|^2-\left(\overline{\overline{|A|^2}}-\overline{\overline{|B|^2}}\right)\right)=0,\qquad x_1=\varepsilon L. \tag{4.43}$$

Substituting (4.33), multiplying by $e^{2i\Omega t_1}$ and taking the $t_1$-average gives

$$\frac{\partial\widetilde{\phi_1^{[0]}}}{\partial x_1}=-\frac{A_o}{A_b}\frac{gK}{\omega^2}\frac{k}{H}\left(\widehat{\mathcal{A}}_+^*\widehat{\mathcal{A}}_--\widehat{\mathcal{B}}_+^*\widehat{\mathcal{B}}_-\right),\qquad x_1=\varepsilon L. \tag{4.44}$$

We also specify $\partial\widetilde{\phi_1^{[0]}}/\partial x_1$ at the seaward end of the bar patch ($x_1=0$). The forms of the long wave potential $\widetilde{\phi_1^{[0]}}$ and the short waves seaward of the bar patch must first be considered.

**Seaward of the bar patch**

Seaward of the bar patch ($x_1<0$), we assume the mean depth $H$ is constant $H=H(0)$, and hence $k$, $C_g$ are also constant. Since the bar height is zero ($D_1=0$), Eqs. (4.12) and (4.13) for the short wave envelope become

$$\widehat{\mathcal{A}}_{\pm x_1}\pm i\frac{\Omega}{C_g}\widehat{\mathcal{A}}_\pm=0,\qquad \widehat{\mathcal{B}}_{\pm x_1}\mp i\frac{\Omega}{C_g}\widehat{\mathcal{B}}_\pm=0.$$

Since $\Omega/C_g$ is constant and $\widehat{\mathcal{A}}_\pm(0)=\left|\widehat{\mathcal{A}}_0\right|$, these equations integrate to

$$\widehat{\mathcal{A}}_\pm=\left|\widehat{\mathcal{A}}_0\right|\exp\left(\mp i\frac{\Omega}{C_g}x_1\right),\qquad \widehat{\mathcal{B}}_\pm=\widehat{B}_\pm(0)\exp\left(\pm i\frac{\Omega}{C_g}x_1\right). \tag{4.45}$$

Eq. (4.41) for the oscillatory long wave component $\widetilde{\phi_1^{[0]}}$ simplifies to

$$\frac{\partial^2\widetilde{\phi_1^{[0]}}}{\partial x_1^2}+\frac{4\Omega^2\omega^2}{gKH}\widetilde{\phi_1^{[0]}}=-2ik\Omega\frac{A_o}{A_b}\left(\frac{1}{\sinh 2kH}+\frac{gK}{\omega^2C_g}\right)\left(\widehat{\mathcal{A}}_+^*\widehat{\mathcal{A}}_-+\widehat{\mathcal{B}}_+^*\widehat{\mathcal{B}}_-\right).$$

Substituting $\widehat{\mathcal{A}}_\pm$, $\widehat{\mathcal{B}}_\pm$ from (4.45) gives

$$\frac{\partial^2\widetilde{\phi_1^{[0]}}}{\partial x_1^2}+\kappa_{LW}^2\widetilde{\phi_1^{[0]}}=-2ik\Omega\frac{A_o}{A_b}\left(\frac{1}{\sinh 2kH}+\frac{gK}{\omega^2C_g}\right)\times\left(\left|\widehat{\mathcal{A}}_0\right|^2e^{2i\Omega x_1/C_g}+\widehat{\mathcal{B}}_+^*(0)\,\widehat{\mathcal{B}}_-(0)\,e^{-2i\Omega x_1/C_g}\right), \tag{4.46}$$

where

$$\kappa_{LW} = \frac{2\Omega\omega}{\sqrt{gKH}} = \frac{2\Omega\omega}{\sqrt{gKH(0)}}.$$

The subscript "$LW$" stands for long wave. The general solution to the inhomogeneous ODE (4.46) is the sum of a homogeneous solution plus a particular solution,

$$\begin{aligned}\widetilde{\phi_1^{[0]}} &= f_0 e^{-i\kappa_{LW}x_1} + f_1 e^{i\kappa_{LW}x_1} \\ &\quad - \frac{ik}{2\Omega H}\frac{A_o}{A_b}\frac{\frac{1}{\sinh 2kH} + \frac{gK}{\omega^2 C_g}}{\frac{\omega^2}{gKH} - \frac{1}{C_g^2}}\left(\left|\widehat{\mathcal{A}}_0\right|^2 e^{2i\Omega x_1/C_g} + \widehat{\mathcal{B}}_+^*(0)\,\widehat{\mathcal{B}}_-(0)\,e^{-2i\Omega x_1/C_g}\right).\end{aligned} \tag{4.47}$$

The terms proportional to $\exp(\pm i\kappa_{LW}x_1)$ are radiated free waves, i.e. solutions to the homogeneous part of Eq. (4.46), whose amplitudes $f_0$, $f_1$ remain to be determined. We assume the free waves are generated by the bar patch and are not present in the incident waves. Therefore, the free waves must be outgoing seaward of the bar patch, and hence $f_1 = 0$ and Eq. (4.47) becomes

$$\widetilde{\phi_1^{[0]}} = f_0 e^{-i\kappa_{LW}x_1} - \frac{ik}{2\Omega H}\frac{A_o}{A_b}\frac{\frac{1}{\sinh 2kH} + \frac{gK}{\omega^2 C_g}}{\frac{\omega^2}{gKH} - \frac{1}{C_g^2}}\left(\left|\widehat{\mathcal{A}}_0\right|^2 e^{2i\Omega x_1/C_g} + \widehat{\mathcal{B}}_+^*(0)\,\widehat{\mathcal{B}}_-(0)\,e^{-2i\Omega x_1/C_g}\right). \tag{4.48}$$

**Seaward boundary condition for the oscillatory long wave potential**

At $x_1 = 0$, the surface elevation and horizontal velocity must be continuous, since the pressure is constant at the surface. Thus $\widetilde{\phi_1^{[0]}}$ and $\partial\widetilde{\phi_1^{[0]}}/\partial x_1$ must be continuous at $x_1 = 0$ and given by Eq. (4.48),

$$\widetilde{\phi_1^{[0]}} = f_0 - \frac{ik}{2\Omega H}\frac{A_o}{A_b}\frac{\frac{1}{\sinh 2kH} + \frac{gK}{\omega^2 C_g}}{\frac{\omega^2}{gKH} - \frac{1}{C_g^2}}\left(\left|\widehat{\mathcal{A}}_0\right|^2 + \widehat{\mathcal{B}}_+^*\widehat{\mathcal{B}}_-\right), \qquad x_1 = 0, \tag{4.49}$$

$$\frac{\partial\widetilde{\phi_1^{[0]}}}{\partial x_1} = -i\kappa_{LW}f_0 + \frac{k}{HC_g}\frac{A_o}{A_b}\frac{\frac{1}{\sinh 2kH} + \frac{gK}{\omega^2 C_g}}{\frac{\omega^2}{gKH} - \frac{1}{C_g^2}}\left(\left|\widehat{\mathcal{A}}_0\right|^2 - \widehat{\mathcal{B}}_+^*\widehat{\mathcal{B}}_-\right), \qquad x_1 = 0. \tag{4.50}$$

Eliminating $f_0$ from (4.49) and (4.50) gives a mixed boundary condition for $\widetilde{\phi_1^{[0]}}$ at $x_1 = 0$,

$$\frac{\partial\widetilde{\phi_1^{[0]}}}{\partial x_1} + i\kappa_{LW}\widetilde{\phi_1^{[0]}} = \frac{kA_o}{HA_b}\left(\frac{1}{\sinh 2kH} + \frac{gK}{\omega^2 C_g}\right)\left(\frac{\left|\widehat{\mathcal{A}}_0\right|^2}{\frac{\omega}{\sqrt{gKH}} - \frac{1}{C_g}} + \frac{\widehat{\mathcal{B}}_+^*\widehat{\mathcal{B}}_-}{\frac{\omega}{\sqrt{gKH}} + \frac{1}{C_g}}\right). \tag{4.51}$$

Lastly, note that $\left|\widehat{\mathcal{A}}_0\right|$ is specified, but $\widehat{\mathcal{B}}_\pm(0)$ are computed from the short wave envelope equations (4.12) and (4.13).

### 4.3.2 Solution of oscillatory long wave potential

Once the short wave amplitudes $\widehat{\mathcal{A}}_\pm$ and $\widehat{\mathcal{B}}_\pm$ are found from the Bragg Scattering equations (4.12) and (4.13), the oscillatory long wave potential $\widetilde{\phi_1^{[0]}}$ over the bar patch $0 < x_1 < \varepsilon L$ is found from the ODE (4.41) subject to two boundary conditions. At the shoreline, $x_1 = \varepsilon L$, imposing zero mass flux led to the boundary condition (4.44),

$$\frac{\partial\widetilde{\phi_1^{[0]}}}{\partial x_1} = -\frac{A_o}{A_b}\frac{gK}{\omega^2}\frac{k}{H}\left(\widehat{\mathcal{A}}_+^*\widehat{\mathcal{A}}_- - \widehat{\mathcal{B}}_+^*\widehat{\mathcal{B}}_-\right) = -\frac{A_o}{A_b}\frac{\widehat{\mathcal{A}}_+^*\widehat{\mathcal{A}}_- - \widehat{\mathcal{B}}_+^*\widehat{\mathcal{B}}_-}{H\tanh kH}, \qquad x_1 = \varepsilon L.$$

At the seaward end of the bar patch, continuity of surface elevation and horizontal velocity led to the boundary condition (4.51),

$$\frac{\partial\widetilde{\phi_1^{[0]}}}{\partial x_1} + i\kappa_{LW}\widetilde{\phi_1^{[0]}} = \frac{kA_o}{HA_b}\left(\frac{1}{\sinh 2kH} + \frac{gK}{\omega^2 C_g}\right)\left(\frac{\left|\widehat{\mathcal{A}}_0\right|^2}{\frac{\omega}{\sqrt{gKH}} - \frac{1}{C_g}} + \frac{\widehat{\mathcal{B}}_+^*\widehat{\mathcal{B}}_-}{\frac{\omega}{\sqrt{gKH}} + \frac{1}{C_g}}\right), \quad x_1 = 0.$$

The oscillatory potential $\widetilde{\phi_1^{[0]}}$ can be solved via the shooting method.

We write $\widetilde{\phi_1^{[0]}}$ in terms of a second function $\phi_{SH}$ so that $\widetilde{\phi_1^{[0]}}$ satisfies the shoreward BC (4.44) automatically,

$$\widetilde{\phi_1^{[0]}} = \phi_{SH} - \frac{i}{\kappa_{LW}}\sqrt{\frac{H(\varepsilon L)}{H(0)}}\left[\frac{\partial\phi_{SH}}{\partial x_1} + \frac{A_o\left(\widehat{\mathcal{A}}_+^*\widehat{\mathcal{A}}_- - \widehat{\mathcal{B}}_+^*\widehat{\mathcal{B}}_-\right)}{A_b H\tanh kH}\right]_{x_1=\varepsilon L} \times \exp\left\{i\kappa_{LW}\int_{x_1}^{\varepsilon L}\sqrt{\frac{H(0)}{H(x_1)}}dx_1\right\}, \tag{4.52}$$

where $\phi_{SH}$ satisfies the boundary conditions

$$\phi_{SH}(0) = -\frac{ik}{2\Omega H}\frac{A_o}{A_b}\frac{\frac{1}{\sinh 2kH} + \frac{gK}{\omega^2 C_g}}{\frac{\omega^2}{gKH} - \frac{1}{C_g^2}}\left(\left|\widehat{\mathcal{A}}_0\right|^2 + \widehat{\mathcal{B}}_+^*\widehat{\mathcal{B}}_-\right), \qquad x_1 = 0, \tag{4.53}$$

$$\frac{\partial\phi_{SH}}{\partial x_1}(0) = \frac{k}{HC_g}\frac{A_o}{A_b}\frac{\frac{1}{\sinh 2kH} + \frac{gK}{\omega^2 C_g}}{\frac{\omega^2}{gKH} - \frac{1}{C_g^2}}\left(\left|\widehat{\mathcal{A}}_0\right|^2 - \widehat{\mathcal{B}}_+^*\widehat{\mathcal{B}}_-\right), \qquad x_1 = 0. \tag{4.54}$$

Also, with the BCs (4.53) and (4.54) on $\phi_{SH}$, the form (4.52) for $\widetilde{\phi_1^{[0]}}$ guarantees that $\widetilde{\phi_1^{[0]}}$ satisfies the seaward BC (4.51).

Substituting (4.52) into the ODE (4.41) gives

$$\begin{aligned}\frac{\partial}{\partial x_1}\left(H\frac{\partial}{\partial x_1}\phi_{SH}\right)+\frac{4\Omega^2\omega^2}{gK}\phi_{SH} &= \frac{1}{2}\left[\frac{\partial\phi_{SH}}{\partial x_1}+\frac{A_o\left(\widehat{\mathcal{A}}_+^*\widehat{\mathcal{A}}_- - \widehat{\mathcal{B}}_+^*\widehat{\mathcal{B}}_-\right)}{A_bH\tanh kH}\right]_{x_1=\varepsilon L} \\ &\quad\times\sqrt{\frac{H(\varepsilon L)}{H(x_1)}}\frac{dH}{dx_1}\exp\left\{i\kappa_{LW}\int_{x_1}^{\varepsilon L}\sqrt{\frac{H(0)}{H(x_1)}}dx_1\right\} \\ &\quad-2ik\Omega\frac{A_o}{A_b}\left(\frac{1}{\sinh 2kH}+\frac{gK}{\omega^2C_g}\right)\left(\widehat{\mathcal{A}}_+^*\widehat{\mathcal{A}}_- + \widehat{\mathcal{B}}_+^*\widehat{\mathcal{B}}_-\right) \\ &\quad-\frac{A_o}{A_b}\frac{gK}{\omega^2}\left(\frac{k}{C_g}\right)_{x_1}C_g\left(\widehat{\mathcal{A}}_+^*\widehat{\mathcal{A}}_- - \widehat{\mathcal{B}}_+^*\widehat{\mathcal{B}}_-\right).\end{aligned} \tag{4.55}$$

The right hand side, though lengthy, is straightforward to compute given the mean depth $H(x_1)$ and short wave amplitudes $\widehat{\mathcal{A}}_\pm$, $\widehat{\mathcal{B}}_\pm$ computed prior to solving the long wave equation. Notice that the r.h.s. of the ODE (4.55) depends on the unknown $\partial\phi_{SH}/\partial x_1(\varepsilon L)$, which suggests (4.55) should be solved by iteration, characteristic of the shooting method.

The shooting method proceeds as follows. Initially, we set $\partial\phi_{SH}/\partial x_1(\varepsilon L)=0$. With $\phi_{SH}(0)$ and $\partial\phi_{SH}/\partial x_1(0)$ given by Eqs. (4.53) and (4.54), the ODE (4.55) is integrated from $x_1=0$ to $\varepsilon L$ yielding an estimate of $\phi_{SH}$. The newly computed value of $\partial\phi_{SH}/\partial x_1(\varepsilon L)$ is then substituted back into the r.h.s. of the ODE, which is integrated again from $x_1=0$ to $\varepsilon L$ yielding a new estimate of $\phi_{SH}$. The process repeats until the value of $\partial\phi_{SH}/\partial x_1(\varepsilon L)$ converges, at which point the solution $\phi_{SH}$ of the ODE (4.55) and BCs (4.53) and (4.54) has been found. The oscillatory long wave potential $\widetilde{\phi_1^{[0]}}$ is then found from (4.52). Note that for constant depth, no iteration is required since Eq. (4.55) becomes

$$\frac{\partial^2\phi_{SH}}{\partial x_1^2}+\kappa_{LW}^2\phi_{SH}=-\frac{2ik\Omega A_o}{HA_b}\left(\frac{1}{\sinh 2kH}+\frac{gK}{\omega^2C_g}\right)\left(\widehat{\mathcal{A}}_+^*\widehat{\mathcal{A}}_- + \widehat{\mathcal{B}}_+^*\widehat{\mathcal{B}}_-\right). \tag{4.56}$$

Finally, the oscillatory component of the return flow, present in both the bedload and

suspended load forcing terms, is given by substituting (4.52) into (4.38),

$$\widetilde{U_2^{[0]}} = \frac{A_o}{A_b}\frac{\partial \phi_{SH}}{\partial x_1} - \frac{A_o}{A_b}\sqrt{\frac{H(\varepsilon L)}{H(x_1)}}\left[\frac{\partial \phi_{SH}}{\partial x_1} + \frac{A_o\left(\widehat{\mathcal{A}}_+^*\widehat{\mathcal{A}}_- - \widehat{\mathcal{B}}_+^*\widehat{\mathcal{B}}_-\right)}{A_b H \tanh kH}\right]_{x_1=\varepsilon L} \times \exp\left\{i\kappa_{LW}\int_{x_1}^{\varepsilon L}\sqrt{\frac{H(0)}{H(x_1)}}dx_1\right\}. \tag{4.57}$$

## 4.4 Numerical results and discussion

The computational steps necessary to simulate bar formation under narrow banded waves are similar to those used in chapters 2 and 3. First, the constant parameters are computed as outlined in §2.3.1 and §3.7. The short wave amplitudes are computed from Eqs. (4.12) and (4.14) in §4.2. The wave amplitudes $A$ and $B$ are found from Eq. (4.2) and are used to compute the components of the orbital velocity $U_1^{[1]}$, $U_2^{[2]}$ from Eqs. (1.83) and (1.85). The oscillatory long wave potential is then found from Eq. (4.55), as outlined in §4.3.2, and the return flow $U_2^{[0]}$ is found from Eq. (4.38) with $\overline{\overline{U_2^{[0]}}}$ given in (4.40) and $\widetilde{U_2^{[0]}}$ in (4.57). These components of the orbital amplitude are then used to compute the gravity-driven diffusivity $D_\nu$ (Eq. (2.86)), the bedload forcing $q_\tau$ (Eq. (2.105)), and the suspended load forcing $\overline{q_S}$ (Eq. (4.11)). The $t_1$-average of the diffusivity and forcing terms are then used with the sand bar equation (4.9) to compute the sand bar elevation $\widetilde{h}$.

We first consider numerical simulations of sand bars on a horizontal bed of mean depth $H = H_o = 5$ m under partially standing narrow banded waves with period $T = 8$ s, wave height $2A_o(1 + |R_L|) = 100/\sqrt{2}$ cm, shoreline reflection $R_\pm(\varepsilon L) = 0.1$ and detuning $\Omega = \Delta\omega/(\varepsilon\omega) = 1$. The scaled incident wave amplitude is set at $\mathcal{A}_\pm(0) = 1$. Zero boundary conditions are imposed on the sand bar elevation at the ends of the bar patch. The water is assumed to be seawater. The sediment diameter is $d = 0.5$ mm and the ripple height is $\eta_r' = \eta_{ro} = 5.5$ cm. Figure 4-1 shows the rms wave amplitude and the bar profiles after 1 and 3 days of wave action. The scaled time corresponding to 3 days is $\bar{t} = 0.08$, indicating that the bars and waves are in an early stage of evolution. The wave envelope oscillates between $\zeta_{\max}$ and $\zeta_{\min}$ with rms $\zeta_{\rm rms}$ (Figure 4-1(a) and definitions in Eqs. (4.21), (4.22), and (4.23)).

The bars exhibit variations in the short and long spatial scales (Figure 4-1(b)). The $t_1$-oscillating return current $U_2^{[0]}$ contributes to the long scale variation and is plotted in

Figure 4-1(d). The coupling coefficient $\Im\left\{D_1 e^{i\theta_R}\right\}$, plotted in Figure 4-1(c), is positive over the left (seaward) half of the bar patch and is negative over the right (shoreward) half. As we discussed previously, this implies the wave and bar heights increase and decrease in the shoreward direction over the left and right halves of the bar patch, respectively, as shown in Figure 4-1(b). The situation is reversed if we take $R_\pm(\varepsilon L) = 0.1e^{\pm i\pi/2}$ (Figure 4-2). Now, $\Im\left\{D_1 e^{i\theta_R}\right\} < 0$ and the bar and wave heights decrease in the shoreward direction over the left half of the bar patch, while the opposite occurs in the right half of the bar patch. Finally, the corresponding relative detuning $\Omega_0|D_1|/\Omega$ is plotted in Figures 4-1(e) and 4-2(e), illustrating that the detuning $\Omega$ is always above the cutoff $\Omega_0|D_1|$. The bars would have to grow significantly larger to force the detuning below cutoff.

The results for narrow banded waves are compared to bars under perfectly tuned waves in Figure 4-3. The scale of the wave height for the perfectly tuned waves is $2A_o(1+|R_L|) = 100$ cm. This choice gives the perfectly tuned waves the same energy as the narrow banded waves. The scaled incident wave amplitude is set at $A(0) = 1$ and the shore reflection is taken as $R_L = 0.1$. All other parameters are outlined in the previous paragraph. The computation for perfectly tuned waves follows the steps used in §3.7 of Chapter 3. Figure 4-3 illustrates that the effect of the narrow banded waves is to periodically alter the energy exchange between the incident and reflected wave trains, which modulates the bar and wave height across the bar patch. For perfectly tuned waves, the wave and bar heights decrease shoreward, monotonically, while those for narrow banded waves increase and then decrease shoreward. Also, the bar crest and trough positions are significantly different over the first half of the bar patch for perfectly tuned and narrow banded waves. Lastly, both long scale and short scale bars are generated under narrow banded waves, while only short scale bars are generated under perfectly tuned waves.

Next, we present numerical results of bar formation on the prototypical beach (2.151) under narrow banded waves with period $T = 10$ s, incident wave amplitude $\mathcal{A}_\pm = 22.2$ cm, and detuning $\Omega = \Delta\omega/(\varepsilon\omega) = 1$. The numerical methods used on the sloping beach are the same as those used in §2.7.3. In Figure 4-4, bars are shown due to strong shoreline reflection $R_\pm(\varepsilon L) = 1$ and coarse and fine grains. The difference between the bars of coarse and fine grains is essentially the same as that considered in chapter 3, but now, under narrow banded waves, the bar amplitude is modulated. In Figure 4-5, bars are shown under narrow banded and perfectly tuned waves and strong shoreline reflection $R_\pm(\varepsilon L) = 1$. For

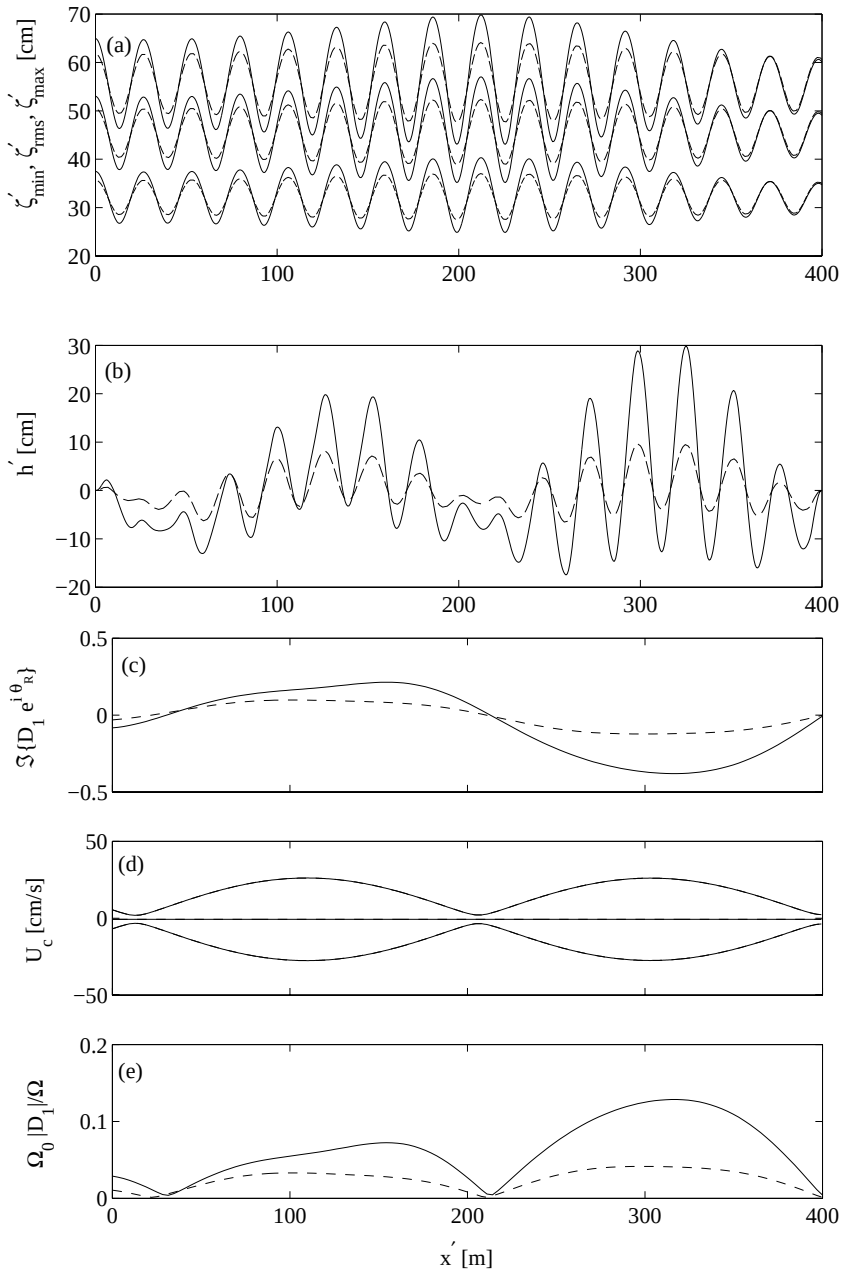


Figure 4-1: The min, rms, and max surface envelopes (a) and bar profiles (b) under narrow banded waves, after 1 (dash) and 3 (solid) days of wave action. Also plotted are (c) the Bragg scattering coupling coefficient $\Im\left\{D_1 e^{i\theta_R}\right\}$, (d) the $t_1$-mean and extrema of the return flow amplitude $U_2^{[0]}$, and (e) the relative detuning $\Omega_0|D_1|/\Omega$. The mean depth is constant, $H = H_o = 4$ m, and the shore reflection is $R_\pm(\varepsilon L) = |R_L| = 0.1$. The other parameters are $T = 10$ s, $A_o(1 + |R_L|) = 50/\sqrt{2}$ cm, $d = 0.5$ mm, $\eta_r' = \eta_{ro} = 5.5$ and $\Lambda_2^{[0]}$=2.

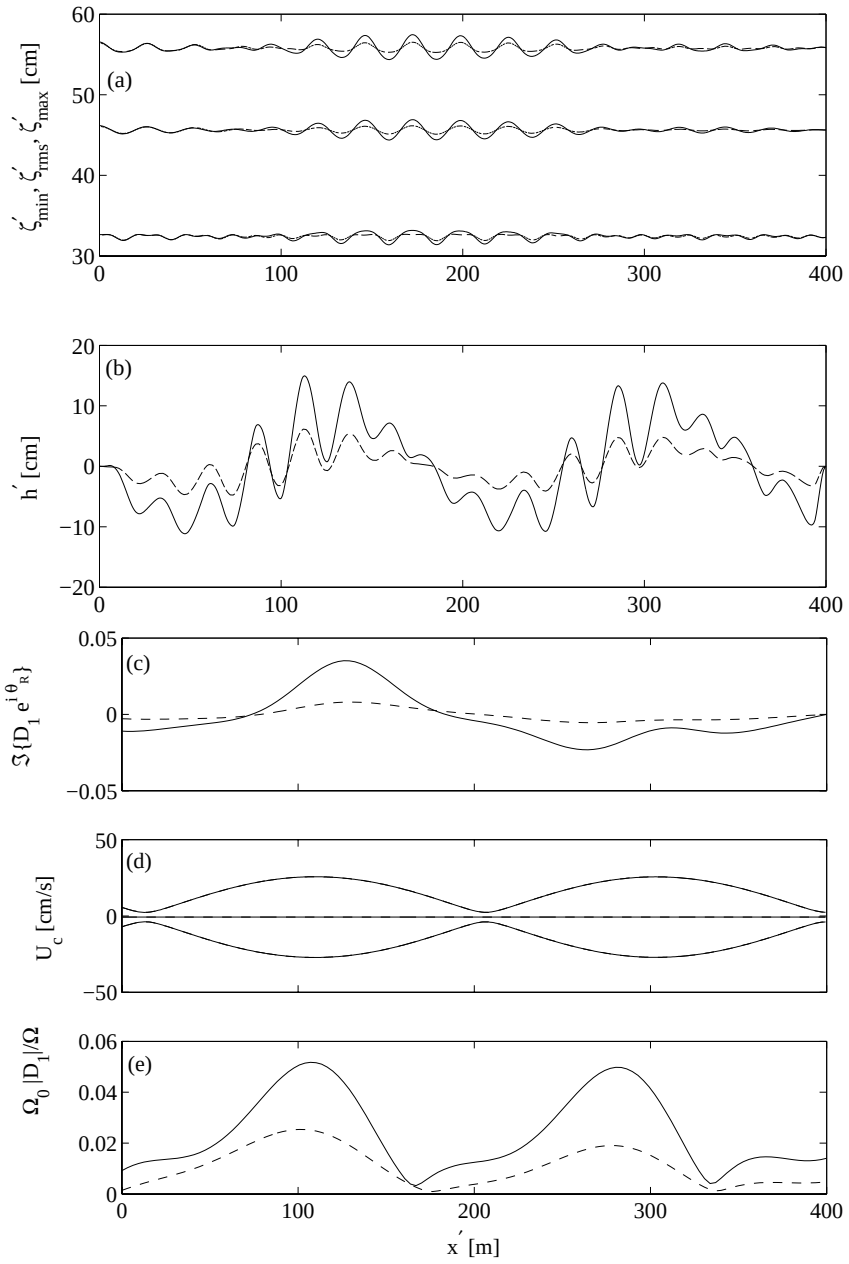


Figure 4-2: Same as Figure 4-1, except the shore reflection is $R_{\pm}(\varepsilon L) = 0.1e^{\pm i\pi/2}$.

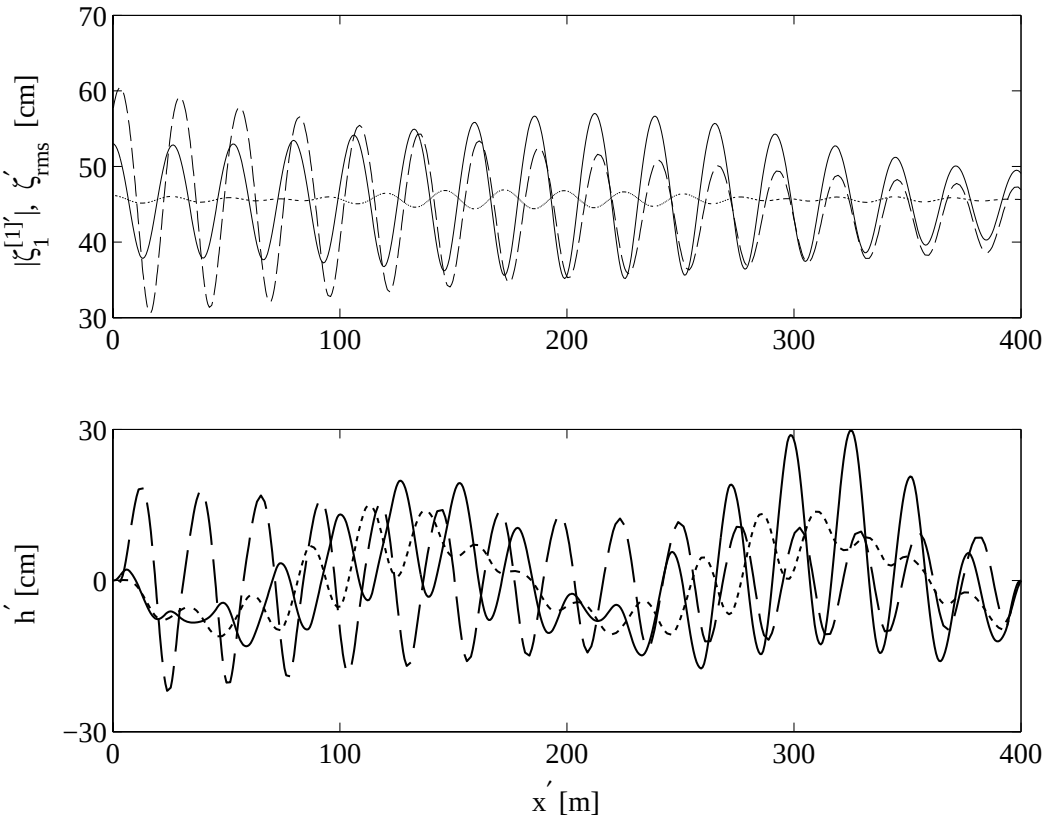


Figure 4-3: Comparison of bars under narrow banded (solid, short dash) and perfectly tuned (long dash) waves, after 3 days of wave action. The shoreline reflection for the narrow banded waves is $R_{\pm}(\varepsilon L) = 0.1$ (solid) and $R_{\pm}(\varepsilon L) = 0.1e^{\pm i\pi/2}$ (short dash) and for the perfectly tuned waves, $R_L = 0.1$ (long dash). The other parameters are the same as those in Figure 4-1, except the wave amplitude of the perfectly tuned waves is $A_o(1 + |R_L|) = 50$ cm.

perfect reflection, the return current vanishes and the bars are similar in shape to those in the monochromatic (perfectly tuned) case, but their amplitude is modulated by the narrow banded waves.

In Figure 4-6, bars on a prototypical beach of coarse grains ($d = 0.5$ mm) with weak shore reflection $R_{\pm}(\varepsilon L) = 0.25$ are shown after 3 days of wave action, under narrow banded (solid) and perfectly tuned (dash) waves. The long spatial modulation of the bar amplitudes are due to both the modulation of the wave amplitude and the oscillatory component of the return flow.

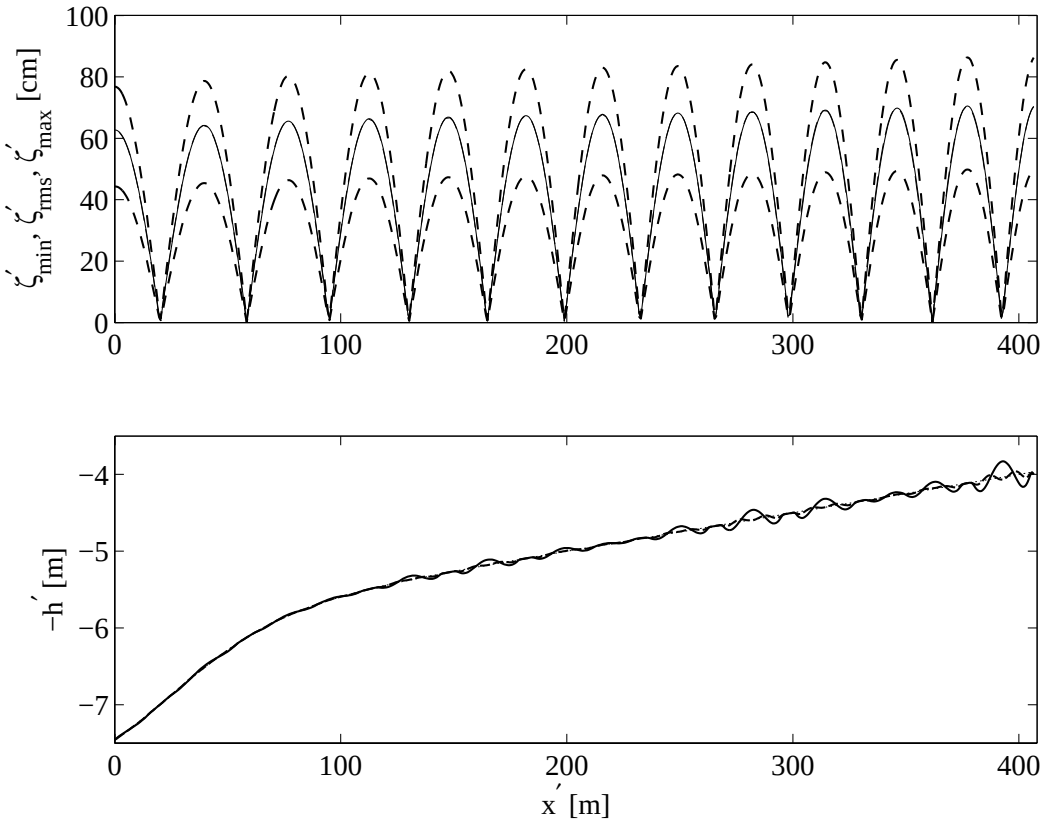


Figure 4-4: The surface envelope and seabed profiles under narrow banded waves on a prototypical sloping beach (2.151) in front of a wall, $R_{\pm}(\varepsilon L) = 1$, after 3 days of wave action. The grain diameter and ripple height is $d = 0.5$ mm and $\eta_r' = 5.5$ (solid) and $d = 0.2$ mm and $\eta_r' = 1.0$ (dash). The other parameters are $T = 10$ s, $\mathcal{A}_{\pm}(0) = 0.90$, $A_o = 50$ cm.

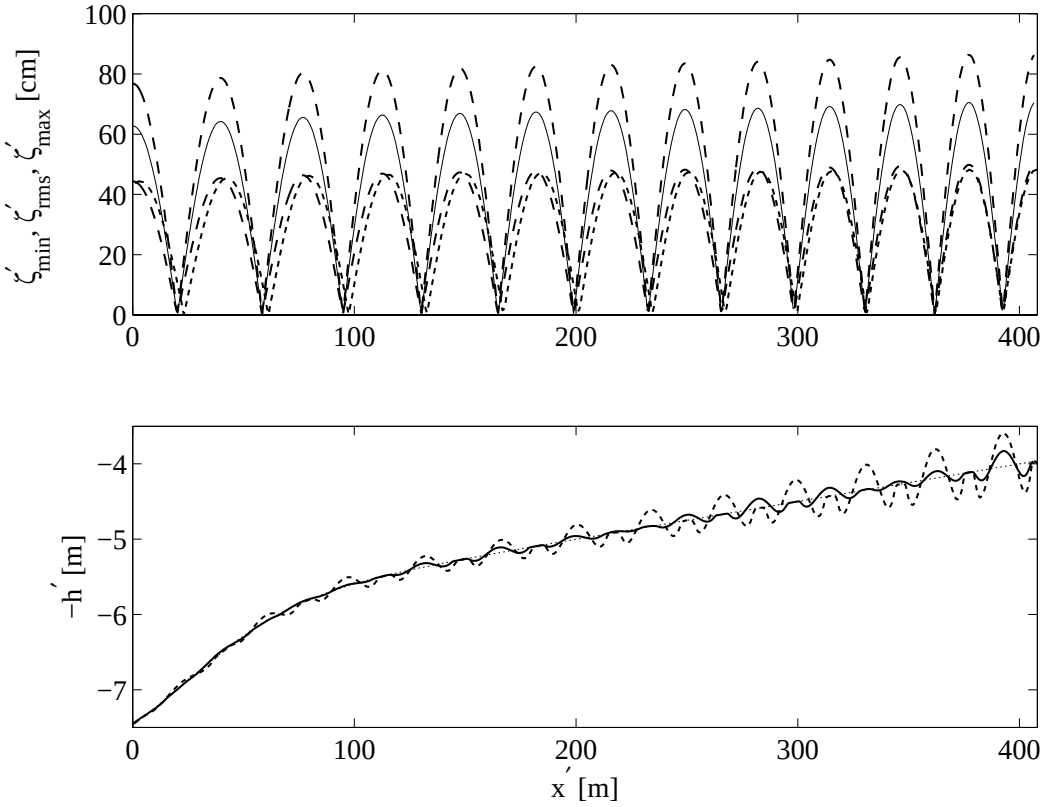


Figure 4-5: The surface envelope and seabed profiles under narrow banded and perfectly tuned waves on a prototypical sloping beach (2.151) in front of a wall, $R_{\pm}\left(\varepsilon L\right) = 1$, after 3 days of wave action. The min, max (long dash) and rms (solid) wave envelopes are given for the narrow banded waves, and the wave envelope $|\zeta_1^{[1]\prime}|$ for the perfectly tuned waves is the short dash line. The solid and dashed seabed profiles correspond to the narrow banded and perfectly tuned waves, respectively, and the dotted line denotes the mean depth (also the initial seabed profile). The other parameters are $T = 10$ s, $\mathcal{A}_{\pm}(0) = 0.90$, $A_o = 25$ cm, $d = 0.5$ mm, and $\eta_r' = 5.5$. The perfectly tuned waves have incident scaled amplitude $A(0) = 0.90$.

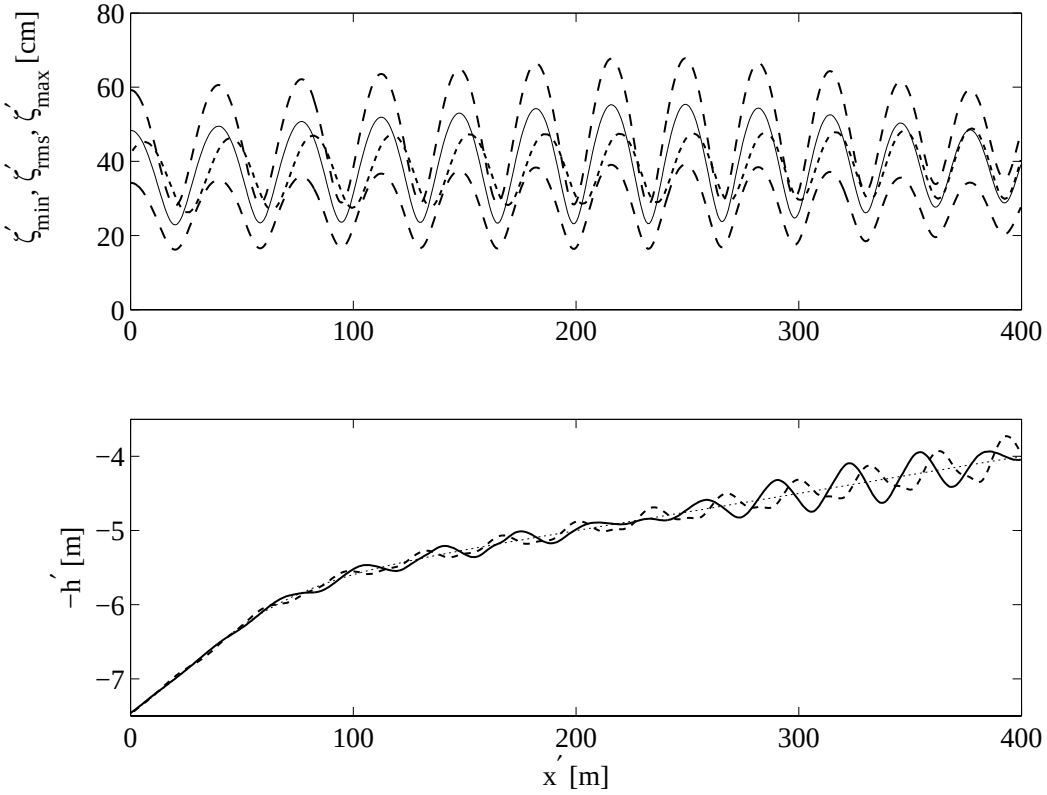


Figure 4-6: The surface envelope and seabed profiles under narrow banded and perfectly tuned waves on a prototypical sloping beach (2.151) with shore reflection $R_{\pm}(\varepsilon L) = 0.25$, after 3 days of wave action. The min, max (long dash) and rms (solid) wave envelopes are given for the narrow banded waves, and the wave envelope $|\zeta_1^{[1]\prime}|$ for the perfectly tuned waves is the short dash line. The solid and dashed seabed profiles correspond to the narrow banded and perfectly tuned waves, respectively, and the dotted line denotes the mean depth (also the initial seabed profile). The other parameters are $T = 10$ s, $\mathcal{A}_{\pm}(0) = 0.887$, $A_o = 40/\sqrt{2}$ cm, $d = 0.5$ mm, $\eta_r' = 5.5$, and $\Lambda_2^{[0]} = 2$. The perfectly tuned waves have incident scaled amplitude $A(0) = 0.887$ and characteristic amplitude $A_o = 40$ cm.

# Chapter 5

# Additional MIT experiments

In this chapter, we review our experimental results on sand bar formation under polychromatic waves and on sediment sorting. The presence of a second harmonic free wave component significantly changes the bar growth rate and bar shape. Also, motivated by the marked difference in bar profiles associated with fine and coarse grains, and also by the sorting experiment of De Best *et al.* [12], we performed a test with coarse red and fine white sands, initially evenly mixed along the entire 15.2 m sediment bed. Under pure standing waves, the sands were sorted into alternating red and white bands. We present both the bar profiles and wave data, as well as the mean grain diameter and thickness of the various deposited layers along the sand bed. Though full theoretical descriptions of the phenomena described here are still lacking, the experimental findings are presented in the hope that complete theories can be found in the future.

## 5.1 Effect on bars due to second harmonic free wave

For constant mean depth, the second harmonic amplitude (1.42) simplifies to

$$\zeta_2^{[2]\prime} = \frac{k'\left(1+2\cosh^2 k'H'\right)\cosh k'H'}{4\sinh^3 k'H'}\left(A'^2 e^{2ik'x'} + B'^2 e^{-2ik'x'}\right) + A^{[2]} e^{ik^{[2]\prime}x'} + B^{[2]} e^{-ik^{[2]\prime}x'}. \tag{5.1}$$

The free wave component, with wavenumber $k^{[2]\prime}$, modulates the forced component, with wavenumber $k' \neq k^{[2]\prime}/2$. The free wave component was initially present due to a monochromatic wavemaker piston displacement, which we later adjusted to cancel the free wave (see §2.6.2). Observing the impact this second harmonic free wave had on the bars, we ran

| Test | $T$ [s] | $H_o$ [cm] | $d$ [mm] | $t'_f$ [days] | $\xi_1$ [cm] | $\xi_2$ [cm] | $\psi_2$ | $A_o$ [cm] | $\lvert R_L \rvert$ |
|---|---|---|---|---|---|---|---|---|---|
| 123 | 2.63 | 60 | 0.20 | 1.00 | 6.0 | 0 | 0 | 4.71 | 0.26 |
| 124 | 2.63 | 60 | 0.20 | 1.00 | 7.5 | 0 | 0 | 5.80 | 0.24 |
| 212 | 2.63 | 60 | 0.20 | 2.00 | 7.5 | 0 | 0 | 5.83 | 0.25 |
| 226 | 2.63 | 60 | 0.20 | 3.00 | 6.5 | 0 | 0 | 3.62 | 0.29 |
| 505 | 2.5 | 60 | 0.20 | 2.50 | 9.0 | 2.0 | 1.5 | 3.27 | 1.0 |
| 513 | 2.5 | 60 | 0.20 | 2.25 | 7.0 | 2.0 | 1.5 | 4.61 | 0.24 |
| 523 | 2.5 | 60 | 0.125 | 1.50 | 9.0 | 2.0 | 1.5 | 3.16 | 1.0 |

Table 5.1: Parameters for the MIT experiments on the effects of moderate and large free second harmonic wave components.

additional tests with large second harmonic free waves. In these latter cases, the flow had two dominant free wave harmonics.

Two dominant harmonics in the wave field will force corresponding harmonics in the boundary layer, in particular, in the bed shear stress. The bedload transport rate will also have two dominant harmonics,

$$\overline{q_B} = \frac{Q_B}{1-\mathcal{N}} \overline{\left|\frac{\Theta}{\widehat{\Theta}}\right|^4 \frac{\Theta}{|\Theta|}} + O(\varepsilon) \tag{5.2}$$

The mean bedload transport rate over a wave period is thus a nonzero quantity. This differs from the near-monochromatic case where the mean bedload transport rate is zero to leading order. Hence, with a larger net bedload transport rate, the bar growth rate is an order of magnitude larger. Bar shape is also affected too. We attempted to derive a quantitative theory for bar formation. Since the mean bedload transport does not average to zero at leading order, a theory can be constructed using only the leading order flow terms in the boundary layer. However, using a depth-linear but time invariant eddy viscosity similar to Eq. (2.1), the sand bar predictions, although different from those under monochromatic waves, could not properly predict the measured crest locations. In fact, the discrepancy was so large that we must admit that a key component to the physical mechanism is missing. In any case, the experimental findings are reported here. A theoretical description of these should be a subject of future research.

The experimental setup is described in §2.6. The parameters for the additional tests are listed in Table 5.1.

### 5.1.1 Second harmonic free waves due to monochromatic piston displacement

In this section, we review results from tests whose second harmonic free wave component was due purely to a monochromatic wavemaker piston displacement, $\xi'(t') = \xi_1 \cos \omega t'$. The tests include 123, 124, 212, and 226 and the associated parameters, including the wavemaker piston displacement, are listed in Table 5.1. For each of these tests, the final wave amplitudes and seabed profiles are shown in Figures 5-1, 5-3, 5-4, and 5-7. The time evolutions of the bar heights are shown in Figures 5-2, 5-6, and 5-8. The presence of the second harmonic is indicated by the modulation of the second harmonic amplitude, due to the interaction of the second harmonic wave components of wavenumber $2k^{[1]\prime}$ and $k^{[2]\prime}$, where $(n\omega)^2 = gk^{[n]\prime} \tanh k^{[n]\prime} H_o$. Lastly, tests 124 and 212 had the same wavemaker settings, sediment diameter and mean water depth. Therefore, comparing the resulting seabed and wave profiles yields an estimate of our experimental variability. Figures 5-5 and 5-6 demonstrate that the variability in the seabed elevation is approximately 1 cm, and that of the first harmonic amplitude is approximately 0.25 cm.

### 5.1.2 Strong second harmonic free wave

In this section, we review results from tests with large second harmonic free wave components generated by adding a large second harmonic to the wavemaker piston displacement, $\xi'(t') = \xi_1 \cos \omega t' + \xi_2 \sin 2\omega t' + \psi_2$. The tests include 505, 513, and 523 and the associated parameters, including the wavemaker piston displacement, are listed in Table 5.1.

In test 505, we investigated the effect of a large free second harmonic on a seabed of coarse grains, under perfect shoreline reflection $R_L = 1$. The wave amplitudes and seabed profiles are shown in Figure 5-9. The effect of the free second harmonic is illustrated by comparing the results to those of test 430, which had the same sediment diameter, reflection coefficient, and mean water depth. The free second harmonic modulates the wave phase, thereby significantly changing the seabed profiles. Bar crests in test 430 become troughs in test 505, and vice versa. The presence of the second harmonic almost doubles the growth rate and bar height over that in the monochromatic test 430 (Figure 5-10).

In test 513, we investigated the effect of a large free second harmonic on a seabed of coarse grains, under weak shoreline reflection $R_L = 0.24$. The wave amplitudes and seabed

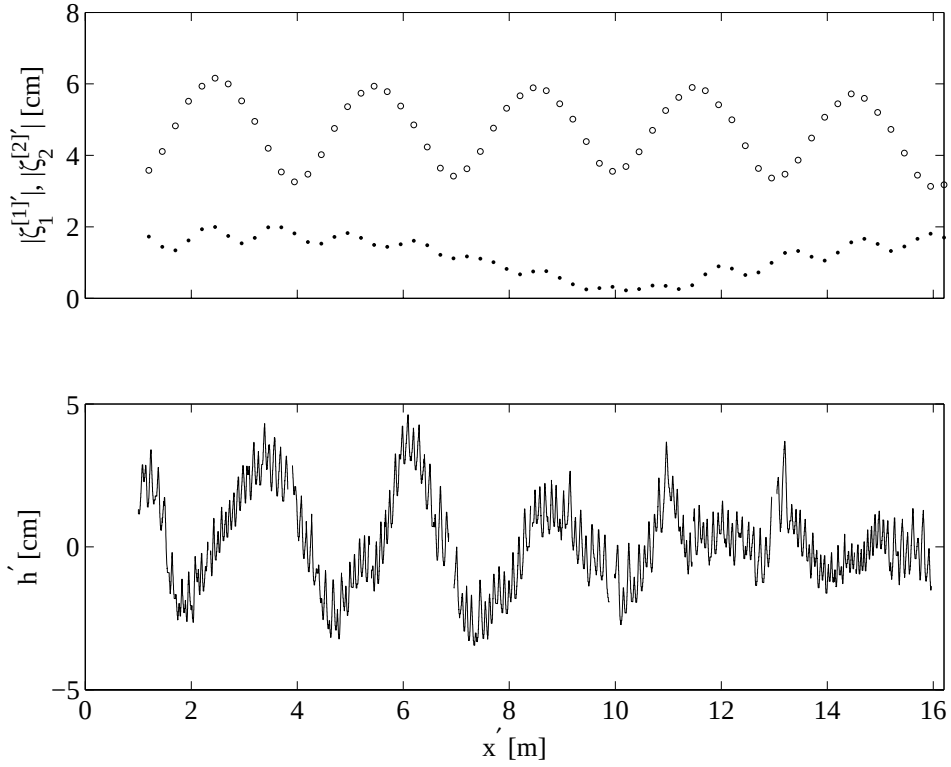


Figure 5-1: Measured wave amplitudes (top) and seabed profile (ripples and bars, bottom) for test 123 after 1.0 days of wave action. The first and second harmonic wave amplitudes are denoted as $\zeta'_{env} = |\zeta_1^{[1]\prime}|$ (∘) and $|\zeta_2^{[2]\prime}|$ (•). $x' = 0$ is 2.80 m from the mean wavemaker position. Gaps in the seabed data are due to vertical tank supports blocking the view.

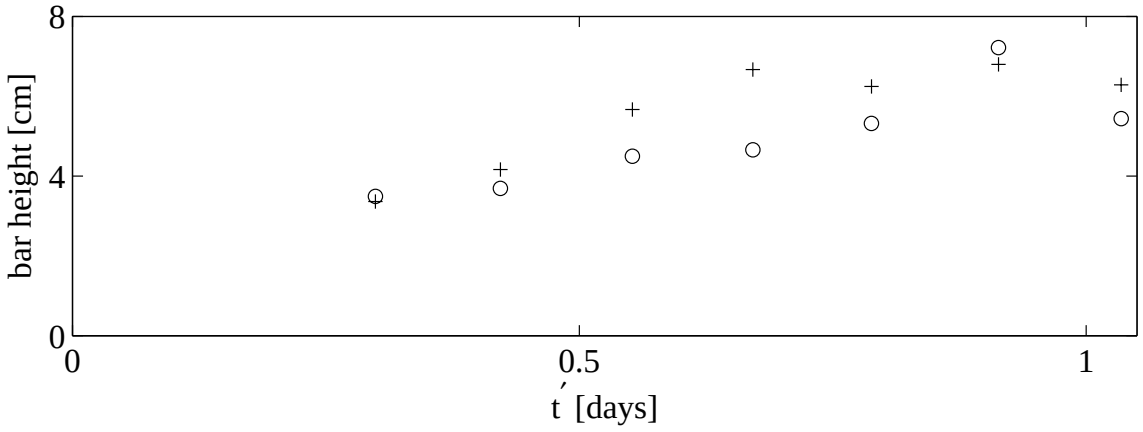


Figure 5-2: Time evolution of bar height for test 123, for the first (∘) and second (+) bars counted from the left in Figure 5-1.

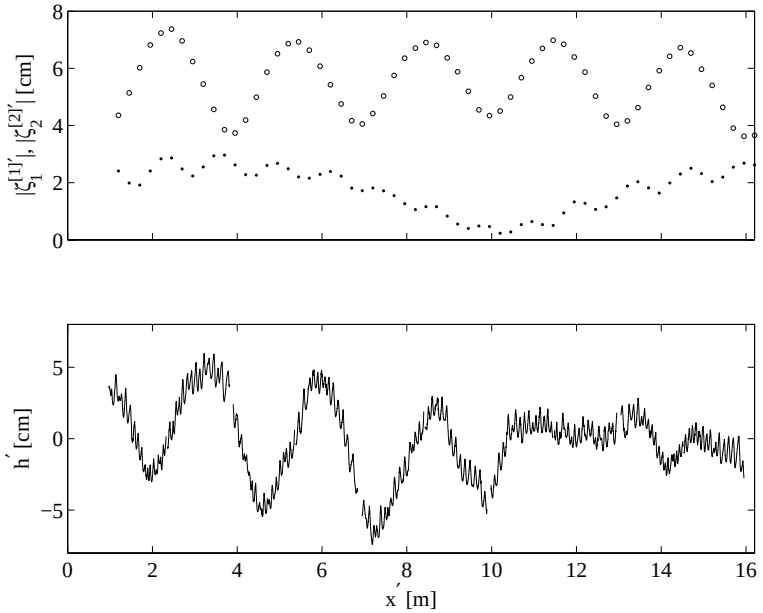


Figure 5-3: Measured wave amplitudes (top) and seabed profile (ripples and bars, bottom) for test 124 after 1.0 days of wave action. The first and second harmonic wave amplitudes are denoted as $\zeta'_{env} = |\zeta_1^{[1]\prime}|$ ($\circ$) and $|\zeta_2^{[2]\prime}|$ ($\bullet$). $x' = 0$ is 2.80 m from the mean wavemaker position. Gaps in the seabed data are due to vertical tank supports blocking the view.

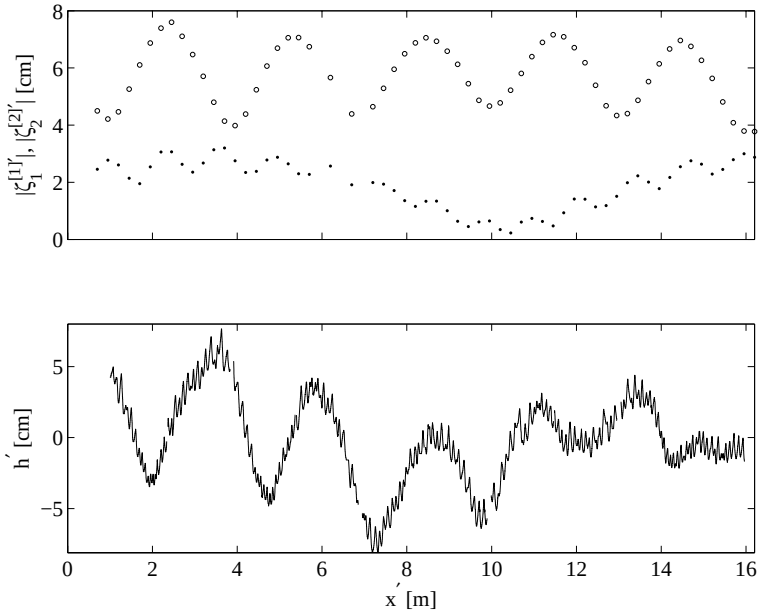


Figure 5-4: Measured wave amplitudes (top) and seabed profile (ripples and bars, bottom) for test 212 after 2.0 days of wave action. The first and second harmonic wave amplitudes are denoted as $\zeta'_{env} = |\zeta_1^{[1]\prime}|$ ($\circ$) and $|\zeta_2^{[2]\prime}|$ ($\bullet$). $x' = 0$ is 2.80 m from the mean wavemaker position. Gaps in the seabed data are due to vertical tank supports blocking the view.

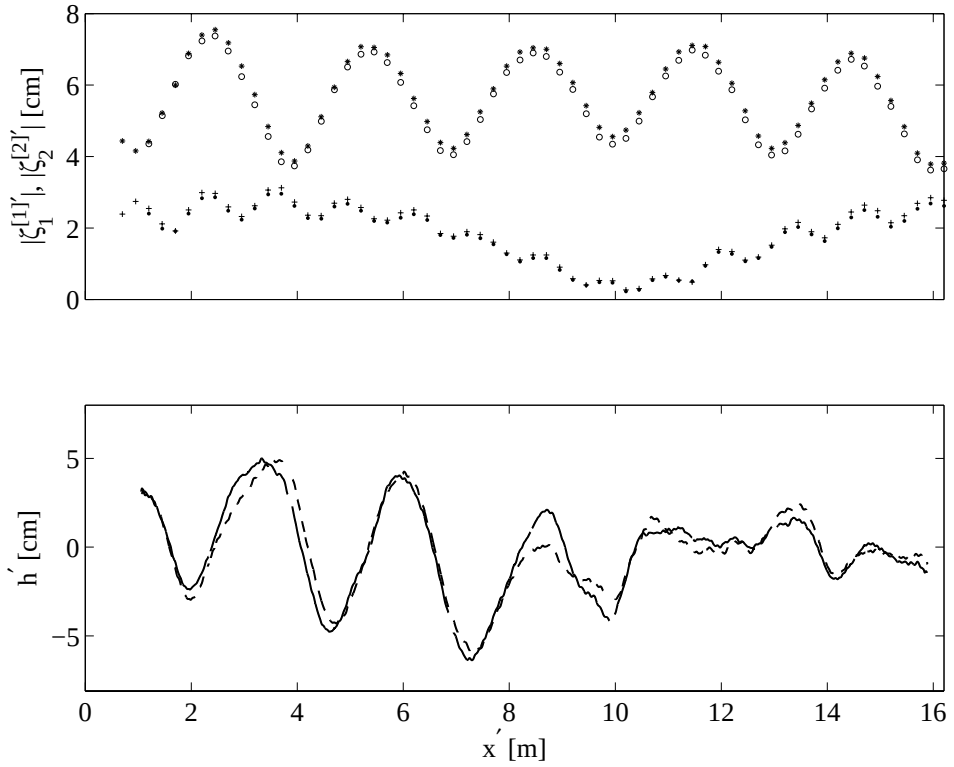


Figure 5-5: Comparison of measured wave amplitudes and seabed profiles for tests 124 and 212 after 1.0 days of wave action. Top: first and second harmonic wave amplitudes $\zeta'_{env} = |\zeta_1^{[1]\prime}|$ and $|\zeta_2^{[2]\prime}|$ for tests 124 (∘, •) and 212 (□, +). Bottom: averaged seabed profiles (bars only) for tests 124 (dash) and 212 (solid). $x' = 0$ is 2.80 m from the mean wavemaker position. Gaps in the seabed data are due to vertical tank supports blocking the view.

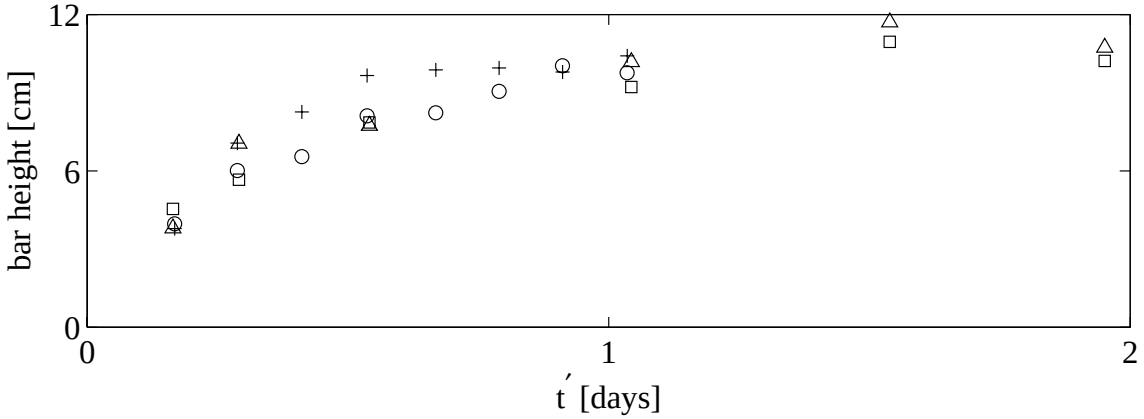


Figure 5-6: Comparison of the time evolution of the heights of the first (∘) and second (+) bars in test 124, to the heights of the first (□) and second (△) bars in test 212, counted from the left in Figure 5-5.

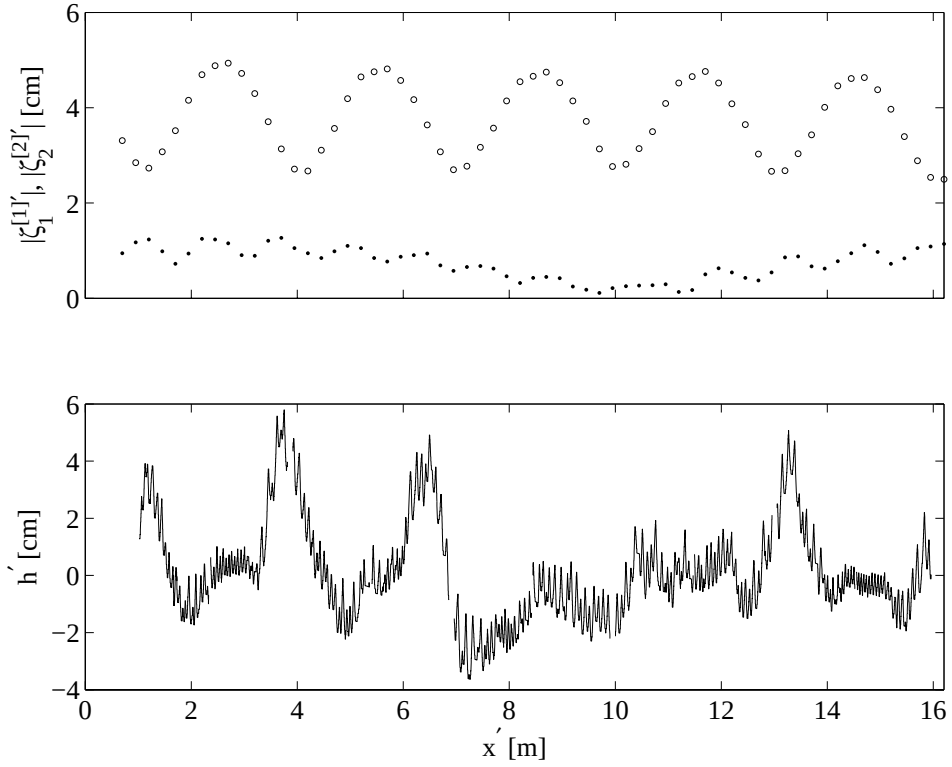


Figure 5-7: Measured wave amplitudes (top) and seabed profile (ripples and bars, bottom) for test 226 after 3.0 days of wave action. The first and second harmonic wave amplitudes are denoted as $\zeta'_{env} = |\zeta_1^{[1]\prime}|$ (○) and $|\zeta_2^{[2]\prime}|$ (●). $x' = 0$ is 2.80 m from the mean wavemaker position. Gaps in the seabed data are due to vertical tank supports blocking the view.

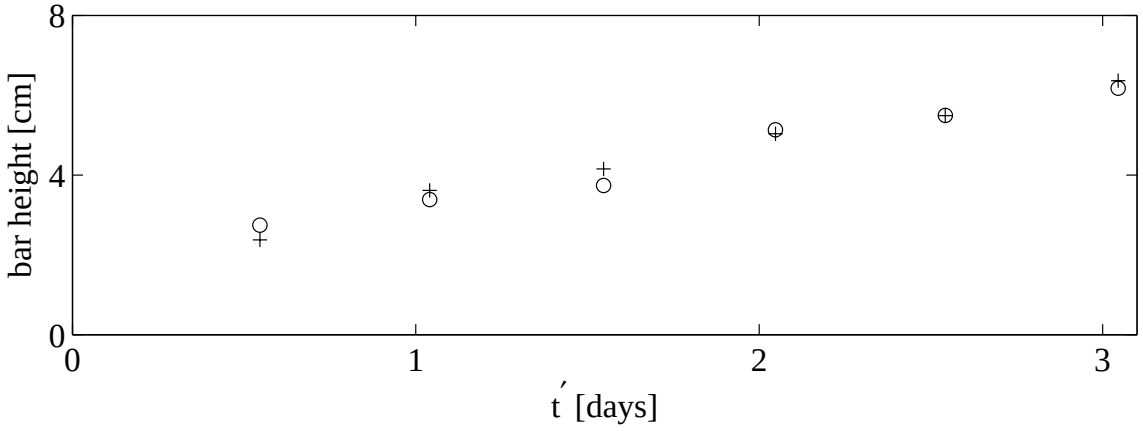


Figure 5-8: Time evolution of bar height for test 226, for the first (○) and second (+) bars, counted from the left in Figure 5-7.

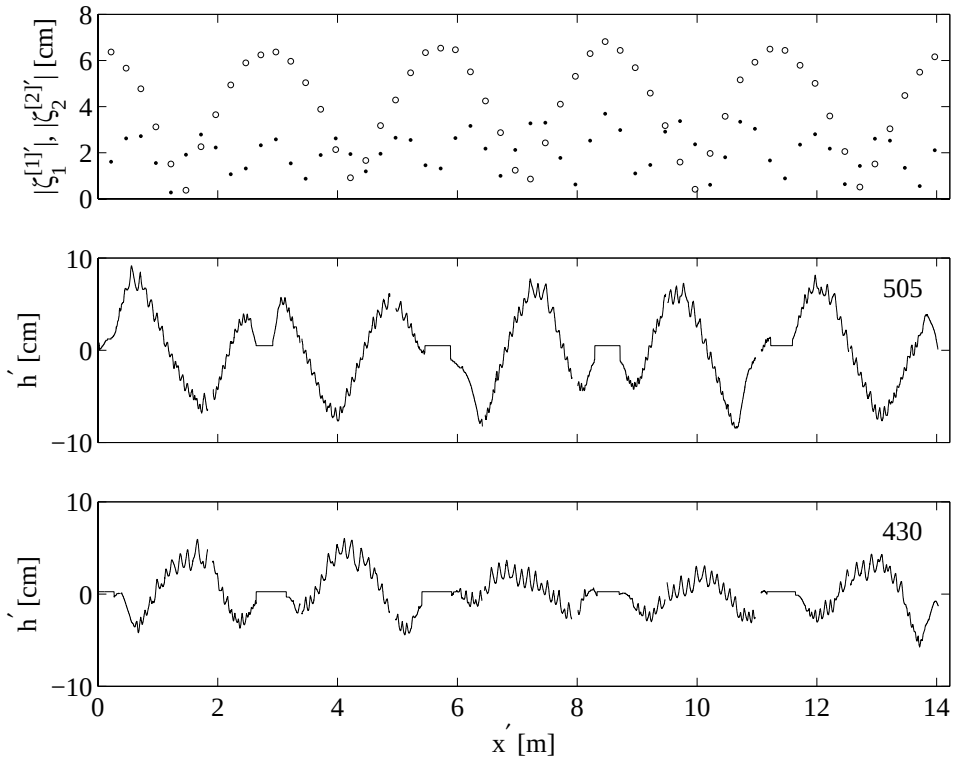


Figure 5-9: Final wave amplitudes and seabed profile for test 505 after 2.5 days of wave action. Top: first and second harmonic wave amplitudes $\zeta'_{env} = |\zeta_1^{[1]\prime}|$ (○) and $|\zeta_2^{[2]\prime}|$ (●). Middle: seabed profile (ripples and bars). Bottom: for comparison, seabed profile for test 430 after 4.0 days. $x' = 0$ is 4.78 m from the mean wavemaker position. Gaps in the seabed data are due to vertical tank supports blocking the view.

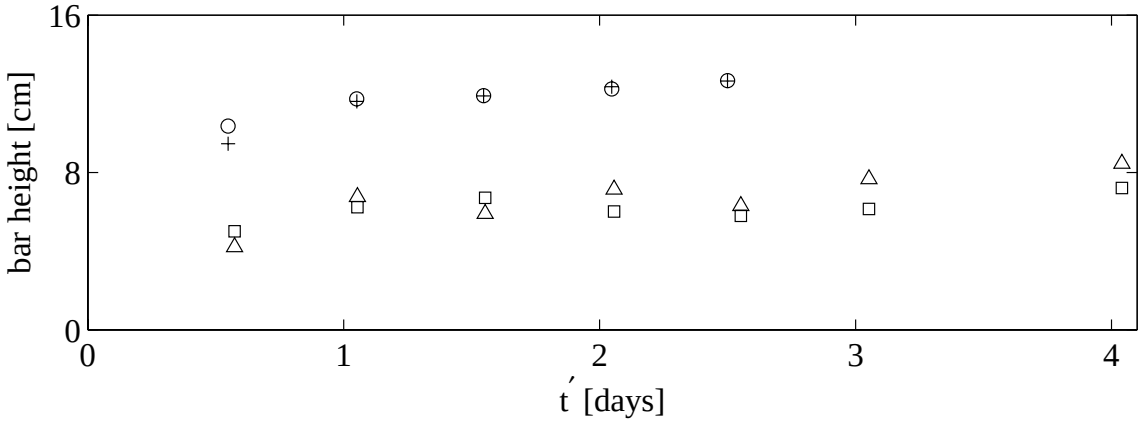


Figure 5-10: Comparison of the time evolution of the heights of the first (○) and third (+) bars in test 505, to the heights of the first (□) and second (△) bars in test 430, counted from the left in Figure 5-9.

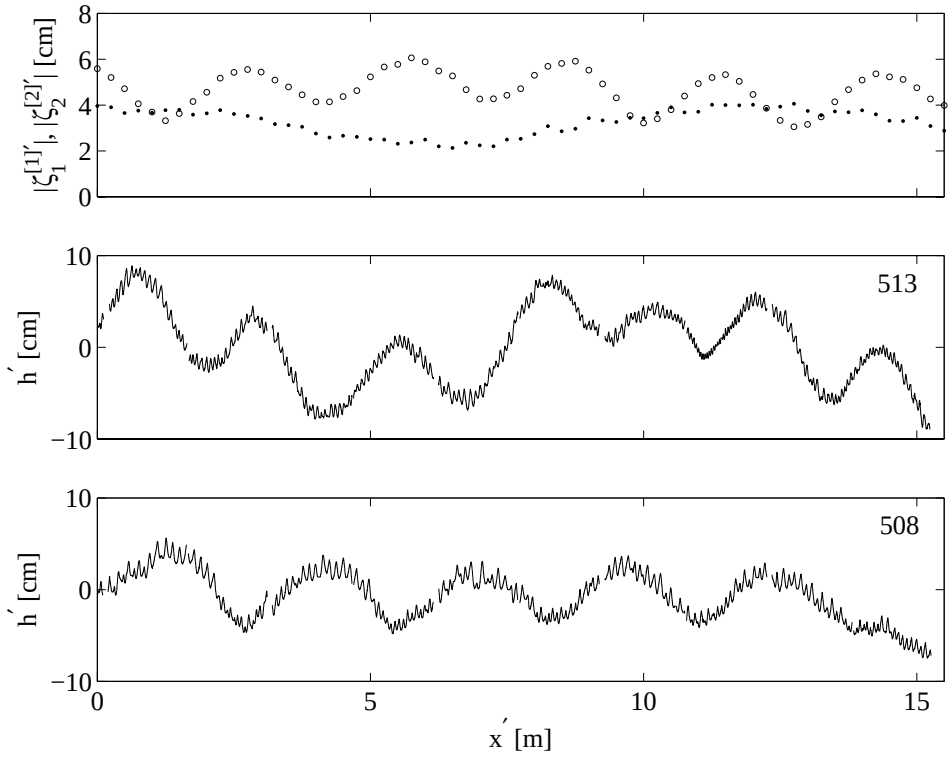


Figure 5-11: Final wave amplitudes and seabed profile for test 513 after 2.3 days of wave action. Top: first and second harmonic wave amplitudes $\zeta'_{env} = |\zeta_1^{[1]\prime}|$ (○) and $|\zeta_2^{[2]\prime}|$ (●). Middle: seabed profile (ripples and bars). Bottom: for comparison, seabed profile for test 508 after 4.0 days. $x' = 0$ is 3.5 m from the mean wavemaker position. Gaps in the seabed data are due to vertical tank supports blocking the view.

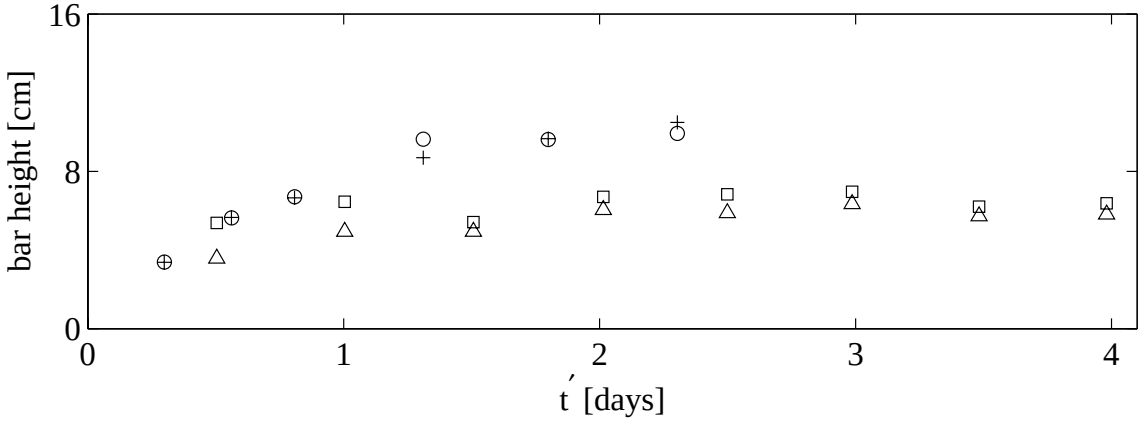


Figure 5-12: Comparison of the time evolution of the heights of the first (○) and third (+) bars in test 513, to the heights of the first (□) and second (△) bars for test 508, counted from the left in Figure 5-11.

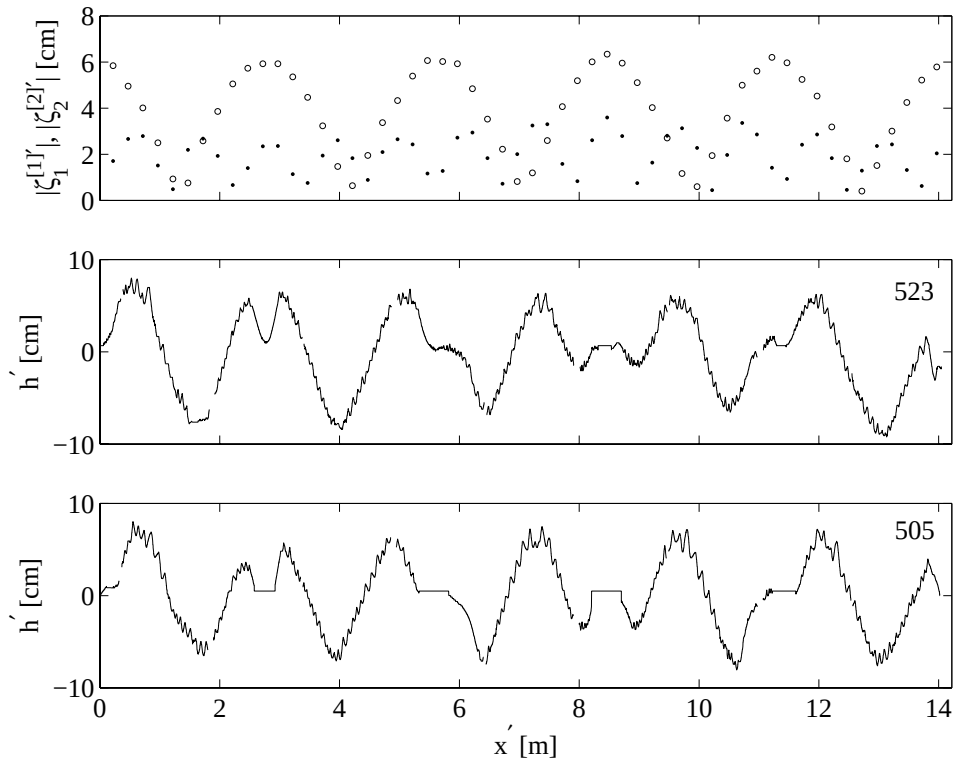


Figure 5-13: Wave amplitude and seabed profiles for test 523 after 1.5 days of wave action. Top: first and second harmonic wave amplitudes $\zeta'_{env} = |\zeta_1^{[1]\prime}|$ ($\circ$) and $|\zeta_2^{[2]\prime}|$ ($\bullet$). Middle: seabed profile (ripples and bars). Bottom: for comparison, seabed profile for test 505 after 1.5 days. $x' = 0$ is 4.78 m from the mean wavemaker position. Gaps in the seabed data are due to vertical tank supports blocking the view.

profiles are shown in Figure 5-11. The effect of the free second harmonic is illustrated by comparing the results to those of test 508, which had the same sediment diameter, reflection coefficient, and mean water depth. Again, the free second harmonic modulates the wave phase, thereby significantly changing the seabed profiles. Bar crests in test 508 become troughs in test 513, and vice versa. Also, long spatial scale ($x_1$) undulations are evident in the seabed profile of test 513, while the seabed profile of test 508 primarily contains short spatial scale ($x$) undulations. The presence of the second harmonic again increases the bar growth rate and height over that in the monochromatic test 508 (Figure 5-12).

In test 523, we investigated the effect of a large free second harmonic on a seabed of fine grains, under perfect shoreline reflection $R_L = 1$. The wave amplitudes and seabed profiles are shown in Figure 5-13. The effect of the free second harmonic is illustrated by comparing the results to those of test 505, which had the same wavemaker piston displacement, reflection coefficient, and mean water depth, but a mean grain diameter of $d = 0.20$

| Test | $T$ [s] | $H_o$ [cm] | $d$ [mm] | $t'_f$ [days] | $\xi_1$ [cm] | $\xi_2$ [cm] | $\psi_2$ | $A_o$ [cm] | $\|R_L\|$ |
|---|---|---|---|---|---|---|---|---|---|
| 603 | 2.5 | 60 | 0.21 & 0.11 | 6.00 | 10.0 | 0.402 | 0 | 3.59 | 1.0 |

Table 5.2: Parameters for the MIT test 603 on sediment sorting under standing waves.

mm. The two seabed profiles are strikingly similar, indicating the two grain sizes act in a similar manner under these polychromatic waves. Under monochromatic waves with perfect reflection in tests 430 and 519, the seabed profiles corresponding to these two grain sizes were markedly different (see Chapter 3).

## 5.2 Sediment sorting

Sands on real beaches have a distribution of grain sizes. Past and current experiments have shown and our theory has explained the migration of sand on uniform beds. Coarse sand tends to be transported toward wave nodes as bedload, and fine sand toward wave antinodes as suspended load. It is important to also study sand bar formation on a bed of multiple grain sizes where the two modes of sediment transport coexist. For a sand bed consisting of multiple grain sizes, De Best *et al.* [12] demonstrated experimentally that under pure standing waves, fine grains are transported toward the wave antinodes as suspended load and the coarser grains toward the nodes as bed load, thereby achieving sediment sorting on the seabed. De Best *et al.* only reported the profiles and grain diameters over one bar.

The MIT sediment sorting test 603 was run in collaboration with Blake J. Landry, and was a larger scale version De Best *et al.*'s test with almost twice the water depth ($H_o = 60$ cm), over twice the wave height, and five sand bars. Sands of different colors were used to visually elucidate the sediment sorting. Many sediment samples were taken before and after the experiment to measure the initial and final sediment distributions.

The experimental setup was outlined in §2.6. Our sediment sorting test 603 was run with the wall configuration of the wave tank to obtain a reflection coefficient of $R = 1$. The pure standing waves generated had a period of $T = 2.5$ s and an incident amplitude of $A_o = 3.59$ cm. The setup parameters are summarized in Table 5.2.

Initially, the seabed consisted of a mixture of two grain sizes of Ottawa silica sand, $d = 0.21$ mm and $d = 0.11$ mm. The coarse $d = 0.21$ mm sand was colored red by the

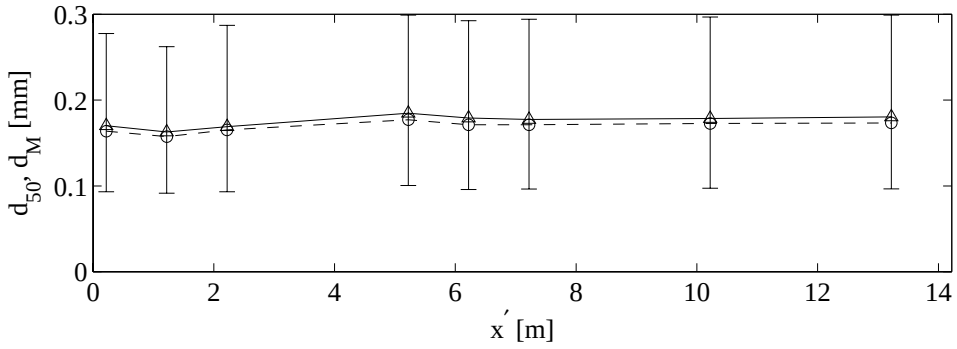


Figure 5-14: Initial mean grain diameter $d_M$ ($\circ$) and median grain diameter ($\triangle$) along sediment bed test 603. Vertical bars from $d_{16}$ to $d_{84}$ at each data point for $d_{50}$ quantify the spread of the grain size distribution. $x' = 0$ is 4.78 m from the mean wavemaker position.

manufacturer (Clifford W. Estes Company) through a painting/baking process. The fine $d = 0.11$ mm sand was its natural color. The sands were initially dry-mixed using a cement mixer, and then hand mixed in small quantities with water and drops of Windex. The small quantities were then individually placed on the sand bed. Once the sand bed was in place, it was leveled. Ten vertical core samples, 3.2 cm in diameter, were then taken along and across the initial bed to ensure the sediment distribution was constant along the bed (see Landry [33] for further details including sieve analyses).

To quantify the sediment distribution, we employ $d_{16}$, $d_{50}$, and $d_{84}$, the grain diameters that are coarser than 16%, 50%, and 84% of the total sampled mass of sediment, respectively. These are typically called "% finer" since 16%, 50%, and 84% of the total sampled mass of sediment is finer than $d_{16}$, $d_{50}$, and $d_{84}$, respectively (Coastal Engineering Manual [51]). The median grain diameter is defined as $d_{50}$ and the mean grain diameter is defined as [51]

$$d_M = (d_{16} d_{50} d_{84})^{1/3} .$$

Note that for sand of a uniform grain size, $d_{16} = d_{50} = d_{84}$ and hence the mean and median diameters are the same, $d_M = d_{50}$. The mean and median grain diameters $d_{50}$ and $d_M$ of the initial bed are plotted along the tank in Figure 5-14, and are approximately $d_{50} \approx 0.175$ mm and $d_M \approx 0.169$ mm. The variability is estimated by plotting vertical bars from $d_{16}$ to $d_{84}$ at each data point for $d_{50}$ along the tank (Figure 5-14). The consistent values of $d_{16}$, $d_{50}$, $d_{84}$, and $d_M$ along the tank indicate the initial bed was well mixed with a nearly uniform sediment distribution.

During test 603, the wave amplitudes and seabed profiles were periodically measured in the manner discussed in §2.6. Digital images of the top view of the sediment bed were also taken periodically to further record the sediment sorting and the ripple and bar evolution.

Within 30 minutes of the wavemaker starting, a thin layer of fine white sand covered the seabed under the antinodes. Clouds of suspended white sand were visible under the wave nodes, as the white sand was lifted from the nodes and transported toward the antinodes. As the ripples moved along the seabed under the nodes, more white sand was exposed and brought into suspension. Red sand from the troughs between the nodes and antinodes was transported toward the nodes. Alternating red and white bands so developed along the bed. Red bar crests formed under the wave nodes and white regions delineated with small white crests formed under the wave antinodes. Figures 5-15 and 5-16 illustrate the bed evolution. After approximately a day, most of the sand under the wave nodes was coarse red sand, and the water under the nodes was clear, indicating a significantly reduced suspended sediment concentration. The experiment was run for 10 days; an equilibrium was achieved after a few days. Photographs of the final seabed are shown in Figures 5-17 and 5-18. The wave amplitudes and bar profiles are shown in Figure 5-19 after 5 days of wave action.

After the wavemaker was stopped, two types of sediment samples were taken. Horizontal scrapings were taken across the width of the tank at specific x-coordinates to obtain samples of the top 1 cm of the sand bed. A PVC pipe of diameter was cut in half to obtain the scrapings. The sand samples were then dried in air and in an oven and the grain size distribution of the dry sediment was found from sieve analyses. The mean and median grain diameters $d_{50}$ and $d_M$ are plotted along the tank in Figure 5-20. On the red bar crests under the wave nodes, the sand had a median diameter $d_{50}$ between 0.25 mm and 0.28 mm, larger than that ($d = 0.21$ mm) of the relatively coarse pure red sand. On the white regions under the wave antinodes, the mean grain diameter was between 0.8 mm and 0.9 mm, smaller than that ($d = 0.11$ mm) of the relatively fine pure white sand. The variability is estimated by plotting vertical bars from $d_{16}$ to $d_{84}$ at each data point for $d_{50}$ along the tank (Figure 5-20). In the white regions under the wave antinodes, $d_{84} - d_{16}$ is relatively small, indicating the sediment in these regions was well-sorted (i.e. had little variation). In the troughs between the nodes and antinodes, the variability and mean grain diameters are close to that of the initial seabed. Along the red crests under the wave nodes, the variability was moderate, but still shifted toward the coarse grain range relative to the initial grain

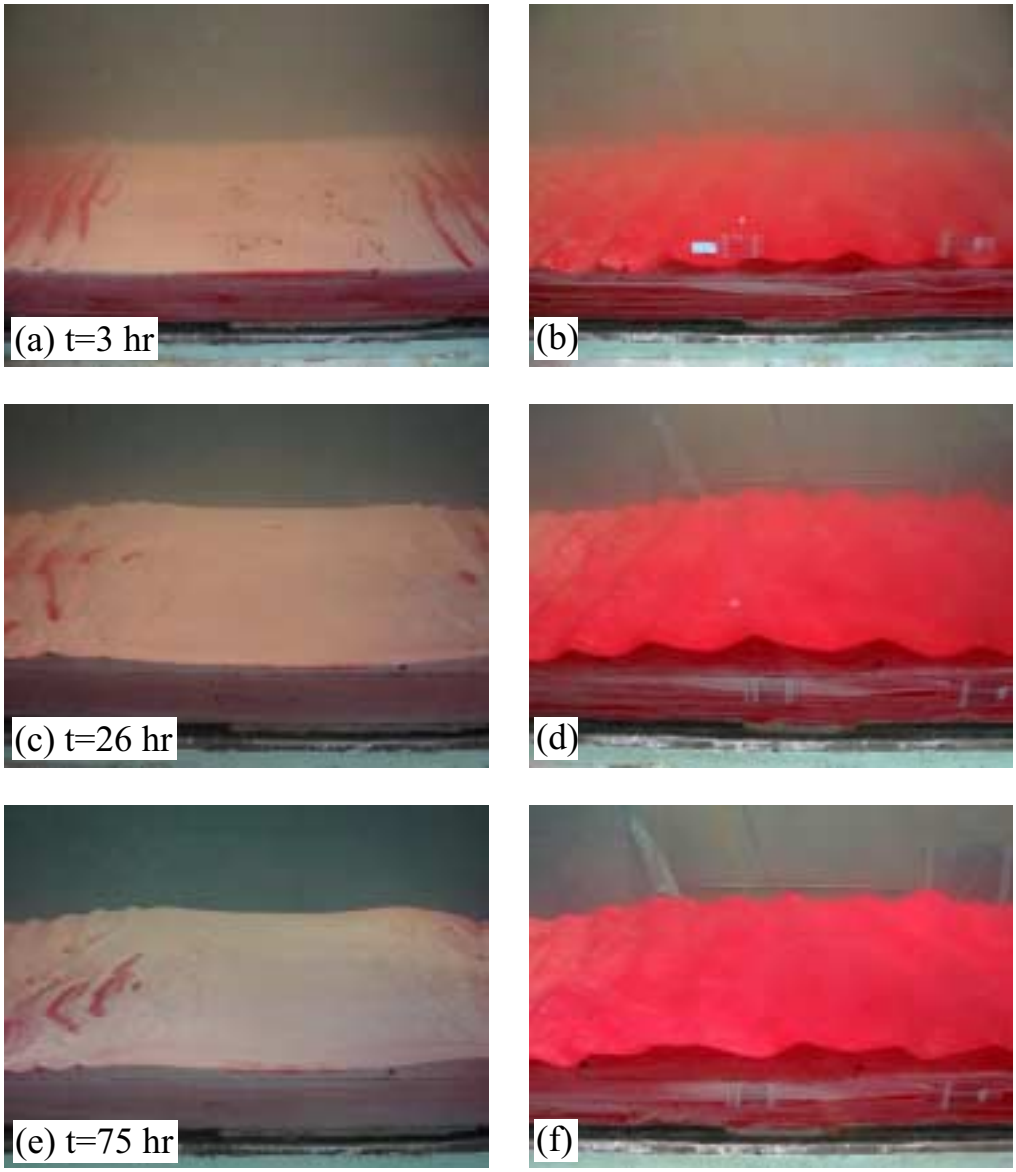


Figure 5-15: Sediment accumulation and movement for test 603 after 3 hrs (a), (b), 26 hrs (c), (d), and 75 hrs (e), (f) of wave action. Seabed portions shown are under a wave antinode (a), (c), (e) and under a wave node (b), (d), (f). Picture clarity indicates the concentration of suspended fine sediments in the water column.

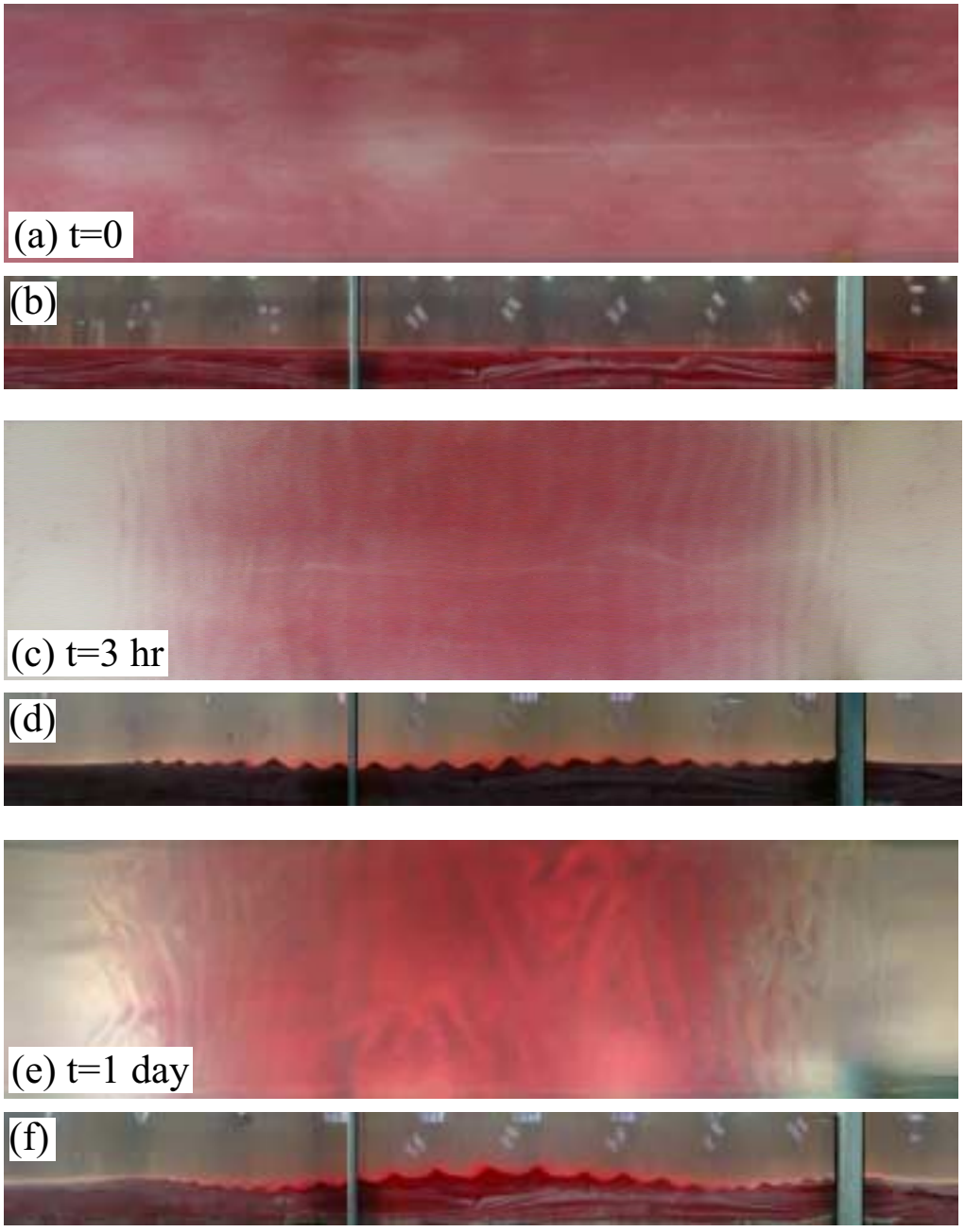


Figure 5-16: Seabed profiles for test 603 initially (a), (b) and after approximately 3 hrs (c), (d) and 1 day (e), (f) of wave action. Images (a), (c), and (e) are top views, and (b), (d), (f) are side views of the same sand bar.

Figure 5-17: Top and side views of a portion of the final seabed profile (after 10 days of wave action) spanning three bar lengths for test 603.

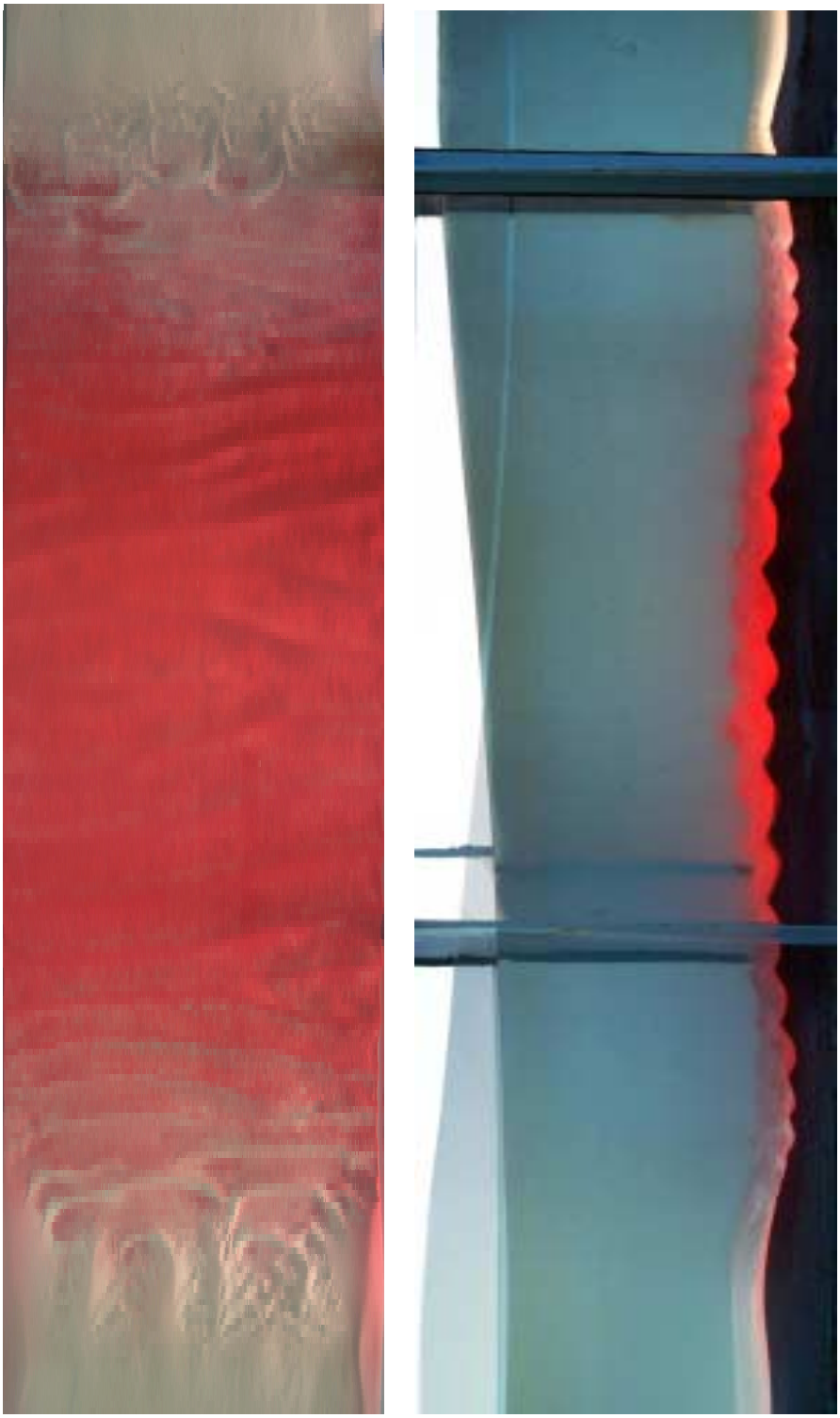

Figure 5-18: Top view (left) and side view (right, courtesy of Felice Frankel / Blake J. Landry / Matthew J. Hancock) of one bar length of seabed for test 603, after 10 days of wave action. Wave profiles in side view are approximately $180^o$ out of phase.

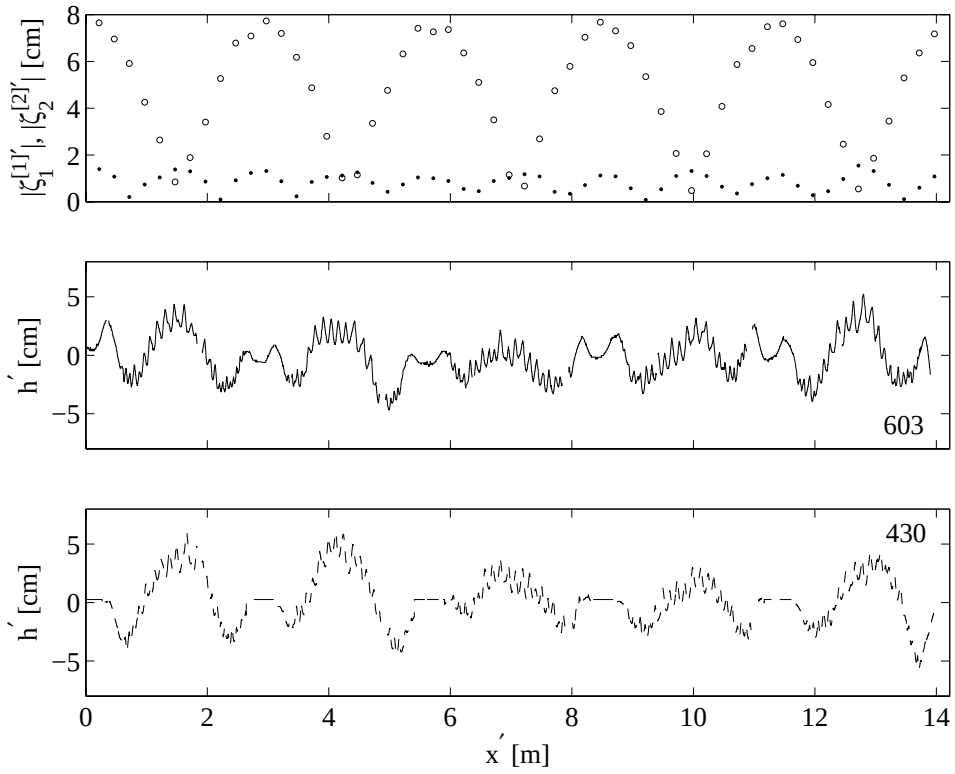


Figure 5-19: Wave amplitudes and seabed profile for test 603 after 5.1 days of wave action. Top: first and second harmonic wave amplitudes $\zeta'_{env} = |\zeta_1^{[1]\prime}|$ ($\circ$) and $|\zeta_2^{[2]\prime}|$ ($\bullet$). Middle: seabed profile (ripples and bars). Bottom: for comparison, seabed profile for test 430 after 4.0 days. $x' = 0$ is 4.78 m from the mean wavemaker position. Gaps in the seabed data are due to vertical tank supports blocking the view.

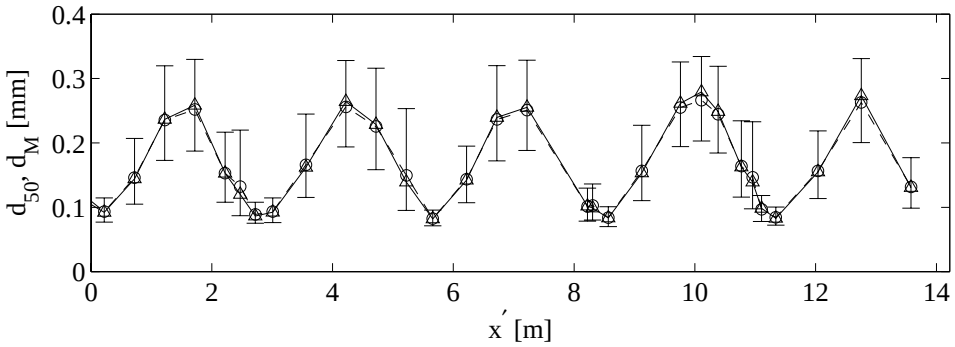


Figure 5-20: Mean grain diameter $d_M$ ($\circ$) and median grain diameter $d_{50}$ ($\triangle$) along the final sediment bed (after 10 days of wave action) for test 603. Vertical bars from $d_{16}$ to $d_{84}$ at each data point for $d_{50}$ quantify the spread of the grain size distribution. $x' = 0$ is 4.78 m from the mean wavemaker position.

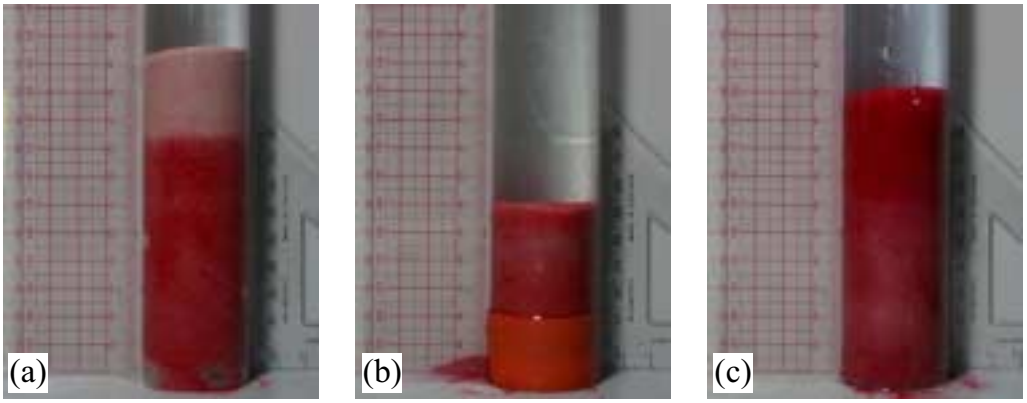


Figure 5-21: Vertical core samples of final seabed for test 603, from under a wave antinode (a), a bar trough (b), and under a wave node (c).

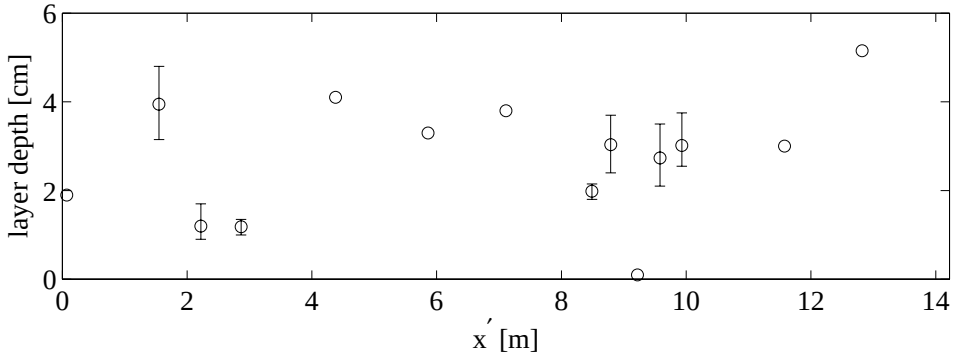


Figure 5-22: Thickness of modified layer (∘) along final seabed profile (after 10 days of wave action) for test 603. Error bars denote variability of thickness laterally across the bed. $x' = 0$ is 4.78 m from the mean wavemaker position.

size distribution.

Vertical core samples of the final seabed were also taken at over 20 locations along the seabed to assess the vertical change in the sediment distribution. The lower portions of the vertical cores consisted of the untouched initial seabed mixture, while the upper portions, which we call the modified layer, were the result of the sediment sorting under wave action. The thickness of the deposition layer in the white regions (under the wave antinode) is clearly visible in Figure 5-21(a). The thickness of the red coarse sand layer under the wave node is also well-defined in Figure 5-21(c). The core samples in the troughs between the wave nodes and antinodes consists primarily of the initial sand mixture (Figure 5-21(b)). Measurements of the modified layer thickness along the seabed are shown in Figure 5-22. On the bar crests, the variability in the layer thickness is on the order of the ripple height.

In the troughs, the layer thickness is negligible.

# Chapter 6

# Discussion and Conclusions

By assuming the slopes of the waves and seabed are comparably gentle, we have combined models for bedload and suspended sediment transport and wave-induced fluid flow to examine the dynamics of sand bar formation. For a coarse sand bed under nearly-monochromatic waves in water of constant depth, previous work (Yu & Mei [70] and Yu [68]) has shown that sand bar formation is a process of forced diffusion, with gravity-driven diffusion and forcing due to both the leading and second order fluid flow field. The research here has extended this theory to a sand bed of fine or coarse grains in water of variable finite mean depth, under perfectly tuned and narrow banded waves. We have also tested our model extensively over laboratory and field data.

Several important improvements have been made to the original theory of Yu & Mei [70]. First, the grain roughness Shields parameter is used to correctly predict $Q_B$, the net bedload discharge over a half cycle and also a multiplying factor in the diffusivity and bedload forcing in the sand bar equation. Using this parameter allows the prediction of the large sub-critical regions observed under wave antinodes when the reflection is strong. Also, under strong reflection, increases in the reflection coefficient lead to increases in the size of the sub-critical region, which in turn lead to a decrease in the total bar height.

A depth-linear eddy viscosity replaces Yu & Mei [70]'s constant eddy viscosity in the bedload transport calculation. Additionally, an order of magnitude estimate has been made of the bed stress induced by the inviscid return flow $U_2^{[0]}$, an artifact of wave propagation in a semi-infinite domain (i.e., with shoreline or wall boundaries). This new bed stress has no effect for high reflection, where $U_2^{[0]}$ is small, but for low reflection, the stress moves the

bar crests seaward of the wave nodes, changing the energy exchange between incident and reflected waves so that both wave height and bar height decrease shoreward. This decrease has been well documented in our laboratory experiments. Focusing on bars in an infinite region, Yu & Mei [70] did not include this stress, and predicted that the total wave and bar heights increase in the direction of wave propagation.

In addition to the effects of bedload considered before by Yu & Mei [70], it is found that suspended load provides a new forcing mechanism affecting sand bar geometry when the seabed is composed of fine sediments. Under weak reflection, as the grain diameter becomes finer, the bar heights increase and the bar crests shift seaward behind the wave node, although the bars grow and evolve more slowly. Under strong reflection, bar troughs occur under the wave node and bar crests form adjacent to sub-critical regions, in stark contrast to the corresponding bars of coarse grains.

We have conducted a survey of small scale laboratory sand bar experiments. For coarse grains, agreement between our theoretical predictions and the laboratory data was satisfactory to good, depending on the magnitude of the wave slope in the experiments. Better agreement was achieved with the experiments involving smaller wave slopes. Due to the large variability associated with fine grains, agreement was often more qualitative than quantitative between our predictions and laboratory experiments of fine-grained sand bars. However, the relatively good quantitative agreement between our predictions and the experiments of Dulou *et al.* [16] of bars of fine grains on a slope is very encouraging.

Due to lack of large scale laboratory data, we conducted our own set of lab experiments in a large wave flume to validate our theory and to study additional aspects of sand bar evolution. Tests involving monochromatic waves validated our theory, for low and high reflection. In particular, our theoretical predictions agreed remarkably with our sand bar tests under pure standing waves. Good agreement was also achieved between our predictions and sand bar tests under weak reflection by adjusting the coefficient of the return flow induced bed stress. Our sand bar tests with moderate and large second harmonic free wave components showed that higher free wave harmonics have a marked effect on sand bar geometry and growth rate. This suggests that sand bars generated by spectral waves could have new features compared with those under nearly monochromatic waves. Also, sediment sorting was demonstrated under standing waves when the seabed consisted of initially well mixed sand of two grain sizes. This led to an array of alternating red and white colored

sand bands along the seabed - a striking feature that begs future theoretical consideration.

We have also made preliminary predictions of bars on real beaches and have compared these to the observations of Dolan & Dean (1985) [15] and Elgar *et al.* (2003) [17]. The agreement is encouraging, despite having to guess some of the wave parameters. Some preliminary conclusions are that wave breaking is likely an important mechanism affecting bar evolution in shallow water. Also, the number of bars on beaches is determined more by the underlying mean beach topography than by Bragg Scattering. Beaches with longer shallow sections will have more sand bars.

To investigate bar formation under waves with frequencies spread over a finite spectrum, we have considered bar formation under narrow banded waves. Under strong shoreline reflection, bars that form under narrow banded waves have significantly smaller heights than those that form under monochromatic waves of similar wave energy flux. Under weak reflection, similar bar heights are predicted under narrow banded and monochromatic waves of similar wave energy flux, but the bar amplitude is modulated across the bar patch under narrow banded waves. For both levels of shoreline reflection, bar crest and trough positions differ significantly between bars generated by narrow banded and monochromatic waves, due to the differences in wave phase. Also, long spatial scale variations in the seabed elevation are noticeable under narrow banded waves, due to a slowly oscillating return flow.

There are several directions for future work. The boundary layer analysis carried out here does not treat the ripple elevation explicitly, as our seabed elevation $\zeta$ is assumed to be smooth. Correlations between the ripple-induced flow are not considered. The effect of ripples is added *a posteriori* when calculating the eddy viscosity and boundary layer thickness. However, based on experimental evidence, the ripple height is on the same order as the boundary layer thickness, in both the laboratory and the field. In this case, the effect of the ripples on the boundary layer flow should be more closely analyzed.

All eddy viscosity models considered in this work are time-invariant. This proved sufficient for making predictions of bar formation under monochromatic waves. However, preliminary work suggests that to understand bar formation under polychromatic waves, a time varying eddy viscosity should be considered. This would allow bar predictions under polychromatic waves in both intermediate and shallow depths.

To properly model bar formation on real beaches under ocean swell, the boundary layer flow and sediment transport must be found under spectral waves. An understanding of

seabed evolution under spectral waves may also allow predictions of the long time evolution of the mean beach topography.

An integral component of this work was the validation of our theory with experiments. Experimental comparisons are necessary, not just desirable, because of the plethora of empirical and practical assumptions on turbulent mixing, return flow stress, and sediment transport. Far more field measurements of simultaneous wave and bar evolution are needed to properly assess the current or any future sand bar model. Further laboratory experiments for fine grains would also be useful. In particular, experiments on the vertical exchange of sediment on a bed of multiple grain sizes is needed to complete a model for sediment sorting under waves.

# Bibliography


[1] M. Abramowitz and I. A. Stegun, editors. *Handbook of Mathematical Functions*. Dover, New York, 1972.

[2] B. Boczar-Karakiewicz, J. L. Bona, and D. L. Cohen. Interaction of shallow-water waves and bottom topography. *Dynamical problems in continuum physics*, 4:131–176, 1987.

[3] B. Boczar-Karakiewicz and R. G. D. Davidson-Arnott. Nearshore bar formation by non-linear wave processes - a comparison of model results and field data. *Marine Geology*, 4:287–304, 1987.

[4] B. Boczar-Karakiewicz, D. L. Forbes, and G. Drapeau. Nearshore bar development in southern gulf of st. laurence. *J. Waterway, Port, Coastal and Ocean Eng*, 121(1):49–60, 1995.

[5] B. Boczar-Karakiewicz and L. A. Jackson. The analysis and role of bars on the protection of a beach system. In *Proc. Int'l Conf. Coastal Eng.*, pages 2265–2278. Am. Soc. Civ. Eng., 1990.

[6] B. Boczar-Karakiewicz, B. Paplinska, and J. Winiecki. Formation of sand bars by surface waves in shallow water. laboratory experiments. *Polska Akademia Nauk, Inst. Budownictwa Wodnego Gdansk, Rozpr. Hydrotech*, 43:111–125, 1981.

[7] B. Boczar-Karakiewicz, W. Romanczyk, and J. L. Bona. Sand bar dynamics and offshore beach nourishment. In *Proc. Coastal Dynamics 97*, pages 873–882. Am. Soc. Civ. Eng., 1997.

[8] J. D. Carter. *Experiments on waves and currents over a movable bed*. M.s. thesis, Dept. of Civil Engineering, Mass. Inst. Tech., 2002.

[9] T. G. Carter, L.-F. P. Liu, and C. C. Mei. Mass transport by waves and offshore sand bedforms. *J. Waterways, Harbors, Coastal Eng. Div. ASCE*, 99:165–184, 1973.

[10] A. G. Davies. The reflection of wave energy by undulations on the seabed. *Dynamics of Atmospheres and Oceans*, 6:207–232, 1982.

[11] A. G. Davies. A model of oscillatory rough turbulent flow. *Est. Coast. Shelf Sci.*, 23(3):353–374, 1986.

[12] A. de Best, E. W. Bijker, and J. E. W. Wichers. Scouring of a sand bed in front of a vertical breakwater. In *Proc. Int'l Conf. on Port and Ocean Engineering Under Arctic Conditions, Vol. II*, pages 1077–1086. Technical University of Norway, 1971.

[13] P. Devillard, F. Dunlop, and B. Souillard. Localization of gravity waves on a channel with a random bottom. *J. Fluid Mech.*, 186:521–538, 1988.

[14] T. J. Dolan. *Wave Mechanisms for the Formation of Multiple Longshore Bars with Emphasis on the Chesapeake Bay.* M.c.e. thesis, University of Delaware, Newark, 1983.

[15] T. J. Dolan and R. G. Dean. Multiple longshore sand bars in the upper chesapeake bay. *Estuarine Coastal and Shelf Science*, 21:727–743, 1985.

[16] C. Dulou, M. Belzons, and V. Rey. Laboratory study of wave bottom interaction in the bar formation on an erodible sloping bed. *J. Geophys. Res.*, 105:19745–19762, 2000.

[17] S. Elgar, B. Raubenheimer, and T. H. C. Herbers. Bragg reflection of ocean waves from sandbars. *Geophys. Res. Lett.*, 30(1):1016, 2003.

[18] J. Fredsoe. On the development of dunes in erodible channels. *J. Fluid Mech.*, 64:1–16, 1974.

[19] W. D. Grant and O. S. Madsen. Combined wave and current interaction with a rough bottom. *J. Geophys. Res.*, 84(C4):1797–1808, 1979.

[20] W. D. Grant and O. S. Madsen. Movable bed roughness in unsteady oscillatory flow. *J. Geophys. Res.*, 87:469–481, 1982.

[21] W. D. Grant and O. S. Madsen. The continental shelf bottom boundary layer. *Ann. Rev. Fluid Mech.*, 18:265–305, 1986.

[22] T. Hara and C. C. Mei. Bragg scattering of surface waves by periodic bars: theory and experiment. *J. Fluid Mech.*, 178:221–241, 1987.

[23] A. D. Heathershaw. Seabed-wave resonance and sand bar growth. *Nature*, 296:343–345, 1982.

[24] J. B. Herbich, H. D. Murphy, and B. Van Weele. Scour of flat sand beaches due to wave action in front of sea walls. In *Int'l Conf. Coastal Eng., Santa Barbara Specialty Conference*, pages 705–726. Am. Soc. Civ. Eng., 1965.

[25] F. B. Hildebrand. *Advanced Calculus for Engineers*. Prentice-Hall, Englewood Cliffs, N. J., 1964.

[26] M. Homma, K. Horikawa, and R. A. Kajima. Study on suspended sediment due to wave action. *Coastal Engineering in Japan*, 8:85–103, 1965.

[27] Z. Huang and C. C. Mei. Effects of surface waves on a turbulent current over a smooth or rough seabed. *J. Fluid Mech.*, 497:253–287, 2003.

[28] C.-D. Jan and M.-C. Lin. Bed forms generated on sandy bottom by oblique standing waves. *J. Waterway, Port, Coastal, and Ocean Eng.*, 124:295–302, 1998.

[29] I. G. Jonsson. Wave boundary layers and friction factors. In *Int'l Conf. Coastal Eng.*, pages 127–148. Am. Soc. Civ. Eng., 1966.

[30] K. Kajiura. A model of the bottom boundary layer in water waves. *Bull. Earthquake Res. Inst.*, 46:75–123, 1968.

[31] J. Kamphuis. Friction factors under oscillatory waves. *Proc. ASCE J. Waterway, Harbors, Coastal Engng. Div.*, 101:135–144, 1975.

[32] D. B. King. The effect of beach slope on oscillatory flow bedload transport. In *Coastal Sediments '91*, pages 734–744. Am. Soc. Civ. Eng., 1991.

[33] B. J. Landry. *Bathymetric evolution of sand bed forms under partially standing waves*. M.s. thesis, Dept. of Civil Engineering, Mass. Inst. Tech., 2004.

[34] J. W. Lavelle and H. O. Mofjeld. Effects of time-varying eddy viscosity on oscillatory turbulent channel flow. *J. Geophys. Res.*, 88(C12):7607–7616, 1983.

[35] G.-H. Lee, W. B. Dade, C. T. Friedrichs, and C. E. Vincent. Examination of reference concentration under waves and currents on the inner shelf. *J. Geophys. Res.*, 109(C2):2021, 2004. doi:10.1029/2002JC001707.

[36] O. S. Madsen. On the generation of long waves. *J. Geophys. Res.*, 76:8672–8683, 1971.

[37] O. S. Madsen. Mechanics of cohesionless sediment transport in coastal waters. In *Coastal Sediments '91*, pages 15–27. Am. Soc. Civ. Eng., 1991.

[38] O. S. Madsen. Spectral wave-current bottom boundary layer flows. In *Int'l Conf. Coastal Eng.*, pages 384–398. Am. Soc. Civ. Eng., 1994.

[39] O. S. Madsen. Sediment transport on the shelf. 1.67 Sediment Transport course notes, Dept. of Civil & Environmental Engineering, M.I.T., 1999.

[40] O. S. Madsen and P. Salles. Eddy viscosity models for wave boundary layers. In *Int'l Conf. Coastal Eng.*, pages 2615–2627. Am. Soc. Civ. Eng., 1998.

[41] P. P. Mathisen. *Bottom roughness for wave and current boundary layer flows over a rippled bed*. Ph.d. thesis, Dept. of Civil Engineering, Mass. Inst. Tech., 1993.

[42] C. C. Mei. Resonant reflection of surface water waves by periodic sandbars. *J. Fluid Mech*, 152:315–335, 1985.

[43] C. C. Mei and C. Chian. Dispersion of small suspended particles in a wave boundary layer. *J. Phys. Oceanography*, 24:2479–2495, 1994.

[44] C. C. Mei and Ü Ünlüata. Harmonic generation in shallow water waves. In R. E. Meyer, editor, *Waves on Beaches*, pages 181–202. Academic Press, New York, 1972.

[45] Chiang C. Mei. *The Applied Dynamics of Ocean Surface Waves*. World Scientific, Singapore, 1994.

[46] M. Naciri and C. C. Mei. Bragg scattering of water waves by a doubly periodic seabed. *J. Fluid Mech.*, 192:51–74, 1988.

[47] T. Nakato, F. A. Locher, J. R. Glover, and J. F. Kennedy. Wave entrainment of sediment from rippled beds. *J. Waterway, Port, Coastal and Ocean Division, ASCE*, 103(WW1):83–99, 1977. See Errata, ASCE, no. WW1, Feb 1978, pp. 96.

[48] P. Nielsen. Dynamics and geometry of wave generated ripples. *J. Geophys. Res.*, 86:6467–6472, 1981.

[49] P. Nielsen. Suspended sediment concentration under waves. *Coastal Eng.*, 10:23–31, 1986.

[50] P. Nielsen. *Coastal Bottom Boundary Layers and Sediment Transport*. World Scientific, Singapore, 1992.

[51] U.S. Army Corps of Engineers. *Coastal Engineering Manual*. US Army Corps of Engineers, Washington, D.C., 2002.

[52] T. J. O'Hare and A. G. Davies. Sand bar evolution beneath partially-standing waves: laboratory experiments and model simulations. *Continental Shelf Research*, 13:1149–1181, 1993.

[53] J. M. Restrepo and J. L. Bona. Three-dimensional model for the formation of longshore sand structures on the continental shelf. *Nonlinearity*, 8:781–820, 1995.

[54] J. S. Ribberink and A. A. Al-Salem. Sediment transport in oscillatory boundary layers in cases of rippled beds and sheet flow. *J. Geophys. Res.*, 99:12707–12727, 1994.

[55] M. M. Rosengaus. *Experimental study on wave generated bedforms and resulting wave attenuation*. Sc.d. thesis, Dept. of Civil Engineering, Mass. Inst. Tech., 1987.

[56] R. C. Seaman and T. O'Donoghue. Beach response in front of wave-reflecting structures. In *Int'l Conf. Coastal Eng.*, pages 2284–2297. Am. Soc. Civ. Eng., 1996.

[57] J. F. A. Sleath. Measurements of bed load in oscillatory flow. *J. Waterway Port Coastal Ocean Engng. Div., ASCE*, 104(WW4):291–307, 1978.

[58] J. F. A. Sleath. The suspension of sand by waves. *J. Hydraulic Res.*, 20(5):439–452, 1982.

[59] J. F. A. Sleath. Seabed boundary layers. In B. Le Méhauté and D. M. Hanes, editors, *The Sea*, volume 9, pages 693–727, 1990.

[60] J. D. Smith and S. R. McLean. Spatially averaged flow over a wavy surface. *J. Geophys. Res.*, 82:1735–1746, 1977.

[61] C. Staub, I. G. Jonsson, and I. A. Svendsen. Sediment suspension in oscillatory flow : measurements of instantaneous concentration at high shear. *Coastal Eng.*, 27:67–96, 1996.

[62] J. Trowbridge and O. S. Madsen. Turbulent wave boundary layers 1. model formulation and first-order solution. *J. Geophys. Res.*, 89:7989–7997, 1984.

[63] J. Trowbridge and O. S. Madsen. Turbulent wave boundary layers 2. second-order theory and mass transport. *J. Geophys. Res.*, 89:7999–8007, 1984.

[64] C. E. Vincent and M. O. Green. Field measurements of the suspended sand concentration profiles and fluxes and of the resuspension coefficient over a ripple bed. *J. Geophys. Res.*, 95(C7):11591–11601, 1990.

[65] P. N. Wikramanayake and O. S. Madsen. Calculation of movable bed friction factors. Technical Progress Report 2, Dredging Research Program, U. S. Army Corps of Engineers, Coastal Engineering Research Center, Vicksburg, Mississippi, 1990.

[66] P. N. Wikramanayake and O. S. Madsen. Calculation of suspended sediment transport by combined wave-current flows. Final report, Dredging Research Program, U. S. Army Corps of Engineers, Coastal Engineering Research Center, Vicksburg, Mississippi, 1994.

[67] S.-L. Xie. Scouring patterns in front of vertical breakwaters and their influences on the stability of the foundations of the breakwaters. Technical report, Coastal Engineering Group, Dept. of Civil Engineering, Delft University of Technology, Delft, The Netherlands, 1981.

[68] J. Yu. *Generation of sand ripples and sand bars by surface waves.* Ph.d. thesis, Dept. of Civil & Environmental Engineering, Mass. Inst. Tech., 1999.

[69] J. Yu and C. C. Mei. Do longshore bars protect the shore? *J. Fluid Mech.*, 404:251–268, 2000.

[70] J. Yu and C. C. Mei. Formation of sand bars under surface waves. *J. Fluid Mech.*, 416:315–348, 2000.